Proceedings of the 5th ISSE National Conference (INAC-05) on Systems Approach for Self-Reliance in Advanced Technologies (SASAT-2023)

24 – 25 March, 2023

Editors

Dr. M. Manickavasagam, DRDO
Prof Sriram Venkatesh, UCE, OU
Dr J.V. Satyanarayana, DRDO
Prof L Siva Rama Krishna, UCE, OU
Dr G.Naresh Kumar, DRDO
Prof P. Prem Kiran, UOH
Mr. O. R. Ashwin Chander, DRDO

Organized by

INDIAN SOCIETY OF SYSTEMS FOR SCIENCE AND ENGINEERING (ISSE)
HYDERABAD CHAPTER

In Association with

BS Publications
An imprint of **BSP Books Pvt. Ltd.**

© ISSE 2023

No part of the Proceedings protected by this copyright notice may be reproduced or utilized in any form or by means of electronics or mechanical including photocopying, recording or by any information storage and retrieval system, without the prior permission from the copyright owners.

Disclaimer

The Publisher and Organisers do not claim any responsibility for the accuracy of the data, statements made, and opinions expressed by authors. The authors are solely responsible for the contents published in the paper.

Published by

BSP BS Publications

An imprint of **BSP Books Pvt. Ltd.**
4-4-309/316, Giriraj Lane, Sultan Bazar,
Hyderabad - 500 095
Phone: 040 - 23445688
e-mail: info@bspbooks.net
www.bspbooks.net

ISBN: 978-93-95038-50-8 (Paperback)

SASAT-2023 – COMMITEES

CHIEF PATRONS

Dr. G. Satheesh Reddy, SA to RM

Dr. S. Somnath, Chairman, ISRO

Dr. Samir V. Kamat, Chairman DRDO

Sr. Prof. D. Ravinder, Vice Chancellor, OU

National Advisory Committee (NAC)

- **Dr. V. Narayanan, Director, LPSC, ISRO and National President, ISSE**
- **Dr. BHVS Narayanamurthy, Chairman, DG(MSS), DRDO and National Vice-President, ISSE and Chairman NAC (SASAT-2023)**
- **Sr. Prof. P. Laxminarayana, Registrar, OU**
- **Sr. Prof. Sriram Venkatesh, Principal, UCE, OU, and Vice-President, ISSE, Hyderabad Local Chapter, Co-Chairman NAC & Vice-President, Hyd. Chapter, ISSE.**
- **Sr. Prof. M. Kumar, Dean, Faculty of Engineering, OU**
- Dr. M. Rama Manohara Babu, Director, ASL, DRDO
- Mr. U. Raja Babu, Director, RCI, DRDO
- Mr. GA Srinivasa Murthy, Director, DRDL, DRDO
- Mr. Rajaraman, GM, BDL, Hyderabad
- Mr. Nilesh M. Desai, Director SAC, Ahmedabad, ISRO
- Dr. P. V. Radhadevi, Director, ADRIN,, Hyderabad
- Dr. S. Unnikrishnan Nair, Director, VSSC, Trivandrum
- Mr. A. Rajarajan, Director, SHAR, ISRO, Sriharikota
- Dr. Prakash Chauhan, Director, NRSC, Hyderabad
- Mr. M.Sankaran, Director, URSC, Bengaluru.
- Mr. Prateek Kishore,Director, TBRL, DRDO
- Mr. BV. Papa Rao, Director, CAS, Hyd.
- Mr. N. Srinivas Rao, Director, DLRL, DRDO
- Dr. Jagannath Nayak, Director, CHESS, DRDO
- Dr. PSRS Sastry, Director, DSP, DRDO
- Mr. Hare Krishna Ratha, Director, ITR, DRDO
- **Dr. M. Manickavasagam, Convener, Director, SPIC, DRDO and President, Hyderabad Chapter, ISSE.**

Local Organizing Committee

- **Dr. M Manickavasagam, Chairman, LOC (SASAT-2023) , and Director, SPIC, DRDO and President, Hyderabad Chapter, ISSE**
- **Prof. L. Siva Rama Krishna,Co-Chairman LOC (SASAT-2023) & Professor, MED, UCE, OU, Hyd.**
- Mr. PV Rajaram, GM, SAM BDL, Hyd.
- Mr. R. Venkatram Reddy, Sc. 'G' RCI
- **Dr. G. Naresh Kumar, Sc. 'F' DRDL, & Joint-Secretary, ISSE Hyderabad Chapter**
- Dr. Prem Kiran Paturi, School of Physics, University of Hyderabad
- **Mr. Pradeep Kumar Agrawal, Sc. 'F', DSP, DRDO & Treasurer, ISSE Hyderabad Chapter.**
- Mr. J. Narendran, Sc. 'F', NRSC, ISRO, Hyderabad
- Mr. Sriram Sista, Sc. 'F', DLRL, DRDO
- Mr. K. Vamshi Krishna Reddy, Sc. 'F', RCI, Hyderabad
- Mr Ashwin Chandar, Sc. 'F', ASL, Hyd.
- Mr. Garapati Ramu, Sc. 'E', DSP, Hyd.
- Prof G. Mallesham, Dean, Development & UGC, OU, Hyd.
- Prof. P. Chandrasekhar, Vice-Principal, UCE, OU
- Prof. P. Raja Sekhar, HoD, Dept. of Civil Engineering, UCE, OU
- Prof. M. Chandra Sekhar Reddy, HoD, Dept. of Mechanical Engineering, UCE, OU
- Prof. G. Yesuratnam, HoD, Dept. of Electrical Engineering, UCE, OU
- Prof. L. Nirmala Devi, HoD, Dept. of Electronics and Communication Engineering, UCE, OU
- Dr. D. Suman, HoD, Dept. of Biomedical Engineering, UCE, OU
- Prof. K. Shyamala, HoD, Dept. of Computer Science Engineering, UCE, OU
- **Dr. J. V. Satyanaarayana, Sc. 'G', RCI, Secretary, ISSE,Hyderabad LOC & Convener SASAT-2023**

SASAT-2023 – Technical Paper Review Team

1. OSMANIA UNIVERSITY

1. Prof. Sriram Venkatesh, Mech. Eng. Dept. UCE, OU
2. Prof. M Chandrashekhar Reddy, Mech. Eng. Dept. UCE, OU
3. Prof. A Krishanaiah, Mech. Eng. Dept. UCE, OU
4. Prof. Narsimhulu Sanke, Mech. Engineering Department
5. Prof. L Siva Rama Krishna, Mech. Eng. Dept. UCE, OU
6. Prof. G Narender, Mech. Eng. Dept. UCE, OU
7. Prof. V. Uma Maheshwar, Mech. Eng. Dept. UCE, OU
8. Prof. P. Chandrashekhar, ECE Dept. UCE, OU
9. Prof. D Rama Krishna, ECE Dept. UCE, OU
10. Prof. P Naveen Kumar, ECE Dept. UCE, OU
11. Prof. PV Sudha, CSE Dept. UCE, OU
12. Dr. MA Hameed, CSE Dept. UCE, OU

2. University of Hyderabad

1. Prof. P Prem Kiran, School of Physics, UOH
2. Dr. VS Ashok, School of Physics
3. Dr. Sree Harsha, ACRHEM

3. DEFENCE RESEARCH & DEVELOPMENT ORGANISATION (DRDO)

1. Dr. M. Manickavasagam, Sc. ‘H’, Director, SPIC
2. Dr. J. V. Satyanaarayana, Sc. ‘G’, RCI
3. Dr. G. Naresh Kumar, Sc. ‘F’, DRDL
4. Dr. M. Sree Ramana, Sc. ‘F’, DLS
5. Mr. O. R. Ashwin Chandar, Sc. 'F', ASL, Hyd.
6. Mr. Sriram Sista, Sc. 'F', DLRL, Hyd.

PREFACE

This proceeding records the papers selected for presentation at the 5th Indian Society of Systems for Science and Engineering (ISSE) National Conference (INAC – 05) on Systems Approach for Self- Reliance in Advanced Technologies (SASAT 2023) held in University College of Engineering, Osmania University, Hyderabad. This event is organized by ISSE Hyderabad Local Chapter in association with ISRO, DRDO and University College of Engineering, Osmania University. Hyderabad is a cosmopolitan city with a deep-rooted rich and legendary past. It is one of the fastest growing metropolitan cities in India in the areas of information technology, biotechnology, pharmaceutical and having prestigious Defense and Space organizations like DRDO and NRSC.

The main objective is to encourage networking among the participants working in the areas of Defense and Space related activities through contributed paper presentations, keynotes/invited talks, panel discussions and exhibitions of components, hardware, and Systems. The conference covers wide range of topics like AI & ML in system Engineering, Anti-Drone Systems, Big Data Analytics & Cloud Computing, Bio-Medical and Health Care Systems, Cyber-Physical Systems & IOT: Engineering Issues, Cognitive Science in Engineering, Control, Guidance and Estimation Theory, Decision Making & Intelligent systems, Energy systems, Smart Grid Technology, Environmental Systems, EO based Systems, EW Systems: Engineering, Testing & Evaluation, Ocean science and Engineering systems, Robotic systems, Intelligent Autonomous Vehicles, (UAVs, ROVs, Drones), Robust & Fault Tolerance Systems, Additive and Digital Manufacturing, Multi-Disciplinary System Design & Optimization, System Eng. for Human Space Transportation, System Simulation, Modelling & Analysis and Transportation Systems.

The response to the conference is overwhelming as we have received more than 75 papers from premier research organizations, academia and industries. All the papers were peer reviewed by experts drawn from academia, research and industry. The technical committee after peer review selected 55 papers for presentation and publication in the proceedings of the conference. Key note address, plenary talks, Invited lectures, Sponsor Presentations, Exhibition of latest technologies in Space and defence are scheduled at the conference by the experts in the area of Systems Engineering. We are grateful to many organizations for their support to the conference through sponsorships. We are also indebted to all the speakers and authors from different parts of the country. We sincerely thank members of the advisory committee, organizing committee and other functional subcommittees and student volunteers for their active involvement in the conduct of the conference.

We hope that the deliberations in the conference will promote fruitful interactions among the participants thus benefiting in understanding the latest cutting edge technologies in the field of Systems Engineering and provide valuable information to all concerned in general. The proceedings will serve as a reference volume for practicing engineers, researchers and academicians in the area.

Dr. M. Manickavasagam
Prof. Sriram Venkatesh
Dr. J.V. Satyanarayana
Prof. L. Siva Rama Krishna
Dr. G. Naresh Kumar
Prof. P. Prem Kiran

CONTENTS

Preface (v)

Session Code/Paper ID	Title	Page No.
	System Engineering Concepts	
3A-1 INAC-05_19_16	Systems Engineering Role and Importance in Weapon Development *G. Naresh Kumar*	1
3A-2 INAC-05_17_1	System Engineering Challenges in Development of LOX-Isrosene Booster Stage for Future Launch Vehicle of ISRO *B Suresh Babu, Reji Joseph, and S Jagannathan*	12
3A-3 INAC-05_19_7	Design and Mathematical Modeling of Fuel Feed System for Dual Fuel Scramjet *Kesava Vishnu G, Vishnu Suresh Nair, Anoop V M, Arun G S, and Kuldeep Singh Naruka*	20
3A-4 INAC-05_19_6	Monte Carlo Based Tolerance Analysis of Sub-systems in Cryogenic Umbilicals *Jishnu T R, Vaibhav Amalak Ahire, Hemendra Kumar Dhurandher, Dilip V, Sathis Kumar B, and Alex A*	28
	System Engineering for Rocket Applications	
3B-1 INAC-05_17_11	Novel Design of a Joint with Translational Freedom for Propellant Tank Anti-Slosh Baffle System *Deepak K, Jayesh P, Ravi Ranjan Kumar and Reji Joseph*	36
3B-2 INAC-05_19_14	Modelling and Dimensional Analysis of Spring-Loaded Pressure Regulator for Performance Prediction and Characterization *Rishabh Garg, Kailas S. Kuhite, Sunil S., D. Venkittaraman, and Alex A.*	47
3B-3 INAC-05_19_9	Numerical Study of the Liquid Oxygen Draining in a Spinning Tank with Baffles for Hybrid-Propulsion Rocket *Anant Singhal, Deepak K. Agarwal, T. John Tharakan, and S. Sunil Kumar*	56
3B-4 INAC-05_19_10	Numerical Study on De-Icing of Aeroplane Wing Using Piezoelectric Materials *K. Guru Brahmam, M. Chandra Sekhar Reddy, and T Ramamohan Rao*	62
	Aerodynamics, Control, Guidance and Estimation	
4A-1 INAC-05_7_1	Terminal Phase Guidance Design for an Anti-Ship Bank-To-Turn (BTT) Cruise Missile *N. Akilandeswari, Mallikarjun. Bangi, K.K. Mangrulkar, and G. Naresh Kumar*	73

4A-2 INAC-05_19_8	Aerodynamic Parameter Estimation of RLV from Telemeter Sensor Output *Ashwin Chandar O.R., A.K. Sarkar and R. Mukesh*	83
4A-3 INAC-05_19_12	Terrain Referenced Navigation Technique Using Correlation Algorithms for Cruise Vehicle *Suresh Mamidipalli, Mallikarjun Bangi and G. Naresh Kumar*	98
4A-4 INAC-05_19_17	Impact of Deblurring on Image Matching Algorithms *Vaddi Chandra Sekhar, Boda Nehru, D Penchalaiah, Akula Naresh, G Naresh Kumar and Abhijit Bhattacharyya*	108
4A-5 INAC-05_16_2	Computational Analysis of Horizontal Axis Wind Turbine Blade NACA 63(4)221 *Uma Maheshwar Vanamala, and Purna Visishta Battu*	116
4A-6 INAC-05_19_19	Self-reliance in Salvo Launch of an Article *Ashish Kumar Gupta*	135
System Engineering in Design of Rocket Sub-Systems		
4B-1 INAC-05_17_2	Experimental Investigation on the Interaction of Supersonic Plume with Launch Pad Structure *B.N.V Sai Aditya, M. Deepthi, G. Venkatesh, T. Srinivas Reddy and S. Sankaran*	140
4B-2 INAC-05_17_6	Characterization of a Pressurized Convoluted Metallic Flexible Hose under Large Bending Angles for Systems Engineering of High Pressure Swiveling Thruster *B. Kartik Surendra, Sourabh Karmarkar, B Suresh Babu, Reji Joseph and Jagannathan S*	147
4B-3 INAC-05_17_7	Development of Shock Test Fixture for a Heavy Rocket Valve *Renjith James, Surya Mani Tripathi, B. Sathis Kumar and A. Alex*	156
4B-4 INAC-05_17_18	Design and Development of Sealing Mechanism for Gaseous Medium Cryogenic Safety Valve for ISRO Launch Vehicle Application *Arun Baby, Gaurav Sharma, Sunil S., D Venkittaraman and A Alex*	165
4B-5 INAC-05_17_16	Multifractal Detrended Fluctuation Analysis for Onset of Combustion Instability in Liquid Rocket Engines *Varghese Mathew Thannickal, T. John Tharakan, and S. R. Chakravarthy*	175
4B-6 INAC-05_17_10	Reflection and Review of Fuel Delivery Systems *Sadan Kanchanapalli and Ramanathan Subramanian*	183
Systems Engineering for Space Missions		
4C-1 INAC-05_18_1	Realization of Integrated Data Acquisition for Testing of Human Rated GAGANYAAN Vikas Engine *Priya Esther, Vineeth Marella, Ethamukkala Bala Krishna, Vinoth B, Gilbert Chandra and Murugananda Bhaskaran*	195

4C-2 INAC-05_19_15	Roll Damping Analysis of Crew Escape Vehicle with Grid Fins at Subsonic and Transonic Mach Numbers *M Jathaveda, Kunal Garg, P Balasubramanian, Harish A and G Vidya*	209
4C-3 INAC-05_7_3	Synthetic Aperture Radar Data Quality Characterization and Calibration Analysis of EOS-04 *S. Sri Sudha, S. Jaya Bharathi, S. Hari Priya and B. Santhisree*	218
4C-4 INAC-05_7_2	Emitter Geolocation from Near-Space Platform Using 3D TDOA *Suman Agrawal*	227
4C-5 INAC-05_5_1	Performance Observation of IRNSS in Terms of Receiver Geometry and Position Accuracy Over Hyderabad Region *R. Anil Kumar and P. Naveen Kumar*	235
AI, ML & Fault Tolerance		
5A-1 INAC-05_15_2	Fault Management of Guidance and Control System for Aerospace Vehicles *M. Reshma Gopal, O. R. Ashwin Chandar and P. Koti Lakshmi*	242
5A-2 INAC-05_17_14	Immunotronics Inspired Novel Self Repairing Finite State Machine for RISC-V based Processor *Deepanjali.S, Noor Mahammad, Balasubramanian. P and G Venkat Reddy*	251
5A-3 INAC-05_1_1	Electro Cardiogram (ECG) Monitoring using Internet of Things and Predict Future in Advance using Artificial Intelligence *G. Sasikala, and G. Satya Krishna*	258
5A-4 INAC-05_1_4	Real Time Face Recognition System using Jetson Nano *Vaddi Chandra Sekhar, D Penchalaiah, G Naresh Kumar, and Abhijit Bhattacharyya*	267
5A-5 INAC-05_19_13	SAR Image based Target Detection & Identification using Deep Learning Model YOLOv7 *B Nehru, Vaddi Chandra Sekhar, A Naresh, D Penchalaiah, and Abhijit Bhattacharya*	273
5A-6 INAC-05_1_7	Adversarial Machine Learning Problems: Threats and Attacks *Revathi Lavanya Baggam, V. Valli Kumari, and Gowri Shankar Wuriti*	279
AI, ML for System Design & Applications		
5B-1 INAC-05_12_1	Artificial Intelligence based Electronic Warfare Systems: A Review *Kiran Garje*	289
5B-2 INAC-05_3_1	Efficient Biometric Service Protocol for Cloud Services *Swathi Gowroju, S. Sai Satyanarayana Reddy, V. Swathi, R. Srinija, and P. Rishika, K Naveen Reddy*	297

5B-3 INAC-05_1_3	Transfer-learning Enhanced Physics Informed- Neural-Networks for Burgers' Equation with High Reynolds' Number *Nishant Kumar, Manish Kr. Tiwari, P.S Gurugubelli, Anil Kumar, and M. Raghavendra Rao*	309
5B-4 INAC-05_1_8	Driver Drowsiness Monitoring System using Visual Behaviour and Machine Learning *Ambika Sahitya Batchu, Madhuvani Patnam, and Goutham Karnati*	319
5B-5 INAC-05_3_1	Design and Implementation of Private Cloud Infrastructure based on OpenStack for Strategic Organizations *M. Swapna, and Devanahalli Sunil Archana*	327
5B-6 INAC-05_17_8	Design of High Speed Drive System for Rocket Subsystem Tests *Deepak Dinesh, Arun Kumar S, Remya KP, Harikumar K, Unnikrishnan Nair P, N. Jayan, and Jose Paul*	336
System Synthesis & Analysis		
5C-1 INAC-05_19_3	High Resolution Spectral Analysis of Pressure Oscillations in Large Segmented Solid Rocket Motors *Kali Prasad KVASN, Sankaran S and Anuj Nigam*	345
5C-2 INAC-05_17_3	Predicting the Shear Properties in S-glass Epoxy Composite by Finite Element Analysis *Pullela Ramalakshmi, Kongari Akshaya, and Pinninti Ravinder Reddy*	355
5C-3 INAC-05_19_4	Visualization of Spokes Mode in a Hall Effect Thruster *Souradeep Roy Choudhury, Samvram Sahu, Vara Prasad Kella, and Vikash Kumar*	362
5C-4 INAC-05_17_4	Experimental Study of Magnetic Field Effects on SPT Performance *Vara Prasad K, Umesh R Kadhane, M Rafi, Anish A and Anooja S*	370
5C-5 INAC-05_17_17	Studies to Investigate the Effect of Feed Line Orientation on Chill-Down Performance of Cryogenic Feed Lines *Venkatesh N, Anant Singhal, Deepak Kumar Agarwal, A Salih and S Sunil Kumar*	378
5C-6 INAC-05_16_1	Cold Flow Characterization of Triplet Injector Head Realized Through Additive Manufacturing *Vikash Kumar, Rafeeque T.A, Madhukumar T, and John Tharakan T*	387
Systems Engineering in Mechanical Systems		
6A-1 INAC-05_17_1	Study on Effect of Vibration Loading of Beam Specimens on its Dynamic Characteristics	395

	C Raja Kumaran, V. Srinivasulu, V. Venkata Ramakrishna, T. Srinivas Reddy, and S. Sankaran	
6A-2 INAC-05_19_5	Optimization of a Stiffened Interstage Structure of a Launch Vehicle using Differential Evolution Algorithm in Indigenous FE Software *Manash Kumar Bhadra, Shachindra Nath Sharma, Partha Ajit Surve, and Vinod G*	405
6A-3 INAC-05_17_9	Multi Optimization of Friction Stir Welding of Aluminium AA 6061 Alloy using Grey based Taguchi Method *Pranav Ravindrannair, K Kishore, P Laxminarayana, U Ashok Kumar, and F Hayat Khan*	413
6A-4 INAC-05_19_11	Design & Development of Four-Wheel Steering Mechanism for Minimum Turning Radius: A Case Study of CM Transportation Trolley *V Venkateswarlu, and Jaiteerth R Joshi*	420
6A-5 INAC-05_17_5	Optimization of Process Parameters in Pulsed Current GTA Welding Process on ASTM 106 Grade-B Steel Pipes using Linear Regression *G Prakasham, L Siva Rama Krishna, and J Kandasamy*	433
6A-6 INAC-05_19_1	Fire Safety Assessment Studies in High Rise Assembly Buildings using Fire Dynamic Simulator *Sanka SVD Sairam, V Vinodh, and T Subbananthan*	441
Systems Engineering in Electrical Systems		
6B-1 INAC-05_13_1	The Radar Cross Section of Marine Vessels *G. Sunil Sriharsha, P.C. Bhuvana, N. Harini, Mallikarjun. Bangi, M. Jyoti, and G. Naresh Kumar*	448
6B-2 INAC-05_7_3	Radar Cross Section Modelling using Swerling Probability Density Function for Target Signal Strength Estimation *Raveen Kumar K, Sabina Esther K, MMV Dhanumjaya Rao, and G Grahadurai*	456
6B-3 INAC-05_19_2	Simulation of DSTATCOM for Distribution Generation based System with Various Algorithms *K. Bhavya, P.V.V.Rama Rao, and L.Ravi Srinivas*	464
6B-4 INAC-05_19_18	Optimal Placement and Sizing of DSTATCOM in Radial Distribution System Using Gravitational Search Algorithm *U. Chandra Rao, Rama Rao PVV and N Sumathi*	471
6B-5 INAC-05_17_15	Multi Objective Optimization of Process Parameters of Electro Discharge Machining on Nimonic 80A Using Grey Relational Analysis *K.L.Uday Kiran, K.Saraswathamma, and M.Rajesh*	487
6B-6 INAC-05_19_20	Mitigation of Voltage Sag and Swell in Smart Grid by using ANT-LION Intelligent Controller *D. Chandra Sekhar, P.V. V Rama Rao and R. Kiranmayi*	503

Systems Engineering Role and Importance in Weapon Development

G. Naresh Kumar*

Scientist, Directorate of Systems,
Defense Research Development Laboratories (DRDL), Kanchanbagh, Hyderabad, Telangana, India
Email: gaddam.nareshkumar@gmail.com

ABSTRACT

Defence industry is involved in numerous weapon development programs to meet the requirement armed forces. Aerospace platforms, underwater systems and other major systems often comprise a large number of interacting subsystems that have to collectively satisfy a set of specified goals. Moreover, these requirements often evolve throughout the development cycle and improvements during the life of the system. Additionally, these may be contradicting requirements. Systems Engineering (SE) provides designers the capability to manage complex relationships within a subsystem design and across the rest of the subsystems. Systems engineering ensures that, the primary system complies with the most challenging requirements from concept development through production and then the extended service life.

The purpose of this article is to share my experience in Systems engineering during the design and development phase of weapon systems. The concept of connectivity diagram is used here.

Keywords: *Systems Engineering (SE), Systems Analysis (SA), System of System (SoS)*

1. INTRODUCTION

Defense Research Development Laboratories (DRDL) is involved in design and development of weapons for armed forces. These weapons are in general, highly complex and involve multidisciplinary systems to meet the mission objectives. Mission of DRDL is stated as:

- Develop the state-of-the-art infrastructure and technologies for different classes of missile. Transfer the technology to production agency for guided missile products.

System is defined as an integrated set of elements, subsystems, and assemblies that accomplish a defined objective. These elements include products (hardware, software, and firmware), processes, people, information, techniques, facilities, services, and other support element. The main characteristics of systems are interaction of the different elements in it. In general, a system is the product of several disciplines makes it interdisciplinary characteristics.

Highly sophisticated weapons are outcome of System of System (SoS). The general understanding of the SoS is it is a large-scale interdisciplinary system involving multiple, heterogeneous, distributed elements. Design and development of large-scale complex system becomes the union of several systems as indicated in Fig. 1. Realization of such systems is a tough task as extremely tight feasible design space is available. Following challenges which influence the development of systems of systems:

- System elements may operate independently.
- System elements have different life cycles.
- The initial requirements are likely to be ambiguous in some cases where user itself not able to define what he/she want.
- Complexity is a major issue for initial modelling, visualization and prototyping.

*Corresponding author: E-mail: gaddam.nareshkumar@gmail.com

ISBN - 978-93-95038-50-8 https://doi.org/10.37285/bsp.sasat2023.01

- Management can overshadow engineering as the budget constraints, schedules, interfaces, and technology upgrades further complicate the development of SoS.
- Fuzzy boundaries cause confusion while specification generation.
- System of Systems engineering is never finishing, continuos improvements and changes may be needed. Project management must continue to account for changes in the various system element life cycles.

Systematic approach required to design and develop such complex and large-scale products. A unique design environment to address the above issues is "Systems Engineering"

2. OVERVIEW OF SYSTEMS ENGINEERING

There is no commonly accepted definition/approach for systems engineering, often confused with "System Analysis", "System Science", "Operations Research" or other.

A suitable definition which reflects the nature and type of work carried out by DRDL, DRDO is given in military standard MIL-STD-499A [3]:

System engineering is the application of scientific and engineering efforts to:

1. *Transform an operational need into a description of system performance parameters and a system configuration through the use of an iterative process of definition, synthesis, analysis, design, test and evaluation;*
2. *Integrate related technical parameters and ensure compatibility of all physical, functional and program interfaces in a manner that optimizes the total system definition and design;*
3. *Integrate reliability, maintainability, safety, survivability, human engineering, and other factors into the total engineering effort to meet cost, schedule, supportability and technical performance objective.*

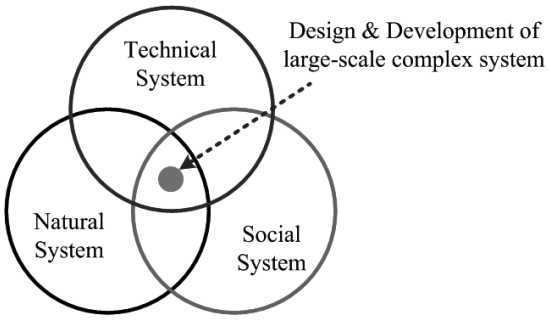

Figure 1: SoS - An extremely tight feasible design space

The above definition and terminology of systems engineering may look very complex but it is a very useful tool to accomplish the objective. An alternative and simple definition of SE in my view is "*Systems engineering is a logical approach taken by multidisciplinary team/teams to engineer and integrate a system to ensure that the product meets customers need*".

Equipped with this definition of a systems engineering, one can expand on the systems engineering methodology in the following steps:

1. Definition of the objectives or goals of the system
2. Elaboration of the interdependencies between the processes of the system
3. Clarification of the roles of the constituent system elements necessary to achieve objectives (thereby reducing cross-functional barriers)
4. Definition of the system's capabilities
5. Establishment of performance expectations prior to operational employment

ISBN - 978-93-95038-50-8

6. Measurement and evaluation of performance to continually improve the system through measurement and evaluation

From the above requirements it is clear that, systems engineering is a unique discipline that concentrates on the design and development of the whole system as distinct from the parts. It involves looking at a problem in its entirety, taking into account all the facets and all the variables and relating the social to the technical aspect. Systems engineering is an iterative process of top-down synthesis, analysis, development, and operation of a real-world system that satisfies, in a near optimal manner, the full range of requirements for the system [2]. It is a tightly coupled interdisciplinary approach and meant to enable the realization of successful systems. It focuses on defining customer needs and required functionality at initial stage of the development cycle, documenting the requirements and qualitative requirements, and then only proceeding with design synthesis, analysis and system validation while considering the complete problem. In addition to design and development SE also considers the cost and schedule for product development, training needs and future product/spares support, and safe disposal of life out products.

Waterfall Process Model (WPM) is the first SE model was introduced by Royce in 1970 for software development activity [4].

The waterfall model is a sequential (non-iterative) design process, used in product (mainly used in software) development processes, in which progress is seen as flowing steadily downwards (like a waterfall) through the phases of conception, initiation, analysis, design, construction, testing, production / implementation and maintenance. Fig. 2 indicates the schematic representation of waterfall process model. The main disadvantage of this model is the feedback at the end of development cycle. Clients may not know exactly what there are getting against their requirements before they see working product and so any change leading to redesign, redevelopment, and retesting, and increased costs [5].

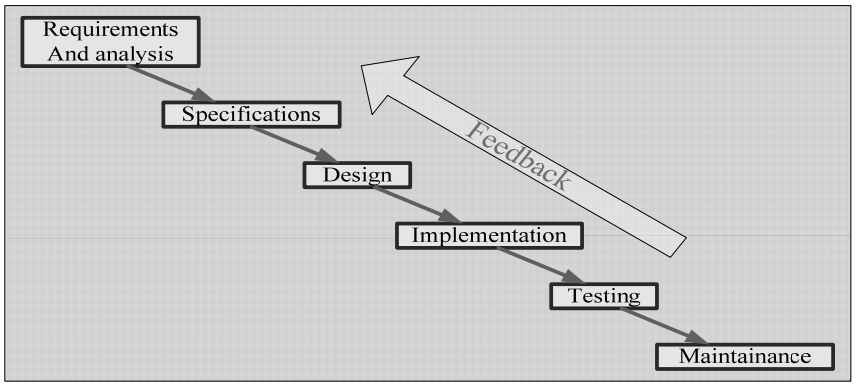

Figure 2: Waterfall Process Model

In 1986, Barry Boehm proposed a new system engineering model called Spiral Process Model (SPM). It is a combination of a waterfall model and iterative model. Each phase in spiral model begins with a design goal and ends with the client reviewing the progress [6]. This model has four phases called, planning, risk analysis, engineering and evaluation. Risk analysis is the main advantages of spiral model over waterfall model. In the risk analysis phase, a process is undertaken to identify risk and alternate solutions. A prototype is produced at the end of the risk analysis phase. If any risk is found during the risk analysis then alternate solutions are suggested and implemented. The main limitation of this model is risk analysis requires highly specific expertise and project's success is highly dependent on the risk analysis phase.

ISBN - 978-93-95038-50-8

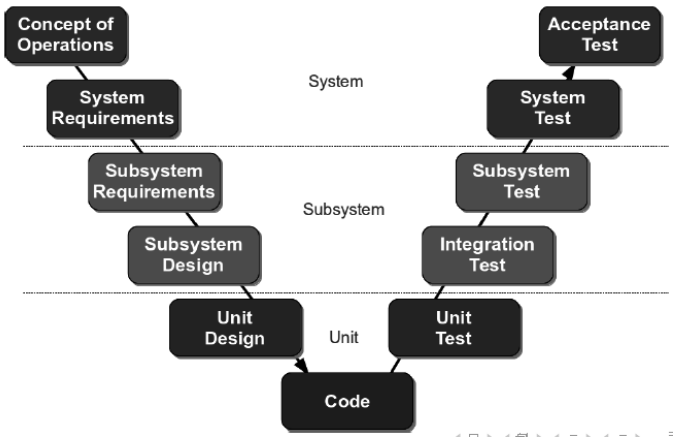

Figure 3: Vee Systems Engineering Process Model

Many different process models have been developed over the years that specify a series of steps that make up the systems engineering approach. Among these models, the "Vee" model is used where requirements are clearly defined and practically fixed. It should be chosen when ample technical resources are available with needed technical expertise. Fig. 3 shows the Vee model used for missile development process. The Vee model is used to visualize the system engineering focus, particularly during the concept and development stages. The Vee highlights the need to define verification plans during requirements development, the need for continuous validation with the stakeholders, and the importance of continuous risk and opportunity assessment.

3. ROLE OF SYSTEMS ENGINEERING TEAM

Exactly the same is performed *by System Engineering Team or Committee (SET or SEC*) of different projects of missile complex. The primary function of the SET in my view is to provide the basis for integrating the technical effort and communicating what will be done, by whom, when and why it is being done. In addition, the SET identifies the roles, responsibility and interfaces of the technical effort and how those interfaces will be managed. Managing this systems architecture and providing traceability and impact during the design lifecycle is an important activity of SE. Forcing designers to articulate testing scenarios as allocated requirements get owned is another important task of systems engineering team.

A general high-level picture of the systems engineering process is indicated in Fig. 4. This process is often repeated multiple times during the course of a complex system design and development process. Its repetition is a function of the system's complexity, system composition and confidence levels on subsystems adopted. Technology Readiness Level (TRL) is plays vital role in number of iterations. In my experience, a project like missile system needs at least three iteration. Submarine launched long range ballistic missile project took just four iteration. For the first two years, we were concentrated on understanding user needs and constraints, current technology and future needs, generated top-level specifications, and initiate the parallel programs to bridge the gap between the technologies available currently and required to meet the user needs. This particular project was in mission mode and supports to research and development activity to build the required technologies. After four iterations, mission review (Conceptual System Design) was conducted and design was cleared for further detailed studies and preliminary designs of different subsystems.

ISBN - 978-93-95038-50-8

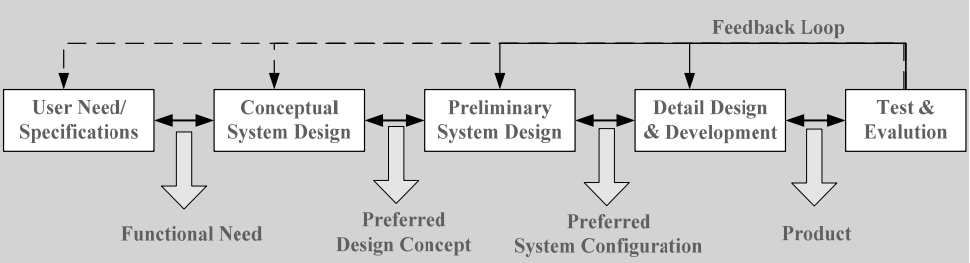

Figure 4: Simplified view of System Engineering Process

SET Work Load: Till this stage system engineer will be having maximum work load. He/she should interact with users, project team and subsystem designers to home on to an optimum system concept. Several times, subsystem designs may be getting rejected due to technical reasons but situations may lead to egotistic problems. Under such situations he/she will face some non-technical pressures additional load/burden on them. Leaving those non-technical issues, typical work load on SET at different stages of design and development phases is shown in Fig. 5.

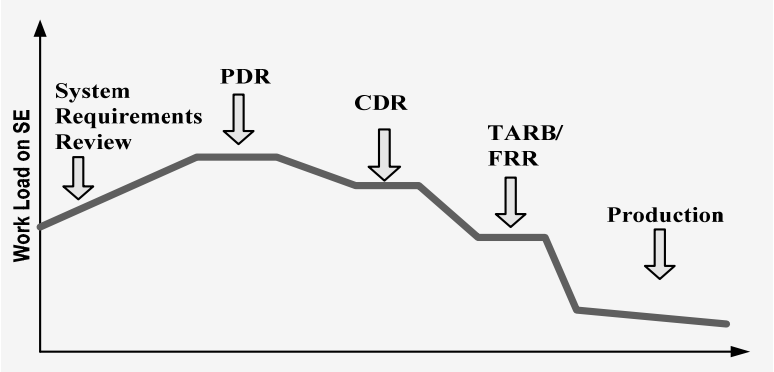

Figure 5: Typical work Load on SET at different phases of development

As it is clear from Fig. 5, most critical and complex stage is the generating overall system requirements which include user needs, constraints from user and designer.

- **Requirements Engineering:** A systems engineer should evolve well-stated requirements which exhibit the following attributes:

  1. The requirement is Necessary - What would happen if you didn't include this requirement. ?
  2. The requirement is Verifiable - How will you know you have met the requirement. ?
  3. The requirement is Attainable - It should be with the current technology or in near future can be developed.

In simple, requirements should be concise and unambiguous. Most of the cases, systems engineers face difficulty in convincing contradictory requirements. Ideally, one should generate consistent (non- contradictory) requirements, but some of the missile systems will have contradictory requirements in performance and safety. Systems engineering team only can visualize the complexity and generate some trade-off solution to meet both performance and safety. In some complex situations, user may not have clear picture of what they want. For example, Indian Navy looking for some state-of-the-art weapon available with USA, but they don't have any information other than end functionality.

ISBN - 978-93-95038-50-8

In such situations, joint team can do some sort of R&D to evolve user needs. SE also concentrates on history of changes and change rationale (if required) is as requirements gets evolve. It also keeps track of change history of design in terms of configuration/data control [10].

- **Risk Assessment:** It is more important aspect of any project. Risk involved from conceptual stage to design, development, production and storage needs to be visualized and necessary step to be initiated at the early stage of project life cycle.
    1. A system engineering demands risk assessment at the beginning of project for all subsystems and also monitors at all critical design stages [9].
    2. Specifically, wherever safety of man is involved, systems studies should bring out different types of possible failure modes and its criticality on safe mission.
    3. When it is important to minimize risk, high fidelity models are required to simulate the failures. Special processing tools are required to analyse the data.
    4. Systems engineering team covers these aspects and generates guidelines for fail-safe system with sufficient redundancy at different subsystems.

During the systems engineering process, peak work load comes when designer starts designing to incorporate system requirements to realize the end goal. Though, preliminary design starts with a simple concept, it goes through different phases and cycles of design, realization, integration, quality control, repeatability/reliability assessment, testing & performance evaluation, life assessment and so on. All these aspects are addressed to the extant at PDR stage itself.

- **System Engineer:** The responsibility of System Engineer *(in DRDL and Missile Complex also called as **System Manager**)* plays a vital role in total SE process of a missile design, development, production, testing and delivery i.e., each and every stage of weapon development life cycle. System manager should focus on interaction of all other subsystems with his own subsystem. The system manager (technical team) works with and for the project / project manager to accomplish the goals of the project. Here, is the list of typical characteristics of a good systems engineer.
    1. Intellectual Curiosity – ability and desire to learn new things and update him self
    2. Ability to make system - wide connections/ thinking
    3. Comfortable with uncertainty and unknowns -
    4. Proper Paranoia – expect the best, but plan for the worst
    5. He/she should be a strong team member and leader
    6. Self Confidence and Decisiveness – short of arrogance
    7. Appreciation for Process - rigor & knowing when to stop
    8. Exceptional Two-way Communicator
    9. Diverse Technical Skills – ability to apply sound technical judgment
    10. Comfortable with change - Rigidness may lead to failure or non-optimal system
    11. Ability to see the big picture even when things are not frozen or yet get into the details

In simple, a system manager should know many things (don't have to be the expert in every field). He must work with many people in different levels and from different disciplines. He should be challenging in nature.

ISBN - 978-93-95038-50-8

- **Benefits of Systems Engineering:** Implementation of this systems approach will enhance core engineering, management, and scientific capabilities and processes to ensure safety and mission success. At the same time systems engineering also helps to increase performance and reduce cost and time. This systems approach needs to be applied to all elements of a system and at all hierarchical levels of a system over the complete project life cycle. Model-based approaches are now available for doing this. Merely what needs to improve in DRDL context is regular and focused interaction of SET teams. The ultimate goal of a good Systems Engineering Efforts (SEE) is to
  1. Address system integration issues as early as possible, and reduce late design changes.
  2. Good understanding of the system interactions
  3. Good coordination among users, designers, production agencies, working teams, and others organizations

4. MODELING AND SIMULATION TOOLS

Technical team generally generates the system specification by *modeling* dynamics of plant and *simulating* in most realistic environment. These tools have very high importance in the whole SE process from problem statement to specification generation, preliminary design, detailed design, testing and performance evaluation. For highly complex problems like aerospace applications, there is a need of using high fidelity models at concept feasibility stage itself.

Trajectory simulation model (in general called as 6-DOF package) is one such critical mathematical model used in Directorate of Systems (DOS) of DRDL. These models should be used appropriately based on its applicability. Table 1 summarize the general guidelines for fidelity of model vs its applicability. Similarly, every small and big sub-system should have reasonably representative mathematical models to evaluate its performance before going for real field testing. This is generally a mandatory requirement for aerospace applications.

Table 1: Fidelity of model vs its applicability

DOF	Applicability
1 DOF	Missile Dynamics on launcher
2 DOF	Missile Dynamics on Launcher with Normal force
3 DOF	System design & optimization, Guidance
6 DOF	Complete Missile Dynamics Simulation

5. DATA MANAGEMENT

In a complex area like missile system design, it is very difficult to assimilate the input data requirements of various subsystems participating in the design process. Data from one subsystem forms input for the other subsystem. Huge amount of data gets generated during design iterations and convergence. Further, for the chosen variant, considerable amount of fine-tuning takes place in almost every subsystem in order to meet the mission requirements. Data management becomes utmost importance so that the correct and appropriate data is used by the concerned subsystems designer. Data management is the key element of systems engineering process and it is treated as a one of the technical management process. The efficient data management essentially provides technical insight and supports management activities as well as decision making. General attributes of data management are as follows:

ISBN - 978-93-95038-50-8

1. Proper acquisition and structuring of data from various sources and working groups
2. Efficient access and retrieval of the “right” data at “right” time
3. Enable sharing and integration of data between user, designer & manufacturing industry as and when needed
4. Every set of should be identified by a unique number for easy of traceability and utility

6. MISSILE SYSTEMS ENGINEERING PROCESS

Design, development and flight testing of a missile system is highly interdisciplinary activity involving various subsystems like aerodynamics, propulsion, structures, control, guidance, navigation, warhead, on-board electronics etc., Each of the said areas have the complexities/intricacies of their own. Hence, it is not possible for a small team like Project Team to have an overall picture of design and development process. It will be highly beneficial, if whole of the mission scenario is divided into various design activities and connectivity can be provided between various parameters that could influence the particular design. Especially, if the criticality of the influencing parameters in the design process is established, it will forewarn the project team as well as the designer during the initial stage itself to take necessary steps for controlling the same. Systems engineering team generates list of such critical parameters for each system and subsystem. Doing so, the foremost task of systems engineering is capturing requirements of all stakeholders and documenting them by paying attention to the best practices. Then comes the top-down systems architecting by involving stakeholders (in case of weapon development, Armed forces and production agency are the stakeholders) who are to be internal to the design team.

In order to achieve user’s multipurpose requirements for "guided missiles" of high kill probability, a hierarchal top down system design methodology has been evolved. This approach will take care of user defined threat profiles, system coverage/kill zone, fire power, mobility, low observability in the presence of constraints of launch platform, safety of launch platforms such as aircrafts and underwater vehicles, availability sensors and actuator and realization time frame and unit cost of missile. The following steps are carried out as part of systems engineering for missile design and development at Directorate of Systems (DOS) of DRDL in consultation with other designers.

1. Stakeholders Requirement Analysis
2. Threat Scenario Definition and Synthesis
3. Generation of System Requirements (also called as "base line specifications")
4. Design Constraints
5. System Architecture Evaluation
    a. Evolving Mission Definition in terms of range, CEP and damage potential
    b. Sizing Propulsion System based on maximum range requirement
    c. Designing Aerodynamic configuration based on lateral acceleration requirement to shape trajectory
    d. Ensuring launch platform safety
    e. Generating Guidance, Control and Actuator requirements
    f. Assess the sensor need and generate specifications
    g. Trajectory design and analysis
6. System Characterization and Sensitivity Analysis
7. Failure Mode Effects and Criticality Analysis (FMECA)

ISBN - 978-93-95038-50-8

8. Methodological Review Mechanism (Mission Review, PDR, CDR, FRR, TRAB and so on)
9. Testing and Evaluation
10. Documentation of design and learning during development.

Normally measure of merit and effectiveness are derived from the mission need statement and used to evaluate the system architecture. It now becomes essential to bring out the *inter-connected connectivity chart* between the various models as indicated in Fig. 6. The result of all these exercises is a System Architecture leading to efficient and faster development. Systems engineering also helps in creating the work breakdown between different subsystems designers. While all the above are the parts essential systems engineering, creative part comes in investigating technology alternatives and supporting decision making through risk analysis.

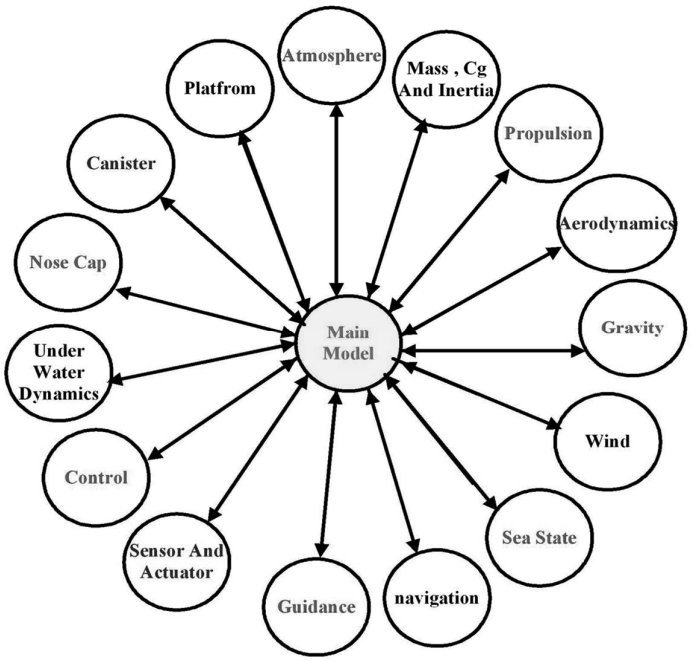

Figure 6: Inter-connected Connectivity Chart

7. CONNECTIVITY CHART

Based on user and mission requirements, subsystem specifications have been evolved by applying systems engineering process. Based on mission profile, critical design areas have been identified that need to be further elaborate as connectivity charts with associated influencing parameters. Connectivity charts is a chart which shows the relation between the outcome and influencing parameters at different degree of interaction levels as indicated in Fig. 7 for one of critical subsystem. Connectivity charts have been developed in a layered approach manner. Outcome of the design activity are indicated on the rightmost side with influencing parameters placed in different layers. Parameters in the innermost 2 layer, i.e., L1 directly influence the outcome of the design process. Parameters that affect L1 are placed in layer-2 (L2) which in turn influenced by the parameters of Layer-3 (L3). These charts are developed to such an extent that a reasonable degree of interaction levels have been achieved. However, it is always possible to further expand the charts or make further connectivity to the parameters in the outermost layer based on complexity of a given subsystem.

ISBN - 978-93-95038-50-8

One of such complex sub-system is explained here as a case study. Control Surface (CS) unfolding is essential to stabilize and control the missile. A powerful pnuemo-hydraulic CS opening mechanism is designed and the operation of this mechanism is greatly effected by an external loads acting on the CS and this needs to be studied in detail. The opening mechanism has got stringent requirements on synchronization of all four fins, angular speed at the time of locking and others, under the conditions where external flow counteracts the opening. The performance of this subsystem depends on missile dynamics as well as pneumatic opening mechanism. Here hydraulic damping system plays vital role to reduce the structural loads. Fig. 7 indicates the connectivity chart for this system. Total five layers provide degree of interaction of different influencing parameters and at the end outcome on system performance.

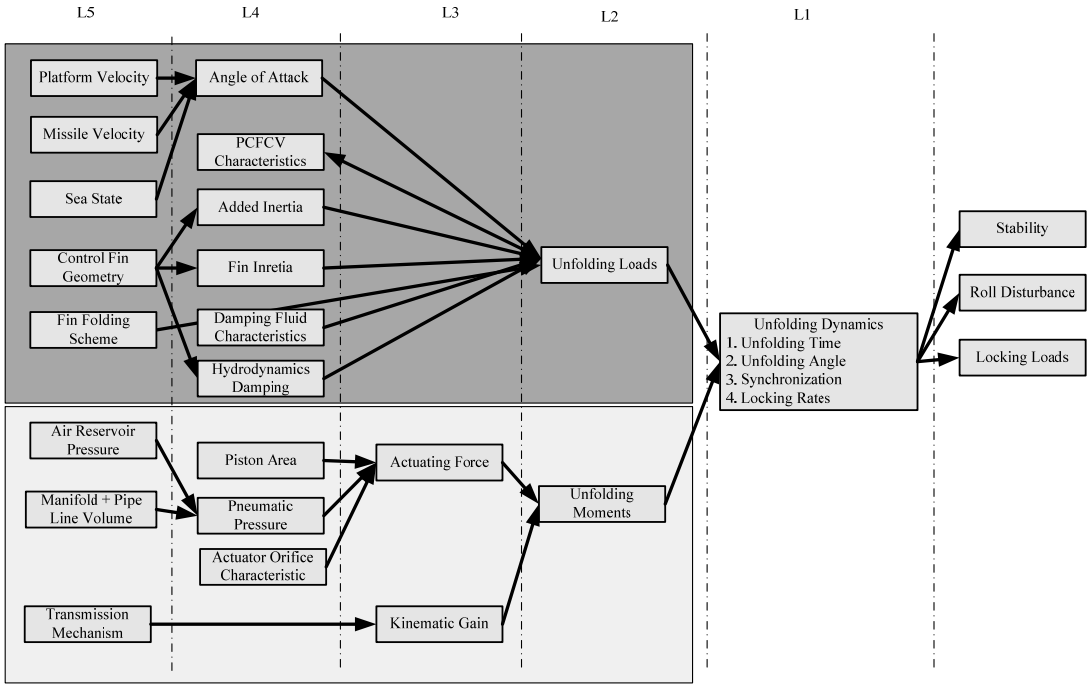

Figure 7: Connectivity chart for CS Unfolding Mechanism

In DRDL the task of systems engineering is accomplished by forming Systems Engineering Teams who discuss on regular basis the various mission requirements and workout the designs to meet them. The designs are discussed in detailed to bring out any shortfalls so that those can be rectified at the right time during the development process. Experience shows that the projects who instituted such forums and followed it up meticulously have experienced minimum problems during flight trials and the overall success rate is very high compared to those who did not follow it meticulously. In my view SET contribution is very high in any successful project.

8. SUMMARY

1. Systems engineering is the art and science of creating a product, it needs dedicated efforts. As there is no unique methodical approach to apply SE on our day to day problems, we (DRDL) should evolve a SE process and articulate it. We must have a curriculum to support individual development in best SE practice for all scientists.

ISBN - 978-93-95038-50-8

2. Need to develop a human resource to eliminate "insufficient understanding of both the individual and System-of-System interdependency of product and process".
3. It is the time to use standard SE tools to properly define the various environments.
4. There exists a large gap in India's technical capability for catering the demands of indigenous production in Aerospace and Defence sector. Indian manufacturing needs to upgrade capabilities in precision engineering, micro engineering to take a big leap into the Aerospace and Defence sector.

ACKNOWLEDGEMENT

The author thanks competent authorities of Defence Research and Development Laboratory (DRDL), Hyderabad for granting permission to publish this piece of work. He also expresses deep gratitude to his team for extended support to strictly follow the system engineering practices.

REFERENCES

1. Blanchard, B. S., Fabrycky, W. J., & Fabrycky, W. J. (1990). Systems engineering and analysis (Vol. 4). Englewood Cliffs, NJ: Prentice Hall.
2. Haskins, C., Forsberg, K., Krueger, M., Walden, D., & Hamelin, D. (2006, June). Systems engineering handbook. In INCOSE.
3. Shishko, R., & Aster, R. (1995). NASA systems engineering handbook. NASA Special Publication, 6105.
4. Royce, W. W. (1970, August). Managing the development of large software systems. In proceedings of IEEE WESCON (Vol. 26, No. 8, pp. 328-338).
5. Parnas, D. L., & Clements, P. C. (1986). A rational design process: How and why to fake it. IEEE transactions on software engineering, (2), 251-257.
6. Boehm, B. W. (1988). A spiral model of software development and enhancement. Computer, 21(5), 61-72.
7. Honour, E. C. (2004, June). 6.2. 3 Understanding the Value of Systems Engineering. In INCOSE International Symposium (Vol. 14, No. 1, pp. 1207-1222).
8. Sheard, S. A. (1996, July). Twelve systems engineering roles. In INCOSE International Symposium (Vol. 6, No. 1, pp. 478-485).
9. Sheard, S. A. (1996, July). The value of Twelve systems engineering roles. In INCOSE International Symposium (Vol. 6, No. 1, pp. 894-902).
10. Honour, E. C. (2013). Systems engineering return on investment. University of South Australia.
11. Valerdi, R., Ross, A. M., & Rhodes, D. H. (2007). A framework for evolving system of systems engineering.
12. Elm, J. P., Goldenson, D. R., Emam, K. E., Donatelli, N., &Neisa, A. (2007). A survey of systems engineering effectiveness (No. CMU/SEI-2007-SR-014). CARNEGIE-MELLON UNIV PITTSBURGH PA SOFTWARE ENGINEERING INST.
13. AK Chakrabarti, "Bird's Nest Network - A Logical Approach in Product Development"
14. G Naresh Kumar and R Krishna Mohan Rao, "Connectivity Chart & Data Management Procedure for B05 Missile System", Report No.: DRDL/B05/GEN/01, Dated: Aug-2012.

System Engineering Challenges in Development of LOX-Isrosene Booster Stage for Future Launch Vehicle of ISRO

B Suresh Babu*, Reji Joseph, and S Jagannathan

Liquid Propulsion Systems Centre
Indian Space Research Organization
Valiamala, Kerala, 695547

ABSTRACT

Liquid Propulsion Systems Centre (LPSC) of ISRO is pioneer in the design and development of liquid propulsive stages. It has undertaken development of Semi-Cryogenic propulsion stage, which will be the largest liquid stage developed so far. The stage with Liquid Oxygen (LOX) and Kerosene based fuel (Isrosene) as its main propellants helps to enhance the payload of GSLV MkIII launcher to beyond 5 tonnes. Design of liquid propulsion stage is complex as it involves components like valves, regulators, flow control devices, functional modules and control sub systems. A typical liquid propulsion stage will have more than 25 sub-systems, each having its own set of components, operating conditions and specification. Systems engineering plays major role in development and realization of such complex Liquid Propellant stages of launch vehicle. Major challenges that are anticipated during mechanical design and development of the LOX-Isrosene (semi-cryogenic) stage are handling large temperature gradients between propellant tanks, its unique storage as well as assembly requirements and management of thermal stresses in adjacent structures. It also warranted the need of combining the system engineering practices followed for Cryogenic and Earth Storable liquid propellant stages, without compromising on the sub system performance. The Semi-Cryogenic stage being developed is planned as a replacement of core booster stage of GSLV-MkIII, heaviest launcher developed by ISRO so far. Though this method reduces development time and cost, it induced additional constraints on the stage development. System engineering practices are utilized for complete assessment of stage systems and for finalization of system configuration with an objective of reduction in development time, cost and without any changes in the remaining systems of the launch vehicle. This paper presents the relevance of systems engineering for launch vehicle development, complexities involved in design and development of Semi-Cryogenic liquid propellant stage and solution strategies implemented for overcoming the design challenges with selected examples.

Keywords: *Semi-Cryogenic, LOX, Launch Vehicle, System engineering*

1. INTRODUCTION

Liquid Propellant stages find a major share in launch vehicles because of their wider operating flexibility, restart capability, reuse capability, throttling etc. A typical bipropellant liquid stage utilizes oxidizer and fuel, stored in independent tanks, for generation of thrust.

Many launch vehicles that are currently in operation like Soyuz, Falcon, Atlas use a semi-cryogenic propellant combination (purified kerosene and liquid oxygen) for large booster stages in view of the advantages that it offers like high density impulse, eco-friendly nature and cost effectiveness. Liquid Propulsion Systems Centre (LPSC), ISRO's lead center for development of liquid propellant stages, is developing a Lox-Isrosene (purified kerosene) engine which can deliver 2000kN thrust for booster stage. This engine will become workhorse engine that will power all semi-cryogenic stages developed by ISRO. Extensive mission studies with different vehicle configurations, wherein semi-cryogenic stages can be either core booster stages and/or strapon stages, were carried out and the payload capabilities assessed. An innovative plan is worked out to design a semi-cryogenic stage that will fit into the existing GSLV-MkIII by replacing the earth-storable lower booster stage. This approach provides the earliest opportunity to demonstrate the Semi-Cryogenic technology in a

*Corresponding author: E-mail: suresh.balabhadra@gmail.com

ISBN - 978-93-95038-50-8 https://doi.org/10.37285/bsp.sasat2023.02

qualified vehicle, in addition to increasing the payload of the GSLV MKIII launcher. The overall vehicle configuration, interfaces with adjacent stages and mission profile remains unchanged, minimizing the development work. However, this method poses additional development challenges in terms of overall configuration, thermal management etc.

2. SYSTEM ENGINEERING-AS APPLICABLE TO LAUNCH VEHICLE DEVELOPMENT

Launch vehicles are designed to place the satellite or the payload into the desired orbit with specified velocity. This objective can be met only with the synchronized effort of all different stages of the launch vehicle and all sub systems of each stage. Hence, the interactions, constraints and responses of various subsystems are to be understood clearly to arrive at an optimum configuration, which makes the design and development of any launch vehicle complex. It involves not only several iterative design procedures and interactions but also certain key design considerations [1]. Sub systems of launch vehicle are complex, combining multiple technical disciplines, and their development posed engineering challenges significantly beyond those that had been presented earlier. Systems engineering, as we know it today, developed to meet these challenges [2].

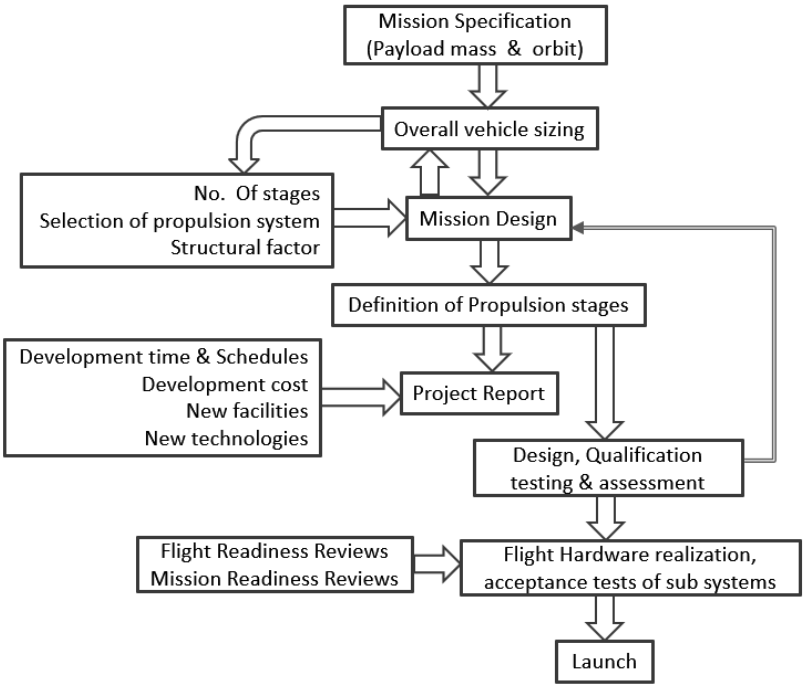

Figure 1: Flow diagram depicting major phases in the development of Launch Vehicle

Design, development, testing and evaluation of any new launch vehicle typically requires a cycle time of not less than 8 to 12 years, especially when new technologies are involved. Hence, the total development activities are divided into major milestones that are considered themselves as independent projects. Figure 1 shows main phases in development of any launch vehicle starting from mission specification till launch. Teams with specialization in materials, mechanical, electronics, propulsion, control and guidance systems have to work in tandem to attain the mission objectives along with exercising strict control on system mass, schedule and budget. Considering the number of disciplines involved, varying type of activities and huge budget, multiple challenges are expected during sub system design. Wherever conflicting requirements are to be met due to the imposed challenges, detailed

ISBN - 978-93-95038-50-8

assessment to be made and specification/requirements of some of the systems to be revisited/adjusted in a way to achieve the goals at integrated level. Today, operational procedures of all launch vehicle missions are worked out based on system engineering approach as it provides the ability to guide such complex development activities with superior knowledge of the system as a whole, its operational objectives and all the technical factors that go into its development.

Gibson et.al. [3] states the importance of system engineering aspects on launch vehicle performance. It analysed many published works and presented a system engineering process performance model that was developed to examine the relationships among management support, organizational commitment, systems engineering support, and systems engineering process performance in US launch vehicle organizations. The hand book [4] gives description of the system engineering methods implemented in launch vehicle programmes of NASA. It lists all the major phases of the design and development of launch vehicle, flow diagrams depicting the interactions between various aspects of the development and also technical risk management.

3. SUBSYSTEMS OF LOX-ISROSENE LIQUID STAGE

A typical liquid propellant stage requires mechanical, propulsion, control systems for its successful functioning. Major load bearing structures that forms external shape of the stage comes under the mechanical systems. Propulsion systems provide smooth flow of propellants to the engine at required inlet conditions and ensure functioning of engine as per requirement. Control systems provide stability and steering of the total vehicle. Auxiliary systems consist of thermal protection, health monitoring, separation/pyro systems etc., and are equally important for successful completion of mission objectives. Table 1 gives summary of major sub systems of Semi-Cryogenic stage. There are 27 sub systems that are to be worked together for the successful functioning of the stage.

Table 1: Major Sub Systems of SemiCryogenic Stage

Mechanical Systems	**Propulsion Systems**		**Control Systems**	**Auxiliary Systems**
	LOX	**Kerosene**		
1. Oxidizer Tank	1. Pressurization	8. Pressurization	1. Anti-Slosh	1. Avionics
2. Fuel Tank	2. Fill and Drain	9. Fill and Drain	2. POGO	2. Insulation
3. Inter Tank Structure	3. Propellant conditioning	10. Feed	3. Pitch and Yaw control	3. Umbilicals
4. Base Shroud	4. Feed		4. Roll Control	4. Instrumentation
5. Thermal Shroud	5. Vent and Relief			5. Destruct
6. Flexible thermal boot	6. Command			6. Pyro
7. Nozzle Closure	7. Engine Purge			

ISBN - 978-93-95038-50-8

Thrust, structural factor and propellant loading to impart required velocity forms the major specification of the stage. The definition and specification of each sub system are derived from the stage definition and specification parameters. Figure 2 shows major steps involved in development of any new liquid stage. Different options and configurations for each of the sub system is worked out and finalized based on thorough review of pros and cons of each configuration. Preliminary design of the finalized configuration is carried out considering influence and requirements of other subsystems, fabrication easiness, integration, testing and launch pad interfaces. Qualification testing will be carried out at various levels, viz, component, sub system and integrated stage, to identify and mitigate the design problems, if any, at the earliest opportunity. Detailed assessment of the sub system performance and the stage performance as a whole will be done and configuration/design of any sub system will be modified, if required.

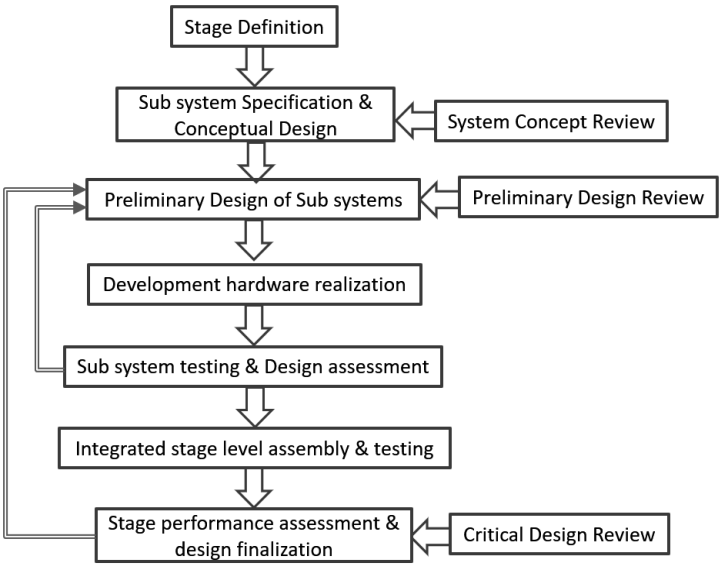

Figure 2: Various phases involved in development of Liquid Propellant stage

3.1. CHALLENGES IN OVERALL STAGE ENGINEERING

The Semi-Cryogenic stage under discussion is configured by maintaining the overall vehicle structure and envelope. With this constraint, maximum possible propellant loading is finalized. For this loading, mission design and mission optimization is done. This led to additional technical challenges as brought out in Table 2. Different studies are carried out with probable stage configurations and is optimized in an iterative process based on the feedback from various studies.

3.2. DESIGN CHALLENGE-1: STAGE CONFIGURATION WITHIN THE AVAILABLE HEIGHT

As the stage height is already fixed, the total propellant loading that can be accommodated in the given envelope depends on the space available after accommodating the necessary structures like Inter stage/tank structures and base structure. The available space is allocated to the propellant tanks considering the Mixture Ratio (MR) and propellant budgeting. Detailed mission studies indicated that the obtained propellant loading gives sub optimal performance of the mission and doesn't increase the payload, which was one of the main

ISBN - 978-93-95038-50-8

objectives of the new stage development. The challenge here is to increase the propellant tank sizes within the available stage envelope and to deal with its influence on other systems.

Table 2: Major Design challenges faced during Semi-Cryogenic stage configuration phase

Design constraint	Affecting parameter	Solution strategy
Stage configuration within available height.	Propellant loading	Optimization of structure heights
Protection of cooling channels in nozzle divergent	Design and configuration of stage aft structures	Detailed aero and thermal studies with different aft structure designs. Jettisonable nozzle protection structure enclosing nozzle divergent
Maintaining auxiliary system layout as in adjacent stages	Cutouts on structures. Interfaces on tanks and structures.	Overall design adapted same as in the earth storable stage being replaced.
Utilization of existing fabrication and integration facilities	Configuration of tanks. Integration procedures.	Configuration of tanks as per established practices. Spatial grouping of LOX and Isrosene modules and systems in all structures.

3.3. SOLUTION STRATEGY IMPLEMENTED FOR DESIGN CHALLENGE-1

In order to maximize the propellant loading, one of the inter stage structure is dispensed with, thus increasing the propellant loading by around 7 tonnes. However, it affected many other sub systems and stage parameters leading to chain of changes. Figure 3 shows the solution strategy implemented, following system engineering practices. It introduced accessibility issues for the avionics sub assembly located in the upper structure and is managed by extension of fuel tank fore end ring. As the fuel tank is moved forward, very near to the strap-on thrust transfer joint, the structural loads have become non-uniform. To optimize tank mass, higher thickness is introduced only for the region where loads are higher. Vehicle loads for remaining structures and oxidizer tank also are re estimated and design is re assessed. Though the modified design induced additional complexities in design and realization of the fuel tank and affected many other systems, it is better trade-off considering the payload advantage gained by the additional propellant loading.

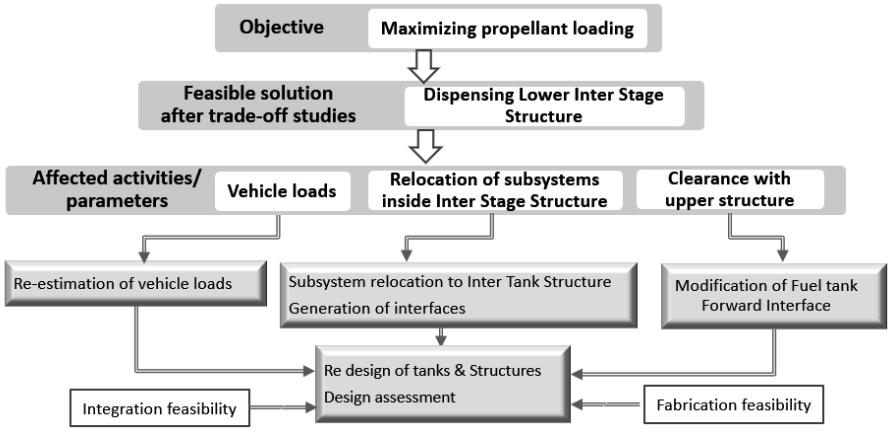

Figure 3: Flow chart of solution startegy for design challenge-1

3.4. DESIGN CHALLENGE-2: PROTECTION OF COOLING CHANNELS IN NOZZLE DIVERGENT

The regenerative cooling channels of nozzle divergent of the engine are filled with fuel before lift-off. However, engine gets ignited only after about 2 minutes in to the flight. During non-operational phase of the engine, nozzle divergent is to be protected from convective and radiative heat loads from exhaust gases of the strapons thereby controlling the temperature of stagnant fuel inside the regenerative cooling channels. The challenge here is to protect/enclose the nozzle divergent till engine ignition.

3.5. SOLUTION STRATEGY IMPLEMENTED FOR DESIGN CHALLENGE-2

To tackle the nozzle divergent heating, an additional nozzle closure is introduced at the stage aft end, interfacing with the thermal shroud. This nozzle closure will be commanded to separate just before engine ignition, using pyro-based devices. Introduction of nozzle closure lead to two distinct aero thermal regimes, before and after nozzle closure separation. Vehicle external configuration also changes during these events. The finalized contour of the nozzle closure and overall configuration of the base region is finalized based on detailed aero, thermal and separation studies. Figure 4 shows the stage base region with nozzle divergent enclosed with nozzle closure. Figure 5 presents the solution strategy implemented following the system engineering practices. The thermal shroud and nozzle closure are considered as a whole and aero studies are carried out for all possible configuration. Though ogive type aft end is the better configuration in aero loads perspective, conical shape with spherical end cap is selected as it provides fabrication and integration easiness.

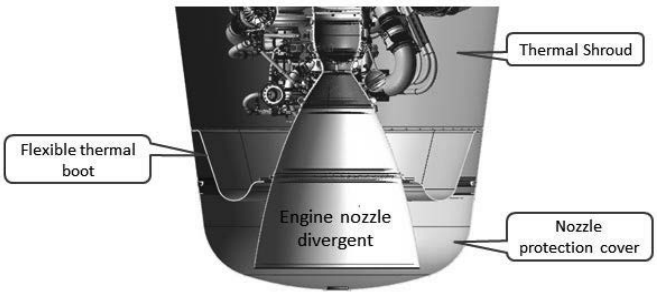

Figure 4: Stage aft end region showing the Nozzle protection cover

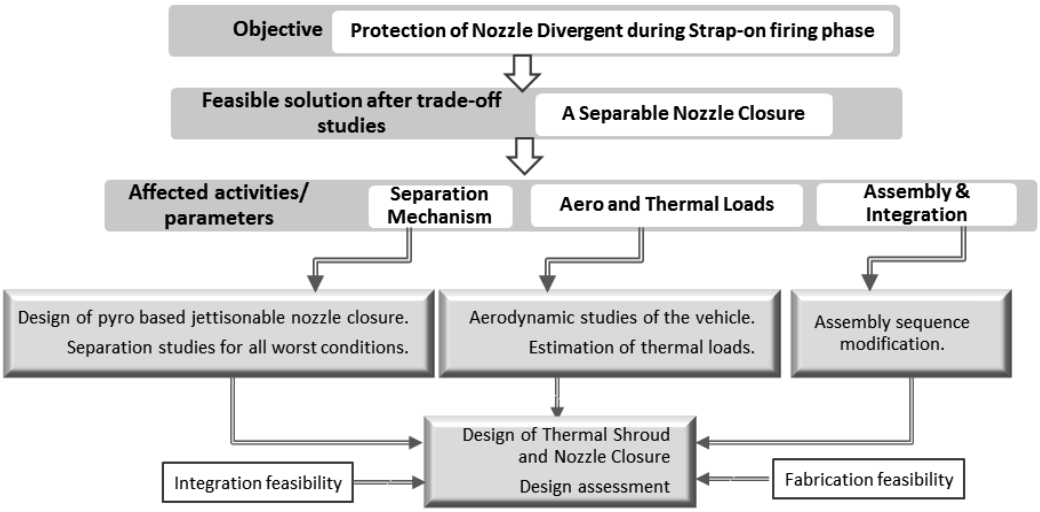

Figure 5: Flow chart of solution strategy for design challenge-2

3.6. DESIGN CHALLENGE-3: MAINTAINING AUXILIARY SYSTEM LAYOUT AS IN ADJACENT STAGES

Auxiliary systems run over the total vehicle, providing instrumentation, power and servicing support independently to each stage and also between the stages. The challenge here is to configure the stage auxiliary systems in line with that of adjacent stages.

3.7. SOLUTION STRATEGY IMPLEMENTED FOR DESIGN CHALLENGE-3

Auxiliary system configuration and layout are maintained same as in the adjacent stages. However, it introduced constraints in working out propulsion sub system layout. The ideal layout of Isrosene feed pipe is found to interfere with that of strapon stage attachment links. Further system integration studies highlighted that the modified feed pipe is very near to external cable layout, introducing access and integration difficulties. Based on detailed studies, an optimum configuration of the structural and auxiliary system were arrived at.

3.8. DESIGN CHALLENGE-4: UTILIZATION OF EXISTING FABRICATION AND INTEGRATION FACILITIES

Cryogenic servicing and storage systems require stringent cleanliness requirements than that of Isrosene systems. Utilization of existing integration facilities requires independent preparation of the LOX and Isrosene tank sub assemblies in Cryogenic and Earth Storable assembly facilities respectively. However, engine also requires to be prepared with stringent cleanliness requirements as that of LOX tank. Hence, stage is configured with LOX tank, base structure and engine as a separate unit that can be assembled in Cryogenic facilities. However, for control system requirements and also for better NPSP margins at pump inlet, it is preferable to place LOX tank at the stage fore end region. Here, the challenge is to finalize the configuration considering the conflicting requirements from integration facilities and vehicle control and LOX feed system.

3.9. SOLUTION STRATEGY IMPLEMENTED FOR DESIGN CHALLENGE-4

Mission studies are carried out and vehicle loads are estimated with LOX tank at stage fore end and aft end. It is found that positioning of LOX tank at the aft increases the tank mass by 100 kg, but the configuration gives advantage on integration and lower stage protrusions. Vehicle controllability and stability with LOX tank at the aft and found to be acceptable. Hence, integration aspects are taken into the consideration and LOX tank is provided at the aft. The change calls for the redesign of tank thickness and change in aero load pattern. Tank design is revisited considering all influencing factors like pump head requirement, aerodynamic projection and structural interfaces.

The above examples gives gist of system engineering applications in design of booster stage with propellants stored at different temperatures and demanding different levels of integration requirement. Breakdown of the stage design into different systems, finding out optimum sub system configuration and integration of all these sub systems utilizing system engineering practices result in birth of optimum stage. Table 4 presents the overall gain in the project deliverables by due consideration from all different sub systems and activities of the stage development.

ISBN - 978-93-95038-50-8

Table 3: Improvement in the stage development activities/parameters

Parameter	Affecting parameter
Propellant loading	Increased by 7 tonnes
Development schedule	Reduced by more than 36 months
Development cost	Reduced by 40% with the utilization of existing facilities

4. CONCLUSIONS

This paper explains the relevance of systems engineering for launch vehicle development programme. A few major challenges faced during development of a large Semi-Cryogenic stage are discussed with the solution strategies. System engineering practices are followed from initial configuration phase till final qualification testing and an optimum solution is attained, considering the conflicting requirements from various sub systems. This approach also helped in increasing the stage performance as a whole.

REFERENCES

1. B.N Suresh, K.Sivan, “Integrated Design for Space Transportation Systems” Springer India, 2015
2. Alexander Kossiakoff, William N. Sweet, Samuel J. Seymour, Steven M. Biemer, “Systems Engineering Principles and Practices” 2nd edition, Wiley, 2011
3. Denton Gibson, Waldemar Karwowski, Timothy Kotnour, Luis Rabelo and David Kern, “The Relationship between Organizational Factors and Systems Engineering Process Performance in Launching Space Vehicles”, Applied Sciences Jounal., 2022, 12, 11541
4. NASA Systems Engineering Handbook, NASA/SP-2007-6015, Rev1

ISBN - 978-93-95038-50-8

Design and Mathematical Modeling of Fuel Feed System for Dual Fuel SCRAMJET

Kesava Vishnu G, Vishnu Suresh Nair*, Anoop V M, Arun G S, Kuldeep Singh Naruka

Liquid Propulsion System Centre
Indian Space Research Organization
Valiamala, Thiruvananthapuram Kerala. Pin Code: 695018

ABSTRACT

A Fuel Feed System (FFS) is designed to supply fuels for a Dual Fuel Scramjet engine. The system design is carried out based on the operational requirements of flow rate, pressure, duration within the envelope constraints. The scramjet engine consists of an effervescent injector with liquid hydrocarbon as the main fuel. Gaseous Hydrogen is used for pilot ignition and for emulsifying the liquid hydrocarbon. Hydrogen gas for both the requirements are met through a single source and supply system. The liquid hydrocarbon storage system consists of a standalone propellant tank with positive expulsion device and cavitating venturis. Mathematical modelling is done on the system and from the model outputs, the operational efficacy of the feed system throughout the flight duration is ensured.

Keywords: *Hypersonic flight, scramjet engine, fuel feed system, effervescent injector*

1. INTRODUCTION

SCRAMJET is a type of air-breathing engine in which the gas flow is supersonic throughout the engine including the combustion chamber. The combustion occurs at supersonic velocity. In scramjet propelled vehicles, fuel has to be carried on-board and once the vehicle reaches required Mach (Above Mach 5), Scramjet can be activated where it takes air (oxidizer) from atmosphere and propels the vehicle using supersonic combustion. Major advantage of using scramjet is that it has a higher specific impulse when compared to conventional rocket engines. Using scramjet engines, it's easy to achieve sustained hypersonic flight for air breathing rockets. A Scramjet engine is totally free from rotating or moving parts.

The major challenge in scramjet is attaining stable supersonic combustion at higher Mach numbers within the low residence time of oxidizer and fuel in chamber. Gaseous hydrogen is used as fuel in scramjet engines due to its higher calorific value, wide flammability range, higher mixing rate with oxidizer and low ignition delay. But on the other hand, GH_2 demands huge storage space due to its lower density. This results in an increase in the size of the launch vehicle which in turn increases the drag and reduces the overall payload capacity. Alternatively, using liquid hydrocarbon which has higher density impulse helps in optimizing the system design within the space constraints. Liquid hydrocarbon has to be injected at the required pressure, and atomized and mixed with ram air to have a proper and stable combustion. The operating sequence will start with a pilot ignition with GH_2 followed by the admission of emulsified liquid hydrocarbon into the engine. The flame from the pilot ignition would help sustain the combustion of the liquid. The scramjet engine under our study operates an effervescent injector. GH_2 is used to emulsify the liquid hydrocarbon flow for a better atomization. The Fuel Feed System (FFS) for scramjet should contain storage tanks for the liquid and gaseous fuels, flow controlling elements, pressure regulating devices, flow lines etc. This work concentrates on the design and mathematical modeling of the FFS.

*Corresponding Author: Email: vishnusureshnair@gmail.com

ISBN - 978-93-95038-50-8 https://doi.org/10.37285/bsp.sasat2023.03

2. LITERATURE REVIEW

The design and mathematical modeling of the system is carried out using independent elemental models and equations mentioned in [1]. The transient analytical model in [1] has flow and thermal models for the gas bottle, fluid flow lines and flow control orifice. Additionally, a thermodynamic model for the pressure regulator is added based on [2]. The solution of flow with friction and heat transfer through the flow lines are based on [3]. Junction elements are added based on [4].

3. FUEL FEED SYSTEM DESIGN

Based on the operating requirements, the FFS is designed. There are two independent feed systems within the FFS. One with Gaseous Hydrogen and the other with the liquid hydrocarbon. Gaseous Hydrogen feed system is designed to store, regulate and deliver the gas at the specified pressure to the scramjet engine. Figure 3 shows the flow schematic of the gaseous hydrogen feed system. A dome loaded pressure regulator is used to regulate the high-pressure gaseous hydrogen to the required lower pressure. Gaseous nitrogen is used for loading the GH2 regulator dome. At the inlet to the combustion chamber, calibrated flow control orifice is used to ensure precise control on the mass flow rate.

Similarly, a liquid circuit is designed to store the liquid hydrocarbon and inject the same to the combustion chamber at the required pressure and flow rate. From Figure 4, it may be noted that a positive expulsion device is used for the tank pressurization. GN2 is filled in the gas side of the pressurization diaphragm. The liquid storage tank is of stand-alone type as there is no active pressurization circuit for the ullage gas. The liquid would flow in blow-down mode during the scramjet engine operation. Cavitating venturis are used to regulate the injection pressure of the liquid and to maintain steady flow irrespective of downstream pressure oscillations.

The major components of Fuel Feed system are as follows,

- Liquid storage tank.
- Hydrogen storage bottle.
- Hydrogen pressure regulator.
- Cavitation venturi for liquid hydrocarbon.
- Flow controlling orifices.

3.1. LIQUID STORAGE TANK

A rubber based positive expulsion device is used in the tank to ensure the continuous flow of liquid hydrocarbon from the tank bottom. Figure 1 shows a typical tank with positive expulsion device. A positive expulsion tank contains a diaphragm which separates the fuel medium from the pressurant. Fuel is stored at the bottom of the tank, whereas pressurant is stored above the diaphragm. Due to system envelope constraints, a standalone tank was used for the storage of the liquid, without an active pressurization system.

ISBN - 978-93-95038-50-8

3.2. HYDROGEN STORAGE BOTTLE

Gaseous Hydrogen is required for both ignition and emulsification of the liquid hydrocarbon. Storing gaseous hydrogen at a high pressure and regulating it to lower pressure helps in designing the system within the available system envelope. A Composite spherical bottle is designed to store gaseous Hydrogen at high pressure (Figure 2).

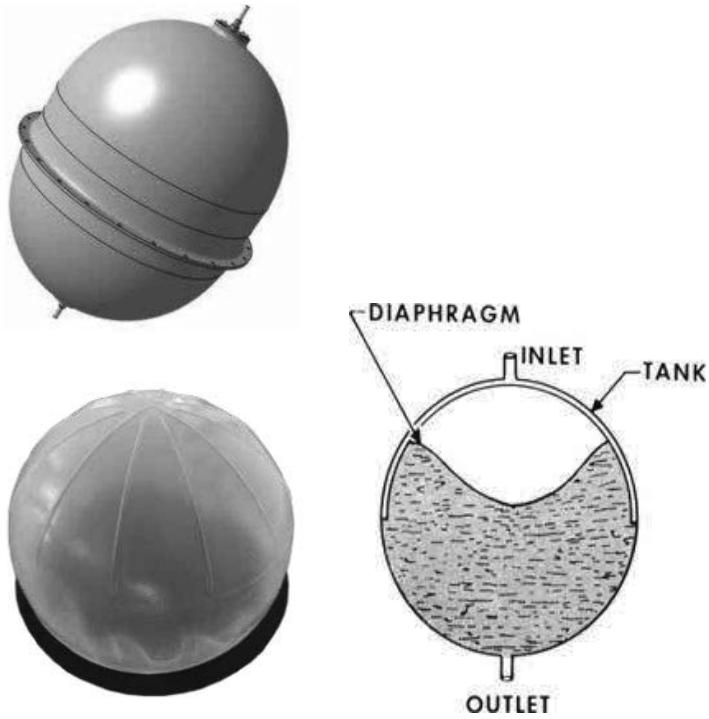

Figure 1: Positive expulsion Tank for liquid storage (Courtesy: https://www.space-propulsion.com/brochures/propellant-tanks)

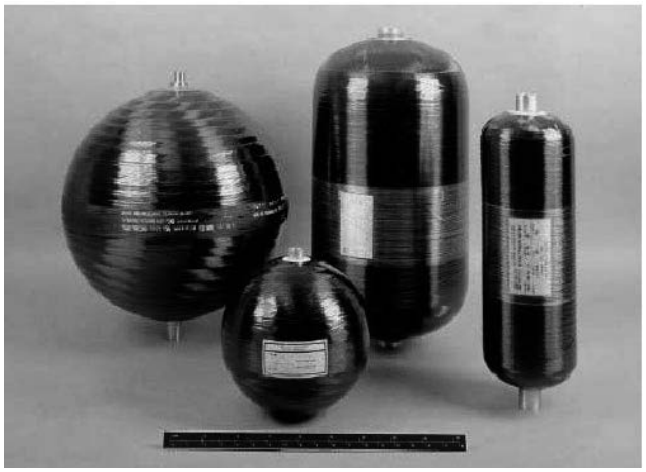

Figure 2: Composite overwrapped pressure vessels for gas storage [6]

ISBN - 978-93-95038-50-8

3.3. HYDROGEN PRESSURE REGULATOR

A dome loaded pressure regulator is designed to regulate gaseous hydrogen from the storage pressure to the required injection pressure. The regulated pressure would be set considering the pressure losses in the feed system downstream to the regulator. The dome loading is supplied by Gaseous Nitrogen from a separate command system.

3.4. SEQUENCE CONTROL VALVES

The sequence of planned scramjet flight is shown below,

Sl. No	Event
1	Injection of GH_2 for pilot ignition
2	Injection of emulsified liquid hydrocarbon
3	GH_2 flow stops

The aforementioned timed sequence of operation is implemented by using sequence control valves.

3.5. FLOW CONTROL ORIFICES

The mass flow rate of GH_2 into the engines are controlled using choked orifices. The orifices avoid the coupling between the pressure oscillations inside the engine combustor and the GH_2 feed system.

3.6. CAVITATING VENTURI FOR LIQUID HYDROCARBON

A cavitating venturi is designed to deliver the liquid at the required injection pressure. The device is designed to have a pressure recovery sufficiently enough to provide the required injection pressure to the scramjet engine injectors. The cavitating venturis ensure decoupling of the liquid feed system from the engine injector and combustor.

4. MATHEMATICAL MODELLING

4.1. GASEOUS HYDROGEN FEED SYSTEM

The gaseous hydrogen feed system is modelled using 13 elements and 16 nodes. Equations on the conservation of mass, momentum and energy are simultaneously solved on all the nodes to determine the mass flow rate, pressure and temperature at each node. The details are shown in Figure 3. Three junction elements are used in the system model. The model outputs are shown from Figure 5 to Figure 8.

4.2. LIQUID SYSTEM

The liquid system is modelled using 14 elements and 17 nodes. At each node, the conservation of mass and momentum are solved to obtain the mass flow rate and pressure. The model outputs are shown from Figure 9 to Figure 12.

ISBN - 978-93-95038-50-8

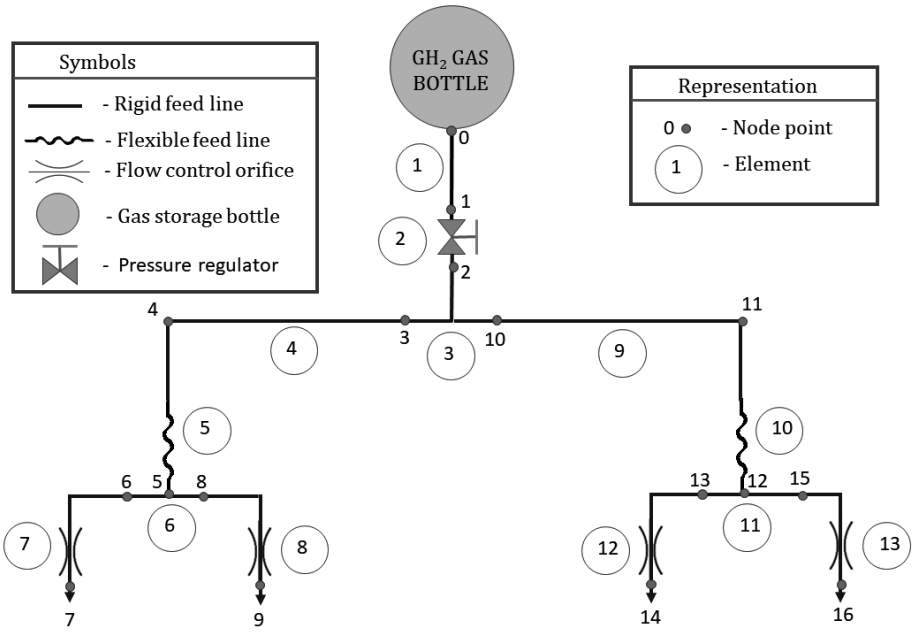

Figure 3: Mathematical model of GH2 feed system

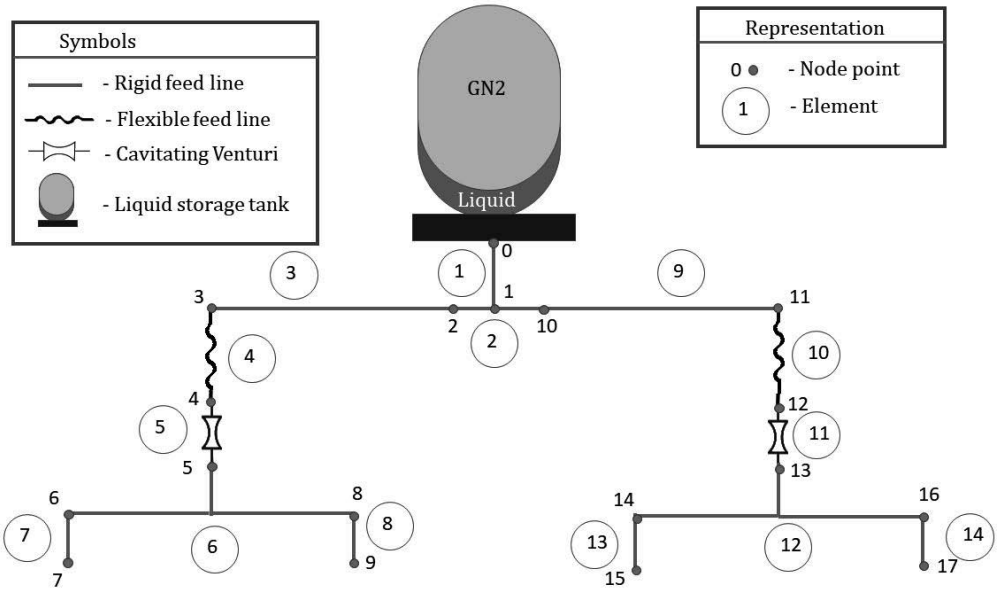

Figure 4: Mathematical model of liquid feed system

5. RESULT AND DISCUSSIONS

The temperature in the GH_2 bottle drops due to adiabatic expansion (Refer Figure 5). The flow control orifices are designed to maintain constant flow rate at constant inlet pressure and temperature. The GH_2 regulator maintains constant pressure at the inlet of the control orifices. The main flow rate and the emulsification flow rate of GH_2 increases as a result of the increase in gas density due to reduction in bottle temperature. Figure 8 shows the variation of regulator

exit temperature versus time and inlet temperature. The rate of change in the emulsification flow rate reduces as the main flow is cut-off at 2 s. Calibrated flow control orifices are passive flow control systems. Steady flow rate of GH_2 in the system can be made by the using a flow control valve which is an active flow control device. But to control the flow using such a valve, a mass flow measurement device and associated instrumentation is also required, which increases the system complexity. Present system configuration is adopted since, the minimum flow rate requirement of GH_2 is met. The increase in GH_2 flow rate as shown in Figure 6 has two effects. It reduces the gas bottle pressure at a rate that is higher than expected. Also, the increased flow rate induces a higher pressure drop in the feed lines. The second problem is solved by appropriately sizing the feed lines. The first problem is solved by increasing the pressure rating of the gas bottle using a composite overwrap. Both the solutions are arrived at considering the system envelope constraints. The envelope constraint on the bend radius of the feed line from gas bottle to regulator decided the maximum line size which could be used. The maximum outer diameter of the composite gas bottle also was decided by the system envelope constraint.

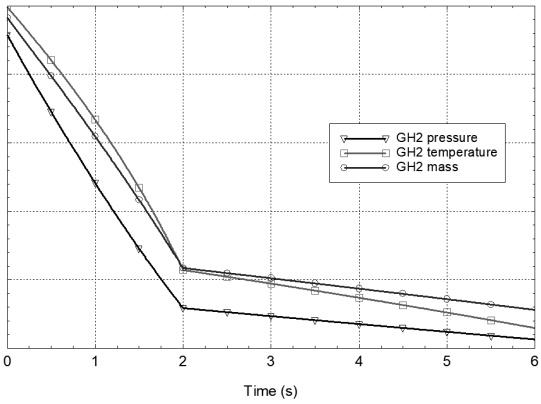

Figure 5: GH2 bottle parameters

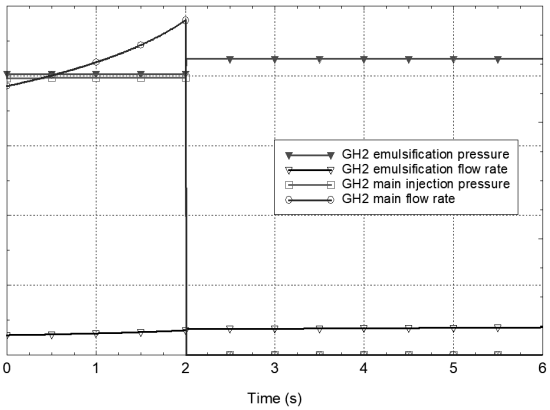

Figure 6: GH2 injection parameters

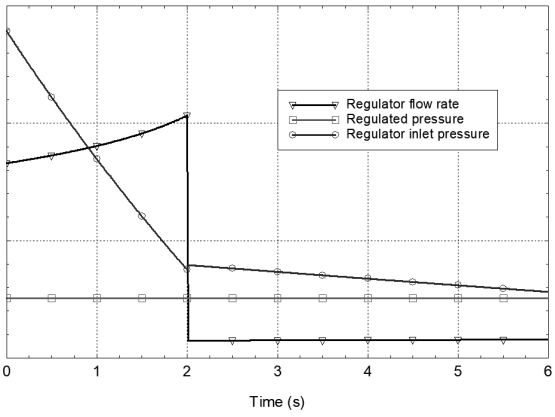

Figure 7: GH2 regulator parameters

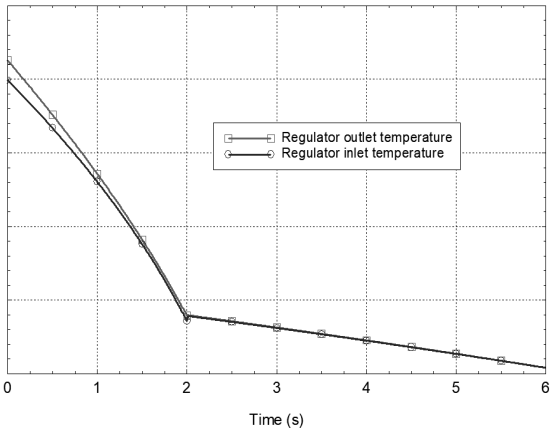

Figure 8: GH2 regulator thermodynamics

Gaseous hydrogen system model outputs

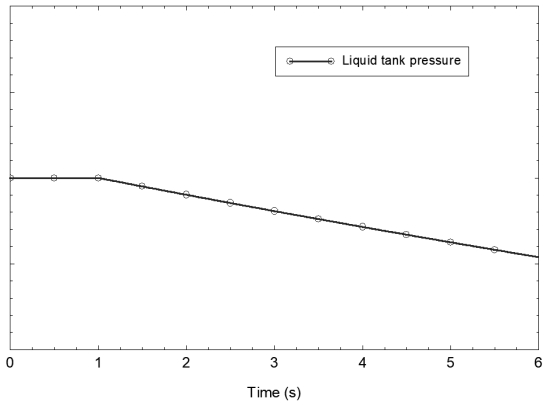

Figure 9: Liquid storage tank parameters

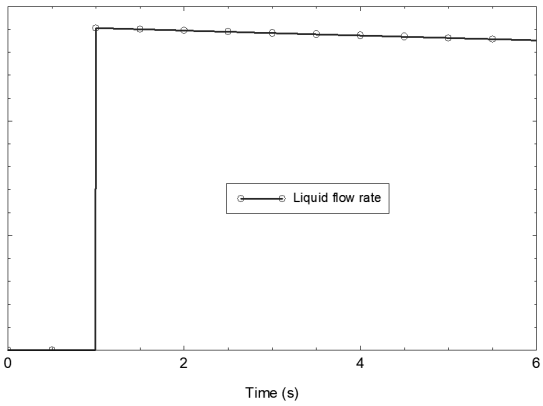

Figure 10: Liquid hydrocarbon flow rate

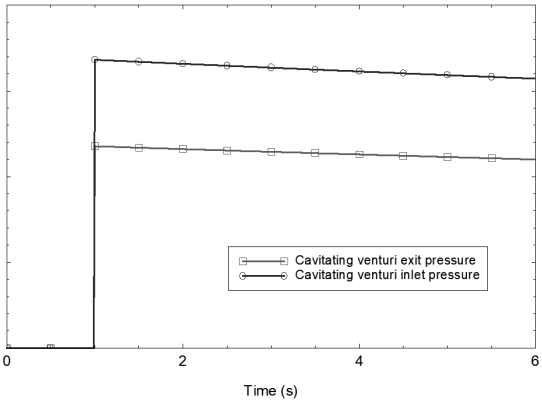

Figure 11: Cavitating venturi parameters

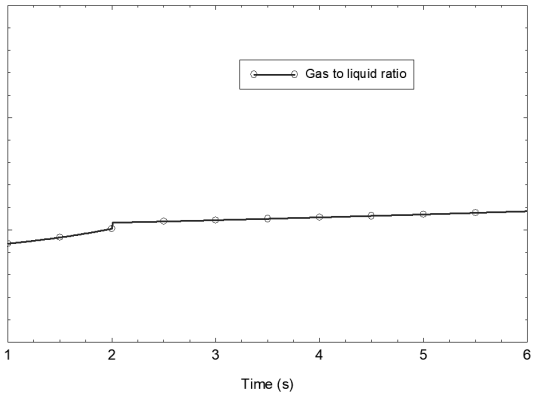

Figure 12: Gas to liquid (GLR) mass ratio

Liquid feed system model outputs

In the absence of an active pressurization system, the liquid storage tank operates in a blow-down mode. It results in reduction of the tank pressure during operation as shown in Figure 9. The reduction in tank pressure also results in a reduction in liquid hydrocarbon flow rate as shown in Figure 10. The presence of cavitating venturi in the system has two effects. The first one is mentioned earlier. The second effect is the presence of recovery factor. The recovery factor which is less than unity ensures that the variation of the venturi downstream pressure is less than that of the upstream pressure, as seen in Figure 11. Hence, the venturi also provides some damping to the upstream pressure variations. The sizing of the venturi is done to ensure the minimum liquid flow rate to the engine at the lowest inlet pressure. A standalone type propellant tank is chosen for the liquid hydrocarbon due to the system envelope constraints. The high volume of the tank ensures a variation in ullage pressure and flow rate within the acceptable limits.

The reduction in liquid flow rate and the increase in GH_2 emulsification flow rate results in an increase in Gas to Liqui Ratio (GLR) for the scramjet engine's effervescent injector. An increase in GLR results in reduction in mean droplet size [5], which results in an enhanced engine performance.

ISBN - 978-93-95038-50-8

6. CONCLUSIONS

A Fuel Feed System is designed for Dual Fuel Scramjet engine using a system approach, considering operational requirements and envelope constraints. Mathematical modelling of the system shows that the throughout the operating duration, the feed system parameters are meeting the operational requirements.

ACKNOWLEDGEMENTS

Sincere thanks to Shri. Mohan Lal B, Dr. C Suresh Kumar, Dr. P Arun Kumar for their valuable guidance throughout the activity.

REFERENCES

1. Agrawal, G., Joseph, J., Agarwal, D.K., Mohanlal, B., Pisharady, J.C., Kumar, S.S. and Babu, C.S., Scramjet Fuel Feed System Modelling for Flight and Ground Expulsion Trials.
2. Bandyopadhyay, A. and Majumdar, A., 2007, August. Modeling of compressible flow with friction and heat transfer using the generalized fluid system simulation program (GFSSP). In Thermal Fluid Analysis Workshop (TSAWS).
3. Sokovnin, O.M., Zagoskina, N.V. and Zagoskin, S.N., 2019. Using a thermodynamic approach to estimate a temperature drop of natural gas in a pressure regulator. Journal of Applied Mechanics and Technical Physics, 60(3), pp.451-456.
4. Oppenheim, B.W. and Rubin, S., 1993. Advanced Pogo stability analysis for liquid rockets. Journal of Spacecraft and Rockets, 30(3), pp.360-373.
5. Sovani, S.D., Sojka, P.E. and Lefebvre, A.H., 2001. Effervescent atomization. Progress in energy and combustion science, 27(4), pp.483-521.
6. Waller, Jess & Nichols, Charles & Wentzel, Daniel & Saulsberry, Regor. (2011). Use of Modal Acoustic Emission to Monitor Damage Progression in Carbon Fiber/epoxy Composites. AIP Conference Proceedings. 1335. 10.1063/1.3592036.

Monte Carlo Based Tolerance Analysis of Sub-systems in Cryogenic Umbilicals

Jishnu T R*, Vaibhav Amalak Ahire,
Hemendra Kumar Dhurandher, Dilip V, Sathis Kumar B, Alex A

Control Systems & Components, Liquid Propulsion Systems Centre,
Indian Space Research Organisation, Thiruvananthapuram, Kerala, 695547
jishnu_tr@lpsc.gov.in

ABSTRACT

The space reforms in India have opened up the space market and in turn opened a window of opportunity for entry of private players into the market. The vision of Indian Space Research Organisation (ISRO) is to change the supply-based model of space sector to demand-based model. To capture the foreign and domestic launch vehicle market, the building costs of the launch vehicle needs to be optimised. The concepts of lean manufacturing, design optimisation, topology optimisation etc., need to be brought in at the design phase to achieve this while mass manufacturing is planned for the launch vehicles. Dimensional Tolerance analysis have been extensively used in mass manufacturing industries to model how the deviations in part level are propagating to assembly. Though computationally expensive, Monte Carlo method is one of the most common tools used for this analysis. Based on a Probability Distribution Function (PDF), number of part dimensions are generated within the tolerance band and the distribution of assembly parameter is evaluated based on geometrical dependency. The sensitivity of dimensional/ geometrical tolerances on assembly critical parameters can be effectively studied by this method. Fluid Control Components in launch vehicles employ a large number of fabricated parts and the assembly of these elements to form a sub-assembly will bring out huge number of critical assembly parameters. Not achieving these specifications can cause hardware rejection, thus increasing the cost of production & delay in project schedule. This study presents the tolerance analysis of certain sub-assemblies used in cryogenic umbilical systems employed in ISRO. The sensitivity analysis of geometrical parameters also presented. These results can of paramount importance to fine tune the design & fabrication drawings at the time of mass manufacturing of parts.

Keywords: *Tolerance Analysis, Monte Carlo Simulation, Probability Distribution Function, Skewness*

1. INTRODUCTION

Geometrical dimensioning and tolerancing has always been an important aspect in mechanical engineering design. The tolerances on each dimension is necessary since absolute dimensions cannot be achieved through any manufacturing process. In an assembly, the tolerances on part level combine to form critical dimensions termed as Functional Critical Dimensions (FCDs).

Tolerance analysis has been one of the major tools by which manufacturing industries improved their production & minimised the cost [1]. Various methods of tolerance analysis are employed by different researchers [2-5]. The dimensions in an assembly is represented as vectors in vector loop method [6,7]. The dimensional, kinematic & geometric variations are taken into considerations in vector loop method. The variation method employs a parametric model in which the geometry is modelled using mathematical equations and the shape & size of various features are studied using this [8,9]. The kinematic relations between two surfaces are modelled using six small displacement vectors and used for tolerance analysis in Small Displacement Torsor (SDT) method [10-12]. In the matrix method, displacement vectors are employed at each tolerance region to derive the mathematical model and analyse the tolerancing [13-15]. The Monte Carlo (MC) analysis gives a probabilistic approach of the tolerances and is the simplest tolerance analysis tool compared to other methods [16-19]. In

*Corresponding author: E-mail: jishnu_tr@lpsc.gov.in

ISBN - 978-93-95038-50-8 https://doi.org/10.37285/bsp.sasat2023.04

MC analysis, functional relationships between the component dimensions is formed. The part dimensions are randomly generated conforming to a particular probability distribution function. The distributions of the FCD/ Assembly Critical Dimensions (ACD) are obtained from the functional relationship [18]. The sensitivity of different geometric tolerance features can also be studied using this tool.

Indian Space Research Organisation (ISRO) employs cryogenic umbilical for the servicing the cryogenic stages of its launch vehicles. Umbilicals are used in launch vehicles for electrical & propellant servicing, environmental conditioning etc., [20]. Essentially any of these systems consist of a flight segment (which will be fastened to the launch vehicle), ground segment (which is the interface to launch pad and separates at a specific time) and a lock with separation mechanism [21]. The cryogenic umbilicals contains two major sub-assemblies namely flight segment & ground segment, which are mated together through collet lock at the centre. The ground plate sub-assembly contains two closely toleranced guide pins and the other sub-assembly contains recesses for these pins. The clearance between the pin & the recess is an important dimension, since it can directly affect the assembly of ground plate sub-assembly to flight plate sub-assembly as well as the separation dynamics of the umbilical. This study finds out the distribution of guide pin clearances using the Monte Carlo tolerance analysis. The sensitivity of geometrical parameter is also studied. The ideal band of clearance is proven during the qualification studies of the umbilical and if the assembly does not meet this the parts will be rejected. The results of the MC analysis can be used to tune the dimensions & geometrical parameters such that the clearance distribution is well within the ideal band.

The paper is organised in four sections. The following section explains the methodology and problem formulation. Section 3 presents the results & discussion followed by conclusions in section 4.

2. METHODOLOGY

2.1 DIMENSIONAL RELATIONSHIPS

The cryogenic umbilical sub-assembly houses two plate sub-assemblies which are mated against each other through centre. Flight plate sub-assembly consists of flight plate & allied sub-assemblies whereas ground plate sub-assembly consists of ground plate and allied sub-assemblies.

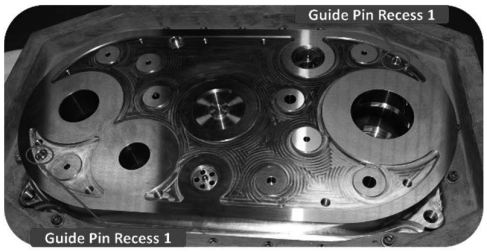

Figure 1: Flight Plate sub-assembly

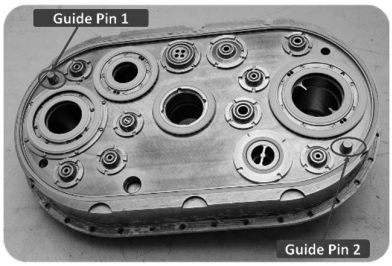

Figure 2: Ground Plate Sub-assembly

There are two guide pins which are assembled in to the ground plate and the flight plate houses the recesses for these pins. Figure 1 & Figure 2 shows the photographs of the plate sub-assemblies employed in Cryogenic Umbilicals. Figure 3 shows the dimensions of the parts in details. In both flight & ground plate sub-assemblies first guide pin location on the left side is dimensioned with respect to the centre (Refer Figure 3 (i), (ii)). The second guide pin location on the right side is dimensioned with respect to the first guide pin location. The ground plate

ISBN - 978-93-95038-50-8

sub-assembly has a female thread into which the guide pin is fastened (Refer Figure 3 (iii)). The assumptions taken for the analysis are as follows;

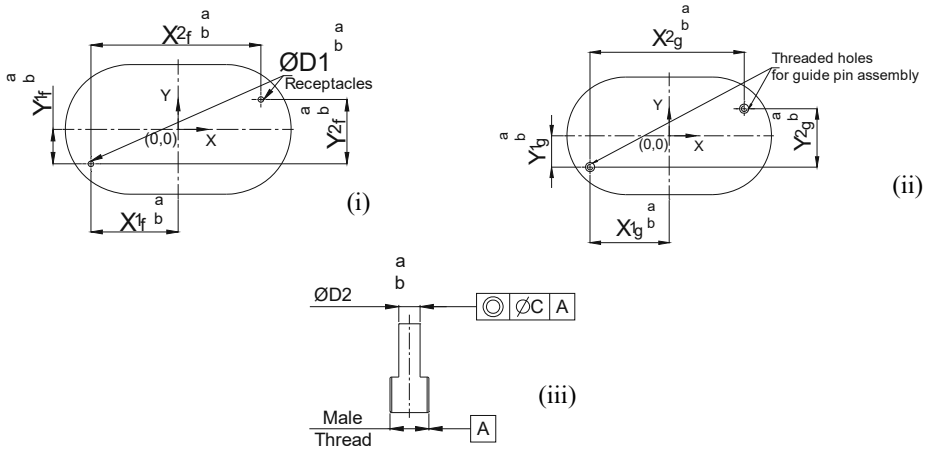

Figure 3: Part Dimensions (i) Flight Plate (ii) Ground Plate (iii) Guide Pin

- The deviation between the centre of the plate sub-assemblies during mating is neglected for the current study. Position of the holes are mentioned with respect to the centre in both flight & ground plate sub- assembly. Hence it is assumed that the centres are perfectly aligning.
- The tolerances on the threads are neglected.

Table 1 shows the details of the parameters from Figure 3. The tolerance band is described as (a, b) for representation. The line diagram to estimate the clearance between guide pin & recess is detailed in Figure 4.

Table 1: Dimensional details of parts

Plate	Dimension	Nominal Value
Flight Plate	Hole 1 X co-ordinate	$-X^1_f$
	Hole 1 Y co-ordinate	$-Y^1_f$
	Diameter of Hole 1 & 2	D_1
	Hole 2 X co-ordinate	$-X^1_f + X^2_f$
	Hole 2 Y co-ordinate	$-Y^1_f + Y^2_f$
Ground Plate	Threaded hole 1 X co-ordinate	$-X^1_g$
	Threaded hole 1 Y co-ordinate	$-Y^1_g$
	Threaded hole 2 X co-ordinate	$-X^1_g + X^2_g$
	Threaded hole 2 Y co-ordinate	$-Y^1_g + Y^2_g$
Guide pin	Concentricity for guide pin 1&2	C
	Angular location of guide pin center	θ
	Diameter of guide pin 1 & 2	D_2

From Figure 4, assuming that the guide pin centre falls at (0.5C, θ), the location of the first guide pin centre with respect to ground plate centre co-ordinate can be represented as;

$$\left(X^1_{gp}, Y^1_{gp}\right) = \left(\left(-X^1_g + (0.5C\cos(\theta))\right), \left(-Y^1_g + (0.5C\sin(\theta))\right)\right) \quad (1)$$

The clearance for first guide pin can be obtained as;

$$Cgp1 = \left(0.5 * D1 - 0.5 * D2 - \sqrt{(X^1gp - X^1{}_f)^2 + (Y^1gp - Y^1{}_f)^2}\right) \quad (2)$$

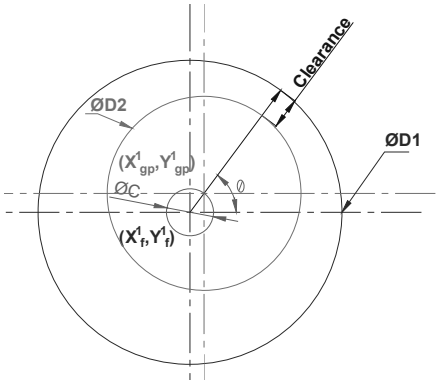

Figure 4: Guide Pin Clearance Details

Similarly, for the second guide pin, the center with respect to ground plate center is;

$$\left(X^2{}_{gp}, Y^2{}_{gp}\right) = \left(\left((-X^1{}_g + X^2{}_g) + (0.5C\cos(\theta))\right), \left((-Y^1{}_g + Y^2{}_g) + (0.5C\sin(\theta))\right)\right) \quad (3)$$

The clearance of second guide pin can be estimated as;

$$Cgp2 = \left(0.5 * D1 - 0.5 * D2 - \sqrt{(X^2{}_{gp} - (-X^1{}_f + X^2{}_f))^2 + (Y^2{}_{gp} - (-Y^1{}_f + Y^2{}_f)^2}\right) \quad (4)$$

Equations (2) & (4) represents the functional relationship of the guide pin clearances, *Cgp1 & Cgp2* with part level dimensions & geometrical parameters.

2.2 MONTE CARLO ANALYSIS

The objective of the study is to carry out the tolerance analysis of guide pin clearances for the plates & conduct the sensitivity study. Equations (2) & (4) gives the functional relationships of the part level dimensions. The parameters taken for the case study is listed in Table 2.

Table 2: Case study parameters (All dimensions in mm)

Sl. No.	Dimension	Nominal Value	Upper Limit	Lower Limit
1	$-X^1{}_f$	*190*	*190.01*	*189.99*
2	$-Y^1{}_f$	*75*	*75.01*	*74.99*
3	D_1	*12.025*	*12.05*	*12*
4	$X^2{}_f$	*370*	*370.01*	*369.99*
5	$Y^2{}_f$	*140*	*140.01*	*139.99*
6	$-X^1{}_g$	*190*	*190.01*	*189.99*
7	$-Y^1{}_g$	*75*	*75.01*	*74.99*
8	$X^2{}_g$	*370*	*370.01*	*369.99*
9	$Y^2{}_g$	*140*	*140.01*	*139.99*
10	*C*	*0*	*+0.03*	*0*
11	D_2	*11.965*	*11.98*	*11.95*

ISBN - 978-93-95038-50-8

The steps for the analysis are as follows;

- Random numbers are generated for all the 11 parameters listed in Table 2 assuming normal distribution. The mean of the distribution is the nominal value and the standard deviation is $1/6^{th}$ of the tolerance band.
- The clearance is estimated for each of these set of dimensions. A computer program was written to get this using MATLAB 2022 software.
- The mean, standard deviation of the clearance data was obtained and the tolerance band is predicted using $\pm 3\sigma$ where σ is the standard deviation.
- The concentricity is varied and the normal plots for each clearance were plotted.

3. RESULTS & DISCUSSIONS

3.1 GUIDE PIN CLEARANCE

The Monte Carlo analysis was done with a sample size of 2000. The random dimensions were generated conforming to normal distribution. The distributions of the generated data for flight plate recess co-ordinates are shown in Figure 5. Similar data was produced for guide pin co-ordinates, hole diameter, concentricity & guide pin diameter.

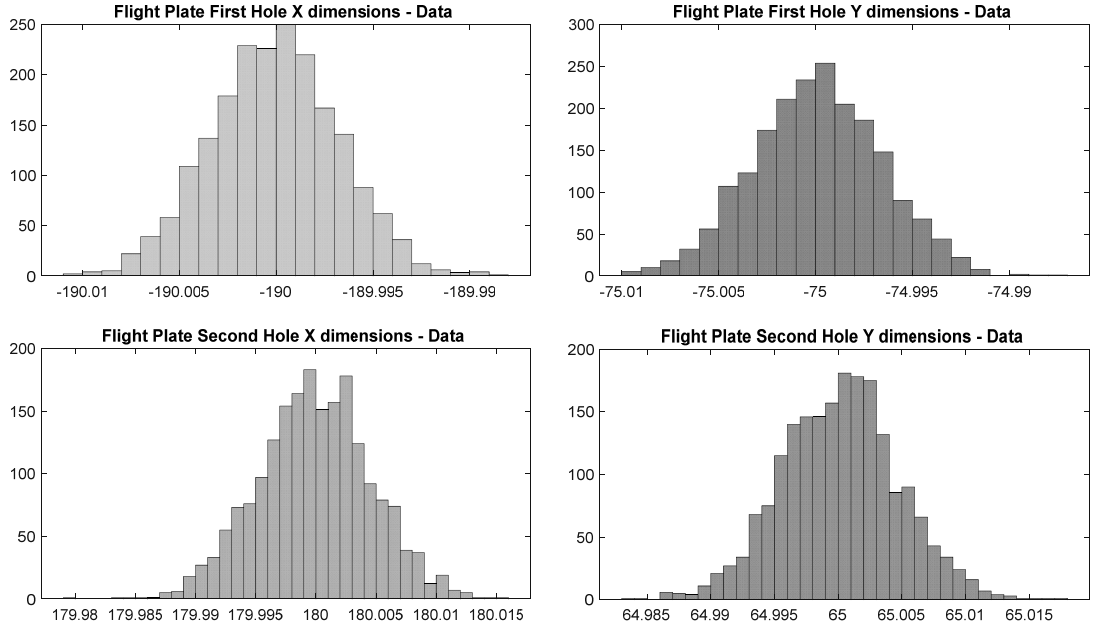

Figure 5: Flight plate hole co-ordinates distribution

Using the MATLAB program, the distribution of guide pin clearances was found out. The Figure 6 shows the histogram plots of the clearance distribution. From the histogram plot, it is evident that the guide pin clearance data follows a normal distribution. The co-efficient of skewness for both the distributions are between -0.5 & 0 and the co-efficient of kurtosis is approximately 3 which ensures the normal distribution.

Table 3: Guide Pin Clearance Distribution

Parameter	Mean (mm)	Standard Deviation	Lower Limit (mm)	Upper Limit (mm)	Co-efficient of Skewness	Co-efficient of Kurtosis
Guide Pin 1 Clearance	*0.026*	*0.006*	*0.009*	*0.043*	*-0.22*	*3.1*
Guide Pin 2 Clearance	*0.024*	*0.006*	*0.006*	*0.045*	*-0.3*	*3.2*

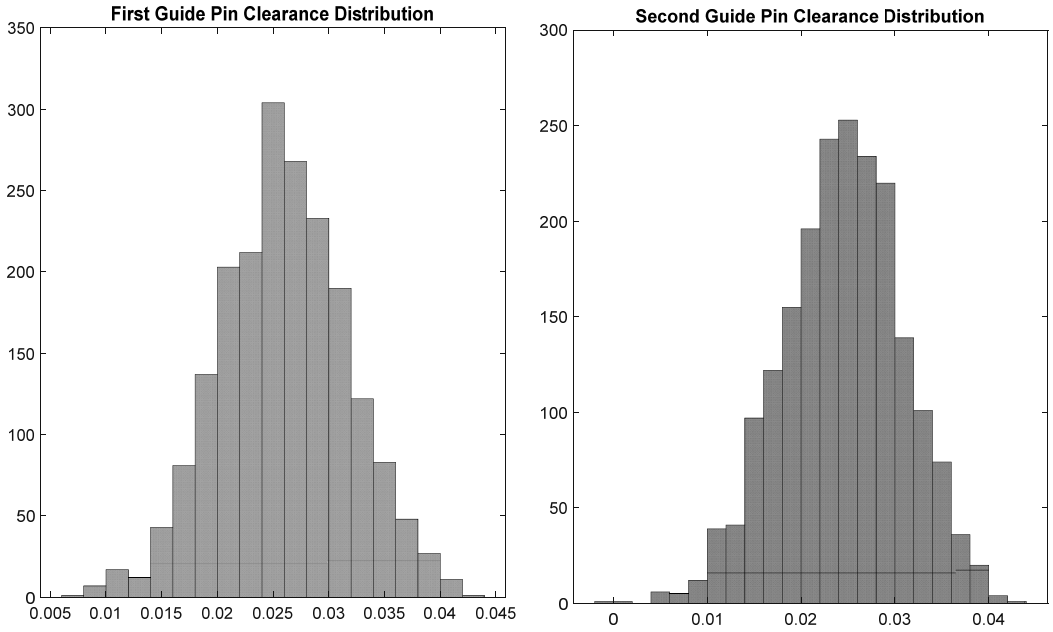

Figure 6: Guide Pin Clearance Data Histograms for Guide Pin 1 & 2

3.2 SENSITIVITY STUDY

The sensitivity analysis was carried out for the concentricity value. The analysis was done for different values. Table 4 shows the results. Figure 7 shows the normal plot of the guide pin 1 & 2 clearances for different concentricity values.

Table 4: Senistivity Study Results

Concentricity (mm)	Guide Pin 1 Mean (mm)	Guide Pin 1 Standard Deviation	Guide Pin 2 Mean (mm)	Guide Pin 2 Standard Deviation
0.03	*0.026*	*0.006*	*0.024*	*0.006*
0.06	*0.025*	*0.006*	*0.024*	*0.007*
0.09	*0.024*	*0.006*	*0.023*	*0.007*
0.12	*0.023*	*0.007*	*0.022*	*0.008*

ISBN - 978-93-95038-50-8

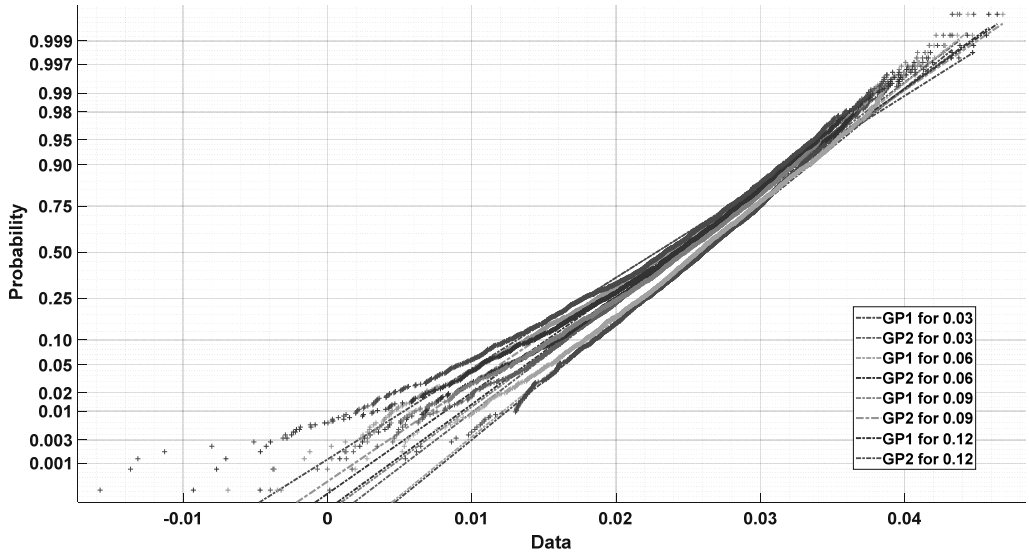

Figure 7: Normal plot of guide pin clearances for different concentricity values

The results indicate that during mass manufacturing, the guide pin clearance will have a mean of 0.026 & 0.024 for guide pin 1 & 2 respectively. The 99% confidence intervals are also estimated from the analysis which is shown in Table 3 upper & lower limit columns. The concentricity variation for four different values did not affect the guide pin clearances significantly.

4. CONCLUSIONS

The conclusions of the study can be listed as follows;

- The Monte Carlo based tolerance analysis was used to find out the distribution of guide pin clearances of plates used in cryogenic umbilicals. The analysis shows that the resulting data follows a normal distribution. The mean and standard deviation of the distribution were found out. The clearance values are well within the clearances qualified for the umbilicals. Hence the dimensions need not be revised.
- The upper & lower limit for the 99% confidence interval of guide pin clearances are found out (refer Table 3). During mass manufacturing, keeping the FCD clearances within this band can maintain the rejection during assembly to <1%.
- Sensitivity study was carried out for the concentricity of the guide pin. Though the variation of concentricity did not affect the mean and standard deviation, as the concentricity error increases, the distribution was found to become long tailed.
- The current study is restricted to a particular case study in a sub-system. This can be extended to various sub-systems to optimize the assembly tolerances & optimize FCD dimensions.

REFERENCES

1. Chase, K.W., Parkinson, A.R. “A survey of research in the application of tolerance analysis to the design of mechanical assemblies”, Research in Engineering Design 3, 23–37 (1991), https://doi.org/10.1007/BF01580066
2. Marziale, M., Polini, W. “A review of two models for tolerance analysis of an assembly: Jacobian and Torsor”, Int J Comput Integr Manuf, 2011;24(1):74-86

3. Laperrière L., Desrochers, A. “Modeling assembly quality requirements using Jacobian or screw transforms: a comparison Assembly and Task Planning”, 2001, Proceedings of the IEEE International Symposium on IEEE, 2001: 330-336
4. Ameta, G., Serge, S., Giordano, M. “Comparison of spatial math models for tolerance analysis: tolerance-maps, deviation domain, and TTRS[J]”, Journal of Computing and Information Science in Engineering, 2011, 11(2): 021004.
5. Chen, H., Jin, S., Li, Z. “A comprehensive study of three-dimensional tolerance analysis methods[J]”, Computer-Aided Design, 2014, 53: 1-13.
6. Chase, K.W., Gao, J. and Magleby, S.P., 1995. “General 2-D tolerance analysis of mechanical assemblies with small kinematic adjustments”, Journal of Design and Manufacturing, 5(4), 263-274.
7. Chase, K.W., Gao, J., Magleby, S.P. and Sorensen, C.D., “Including geometric feature variations in tolerance analysis of mechanical assemblies”, IIE Transactions, 1996, 28(10), 795- 807.
8. Gupta, S., Turner, J U. “Variational solid modeling for tolerance analysis[J]”, Computer Graphics and Applications, IEEE, 1993, 13(3): 64-74.
9. Li, B., Roy, U. “Relative positioning of toleranced polyhedral parts in an assembly[J]”, IIE Transactions, 2001, 33(4): 323-336.
10. Bourdet, P., Mathieu, L., Lartigue, C. “The concept of the small displacement torsor in metrology[J]”, Series on Advances in Mathematics for Applied Sciences, 1996, 40: 110-122.
11. Bourdet, P., Ballot, E. “Geometrical behavior laws for computer-aided tolerancing [M]”, Computer-Aided Tolerancing, Springer Netherlands, 1996: 119-131.
12. Legoff, O., Villeneuve, F., Bourdet, P. “Geometrical tolerancing in process planning: a tridimensional approach[J]. Proceedings of the Institution of Mechanical Engineers, Part B”, Journal of Engineering Manufacture, 1999, 213(6): 635-640.
13. Desrochers, A., Rivière, A. “A matrix approach to the representation of tolerance zones and clearances[J]”, The International Journal of Advanced Manufacturing Technology, 1997, 13(9): 630-636.
14. Whitney, D E., Gilbert, O L., Jastrzebski, M. “Representation of geometric variations using matrix transforms for statistical tolerance analysis in assemblies [J]”, Research in Engineering Design, 1994, 6(4): 191-210.
15. Serrano-Mira, J., Rosado-Castellano, P., Romero-Subirón, F., Bruscas-Bellido, G M., Abellán-Nebot, J.V. “Incorporation of form deviations into the matrix transformation method for tolerance analysis in assemblies”, Procedia Manufacturing 41, 2019, 547-554.
16. DeDoncker, D., Spencer, A. “Assembly tolerance analysis with simulation and optimization techniques[R]”, SAE Technical Paper, 1987.
17. Grossman, D D. “Monte Carlo simulation of tolerancing in discrete parts manufacturing and assembly[J]”, 1976.
18. Huiwen, Yan., Xiangji, Wu., Jiangxin, Yang, “Application of Monte Carlo Method in Tolerance Analysis”, 13th CIRP conference on Computer Aided Tolerancing, Procedia CIRP 27 (2015) 281 – 285
19. Samuel, H. Huang., Qiu, Liu., Rami Musa, “Tolerance-based process plan evaluation using Monte Carlo simulation”, International Journal of Production Research, 42:23, 4871-489, 2004, DOI: 10.1080/0020754042000264608
20. SP-8061, NASA, "Interaction with Umbilicals & Launch Stand," NASA Space Vehicle Design Criteria (Structures), August 1970.
21. Hemendra Kumar Dhurandher, Vaibhav Ahire, Dilip V, B Sathis Kumar and Krishnanandan V, "Fall Trajectory Finalisation for Cryogenic Umbilical," in LAMSYS, Trivandrum, 2017.

ISBN - 978-93-95038-50-8

Novel Design of a Joint with Translational Freedom for Propellant Tank Anti-Slosh Baffle System

Deepak K*, Jayesh P, Ravi Ranjan Kumar and Reji Joseph

Liquid Propulsion Systems Centre,
Indian Space Research Organisation
Thiruvananthapuram, Kerala, 695547
Email: dkavailable@gmail.com

ABSTRACT

Launch vehicles stages are fuelled by different propellants at ambient and cryogenic temperatures, which are stored in propellant tanks. The propellant tanks are subjected to pressure, structural, aerodynamic, thermal and slosh loads. Anti-slosh baffles are provided inside propellant tanks to provide adequate slosh suppression. These baffles are mounted inside tanks within limited space, along with other internal systems. The pressure and structural loads induce axial dilation of propellant tanks and rotation of end rings. Axial freedom at baffle mounting joints is required to reduce the mechanical reaction loads at the joints caused by tank deformation, under pressure and axial loads. The anti-slosh baffle joints should have sufficient freedom to manage such tank dilations, which is achieved by providing translational freedom to the joints, without compromising the structural integrity. Conventional joints with translational freedom have complex joining procedure, demand space and access requirement. Only limited joining techniques like bolting and riveting can be employed in anti-slosh baffle systems to meet the assembly and integration requirements. The assembly of anti-slosh baffle sub-assemblies inside propellant tanks is easier with joints comprising of rivets. This paper presents a novel design of a riveted joint with translational freedom for anti-slosh baffles inside a propellant tank. The design is validated with a quasi-static tensile test and the qualified joint is adopted in engineering of the system for flight.

Keywords: *Propellant tank; Anti-slosh baffle; Tensile test; Translational freedom*

1. INTRODUCTION

Launch vehicles have multiple stages designed to achieve diversified mission requirements. The liquid propulsion stages of a launch vehicle are powered using different propellants. Depending on the requirements, these are stored at ambient or cryogenic temperatures in propellant tanks. Apart from storing propellants, the tanks also act as primary structures of the vehicle [1], because of which these are subjected to various loads namely pressure, structural, aerodynamic, thermal and slosh.

Propellant tanks deform under the structural and pressure loads. The systems mounted to propellant tanks should have sufficient stiffness and freedom of movement to withstand these loads. Also, the inert mass of the vehicle is to be minimized to increase its payload capacity. Hence, designing joints in propellant tanks with sufficient joint strength, stiffness, degrees of freedom, in addition to optimised mass and limited space is challenging.

The slosh, which is the oscillations of the free surface of the propellant tank induce additional load on the tank. The slosh load, if not controlled, can lead to vehicle instability and huge load on tank structure, leading to failure of the mission. Slosh suppression devices are used to dampen the free surface motion of propellants, and prevent vehicle instability induced due to slosh [2]. Anti-slosh baffles used in propellant tanks as an effective way of supressing slosh, reducing the duration and amplitude of oscillations [3]. These are mounted inside tanks within limited space, along with other internal systems. The slosh dampening systems are mass optimised structure made of sheet metal primely to dampen the slosh

*Corresponding author: E-mail: dkavailable@gmail.com

effects. The joints of the slosh dampening system to the tank shall have required translational freedom to avoid the structural load transfer taking place through the slosh members.

The particular tank requires a matrix structure of horizontal and vertical baffles. The baffle structure is connected between the fore and aft end rings of the propellant tank. The internal pressure and structural loads induce axial dilation of the fuel tanks and rotation of end rings. This demand for axial freedom at baffle mounting joints to reduce the mechanical reaction loads at the joints, without compromising the structural integrity. Only limited joining techniques like bolting and riveting can be employed in these joints to meet the assembly and integration requirements.

If the bolted joints are used, high preload of the order of 60% of yield strength of the bolt material is to be applied to avoid bolt loosening under vibration. However, this preload will affect the translational freedom of the joint. To overcome this, special designs with steel bushes in the bolted holes are to be employed. The length of the bush is to be designed in such a way that the preload does not act on the anti-slosh baffle plates. The steel bush should not yield and the anti-slosh baffle plate should not be loose. This will result in a higher hole diameter and only a few fasteners can be provided in the available space, which may not be structurally acceptable.

Riveted joints are prepared for the assembly of anti-slosh baffle sub-assemblies inside propellant tanks made of sheet metal, and it requires lesser space than bolted joints. This paper describes about the novel design of a riveted joint with translational freedom in the anti-slosh baffles of a fuel tank. Detailed FE analysis is carried out to finalise the riveted joint. The design is validated with a quasi-static tensile test and the qualified joint is adopted in engineering of the system for flight.

2. LITERATURE REVIEW

Different studies on bolted and riveted structural joints used in aerospace structures are reviewed to evaluate its performance. Li et al. [4] conducted experiments on composite riveted joints used for aircraft applications. They studied the tensile response and failure of seven CFRP riveted joints with circular holes, at quasi-static (0.5 mm/min) and dynamic (4 m/s and 8 m/s) loading rates.

The variation of tensile strength with loading rate was found to have no effect on the joints. It was also shown that the average total energy absorption of the joints increased and the modes of failure of the joints changed with increase in the loading rate.

Szolwinski and Farris [5] analysed a single-lap joint structure to obtain the residual stress field in the joint. They included the results of rivet installation process parameters viz. quasi-static loading and squeeze force-controlled riveting, obtained from the FE model, to the final residual stress field. A coefficient of friction of 0.2 was used between all contact surfaces, during the FE analysis. The model was validated experimentally. The analysis showed that the residual stress field depended on the through-thickness restraint because of the rivet. It also showed that near the rivet hole periphery, a zone of compressive residual hoop stress is dominant, whereas a zone of tensile residual hoop stress is dominant away from the hole. The residual hoop stress zones can impact the propagation of fatigue cracks.

The quality of rivet formation was studied by Hossein Cheraghi [6] with reference to process parameters like squeeze force, rivet length, tolerances on rivets and hole diameters. The effect of the above-mentioned parameters was studied numerically and statistically. He used a frictional value of 0.2 for modelling all contacts in the numerical model. It was

ISBN - 978-93-95038-50-8

concluded that if the rivet hole diameter decreases, or if the rivet diameter increases, the range of squeeze force increases. It was found that if the rivet length and diameter increase, the amount of squeeze force needed to drive a rivet increases.

Honglun Huan and Min Liu [7] experimentally evaluated the structural behaviour of riveted lap joints with squeeze force. The study comprised of static strength experiments and FE analysis. Three levels of squeeze forces: 28 kN, 31 kN and 34 kN were used for the study. The coefficient of friction was specified as 0.18 for the FE analysis. It was shown that the joint stiffness is not affected by increasing the squeeze force. But the joint strength decreases with an increase in squeeze force. The joint stiffness gradually decreases with an increase in the tensile load. It was also proven that under static load, the first hole of the outer sheet fails first, due to the highest amount of load transmission and secondary bending.

Joints with translational freedom are commonly used in the railway industry, on joints in railway tracks to accommodate axial displacements due to temperature differences in long welded rails. In a switch expansion joint, two running rails viz; a stock rail and a tongue rail, slide against each other [8]. The expansion joints limit the degrees of freedom in lateral direction on Continuously Welded Rail (CWR) tracks.

Wald et al. [9] predicted the stiffness of bolted joints in steel plates with slotted holes, using component method. The slotted holes are perpendicular to the applied force. As compared to circular holes, it was observed that bolted joints with slotted holes perpendicular to the applied force had lower stiffness and higher deformation capacity.

It can be observed that riveted and bolted joints are widely used in aircraft and aerospace industry. Many researchers studied the behaviour of these joints under different influencing parameters. Finite element analysis has been used in predicting the influence of squeeze force on rivet head formation, fatigue life, crack formation, residual stress analysis of riveted joints. The FE models are validated using tensile tests, mainly quasi-static, carried out at a very low loading rate. Though study has been conducted on the behaviour of bolted joints with translational freedom, study of such riveted joints is not conducted. The joint under present study has translational freedom when the propellant tank deforms under loads. Being a new design, a quasi-static tensile test is done on a test specimen simulating the joint, to experimentally validate the design.

3. DESIGN OF RIVETED JOINT WITH TRANSLATIONAL FREEDOM

The baffle in this fuel tank is a matrix structure consisting of 8 vertical and 5 horizontal members. The location of baffles is finalised after detailed slosh analysis. Figure 1 shows the tank internal view with anti-slosh baffles. The vertical baffles are classified as top (in the fore end dome), middle (in the cylindrical shell) and bottom (in the aft end dome) vertical baffles. The middle vertical baffles are attached to the projections on end rings at the fore and aft ends. The middle vertical baffles are connected to brackets fastened to tank end rings by Ø5 mm universal head V65 rivets (ultimate shear strength = 265 N/mm^2). Constrained joint will result in a stress level beyond the ultimate shear strength of the rivet material. The size and arrangement of the rivets are a trade-off between the margin w.r.t the ultimate shear strength and the space constraints in the ant-slosh baffles. The rivets are arranged in such a way that the edge distance between the rivet hole and anti-slosh baffle plates are ensured. In addition to the axial load condition, rotation of the tank end ring flanges is also noticed due to the inward movement of the ring region under internal pressure. For this, extensive Finite

ISBN - 978-93-95038-50-8

Element Analysis (FEA) was carried out using ANSYS 18.1 considering the rotation and translational freedom at the joint.

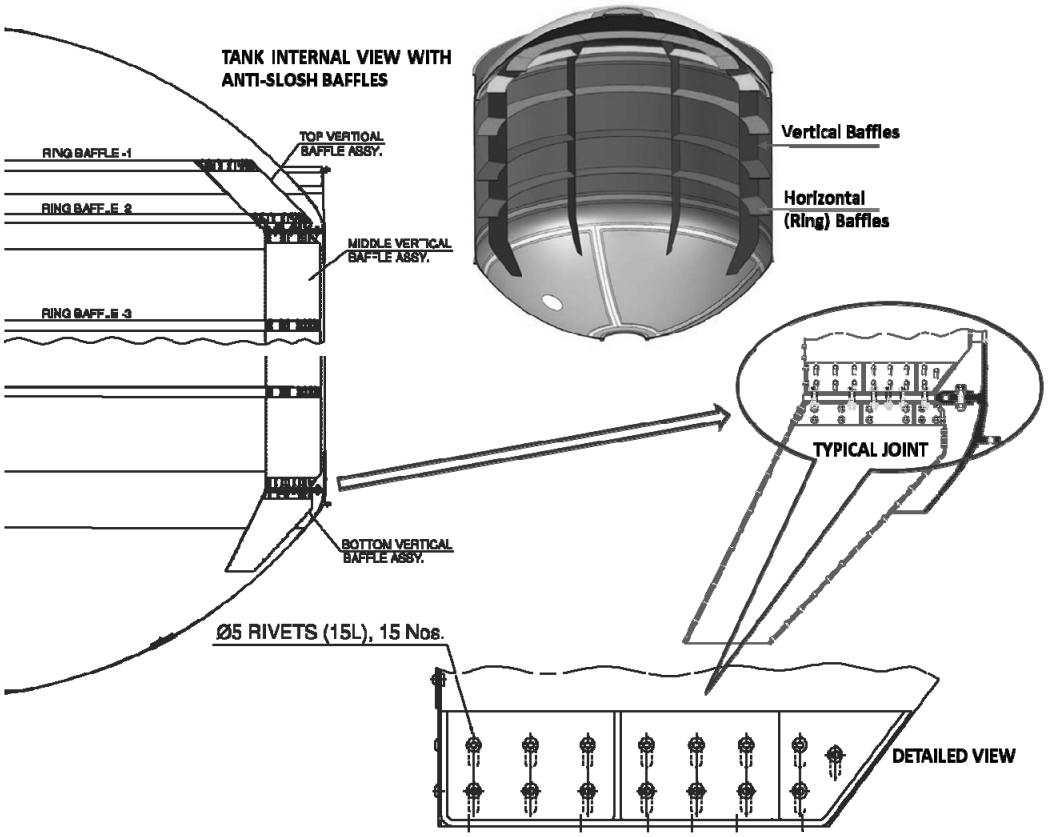

Figure 1: Tank internal view with anti-slosh baffles

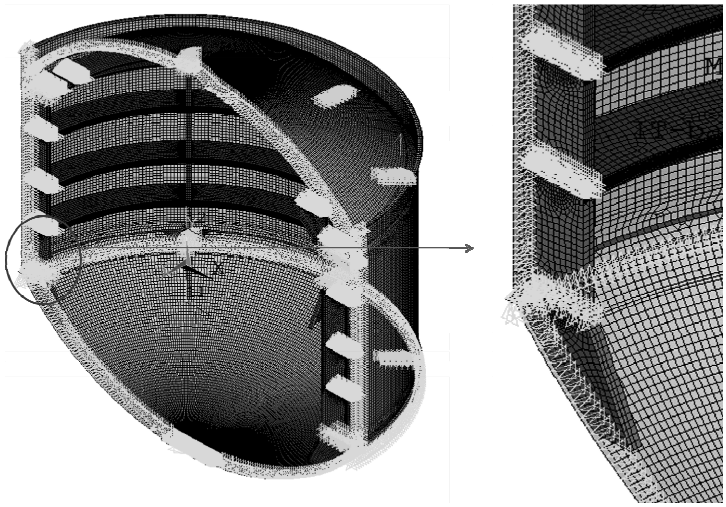

Figure 2: FE model with boundary conditions

ISBN - 978-93-95038-50-8

Figure 2 shows the FE model with boundary conditions. The tank is modelled by 2D shell elements and is assumed to be simply supported at the AE ring flange. The symmetric boundary conditions at the ends of the tank are modelled. The symmetric boundary conditions at the end of the horizontal baffles are also modelled to simulate the hoop continuity. The elongated axial slots at the middle vertical baffle with AE bracket interface is simulated by coupling all degrees of freedom except axial translation at the AE side. There are elongated radial slots at the tank support bracket interface simulated by coupling all degrees of freedom except radial translation. Fasteners are modelled using beam elements.

Three load cases are considered as specified in Table 1.

Table 1: Load cases considered for FE analysis

Load Step	**Loads considered**
Load step 1	Internal pressure
Load step 2	Structural tensile load
Load step 3	Slosh pressure load acting on the horizontal and vertical baffles

The maximum ultimate slosh pressure load applied at the anti-slosh baffles was 11.25 kPa, and the value varied at different baffles. The total baffle deformation under ultimate tank and slosh pressures is shown in Figure 3. It is noticed that deformation under ultimate tank and slosh pressures, a maximum baffle deformation of 36 mm is locally observed at the horizontal baffle in the second horizontal baffle in the FE dome. This is acceptable from the structural and slosh point of view. The von-mises stress distribution in vertical baffles under ultimate tank and slosh pressures is shown in Figure 4. A maximum stress of 280 N/mm^2 is observed locally at the FE of one of the vertical baffles, which is acceptable.

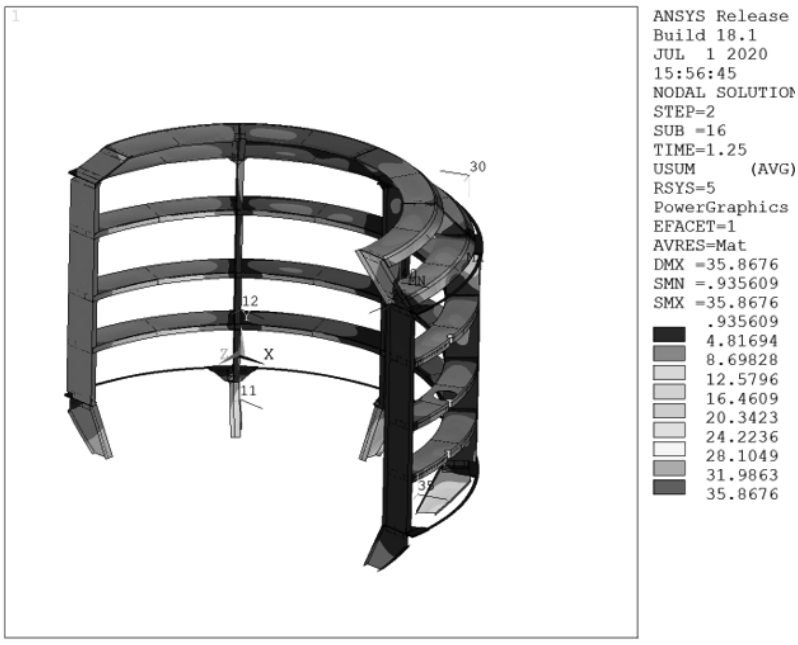

Figure 3: Total baffle deformation under ultimate tank and slosh pressures

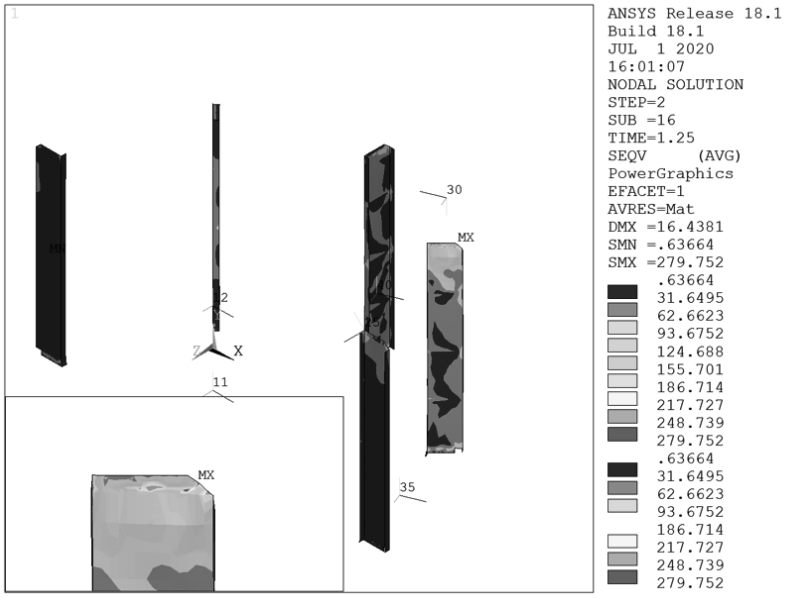

Figure 4: Von mises stress distribution in vertical baffles under ultimate tank and slosh pressures

Modal and harmonic analysis were also done for all critical modes, considering 3% damping. Based on the FE analysis, the maximum shear stress noticed at Ø5 mm rivets connecting middle vertical baffle to brackets is 170 N/mm^2. A margin of 0.55 exists w.r.t the ultimate shear strength of 265 N/mm^2 for V65 rivets.

4. EXPERIMENTAL VALIDATION OF DESIGN

The design of riveted joint with translational freedom for anti-slosh baffles inside propellant tank is experimentally validated. To simulate the actual assembly inside the tank, a test specimen from AA2219-T6 sheets is fabricated, considering four riveted joints in slotted holes.

One AA2219-T6 sheet of 1.5 mm thickness is sandwiched between two AA2219-T6 sheets of 3 mm thickness by Ø5 V65 rivets, to simulate the actual baffle joint in the fuel tank. According to rivet selection procedure by Li et al. [10] rivet length of 15 mm is selected. The configurations of the sheets are shown in Figure 5. Two rows and two columns of the actual riveted joint are simulated in the experiment. Four slotted holes are provided on the 1.5 mm sheet. The length of each slotted hole is 12 mm, and the width is 5.5 mm.

Ø2 mm pilot holes are initially drilled on each of the 3 mm sheets, which are then match drilled and enlarged after suiting with the other sheets. Sheet dimensions of 73 mm x 58 mm simulate the actual joint in the tank. An additional length of 90 mm is provided on each sample for adequate grip length. Hence, sheet samples of dimension 73 mm x 148 mm are used for testing.

The rivet joint is formed using a pneumatic rivet gun with a squeeze force of 9 kN applied on the driven head of the rivet at a pressure of 6 bar. After riveting, it was ensured that the manufactured rivet heads were free of tool marks and no gap exists between the head and the

ISBN - 978-93-95038-50-8

3 mm sheet. It was also ensured that the material around the rivet head on the 3 mm sheet was free of cracks.

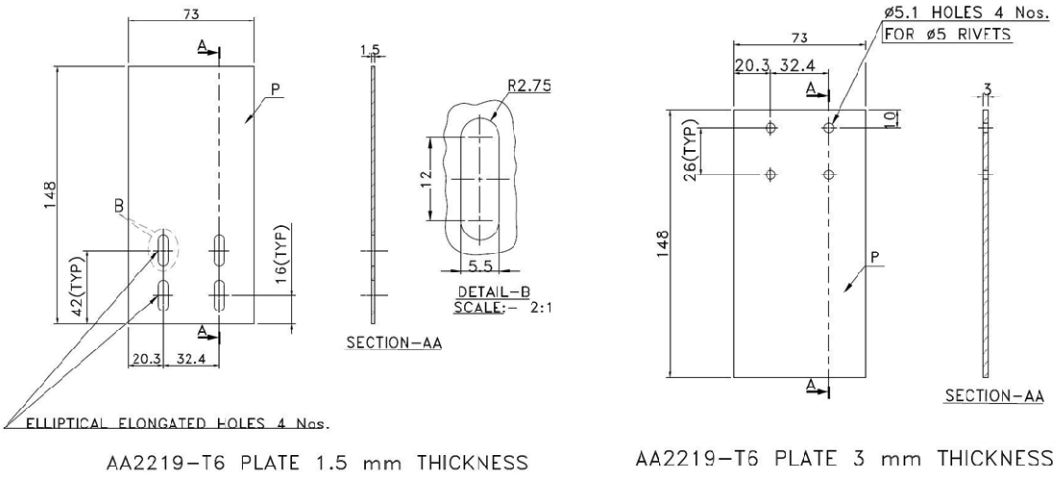

Figure 5: AA2219-T6 sheets for experimental validation of design

The riveted joints of the test specimen were subjected to axial loading. The test specimen is shown in Figure 6. The experiment was carried out on a Zwick Roell- 250 kN universal testing machine. The frictional resistance, F_f, in the riveted joint is obtained by the equation:

$$F_f = \mu R \tag{1}$$

where, μ = coefficient of friction and R = reaction load.

The residual load acting at the rivet joints is estimated to be of the order of 1 kN. Hence, for a joint with four rivets, the expected frictional resistance is of the order of 4000 x 0.2 = 800 N.

The riveted joint is subjected to pure shear by applying a tensile load. A dummy sheet of 1.5 mm thickness is placed between the two 3 mm sheets to ensure proper grip in the UTM. The test setup is shown in Figure 7.

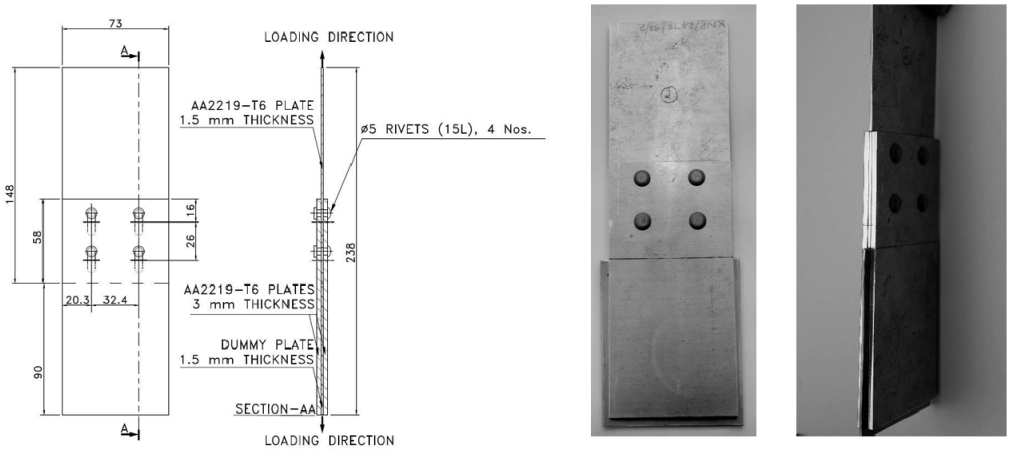

Figure 6: Test specimen for loading rivet joints

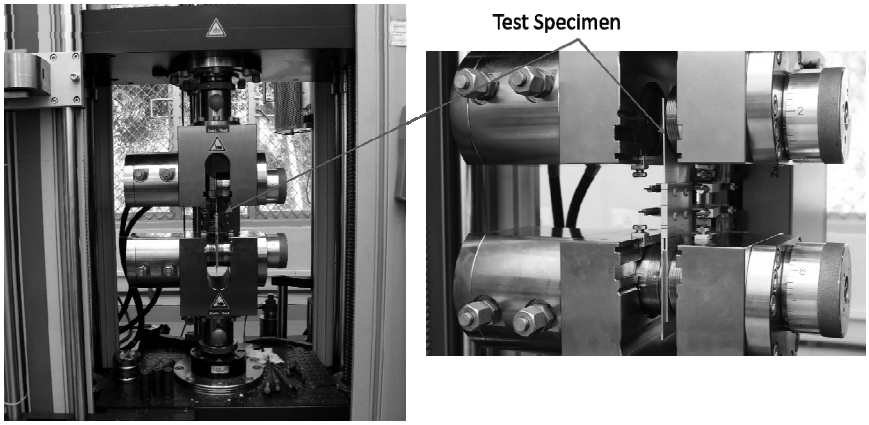

Figure 7: Test setup for loading riveted joints

A quasi-static tensile load was applied to the setup, with a loading speed of 2 mm/min. Step loading of 50 N was applied with a hold time of 5 sec between the load steps. The test continued till 10 mm displacement of the rivets in the slots, or till a maximum load of 500 N, whichever is the earliest.

After testing, the rivet joint was cut as shown in Figure 8. This is to verify that the joint is intact after the movement of the sheets. This ensures the rivet movement due to specimen loading.

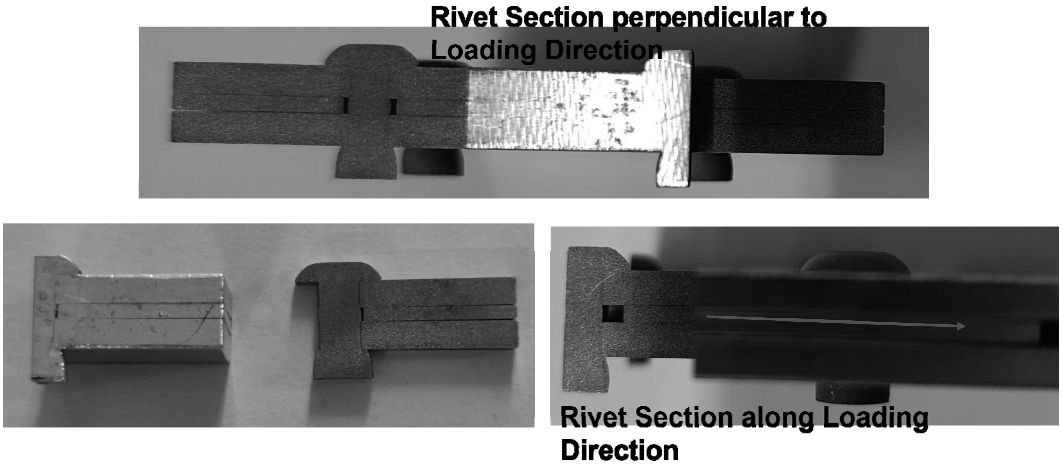

Figure 8: Cross sectional views of rivets after testing

5. Results and Discussions

With the application of tensile load, the joint remained intact till 485 N, before the displacement of the joint commenced, and continued till 10 mm in the slot. Force vs. displacement, displacement vs. test time and force vs. test time were plotted. The results are shown in Figure 9.

ISBN - 978-93-95038-50-8

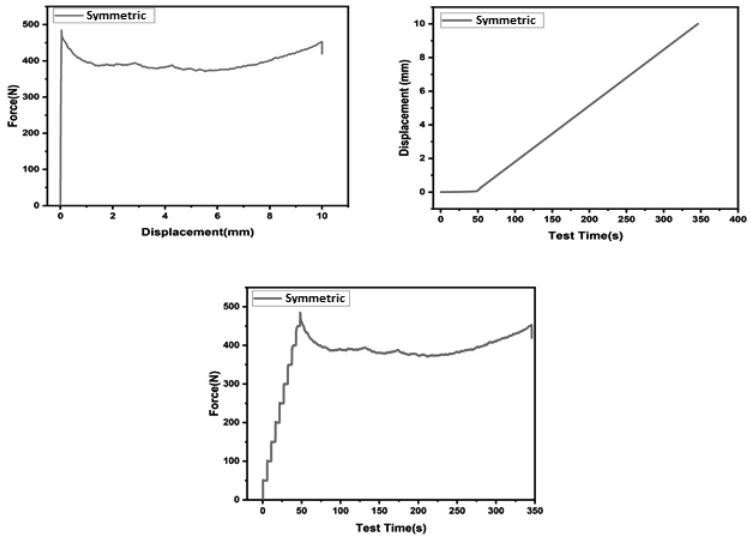

Figure 9: Plots of loading riveted joints

During the riveting process, both ends of the rivets get mechanically deformed and closely butt with the mating surfaces of the adjacent sheets, closing all the nearby gaps and crevices. Cut sections of the rivets after testing shows that the initial gaps between rivet and the mating sheets gets closed due to material flow of the rivet. In this condition, the joint is fully intact till the applied load overcomes the frictional resistance offered by the riveted joint. The load is observed to be 485 N, which is analogous to static frictional force to disturb the initial configuration of the riveted joint. Once the frictional resistance is overcome, slight reduction in the applied load is observed. This corresponds to the force required to move the rivet within the slotted hole, with close contact between the rivet heads and the adjacent sheets. This is analogous to kinetic friction. Once it is about to reach the other end of the slotted hole, slight increase in the load is observed due to the constraints offered by the edges of the plates.

The location of rivets in the slots after testing is shown in Figure 10.

Figure 10: Rivet movement in slots after testing

ISBN - 978-93-95038-50-8

Since the rivet movement in the joints commenced at 485 N, which is within the expected value of 800 N, the adequacy of the design is validated. The uncertainties of the frictional resistance in the riveted joint are a function of parameters like coefficient of friction, squeeze force, rivet length, tolerances on rivet and rivet hole diameter.

6. CONCLUSIONS

A non-conventional riveted joint with translational freedom is designed for anti-slosh baffles in a fuel tank. The joint is design account the limited space inside and ability to maintain integrity in variety of loads acting on the joints. The integration aspects of the joint also taken incorporated considering the accesses and tooling.

Detailed FE analysis was carried out considering the rotation and translational freedom at the joint. Axial elongation considering both tank ultimate internal pressure and structural tensile loads is 8 mm. The designed joint is able to accommodate a ring movement of 12 mm. The size and arrangement of rivets are arrived at after several iterations. Modal and harmonic analysis were also done for all critical modes, considering 3% damping. Based on the FE analysis, the maximum shear stress noticed at Ø5 mm rivets connecting vertical baffle to brackets is 170 N/mm^2. A margin of 0.55 exists w.r.t the ultimate shear strength of 265 N/mm^2 for V65 rivets.

The design is validated with a quasi-static tensile test by loading the riveted joints.

When the riveted joints are axially loaded, these are subjected to pure shear. The rivet movement commenced at 485 N. This is within the expected value of 800 N. Such joints can be adopted in engineering of the system for flight. More tests are planned with different loading conditions of riveted joints, to predict the range of load to initiate the joint movement.

ACKNOWLEDGEMENTS

Authors acknowledge the Mechanical Design and Analysis Entity, Proto Fabrication Facility & Aerospace Materials Lab of Materials & Manufacturing entity and Semi-Cryo Stages Group members of LPSC/ISRO for their valuable support during different stages of study. Authors thank Shri. R Krishnakumar, former Group Director, Mechanical Design and Analysis Entity, for providing valuable design guidance during the study. Authors also thank the Mechanical Integration Facility, VSSC/ISRO for the support extended during test specimen fabrication.

REFERENCES

1. NASA, Liquid Rocket Metal Tanks and Tank Components. NASA SP-8088, May 1974.
2. NASA, Slosh Suppression. NASA SP-8031, May 1969.
3. NASA, Propellant Slosh Loads. NASA SP-8009, May 1968.
4. Li, QM., Mines, R., Birch, RS, “Static and dynamic behaviour of composite riveted joints in tension”, International Journal of Mechanical Sciences, 2001, Vol. 43, pp. 1591-1610. doi:10.1016/s0020-7403(00)00099-0.
5. Szolwinski, MP., Farris, TN, “Linking riveting process parameters to the fatigue performance of riveted aircraft structures”, Journal of Aircraft, 2000, Vol. 37(1), pp.130-137. doi:10.2514/2.2572.

6. Cheraghi, SH., “Effect of variations in the riveting process on the quality of riveted joints”, The International Journal of Advanced Manufacturing Technology, 2008, Vol. 39, pp. 1144-1155. doi:10.1007/s00170-007-1291-6.
7. Huan, H. & Liu, M, “Effects of squeeze force on static behaviour of riveted lap joints”, Advances in Mechanical Engineering, 2017, Vol.9(5), pp. 1-13. doi: 10.1177/1687814016686891.
8. Esveld, C. Ballasted track. Modern railway track, MRT Productions, The Netherlands, 2001. pp. 203-230.
9. Wald, F., Sokol, Z., Moal, M., Mazura, V., Muzeau, JP, “Stiffness of cover plate connections with slotted holes”, Journal of Constructional Steel Research, 2004, Vol. 60, pp. 621-634. doi:10.1016/S0143-974X(03)00133-0.
10. Li, G., Shi, G., Bellinger, NC. Assessing the riveting process and the quality of riveted joints in aerospace and other applications. In Welding and Joining of Aerospace Materials, 2012. pp. 181-214.

ISBN - 978-93-95038-50-8

Modelling and Dimensional Analysis of Spring-Loaded Pressure Regulator for Performance Prediction and Characterization

Rishabh Garg*, Kailas S. Kuhite, Sunil S., D. Venkittaraman, Alex A.

Liquid Propulsion Systems Center
Indian Space Research Organization
Valiamala, Thiruvananthapuram, Kerala 695547
[1]rishabhgarg014@gmail.com, [2]kuhitekailas@gmail.com

ABSTRACT

The successful performance of a typical launch vehicle depends on fault free and reliable performance of different propulsion stages which uses various fluid control systems to control flow, pressure and direction of propellant and pressurant. Liquid propulsion stages require almost constant propellant tank pressure to maintain desired propellant flow into engines and to provide a positive pump suction head to avoid cavitation. In addition, these stages require constant pressure command gas source to operate engine propellant flow control valves, gas generator valves, purge valves etc. Pressure regulator is a variable-area pressure reduction valve, which provides constant outlet pressure at its downstream, irrespective of variations in inlet pressure and flow demand. In active Pressurisation systems, the design of pressure regulator is complex due to the large band of inlet pressure variation at high flow rate demand. A non-linear dynamic mathematical model of pressure regulator is required for predicting the performance in the specified working conditions with respect to initial transients, temperature effects, variation in input/ output conditions, inherent oscillations etc. The model is also effective to carry out post-flight analysis by simulating anomalies seen during ground tests and during flight. The upper stage of PSLV uses liquid pressure-fed engines which has two-stage regulated pressurisation system to maintain constant tank pressure with regulators in series. First rough regulator regulates high pressure GHe stored in gas bottle to intermediate pressure and then precision second regulator regulates to final required tank pressure. A non-linear and 1D time-domain mathematical model of high-pressure regulator simulating transients and working range was made using AMESim software and validated with experiment results. One of the anomalous observations in regulator during ground testing was studied with this model. Later these observations were confirmed by NDT techniques on the hardware. Paper presents the details of the model and parametric study conducted on the regulator. The validation of model with test results and characterization of the model to recreate the anomaly is also presented.

Keywords: *Pressure Regulator, AMESim Model, Performance analysis*

1. INTRODUCTION

Liquid propulsion stages require active control of propellant tank internal pressure. To reduce weight, propellants are stored in thin-walled tanks at low pressure and then injected into the engine at high pressure using turbo pumps. To ensure proper pump performance and avoid cavitation, the pump inlet pressure should be kept above the NPSP. Also, the tank internal pressure should be kept sufficiently higher than the atmospheric pressure to prevent structural failure by buckling due to low pressure difference. Tank pressures are controlled by admitting propellant compatible gas into the ullage volume to volumetrically replace the propellants consumed by the engine. Helium gas is typically used because of its inert nature and compatibility with propellants, low molecular weight which provides high pressure per unit mass and volume. Initially the tanks will be pressurized at ground through a pre-pressurization circuit for engine start-up. The on-board pressurization system takes over for the flight propulsive phase. In a typical Pressurisation system, the pressurant are stored in gas bottles at very high pressure. Isolation valve is used to isolate the high-pressure gas from pressure regulator and downstream elements. Once the isolation valve is opened, pressure is

*Corresponding Author: Email: rishabhgarg014@gmail.com

communicated to regulator which regulates it to required outlet pressure. This regulator can be in single stage or multi-stage with two or more pressure regulators in series. Figure-1 shows the typical configuration of a single stage pressure regulation system.

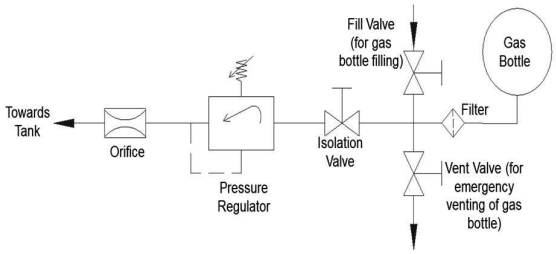

Figure 1: Typical Single-stage Pressure Regulation System

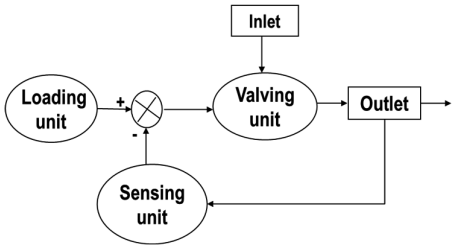

Figure 2: Control System Diagram of a Pressure Regulator

A pressure regulator is a control valve which maintains the pressure to a required level by varying flow across the valve as a function of difference in actual & desired outlet pressure. This is a self-contained close loop control system which senses any difference in outlet pressure w.r.t required outlet pressure and vary the flow area across valve with help of Valving element movement. Control system diagram of a pressure regulator is shown in Figure-2. Pressure regulator is a common device used in many industrial applications, domestic usage and widely used in aerospace application too. A pressure regulator is a self-actuated device which does not need any additional power source to operate which makes it a preferable candidate for pressure controlling in launch vehicle application. Pressure regulator can be broadly classified as modulating pressure regulator and non-modulating pressure regulator [1]. A modulating pressure regulator maintains required regulator outlet pressure at a chosen set point. However, non-modulating pressure regulator maintains regulator outlet pressure between upper and lower limit of required pressure.

Pressuiration system selected for study is a two-stage regulated ambient gas pressurization system which regulates high pressure Helium gas from 330 bar to 35 bar in first stage by primary pressure regulator (PPR) and then finally to 19 bar by secondary pressure regulator (SPR). PPR of first stage regulation is considered for study which a direct acting, Belleville disc loaded pressure regulator. A one-dimensional time domain mathematical model of PPR is developed using AMESim to study the complete behavior of pressure regulator and validated with experimental results. Later, abnormal performance seen during lab test was simulated by model characterization and design of regulator was modified based on model results.

2. MATHEMATICAL MODELLING OF SPRING LOADED PRESSURE REGULATOR

2.1 CONFIGURATION OF PRESSURE REGULATOR

Primary Pressure regulator (PPR) of 2-stage pressure regulation system of upper stage of PSLV is selected. Figure 3 shows the schematic view of PPR. This is a direct acting, Belleville spring loaded, balanced type, normally open regulator. Regulator has conical hard on soft seat configuration. Piston with 'O' ring seals is used as a sensing element. Downstream pressure is maintained constant by regulating the flow across the seat. Belleville spring load will be adjusted to achieve required outlet pressure. Regulator has ambient pressure communication on the loading side which makes a reduction 1 bar in set pressure from ground to flight.

ISBN - 978-93-95038-50-8

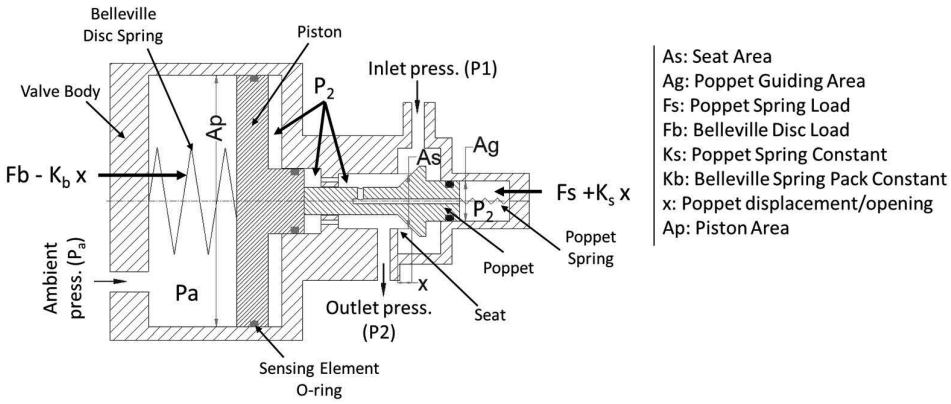

Figure 3: Free-body diagram of Primary Pressure Regulator

Following is the force balance equation of pressure regulator at a particular opening (x):

$$P_1 \times (As - Ag) + Fs + Ks \times x - Fb + Kb \times \mathrm{x} + P_2 \times Ap - P_2 \times (As - Ag) - Pa \times Ap = 0 \quad (1)$$

This regulation system has Helium gas stored at high pressure in upstream of PPR and isolated with isolation valve. In downstream of PPR, another fine secondary pressure regulator (SPR) is mounted followed by solenoid valve (SV) for isolation in downstream which allows the flow through regulator when opened. Initially SV is closed and when isolation valve is opened, the high-pressure helium is communicated to downstream regulators and regulator goes in lock-up mode providing required outlet pressure at downstream. However, there is no flow across regulators since the downstream SV is closed. Once the SV is opened, flow stars and regulator comes into function providing required pre-set outlet pressure.

2.2 MATHEMATICAL MODEL

In a pressurisation system, it is of great importance to predict the behavior of pressure regulator during transient and steady state. In addition to basic governing equations for flow and force balance, the dynamic characteristic of a pressure regulator is highly dependent on various geometrical and physical parameters like static and dynamic friction in sliding pairs, clearances and guidance of various critical moving pairs, lubrication stribeck effects, mass inertia of moving elements, Valving element geometry, coulomb & pneumatic damping, spring stiffness, flow losses, physical properties of working medium, effects of temperature variation etc. This makes the conventional mathematical model complex and difficult to solve by conventional governing differential equations and then solving them by either numerical techniques or conventional software codes. Hence, a one-dimensional time domain mathematical model of PPR is developed using *"Advanced Modelling Environment for performing Simulation for Engineering systems (AMESim)"* to study the complete behavior of pressure regulator. The ability, accuracy, pictorial representation, less post-processing time of modeling tool software's for prediction of system dynamics and its behavior at various operating conditions makes it more popular and convenient to use.

LMS Imagine AMESim® helps in 1D lumped parameter time domain analysis of hydraulic and pneumatic systems. The software interfaces uses symbols to represent individual components in a easily recognizable pictorial form. Each component has its own governing equations to simulate the physical phenomena related to that component in form of algebraic and partial differential equations. It converts a given set of partial differential

ISBN - 978-93-95038-50-8

equations to a system of either ordinary differential equations or algebraic equations and solves them using numerical method such as explicit Runge-Kutta or linear multi step method like adams bashforth or adams moulton method.

Pressure regulator is divided in various sub-system chambers from free body diagram is made and suitable algorithms are selected from software [4]. Figure-4 shows the equivalent mathematical model of PPR along with various upstream and downstream components used during testing. In PPR model, moving element's inertia is simulated by mass simulator module with maximum movement of poppet restricted to its maximum travel possible in actual hardware. A standard O-ring model is used for simulating O-ring static and sliding friction providing the actual geometrical parameters for O-ring and corresponding groove [3]. Spring stiffness, piston, downstream orifice etc. is simulated with respective sub-models. Since the expansion of high pressure gas in upstream gas bottle depends on heat exchange across gas bottle which needs further detailed thermal model of gas bottle, direct pressure & temperature measurement from the flow test is given as input to model to validate it with experimental results. A standard ideal pressure regulator for simulating SPR and orifices & flow lines for simulating downstream components which controls the flow demand are selected.

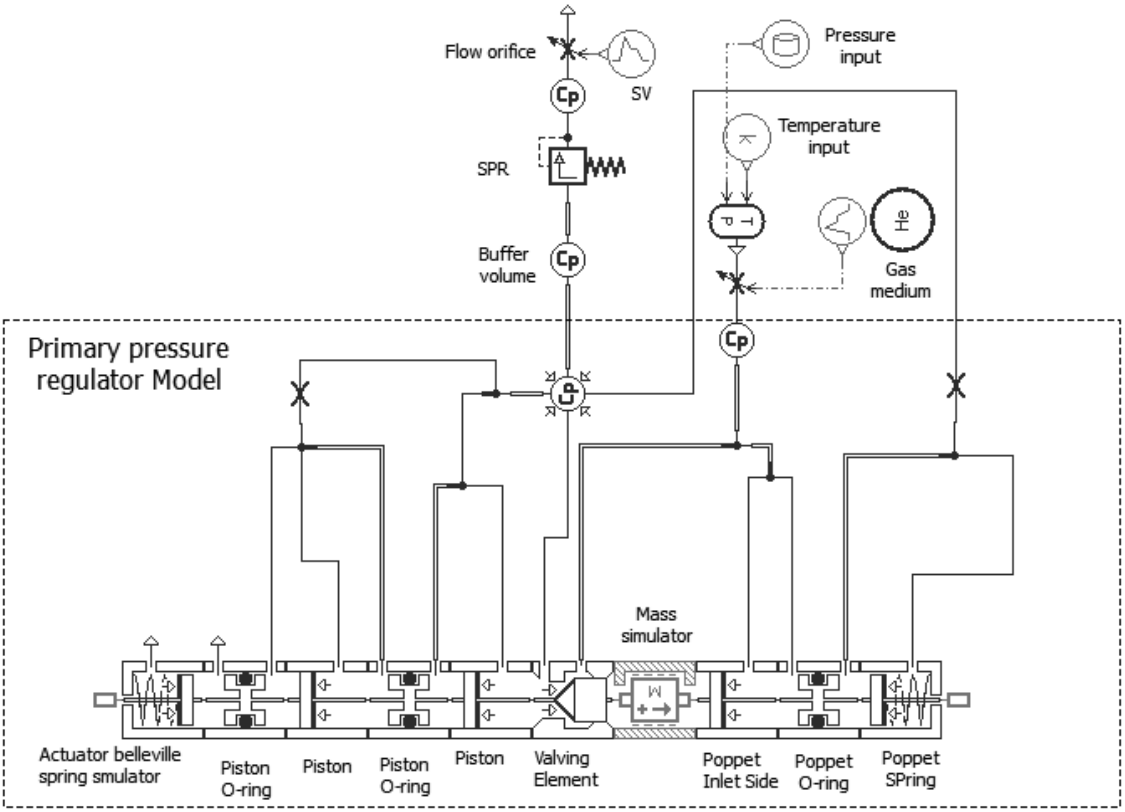

Figure 4: Mathematical Model of Primary Pressure Regulator

For simulating working medium, a real gas sub-model using Vander wall equation of state is selected as follows:

$$\left(P + \frac{a}{V^2}\right) \cdot (V - b) - RT = 0 \tag{2}$$

where, $a = \frac{27.R^2.T_c^2}{64.P_c}$ and $b = \frac{R.T_c}{8.P_c}$; P: Pressure; V: Volume; T: Temperature; R: Characteristic gas constant; Tc: Critical Temperature; Pc: Critical Pressure

The temperature and pressure time-derivatives are evaluated resolving the following system of two equations traducing the mass balance and enthalpy balance:

$$\begin{bmatrix} \mathrm{V}.\left(\frac{\partial \rho}{\partial \mathrm{p}}\right)_{\mathrm{T}} & \mathrm{V}.\left(\frac{\partial \rho}{\partial \mathrm{T}}\right)_{\mathrm{p}} \\ \mathrm{m}.\left(\frac{\partial \mathrm{h}}{\partial \mathrm{p}}\right)_{\mathrm{T}} - \mathrm{V} & \mathrm{m}.\left(\frac{\partial \mathrm{h}}{\partial \mathrm{T}}\right)_{\mathrm{p}} \end{bmatrix} . \begin{bmatrix} \frac{\mathrm{dp}}{\mathrm{dt}} \\ \frac{\mathrm{dT}}{\mathrm{dt}} \end{bmatrix} = \begin{bmatrix} \sum \frac{\mathrm{dm_i}}{\mathrm{dt}} - \rho.\frac{\mathrm{dV}}{\mathrm{dt}} \\ \sum \frac{\mathrm{dm_i}}{\mathrm{dt}}.\mathrm{h_i} - \mathrm{h}.\sum \frac{\mathrm{dm_i}}{\mathrm{dt}} + \delta \mathrm{Q} \end{bmatrix} \quad (3)$$

where density (ρ) and enthalpy (h) partial derivatives depend on the equation of state and m is mass.

These equations are now solved using numerical techniques. The heat exchange is computed using the following relation:

$$\dot{\mathrm{Q}} = \mathrm{k_{th}} \cdot \mathrm{S} \cdot (\mathrm{T_{ext}} - \mathrm{T_w}) \quad (4)$$

Where k_{th} is the thermal exchange coefficient, S is the thermal exchange area, T_{ext} is the external temperature and T_w the working temperature.

2.3 MODEL VALIDATION WITH EXPERIMENTS

To validate the model, lab test was conducted on same hardware and model results are compared with lab test results. Helium is stored in 0.07m^3 gas bottle at 330 bar and fed to PPR. The flow rate in regulator downstream is controlled by ø3.2mm orifice. Comparison of simulation results with actual hardware test results shows a close match during the transients and in steady phase.

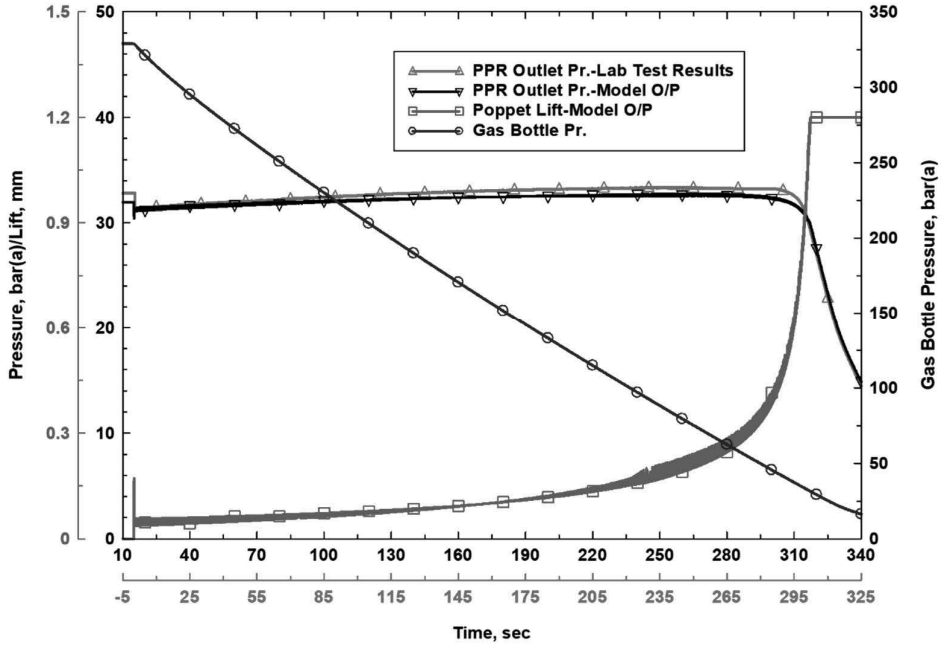

Figure 5: Comparison of Mathematical Model and Experiment Results

3. PERFORMANCE PREDICTION AND CHARACTERIZATION

3.1 PERFORMANCE OBSERVATION IN LAB TEST

During lab flow test, pressure spikes of around 0.3-0.4 bar was seen in pressure regulator outlet pressure during flow test of PPR. Subsequently in another hardware also some pressure spikes and roughness were seen during flow test. Figure-6.1 & 6.2 shows the anomalous observation seen during flow test.

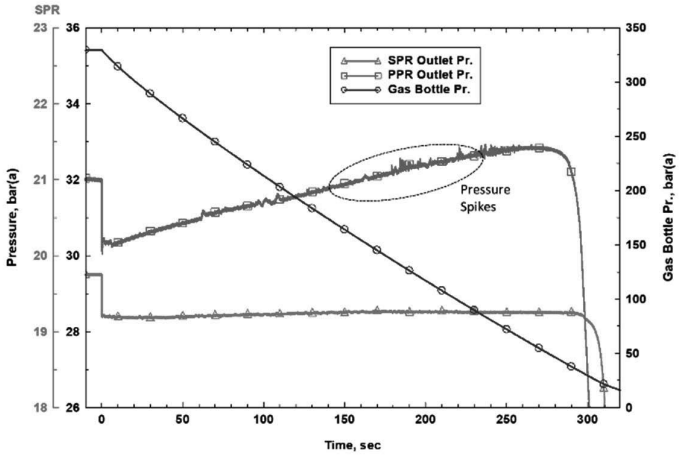

Figure 6.1: Anomalous observation seen in PPR outlet pressure during GHe lab flow test

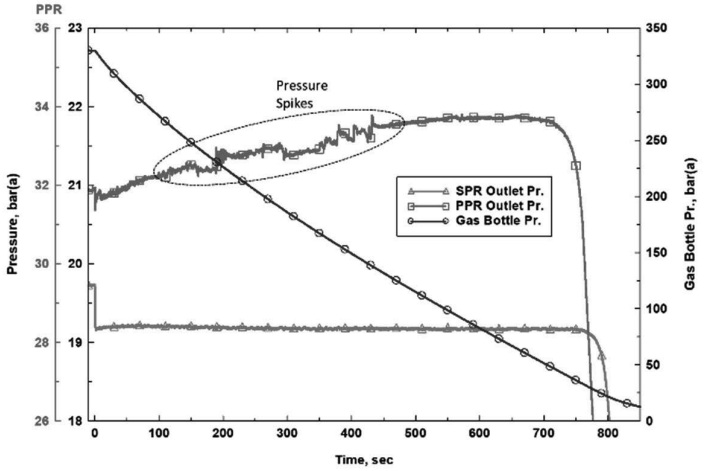

Figure 6.2: Anomalous observation seen in PPR outlet pressure during GN2 lab flow test

3.2 ANOMALY SIMULATION

To find out the exact reason of observation a parametric analysis of mathematical model was carried out to see the effect of various parameters on regulator outlet pressure. It was found that the observation seen in regulator outlet pressure is because of intermittent additional friction in sliding elements during motion which leads to pressure spikes when relieved. In mathematical model of regulator, additional friction force was introduced during functioning and after some seconds it was relieved. Model results shows that there is a dip in outlet pressure when there is additional friction force comes in sliding elements and relieved

ISBN - 978-93-95038-50-8

in the form of kink when it is removed. Figure 7 shows the mathematical model results for anomaly simulation. O-ring design, clearances between sliding pairs, surface finish condition of all sliding elements, geometrical parameters to ensure alignment, guidance of moving elements etc. were rechecked and it was understood that there is a design marginality in spring guidance.

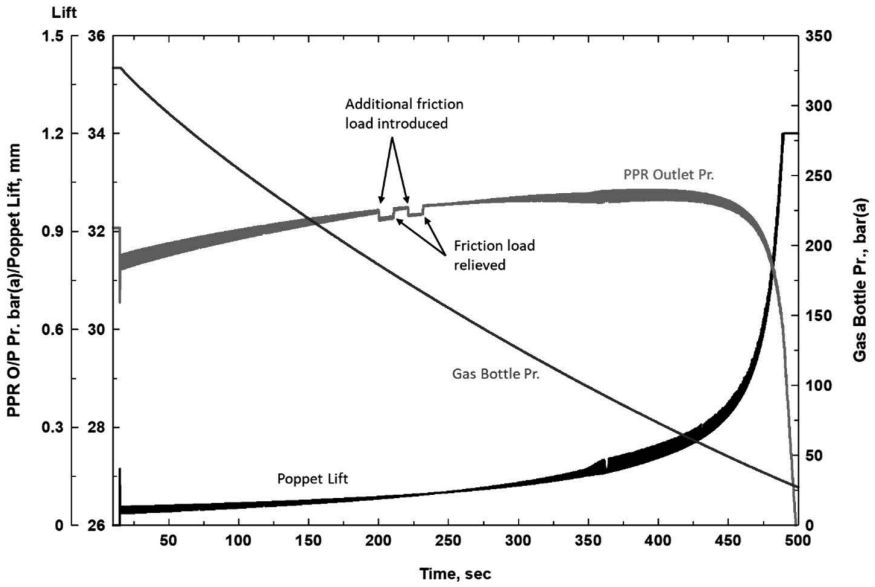

Figure 7: Mathematical Model Simulation results for abnormal lab test observation

To confirm the model results and dimensional analysis results, CT scan of hardware in assembled condition was carried out (results are shown in figure 8) and it was found that spring OD is touching the spring room ID creating the movement restriction and leading to non-smooth movement of sliding elements. Later, this was confirmed when the hardware was dis-assembled and scratches marks were found in spring room ID which was created by spring rubbing during regulator functioning.

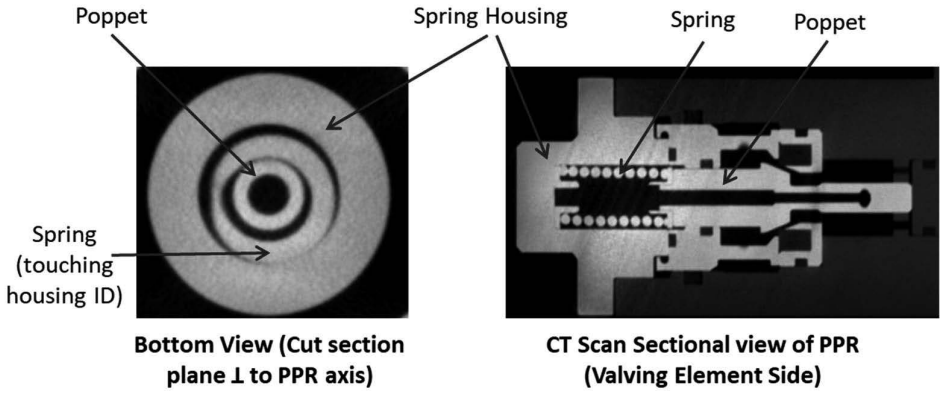

Figure 8: CT scan of PPR in assembled condition

After detailed dimensional analysis, spring was properly guided in ID for a distance of 1.5d-2d mm length at each end with help of spring retainers. It was ensured that with extreme variation in parts dimension and even with lateral shift of spring to extreme position, spring

ISBN - 978-93-95038-50-8

will not touch spring room ID and hence there is no chance of spring rubbing and restricting smooth movement of sliding elements. The regulator design was modified accordingly and hardware was realised with new dimensions. The flow test results of modified regulator were found to be satisfactory. The hardware was subjected to vibration test also followed by flow test to confirm the ruggedness of design. To ensure the consistency in regulator performance hardware's were realised with min/max tolerance band and flow tests were carried out. Performance of all the hardware was found to be satisfactory during flow tests as shown in figure 9.1 & 9.2.

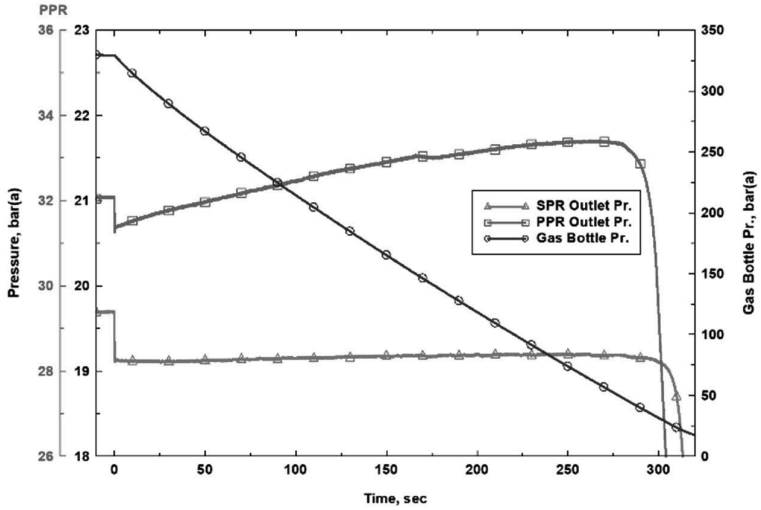

Figure 9.1: Performance of PPR during GHe lab flow test after Design Modification

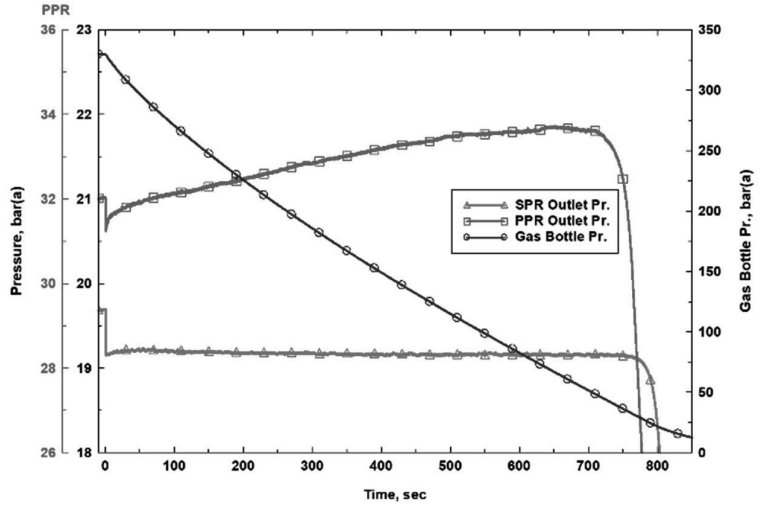

Figure 9.2: Performance of PPR during GN2 lab flow test after Design Modification

4. CONCLUSION

This paper presents the development of dynamic mathematical model for a spring-loaded pressure regulator using LMS AMESim and comparison of lab level performance with simulation test results. Comparison of simulation results with actual hardware test results

ISBN - 978-93-95038-50-8

shows a close match during the transients and in steady phase. This model is considerably used for performance prediction of pressure regulator during lab test and during flight.

From study, it is concluded that additional momentary friction during the regulator movement can cause sudden dips or roughness in regulator outlet pressure which once relieved can manifest in kink. It is proven with modelling and simulation tests. The major reason for the intermittent friction is found to be design marginality in spring guidance, which was found out by dimensional analysis and later confirmed by NDT techniques. Based on model results and analysis, design of regulator was modified and successfully tested at lab.

ACKNOWLEDGEMENT

I would like to thank Shri. Manu Joseph and team, QCNG/LPSC for their kind support and help for carrying out NDT analysis on hardware.

REFERENCES

1. "Aerospace fluid component designer's handbook, Vol. 1", Air Force Rocket Propulsion laboratory, Edwards, California, Technical Documentary Report No. RPL-TDR-64-25, February 1970.
2. Sunil S., Ullekh Pandey, Jeevanlal B. S., M. Radhakrishnan and C. Amarasekaran, "Mathematical modelling of pressure regulator for cryogenic application", Proceedings of the 37th International & 4th National conference on Fluid Mechanics and Fluid Power, FMFP 2010, IIT Madras, Chennai, India, December 16-18, 2010.
3. "Parker O-ring Handbook", Parker Hannifin Corporation – O-ring division,
4. Software Documentation of LMS Imagine AMESim.
5. Al-Ghathian F.M.M., Tarawneh M.S. "Friction Forces in O-ring Sealing", American Journal of Applied Sciences: 626-632, 2005
6. White F.M., 1974, Viscous Fluid Flow, McGraw-Hill, New York

Numerical Study of the Liquid Oxygen Draining in a Spinning Tank with Baffles for Hybrid-Propulsion Rocket

Anant Singhal*, Deepak K. Agarwal, T. John Tharakan, S. Sunil Kumar

Propulsion Research and Studies
Liquid Propulsion Systems Centre
Thiruvananthapuram, Kerala, 695547
mail2anantsinghal@gmail.com

ABSTRACT

Computational Fluid Dynamics (CFD) study of liquid oxygen draining in a spinning tank with and without baffles is carried out for hybrid propulsion rocket. The effect of tank spinning and the presence of baffles on the vortex formation and unusable propellant mass is brought out in this work. The interface of the draining propellant is captured using the Volume of Fluid (VOF) framework while the motion of baffles is simulated through mesh motion technique. Initially, analysis of liquid oxygen draining is carried out in a stationary tank without baffles. It is found that that a vortex is formed in the tank and gas entry in the feed line happens at 21s resulting in unusable propellant of 1.9kg. Subsequent analysis of liquid draining in a spinning tank without baffles shows that gas enters into the feed line earlier as compared to the stationary tank. Finally, the analysis is carried out for propellant draining in spinning tank with baffles. It is found that the momentum imparted by the baffles to the draining fluid increases the unusable propellant mass further compared to tank without baffle.

Keywords: *draining, tank, spinning, baffles*

1. INTRODUCTION

A hybrid propulsion rocket is being developed by ISRO that has solid propellant as fuel and liquid oxygen as the oxidizer. This hybrid propulsion rocket is envisaged to be aerodynamically spin stabilized. In one of the liquid oxygen storage tank configurations, baffles are placed on the tank inner walls along its length. The baffles are placed to reduce the propellant sloshing during flight. However, the spinning of the tank and the presence of baffles may cause vortex formation during propellant draining that can lead to a decrease in the usable propellant mass. In the present study, three-dimensional transient numerical simulations of liquid oxygen tank draining during flight is carried out to study the effect of tank spinning and baffles on the un-usable propellant mass towards the end of the flight.

2. LITERATURE REVIEW

Various experimental studies have been reported on the formation of vortex during draining of liquid in tanks [1-3]. It has been reported that a dip forms on the free surface of the draining liquid which intensifies into a gas-vortex. The gas enters the drain port at a critical height. In the context of rocket engines, this gas entry from the tank drain into the pump may lead to critical failure. Therefore, it is important to study and estimate the formation of gas vortex during draining of the liquid propellant. Various researchers have successfully proven the usability of VOF method to capture the formation of vortex during liquid draining [4-6].

Researchers have also reported the flow field in a stirred tank both with and without baffles on the tank wall. [7, 8]. A detailed experimental study of liquid motion in spinning, nutating tanks was reported in [9] to determine the effect of such liquid motion on the stability of the spacecraft. However, to the best knowledge of the authors, study on the flow

*Corresponding Author: Email: mail2anantsinghal@gmail.com

field during propellant draining in a spinning tank with and without baffles for launch vehicle application is not available in open literature. Therefore, in the present paper, a numerical investigation is carried out to bring out the effect of tank spin motion and baffles on the vortex formation and un-usable propellant in the tank. The following 3D transient CFD analyses were carried out for the draining of liquid oxygen from the tank.

Case1: Analysis of propellant draining in a stationary tank without baffles.

Case 2: Analysis of propellant draining in a spinning tank without baffles.

Case 3: Analysis of propellant draining in a spinning tank with baffles.

3. COMPUTATIONAL DOMAIN AND BOUNDARY CONDITIONS

The 3D computational domain of the liquid oxygen tank is shown in Figure 1. The domain consists of the tank with baffles both in the cylindrical part and in the bottom dome of the tank. The cylindrical part of the tank is 1.76m in height and 0.3m in diameter. A set of four baffles is mounted longitudinally each on the tank cylindrical wall and in the bottom hemispherical portion of the tank. The domain for the cases 1 and 2 is similar as shown in Figure 2 except that the baffles are removed from the tank. The domain is meshed with polyhedral elements having a total mesh count of 27lakhs. The maximum skewness of the mesh is 0.85 while the minimum orthogonal quality is 0.16.

A pressure inlet boundary condition was applied at the vent in the top dome in order to maintain the ullage at a constant pressure of 35bar during liquid oxygen draining. A constant liquid oxygen mass flow rate of 6kg/s is specified at the drain port outlet. The tank was simulated to be spinning at a rate of 6rps. The vehicle acceleration of 50m/s^2 was considered as the body force acting on the propellant. The initial propellant loading of 128kg and resulting ullage volume of 6 litres was considered for the simulation. Each transient simulation was carried out for a duration of 22s.

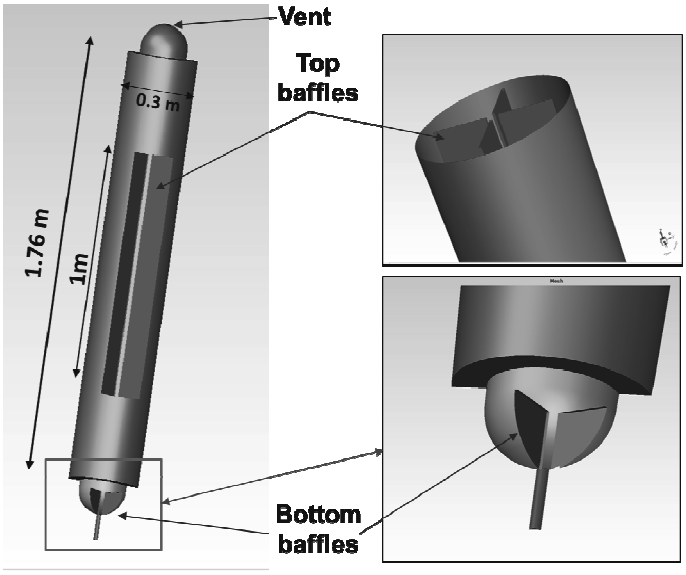

Figure 1: Computational domain of the LOX tank

ISBN - 978-93-95038-50-8

4. NUMERICAL METHODOLOGY

The numerical simulations were carried out using ANSYS Fluent. The spinning of the tank having baffles is simulated using the mesh motion technique. The interface of the draining liquid oxygen is captured using Volume-of-Fluid (VOF) methodology with SST k-ω turbulence model. The pressure and velocity coupling is achieved using the Pressure-Implicit with Splitting of Operators (PISO) scheme. The discretization of the governing equations was carried out using second order upwind scheme in space. First order implicit scheme was used for time marching with a time step of $1x10^{-4}$s. Non-iterative time advancement was invoked for improved stability of the solution at each time step.

The tracking of the interface(s) between the phases is accomplished by the solution of a continuity equation for the volume fraction of one (or more) of the phases. For the qth phase in absence of mass transfer, this equation has the following form:

$$\frac{\partial}{\partial t}\left(\rho_q \alpha_q\right) + \nabla \cdot \left(\rho_q \alpha_q \vec{v}\right) = 0 \tag{1}$$

Volume fraction equation will not be solved for the primary phase; since it is computed based on the constraint,

$$\sum_{q=1}^{n} \alpha_q = 1 \tag{2}$$

Volume fraction equation is solved using the implicit formulation in this study. In the VOF model, a single momentum equation is solved throughout the domain.

$$\frac{\partial}{\partial t}(\rho\vec{v}) + \nabla \cdot (\rho\vec{v}\vec{v}) = -\nabla p + \nabla \cdot [\mu(\nabla\vec{v} + \nabla\vec{v}^T)] + \rho\vec{g} + \overrightarrow{F_t} \tag{3}$$

where ρ, μ are volume-weighted averaged properties. F_t represents the surface tension force at the interfaces.

Continuum surface force (CSF) model which accounts for surface tension between a phase pair as a continuous, volumetric body force term is applied in this study. It has the following form:

$$F_t = \sigma_{ij} \frac{\alpha_i \rho_i \kappa_j \nabla\alpha_j + \alpha_j \rho_j \kappa_i \nabla\alpha_i}{\frac{1}{2}\left(\rho_i + \rho_j\right)} \tag{4}$$

where curvature $\kappa = -\nabla \cdot \hat{n}$, interface unit normal $\hat{n} = \nabla\alpha / |\nabla\alpha|$

5. RESULTS AND DISCUSSION

VALIDATION STUDY

Initially, as a model validation, steady state axisymmetric analysis of liquid in a spinning tank was carried out. The obtained shape and rise of the liquid free surface was compared with the analytical result. A cylindrical tank having 200mm diameter and 600mm height was taken for the validation study. The tank was considered to be rotating at a speed of 12rad/s. The contour of liquid volume fraction obtained from CFD analysis is shown in Figure 2. It can be seen that CFD estimates the distance between the minimum and maximum height of the liquid free surface to be 75mm. The expression given by Eq. (5) was used to analytically

estimate the height of the liquid free surface. The height of the free-surface is estimated to be 73.39mm using Eq. (5). Thus, error in the CFD model is within 2.2%.

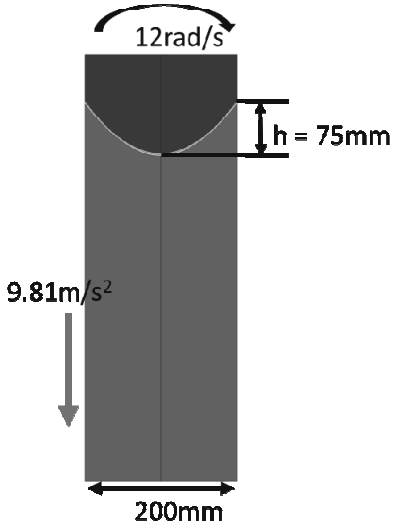

Figure 2: Shape of liquid free-surface in a spinning tank for model validation

$$h = \frac{R^2.\omega^2}{2g} \tag{5}$$

where R is the tank radius, ω is the angular velocity and g is the gravitational acceleration.

CASE 1: ANALYSIS OF PROPELLANT DRAINING IN A STATIONARY TANK WITHOUT BAFFLES

Initially, analysis of liquid oxygen draining in a stationary tank without baffles was carried out to estimate the propellant left-out in the tank at the instant when vapor enters the drain line. Figure 3 shows the liquid volume fraction in the tank at the start of draining (t=0s), 1s, 10s and the time instant at which the ullage gas enters the drain port (21s).

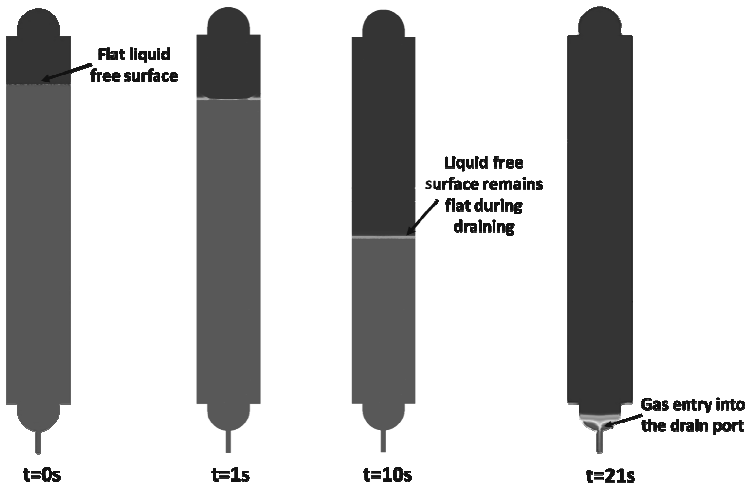

Figure 3: Contours of liquid (red color) volume fraction at various time instants for Case 1

It can be seen that when the tank is not spinning, the free surface of the liquid that was flat initially remains to be flat throughout the draining. A dip is formed at the free surface of the propellant towards the end of the draining and the ullage gas enters the drain port at 21s. The mass of liquid oxygen remaining in the tank at this instant is 1.9kg and is termed as unusable propellant.

CASE 2: ANALYSIS OF PROPELLANT DRAINING IN A SPINNING TANK WITHOUT BAFFLES

Subsequent to case 1, analysis was carried out for a spinning tank without baffles to determine the effect of spin motion on the flow behavior and un-usable propellant. The initial condition for this case was the same as that for case 1. Figure 4 shows the contours of liquid volume fraction at t=5s, 10s and 20.28s (the time at which ullage gas enters the drain port).

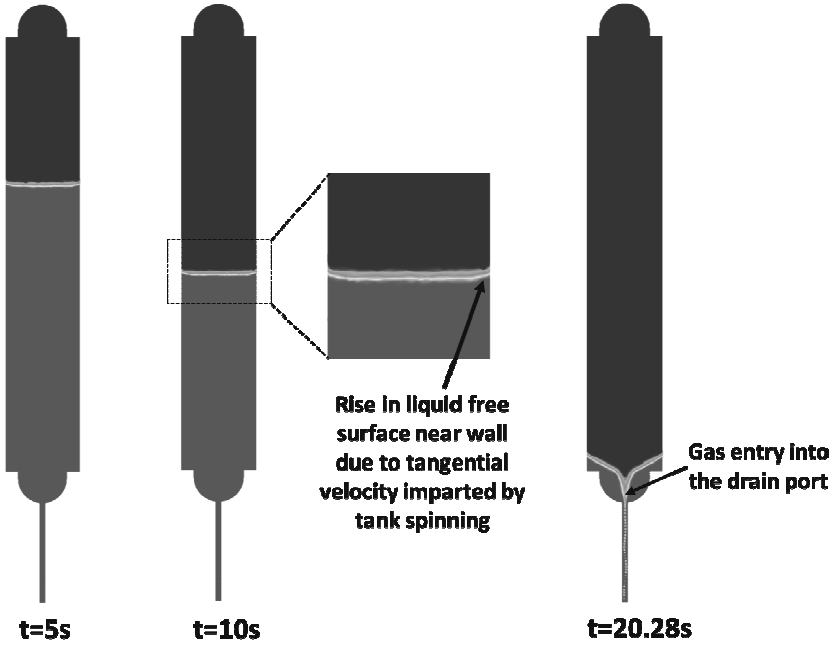

Figure 4: Contours of liquid (red color) volume fraction at various time instants for Case 2

It can be seen from Figure 4 that the free surface of the liquid assumes a curved shaped due to centrifugal force acting on the liquid resulting from spinning of the tank. The ullage gas enters the tank drain port at 20.28s and the un-usable mass of liquid oxygen in the tank is 6.3kg at this instant. The spinning motion of the tank imparts angular momentum in the draining liquid, thus increasing the vorticity of the liquid. The increased vorticity results in earlier dip formation in the liquid free surface which results in a higher left-out mass in case 2.

CASE 3: ANALYSIS OF PROPELLANT DRAINING IN A SPINNING TANK WITH BAFFLES

Figure 5 shows the contours of liquid volume fraction at various time instants for propellant draining in a spinning tank having baffles. The baffles that are fastened to the tank walls also spin along with the tank. The spinning baffles impart additional angular momentum to the liquid that results in a dip formation at the free-surface of the liquid during early stage of the draining at t=1s. The dip formation in case 3 results in early gas entry into the drain port compared to that in cases 1 and 2. The gas enters into the drain port at 20.02s in case 3 and the left-out propellant in the tank, at this time instant, is found to be 7.9kg.

ISBN - 978-93-95038-50-8

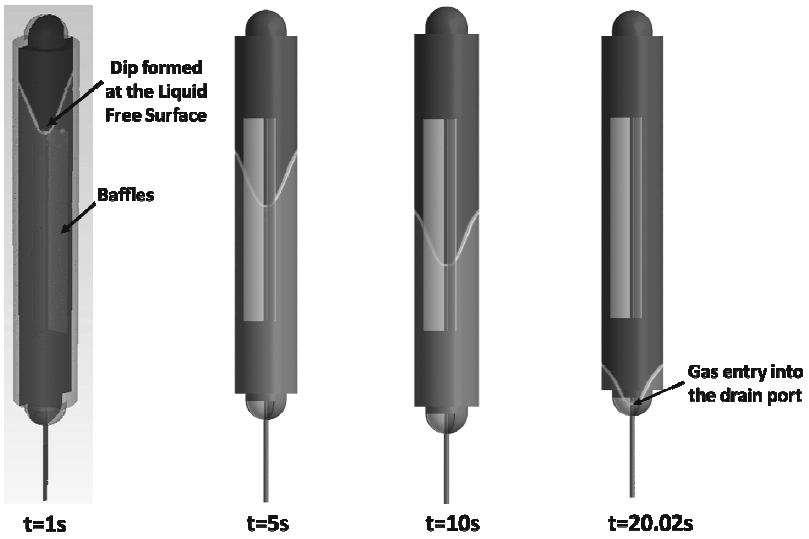

Figure 5: Contours of liquid (red color) volume fraction at various time instants for Case 3

6. CONCLUSIONS

Two-phase CFD simulations of liquid oxygen draining in the tank of a spin stabilized hybrid propulsion rocket is reported in the current paper. The simulations are carried out for spinning tank with and without baffles on its inner wall to determine the effect of spin motion and baffles on the un-usable propellant in the tank. It is found that the spinning of the tank increases the un-usable propellant mass from 1.9kg for a stationary tank to 6.3kg for a spinning tank without baffles. Further, adding anti-slosh baffles to the tank of a spin stabilized rocket increases the left out propellant to 7.9kg, thus increasing the mass penalty.

REFERENCES

1. Ramamurthi, K. & Tharakan, T.J, “Intensification of a vortex during draining”, Can. J. Chem. Eng. 73 (1995) 292–299.
2. Ramamurthi, K. & Tharakan, T.J, “Flow visualisation experiments on free draining of a rotating column of liquid using nets and tufts”, Exp. Fluids 21 (1996) 139–142.
3. Lubin, B.T. & Springer, G.S, “The formation of a dip on the surface of a liquid draining from a tank”, J. Fluid Mech. 29 (1967) 385–390.
4. Robinson, A, Morvan, H, Eastwick, C, “Computational investigations into draining in an axisymmetric vessel”, J. Fluids Eng. 132 (2010).
5. Zhou, Q.N. & Graebel, W.P, “Axisymmetric draining of a cylindrical tank with a free surface”, J. Fluid Mech. 221 (1990) 511–532.
6. Agarwal, D, Basu, P, Tharakan, T.J, Salih, A, “Prediction of gas-core vortices during draining of liquid propellants from tanks”, Aerospace Science and Technology 32 (2014) 60–65.
7. Rajavathsavai, D, Khapre, A, Munshi, B, “Numerical Study of Vortex Formation inside a Stirred Tank”, International Journal of Chemical, Molecular, Nuclear, Materials and Metallurgical Engineering Vol:8, No:12, 2014.
8. Tamburini A, Gagliano G, Scargiali F, Micale G, Brucato A, Ciofalo M, “CFD Simulation of Radially Stirred Baffled and Unbaffled Stirred Tanks”, Chemical Engineering Transactions, 2019, 74, 1033-1038 DOI:10.3303/CET1974173.
9. David J. Chato, D.J, Dalton, P.J, Dodge, F. T, Green, S. Liquid Motion Experiment Flight Test Results. NASA, NASA/TM—1998-208479. July 1998.

Numerical Study on De-Icing of Aeroplane Wing Using Piezoelectric Materials

K. Guru Brahmam*, M. Chandra Sekhar Reddy, T Ramamohan Rao

* Department of Mechanical Engineering, Chaitanya Bharathi Institute of Technology, Gandipeta, Hyderabad, 500075, Telangana, India.
[2]Department of Mechanical Engineering, University College of Engineering (Autonomous), Osmania University, Hyderabad, 500007, Telangana, India.
[1]Department of Mechanical Engineering, Vasavi College of Engineering, Ibrahim Bagh, Hyderabad, 500089, Telangana, India.
Email: gurubrahmam_mech@cbit.ac.in

ABSTRACT

The focus of the present investigation is to de-ice an airfoil wing using vibration induced by piezoelectric material. We selected symmetrical airfoil (NACA0015) for the numerical simulation. Airfoil is designed using solid works as airfoil data. Piezo electric patches and ice layer are designed and assembled to the airfoil wing using solid works. The final model is imported into ANSYS. Modal analysis is carried out for extraction of frequencies and mode shapes. Harmonic analysis is carried out for maximum shear stress. The results of these simulations allowed optimizing the positioning of the patches and angle of piezo on the structure and the optimal excitation voltage for the piezoelectric patches. Results are presented in the form of tabular data and digital photographs

Keywords: *De-Icing, wing, Piezoelectric Materials, Modal Analysis, Voltage.*

1. INTRODUCTION

Flight safety is undoubtedly the most important requirement for modern aircraft design and operation. However, in reality, aircraft flight performance and safety are inevitably affected by adverse meteorological conditions, one such weather condition is icing. Aircraft icing can cause severe aerodynamic and flight mechanical effects, thus threatens aircraft flight safety. Ice formation affects an airplane's performance by degrading its ability to generate lift. Ice accretes near the leading edge of an aircraft wing as it is a stagnation point. Ice deposition changes the leading-edge profile of the air foil and severely affects the lift generating ability of the wing. Ice formation takes place either on the ground or in flight.

The term de-icing means removal of the layer of ice from the surface of the body. Many de-icing techniques are implemented to prevent and remove ice from aircraft. The most commonly used de-icing techniques are chemical de-icing and anti-icing, electro-thermal de-icing, pneumatic de-icing, electro-impulse de-icing, and electro-vibratory de-icing. Piezoelectric de-icing, a new electro-vibratory de-icing technology, recently is proposed to apply to the aircrafts. This system has such characters as simple structure, less energy consumption and convenient maintenance. It is promising with low power requirement of the order of 1-3 kW which indicates good application prospect in the future.

2. LITERATURE REVIEW

The literature survey has revealed that several researchers attempted to find the widely interested study in a numerical model of a simple flat plate was elaborated to understand phenomena involved in vibration-based de-icing and assist with the design of the piezoelectric de-icing system. Ramanathan [1] et al. studied that resonating piezoelectric

*Corresponding author: E-mail: gurubrahmam_mech@cbit.ac.in

elements were used to generate ultrasonic surface waves to produce shear stress at the ice interface and used an aluminum plate on which a piezoelectric actuator patch was bonded. The actuator was excited at a frequency of 1 MHz, the resonant frequency of the actuator, to remove an ice layer accreted a few centimeters ahead of the actuator. Delamination of the ice occurred after more than a hundred seconds and thermal energy released from the actuator played an important role in it. **Kandagal and Venkatraman [2]** investigated Similar to the de-icing mechanism explored by Venna partially, Kandagal and Venkatraman succeeded in de-icing a cantilevered flat plate with piezoelectric actuators by exciting its resonant frequencies. Excitation of the fourth mode, at 805 Hz, resulted in instantaneous delamination of the ice at several locations on the plate, without any trace of heating from the actuators. Analysis of the results showed that shear stress generated at the interface seemed to be responsible for breaking the ice adhesion to the substrate.**M. Matbou Riahi [3],** et al. mainly examines the mechanical behavior at the ice/aluminum interface in order to develop a numerical model simulating de-icing. The numerical results obtained using the beam theory show important differences compared to experimental data. **Tian Baz [4]** et al studied the analytic and experimental research of a vibration de-icing method for aircrafts with piezoelectric transducer as the actuator. The power consumption for vibration de-icing is about 36.5 w/m^2, which is only 1.57 % of the power consumption when using the latest electro-thermal de-icing method. **Palacios [5]** et al. studied ultrasonic waves and their dispersion on a flat plate. It was showed that as the excitation frequency approached the resonant frequency of the actuator, the adhesion of the ice diminished, and the plate temperature increased. The study concluded that the excitation frequency should be below 100 kHz since strains generated diminished with a frequency increase. **Kalkowski [6]** et al. used numerical simulations to estimate the shear stress at the interface generated by piezoelectric actuators and the matching power consumption of the actuators. **Habibi [7]** et al. investigated the use of piezoelectric actuators to excite shear stresses on Carbon-Fiber-Reinforced Polymer (CFRP) as a de-icing system. They used FEM to study the wave propagation through this material. With the results they established an optimal excitation of the system by comparing the resulting shear stress with the adhesive shear strength of ice. The obtained results will be tested experimentally in a later study. **Budinger [8]** et al. developed an analytical model for piezoelectric de-icing at ultrasonic frequencies. The model showed that flexural modes generate more shear stress at the ice/substrate interface than extensional modes.

Yin [9] et al. studied a new non-thermal method–ultrasonic de-icing for wind turbine blade is proposed. Firstly, based on the theory of ultrasonic de-icing, the harmonic analysis of the structure of the composite plate-ice layered system is investigated using the finite element method. The simulation results showed that ultrasonic de-icing method is feasible for wind turbine blade de-icing purposes. **Palacios [10]** implemented a 3D finite element model and used it to design de-icing system experimental setups. With the help of this tool, they investigated the impedance matching for excitation, which lead to promising experimental results. **Yihua Cao [11] et al,** a brief review of the research on aircraft icing is presented. The following aspects are discussed. First, the causes, types, severity and natural parameters of aircraft icing are introduced. Then, the various effects of ice accretion on aircraft aerodynamic performance, stability, controllability as well as the existing estimation methods are summarized and analyzed. **Prashanth Sagar Reddy, Beeram [12] et al. C**omprehensive study was conducted to characterize ice adhesion strength over various surfaces by using a custom-built shear strength tester. **Boutros [13]**proposed a de-icing solution using lightweight Macro Fiber Composite (MFC) actuators on the leading edge of a wing. The developed numerical model for MFC actuators was validated experimentally on cantilever

ISBN - 978-93-95038-50-8

beams. **Harvey [14]** followed by **Villeneuve [15] et al.** demonstrated a proof of concept for de-icing with actuator patches at structural resonant frequencies matching the first modes of the structures on which they were bonded. Total or partial de-icing was successfully achieved for a flat plate, a thinned Bell 206 main rotor blade, and a Bell 206 tail rotor blade sections. Numerical simulations were used to predict the resonant frequencies and the mode shapes to optimally position and drive the actuators.

In this paper The modal analysis of Testing Skin with Piezoelectric Ceramics is done by generating mesh and giving fixed support. The following frequencies and their corresponding mode shapes are extracted as the result of modal analysis. Harmonic Analysis is carried out for maximum shear stress by taking frequencies extracted from modal analysis and voltage as input, evaluating results, Observing and recording shear stress.

The Harmonic analysis is carried out with the frequency from 0 to 1000Hz and the excitation voltage 300V. The maximum shear stress is obtained with the natural frequency 977.5 Hz in harmonic response. The above procedure is repeated with PZT at different locations on the wing.

3. PROBLEM STATEMENT

The finite element analysis software ANSYS has been proved effective in years of applications on vibration analysis, it is employed here to investigate the influence of the length of piezoceramic actuator to the vibration excitation of the wing. In the finite element model the length of the wing is 395 mm and the thickness is 2mm, and the material properties are also defined. The material of the square actuator is PZT5H with the thickness 0.5mm. The wing is fixed on one side, and multiple PZT patches are bonded on the plate at the wave crest or trough where produces the largest strain energy. Alternating voltage is applied to the PZT to excite the vibration of the wing through reverse piezoelectric effect, and the length of the PZT will be changed to search for its relationship with the vibration intensity of certain mode. For our model we have taken 50.8x50.8x0.5mm as PZT dimensions as we are studying wing with smaller dimensions when compared to original aeroplane wing.

4. RESEARCH METHODOLOGY

This numerical model was developed to design and predict optimal excitation of structures for de-icing purpose. This study allowed to develop a numerical model of a wing with piezoelectric patches and understand optimal phasing of the actuators. The numerical model is used in the further phase of the project by adding ice layers for investigation of vibration-based de-icing, with the final objective of developing and integrating a piezoelectric actuator de-icing system to an Aircraft wing structure.

The results of these simulations allowed to optimize the positioning of the actuators on the structure and the optimal phasing of the actuators for mode activation. A numerical model of the final setup was elaborated with the piezoelectric actuators optimally positioned on the wing and meshed with piezoelectric elements. Electrical boundary conditions were applied to the actuators to excite the vibration of the Aero plane wing. The results validated the model when the Aero plane wing is optimally excited.

ISBN - 978-93-95038-50-8

4.1. FLOW CHART FOR SIMULATION

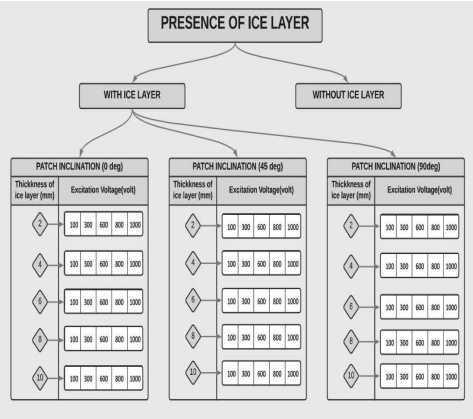

Figure 1. Flow chart for analysis
.

Figure 2. Design of aero plane wing with PZT patch and Ice Layer in Solid works

4.2. DESIGN OF AERO PLANE WING WITH PZT PATCH AND ICE LAYER

After modelling of airfoil wing ice layer is assembled on the leading edge of the wing with different thickness for each model. Piezoelectric patches are also attached to the wing at different locations and in different numbers.

4.3 MODAL ANALYSIS AND HARMONIC RESPONSE ON AERO PLANE WING WITH PIEZOELECTRIC PATCHES AND ICE LAYER

Table 1. Modal analysis

Tabular Data

	Mode	Frequency [Hz]
11	11.	575.33
12	12.	667.91
13	13.	692.4
14	14.	707.96
15	15.	710.62
16	16.	815.97
17	17.	828.07
18	18.	840.82
19	19.	913.81
20	20.	929,39

4.4 SUMMARY

The de-icing of Aero plane wing using piezo electric material has been done using SOLID WORKS and ANSYS. The modal and harmonic analysis of aero plane wing has been done. Mode shapes and frequencies are obtained from modal analysis and from the harmonic analysis we can determine the shear stress required to break the ice. To remove ice successfully from aluminum wing we need 0.52 MPa of shear stress. To achieve this goal, trial and error voltages have been taken and resulting shear stress values are found and recorded. The results obtained from harmonic response are compared with the literature study. These results would further be interpreted in results and discussion.

ISBN - 978-93-95038-50-8

5. RESULTS AND DISCUSSION

The main objective of our work is to break ice on the Aero plane wing by applying voltage to the PZT and getting required shear stress at that particular location, so ice adhesion properties are also studied while doing project, the same details are mentioned below Ice adhesion is based on physical and chemical processes that exist between the ice and solid interface. In general, the adhesion forces can be categorized into three different types: chemical adhesion that includes covalent and electrostatic forces; thermodynamic adhesion involving van der Waals forces and hydrogen bonding; mechanical adhesion due to solid surface roughness. So, from reference paper (characterisation of ice adhesion strength over different surfaces pertinent to aircraft anti-/de-icing by Prasanth Sagar Reddy Beeram) we have taken ice adhesion strength of aluminium alloy taken as 0.09Mpa for aluminium 6061.

We have recorded shear stress values on the aero plane wing by giving different voltages to the PZT material in the ANSYS simulation software, and the same process is repeated for various models with PZT at different locations from the fixed end.

We have analysed harmonic response at maximum deformation frequency as mentioned in the methodology chapter. So, for the first model we obtained shear stress values for different voltage inputs and the same process is repeated for remaining models. The same is presented below as tabular form.

Table 2. Shear stress values of the first mode with 100V

S.NO	Frequency (Hz)	Max shear stress (MPa)	Shear stress (XY) MPa	Shear stress (YZ) MPa	Shear stress (XZ)MPa
1	150	0.0090787	0.0041753	0.0028347	0.0061255
2	200	0.0090233	0.0040877	0.0028384	0.0060105
3	250	0.0090367	0.0041114	0.0028364	0.0060394
4	300	0.0090515	0.0041214	0.0028368	0.0060419
5	350	0.0090523	0.004128	0.0028421	0.0061272
6	400	0.0090868	0.0041922	0.0028377	0.0061084
7	450	0.0090212	0.0040642	0.0028345	0.0060486
8	500	0.0090377	0.0040893	0.00283	0.0060705
9	550	0.0089735	0.0040647	0.0027886	0.0059402
10	600	0.0090941	0.0041259	0.0028569	0.006181

Table 3. Shear stress values for second mode with 100V

S.No	Frequency (Hz)	Max shear stress (MPa)	Shear stress (XY) MPa	Shear stress (YZ) MPa	Shear stress (XZ)MPa
1	150	0.047805	0.028671	0.023949	0.018797
2	200	0.047679	0.028438	0.023983	0.018737
3	250	0.047717	0.028472	0.023976	0.018757
4	300	0.047722	0.028499	0.023973	0.018793
5	350	0.047751	0.02852	0.023974	0.018789
6	400	0.047802	0.028645	0.02393	0.018886
7	450	0.047575	0.028333	0.024006	0.018724
8	500	0.047624	0.028216	0.023995	0.01877
9	550	0.047244	0.02769	0.024063	0.019022
10	600	0.047828	0.028724	0.023961	0.018759

ISBN - 978-93-95038-50-8

Table 4. Shear stress values for third mode with 100V

S.No	Frequency (Hz)	Max shear stress (MPa)	Shear stress (XY) MPa	Shear stress (YZ) MPa	Shear stress (XZ)MPa
1	100	0.0041437	0.0017046	0.00089307	0.0017183
2	200	0.0041367	0.0017005	0.00089199	0.0017173
3	300	0.0042967	0.0017104	0.0010235	0.0015551
4	400	0.0041605	0.0017051	0.0008961	0.0016993
5	500	0.0041548	0.0017085	0.00088868	0.0017229
6	600	0.0041368	0.0017103	0.00089164	0.001763
7	700	0.0046788	0.0035704	0.0024507	0.0023381
8	800	0.016048	0.0077932	0.0079443	0.0054846
9	900	0.0042071	0.0016178	0.00095532	0.0016707
10	1000	0.0041521	0.0017054	0.00088702	0.0017061

Table 5. Shear Stress values for the fourth mode with 300V

S.NO	Frequency (Hz)	Max shear stress (MPa)	Shear stress (XY) MPa	Shear stress (YZ) MPa	Shear stress (XZ)MPa
1	122.5	0.076108	0.021041	0.061969	0.018795
2	145	0.075702	0.021277	0.06155	0.018959
3	302.5	0.076452	0.020846	0.06236	0.018698
4	415	**0.11178**	0.058249	0.069522	0.05213
5	527.5	0.076852	0.020822	0.062816	0.018579
6	572.5	0.076767	0.020731	0.062683	0.018713
7	617.5	0.076698	0.020818	0.062694	0.018938
8	662.5	0.076609	0.020773	0.062498	0.018495
9	707.5	0.076529	0.020773	0.062444	0.018623
10	752.5	0.076261	0.021019	0.062438	0.018739
11	797.5	0.076037	0.021127	0.06213	0.018907
12	842.5	**0.76507**	**0.60332**	**0.17558**	**0.12334**
13	887.5	0.077714	0.021307	0.063222	0.018623
14	977.5	**1.0086**	**0.84915**	**0.4491**	**0.35533**
15	1000	0.076801	0.021104	0.06257	0.018458

Table 6. Shear Stress values for the fifth mode with 300V

S.NO	Frequency (Hz)	Max shear stress (MPa)	Shear stress (XY) MPa	Shear stress (YZ) MPa	Shear stress (XZ)MPa
1	150	0.14342	0.086013	0.071847	0.056392
2	200	0.14304	0.085313	0.07195	0.056211
3	250	0.14315	0.085417	0.071927	0.056271
4	300	0.14317	0.085496	0.071918	0.056378
5	350	0.14325	0.085559	0.071922	0.056368
6	400	0.14341	0.085934	0.07179	0.056659
7	450	0.14273	0.084998	0.072018	0.056173
8	500	0.14287	0.084649	0.071985	0.05631
9	550	0.14173	0.083071	0.07219	0.057065
10	600	0.14348	0.086172	0.071883	0.056278

ISBN - 978-93-95038-50-8

Table 7. Shear Stress values for sixth mode with 600V

S.NO	Frequency(Hz)	Max shear stress(MPa)	Shear stress(XY) MPa	Shear stress(YZ) MPa	Shear stress(XZ)MPa
1	190	0.31488	0.07216	0.1436	0.031461
2	280	0.31481	0.072054	0.14352	0.03156
3	370	0.31499	0.072247	0.14365	0.031368
4	460	0.31493	0.072198	0.14362	0.031438
5	540	0.31501	0.07214	0.14359	0.031497
6	640	0.31481	0.072155	0.14358	0.031529
7	730	0.3147	0.072095	0.14353	0.031661
8	820	0.31439	0.071368	0.14296	0.032954
9	910	0.31522	0.072447	0.14372	0.030746
10	1000	0.31501	0.072231	0.14362	0.031242

Table 8. Shear Stress values for seventh mode with 600V

S.NO	Frequency (Hz)	Max shear stress (MPa)	Shear stress (XY) MPa	Shear stress (YZ) MPa	Shear stress (XZ)MPa
1	150	0.054472	0.025052	0.017008	0.036753
2	200	0.05414	0.025052	0.01703	0.036063
3	250	0.05422	0.024669	0.017018	0.036236
4	300	0.054309	0.024728	0.017021	0.036252
5	350	0.054314	0.024768	0.017053	0.036763
6	400	0.054314	0.025153	0.017026	0.03665
7	450	0.054127	0.024536	0.017007	0.036291
8	500	0.054226	0.024536	0.01698	0.036423
9	550	0.053841	0.024388	0.016732	0.035641
10	600	0.054565	0.024755	0.017141	0.037086

Table 9. Shear Stress values for seventh mode with 600V

S.NO	Frequency (Hz)	Max shear stress (MPa)	Shear stress (XY) MPa	Shear stress (YZ) MPa	Shear stress (XZ) MPa
1	150	0.06387	0.011677	0.011677	0.036174
2	200	0.063744	0.015502	0.011697	0.03598
3	250	0.063774	0.015567	0.01168	0.036072
4	300	0.06387	0.015597	0.011698	0.036069
5	350	0.06385	0.01563	0.011667	0.03116
6	400	0.064031	0.015997	0.01653	0.036333
7	450	0.063706	0.015336	0.011693	0.036176
8	500	0.063657	0.015477	0.011681	0.03624
9	550	0.064247	0.015628	0.011786	0.037548
10	600	0.06392	0.015753	0.011628	0.036127

ISBN - 978-93-95038-50-8

Table 10 Shear Stress values for ninth mode with 800

S.NO	Frequency (Hz)	Max shear stress (MPa)	Shear stress (XY) MPa	Shear stress (YZ) MPa	Shear stress (XZ)MPa
1	150	0.08516	0.021009	0.015569	0.048232
2	200	0.084993	0.020669	0.015596	0.047974
3	250	0.085032	0.020756	0.015574	0.048096
4	300	0.08516	0.02084	0.015597	0.048092
5	350	0.085133	0.02084	0.015569	0.048155
6	400	0.085374	0.02133	0.015537	0.048445
7	450	0.084941	0.020448	0.01559	0.048235
8	500	0.084876	0.020636	0.015574	0.04832
9	550	0.085663	0.020837	0.015715	0.050065
10	600	0.085227	0.021003	0.015504	0.048169

Table 11.: Shear Stress values for tenth mode with 800V

S.NO	Frequency (Hz)	Max shear stress (MPa)	Shear stress (XY) MPa	Shear stress (YZ) MPa	Shear stress (XZ)MPa
1	150	0.072629	0.033403	0.022678	0.049004
2	200	0.072186	0.032702	0.022707	0.048084
3	250	0.072294	0.032892	0.022691	0.048315
4	300	0.072412	0.032971	0.022694	0.048335
5	350	0.072412	0.033024	0.022737	0.049017
6	400	0.072694	0.033537	0.022701	0.048867
7	450	0.072169	0.032514	0.022676	0.048389
8	500	0.072301	0.032714	0.02264	0.048564
9	550	0.071788	0.032518	0.022309	0.047522
10	600	0.072753	0.033007	0.022855	0.049448

Table 12. Shear stress values for Eleventh model for the excitation voltage of 1000V

S.NO	Frequency (Hz)	Max shear stress (MPa)	Shear stress (XY) MPa	Shear stress (YZ) MPa	Shear stress (XZ)MPa
1	122.5	**0.76108**	0.21041	0.61969	0.18795
2	145	0.76108	0.21277	0.6155	0.18959
3	167.5	0.89829	0.4111	0.71335	0.17614
4	190	0.77024	0.20903	0.63032	0.18518
5	212.5	0.76737	0.20771	0.62689	0.18605
6	235	0.76624	0.20742	0.62558	0.1864
7	257.5	0.76555	0.20783	0.6248	0.18662
8	280	0.76511	0.20811	0.62415	0.18681
9	302.5	0.76452	0.20846	0.6236	0.18698
10	325	0.76393	0.20883	0.62294	0.18719
11	347.5	0.76312	0.20932	0.62208	0.18745
12	370	0.76197	0.21011	0.62074	0.1877
13	392.5	0.75926	0.21153	0.61782	0.18927
14	415	1.1178	0.58249	0.69522	0.5213
15	437.5	0.85768	0.33312	0.69147	0.16607
16	460	0.77639	0.21219	0.63619	0.18285
17	482.5	0.77147	0.20978	0.63114	0.18285

Contd…

S.NO	Frequency (Hz)	Max shear stress (MPa)	Shear stress (XY) MPa	Shear stress (YZ) MPa	Shear stress (XZ)MPa
18	505	0.76972	0.20866	0.62915	0.18533
19	527.5	0.76852	0.20822	0.62816	0.18579
20	550	0.7684	0.2087	0.62755	0.18614
21	572.5	0.76767	0.20731	0.62683	0.18713
22	595	0.76698	0.20729	0.62673	0.18732
23	617.5	0.76647	0.20818	0.62694	0.18938
24	640	0.76679	0.20974	0.62415	0.18743
25	662.5	0.76609	0.20773	0.62498	0.18495
26	685	0.76566	0.20757	0.62481	0.18575
27	707.5	0.76529	0.20789	0.62444	0.18623
28	730	0.76471	0.20789	0.62444	0.1868
29	752.5	0.76261	0.2082	0.62379	0.18739
30	775	0.76213	0.21019	0.62438	0.18758
31	797.5	0.76037	0.21019	0.62309	0.18907
32	820	0.75933	0.21127	0.6213	0.19562
33	842.5	7.6507	0.22121	0.61975	1.2334
34	865	0.76394	6.0332	0.61975	0.18458
35	887.5	0.77714	0.21948	1.7558	0.18623
36	910	0.7719	0.21307	0.62773	0.18623
37	932.5	0.77013	0.21019	0.63222	0.18667
38	955	0.77026	0.20888	0.63066	0.18912
39	977.5	**10.086**	8.4915	4.491	3.5533
40	1000	0.76801	0.21104	0.6257	0.18458

Table 13. Shear Stress values for twelfth mode with 1000V

S.NO	Frequency (Hz)	Max shear stress (MPa)	Shear stress (XY) MPa	Shear stress (YZ) MPa	Shear stress (XZ)MPa
1	122.5	**0.76108**	0.21041	0.61969	0.18795
2	145	0.76108	0.21277	0.6155	0.18959
3	167.5	0.89829	0.4111	0.71335	0.17614
4	190	0.77024	0.20903	0.63032	0.18518
5	212.5	0.76737	0.20771	0.62689	0.18605
6	235	0.76624	0.20742	0.62558	0.1864
7	257.5	0.76555	0.20783	0.6248	0.18662
8	280	0.76511	0.20811	0.62415	0.18681
9	302.5	0.76452	0.20846	0.6236	0.18698
10	325	0.76393	0.20883	0.62294	0.18719
11	347.5	0.76312	0.20932	0.62208	0.18745
12	370	0.76197	0.21011	0.62074	0.1877
13	392.5	0.75926	0.21153	0.61782	0.18927
14	415	1.1178	0.58249	0.69522	0.5213
15	437.5	0.85768	0.33312	0.69147	0.16607
16	460	0.77639	0.21219	0.63619	0.18285
17	482.5	0.77147	0.20978	0.63114	0.18285
18	505	0.76972	0.20866	0.62915	0.18533
19	527.5	0.76852	0.20822	0.62816	0.18579
20	550	0.7684	0.2087	0.62755	0.18614

Contd…

S.NO	Frequency (Hz)	Max shear stress (MPa)	Shear stress (XY) MPa	Shear stress (YZ) MPa	Shear stress (XZ)MPa
21	572.5	0.76767	0.20731	0.62683	0.18713
22	595	0.76698	0.20729	0.62673	0.18732
23	617.5	0.76647	0.20818	0.62694	0.18938
24	640	0.76679	0.20974	0.62415	0.18743
25	662.5	0.76609	0.20773	0.62498	0.18495
26	685	0.76566	0.20757	0.62481	0.18575
27	707.5	0.76529	0.20789	0.62444	0.18623
28	730	0.76471	0.20789	0.62444	0.1868
29	752.5	0.76261	0.2082	0.62379	0.18739
30	775	0.76213	0.21019	0.62438	0.18758
31	797.5	0.76037	0.21019	0.62309	0.18907
32	820	0.75933	0.21127	0.6213	0.19562
33	842.5	7.6507	0.22121	0.61975	1.2334
34	865	0.76394	6.0332	0.61975	0.18458
35	887.5	0.77714	0.21948	1.7558	0.18623
36	910	0.7719	0.21307	0.62773	0.18623
37	932.5	0.77013	0.21019	0.63222	0.18667
38	955	0.77026	0.20888	0.63066	0.18912
39	977.5	**10.086**	8.4915	4.491	3.5533
40	1000	0.76801	0.21104	0.6257	0.18458

The coupling element type is PZT for the piezoelectric material (Patch) and Aluminium for testing skin i.e., wing. The freedom of the nodes on the testing edge is constrained too. However, the deformation position of the testing skin with PZT patch differs a little from the skin without PZT patches. As we have already discussed in methodology, we have taken PZT patches at different locations and studied shear stress at different voltages for each location. The harmonic analysis is carried out with the frequency extracted from modal analysis and corresponding shear stress varying with different voltage inputs is illustrated in above figures.

As we have discussed the ice adhesion strength for aluminium alloy is 0.52 MPa. Once the shear stress at that location reaches ice adhesive shear strength, this force can remove the ice adhered to the skin, which means it is feasible to design this piezoelectric de-icing system in this Simulation of “De-icing on aero plane wing with piezo electric material”.

6. CONCLUSION

The existing de-icing methods have some disadvantages. To solve these problems, de-icing with piezo electric materials is studied in this project. Piezoelectric materials are used and bonded on the surface of the structure to act as the actuators. At different PZT locations, shear stress values are determined at maximum deformation frequency. To remove ice successfully from aluminum wing we need 0.52 MPa of shear stress. To achieve this goal, trial and error voltages have been taken and resulting shear stress values are found and recorded.

Based on the Numerical Analysis and Simulation in ANSYS, the following conclusions can be drawn: The present method can be used to remove ices at any position when the piezoelectric patches are evenly distributed on the whole structure. On the other hand, when

ISBN - 978-93-95038-50-8

the icing positions are fixed, through the reasonable arrangement of piezoelectric patches, less piezoelectric patches are needed.

REFERENCES

1. Ramanathan, S. An Investigation on the Deicing of Helicopter Blades Using Shear Horizontal Guided Waves. Ph.D. Thesis, The Pennsylvania State University, University Park, PA, USA, 2005.
2. Kandagal, S.; Venkatraman, K. Piezo-actuated vibratory deicing of a flat plate. In Proceedings of the 46th AIAA/ASME/ASCE/AHS/ASC Structures, Structural Dynamics and Materials Conference, Austin, TX, USA, 18–21 April 2005; p. 2115
3. M. Matbou Riahi, D. Marceau a, C. Laforte, J. Perron The experimental/numerical study to predict mechanical behaviour at the ice/aluminum interface (2011)
4. Tian Baz, Chunling Zhu, Bo Miao, Kai Li, Chengxiang Zhu., Vibration de-icing method with piezoelectric actuators (2014)
5. Palacios, J.L.; Zhu, Y.; Smith, E.; Rose, J. Ultrasonic Shear and Lamb Wave Interface Stress for Helicopter Rotor Deicing Purposes. In Proceedings of the 47th Structures, Structural Dynamics and Materials Conference, Newport, RI, USA, 1–4 May 2015.
6. Kalkowski, M.; Waters, T.; Rustighi, E. Removing surface accretions with piezo-excited high-frequency structural waves. In Active and Passive Smart Structures and Integrated Systems 2015; International Society for Optics and Photonics: Bellingham, WA, USA, 2015.
7. Habibi, H.; Chong, A.; Kanfoud, J.; Selcuk, C.; Gan, T.H.; Mayhew, D. Simulation of an electro-mechanical ice protection system for aircraft structure based on ultrasonic guided wave. In Proceedings of the Greener Aviation 2016, Brussels, Belgium, 11–13 October 2016.
8. Budinger, M.; Pommier-Budinger, V.; Napias, G.; Costa da Silva, A. Ultrasonic Ice Protection Systems: Analytical and Numerical Models for Architecture Tradeoff. J. Aircr. 2016, 53, 680–690.
9. Congbo Yin, Zhendong Zhang, Zhenjun Wang, Hui Guo. Numerical simulation and experimental validation of ultrasonic de-icing system for wind turbine blade (2016)
10. Palacios, J.; C Smith, E.; Zhu, Y.; L Rose, J.; Morrow, P. Global Ultrasonic Shear Wave Anti-Icing Actuator for Helicopter Blades. In Annual Forum Proceedings-American Helicopter Society; American Helicopter Society, Inc.: Virginia Beach, VA, USA, 2017.
11. Aircraft icing: an ongoing threat to aviation safety (2017) Yihua Cao, Wenyuan Tan, Zhenlong Wu.
12. by Prashanth Sagar Reddy Beeram Characterization of ice adhesion strength over different surfaces pertinent to aircraft anti-/de-icing (2017).
13. Boutros Azizi, Richard J. Prazenica, and Daewon Kim, Finite Element Modeling of Macro-Fiber Composite Actuators for Wing De-Icing Applications (2018).
14. LI Qingying, ZHU Yongjiu, Analysis of the Application of Piezoelectric Ceramic Material in the De-Icing Technique of the Aircrafts (2018).
15. Villeneuve, E.; Harvey, D.; Zimcik, D.; Aubert, R.; Perron, J. Piezoelectric De-Icing System for Rotorcraft. J. Am. Helicopter Soc. (2020).

ISBN - 978-93-95038-50-8

Terminal Phase Guidance Design for an Anti-Ship Bank-To-Turn (BTT) Cruise Missile

N. Akilandeswari[1*], Mallikarjun. Bangi[1*], K.K. Mangrulkar[2], and G. Naresh Kumar[3]

[1]Engineer, Hyderabad, Telangana, India,
[1]Associate Professor, DIAT, Pune, Maharashtra, India,
[3]Scientist, DRDL, Hyderabad, Telangana, India,

ABSTRACT

In this paper, a different approach guidance technique is evolved by generating an angle, to guide an anti-ship cruise missile in terminal phase. The present work focuses to model and simulate a guidance scheme for terminal phase of an anti-ship Bank to Turn (BTT) cruise missile. The targeted ships are relatively slow compared to missile speeds. The modified guidance law of Pure Pursuit and Proportional Navigation (PN) in terms of course angle is implemented for stationary as well as moving targets in the lateral plane. The longitudinal guidance is achieved by computing the commanded altitude as a function of range to go.

Keywords: *Course Angle, Bank-to-Turn, Proportional Navigation, Pure Pursuit*

1. INTRODUCTION

Anti-ship missiles are guided missiles designed to attack moving ship targets. The target ships are relatively slow moving with respect to the interceptor. Hence, cruise missiles are designed to maintain constant speed over a long range where maneuverability is not a primary concern. They are categorized into Bank-To-Turn (BTT) missiles as they have wings and mimic an aircraft. In order to change the direction of flight, the vehicle banks, generating a component of lift along the lateral axis. Guidance forms a major component of the missile system. The reasons for perturbation in trajectory arise due to motion of target, launching errors, external and internal disturbances.

Guidance of BTT missiles is a widely researched topic. Proportional navigation (PN) is commonly used guidance law for anti-ship missiles. Biased Proportional Navigation (BPN) is proved superior to PN in presence of sensor noise. Jang et.al Jang Gyu Lee, Hyung Seok Han, and Young Jin Kim (1999) attempted to analyse and make a comparison of PN and BPN laws. Kent B. Watterson Kent B. Watterson (1983), discussed mainly about baseline guidance scheme with a pop-up maneuver, and sea-skimming guidance scheme. In his work, for terminal homing. PN guidance is used in azimuth plane and altitude hold cruising in elevation plane. It is also stated that PN is used separately in yaw and pitch plane at terminal impact phase. Cunningham, EP (1974) devised a zero heading error scheme and stated that, it is better than 3-D PN guidance by generating roll and pitch acceleration commands. A guidance law using Lyapnov function is formulated by Tae et.al Tae Soo No, John E. Cochran, Jr. and Eul Glon Kim (2001) where he explained about computing roll angle and pitch acceleration using non-zero effort miss by eliminating polar conversion and he also compared it with PN.

Terminal phase of BTT missile guidance along with impact angle and impact time constraints have been emphasized in works Qingchun Li, Wensheng Zhang, Gang Han and Yehui Yang (2015), Wei Lei, Shunli Li, and Yuqi Zhao (2012) and Hyo-Sang Shin, Jin Ik Lee, and Min-Jea Tahk (2006).

[*]Corresponding Author: Email: mallikarjun.bangimatam@gmail.com

Many guidance laws are evolved either to improve the guidance performance of the conventional Proportional Navigation and Pure Pursuit Guidance law are to achieve some specific requirements. Normally, BTT missile guidance involves conversion from Cartesian coordinates to roll angle and pitch acceleration using Polar Conversion Logic (PCL).

2. PROBLEM DEFINITION

The objective of all navigation, guidance and control (NGC) systems had been that the control system is designed efficiently to make the air frame follow the generated commands. The guidance system provides the necessary corrections in the flight path which are then translated to mechanical commands to the system's actuators by the autopilot. The vehicle considered is a BTT subsonic cruise missile with 0.75 Mach, which can be launched from multiple platforms. Its launch phase involves a solid propellant and once it enters cruise phase, the wings are deployed and the propulsion is switched to a turbofan engine.

The BTT missile guidance commonly involves conversion from Skid-To-Turn (STT) commands to pitch acceleration and roll angle. A course angle autopilot is suggested in place of a lateral acceleration autopilot in horizontal/yaw plane. The guidance is achieved using line of sight angle in yaw plane. Guidance algorithm generates course angle, which is provided as input to the autopilot. Here, an attempt is made to implement the same using different guidance laws, mainly Pure pursuit guidance, deviated pursuit guidance and with Proportional Navigation guidance.

3. MATHEMATICAL MODELLING

A non-linear 6-DOF model of the missile using Newton-Euler method is used for simulation. Typical axis convention for BTT missile using right handed co-ordinate system is shown in fig. 1. The body axis frame is denoted by (XB, YB, ZB) while the inertial co-ordinate frame is represented in NED Frame.

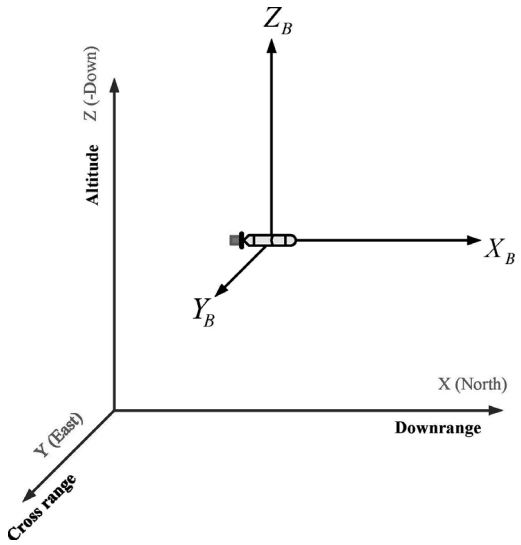

Figure 1: Axis convention of a missile

The various assumptions considered for analysis include:

1) The earth is at, non-rotating and is fixed in inertial space.
2) The atmospheric density is constant.
3) The vehicle is a rigid body.
4) The mass is constant as the fuel consumed by the turbofan engine is less and their effects are neglected.
5) The rate of change of inertia is negligible.
6) The thrust is assumed to be aligned with the center line of body X-axis and hence creates no moment about the center of mass of the vehicle.
7) As the missile is symmetric along both XY-plane and XZ-plane, the product of moments of Inertia IXY and IY Z are considered to be zero.

ISBN - 978-93-95038-50-8

3.1 MISSILE EQUATIONS OF MOTION

The mathematic model Randal W Beard and Timothy W McLain (2012) of a generic BTT missile is derived in this section. The non-linear translational kinematic equations that relate the inertial velocities $(\dot{p}_n, \dot{p}_e, \dot{p}_d)$ with the body frame velocities (u, v, w) are represented as:

$$\begin{aligned}
\dot{p}_n &= u\cos\theta\cos\phi + v(\sin\phi\sin\theta\cos\psi - \cos\phi\sin\psi) + w(\cos\phi\sin\theta\cos\psi + \sin\phi\sin\psi) \\
\dot{p}_e &= u\cos\theta\sin\psi + v(\sin\phi\sin\theta\sin\psi + \cos\phi\cos\psi) + w(\cos\phi\sin\theta\sin\psi - \sin\phi\cos\psi) \\
\dot{p}_d &= -u\sin\theta + v(\sin\phi\cos\theta) + w(\cos\phi\cos\theta)
\end{aligned} \quad (1)$$

The non-linear relationship between the Euler angle rates $(\dot{\phi}, \dot{\theta}, \dot{\psi})$ and angular velocities (p, q, r) is given by the following kinematic equations:

$$\begin{aligned}
\dot{\phi} &= p + q\sin\phi\tan\theta + r\cos\phi\tan\theta \\
\dot{\theta} &= q\cos\phi - r\sin\phi \\
\dot{\psi} &= q\sin\phi\sec\theta + r\cos\phi\sec\theta
\end{aligned} \quad (2)$$

The six-DOF equations of motion of the flight vehicle are

$$\begin{aligned}
\dot{u} &= rv - qw + \frac{F_x}{m} \\
\dot{v} &= pw - rq + \frac{F_y}{m} \\
\dot{w} &= qu - pv + \frac{F_z}{m} \\
\dot{p} &= \frac{I_{xz}(I_x - I_y + I_z)}{I_x I_z - I_{xz}^2} pq - \frac{I_z(I_z - I_y) + I_{xz}^2}{I_x I_z - I_{xz}^2} qr + \frac{I_z}{I_x I_z - I_{xz}^2} M_x + \frac{I_z}{I_x I_z - I_{xz}^2} M_x \\
\dot{q} &= \frac{(I_z - I_x)}{I_y} pr - \frac{I_{xz}}{I_y}(p^2 - r^2) + \frac{M_x}{I_y} \\
\dot{r} &= \frac{I_z(I_z - I_y) + I_{xz}^2}{I_x I_z - I_{xz}^2} pq - \frac{I_{xz}(I_x - I_y + I_z)}{I_x I_z - I_{xz}^2} qr + \frac{I_{xz}}{I_x I_z - I_{xz}^2} M_x + \frac{I_x}{I_x I_z - I_{xz}^2} M_x
\end{aligned} \quad (3)$$

Here, M_x, M_y and M_z represents the rolling, pitching and yawing moments about body X, Y and Z axes respectively while F_x, F_y and F_z represent the forces along body X, Y, and Z axes respectively. The dynamics of the flight vehicle are described by the following force and moment equations along the three co-ordinate axes.

$$M_x = QbSC_1, M_y = QbSC_m, M_z = QbSC_n \quad (4)$$

Where the moment co-efficient are given by the following equation:

$$\begin{pmatrix} C_1 \\ C_m \\ C_n \end{pmatrix} = \begin{pmatrix} C_{10} \\ C_{m0} \\ C_{n0} \end{pmatrix} + \begin{pmatrix} 0 & C_{l\beta} \\ C_{m\alpha} & 0 \\ 0 & C_{n\beta} \end{pmatrix} \begin{pmatrix} \alpha \\ \beta \end{pmatrix} + \frac{1}{2V_m} \begin{pmatrix} bC_{lp} & 0 & bC_{lr} \\ 0 & cC_{mq} & 0 \\ bC_{n_p} & 0 & bC_{n_r} \end{pmatrix} \begin{pmatrix} p \\ q \\ r \end{pmatrix} + \begin{pmatrix} C_{l\delta a} & 0 & C_{l\delta r} \\ 0 & C_{m\delta e} & 0 \\ C_{n\delta a} & 0 & C_{n\delta r} \end{pmatrix} \begin{pmatrix} \delta_a \\ \delta_e \\ \delta_r \end{pmatrix} \quad (5)$$

Here, $C_{l\beta}, C_{m\alpha}, and\ C_{n\beta}$ are known as the stability derivatives due to the effect of angle of attack (α) and side slip angle (β) while C_{lp}, C_{mq} and C_{nr} act as the damping derivatives. Also, $C_{l\delta a}, C_{m\delta e}, and\ C_{n\delta r}$ associated with the control surface deflections are called the primary control derivatives while $C_{l\delta a}, and\ C_{n\delta a}$ are known as the cross control derivatives that effect due to the coupling of roll and yaw motions. Similarly, the forces along various axes are given by:

$$\begin{pmatrix} F_x \\ F_y \\ F_z \end{pmatrix} = QS \begin{pmatrix} \sin\alpha & 0 & -\cos\alpha \\ 0 & 1 & 0 \\ -\cos\alpha & 0 & -\sin\alpha \end{pmatrix} \begin{pmatrix} C_L \\ C_Y \\ C_D \end{pmatrix} + \begin{pmatrix} T \\ 0 \\ 0 \end{pmatrix} + \begin{pmatrix} G_x \\ G_y \\ G_Z \end{pmatrix} \quad (6)$$

The dynamic pressure at a velocity 'Vm' is given by: $Q = \frac{1}{2}\rho V_m^{\,2}$ (7)

Here, the aerodynamic force co-efficients are described by

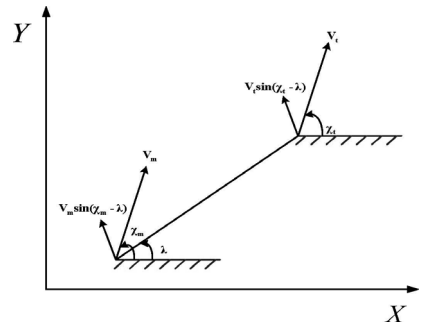

Figure 2: PN Guidance law in lateral plane

$$\begin{pmatrix} C_L \\ C_Y \\ C_D \end{pmatrix} = \begin{pmatrix} C_{L0} \\ C_{Y0} \\ C_{D0} \end{pmatrix} + \begin{pmatrix} C_{L\alpha} & 0 \\ 0 & C_{Y\beta} \\ C_{D\alpha} & 0 \end{pmatrix} \begin{pmatrix} \alpha \\ \beta \end{pmatrix} + \frac{1}{2V_m} \begin{pmatrix} 0 & cC_{Lq} & 0 \\ 0 & cC_{Dq} & 0 \\ bC_{Yp} & 0 & bC_{Yr} \end{pmatrix} \begin{pmatrix} p \\ q \\ r \end{pmatrix} + \begin{pmatrix} 0 & C_{L\delta e} & 0 \\ C_{Y\delta\alpha} & 0 & C_{Y\delta r} \\ 0 & C_{D\delta e} & 0 \end{pmatrix} \begin{pmatrix} \delta_\alpha \\ \delta_e \\ \delta_r \end{pmatrix} \quad (8)$$

Here, $C_{L\alpha}, C_{D\alpha}, C_{Y\beta}, C_{Lq}, C_{Dq}, C_{Yp}, and\, C_{Y\alpha}$ are known as the stability derivatives. $C_{L\delta_e}, C_{D\delta_e}, C_{Y\delta_a}, C_{Y\delta_r}$ are called as control derivatives. Thrust is assumed to be oriented along the nose of the missile. The gravity components in Eqn. 6 along the axes in body frame is represented as

$$\begin{pmatrix} G_x \\ G_y \\ G_z \end{pmatrix} = mg \begin{pmatrix} -\sin\theta \\ \cos\theta\sin\phi \\ \cos\theta\cos\phi \end{pmatrix} \quad (9)$$

3.2 MISSILE PARAMETERS

The following data is used for simulation: Kent B. Watter-son (1983). The elevator, aileron and rudder deflections are limited to ±15.

Table 1: Missile Parameters

S.No.	Parameter	Data	Units	S.No.	Parameter	Data	Units
1	Wing span, 'b'	2.58622	m	7	I_x	37.691731	kgm^2
2	Platform area, 'S'	1.11484	m^2	8	I_y	2043.217	kgm^2
3	Maximum chord 'c'	0.43098	m	9	I_z	2043.996	kgm^2
4	Missile velocity, "V_m"	255.72	ms^{-1}	10	I_{xz}	15.8630	kgm^2
5	Sea level Density, "p"	1.22505	kgm^{-3}	11	Thrust	2668.993	N
6	Mass of the missile, "m"	1000	kg				

3.3 SEEKER MODEL

Consider the 2D engagement geometry in a yaw plane as shown in fig 2. The components of relative missile to target separations along X and Y co-ordinates are expressed below:

$$\Delta X = X_t - X_m,\ \Delta Y = Y_t - Y_m \qquad (10)$$

Where (X_m & Y_m) are the missile positions, and (X_t & Y_t) are the target positions along north and east respectively. The relative velocity components in Earth co-ordinates are given by

$$\Delta V_x = V_{tx} - V_{mx},\ \Delta V_y = V_{ty} - V_{my} \qquad (11)$$

Where (V_{mx} & V_{my}) are the missile velocities and (V_{tx} &V_{ty}) are the target velocities along north and east respectively.

The relative separation or the relative range-to-go `R' between missile and target expressed in terms of its inertial components as

$$R = \sqrt{\Delta X^2 + \Delta Y^2} \qquad (12)$$

Differentiating the above equation, the closing velocity `Vc' is expressed as:

$$V_c = \frac{-\Delta X \times \Delta V_x + \Delta Y + \Delta V_y}{R} \qquad (13)$$

The Line of Sight (LOS) angle, `λ' and line of sight rate, `$\dot{\lambda}$' are expressed in terms of relative separation components as:

$$\lambda = \tan^{-1}\left(\frac{\Delta Y}{\Delta X}\right) \qquad (14)$$

$$\dot{\lambda} = \frac{\Delta X \times \Delta V_y - \Delta Y \times \Delta V_x}{R^2} \qquad (15)$$

3.4 REPRESENTATION OF COURSE ANGLE

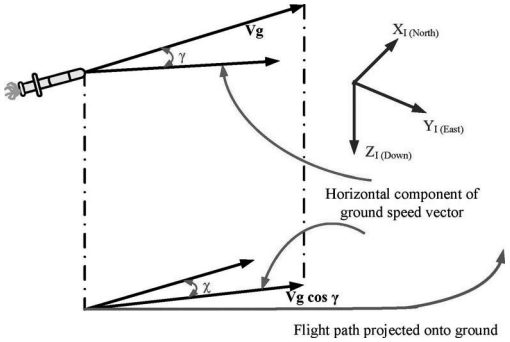

Figure 3: Visualization of Course angle

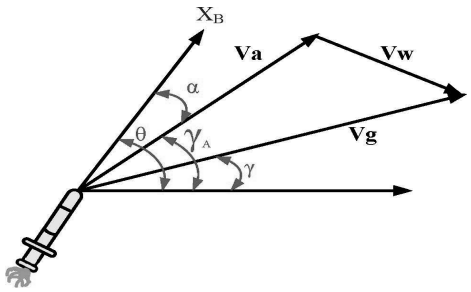

Figure 4: Schematic in Vertical plane

The direction of the ground speed vector relative to inertial frame as seen in fig. 3 is specified using two angles viz. the course angle (X) and the flight path angle (γ). Fig. 4 shows the flight path angle between the horizontal plane and the ground velocity vector V_g, while the course is the angle between the projection of the ground velocity vector onto the horizontal plane and true north as shown in fig. 5. The simulation is carried out in MATLAB

using Runge-Kutta-4 (RK4) method. When the altitude falls below ground level and when the instantaneous relative range between targets to missile is higher than its previous recorded value indicating that the missile is receding away from the target act as stopping criteria of simulation.

The maximum target velocity is assumed to be 30 m/s.

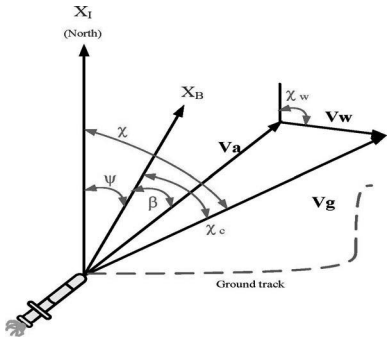

Figure 5: Schematic in Horizontal plane

4. GUIDANCE TECHNIQUES

The target ship's manoeuvrability and speed are negligible with those of anti-ship missiles which attain high-subsonic or supersonic speeds. Assumed that the missile speed is constant throughout the engagement. Guidance design assumes seeker to provide (λ), ($\dot{\lambda}$), (R) and (V_c) between the missile and target as inputs to the system. It is implemented separately in 2D planes i.e., in lateral (yaw-plane) and longitudinal (pitch-plane) guidance separately. Pure pursuit, Deviated pursuit and Proportional navigation guidance are used in the lateral plane. For altitude guidance, an altitude profile depending on relative range is generated and used as the commanded reference. The outputs are directed to second-order autopilot [7].

4.1 PURE PURSUIT GUIDANCE

Table 2: Pure Pursuit Guidance

Initial X_t (km)	Initial Y_t (km)	V_{tx} (m/s)	V_{ty} (m/s)	Miss Distance (m)
5	0.1	0	0	0.09899
5	0.5	0	0	0.08864
5	0.1	0	10	13.41
8	0.5	0	0	0.02358
8	0.2	0	0	0.08077
5	0.1	0	30	90.94

ISBN - 978-93-95038-50-8

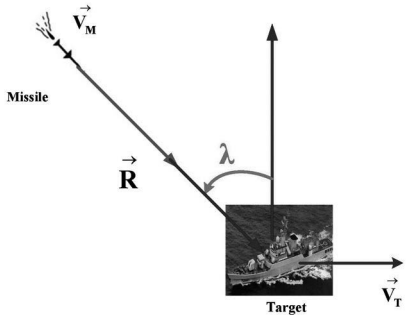

Figure 6: Pure pursuit guidance law

In principle, the pure pursuit guidance states that if the pursuer keeps pointing at the target, it shall collide with the target at one point, if the missile's velocity vector points at the target's current position at every instant of time. It is implemented by commanding the required course angle of the missile to be the line of sight angle between the missile and target as shown in fig 6 obtained from the seeker. $X = \lambda$ (16)

Table 3. Deviated Pursuit Guidance with k_λ=8

Initial X_t (km)	Initial Y_t (km)	V_{tx} (m/s)	V_{ty} (m/s)	Miss Distance
5	0.5	5	10	0.8045 m
5	0.1	0	10	0.8401 m
5	0.1	0	30	3.153 m
5	0.1	0	0	0.7033 m

While pure pursuit guidance works well with stationary targets, an anticipation is required to track the target in case of moving targets.

Results: Few test cases are simulated using pure pursuit guidance and the result is tabulated below in Table 2. The results show that as the target is simulated with a velocity, miss distances are huge for moving targets.

4.2 MODIFIED DEVIATED PURSUIT GUIDANCE

Table 4. Deviated Pursuit Guidance with Filter of DC Gain=1 and Time constant T=10

Initial X_t (km)	Initial Y_t (km)	V_{tx} (m/s)	V_{ty} (m/s)	Miss Distance (m)
5	0.5	5	10	0.8118
5	0.1	0	10	1.079
5	0.1	0	30	19.15
5	0.1	0	0	0.01144

Deviated pursuit is a form of pursuit guidance, there is a constant additional deflection added to the pure pursuit input. An (k_λ) additional term is introduced which is continuously varying along the missile downrange. The LOS rate is multiplied by a gain

ISBN - 978-93-95038-50-8

factor and is added to the LOS angle (pure pursuit input), thus calculating the required commanded course angle. $X = \lambda + k_\lambda \dot{\lambda}$ (17)

But, the miss distances depend upon the target velocity and relative initial error along the y-direction between missile and target in the inertial frame. The control demand from guidance loop increases as the missile approaches the target. A low pass filter of the form $\left[\frac{a}{s+a}\right]$ is added to the product of gain and LOS rate, with different filter time constants to remove high frequencies. The errors do not have a pattern and result in huge miss distances for some cases. Limiting the filter output or introducing non-linear gain at different ranges were not useful.

Results Few test cases are studied and the results have been tabulated in Table 3. A filter was added to the product of gain and rate of line of sight but errors changed depending on different filter time constants, and did not show a pattern. Large miss distances were found from case to case. Limiting the filter output or introducing non-linear gain at different ranges were not improving miss distances. Some of the cases are tabulated in Table 4.

4.3 PROPORTIONAL NAVIGATION GUIDANCE

By definition of Proportional Navigation (PN), the rate of change of line of sight (LOS) angle is zero. PN Guidance using Course Angle in order to achieve zero rate of change of LOS, the missile's velocity component perpendicular to the line of sight must be equal to the target's velocity component perpendicular to the line of sight.

$$V_m \sin(X_m - \lambda) = V_t \sin(X_t - \lambda) \quad (18)$$

$$Resolving\ (X_t - \lambda)\ X_m = \lambda + \sin^{-1}\left(\frac{V_{ty}\cos\lambda - V_{tx}\sin\lambda}{V_m}\right) \quad (19)$$

Proportional Navigation Guidance Using Roll Angle

By directly using roll angle, fig. 7 shows the block diagram of PN guidance law implementation.

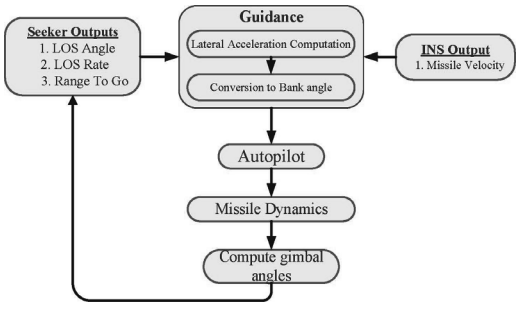

Figure 7: Block diagram of PN Guidance

$$a_c = N' V_c \dot{\lambda} \quad (22)$$

Re-writing lateral acceleration in terms of course angle is

$$V_m \dot{X} = N' V_c \dot{\lambda} \quad (23)$$

$$\text{Assuming } V_m \ ?\ V_t, \text{and hence. } V_c = V_m \Rightarrow \dot{X} = N' \dot{\lambda} \quad (24)$$

Relating $\dot{X}$ and $\phi \Rightarrow \phi = \tan^{-1}\left(\frac{N' V_m \dot{\lambda}}{g}\right) = \tan^{-1}\left(\frac{\dot{X} V_m}{g}\right)$ (25) This is limited to a maximum of ±30° and given as input to the roll autopilot directly.

Results: Few test cases have been simulated and results are tabulated in Table 5.

Table 5. PN Guidance using Course Angle

Initial X_t (km)	Initial Y_t (km)	V_{tx} (m/s)	V_{ty} (m/s)	Miss Distance
5	0.5	5	10	0.1232 m
5	0.2	0	30	0.1041 m
5	0.5	30	30	0.0250 m
5	0.1	0	30	0.0459 m
5	0.1	0	0	0.0989 m
5	0.1	0	10	0.0126 m

Designed a math model by representing lateral acceleration in terms of course angle, and directly commanding roll autopilot were developed. A test case was generated by following assumptions with initial distances 5 km and 0.5 km along inertial X-axis and Y-axis respectively with target velocity along north is 10 m/s and along east it is to be 30 m/s, and with Navigation Constant (N) = 3, the simulation were carried out and observed a miss distance error as 0.07913 metres.

4.4 COLLISION TRIANGLE IN PN GUIDANCE

For a simulation case using PN guidance, with initial target co-ordinates (Xt &Yt) of (5km&0.1km) and with initial velocity of 10m/s along the east direction, the miss distance and altitude error turns out to be 0.1237 m and 0.1840 m respectively.

The engagement trajectory is shown below in fig. 8. When the rate of change of line of sight becomes zero, the missile gets onto the collision course, and from then the current LOS remains parallel to the previous LOS. Data of missile and target positions have been generated for every 0.5 sec and the collision triangle is plotted in fig. 9.

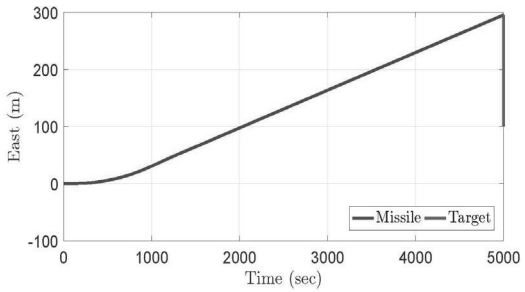

Figure 8: Trajectory

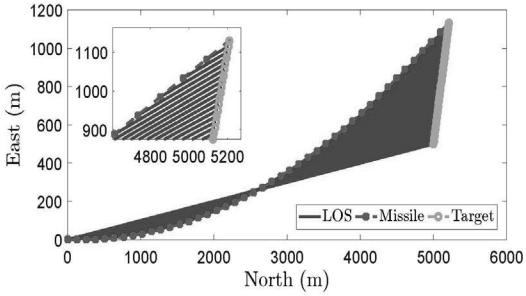

Figure 9: Collision Triangle

4.5 LONGITUDINAL GUIDANCE

In the longitudinal plane, a reference altitude signal needs to be generated from the start of terminal phase. Let h_0 and R_0 be the altitude and horizontal range at the start of terminal phase. The commanded altitude h_c needs to be proportional to the instantaneous horizontal

range. Assuming the target height is around 3 m, we aim to hit at 1.5 m and hence, we have,

$$\frac{h_c - 1.5}{h_o - 1.5} = \frac{R}{R_o} \Rightarrow h_c = \frac{h_o - 1.5}{R_o} R + 1.5 \quad (26)$$

On generalizing at every instant of time, $h_c = \frac{h_o - 1.5}{R_o}\left(R + \dot{R}dt\right) + 1.5 \quad (27)$

Thus, a smooth ramp signal is generated as the commanded reference such that the missile dives close to sea level only near to the point of engagement.

5. CONCLUSION

The guidance design using course angle is implemented in lateral and longitudinal planes separately. Guidance in the horizontal plane is achieved by modification of two different guidance principles. Analyses with various test cases show that final errors in miss distance at the point of impact are comparable thus indicating the robustness of the algorithm. Further, the work may be expanded into many areas including incorporating seeker model, including seeker noise and sea-clutter in the background.

ACKNOWLEDGEMENT

The authors thank competent authorities of Defence Research and Development Laboratory (DRDL), Hyderabad for granting permission to publish this piece of work.

REFERENCES

1. Cunningham, EP (1974). Guidance of a bank-to-turn missile with altitude control requirements. Journal of Spacecraft and Rockets, 11(5), 340-342.
2. Hyo-Sang Shin, Jin Ik Lee, and Min-Jea Tahk (2006). Guidance synthesis to control impact angle and time. KSAS International Journal, 7(1), 129-136.
3. Jang Gyu Lee, Hyung Seok Han, and Young Jin Kim (1999). Guidance performance analysis of bank-to-turn (btt) missiles. International Conference on Control Applications, 991-996.
4. Kent B. Watterson (1983). Bank-to-turn cruise missile terminal guidance and control law comparison. Ph.D. thesis, Naval Postgraduate School Monterey, California.
5. Paul Zarchan (2012). Tactical and strategic missile guidance, volume 157. American Institute of Aeronautics and Astronautics, Inc.
6. Qingchun Li, Wensheng Zhang, Gang Han and Yehui Yang (2015). Adaptive neuro-fuzzy sliding mode control guidance law with impact angle constraint. IET Control Theory and Applications, 09(14), 2115{2123. doi:10.1049/iet-cta.2014.1206.
7. Randal W Beard and Timothy W McLain (2012). Navigation, Guidance, and Control of Small Unmanned Air-craft. Princeton university press.
8. Tae Soo No, John E. Cochran, Jr. and Eul Glon Kim (2001). Bank-to-turn guidance law using Lyapnov function and nonzero effort miss. Journal of Guidance, Control, and Dynamics, 24(02), 255-260.
9. Wei Lei, Shunli Li, and Yuqi Zhao (2012). Design of anti-ship missile's terminal guidance law with multiple constraint based on back stepping. In Second International
10. Conference on Instrumentation, Measurement, Computer, Communication and Control, 892{895. IEEE. doi:10.1109/IMCCC.2012.214.

Aerodynamic Parameter Estimation of RLV from Telemeter Sensor Output

Ashwin Chandar OR*[1], AK Sarkar[2], R Mukesh[3]
[1]Technology, Director, MDSA, Advanced Systems Laboratory, Hyderabad.
[2]Professor, Department of Aeronautical Engineering, ACS College of Engineering, Bangalore, India
[3]Professor, Department of Aerospace Engineering, ACS College of Engineering, Bangalore, India
ashwin.asl@gov.in[1], achintya.drdl@gmail.com[2], mukeshprm@gmail.com[3]

ABSTRACT

An important applications of System Identification in aerospace science is aerodynamic parameter estimation from flight data. Though plenty of literature exist for aircraft on this topic, scanty for flight vehicles. An unified methodology of aerodynamic parameter estimation of flight vehicles is developed using Estimation Before Modeling technique under practical constraints of limited external measurements and mild or no excitations during flight. This technique has been extensively validated using flight data of different types of flight vehicles. In this paper, aerodynamic parameter estimation of Reusable Launch Vehicle during descend phase of flight is presented. Available onboard measurements are very noisy and also telemeter accelerometer and gyro signals are with intermittently missing data. Here no external measurements are available and it underwent maneuver only along pitch plane, considered for aerodynamic parameter estimation. Under these practical constraints, aerodynamic moment coefficients have been estimated and compared with preflight values in present research.

Keywords: *Aerodynamic Parameter Estimation, Estimation Before Modeling, Extended Kalman Filter, Filter Tuning, Multiple Linear Regression*

NOMENCLATURE

(a_x, a_y, a_z)	Accelerameter Sensed acceleration for SDINS
J	NIS Cost function
M, N	Mach Number, Total measurements
(I_{xx}, I_{yy}, I_{zz})	Moment of Inertia about (X,Y,Z) axes
R	Measurement Noise Covariance
S	Reference Area
V	Resultant Velocity
h	Altitude
m	FV mass
v_k	Innovation of kth measurement sample
(p,q,r)	Gyro sensed body rates from SDINS
(α_b, β_b)	Angle of attack, slip angle (Body Frame)
$(\alpha_{db}, \beta_{db})$	Angle of attack, slip angle (DB, Body Frame)
(α_f, β_f)	Angle of attack, slip angle (Fin Frame)
$(\alpha_{df}, \beta_{df})$	Angle of attack, slip angle (DB, Fin frame)
(α_r, ϕ_r)	Resultant α, Aero-phi
(α_{dr}, ϕ_{dr})	Resultant α, Aero-phi (DB)
P	Density

*Corresponding Authors: Email: ashwin.asl@gov.in

ABBREVIATION

ADC	AeroDynamic Control
APE	Aerodynamic Parameter Estimation
CFD	Computational Fluid Dynamics
DB	Data Base
DOF	Degrees of Freedom
EBM	Estimation Before Modeling
EKF	Extended Kalman Filter
FV	Flight Vehicle
GM	Gauss Markov
GPS	Global Positioning Systems
MBFS	Modified Bryson Frazier Smoother
SDINS	Strap Down Inertial Navigation System
MLR	Multiple Linear Regression
NIS	Normalized Innovation Sequence
PFA	Post Flight Analysis
RLV	Reusable Launch Vehicle
SFV	Strategic Flight Vehicle
TFV	Tactical Flight Vehicle

1. INTRODUCTION

Techniques for Aerodynamic Parameter Estimation (APE) have led to three different, but complementary techniques 1) Analytical / Computational Fluid Dynamics (CFD) 2) Wind Tunnel Testing 3) Flight Data Extraction. Analytical and Wind Tunnel measurements though offer a good estimate of the aerodynamic parameters, extraction of same from flight data will be considered as more authentic as there are no scaling down or numerical approximations. Therefore it is required to use it for estimation of these parameters. But flight data has the inherent problems like sensor noise, Intermittent data loss due to high dynamics during descend phase, bias and scale factor in data and so on. However, the estimates from flight are more authentic. So it need to be processed and the relevant parameters need to be extracted. Based on flight measurements, APE is very important and necessary to reduce the limitations and uncertainties of aforementioned two methods. This study results in typically airframe / autopilot modification through post flight analysis (PFA). APE of aircraft from many onboard measurements like linear accelerometers, angular accelerometers, rate gyros, free gyros, air speed sensor, angle of attack sensors in both pitch and yaw plane and altimeter under manueuver has been attempted by lot of researchers. Plenty of literatures exist in this topic (1, 2). But same from flight test data of flight vehicle (FV) are very scanty. The practical difficulties encountered in different types of FVs for APE in authors' organization are 1) Tactical FVs (TFVs) are equipped with only telemeter on board accelerometer and gyro without any available external measurement. They undergo some maneuvers not continuously but only while any event switch over based on guidance requirement. But in

ISBN - 978-93-95038-50-8

aircraft pilot executes 3-2-1-1 doublet maneuver in required plane to excite it for parameter estimation which is of much larger magnitude than in FV [3] (pp. 29-46). 2) Strategic FVs (SFVs) are equipped with on board accelerometer and gyro outputs from strap down inertial navigation system (SDINS). Sometimes radar tracked position data is only available as external measurement. But during entire flight regime angle of attack and sideslip angle very low and it undergoes a less amount of maneuver. So input accelerometer and gyro data for parameter estimation consist of constant or DC biases and scale factors along with random noise. Under such practical constraints on available flight data, an unified methodology is developed to estimate crucial aerodynamic coefficients with some engineering assumptions by exploiting available data judiciously (Fig. 1). So limited sensor and mild maneuver throws challenge on APE of FV. The aerodynamic parameters estimated for different TFVs and SFVs were aerodynamic coefficients (a_r) as a part of PFA [4, 5]. Present research is extension of above activities for an Experimental Reusable Launch Vehicle (RLV). The new problems associated with present flight data are 1) Sensor outputs are very noisy along with intermittently missing data in all channels simultaneously. 2) Aerodynamic model is nonlinear and function of resultant angle of attack and aero-phi ($\sigma\rho, \phi\alpha$) in It underwent maneuver in Pitch plane, which is only considered for the analysis. So moment coefficients $\left(C_{DO} C_M^{\alpha}, C_M^{\delta}\right)$ along with Roll Moment Coefficients have been estimated. These are novel elements in present research over previously ones as cited above. There is a strong assumption in present activity that preflight force coefficients are invariant during flight. At first overall problem formulation is described. Next APE along pitch and roll channel both from simulated as well as flight data have been discussed. The paper concludes with immediate future activities being carried out for further improvement on present results.

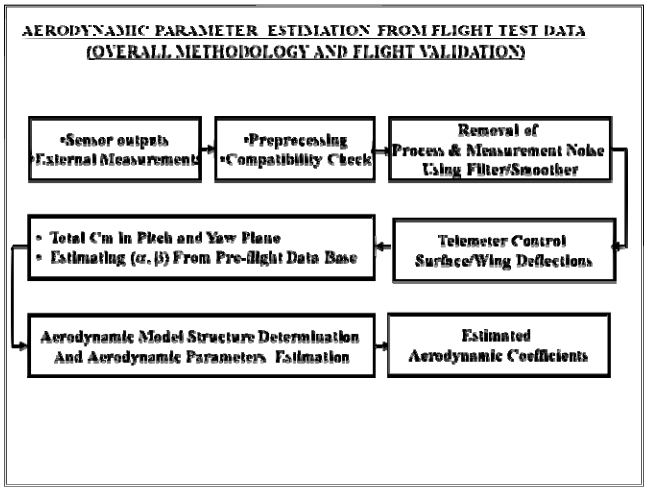

Figure 1: Steps in FV Aero. Parameter Estimation

PROBLEM FORMULATION

Present estimation problem is described in a nutshell consists of three major steps such as a) To obtain $\left(\hat{a}_x, \hat{a}_y, \hat{a}_z, \hat{p}, \hat{q}, \hat{r}\right)$ using EKF/MBFS as Estimation Before Modeling (EBM) from accelerometer and gyro outputs (a_{xm}, a_{ym}, a_{zm}, p_m, q_m, r_m) of SDINS b) Estimation of angle of attack and sideslip angle (α_{db}, β_{db}) by equating aerodynamic data base with flight sensed lateral acceleration (Latax) components $\left(\hat{a}_x, \hat{a}_y\right)$ c) Estimation of moment coefficients from $(\hat{p}, \hat{q}, \hat{r})$ using Multiple Linear Regression (MLR) based model structure determination.

ISBN - 978-93-95038-50-8

PLANT AND MEASUREMENT MODEL FOR EKF/MBFS

Plant is 3rd order Gauss Markov (GM) (1, 4), SDINS sensed accelerations and body rates are the present measurements.

STATE EQUATIONS

Equivalent state equations of form $\dot{X}(t) = f(X(t), u(t), t) + G\, w(t)$ and size (21 × 1) are

$\dot{p} = C_1pq + C_2qr + N_1C_4 + L_1$

$\dot{q} = C_5pr + C_6 (r^2 - p^2) + M_1$

$\dot{r} = C_8pq + C_9qr + L_1C_{11} + N_1$

$$\begin{bmatrix} \dot{X}_1 \\ \dot{X}_2 \\ \dot{X}_3 \end{bmatrix} = \begin{bmatrix} 0 & 1 & 0 \\ 0 & 0 & 1 \\ 0 & 0 & 0 \end{bmatrix} \begin{bmatrix} X_1 \\ X_2 \\ X_3 \end{bmatrix} + \begin{bmatrix} wx_1 \\ wx_2 \\ wx_3 \end{bmatrix}$$

$$\begin{bmatrix} \dot{Y}_1 \\ \dot{Y}_2 \\ \dot{Y}_3 \end{bmatrix} = \begin{bmatrix} 0 & 1 & 0 \\ 0 & 0 & 1 \\ 0 & 0 & 0 \end{bmatrix} \begin{bmatrix} Y_1 \\ Y_2 \\ Y_3 \end{bmatrix} + \begin{bmatrix} wy_1 \\ wy_2 \\ wy_3 \end{bmatrix}$$

$$\begin{bmatrix} \dot{Z}_1 \\ \dot{Z}_2 \\ \dot{Z}_3 \end{bmatrix} = \begin{bmatrix} 0 & 1 & 0 \\ 0 & 0 & 1 \\ 0 & 0 & 0 \end{bmatrix} \begin{bmatrix} Z_1 \\ Z_2 \\ Z_3 \end{bmatrix} + \begin{bmatrix} wz_1 \\ wz_2 \\ wz_3 \end{bmatrix}$$

$$\begin{bmatrix} \dot{L}_1 \\ \dot{L}_2 \\ \dot{L}_3 \end{bmatrix} = \begin{bmatrix} 0 & 1 & 0 \\ 0 & 0 & 1 \\ 0 & 0 & 0 \end{bmatrix} \begin{bmatrix} L_1 \\ L_2 \\ L_3 \end{bmatrix} + \begin{bmatrix} wl_1 \\ wl_2 \\ wl_3 \end{bmatrix}$$

$$\begin{bmatrix} \dot{M}_1 \\ \dot{M}_2 \\ \dot{M}_3 \end{bmatrix} = \begin{bmatrix} 0 & 1 & 0 \\ 0 & 0 & 1 \\ 0 & 0 & 0 \end{bmatrix} \begin{bmatrix} M_1 \\ M_2 \\ M_3 \end{bmatrix} + \begin{bmatrix} wm_1 \\ wm_2 \\ wm_3 \end{bmatrix}$$

$$\begin{bmatrix} \dot{N}_1 \\ \dot{N}_2 \\ \dot{N}_3 \end{bmatrix} = \begin{bmatrix} 0 & 1 & 0 \\ 0 & 0 & 1 \\ 0 & 0 & 0 \end{bmatrix} \begin{bmatrix} N_1 \\ N_2 \\ N_3 \end{bmatrix} + \begin{bmatrix} wn_1 \\ wn_2 \\ wn_3 \end{bmatrix}$$

MEASUREMENT EQUATIONS:

It can be written in the form $Z(t_k) = h(X, t_k) + \eta(t_k)$, $k = 1,2, \ldots N$ as

$$\begin{bmatrix} a_{xm} \\ a_{ym} \\ a_{zm} \end{bmatrix} = \begin{bmatrix} X_1 - (r^2 + q^2)x_{cg} + (pq - r)y_{cg} + (pr + q)z_{cg} \\ Y_1 - (p^2 + r^2)y_{cg} + (pq + r)x_{cg} + (qr - p)z_{cg} \\ Z_1 - (q^2 + p^2)z_{cg} + (pr - q)x_{cg} + (qr + p)y_{cg} \end{bmatrix} + \begin{bmatrix} \eta_1 \\ \eta_2 \\ \eta_3 \end{bmatrix} \quad (2)$$

ISBN - 978-93-95038-50-8

$$\begin{bmatrix} p_m \\ q_m \\ r_m \end{bmatrix} = \begin{bmatrix} p \\ q \\ r \end{bmatrix} + \begin{bmatrix} n_4 \\ n_5 \\ n_6 \end{bmatrix}$$

The available measurements are contaminated by Gaussian white noise of covariance $\left(\sigma_{a_x}^2,\ \sigma_{a_y}^2,\ \sigma_{a_z}^2,\ \sigma_p^2,\ \sigma_q^2,\ \sigma_r^2\right)$. These are diagonal elements of Measurement Covariance Matrix R. The notations used in above Eqns. (1-2) are

$$C_1 = \frac{\left[I_{zz}\left(I_{zz} + I_{zz} - I_{yy}\right)\right]}{I^2} \qquad C_2 = \frac{\left[I_{22}\left(I_{yy} - I_{zz}\right)I_{xx}^2\right]}{I^2} \qquad C_4 = \frac{I_{xx}}{I_{zz}}$$

$$C_5 = \frac{\left(I_{zz} - I_{zz}\right)}{I_{yy}} \qquad C_6 = \frac{I_{22}}{I_{yy}} \qquad C_8 = \frac{\left[I_{xx}\left(I_{xx} - I_{yy}\right) + I_{zz}^2\right]}{I^2}$$

$$C_9 = \frac{\left[I_{xx}\left(I_{yy} - I_{zz}\right) - I_{zz}^2\right]}{I^2} \qquad C_{11} = \frac{I_{22}}{I_{xx}};\ I^2 = \left(I_{xx}I_{zz} - I_{xx}^2\right)$$

EKF/MBFS has been mechanized with 21 state variables (Eqn. 1) and 6 measurements (Eqn. 2).

FILTER INITIALIZATION AND FILTER TUNING

In filtering /estimation problem evaluation of **(X_0, P_0)** is filter initialization and proper choice of **(X_0, P_0, Q, R)** is Filter Tuning [6]. The methodology is discussed now.

Evaluation of (X_0, P_0): First seven points of a measured signal from t_0 is approximated to a pararabola.

$$y_s(t_3) = c_0 + c_1(t_3 - t_0) + c_2(t_3 - t_0)^2 \qquad \text{j = 1, ...,7} \tag{3}$$

Coefficients (C_0, C_1, C_2) and their variances $\left(\sigma_0^2, \sigma_1^2, \sigma_2^2\right)$ are determined by least square and is shown as

$$\sigma_y^2,(t) = \sigma_0^2 + \sigma_1^2(t - t_0)^2 + \sigma_2^2(t - t_0)^4;\ \sigma_{yx}^2(t) = \sigma_1^2 + 4\sigma_2^2(t - t_0)^2;\ \sigma_{yx}^2(t) = 4\sigma_2^2 \tag{4}$$

For all measurements above method is used to compute (X_0, P_0) [4]. Based on Eqn. 3 (position, velocity, acceleration) components $\left(y_a, \dot{y}_a, \ddot{y}_a\right)$ of a measured signal are evolved. Eqn. 4 is used to compute diagonal $\left(\sigma_y^2, \sigma_{\dot{y}}^2, \sigma_{\ddot{y}}^2\right)$ of above measurement channel. This is carried out for all measurement channels and (X_0, P_0) are evolved at $t = t_0$. Initially only the diagonal elements of P_0 at keeping off-diagonal elements to zero.

Evaluation of Q: During time interval (t_1, t_f) measured signal is analyzed in frequency domain to find out f_{max} upto 4 Hz sufficient enough to regenerate peak variations of the valid signal in measurements. So all measured signals are analyzed in frequency domain to calculate amplitudes within [0-f_{max}]. Then Q-matrix diagnonal elements of Eqn. 1 are evaluated [4].

ISBN - 978-93-95038-50-8

Evaluation of R: The measurement variance can be calculated as $r_{aa} = \left(\frac{\Delta w}{3}\right)^2$ where Δy_i is the maximum dispersion of noise over mean. The diagonal elements of R-matrix are depicted in Table 2.

Proper filter tuning is based on Normalized Innovation Sequence (NIS) cost function which should be close to the number of measurement channels with near optimal filter tunning parameter [7].

Computation of Angle of Attack and Sideslip Angle from Aerodynamic Data Base

For APE, it is always customary to estimate angle of attack and sideslip angle (α_{bf}, β_{bf}) in fin frame from aerodynamic Data Base (DB). This experimental RLV undergoes no specific maneuver during initial phase and then followed by guidance demanded planned maneuver during the later part of the flight path regime. Moreover, maneuver is along pitch plane along body frame. The yaw plane along body frame is only for disturbance rejection. This makes fins along yaw plane are of lesser size (Fig. 2). Telemeter (α_b, β_b) from SDINS will be having effect of Bias and can not be used for aerodynamic coefficient estimation. So (α, β) is estimated from DB assuming invariance of preflight force coefficients. This is carried out by computing (α_{db}, β_{db}) in body frame from DB values of (C_N, C_S) along with telemeter flight control deflections (δ_1, δ_2, δ_3, δ_4). These angles are transformed to fin frame and (α_{df}, β_{df}) is used for aerodynamic moment coefficient estimation using Multiple Linear Regression (MLR) through model structure determination. It is to be noted that here fins are in (+) position. So body and fin frame are identical. The sensors are in body frame. Also complete aerodynamic data is in body frame with respect to total angle of attack, roll orientation and mach number (α_r, ϕ_r, M).

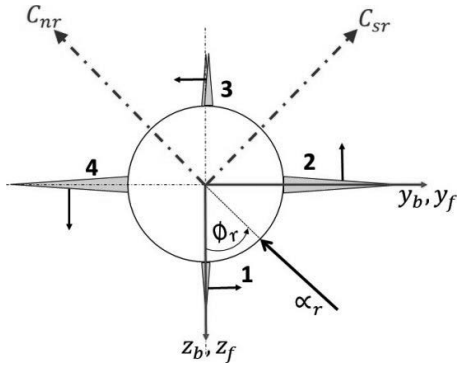

Figure 2: (C_N,C_S), (ϕ_r, α_r) ADC Sign Convention

Aerodynamic control (ADC) along (roll, pitch, yaw) are carried out by these fin surfaces (δ_1, δ_2, δ_3, δ_4). The sign convention of (δ_r, δ_p, δ_y) are given in Table 1. Corresponding sign convention is

$$\delta_{pb}^{(+)} \rightarrow q_b^{(+)} \rightarrow a_b^{(+)} \rightarrow C_{Nb}^{(+)} \rightarrow a_{zb}^{(-)} \quad \text{(pitch plane)} \tag{5}$$

$$\delta_{yb}^{(+)} \rightarrow r_b^{(-)} \rightarrow \beta_b^{(+)} \rightarrow C_{Yb}^{(+)} \rightarrow a_{yb}^{(-)} \quad \text{(yaw plane)}$$

ISBN - 978-93-95038-50-8

Table 1: ADC Sign Convention (Fig.2)

Descrip.	Expression	Direction
(δ_r) roll (+) ve Counterclockwise	$\delta_r = (\delta_1 + \delta_2 + \delta_3 + \delta_4)$	p (–)ve
(δ_{pf}) pitch (+ ve) along zf	$\delta_{pf} = (-\delta_2 + \delta_4)$	qf (+) ve
(δ_{yf}) yaw (– ve) along yf	$\delta_{yf} = (-\delta_1 + \delta_3)$	rf (+) ve

Methodology of (α_{db}, β_{db}) computation is explained now. Measured sensor outputs are smoothened using EKF/MBFS filter/smoother algorithm has been discussed before. The smoothened $\left(\hat{a}_x, \hat{a}_{yb}, \hat{a}_{zb}, \hat{p}, \hat{q}b, \hat{r}b, \hat{p}, \hat{q}_b, \hat{r}_b\right)$ will be used now for present study. Total aerodynamic force coefficients along (pitch, yaw) in body and fin plane are

$$C_{zb}^{Total}(\text{flight}) = \frac{m\dot{a}_{zb}}{\frac{1}{2}\rho V^2 S} \qquad C_{zf}^{Total}(\text{flight}) = \frac{m\dot{a}_{zf}}{\frac{1}{2}\rho V^2 S}$$

$$C_{yb}^{Total}(\text{flight}) = \frac{m\dot{a}_{yb}}{\frac{1}{2}\rho V^2 S} \qquad C_{yf}^{Total}(\text{flight}) = \frac{m\dot{a}_{yf}}{\frac{1}{2}\rho V^2 S} \tag{6}$$

$$C_N^R(\text{flight}) = \sqrt{C_{yb}^{Total}(\beta_b)^2 + C_{zb}^{Total}(a_b)^2}$$

for given $(\alpha_{df}, \beta_{df})$ from DB along fin frame using Eqn. 6

$$C_{yf}(\beta_{df}) = C_{yf}^{Total}(\text{flight}) - C_{yf}^{\delta yf\frac{(\delta_1-\delta_2)}{2}}$$

$$C_{zf}(\alpha_{df}) = C_{zf}^{Total}(\text{flight}) - C_z^{\delta yf\frac{(-\delta_2+\delta_4)}{2}}$$

$$C_N^R(\text{DB}) = \sqrt{C_{yf}(\beta_{df})^2 + C_z(\alpha_{df})} \tag{7}$$

Here $C_N^R(\alpha_r, M)$ is resultant normal force coefficient along α_r plane for given Mach number. Our aim is to evolve $(\alpha_{dr}, \phi_{dr}, \alpha_{df}, \beta_{df})$ by equating $\left(C_{yf}^{Total}, C_{zf}^{Total}, C_N^R\right)$ from flight and nominal zero DB using Eqns. (6-7). By defining cost function, this will be discussed now.

$$C_{yb}^{Total}(\beta_{db}) = -C_N^R(\alpha_{dr})\sin\phi_{dr}$$

$$\tan\beta_{db} = \tan\alpha_{dr}\sin\phi_{dr}$$

$$C_{zb}^{Total}(\alpha_{db}) = -C_N^R(\alpha_{dr})\cos\phi_{dr}$$

$$C_{yf} = C_{yb}; C_{zf} = C_{zb}$$

$$\tan\beta_b = \tan\alpha_r\sin\phi_r \tag{8}$$

$$\tan\alpha_b = \tan\alpha_r\cos\phi_r$$

$$\beta_f = \beta_b; \alpha_f = \alpha_b$$

ISBN - 978-93-95038-50-8

$$\tan\alpha_{db} = \tan\alpha_r \cos\phi_r$$

$$e_1 = C_{yf}(\text{flight}) - C_{yf}^{\text{Total}}(\text{DB}, \beta_{df})$$

$$e_2 = C_{zf}(\text{flight}) - C_{zf}^{\text{Total}}(\text{DB}, \alpha_{df})$$

$$e_3 = C_N^R(\text{flight}) - C_N^R(\text{DB})$$

Cost function to be optimized for equating total normal force from flight and DB and to evolve the parameters $\Theta = (\alpha_{dr}, \phi_{dr}, \alpha_{df}, \beta_{df})$ is,

$$J(\Theta) = (J_1 + J_2 + J_3) = \mathbf{e}^{\mathbf{T}}\mathbf{R}\mathbf{e} \tag{9}$$

where $e = (e_1\ e_2\ e_3)^T$ and **R** = Diagonal [1 1 1]. Eqns (6.9) have been solved together using **fmincon** of **MATLAB Optimization Toolbox** to evolve Θ (Fig. 3).

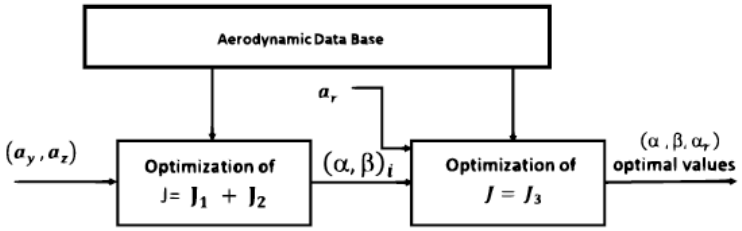

Figure 3: Optimization for $(\alpha_{dr}, \phi_{dr}, \alpha_{df}, \beta_{\partial f})$ (DB)

AERODYNAMIC MODEL STRUCTURE FOR APE USING MLR

Total moment coefficients in fin frame along (roll, pitch and yaw) channels are computed as

$$C_{mx}^{\text{Total}} = \frac{l_{zz}\ddot{\phi}}{\frac{1}{2}\rho V^2 Sd}; C_{myf}^{\text{Total}} = \frac{l_{yy}\ddot{\theta}}{\frac{1}{2}\rho V^2 Sd}; C_{mzf}^{\text{Total}} = \frac{l_{zz} f_f}{\frac{1}{2}\rho V^2 Sd} \tag{10}$$

The aerodynamic model structure in fin frame along pitch plane with inputs as $(\alpha_{df}, \delta_{pf})$ is

$$C_{zf}^{\text{Total}} = C_N^O + C_N^\alpha\ \alpha_{df} + \frac{C_N^\delta}{2}\delta_{pf}$$

$$C_{myf}^{\text{Total}} = C_{my}^O + C_{my}^\alpha\ \alpha_{df} + \frac{C_{my}^{\delta p}}{2}\delta_{pf} \tag{11}$$

Yaw plane model with inputs as $(\beta_{df},\ \delta_{yf})$ is

$$C_{yf}^{\text{Total}} = C_Y^O + C_Y^\delta\ \beta_{df} + \frac{C_Y^\delta}{2}\delta_{yf}$$

$$C_{mzf}^{\text{Total}} = C_{mz}^O + C_{mz}^\beta\ \beta_{df} + \frac{C_m^\delta y_z}{2}\delta_{yf} \tag{12}$$

ISBN - 978-93-95038-50-8

Roll model structure with inputs as (α_{dr}, δ_r) is

$$C_i^{Total} = C_i^O + C_i^{ar}\ \alpha_{dr} + C_i^{\phi r} \cos(4\phi_{dr}) + C_i^{\delta} r \delta r \tag{13}$$

$(\delta_r, \delta_{pf}, \delta_{yf})$ are function of $(\delta_1, \delta_2, \delta_3, \delta_4)$ (Table 1).

RESULTS AND DISCUSSION

Three major steps of present APE have been discussed before. Now they have been validated first using simulated flight data and later used to process flight data.

CASE STUDY WITH SIMULATED DATA

Noisy sensor outputs based on Table 2 obtained from flight data have been processed by EKF/MBFS filter smoother, NIS cost is high while filtering by EKF. But through smoothing the cost becomes very close to total number of measurement channels (Table 2). So smoothened estimates are very close to truth model. Due to brevity discussion on filtering results are skipped. Based on smoothened $(\hat{a}_z f, \hat{a}_z f), C_N^R$ along with (α_{dr}, ϕ_{dr}, α_{df}, β_{df}) have been estimated using cost function optimization (Eqn. 6). Time history of (C_N^R, α_{dr}) along with very small estimation error are depicted in Figs. (4-5). Using smoothened qf total pitching moment coefficients in fin frame C_{myf}^{Total} are also evolved (Eqn. 10). Now (α_{df}, δ_{pf}) are used to estimate aerodynamic moment coefficients along pitch (Eqn. 11). Comparison of estimated moment coefficients $(C_m^{\alpha}, C_m^{\delta})$ along with preflight values is shown in Table 3. C_{myf}^{Total} from flight and model output are compared in Fig. 6. Being simulated data the goodness of fit is very good because of high $F_{statistics}$ value. Study of roll channel being similar, not discussed herein. No attempt has been made to estimate yaw channel coefficient due to no excitation.

Table 2: Sensor Noise and NIS Cost

(1 – σ) Sensor Measurement Noise					
a_{xm} (m/s²)	**a_{ym} (m/s²)**	**a_{zm} (m/s²)**	**p_m (d/s)**	**q_m (d/s)**	**r_m (d/s)**
0.80	1.00	2.00	4.00	2.00	1.00
NIS Cost Function					
Description		Sim. Data		Flt. Data	
EKF Filter		12.16		14.25	
MBFS Smoother		6.35		6.86	
True		6		6	

ISBN - 978-93-95038-50-8

Table 3: Estim. Aero. Coeff. (Simulation, MLR) (M = 12.4, $\alpha = 1.6^{o}$, $\frac{x_{eg}}{d} = 1.675$)

Pitch Channel (a_f Effect)				
Case	C_N^{α} (/deg)	C_m^{α} nose (/deg)	$C_m^{\alpha}\big\|_{cG}$ (/deg)	F_{stat}
Preflight	0.0305	–0.0578	–0.0067	-
Flight	0.0318 $(4.5 \times 10^{-5})^{(+)}$	-0.0579	-0.0047 (6.6×10^{-6}) (+)	5306089 C_N^{Total}
Pitch Channel (δp Effect)				
Case	C_N^{δ} (/deg pair)	$C_m^{\delta}\big\|_{nose}$ (/deg pair)	$C_m^{\delta}\big\|_{CG}$ (/deg pair)	F_{stat}
Preflight	0.0012	0.00277	0.00075	
Flight	0.0013 $(6.0 \times 10^{-6})^{(t)}$	0.00278	0.00061 (8.8×10^{-6})	18929 C_M^{Total}

(†) is (Standard Deviation (±a))

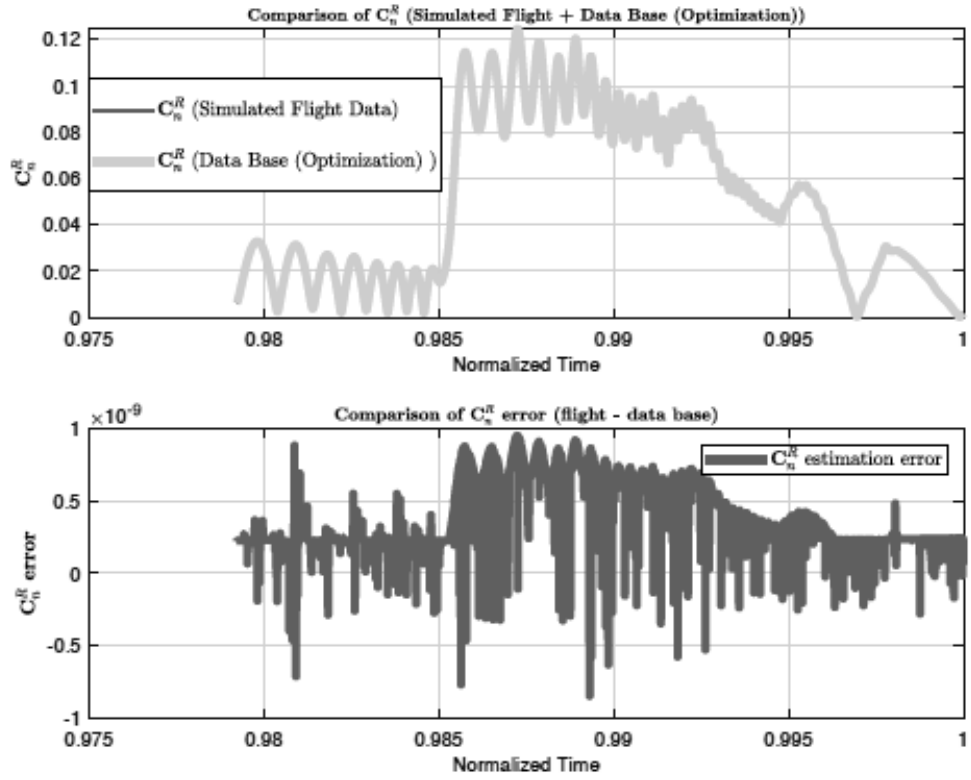

Figure 4: Time history comparison of C_N^R and estimation error (Simulated Flight + DB)

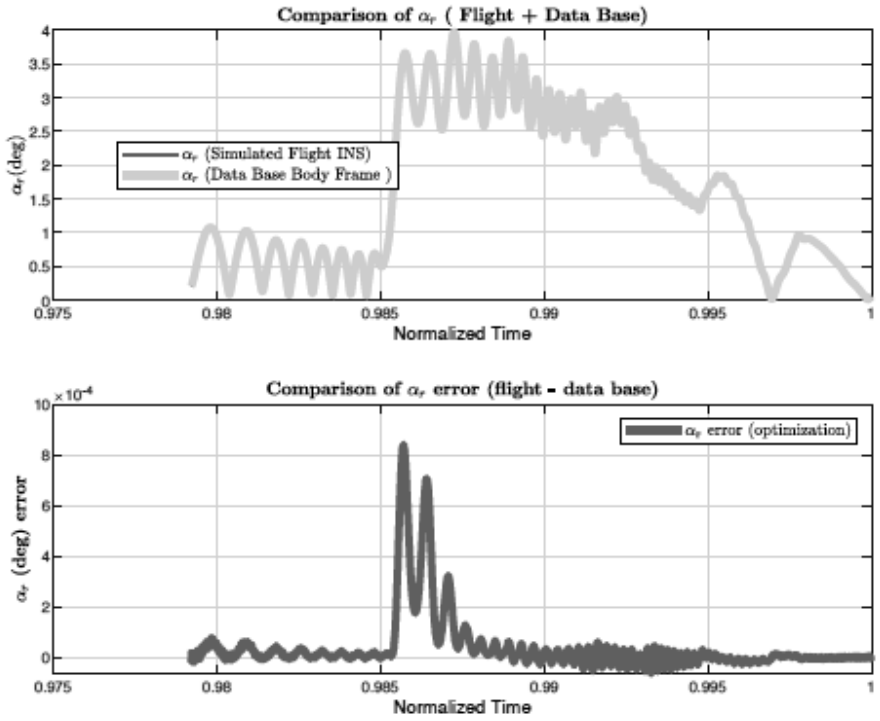

Figure 5: Time history comparison of $\alpha_{dr}(\deg)$ and estimation error (Simulated Flight + DB)

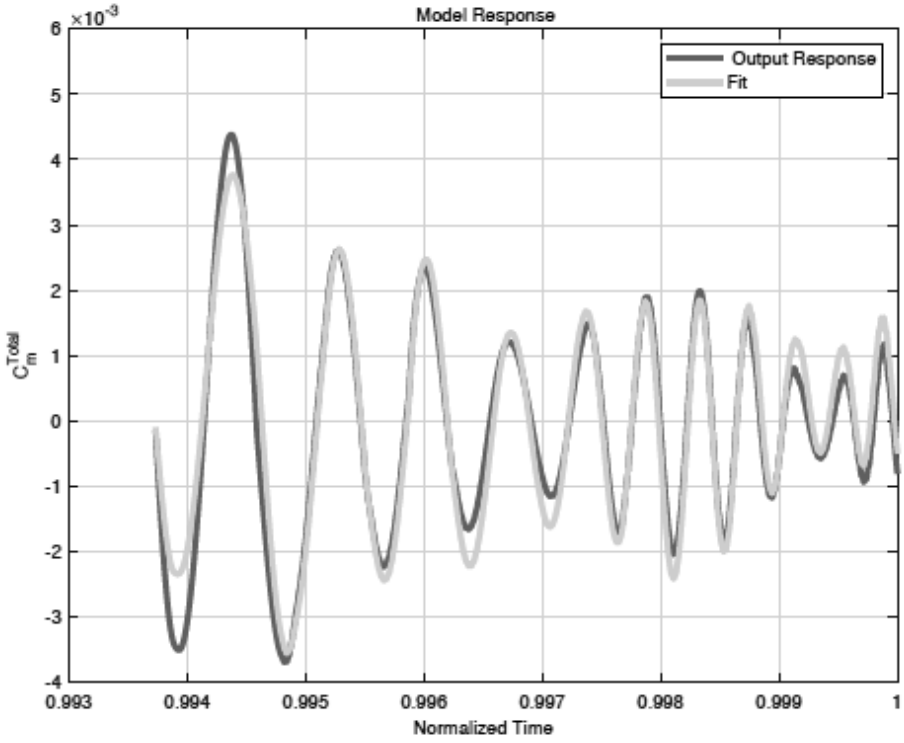

Figure 6: Time history comparison of C_m^{Total} (Simulated Flight + Pitch Plane model response)

CASE STUDY WITH FLIGHT DATA

Carefully noisy flight data with lot of missing data points and outliers have been preprocessed. Then EKF/MBFS filter / smoother has been used to estimate the states and their derivatives as discussed before. Smoothened pitch rate used for C_{myf}^{Total} estimation is shown in Fig. 7. NIS cost during smoothening is close to total number of measurement channels (Table 2) which ensures estimates are near optimal. Based on smoothened latax components, C_N^R along with (α_{dr}, ϕ_{dr}, α_{df}, β_{df}) have been estimated. Time history of C_N^R along with very small estimation error evolved during optimization are depicted in Fig. 8. Now using smoothened $(\hat{p},\hat{q}f),\left(C_l^{Total},C_{myf}^{Total}\right)$ have been evolved (α_{df}, α_{dr}, ϕ_{dr}) along with (δ_{rf}, δ_{pf}) are used to estimate aerodynamic moment coefficients both along pitch and roll channel (Eqns. (11-13)). Comparison of estimated aerodynamic moment coefficients along with preflight values is shown in Table. 4. $\left(C_l^{Total},C_{myf}^{Total}\right)$ from flight and model output are compared in Figs. (9-10) respectively. Inferences based on present flight data analysis are 1) Due to lack of strong maneuver unlike in aircraft, the $F_{statistics}$ for moment coefficient estimation along pitch and roll channel are (750, 666) which is of good acceptance level. Based on authors flight data analysis experience it is of order of (500-800) for SFVs. Generally for TFVs it is of order of (1500-5000). Had there been strong maneuver, $F_{statistics}$ which dictates goodness of fit would have been more. 2) Control effectiveness for both channels are less than preflight and configuration experienced considerable C_i^{ar} as disturbance during flight. 3) All estimated parameters can be reasoned out as authentic due to small standard derivation.

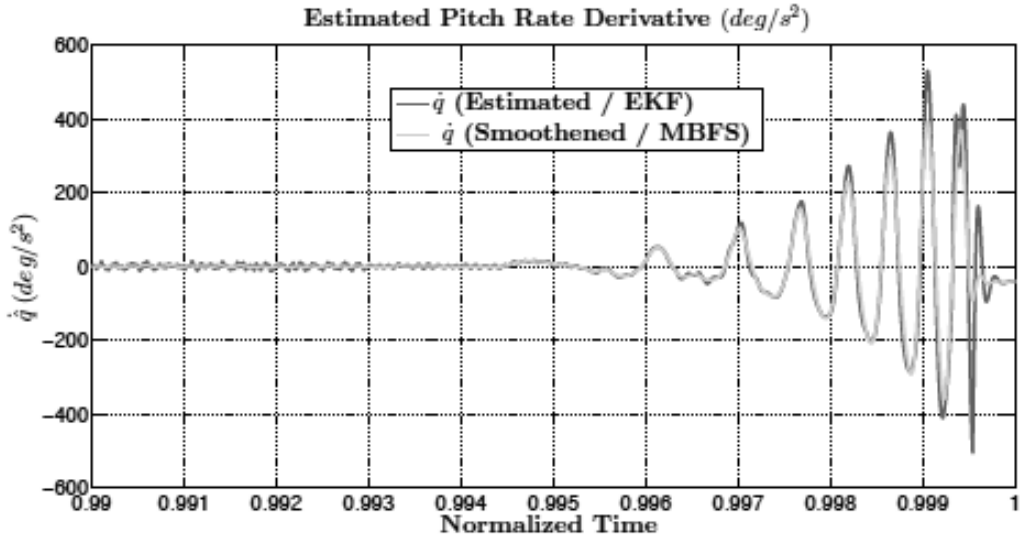

Figure 7: Time history comparison of $\dot{q}$ (Flight, EKF + MBFS)

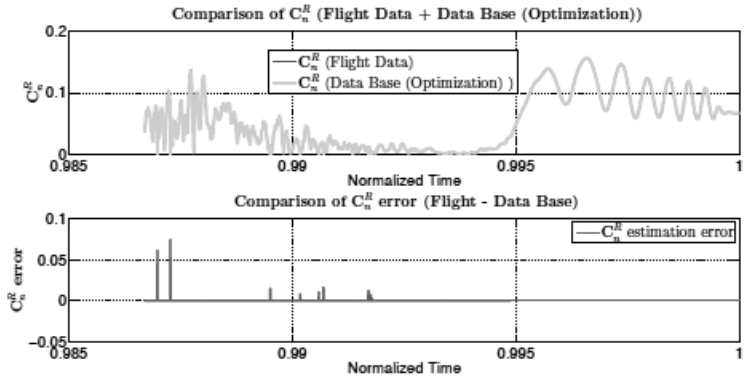

Figure 8: Time history comparison of C_{RN} and estimation error (Flight + DB)

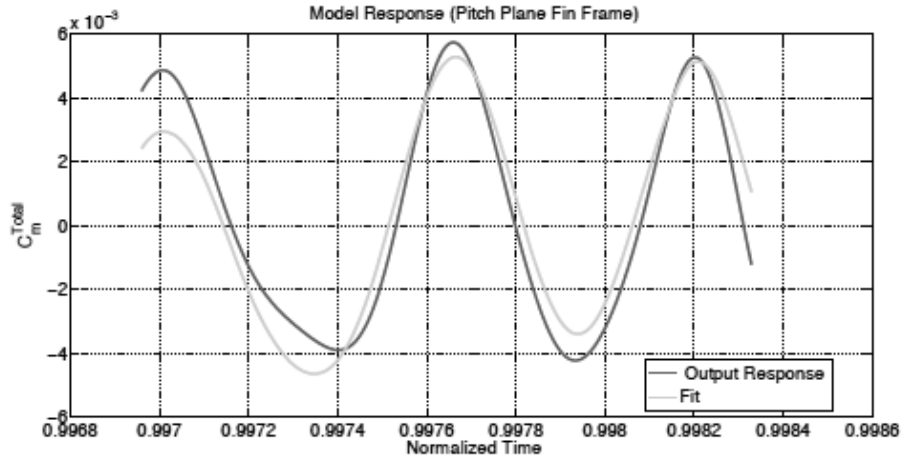

Figure 9: Time history comparison of C_M^{Total} (Flight + Pitch Plane model response)

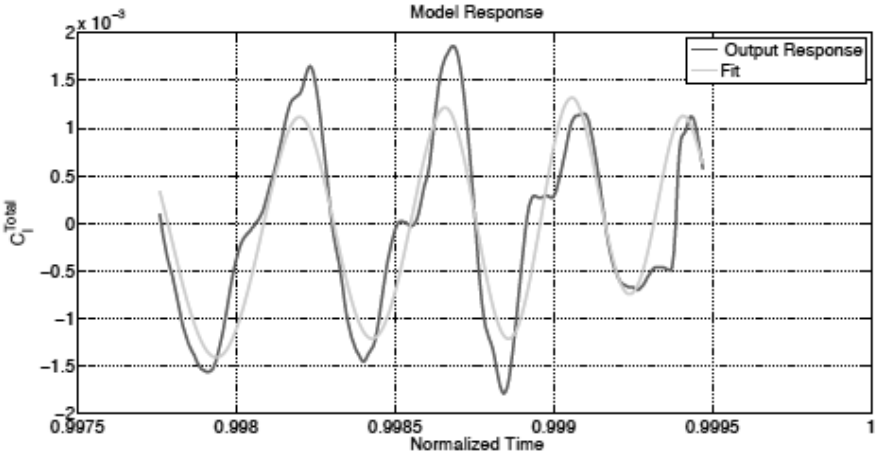

Figure 10: Time history comparison of C_l^{Total} (Flight + Roll Channel model response)

Table 4: Estim. Aero. Coeff. (Flight, MLR) (M=12.4,$\alpha = 1.6^0$, $\frac{x_{cg}}{d} = 1.675$)

Pitch Channel α_f Effect				
Case	C_N^{α} (/ deg)	$C_m^{\alpha}\big\|_{nose}$ (/deg)	$C_m^{\alpha}\big\|_{CG}$ (/deg)	F_{stat}
Preflight	0.0305	-0.0578	-0.00057	-
Flight	0.0310 (5.0×10^{-5}) (+)	-0.0550	-0.0020 (1.0×10^{-4})(+)	1769555 C_N^{Total}
Pitch Channel δ_p Effect				
Case	C_N^{δ} (/ deg pair)	$C_m^{\delta}\big\|_{nose}$ (/deg pair)	$C_m^{\delta}\big\|_{CG}$ (/deg pair)	F_{stat}
Preflight	0.0012	0.00278	0.00071	-
Flight	0.0013 (5.5 × 10−6)(†)	0.00252	0.00030 (1.4×10^{-5}) (†)	750 C_m^{Total}
Roll Channel (α_r, ϕ_r, δ_r) Effect				
Preflight	-	-	0.000332	-
Flight	0.00011 (3.0×10^{-5})(+)	-	0.0000 (1.3×10^{-5})(+)	666 C_t^{Total}

(†) is (Standard Deviation ($\pm\sigma$))

CONCLUSION AND FUTURE WORK

APE problem is carried out using MLR where pitch and roll channel have been processed separately through EBM. The same activity will be carried out by mechanizing complete 6 DOF plant state equations with available measurements using EKF/MBFS filter smoother ([8,9]). There the aerodynamic parameters will be augmented in plant equations as time-invariant during this phase of flight. Also in present experimental RLV, GPS aided SDINS is used for Navigation. So sensor outputs have negligible bias and this technique should give meaningful estimates. Estimated parameters using present method as well as proposed method should be consistent before using them for subsystem modifications as part of PFA.

ACKNOWLEDGEMENT

Authors thank Director ASL, Dr M Manickavasagam, Outstanding Scientist DRDO and ACS College of Engineering Management for permitting to publish present research. They also thank Mr Sanket Neharkar, research scientist for manuscript preparation help.

REFERENCES

1. M Sri-Jayantha and R F Stengel. Determination of nonlinear aerodynamic coefficients using estimation before modelling method. *Journal ofAircraft*, 25(9):769–804, September 1988.

2. P G Hamel and R V Jategaokar. Evolution of flight vehicles system identification. *Journal of Aircraft*, 33(1):9–28, January 1996.

3. R V Jategaokar. *FlightVehicle System Identication: A Time Domain Methodology*. American Institute of Aeronautics and Astronautics,Inc., Reston, Virginia, First Edition, 2006.

4. A K Sarkar and S Panneerselvam. Aerodynamic coefficients estimation of a tactical flight vehicle from noisy flight test data under limited measurements. *Paper No. AIAA-98-4260-CP*, Proceedings of AIAA Flight Mechanics Conference in Boston, Massachuset, August 1998.

5. P K Kar, A K Sarkar, J Umakant, and Radhakant Padhi. Aerodynamic coefficients estimation of a flight vehicle from different flight trials under limited measurements. *Paper No. AIAA-2011-6274-CP*, Proceedings of AIAA Atmospheric Flight Mechanics Conference and Exhibit, Portland, Oregon, Oregon Convention Center, August 2011.

6. R M O Gemson and M R Ananthasayanam. Importance of initial state covariance matrix for the parameter estimation using an adaptive extended kalman filter. *Paper No.AIAA-98-4153-CP*, 1998.

7. Y Bar-Shalom and X R Li. *Estimation and Tracking, Principles, Techniques and Software*. Artech House, Boston, First Edition, 1993.

8. R V Jategaokar and E Plaetschket. Algorithms for aircraft parameter estimation accounting for process and measurement noise. *Journal ofAircraft*, 26(4):360–372, April 1989.

9. Kai Zhang, Tingting Fu, and Jiajun Xiong. Estimation of aerodynamic parameter for maneuveringre entry vehicle tracking. *Paper No.AIAA-2011-6274-CP*, Proceedings of the 36th Chinese Control Conference, Dalian, China, July, 26-28 2017.

ISBN - 978-93-95038-50-8

Terrain Referenced Navigation Technique Using Correlation Algorithms for Cruise Vehicle

Suresh Mamidipalli*[1], Mallikarjun Bangi[2], G. Naresh Kumar[1]

[1]Scientist, DRDL, Hyderabad, Telangana, India,
[2]Engineer, Hyderabad, Telangana, India,

ABSTRACT

The Cruise vehicle is guided by an Inertial Navigation Systems (INS) and Satellite Navigation (SatNav). Where INS provide very accurate and reliable solution for navigation, but gyroscope and accelerometers errors accumulate with time, and accordingly navigation errors also grow w.r.to time leading to very high Position drifts for long duration missions. While in SatNav performance is poor due to the signal interference and jamming. The solution to these problems leads to an introduction of another device to perform precise measurements of the vehicle's geographical position along its flight path. TERCOM is a well approved navigation technique which deals with terrain elevation. TERCOM compares the measured elevation value and on-board stored elevation value using correlation algorithm. A TERCOM system is a self-contained and provides positional fixes to cruise vehicle, aircraft, and drones. TERCOM is the only fix-taking system that can operate autonomously in a RF/ SatNav denied scenarios. TERCOM can be used in both tactical and strategic systems and operates under ECM (electronic countermeasures) conditions and provides day/night, all weather capability in low altitude terrain following scenarios. This paper presents correlation algorithm and its performance evaluation in the Western Ghats of India.

Keywords: *Baro Altimeter (BA), Cruise Vehicle, MAD, MSD, Radio Altimeter (RA), TERCOM*

1.0 INTRODUCTION

A Cruise vehicle is a self-guided, continuously powered, pilotless, air-breathing which is supported by an aerodynamic surface. INS determine position, velocity & attitude of the vehicle [1-2]. With flight time, the drift and errors in inertial system increases as inertial system positioning errors are cumulative resulting in many kilometers of accumulated positioning error with flight duration. On the other hands, *SatNav* allows the vehicle to continuously correct its inertial errors, regardless of terrain and weather conditions and works well over water as well as land. These advantages were offset by problems with vulnerability to jamming.

Due to its long flight duration, navigational accuracy degrades with time especially in *SatNav* denied environments and lands into unacceptable error basket. A navigational aid like TERCOM which can correct the INS errors during midcourse phase of the flight is of great help to achieve the mission objectives in *SatNav* denied. Additionally, it also assists the vehicle to enter terminal phase with reasonable positional accuracy where a terminal sensor (RF or IR seeker) can take over. A Terrain-referenced navigation (TRN) is a well approved navigation technique which deals with terrain elevation [3, 14]. It compares the measured elevation value with on-board stored elevation value using correlation algorithm.

2.0 TERCOM TECHNIQUE

Terrain Contour Matching (TERCOM) is defined as the process of finding the location of the vehicle through correlation with terrain over which the vehicle is flying [4]. It is also known as the correlation guidance as the comparison between the features of the terrain over which the vehicle is flying and pre-stored features of the planned trajectory. This navigation aid technique can be employed for any type of launch condition (air, ground, sea or

*Corresponding Author: Email: sk.mamidipalli@gmail.com

underwater). The prerequisite being terrain hugging trajectory with very low cruising altitude as indicated in fig. 1.

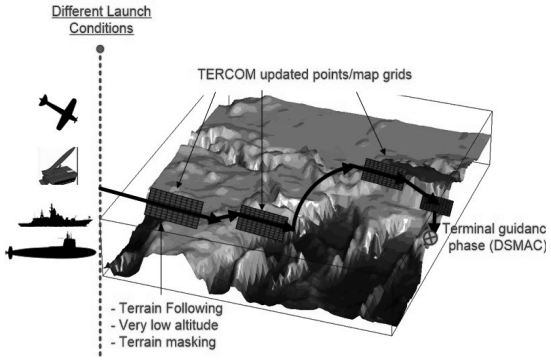

Figure 1: TERCOM Principle

These pre-stored features are obtained by measuring the terrain of interest prior to the mission. Terrain features are stored in the form of a horizontal matrix based on the elevation of the terrain of interest. Each map is then divided into equal size squares such that each square represents the average height of that region. This constitutes the Map Database and is stored in the on-board computer of the vehicle.

The profile of the terrain underneath is captured by a sophisticated data acquisition system composed of RA and BA. RA records the radio wave traveling time by sending and receiving back the reflected radio wave from the underlying terrain. This time is used in calculating the altitude of the vehicle [5-6]. The BA is used to measure vehicles altitude w.r.to mean sea level since it works on the principle of measuring atmospheric pressure.

This paper mainly describes about the TERCOM implementation and performance analysis. Different techniques are explored in literature, where effective use of **data correlation** and **image processing** techniques have been used to navigate a flying vehicle during mid-course trajectory. In this paper, TERCOM navigation technique is presented where data correlation-based guidance is achieved [8-9]. As the flying vehicle reaches the matrix area, the profile of the terrain beneath the flying vehicle is obtained by the combination of the two altimeters, each giving its output specific intervals. These real time actual data values are then correlated with the pre-stored terrain elevations [2] which then provide the horizontal position.

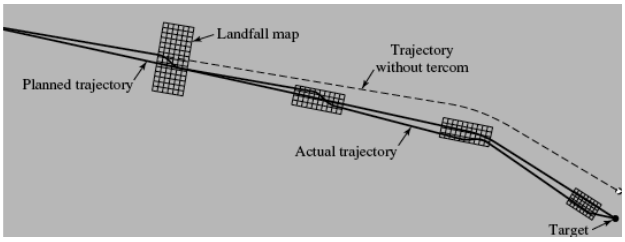

Figure 2: Vehicle flying over stored maps (TERCOM)

In view of high positional error at the start of TERCOM, the requirement of map size is high & as the flight path corrected to the desired path the map size reduce as shown in fig. 2.

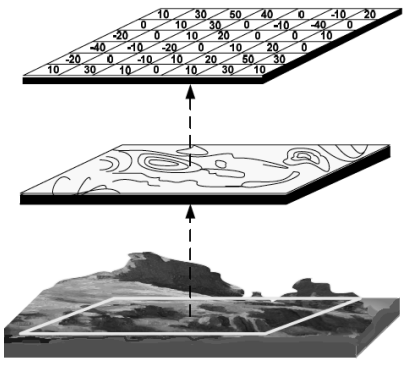

Figure 3: Data Preparation

3.0 STEPS IN TERCOM

The determination of vehicle position by means of terrain contour matching involves three basic steps mainly the first step is an off-line planning, sampling and correlation need to take place in real time at flying vehicle OBC.

Mission Planning: It is the process which takes place much prior to any flight. It is also known as Data Preparation Stage, where the maps of the area of interest are acquired either using topographic charts or stereo aerial photographs. These maps are then digitized and converted into matrix form as shown in fig. 3. Each cell is replaced with discrete average terrain height with respect to the reference datum WGS84.

The size of map (matrix) corresponds to the resolution of the cell size. The digitized map is stored in on-board computer of the flying vehicle.

D*ata Sampling:* The altitude above the terrain is generated by taking difference of BA and RA measurements. The difference in altitudes indicates terrain height w.r.to reference datum which is similar to stored map elevations. It is always not possible to acquire the altitude information for BA and RA at equal interval. It is required to synchronize output of these two sensors w.r.to cell size. This synchronized data is ready for correlation. The data sampling or acquiring process is depicted in the fig. 4.

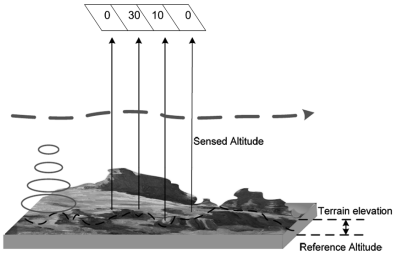

Figure 4: Data Acquisition Process

Data Correlation: The acquired data and the digitized map are correlated to get the highest similarity along the columns. The column which matches with highest correlation, is the trajectory of the terrain where the vehicle has flown. Normally this should be center column of map, assuming no navigation error. In case the correlating column is other than the center column, distance from the center column are called the cross-track and along-track errors as shown in fig. 5. These errors are used to correct the trajectory of the vehicle such that the center column becomes the steering track. All this happens in real time as the flying vehicle has to be kept on the intended track all the time and any delay here would allow the vehicle to go beyond controllable bounds.

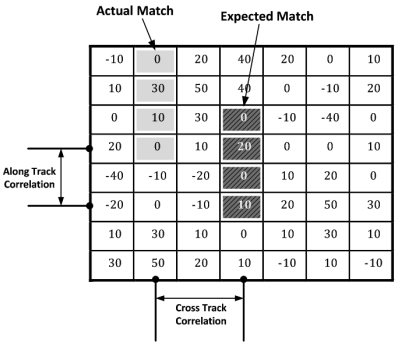

Figure 5: Data Correlation

The most computationally efficient correlation techniques used are Mean Absolute Difference (MAD) and Mean Square Difference (MSD).

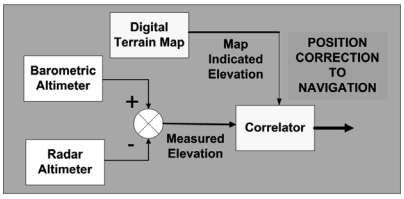

Figure 6: Major Subsystems of TERCOM

4.0 TERCOM SYSTEM ARCHITECTURE

Functional block diagram of the TERCOM is indicated in fig. 6. TERCOM system uses following onboard hardware & software modules:

1) ***Radar Altimeter***: Measures the ground clearance or altitude above Ground Level (AGL) [5-7].
2) ***Barometric Altimeter***: Provides altitude above Mean Sea Level (MSL)

3) ***On-board Digital Elevation Map (DEM)*** as a reference terrain
4) ***Correlator:*** Computation of MAD or MSD algorithm to find best match.

The critical part of TERCOM process is the data correlation. The RA acquires altitude measurement above terrain and BA provides w.r.to mean sea level. The difference between BA and RA is the sensed vertical terrain profile w.r.to WGS-84. This terrain profile is correlated with the sequence of altitudes retrieved from the DEM for parallel paths that are offset from the predicted flight path by increments in the cross-track & along-track directions.

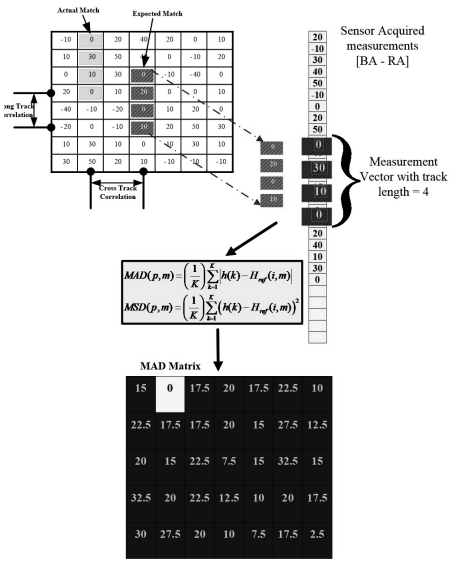

Figure 7: MAD & MSD Correlation Algorithms

5.0 TERRAIN NAVIGATION TECHNIQUES

There are several varieties of algorithms available in literature [2], which can be used for navigational aiding. In general, they are categorized as:

Batch Processing: In this method, the location update takes place in one go. A set of measurements called track are processed (correlated) together. TERCOM, TERPROM, CAROTE, GOEBEL etc. are falls under this category. Batch processing algorithm is generally selected for cruise vehicle, because no linearization of terrain profile is necessary & this technique is applicable to both small discrete and large maps which can support continuous navigation updating [10-11].

Recursive Processing: In this processing, a filter is employed to estimate the offset from desired location eg. SITAN, VATAN [12-13] etc. Here, the location offset is highly coupled with the filter states performance. It is best suitable for small maps with fairly small initial position error.

There are number of batches processing-based correlation algorithms of varying complexities and accuracies are available in literature as follows:

1. Mean Squared Difference (MSD)
2. Mean Absolute Difference (MAD)
3. Normalized MAD (N-MAD)
4. Normalized MSD (N-MSD) and
5. Product Method

5.1 MEAN ABSOLUTE DIFFERENCE CORRELATION ALGORITHM

The MAD method calculates the mean of absolute value of differences between corresponding measured sample (i.e., difference between BA and RA) and the reference map indicated terrain elevation values. The MAD algorithm provides the best combination of accuracy and computational efficiency for performing real-time terrain contour matching in an on-board computer environment. The formulation of MAD is as follows:

$$MAD(p,m)=\frac{1}{K}\sum_{k=1}^{K}|h(k)-H_{ref}(i,m)| \qquad (1)$$

5.2 MEAN SQUARED DIFFERENCE CORRELATION ALGORITHM

The MSD method, as the name implies is mean of the squares of differences between the measured sample (i.e., difference between BA and RA) and the corresponding reference map indicated terrain elevation profile. This is a quadratic function of error and hence affected by outliers. However, the major advantage of using this method is that it provides higher weightage to large errors, in turn narrowing down the uncertain zones.

$$MSD(p,m)=\frac{1}{K}\sum_{k=1}^{K}\left(h(k)-H_{ref}(i,m)\right)^2 \qquad (2)$$

Where,

N = the number of rows of reference matrix

M = the number of columns of reference matrix

K = Track length (the number of samples measured/used for correlation)

k = Track length index, & p = MAD starting index

m = column index, $1< m \leq M$

n = row index, $1< n \leq N$

$i = p+k-1$ which is reference terrain altitude from MAD starting point to track length

$H_{ref}(n, m)$ = the stored reference matrix data: $1 \leq n \leq N$ and $1 \leq m \leq M$

$H(k) = k^{th}$ measured terrain elevation. The size of MAD matrix is $(N - K + 1) \times M$

6.0 SIMULATION STUDIES

Simulation studies are carried out by considering the real time data collected from the RA and BA information from su-30 MKI aircraft. The required digital elevation database collected from NRSC, ISRO Hyderabad. In order to assess the efficacy of MAD & MSD algorithms simulation studies are carried out using Ideal Measurement (Error Free), Erroneous Measurement (By Injecting Random Errors), and Real Measurement. Correlation is carried out with available sortie data around Western Ghats.

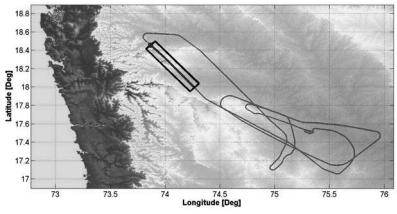

Figure 8: Su-30 aircraft sortie

Case 1: Ideal Measurement (Error Free): The performance of MAD and MSD are evaluated under error free situation. This is an ideal situation for correlation. The correlation output is presented in terms of surface plot. The fig. 9 and 10 indicates one distinct peak over the surface of 1/MAD and 1/MSD. This indicates perfect correlation w.r.to desired column.

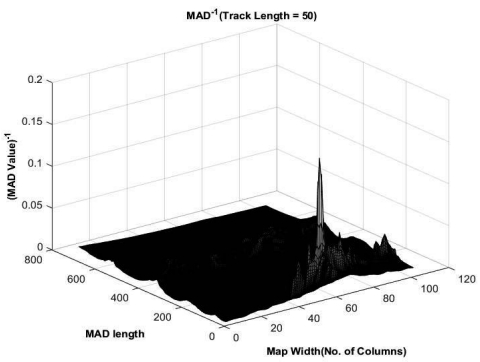

Figure 9: Case-1: MAD method

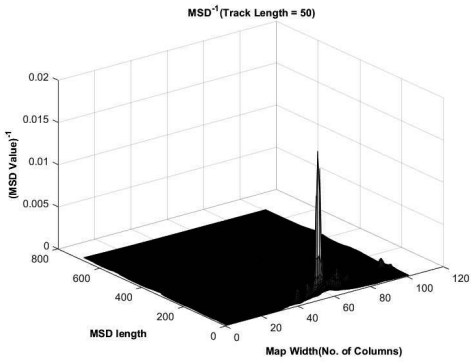

Figure 10: Case-1: MSD method

Case 2: Erroneous Measurement (By Injecting Random Errors): Measurement vector is generated similar to case 1 and corrupted with random noise within the sensor 3σ noise characteristics. Correlation is carried out with corrupted measurement, this gives accuracy of position estimate w.r.to noisy measurements. Fig. 11 indicates the effect of error on estimated position. These results are arrived by carrying out 500 Monte Carlo runs using normal distribution. Present study can be used to decide the gross error budget for given terrain area. So, the contribution of errors in BA, RA and Map database are accounted together.

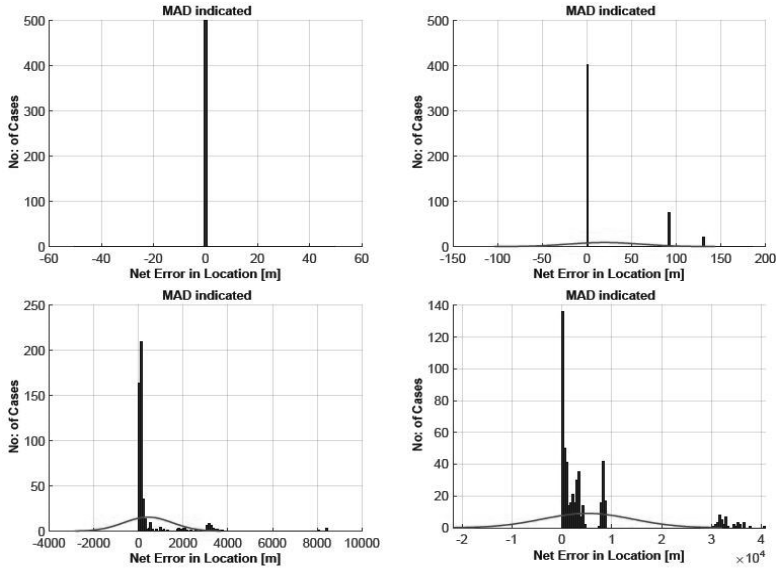

Figure 11: MAD: Location error with Track Length = 50 &Measurement error = 10, 50, 100 & 200m

Case 3: Real Measurement: Measurement vector in generated by using the RA [7] and BA readings as indicated in the eq. 3.

$$H_{meas} = H_{baro} - H_{rc} \qquad (3)$$

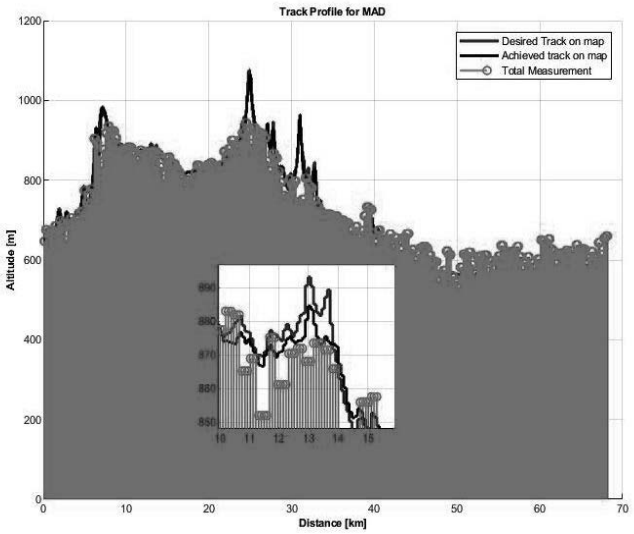

Figure 12: Measurement Vector

Table 1. MAD Position Error with varying Track length

Track Length	MAD		MSD	
	CRE [km]	DRE [km]	CRE [km]	DRE [km]
10	3.0610	52.4100	4.3590	3.0611
20	3.7104	3.1539	3.7104	3.1539
50	2.7828	2.6901	3.7104	4.7308
150	3.2466	3.8032	3.2466	3.7104
250	2.3190	2.8756	3.1539	3.7104
500	1.7625	2.1335	1.3914	1.9480
734	1.2040	0	1.2040	0

H_{baro} is the direct measurement and H_{rc} is the corrected measurement from radar altimeter. Figure 8 indicates the selected section of trajectory and respective terrain. Figure 12 indicates measurement vector and the desired terrain elevation. The obtained cross range error is 1204 m and downrange error is 0m for full track length. This figure also indicates the track with maximum correlation (i.e., Achieved track). The position error also depends on track length, in addition to the errors associated with measurement, data association, and database and flight errors. Figures 13 and 14 indicates the convergence of distinct peaks as the track length increase from 10 to 150. The effect of track length on position error is tabulated in table 1 for both MAD and MSD correlation algorithms.

ISBN - 978-93-95038-50-8

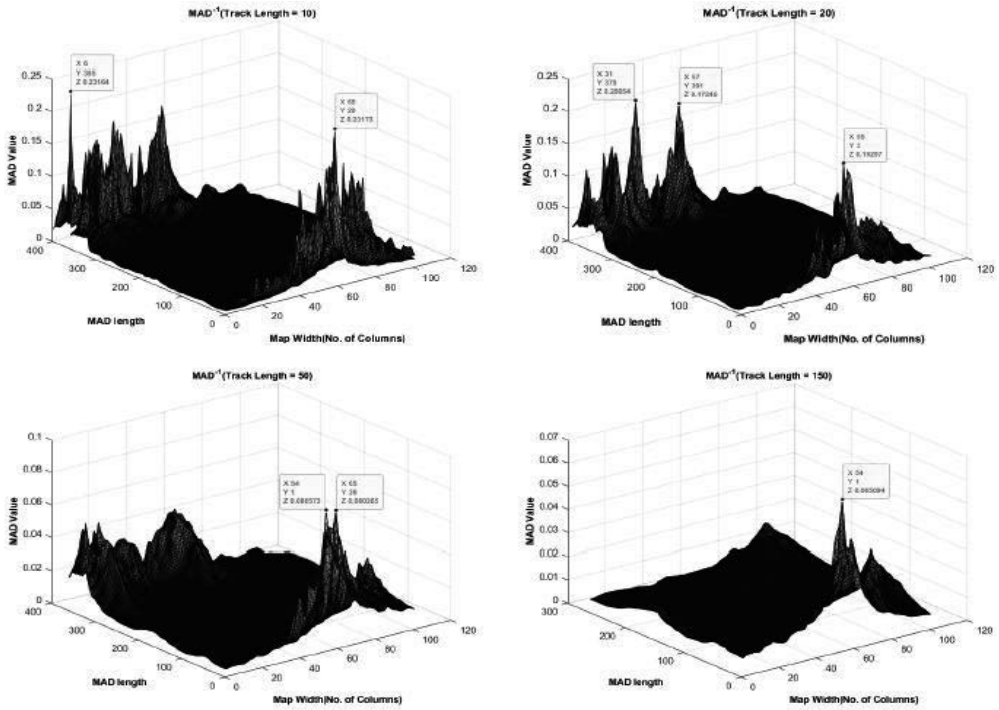

Figure 13: MAD: Convergence of distinct peaks as track length varies from 10 to 150

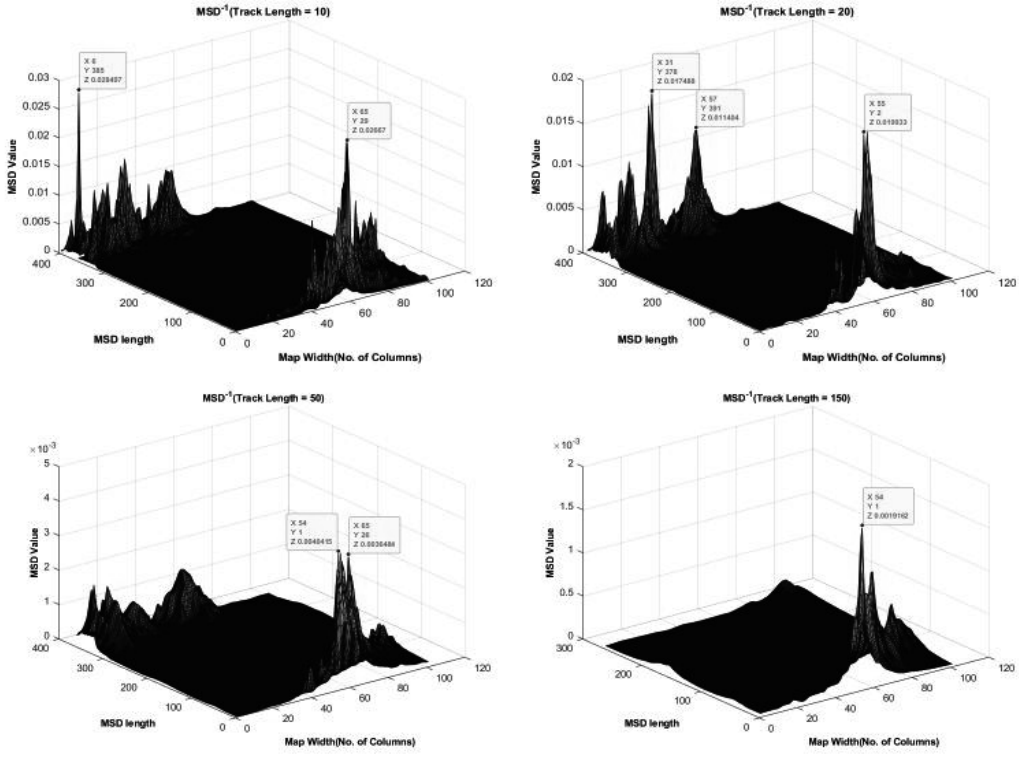

Figure 14: MSD: Convergence of distinct peaks as track length varies from 10 to 150

COMPARISON OF MAD AND MSD

MAD works better in cases of high terrain roughness and difference in correlation terms are higher than 1. MSD works better even in cases of flatter terrain and when difference in correlation terms are in fraction. Since in MSD the correlation terms are squared, so the separation between fractions increase further. So, while processing, both algorithms are executed simultaneously and based on the selection is made to choose MAD or MSD. Computational burden is more for MSD.

7. CONCLUSION

In the present study, correlation algorithm for TERCOM navigational aid has been developed.

Efficacy of TERCOM algorithm under different situations like, ideal measurements, intentionally corrupted measurements and under realistic measurements has been studied. Based on the available literature, the basic MAD and MSD algorithms are developed. These algorithms are analyzed over the realistic sortie data obtained from Su-30 Aircraft sortie trial. Monte Carlo simulation runs (500) were carried out to ascertain the effect of track length for given terrain. Different terrain database like DTED, SRTM and GEOTIFF formats were analyzed and necessary interface developed.

ACKNOWLEDGEMENT

The authors thank competent authorities of Defence Research and Development Laboratory (DRDL), Hyderabad for granting permission to publish this piece of work.

REFERENCES

1. V. EkUtekin, "Navigation and control studies on cruise missiles," Ph. D. dissertation, The Graduate School of Natural and Applied Sciences of Middle East Technical University, 2007.
2. P.D. Groves, “Principles of GNSS, Inertial, and Multisensor Integrated Navigation Systems”, Artech house, 2008.
3. G. M. Siouris, “Missile Guidance and Control Systems”, Springer, 2004.
4. Mark W. Cannon, Jr., “TERCOM Performance: Analysis and Simulation, Technical Report AMRL-TR-73 J30”, Wright-Patterson AFB, Ohio, June 1974.
5. G.S. Brown. “The average impulse response of a rough surface and its applications”. IEEE Trans. Antennas Propagat, vol AP-25, pp. 67-74, Jan. 1977
6. Jensen J R,” Radar altimeter gate tracking theory and extension”, [J]. IEEE Trans Geosci and Remote Sensing,1999, 37(2) 651-657
7. Zhang Hua, Hu Xiulin, “A Height-Measuring Algorithm Applied to TERCOM Radar Altimeter”, 3rd ICACTE, vol 05, pp 43-46, 2010
8. Golden, JP, Wiener, Thomas, “Image Processing for Missile Guidance-Terrain Contour Matching (TERCOM): A Cruise Missile Guidance Aid”, SPIE Proceedings, vol-238, pp 10-18, 1980.
9. Y.M. Yoo, W.H. Lee, S.M. Lee, C.G. Park, I.H. Kwon, “Improvement of TERCOM Aided Inertial Navigation System by Velocity Correction”, Proceedings of the 2012 IEEE, pp 1082-1087 .
10. Geofrey, BI, “Image processing for tomahawk scene matching”, vol 5, pp 250-264, 1994.
11. Zhao, Long and Gao, Nan and Huang, Baoqi and Wang, Qingyun and Zhou, Jianhua, “A novel terrain-aided navigation algorithm combined with the TERCOM algorithm and particle filter”, IEEE Sensors Journal, vol 15, no. 2, pp 1124-1131, 2014.

12. J. Hollowell, “Heli /SITAN: A terrain referenced navigation algorithm for helicopters,” in Proc. IEEE Posit. Location Navigat. Symp. Las Vegas, NV, USA, Mar. 1990, pp. 616–625.
13. CA Baird, FB Snyder, and M Beierle, “Terrain-aided altitude computations on the AFTI/F-16,” in Proc. IEEE Posit. Location Navigat. Symp, Las Vegas, NV, USA, Mar. 1990, pp. 474–481.
14. O. Eroglu and G. Yilmaz, “A terrain referenced UAV localization algorithm using binary search method,” J. Intell. Robot. Syst., vol. 73, nos. 1–4, pp. 309–323, Jan. 2014.
15. Han, Yurong and Wang, Bo and Deng, Zhihong and Fu, Mengyin, “An improved TERCOM-based algorithm for gravity-aided navigation”, vol16, no 09, pp 2537-2544, 2016.
16. Rajendra Naik Bhukya and Swetha Kodepaka and Vennela Dharavath and Ravi Boda, “Position and Velocity Errors Reduction Using Advanced TERCOM Aided Inertial Navigation System”, vol 1165. Springer, isbn: 978-981-15-5112-3, pp 801-809, 2021,

Impact of Deblurring on Image Matching Algorithms

Vaddi Chandra Sekhar*, Boda Nehru, D Penchalaiah, Akula Naresh, G Naresh Kumar, Abhijit Bhattacharyya

Defense Research and Development Laboratory
Hyderabad, Telangana, 500058

ABSTRACT

Motion blur can have a significant impact on the performance of image matching tasks, particularly when using feature-based matching algorithms like SIFT (Scale-Invariant Feature Transform) or SURF (Speeded Up Robust Features). In this work we explore the impact of image deblurring on image matching algorithms. For our work we chose one classical algorithm SIFT and one Neural network model D2NET. For deblurring the images we used the state of the art deblurGAN model. It is observed that Image matching has significantly improved on the deblurred images compared to the blurred images as observed from the precision recall curves.

Keywords: *DeblurGAN, SIFT, D2NET, Image matching, Neural Network, Computer Vision*

1. INTRODUCTION

In vision-based navigation systems cameras mounted on moving and vibrating platforms like UAV's causes blurring in the images which reduces the visual perception quality and also severely degrade the performance of image matching tasks [1]. Image matching involves finding correspondences between two or more images. This can be used for tasks like image registration, object recognition, and 3D reconstruction.

Feature-based matching algorithms like SIFT [2] and SURF [3] identify distinctive keypoints in images and match them based on their descriptors. When images are affected by motion blur, the distinctive keypoints can become difficult to detect and match accurately, leading to errors in feature matching. Motion blur causes objects in the image to appear blurred or smeared, which can change the appearance and location of keypoints. This can result in a lower number of matched keypoints and a higher rate of false matches, which can reduce the accuracy of image matching.

Most of the literature available on image matching have tested the performance of image matching algorithms on Gaussian blur with varied sigma [4], However most of the work in literature ignore the effects on motion blur on image matching algorithms. In this work we tested the degradation of image matching performance because of different kinds of motion blur.

To mitigate the effects of motion blur on image matching tasks, it is important to use appropriate preprocessing techniques to reduce or remove the blur. This can include image deblurring, motion estimation, and motion compensation techniques. In this work we have explored the impact of deblurring on image matching, we have used the state of the art DeblurGan [5] model to deblur the blurred images and have studied the performance of image matching on the deblurred images.

*Corresponding Author: Email: vcsekhar.drdl@gov.in

2. LITERATURE REVIEW

Deblurring images can have a significant impact on matching techniques. Juncai Peng et al [6] proposed a joint image deblurring and matching method unlike the traditional method of deblurring the image first and then applying the image matching techniques.. By combining image deblurring and matching tasks, their approach could obtain significant improvements over the state-of-the-art image matching algorithms. However the blur kernels used are gaussian blur kernels and the work has not been tested on images with motion blur. T. Sieberth et al [7] used an approach of using Fourier transformation to obtain good deblurred results and improved feature matching . Jian W et al [8] compared different variants of SIFT and have tested the performance of SIFT variants under different blur conditions and have found that color invariant scale invariant feature transform CSIFT has improved performance on blurred images compared to sift, however the improvement is not very high compared to sift. In all these works the blur used to corrupt the images are Gaussian blur and none of them have used motion blur for testing.

3. RESEARCH METHODOLOGY AND PROPOSED METHOD

We first generate motion blur on the INRIA Graffiti dataset [8] and find the precision recall curves for both sift and D2Net [9]. Next we deblur the images using deblurGAN and find the precision recall curves and compare the results.

Motion Blur Generation: We introduce synthetic blur on the images by convolving clean natural images with one out of 73 possible linear motion kernels [10].

Figure 1: Figure shows the kernel and the corresponding blurred image. Kernel size chosen to generate the blur is 50x50

FEATURE EXTRACTION

Scale-Invariant Feature Transform (SIFT) is a computer vision algorithm used for object recognition and image matching. It was introduced by David Lowe in 1999 and has since become one of the most widely used methods for feature detection and extraction in computer vision.

The SIFT algorithm identifies local key points in an image that are invariant to scale and rotation. It does this by first constructing a scale space representation of the image, which involves repeatedly applying Gaussian blurring and downsampling to create a set of progressively lower-resolution images.

Next, the algorithm identifies potential key points at various scales by looking for local extrema in the difference-of-Gaussian (DoG) images, which are obtained by subtracting

ISBN - 978-93-95038-50-8

adjacent scales of the Gaussian pyramid. These potential key points are then filtered based on their contrast and edge response, and a gradient orientation is assigned to each key point.

Finally, SIFT constructs a descriptor for each key point based on the gradient orientations and magnitudes in its local neighborhood. The resulting descriptors are highly distinctive and invariant to scale, rotation, and illumination changes, making them ideal for image matching and object recognition tasks.

SIFT has been widely used in applications such as image retrieval, 3D reconstruction, and robot navigation.

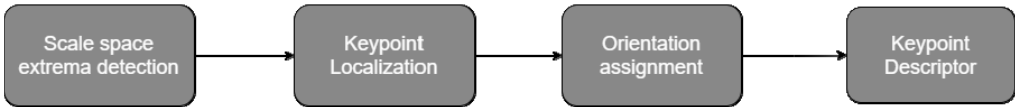

Figure 2: SIFT algorithm

Figure 3: Result of SIFT on original images

D2-Net is a deep learning-based algorithm for feature detection and description in computer vision. It was introduced by Rocco et al. in 2019 as an improvement over existing methods such as SIFT and SURF.

The name "D2-Net" comes from the fact that the algorithm is built around a deep neural network that predicts two types of features: keypoints and their descriptors. The network is trained on a large dataset of image pairs with ground truth correspondences, using a loss function that encourages the predicted keypoints and descriptors to match those in the ground truth.

One of the key advantages of D2-Net over previous methods is its ability to handle large scale changes and viewpoint variations in images. This is achieved through a multi-scale architecture that generates feature maps at different resolutions, allowing the network to capture both fine and coarse image structures.

Another strength of D2-Net is its speed and efficiency. Unlike SIFT and SURF, which require multiple steps of filtering and matching, D2-Net performs feature detection and description in a single forward pass of the neural network. This makes it much faster and more scalable, especially for large-scale applications.

ISBN - 978-93-95038-50-8

D2-Net has shown state-of-the-art performance on several benchmark datasets for feature detection and description, and has been used in applications such as image matching, 3D reconstruction, and object recognition.

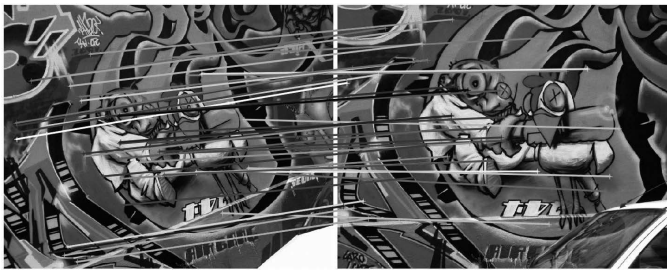

Figure 4: Result of D2NET on original images

DEBLURRING

DeblurGAN is a deep learning-based algorithm for image deblurring, introduced by Kupyn et al. in 2018. It uses a generative adversarial network (GAN) to restore sharp images from blurry ones.

The DeblurGAN architecture consists of two neural networks: a generator and a discriminator. The generator takes a blurry image as input and produces a sharp image as output. The discriminator is trained to distinguish between the sharp output images and the original, unblurred images.

The generator is trained using a loss function that combines two components: a content loss and an adversarial loss. The content loss measures the difference between the generated sharp image and the original unblurred image. The adversarial loss encourages the generator to produce images that are indistinguishable from real, sharp images, according to the discriminator.

DeblurGAN can handle a wide range of blur types, including motion blur and defocus blur, and has shown state-of-the-art performance on several benchmark datasets for image deblurring. It has also been used in real-world applications such as restoring blurry images in surveillance footage and medical imaging.

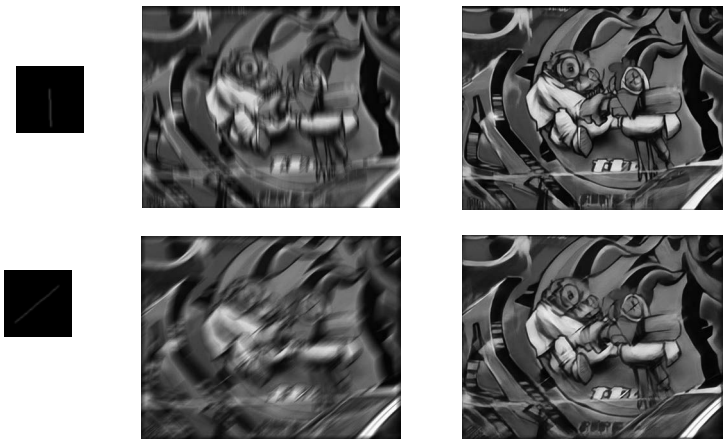

Figure 5: Results of DeblurGan on blurred images

ISBN - 978-93-95038-50-8

5. RESULTS AND DISCUSSIONS

We have tested SIFT and D2NET on blurred images and the deblurred images. Below figures summarizes the results

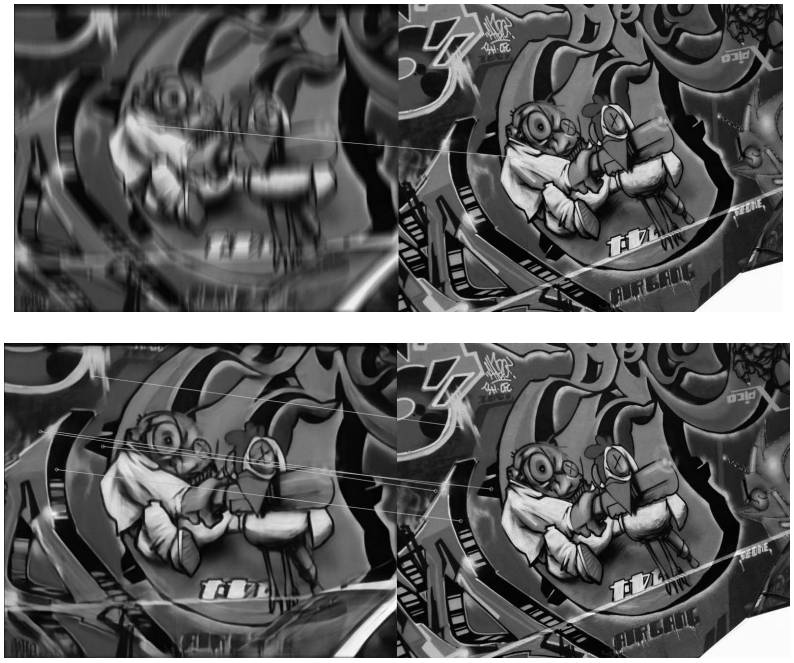

Figure 6: Result of SIFT on blurred and deblurred image

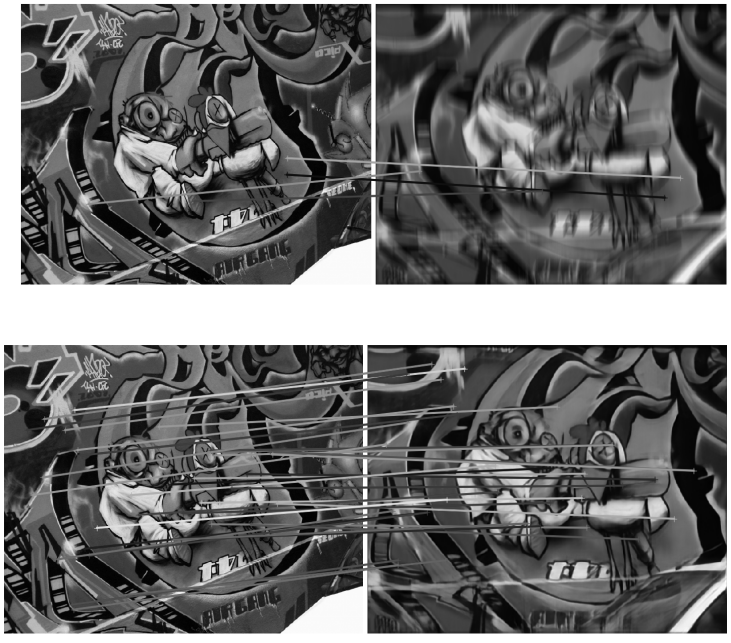

Figure 7: Result of D2NET on blurred and deblurred image

As seen in the above figures the matching has improved on the deblurred images compared to the blurred images, we quantify these results below.

Precison Recall Curves: We use the same evaluation metrics as discussed in [4]. The first step in finding precision recall curves is to find all the keypoints for all of the images in the dataset. Euclidean distance between the descriptors for all pairs of keypoints between the reference image and all other images in the dataset are found. If the Euclidean distance between the descriptors for a particular pair of keypoints falls below the chosen threshold t, these keypoints are termed as a match. A correct-positive is a match where the two keypoints correspond to the same physical location. A false-positive is a match where the two keypoints come from different physical locations. This information is verified by utilizing the homography between the two images. The total number of positives value mentioned is known apriori. From these numbers, we can determine recall and 1−precision [12]:

$$recall = \frac{\text{number of } \textit{correct-positives}}{\text{total number of positives}}$$

$$1-precision = \frac{\text{number of } \textit{false-positives}}{\text{total number of matches (correct or false)}}.$$

We generate the recall vs. 1−precision graphs by varying the threshold t.

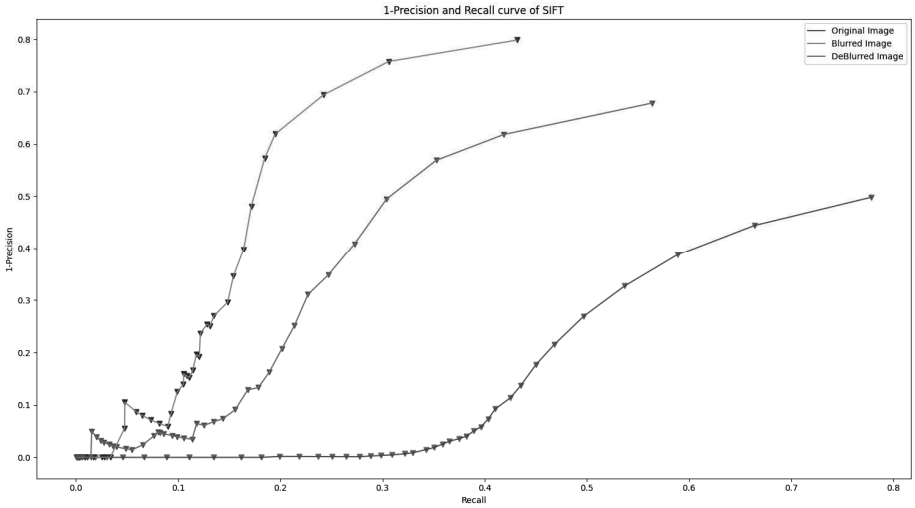

Figure 8: Figure shows 1-precision recall curve for sift on original, blurred and deblurred images

We now discuss the interpretation of these curves. An ideal detector should have recall close to 1, and 1-precision close to zero. We can see that from Fig 8, for the same value of 1-precision the recall value for deblurred image is greater than recall for the blurred image, proving that deblurring the image has significantly improved the true positive rate. Similar observations are made for D2Net from Fig 9. However D2Net has lower 1-precision compared to SIFT, and the curve for deblurred image is very close to the curve for original sharp image, indicating that deblurring as a pre-processing stage for D2Net is very effective.

ISBN - 978-93-95038-50-8

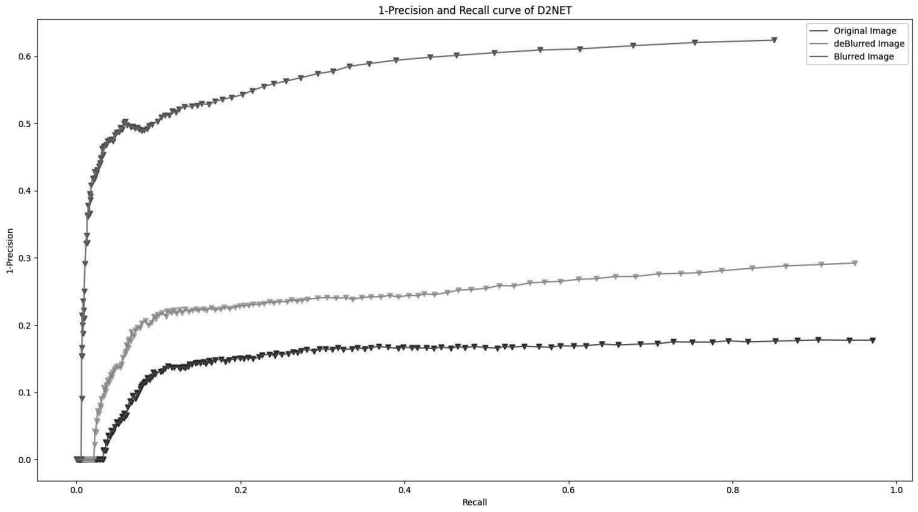

Figure 9: Figure shows 1-precision recall curve for D2NET on original, blurred and deblurred images

6. CONCLUSIONS

We have successfully demonstrated how removing the blur from images improves the accuracy of image matching. 1-precision vs recall curves showed improvement for both SIFT and D2NET on deblurred images compared to blurred images. The results also show that D2NET curve for deblurred images is very close to the original image, showing that deblurring is very effective while using D2NET as image matching technique, and D2Net is a better technique for image matching compared to SIFT because of very less false positives as indicated by very low values of 1-precision.

REFERENCES

1. Guo, Qing, et al. "Exploring the effects of blur and deblurring to visual object tracking." IEEE Transactions on Image Processing 30 (2021): 1812-1824.
2. Lowe, David G. "Object recognition from local scale-invariant features." Proceedings of the seventh IEEE international conference on computer vision. Vol. 2. Ieee, 1999.
3. Bay, Herbert, et al. "Speeded-up robust features (SURF)." Computer vision and image understanding 110.3 (2008): 346-359.
4. Juan, Luo, and Oubong Gwun. "A comparison of sift, pca-sift and surf." International Journal of Image Processing (IJIP) 3.4 (2009): 143-152.
5. Kupyn, Orest, et al. "Deblurgan: Blind motion deblurring using conditional adversarial networks." Proceedings of the IEEE conference on computer vision and pattern recognition. 2018.
6. Peng, Juncai, et al. "Joint image deblurring and matching with feature-based sparse representation prior." Pattern Recognition 103 (2020): 107300.
7. Sieberth, Till, Rene Wackrow, and J. H. Chandler. "INFLUENCE OF BLUR ON FEATURE MATCHING AND A GEOMETRIC APPROACH FOR PHOTOGRAMMETRIC DEBLURRING." International Archives of the Photogrammetry, Remote Sensing & Spatial Information Sciences (2014).
8. Viewpoint change sequences. http://www.inrialpes.fr/ movi/

9. Dusmanu, Mihai, et al. "D2-net: A trainable cnn for joint detection and description of local features." arXiv preprint arXiv:1905.03561 (2019).
10. J. Sun, W. Cao, Z. Xu, and J. Ponce. Learning a Convolutional Neural Network for Non-uniform Motion Blur Removal. 2015. 3, 5, 7, 8
11. K. Mikolajczyk and C. Schmid. A performance evaluation of local descriptors. In Proceedings of Computer Vision and Pattern Recognition, June 2003
12. Ke, Yan, and Rahul Sukthankar. "PCA-SIFT: A more distinctive representation for local image descriptors." Proceedings of the 2004 IEEE Computer Society Conference on Computer Vision and Pattern Recognition, 2004. CVPR 2004.. Vol. 2. IEEE, 2004.

ISBN - 978-93-95038-50-8

Computational Analysis of Horizontal Axis Wind Turbine Blade NACA 63(4)221

Uma MaheshwarVanamala*, PurnaVisishtaBattu

*Department of Mechanical Engineering
University College of Engineering, Osmania University
Hyderabad, Telangana, 500007

ABSTRACT

Wind energy is one of the most sustainable sources of renewable energy. The fast technological development in the wind industry and availability of multi megawatt sized horizontal axis wind turbines has further led to the promotion of wind power utilization globally. The paper presents work on NACA 63(4)-221 aerofoilprofile is taken which is redesigned horizontal axis wind turbine blade (HAWT) for VESTAS RRB V27-225 kW. In a HAWT, aerofoil blades are very essential parts. Forces for lift and drag on the blade play an important role in the aerodynamic efficiency of aerofoil. CFD analysis on the aerofoil blade of wind turbine is carried out and the effect of angle of attack and Reynolds number on performance of the NACA 63(4)-221 aerofoilblade is presented. The ratio of coefficient of lift to coefficient of drag (C_l/C_d) is calculated. Maximum C_l/C_d values are observed at Angle of Attack 6^o degrees.

Keywords: *Horizontal Axis Wind Turbine, Aerofoil, Angle of Attack, Reynolds number.*

1. INTRODUCTION

A wind turbine, or alternatively referred to as a wind energy converter, is a device that converts the wind's kinetic energy into electrical energy. Wind energy is a form of solar energy. Wind is caused by the uneven heating of the earth's atmosphere by the solar radiation, variations in the earth's surface, and rotation of the earth. So the energy is from the Sun.

A Wind turbine uses the wind's kinetic energy and converts it into mechanical energy, that is, rotations the blades of the wind turbine. The blades spin a shaft that is connected through a gearbox to the generator which produces electricity, in conventional wind turbines. The most recognizable parts of a turbine are its blades. Many turbines today have three blades, while some have two. Atmospheric turbulence (unsteady movement of air) produces important various types of aerodynamic forces (lift and drag) on wind turbine blade, where turbulence is a primary source of aerodynamic forces on blade of wind turbine.

2. LITERATURE REVIEW

A lot of work and studies have been done on turbines blades which are described in various research papers. Few of the papers which are referred are described below.

H. Abbott, Albert E. Yondoenhoff and Louis S. Stiyers (1945); in National Advisory Committee for Aeronautics, Report No. 824, Summary of Aerofoil Data, have collected aerofoil data for both flight and wind-tunnel tests and correlated. They found that the NACA 6-series aerofoils also have favourable critical-speed characteristics and do not appear to present unusual problems associated with the application of high-lift and lateral-control devices.UmeshChaudhary; Sisir Kumar Nayak (2015); "Micro and small-scale HAWT blades aerofoils study through CFD for low wind applications" analysis of basic 5 series NACA aerofoils profile for micro and small-scale horizontal axis wind turbine (HAWT) has been

*Corresponding author: E-mail: Mahesh.v@uceou.edu

studied for different angle-of-attack α and fixed Reynolds number and found the optimal angle-of-attack.

MingweiGe,; De Tian,; and Ying Deng (2016); "Reynolds Number Effect on the Optimization of a Wind Turbine Blade for Maximum Aerodynamic Efficiency" have investigated the effect of the Reynolds number on the aerodynamic performance of aerofoils, and influence on the optimal design of a wind rotor aiming to maximize the power coefficient.GiridharRamanujam, HüseyinÖzdemir and H. W. M. Hoeijmakers (2016); in "Improving Aerofoil Drag Prediction" have developed an improved formulation of drag estimation for thick aerofoils. The improved drag formulation predicts the drag accurately for aerofoils with reasonably small trailing-edge thicknesses. The derivation of drag correction is based on the difference between the actual momentum loss thickness based on free stream velocity and that based on the velocity at the edge of the boundary layer. A modification to the existing drag calculation method till then in XFOIL-like methods has been developed.

C.A. Baxevanoua, P.K. Chaviaropoulosb, S.G. Voutsinas c, N.S. Vlachosa (2008); "Evaluation study of a Navier–Stokes CFD aero elastic model of wind turbine aerofoils in classical flutter" described a new aero elastic numerical model, which combines a Navier–Stokes CFD solver with an elastic model and two coupling schemes for the study of the aero elastic behaviour of wind turbine blades undergoing classical flutter. There model is evaluated by comparing with previous numerical results and the corresponding linear analytical solutions. Consequently, a parametric study is carried out. Conclusions are drawn about the ability of the model to handle the aero elastic behaviour of an aerofoil and about the most appropriate coupling scheme in terms of predicting the modal damping and the flutter limiting point. There predictions show that they are only slightly affected by the coupling or the space discretization scheme and mainly by the turbulence model used.

Muhammad FaizanYounas, Awais Ali and Muhammad DaudShafique(2019);" CFD Simulation of HAWT Blade and Implementation of BEM Theory"; designed HAWT implemented Blade Element Momentum Theory (BEM), studied the characteristics of flow over the designed blade in Computational Fluid Dynamics (CFD) and simulations where done using ANSYS Fluent.In present work CFD analysis for airfoil NACA 63(4)-221 for redesigning the blade of VESTAS RRB V27-225 kW Horizontal Axis Wind Turbine (HAWT). In this work the viscous SpalartAllmaras model is used. SpalartAllmaras model is a one equation model which solves a transport equation for a viscosity-like variable, referred to as the Spalart-Allmaras variable.

3. PROBLEM DEFINITION

NACA series blades have been experimented in a wind tunnel and the results were obtained. Computationally the analysis can be done on the blades of the turbine so as to predict the performance before it is experimented and been installed for applications. This can help for better performance, eliminate deficient conditions, reduce time and cost.

3.1 OBJECTIVES

The horizontal axis wind turbine blade for VESTAS RRB V27-225 kW, computational study on the performance of an aerofoil blade profile NACA 63(4)-221 is carried out with the following objectives.

i. To conduct analysis on Horizontal axis wind turbine blade NACA 63(4)221 profile.

ISBN - 978-93-95038-50-8

ii. To determine lift coefficient (C_l), drag coefficient (C_d), ratio of lift coefficient to drag coefficient (C_l/C_d) of the aerofoil.
iii. To determine angle of attack where C_l/C_d is maximum.

The following flow Parameters are varied in the study:

a) Angle of Attack: 4^0, 5^0, 6^0, 7^0, 8^0.
b) Low Reynolds number in the range of $X10^5$ (wind speed: 6 m/s, 7 m/s, 8 m/s, 9 m/s, 10 m/s).
c) High Reynolds number in the range of $X10^6$ (wind speed: 43.8 m/s, 87.6 m/s, 131.5 m/s).

4. RESEARCH METHODOLOGY

4.1. MODELING GEOMETRY

The coordinates of the NACA 634-221 are obtained from literature P. K. Nigam (2020) [7]. The aerofoil is designed by selecting required coordinate file in the Design modeller. A rectangular domain is designed using sketching tool for analysis around the aerofoil. Then the required design is obtained using Boolean operation. Figure 1 shows the designed aerofoil profile of NACA 634-221. The boundary conditions which are defined in setup are been named using named selections of the aerofoil: inlet, outlet, top, bottom, aerofoil top, aerofoil bottom and 2d design profile.

4.2. MESH

Mesh is done around the aerofoil with physics preference CFD and Solver preference is Fluent. Edge sizing of the aerofoil cross-section is done, in inflation the boundary as the aerofoil edges is selected for obtaining finer mesh around the aerofoil. The mesh is generated in ANSYS Workbench 2020 R2 by using ANSYS Fluent 2020 R2, is shown in the figure 2.

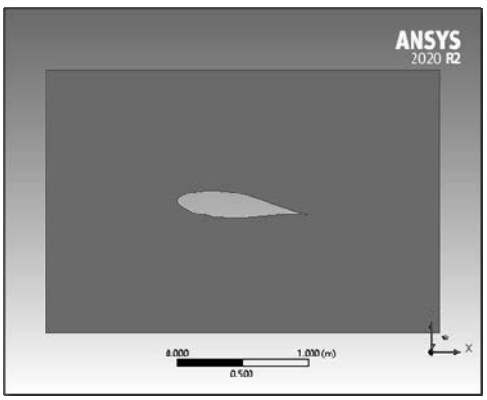

Figure 1: NACA 63_4-221aerofoil profile

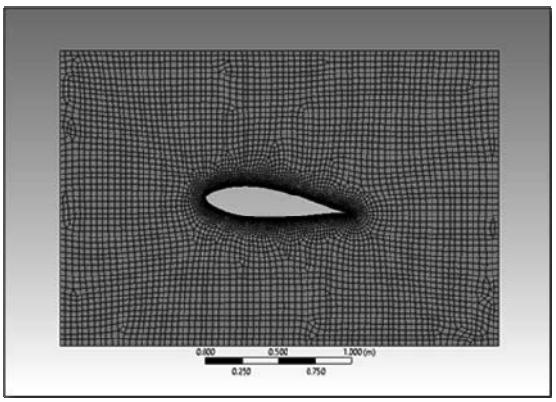

Figure 2: Mesh around NACA 63_4-221

4.3. GRID INDEPENDENCE STUDY

A solution is considered grid-independent if the discretization and solution error are small enough, given sufficient iterations. This is essential to know for comparative results. A mesh convergence study consists of refining elements and comparing the refined solutions to the

coarse solutions. If further refinement (or other changes) does not significantly change the solution, the mesh is an "Independent Grid."

In this analysis, mesh is performed at angle of attack=60, inlet velocity: 6m/s for the aerofoil. When the increase in the change in Cl/Cd coefficient becomes negligible, the optimum mesh number is determined. Table 1 shows the grid independence test results.

From these results, of the grid independence test, mesh is determined at 17866 nodes and 17264 elements for best results.

Element size: 0.04m (linear element order)

Number of divisions (aerofoil edges): 500(Behaviour: Hard)

Inflation between face and edges of aerofoil: 8 layers with 0.01 maximum thickness

In meshing finer mesh is done around the aerofoil to obtain accurate values of Lift and Drag coefficient around the aerofoil

Table 1: Grid Independence Test Results

NODES	Cl/Cd
13838	74.40807477
15099	74.04116318
15488	74.42551651
16009	74.84930386
16512	74.49607027
17866	**75.21509212**
18787	75.1802723
19313	74.63732116
20526	74.84930386

The geometry is designed at varies angle of attack and is been meshed accordingly after the grid independence test. The Table 2 shows the number of nodes obtained at different angle of attack.

Table 2: Mesh size at Angle of Attack

Angle of Attack	Nodes
4^0	17794
5^0	17810
6^0	17866
7^0	17911
8^0	17983

4.4. VALIDATION

At the end of each analysis, the ratio Cl/Cd for a given angle of attack were calculated, compared and validated with the results available in the literature P. K. Nigam (2020) and Abbott I.H (1945).

ISBN - 978-93-95038-50-8

Case1: At low Reynolds Number, inlet velocity=6 m/s for the aerofoil. The values of Cl/Cd are calculated, compared and validated with the results available in the literature P. K. Nigam (2020) [7]. Table 3 shows the validation results at varying angle of attack at low Reynolds number.

Table 3: Validation at low Reynolds number

Angle of Attack(AOA)	C_l/C_d	Reference C_l/C_d[7]
4º	67.820	70.847
5º	73.061	75.814
6º	75.215	78.457
7º	73.731	78.017
8º	70.932	74.662

Case2: At high Reynolds Number, inlet velocity= 43.8 m/s (Re=3x106) for the aerofoil. The values of Cl/Cd are calculated, compared and validated with the results available in the literature Abbott I.H (1945) [1] and P. K. Nigam (2020) [7].Table 4 shows the validation results at varying angle of attack at high Reynolds number.

Table 4: Validation at high Reynolds number

Angle of Attack(AOA)	C_l/C_d	Reference C_l/C_d [1]	Reference C_l/C_d[7]
4º	96.232	0.55/0.0067=82.089	-
5º	102.183	0.77/0.0072=106.944	108.854
6º	105.724	0.86/0.0079=108.861	111.613
7º	104.085	0.975/0.009=108.333	111.120
8º	102.970	1.05/0.0114=92.110	108.280

4.5 SETUP

4.5.1 BOUNDARY CONDITIONS

The analysis consists of flow around an aerofoil at various angles of attack (4º, 5º, 6º, 7º, 8º) and at different Reynolds number in the range of 10^5 and 10^6.

Reynolds Number (Re): The Reynolds number is a dimensionless number used to predict flow patterns in different fluid flow situations. The ratio of inertial forces to viscous forces gives Reynolds number.

$$Re = \frac{Inertial\ Force}{Viscous\ Force} = \frac{\rho v l}{\mu} = \frac{vl}{\vartheta}$$

Where, ρ is the density of the fluid (kg/m3)

v is the wind speed (m/s)

l is a characteristic linear dimension (m)

ISBN - 978-93-95038-50-8

μ is the dynamic viscosity of the fluid (Pa·s) or N·s/m2 or kg/(m·s)

ϑ is the kinematic viscosity of the fluid (m2/s)

From the above equation of Reynolds number, wind velocity is calculated for high values of Reynolds number: 3x106, 6x106, 9 x 106.

$$Wind\ Speed\ \mathrm{v} = \frac{Re\ \mu}{\rho l}$$

Calculations of wind velocities at high Reynolds number:

Here air is the medium so; ρ=1.225 m/s, μ= 1.7894x10^{-5} kg/m-s and chord length l=1m

At Re=3x10^6 $\quad V = \frac{3x10^6 x1.7894x10^{-5}}{1.225x1}$ =43.822 m/s

At Re=6x10^6 $\quad V = \frac{6x10^6 x1.7894x10^{-5}}{1.225x1}$ =87.644m/s

At Re=9x10^6 $\quad V = \frac{9x10^6 x1.7894x10^{-5}}{1.225x1}$ =131.466 m/s

Energy equation and Viscous Spalart-Allmaras(1 Equation) model is been used for the calculation. The Spalart-Allmaras model is a relatively simple one-equation model that solves a modelled transport equation for the kinematic eddy (turbulent) viscosity. The inputs and boundary conditions are shown in the Table 5.

Table 5: The parameters considered in the Fluent Setup

Fluent Setup	
Physics Preference	CFD
Solver Preference	Fluent
Problem Type	2D
Type of Solver	Pressure-Based Solver
Models	
Energy Equation	On
Viscous Model	SpalartAllmaras(1 Equation)
Material Properties	Flowing fluid is air
Density of air	1.225 kg/m^3
Viscosity	1.7894e^{-05} kg/m-s
Boundary Conditions	
Velocity Inlet	
Velocity(m/s)	6, 7, 8, 9, 10, 43.8, 87.6, 131.5
Pressure outlet	
Gauge pressure	0 Pa
Turbulent viscous ratio	10

ISBN - 978-93-95038-50-8

5. SOLUTION METHOD

Table 6 shows solver conditions for obtaining the calculated results of lift coefficient and drag coefficient. The required solutions which are to be calculated are been defined in report definitions to graphically plot and view results. The calculations are done by running with 200 iterations for all parameters varying for the solutions to converge.

Table 6: Solution Method

Solution Method	
Pressure velocity coupling	
Scheme	Coupled
Spatial Discretization	
Gradient	Least Squares Cell Based
Pressure	Second Order
Momentum	Second Order Upwind
Modified turbulent	First Order Upwind
Energy	Second Order Upwind
Report Definitions	
Report File and Report	Lift coefficient, Drag
Solution Initialization	
Initialization Method	Hybrid Initialization
Run Calculations	
Number of iterations	200

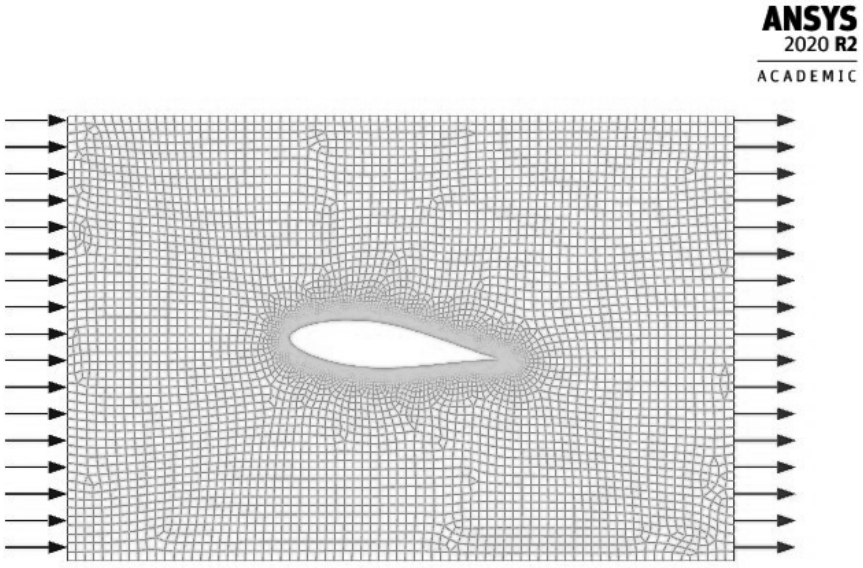

Figure 3: NACA 63_4-221 with inlet and outlet

5. RESULTS AND DISCUSSIONS

From these contours obtained it is observed that they are lower values of pressure on the top of the aerofoil, higher values of pressure on the bottom of the aerofoil, likewise, higher values of velocity on the top of the aerofoil, lower values of velocity on the bottom of the aerofoil. So there is a significant amount of lift on the top of the aerofoil.

Figures 4 to 19 shows the velocity distribution and pressure distribution around aerofoil at Angle of attack=6° at velocities=6m/s, 7m/s, 8m/s, 9m/s, 10m/s, 43.8m/s, 87.6m/s and 131.5m/s.

At a particular angle of attack, as the wind velocity increases there is increase in velocity of the aerofoil. It is also observed that as the angle of attack increases there is an increase in velocity of the aerofoil.

From the velocity contours the following are the observations:

a) As the wind velocity is increased the velocity around the aerofoil is increasing.
b) The velocity is higher on the top of the aerofoil compared to the bottom of the aerofoil.
c) The maximum values of velocity are on the top of the aerofoil.
d) The minimum values of velocity are at the leading edge and trailing edge of the aerofoil.

From the static pressure contours the following are the observations:

a) As the wind velocity is increased the static pressure around the aerofoil is increasing.
b) The pressure is lower on the top of the aerofoil compared to the bottom of the aerofoil.
c) The maximum values of static pressure are at the leading edge the aerofoil.

In viewpoint on effect of AOA on velocity contours and pressure contours, it is observed that with the increase in angle of attack from 4º to 8º

i. The velocity around the aerofoil is increasing.
ii. The range of velocity distribution around the aerofoil is increasing.
iii. The static pressure around the aerofoil is increasing.
iv. The range of static pressure distribution around the aerofoil is increasing.

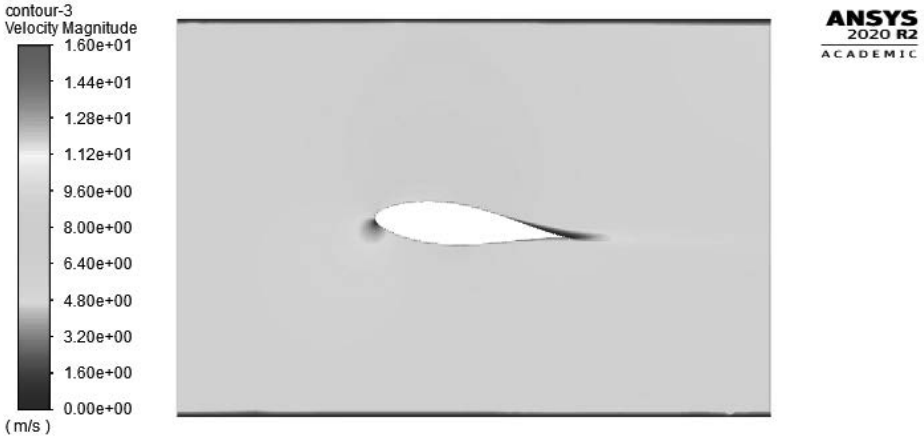

Figure 4: Velocity distribution around Aerofoil-NACA 63(4)-221 at AOA=6° and v=6 m/s

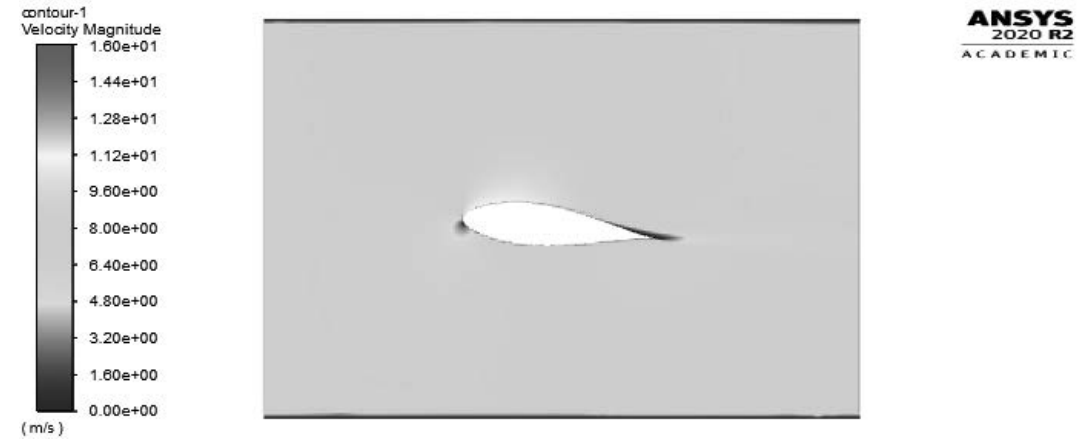

Figure 5: Velocity distribution around Aerofoil-NACA 63(4)-221 at AOA=6° and v=7 m/s

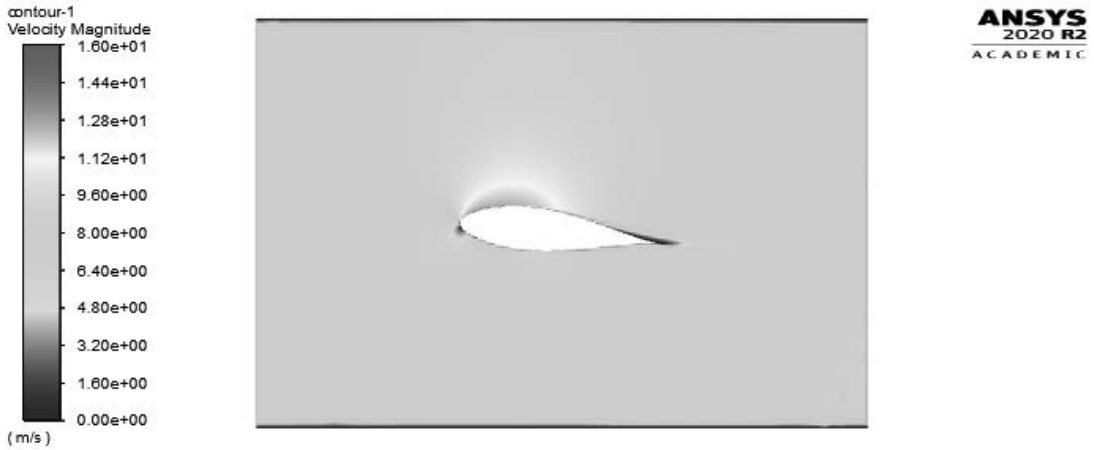

Figure 6: Velocity distribution around Aerofoil-NACA 63(4)-221 at AOA=6° and v=8 m/s

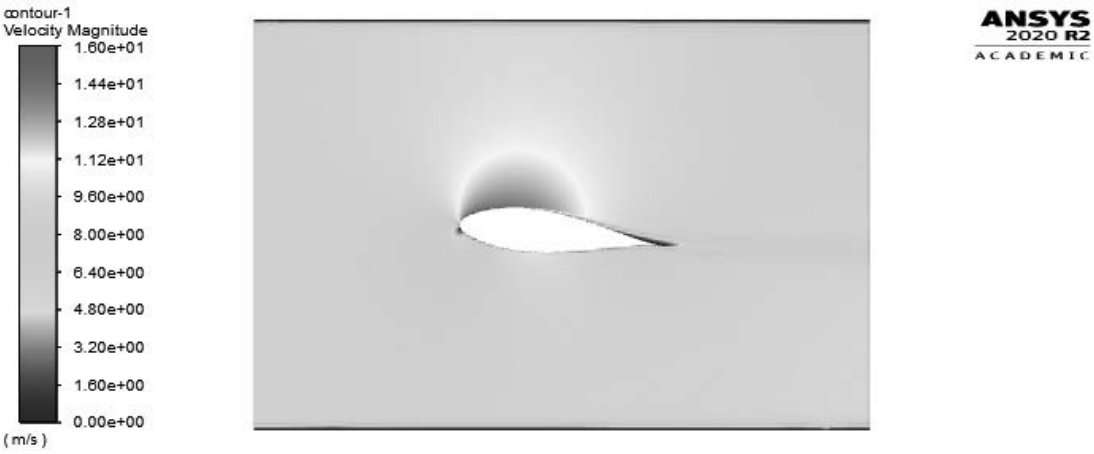

Figure 7: Velocity distribution around Aerofoil-NACA 63(4)-221 at AOA=6° and v=9 m/s

ISBN - 978-93-95038-50-8

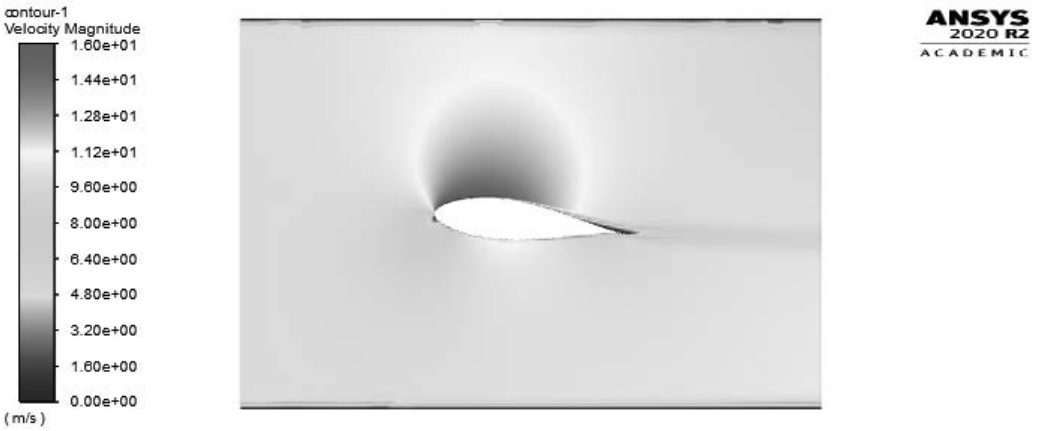

Figure 8: Velocity distribution around Aerofoil-NACA 63(4)-221 at AOA=6° and v=10 m/s

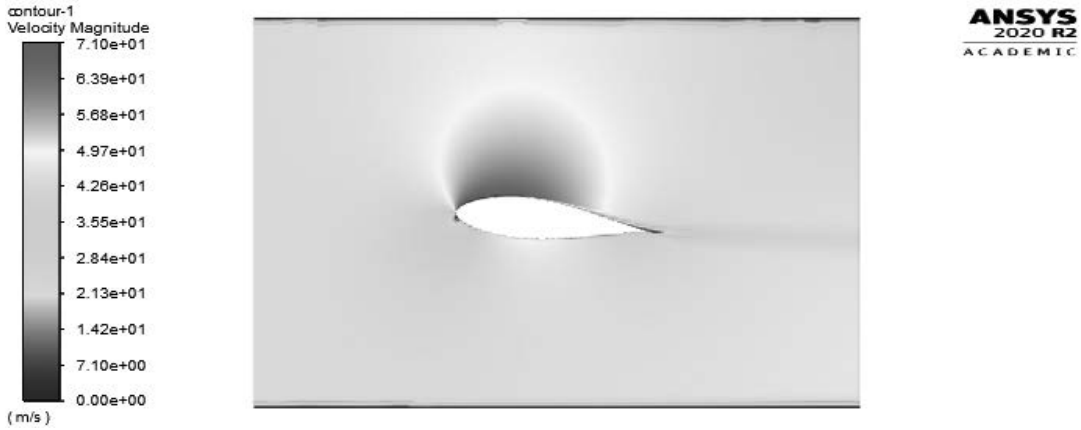

Figure 9: Velocity distribution around Aerofoil-NACA 63(4)-221 at AOA=6° and v=43.8 m/s

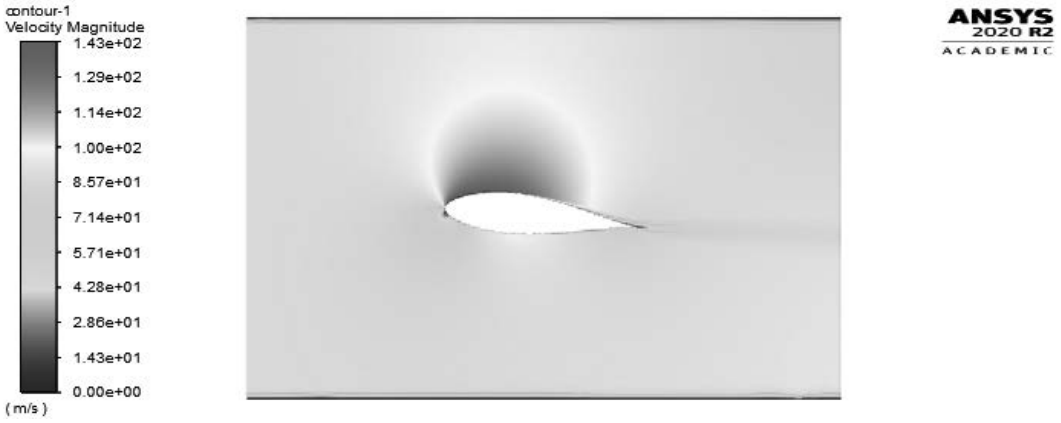

Figure 10: Velocity distribution around Aerofoil-NACA 63(4)-221 at AOA=6° and v=87.6 m /s

ISBN - 978-93-95038-50-8

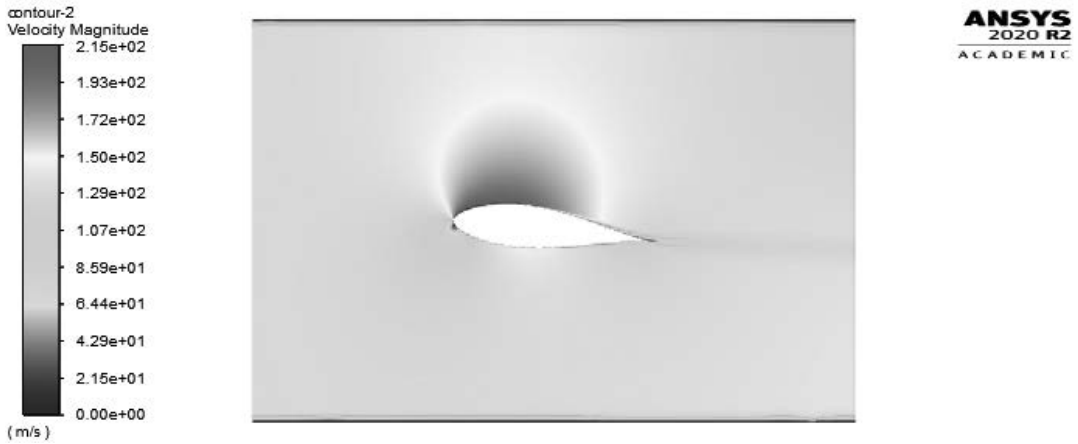

Figure 11: Velocity distribution around Aerofoil-NACA 63(4)-221 at AOA=6° and v=131.5 m /s

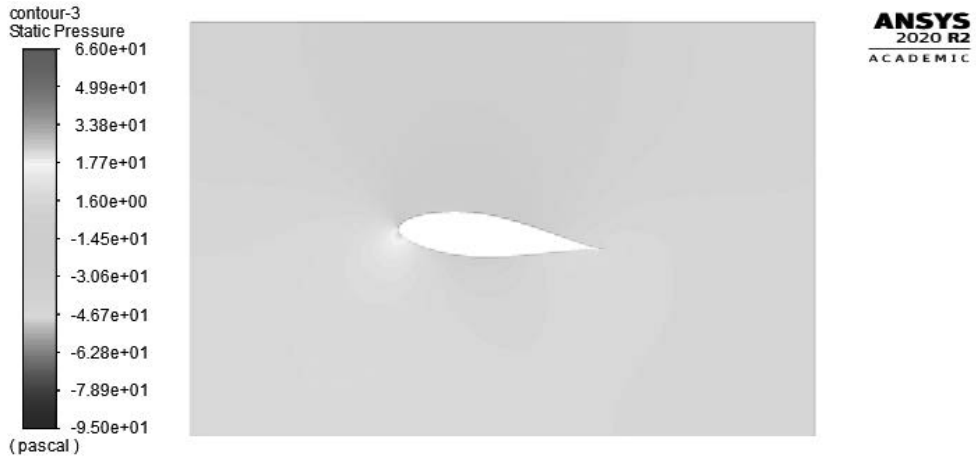

Figure 12: Static Pressure distribution around Aerofoil-NACA 63(4)-221 at AOA=6° and v=6 m/s

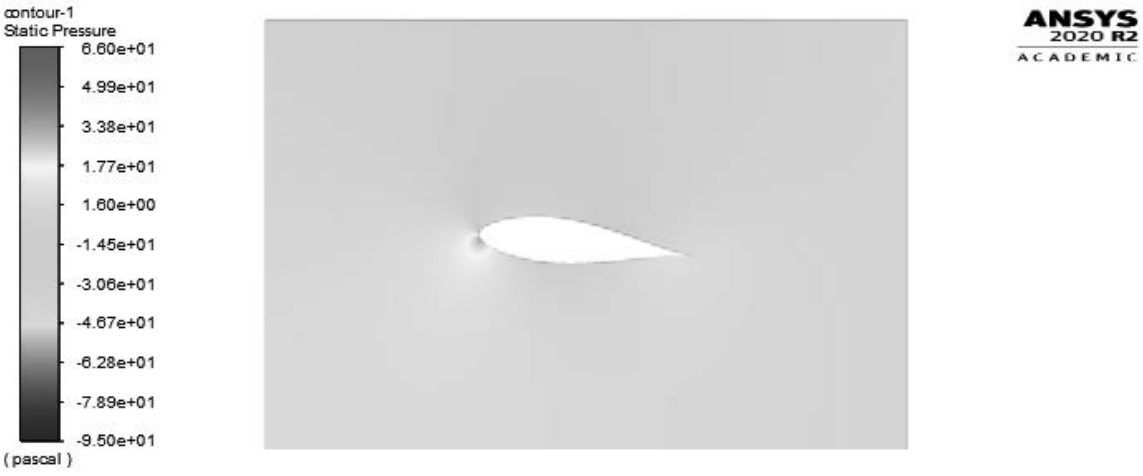

Figure 13: Static Pressure distribution around Aerofoil-NACA 63(4)-221 at AOA=6° and v=7 m/s

ISBN - 978-93-95038-50-8

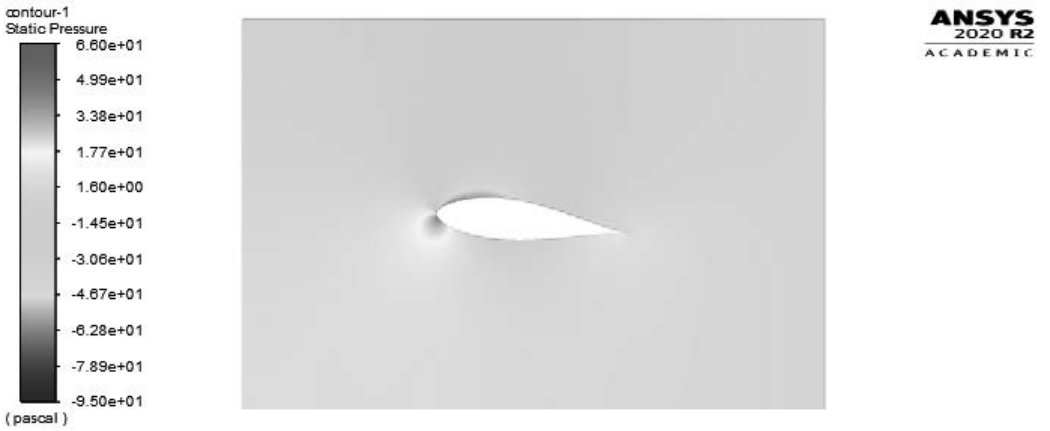

Figure 14: Static Pressure distribution around Aerofoil-NACA 63(4)-221 at AOA=6° and v=8 m/s

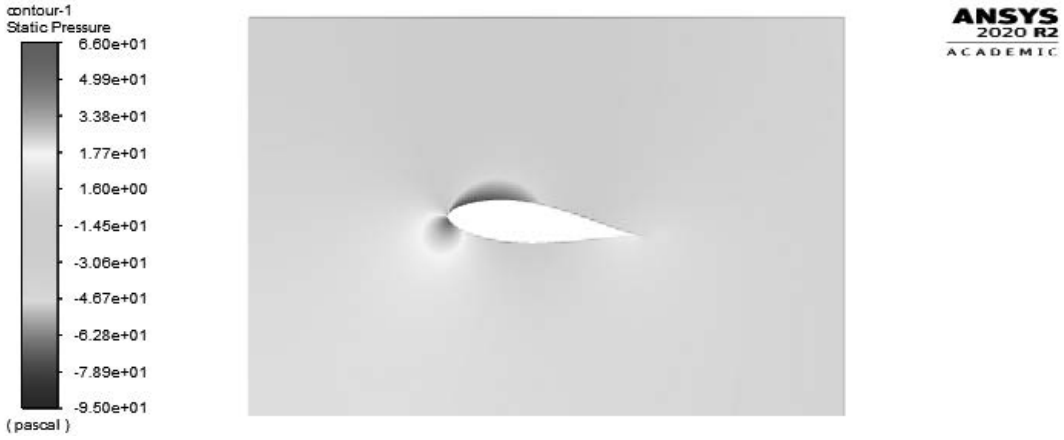

Figure 15: Static Pressure distribution around Aerofoil-NACA 63(4)-221 at AOA=6° and v=9 m/s

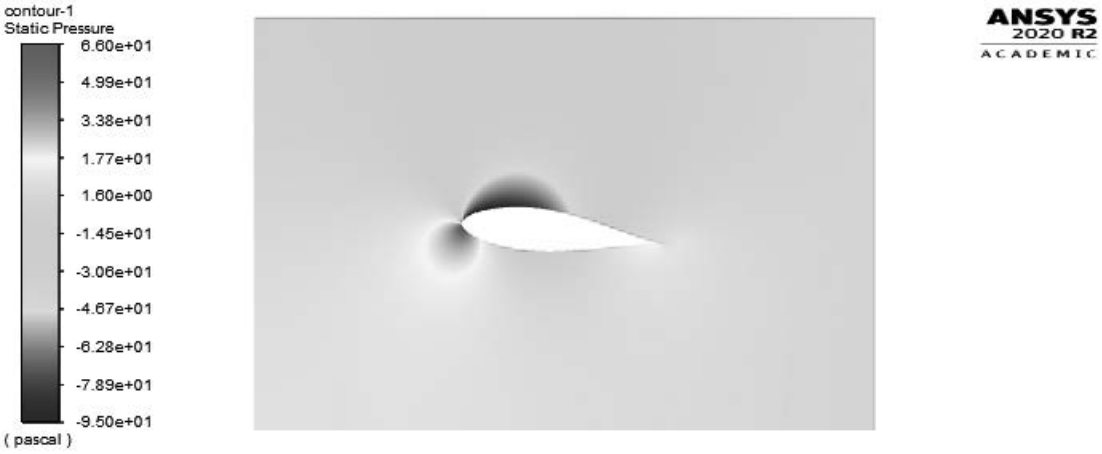

Figure 16: Static Pressure distribution around Aerofoil-NACA 63(4)-221 at AOA=6° and v=10 m/s

ISBN - 978-93-95038-50-8

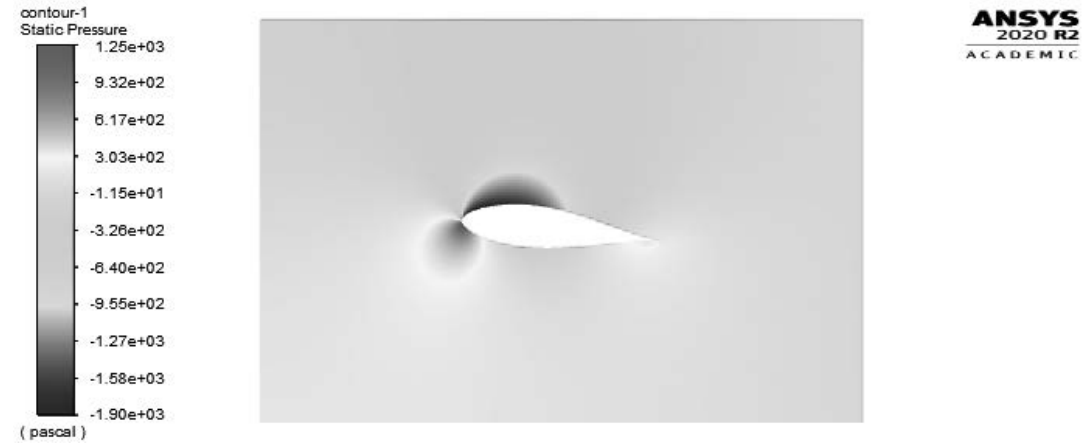

Figure 17: Static Pressure distribution around Aerofoil-NACA 63(4)-221 at AOA=6° and v=43.8 m/s

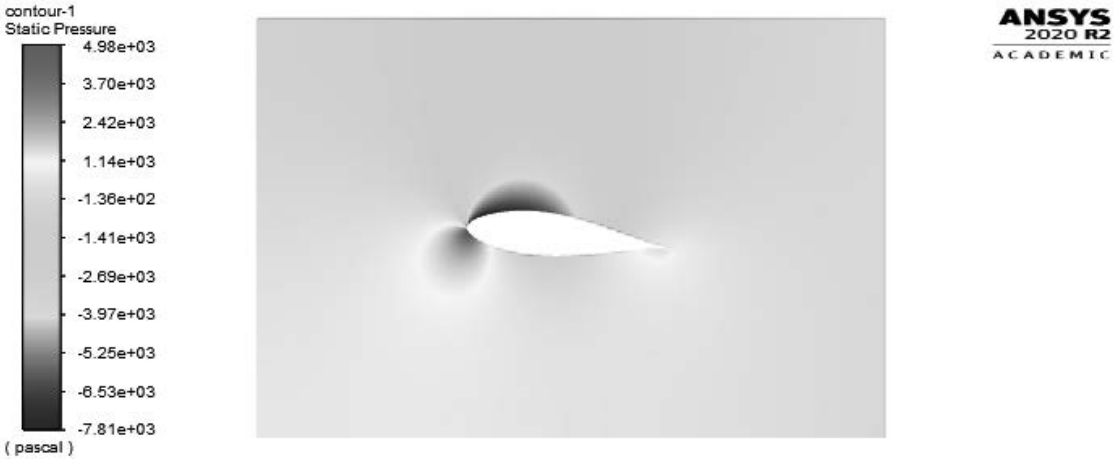

Figure 18: Static Pressure distribution around Aerofoil-NACA 63(4)-221 at AOA=6° and v=87.6m/s

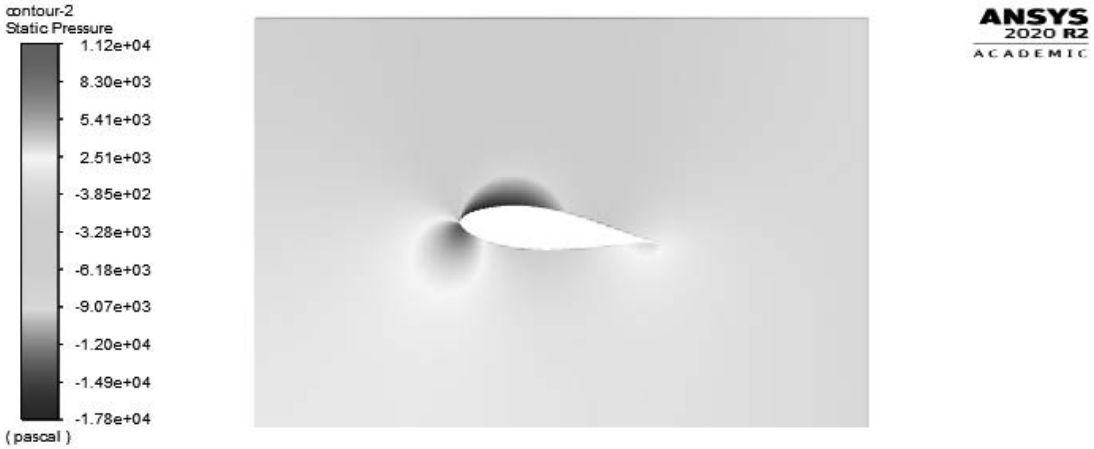

Figure 19: Static Pressure distribution around Aerofoil-NACA 63(4)-221 at AOA=6° and v=131.5 m/s

ISBN - 978-93-95038-50-8

Table 7 shows the calculated values of lift coefficient, drag coefficient at angle of attack 4° to 8° at low values of Reynolds number in CFD and figures 20, 22, 24 shows the graphs plotted from them. Table 8 shows the calculated values of lift coefficient, drag coefficient at angle of attack 4o to 8o at high values of Reynolds number in CFD and figures 21, 23, 25 shows the graphs plotted from them.

The improved drag formulation predicts the drag accurately for aerofoils with reasonably small trailing-edge thicknesses. The derivation of drag correction is based on the difference between the actual momentum loss thickness based on free stream velocity and that based on the velocity at the edge of the boundary layer. A correction factor 0.4 is multiplied to the obtained drag coefficient in CFD to get corrected drag coefficient as explained by GiridharRamanujam (2016) [5].

TABLE 7: CFD analysis results of NACA aerofoil 63(4)-221 at various angle of attack and wind speed for low Reynolds number (x 10^5)

Angle of Attack (degrees)	Reynolds Number	Wind Speed (m/s)	Coefficient of Lift C_l	Coefficient of Drag C_d^1	Corrected Coefficient of Drag $C_d=C_d^1*0.4$	C_l/C_d
4^0	410752.20	6	0.62389	0.022997	0.0091992	67.82
4^0	479210.90	7	0.62784	0.022318	0.0089274	70.32
4^0	547669.60	8	0.63086	0.021846	0.0087383	72.19
4^0	616128.31	9	0.63321	0.021493	0.0085972	73.65
4^0	684587.01	10	0.63538	0.021190	0.0084761	74.96
5^0	410752.20	6	0.74093	0.025353	0.0101412	73.06
5^0	479210.90	7	0.74608	0.024681	0.0098725	75.57
5^0	547669.60	8	0.74917	0.024208	0.0096834	77.36
5^0	616128.31	9	0.75160	0.023835	0.0095341	78.83
5^0	684587.01	10	0.75412	0.023501	0.0094006	80.22
6^0	410752.20	6	0.84433	0.028064	0.0112256	75.21
6^0	479210.90	7	0.85024	0.027361	0.0109445	77.68
6^0	547669.60	8	0.85374	0.026870	0.0107482	79.43
6^0	616128.31	9	0.85685	0.026463	0.0105853	80.94
6^0	684587.01	10	0.85999	0.026097	0.0104389	82.38
7^0	410752.20	6	0.94236	0.031952	0.0127810	73.73
7^0	479210.90	7	0.94921	0.031196	0.0124786	76.06
7^0	547669.60	8	0.95343	0.030661	0.0122645	77.73
7^0	616128.31	9	0.95740	0.030201	0.0120806	79.25
7^0	684587.01	10	0.96072	0.029826	0.0119305	80.52
8^0	410752.20	6	1.02121	0.035992	0.0143969	70.93
8^0	479210.90	7	1.02919	0.035177	0.0140709	73.14
8^0	547669.60	8	1.03484	0.034576	0.0138305	74.82
8^0	616128.31	9	1.03984	0.034047	0.0136190	76.35
8^0	684587.01	10	1.04370	0.033633	0.0134532	77.58

ISBN - 978-93-95038-50-8

MAXIMUM C_l/C_D VALUES ARE OBSERVED AT ANGLE OF ATTACK=6 DEGREE

TABLE 8: CFD analysis results of NACA aerofoil 63(4)-221 at various angle of attack and wind speed for high Reynolds number (x10^6)

Angle of Attack (degrees)	Reynolds Number	Wind Speed (m/s)	Coefficient Of Lift C_l	Coefficient Of Drag $C_d{}^1$	Corrected Coefficient Of Drag $C_d=C_d{}^1*0.4$	C_l/C_d
4^0	3000000	43.8	0.46411	0.012057	0.0048228	96.23
4^0	6000000	87.6	0.45447	0.010459	0.0041837	108.62
4^0	9000000	131.5	0.45838	0.009966	0.0036447	114.98
5^0	3000000	43.8	0.78772	0.019272	0.0077089	102.18
5^0	6000000	87.6	0.80490	0.017807	0.0070229	113.00
5^0	9000000	131.5	0.81369	0.017088	0.0068355	119.04
6^0	3000000	43.8	0.90470	0.021393	0.0085572	105.72
6^0	6000000	87.6	0.92632	0.019884	0.0079535	116.46
6^0	9000000	131.5	0.93658	0.019089	0.0076358	122.65
7^0	3000000	43.8	1.02227	0.024554	0.0098216	104.08
7^0	6000000	87.6	1.04667	0.023060	0.0092241	113.47
7^0	9000000	131.5	1.05839	0.022230	0.0089210	119.02
8^0	3000000	43.8	1.12848	0.027398	0.0109593	102.97
8^0	6000000	87.6	1.16384	0.02562	0.0102470	113.58
8^0	9000000	131.5	1.17842	0.024892	0.0099569	118.35

MAXIMUM C_l/C_D VALUES ARE OBSERVED AT ANGLE OF ATTACK=6 DEGREES

Combined effect of AOA and Wind velocity on Lift Coefficient at low Reynolds number and high Reynolds number

Figure 20 and figure 21 shows the Lift Coefficient at different angle of attack for wind velocities at low Reynolds number and high Reynolds number respectively. The following are the observations from them:

a) The lift coefficient is increasing as the angle of attack is increased.
b) The lift coefficient is increasing as the wind velocity is increased.
c) The difference in increase in lift coefficient is identical as the wind velocity increases and angle of attack increases.
d) The difference in increase in lift coefficient at AOA 4^o to 5^o is more compared to other successive AOA at high Reynolds number.

ISBN - 978-93-95038-50-8

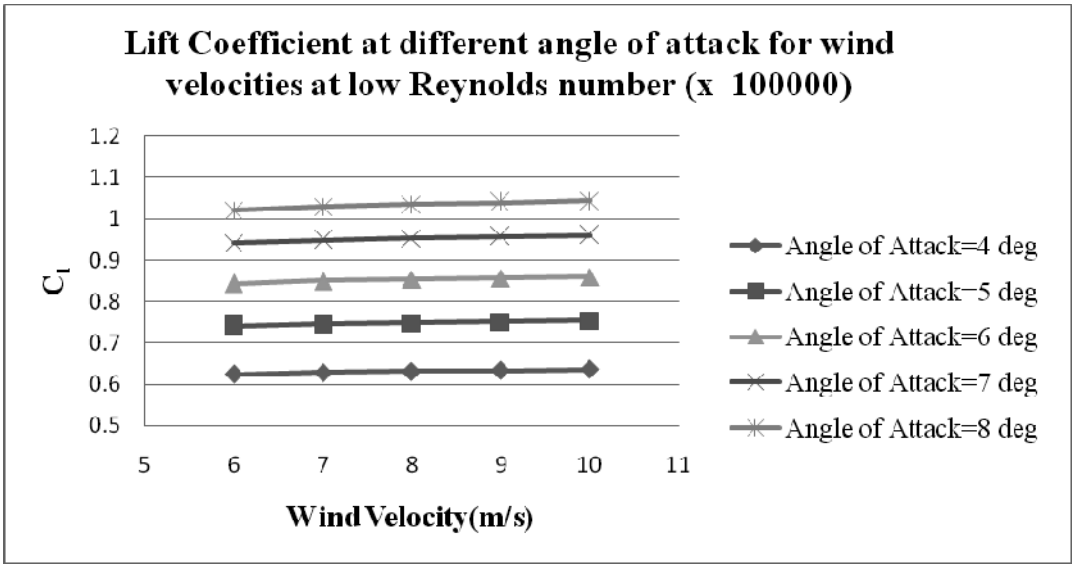

Figure 20: Lift Coefficient at different angle of attack for wind velocities at low Reynolds number (x100000)

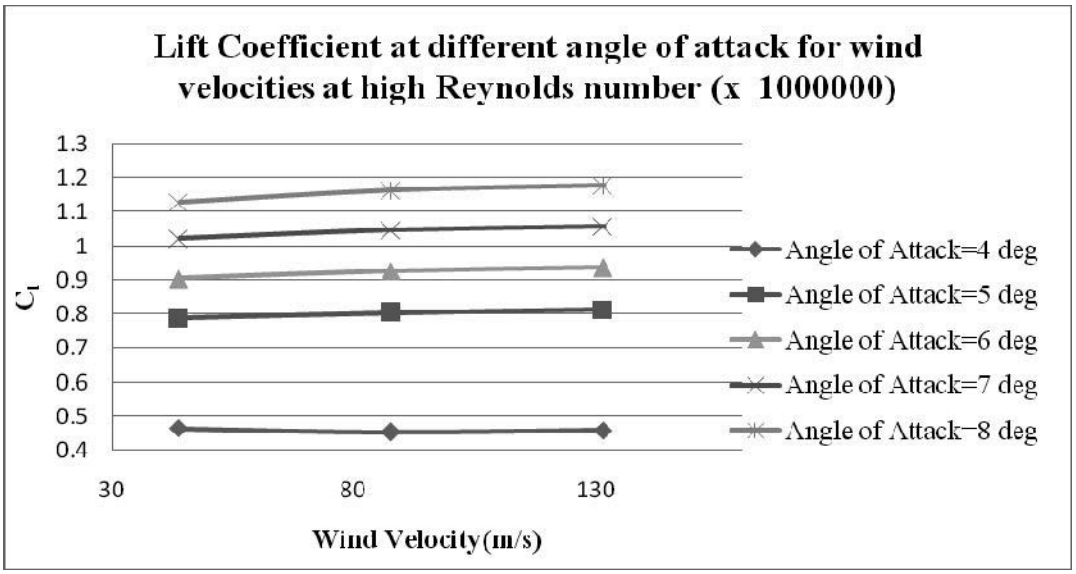

Figure 21: Lift Coefficient at different angle of attack for wind velocities at high Reynolds number (x1000000)

Combined effect of AOA and Wind velocity on Drag Coefficient at low Reynolds number and high Reynolds number

Figure 22 and figure 23 shows the Drag coefficient at different angle of attack for wind velocities at low Reynolds number and high Reynolds number respectively. The following are the observations from them:

a) The drag coefficient is increasing as the angle of attack is increased.
b) The drag coefficient is decreasing as the wind velocity is increased.
c) The difference in increase in drag coefficient at AOA 4^o to 5^o is more compared to other successive AOA at high Reynolds number.

ISBN - 978-93-95038-50-8

d) The difference in decrease in drag coefficient is identical as the wind velocity increases.
e) The difference in increase in drag coefficient is identical as the angle of attack increases.

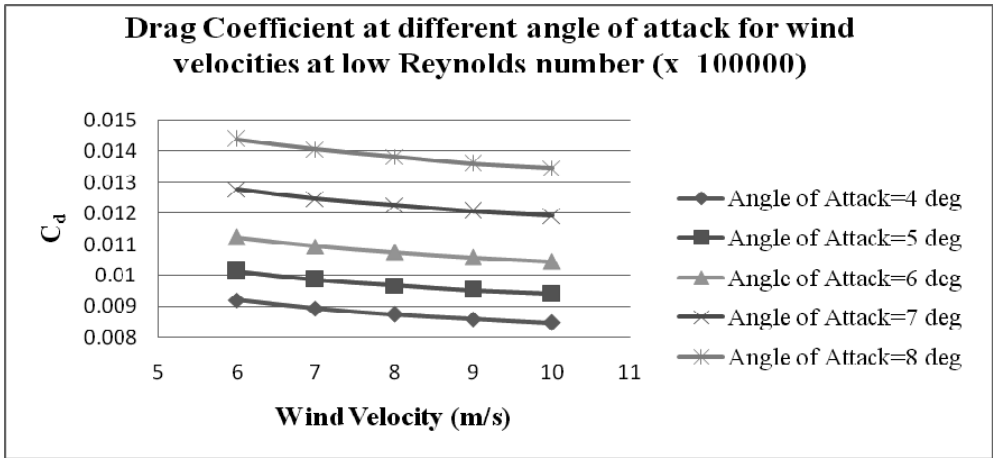

Figure 22: Drag Coefficient at different angle of attack for wind velocities at low Reynolds number (x100000)

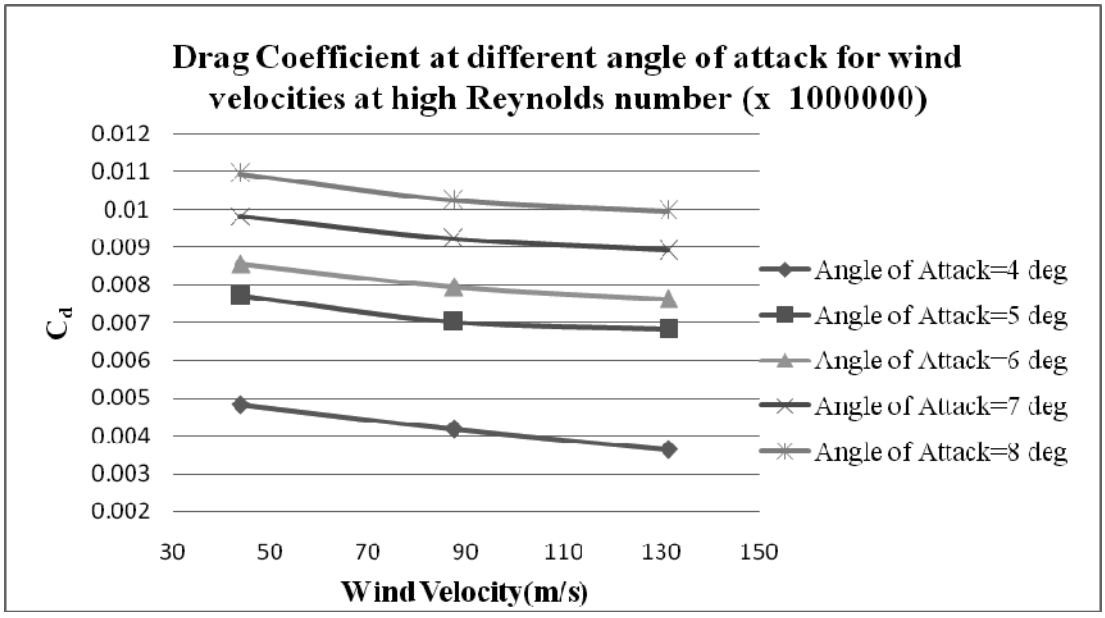

Figure 23: Drag Coefficient at different angle of attack for wind velocities at high Reynolds number (x1000000)

Combined effect of AOA and Wind velocity on Lift Coefficient to Drag Coefficient ratio (C_l/C_d) at low Reynolds number and high Reynolds number

Figure 24 and figure 25 shows the Lift coefficient to Drag coefficient ratio (C_l/C_d) at different angle of attack for wind velocities at low Reynolds number and high Reynolds number respectively. The following are the observations from them:

1. At angle of attack 4° to 8°, the lift coefficient to drag coefficient ratio (C_l/C_d) increases with increase in wind velocity.

2. The lift coefficient to drag coefficient ratio (C_l/C_d) increases with increase in angle of attack 4° to 6° and further decreases with increase in angle of attack.
3. At the angle of attack 6° the maximum C_l/C_d values are obtained at low Reynolds number and high Reynolds number.

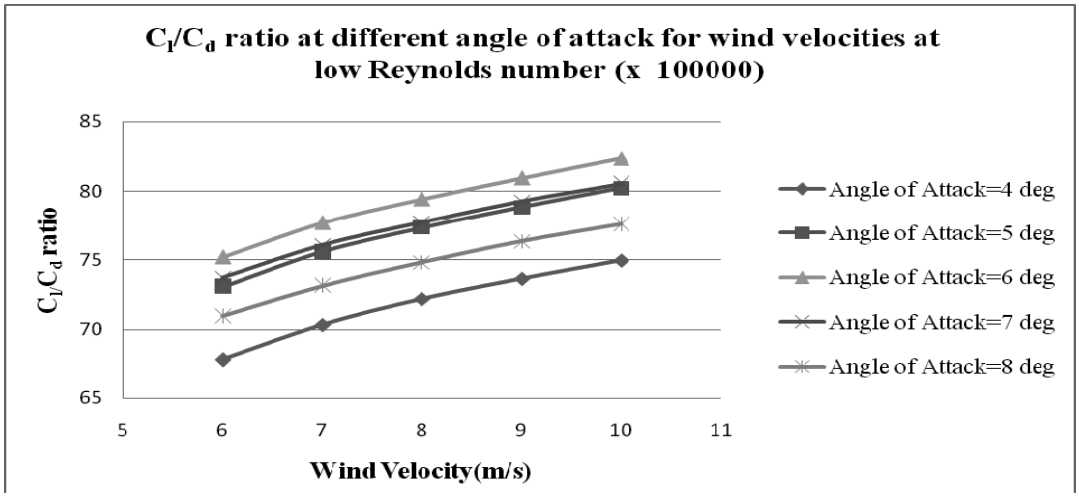

Figure 24: C_l/C_d ratio at different angle of attack for wind velocities at low Reynolds number ($x10^5$)

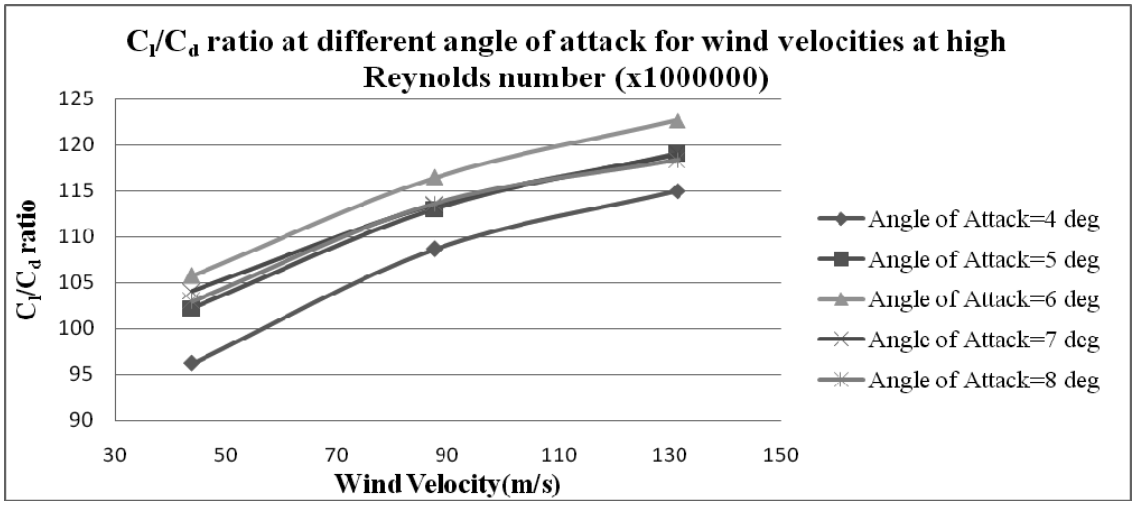

Figure 25: C_l/C_d ratio at different angle of attack for wind velocities at high Reynolds number ($x10^6$)

6. CONCLUSIONS

From the CFD results obtained, the following conclusions are made:

i. The increase in wind velocity increases the velocity of flow on the aerofoil.

ii. The increase in angle of attack 4° to 8° increases the velocity of flow on the aerofoil.

ISBN - 978-93-95038-50-8

iii. Coefficient of lift (C_l) and coefficient of drag (C_d) have increased with the increase in the angle of attack

iv. For angle of attack 4^o to 8^o,Coefficient of lift (C_l) has increased as the Reynolds number is increased.

v. For angle of attack 4^o to 8^o, Coefficient of drag (C_d) has decreased as the Reynolds number is increased.

vi. For angle of attack 4^o to 8^o, the percentage increase in ratio coefficient of lift to coefficient of drag (C_l/C_d) decreases from 3.5% to 1.5% with increase in low values of Reynolds number.

vii. For angle of attack 4^o to 8^o, the percentage increase in ratio coefficient of lift to coefficient of drag (C_l/C_d) decreases from 11.5% to 4% with increase in high values of Reynolds number.

viii. The ratio of lift coefficient to drag coefficient (C_l/C_d) has increased with increase in angle of attack in the range 4^o to 6^o and has decreased with increase in angle of attack beyond 6^o.

ix. For low Reynolds Number study, at angle of attack 6^o, the maximum value of C_l/C_d=82.38 is observed at 10 m/s.

x. For high Reynolds Number study, at angle of attack 6^o, the maximum value of C_l/C_d=122.65 is observed at 131.5 m/s.

REFERENCES

1. Abbott I.H., Von Doenhoff A.E., Stivers L., NACA Report No. 824 – Summary of Airfoil Data, National Advisory Committee for Aeronautics, p 175; 1945.
2. C.A. Baxevanoua, P.K. Chaviaropoulosb, S.G. Voutsinas c, N.S. Vlachosa; Evaluation study of a Navier–Stokes CFD aeroelastic model of wind turbine airfoils in classical flutter; Journal of Wind Engineering and Industrial Aerodynamics;2008.
3. GiridharRamanujam, HüseyinÖzdemir and H. W. M. Hoeijmakers; Improving Airfoil Drag Prediction; American Institute of Aeronautics and Astronautics, Inc.; 2016.
4. Liu, X., Lu, C., Liang, S., Godbole, A., & Chen, Y. "Vibration-induced aerodynamic loads on large horizontal axis wind turbine blades". Applied Energy, 185, pp 1109–1119. 2017.
5. MingweiGe, De Tianand Ying Deng; Reynolds Number Effect on the Optimization of a Wind Turbine Blade for Maximum Aerodynamic Efficiency; Journal of Energy Engineering; 2016.
6. Muhammad FaizanYounas, Awais Ali and Muhammad DaudShafique;"CFD Simulation of HAWT Blade and Implementation of BEM Theory"; Sukkur IBA Journal of Emerging Technologies; Vol 2 No 2; 2019.
7. P. K. Nigam, NitinTenguria and M. K. Pradhan; Verification of Sliding Ratio (Cl/Cd) of Airfoil through CFD Analysis; Journal of Scientific Research; Volume 64, Issue 1, 2020.
8. P.K.Nigam, NitinTenguria and M.K.Pradhan; Analysis of horizontal axis wind turbine blade using CFD; InternationalJournalofEngineering,ScienceandTechnology Vol.9,No.2,2017pp.46-60.
9. Sayed M.A, Kandil H.A, ShaltotA."Aerodynamic analysis of different wind-turbine-blade profiles using finite-volume method" Energy Conversion and Management, Vol. 64pp.541-550, 2012.
10. UmeshChaudhary; Sisir Kumar Nayak; "Micro and small-scale HAWT blades airfoils study through CFD for low wind applications"; Annual IEEE India Conference (INDICON);2015.

ISBN - 978-93-95038-50-8

Self-reliance in Salvo Launch of an Article

Ashish Kumar Gupta*

Defence Research and Development Laboratory (DRDL)
(DRDO)
Hyderabad, TS, 500005
E-mail: ashishkumar.drdl@gov.in

ABSTRACT

Defense-related operations such as firing of torpedo, underwater mines, and submarine-launched missiles and so on can be carried out from underwater platforms. This paper focuses on the activities when articles are launched from submersible platforms. In real-time scenario, after firing of an article, it is ensured that maximum damage is caused to adversary and that the operation must be finished in prerequisite duration and the mobile launcher should flee from that area in a short period. It details the factors that are considered while implementing the schemes for salvo launch in terms of fault tolerance, automated sequences, system modular design and various communication protocols. This system has been successfully implemented and tested for warfare activities.

Keywords: *automated sequence, fault tolerance, salvo launch, underwater platforms*

1. INTRODUCTION

In recent years, there have been significant and ongoing technical advancements that have, in some cases, drastically altered our way of life. The noteworthy thing about the current technological boom is that, in contrast to what happened following World Wars I and II, most advancements came from the non-military sector. Due to the possibility of rogue states and non-state actors to acquire capabilities that might asymmetrically influence the nature of conventional combat, such technological breakthroughs have also led to an extremely complicated strategic environment. For undertaking research, commercial, and naval operations, frequently in hostile and dangerous locations, submersible platforms [1] transporting objects are frequently utilised. In order to enable the successful accomplishment of its job, articles that are launched actually need to have a particular level of fault tolerance built into them. Every technique employed to boost this level of fault tolerance will expand the article's range of operational capabilities. As control engineering technology develops, the operating requirements for commercial, naval, and scientific underwater vehicles become more difficult.

Such vehicles must be equipped with a fault-tolerant or reconfigurable control system in order to survive actuator or sensor failure during a mission. Articles launched in salvo from underwater vehicles involves lot of safety issues which have to be taken care in the development phase itself. As the design and development of an article is a complex task, it requires expertise in almost all phases of engineering, from conception to finally launch stage. While designing and implementing the salvo launch of an article some major aspects that needs to be considered are fault tolerance, timing cyclogram, automated sequence and transfer alignment. This paper covers a brief design and analysis aspects of salvo launch of an article for modern warfare.

* Corresponding author: E-mail: ashishkumar.drdl@gov.in

2. SYSTEM DESCRIPTION

With advances in technology, there has been rising demands to launch an article in salvo mode. Successful launch involves various factors, of which the prime importance is preparation of article in smaller time duration and minimum human intervention. The preparation is carried out in various phases in a systematic phase manner before launch [2]. As a case study Figure 1 below shows the basic block diagram of a system in salvo launch. This paper considers two weapons during salvo launch. System consists of two main consoles which is responsible for controlling all the subsystems following it in conjunction with remote controller.

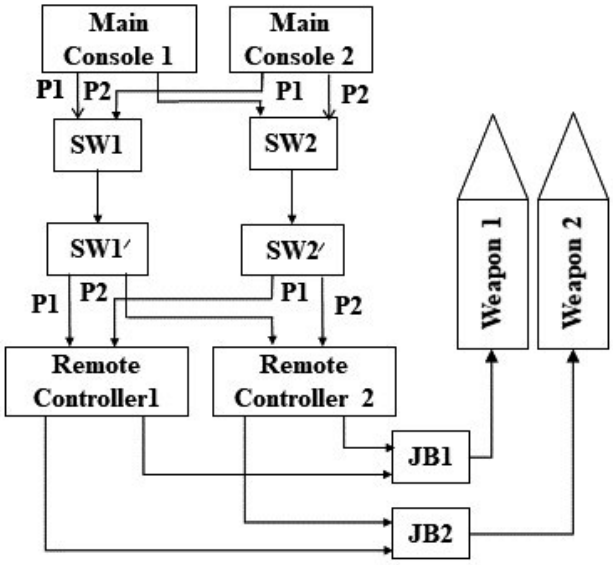

Figure:1 Block diagram of a system in salvo launch

In order to increase the reliability of the system fault tolerance is introduced in the main console and remote controller of the system. Cross connection is made via switches to check for and ensure against any system link failure. It is here whose health check and preliminary data exchange takes place. Provision is made for standby system to take up in case any failure occurs in main system. Redundancy elements have been added across all of the subsystems to account for the space constraints and to improve the whole power management [3] system's reliability and availability.

Subsystem redundancy has improved the power management system's ability to withstand faults. the arrangement of the entire system in a serial-parallel combination. A setup like that ensures the system won't operate with a single point of failure. All of the controls are GUI-based, and in addition to all primary displays, they also show the current drawn by each piece of equipment. The operator can watch both guns' operations via GUI displays prior to ultimate launch.

3. DESIGN CONSIDERATION

Provisions are made to launch the articles either in manual mode or in automated mode. Sequence of operations and launching of articles are predefined. It is ensured that the system has a series of automated phase sequences. It is necessary because for two articles in salvo

ISBN - 978-93-95038-50-8

launch, time scheduling is very important. Proper time delays [4][5] between the articles is ensured which should be free from any manual interventions. Operator sitting at the console has the provision to launch the second article or exit for the ongoing activities.

Fault tolerance [6] is introduced in the system in from of redundancy. Fault-tolerance as a crucial architectural feature of any systems has experienced substantial improvement over the past ten years in both understanding and application. A different approach to the fault problem is provided by fault-tolerance [6], in which the system's internal components handle fault detection and returning it to normal operation. The special quality of a digital system known as fault tolerance allows it to continue operating as a logic machine according to the program's specified behaviour even in the presence of defects. Because fault-goal tolerance's is to bring an error state back to the desired behaviour, ensuring the survival of information processing operations, it is possible to describe fault-tolerance as the logic machine's survival attribute. To reduce the danger of single point failure, fault tolerance is added to the system. Throughput and reaction times are unaffected, and the system does not experience any further changes [7]. Fault tolerance system use redundancy in both main system and subsystem. These systems continuously share the health and data information.

For people who depend on or utilise computers, fault tolerance provides important psychological support. The knowledge that fault-tolerance is being used will probably lessen the anxiety that exists when it is known that the very first component failure will be fatal [8] to the uninterrupted operation of the entire machine, even if the probability of such failure is very low. This is especially true when the failure of a system could endanger a person's safety or financial well-being.

A systematic series of design actions that includes explicitly stating the sorts of defects that are to be tolerated introduces fault-tolerance into the system architecture. Quantitative reliability goals are then set, and after that, a detailed evaluation of the dependability that the system has really reached is assumed. The purpose of recovery algorithms [9] is to restore the system to some level of normal operation or to securely shut it down. They are triggered by signals from fault detection algorithms.

Following the discovery of the defect, recovery refers to all steps that are taken. These might involve fixing errors, finding faults, excluding or changing out failed components, documenting what was done, restarting regular operation, or carrying out a safe shutdown. The failure of the system is caused by recovery algorithms that are unable to fulfil their task. Redesigning control sequences, adding spare processors or bus components, increasing storage capacity, and other changes to the original architecture may be necessary to accommodate the addition of recovery. With the use of analytical modelling, simulation, or a mix of the two, the fault-tolerance of a design is evaluated [11]. It is done to improve the design.

4. EMERGENCY PROCEDURES DURING LAUNCH

Despite the efforts made to prevent failures, numerous systems have experienced faults while in operation. Because of this, most systems incorporate emergency procedures to identify error states that could be caused by design flaws, record them, and get the system to a place where external help could be requested to finish the analysis and restart operation. Although certain fault-tolerance approaches for physical defects are comparable to these emergency procedures, the function that is achieved is just the shutdown of all or a portion of the system.

ISBN - 978-93-95038-50-8

The entire set of hardware, software, and repetition (time) approaches that produce the initial fault signal are used to implement fault detection. Below is a useful breakdown of all these techniques based on when they were used in relation to the system's regular operation.

- Initial testing, which is done before regular usage and is used to spot defective hardware parts that may have flaws introduced during the manufacturing or assembly procedures.
- Concurrent (on-line) detection, which occurs in tandem with regular system operation.
- Scheduled (off-line) detection, which occurs when routine operation is momentarily halted.
- Redundancy testing, which is performed concurrently or at predetermined intervals and checks to see if the different defensive redundancies are fault-free in and of themselves.

5. TIMING CYCLOGRAM

To ensure timing cyclogram in salvo launch, both linear and parallel methods can be used, each with its own advantages and disadvantages. If the articles are launched in a linear manner, then it may cause delays in combat mode of operation which is not desirable in practical real time scenario. It is preferred to opt for parallel approach for operating the articles as it is less time consuming and also acknowledges the fault at the initial stage of launch. However, it makes the checkout system activities complex in nature.

6. CONTROL AND GUIDANCE

For control and guidance, Initial Navigation System is precisely initialized prior to start of any operation. For controlling the power to the article subsystems and firing of pyros, reliability is ensured in the electrical schemes designed for article onboard and also on ground checkout system. Space optimization, redundancy and isolation among articles is ensured at the designing phase itself, GUI is made for proper identification of the weapons either in one screen or split in different pages. Both analog and digital parameters are also provided as displays on console.

7. TESTING OF ARTICLE

The system is tested for functional test, subsystem test, integrated test, phase checks, power consumption test, and failure mode test after design implementation. Software is developed using real time operating system VxWorks. GUI is implemented using Zinc Application framework on C++ language. Individual subsystems are tested using simulator. All protocol level validation is done and communication link failure is also tested in advance. During system level testing, actual system is tested with simulated articles instead of actuals. All ground and operational parameters are monitored and discrepancies if any is observed and tabulated. Electrical phase checks of the article are carried out in phases at subsystem and integrated levels. It is mandatory to carry out these checks before any launch operation activities.

ISBN - 978-93-95038-50-8

8. CONCLUSION

This paper covers in brief the design aspects and analysis of salvo launch of an article which is useful for present scenario where power and safety is of prime concern. Factors which influence the performance of the system during article preparation and launch is thoroughly verified valuated by suitable nominated committees before operating it in real-time scenario. Such study is not just confined to underwater circumstances; it may also be extended to ground-based systems.

REFERENCES

1. Kumar A, Anjaneyulu L. Design and development of power management system of unmanned underwater platform for defence application. Defence Science Journal. 2017;67(1):119.
2. Kumar A, Anjaneyulu L. Design and Development of Redeployable Underwater Data Communication Link for Defence Application. Defence Science Journal. 2018 Jan 1;68(1).
3. Kumar A, Anjaneyulu L. Emerging Trends in Instrumentation in Rocket Motor Testing Over Three Decades. Defence Science Journal. 2015 Jan 1;65(1).
4. Kumar A, Anjaneyulu L. Data Analysis and Validation of Acquired Temperature Data on Underwater Platform. Defence Science Journal. 2018 Nov 1;68(6):597-603.
5. Zhang X, Yu Y. Experimental and numerical research on a novel underwater launching method with high efficiency and low resistance. AIP Advances. 2021 Feb 1;11(2):025212.
6. Wang X. Active fault tolerant control for unmanned underwater vehicle with actuator fault and guaranteed transient performance. IEEE Transactions on Intelligent Vehicles. 2020 Nov 17;6(3):470-9.
7. Xu X, Wei Z, Ren Z, Li S. Fault-tolerant time-varying formation tracking for second-order multi-agent systems subjected to directed topologies and actuator failures with application to cruise missiles. InProceedings of 2018 Chinese Intelligent Systems Conference 2019 (pp. 845-861). Springer, Singapore.
8. Ma X, Dai K, Li M, Yu H, Shang W, Ding L, Zhang H, Wang X. Optimal-Damage-Effectiveness Cooperative-Control Strategy for the Pursuit–Evasion Problem with Multiple Guided Missiles. Sensors. 2022 Nov 30;22(23):9342.
9. Mazare M, Taghizadeh M, Ghaf-Ghanbari P. Pitch actuator fault-tolerant control of wind turbines based on time delay control and disturbance observer. Ocean Engineering. 2021 Oct 15;238:109724.
10. Yibo DI, Xiaokui YU, Guangshan CH, Jiashun SI. Review of control and guidance technology on hypersonic vehicle. Chinese Journal of Aeronautics. 2022 Jul 1;35(7):1-8.
11. Nan H, Zhi-Hua C, Zheng-Lun W. Main Characteristics of Underwater Supersonic Gas Jet Flows. Mathematical Problems in Engineering. 2022 May 31;2022.

ISBN - 978-93-95038-50-8

Experimental Investigation on the Interaction of Supersonic Plume with Launch Pad Structure

B.N.V Sai Aditya*, M. Deepthi, G. Venkatesh, T. Srinivas Reddy, S. Sankaran

Test Facilities, SMP&ETF, SDSC SHAR
Indian Space Research Organization
Sriharikota, Andhra Pradesh, 524121

ABSTRACT

With the advent of increased launch frequency, ISRO is planning to meet the demand by augmenting the existing launch pad at Sriharikota using an innovative scheme of launch vehicle integration and transfer sequence. Under this project, the integrated launch vehicle will be transferred on Mobile Launch Pedestal (MLP) from the integration facility to the First launch pad on a rail track. This rail track will cross the Jet Deflector Duct (JDD) with a rail track span of 7.5m. The rail track will be supported on the girder, which will be subjected to severe thermal environment generated due to the interaction of hot supersonic jet from C-D nozzle with a 9 ^{0}cant angle, through the launch pedestal cut-out during launch vehicle lift-off. In order to design the rail track girder beam, cold and launch pad measurements are initiated to study this thermal & flow related problem and map the extent of interaction of hot supersonic jet on the launch pad structure, simulating the rail beam structure. Pressure, temperature, heat flux and flow visualization results are presented and discussed in this paper. From the flow visualization results and launch pad measurements it is understood that there is no direct impingement of supersonic jet on the launch pad structure, resulting in a benign condition of flow parameters.

Keywords: *Supersonic jet interaction; cold flow, launch pad measurements, surface flow visualization, fluid & thermal environment, launch vehicle lift-of simulation.*

1. INTRODUCTION

Studies were initiated to characteristics the pressure and thermal loads on the proposed girder beam through scaled down cold & hot flow studies. Cold flow studies are carried out using GN2 as surrogate gas and hot flow studies with scaled solid rocket motor, simulating the actual strap-on vehicle both geometrically and thermo-physically. Actual launch pad lift-off environment is simulated during the experiments and lift-off trajectory is maintained by increasing the nozzle exit distance from the initial lift-off condition. Figure 1 shows the typical configuration of study. The MLP with girder column was realized and the supersonic plume interaction with newly proposed girder was studied using surface flow visualization technique for various lift-off heights during cold flow experiments.

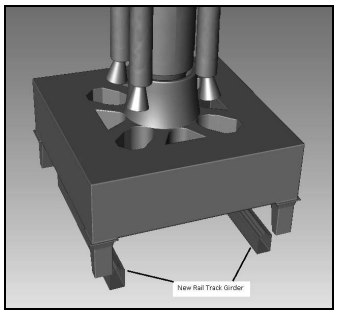

Figure 1: Proposed New Rail Track girder within the launch pedestal and its interaction with strap-on supersonic jet

*Corresponding Author: Email: adityaburle@shar.gov.in

2. EXPERIMENTAL METHODOLOGY

As discussed earlier, the supersonic plume issuing out of strap-on jet of the launch vehicle might interact with the newly prosed rail track girder, which is within the span of the MLP compared to the old track bema which is far away from the hot plume. To investigate this problem cold and hot flow model tests are carried out and are reported in this paper.

2.1. COLD FLOW EXPERIMENTS

The cold flow experiments are carried out using one strap-on jet plume issuing out of C-D nozzle with GN2 as surrogate gas with 1:32 scale. The rail beam girder and the MLP top surface and the cut-out hole were uniformly coated with Titanium dioxide and olive oil in proper suitable mixture to find the shear layer interaction of the jet with the beam. The distance from the nozzle is varied from then initial stand-off distance by a nozzle exit diameter (De as non-dimensional parameter) to simulate the vehicle trajectory to a certain height. In cold flow experiments, the chamber pressure is set as 24.6 bar for compensating the change in the specific heat ratio (γ) between actual hot & cold flow cases as mentioned in Table.1. The flow visualization setup is shown in Figs.2 & 3 below.

Table 1: Simulation Parameters

Parameter	1:1 Strap-on Jet	Cold Flow (1:32)
Chamber Pressure (bar)	36.5	24.6
Nozzle exit pressure (bar)	0.66	0.66
Mach number	3.08	3.08
Mass Flow rate (kg/s)	252.16	0.49
Area ratio (Ae/At)	7.56	4.65
Nozzle Exit Dia. (mm)	982	30.83
Nozzle Throat Dia.	357	14.28
Specific heat ratio (γ =Cp/Cv)	1.2	1.4

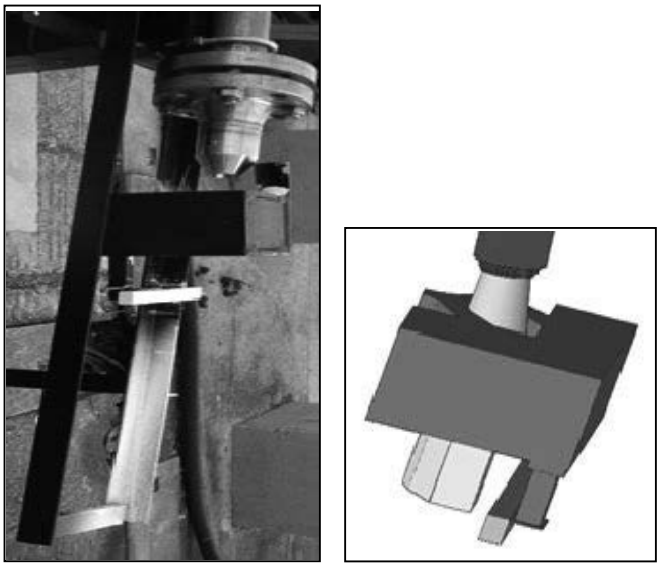

Figure 2: Cold Flow Experimental Set-up for Flow Visualization

ISBN - 978-93-95038-50-8

The cold flow visualization experiments are conducted at various L/De cases (L is the any lift off height and De is the nozzle exit diameter) and the results for specific cases are only presented due to brevity of space in Fig.3. From the cold flow tests, it is observed that no plume impingement is seen on the newly proposed girder at lower lift-off; however, as the L/De increases, the supersonic jet spills over the MLP top and a very weak interaction of plume with Girder is observed as shown in Fig.3. This preliminary study clearly shows that the strap-on supersonic plume is not impinging on the newly proposed rail girder beam. For further confirmation, hot flow tests are planned.

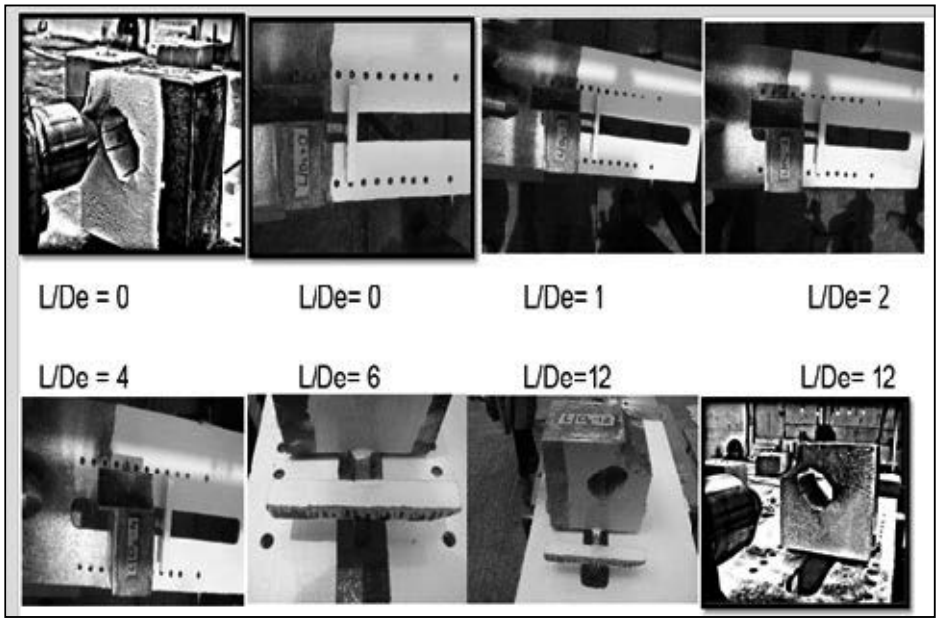

Figure 3: Cold Flow Visualization at various Lift-off Heights

These flow visualization results have given an insight on the probable sensors measurement range required for measuring the heat flux, temperature and pressure on the proposed girder.

2.2. LAUNCH PAD MEASUREMENTS

Launch pad measurements were carried out during the lift-off PSLV launch vehicle. Structure simulating the newly proposed Girder is erected and measurement provisions were made to measure pressure, heat flux and temperature along the length of the girder and depth of the girder. Location plan showing the sensors mounted on the launch pad is shown in Fig. 4 and Fig.5.

Expected depth of the girder is 750mm, hence a vertical member of 900mm is drawn from the launch pedestal simulating the depth of the girder. Level 0 corresponds to the ground level and level 900 corresponds to 900mm below ground level.

An interconnecting member simulating the length of the girder is realized at an elevation of 750mm below ground level simulating the bottom portion of the girder. Temperature measured during the lift-off is shown in Fig.6. Table 2, shows the peak temperature measured at each measurement location.

ISBN - 978-93-95038-50-8

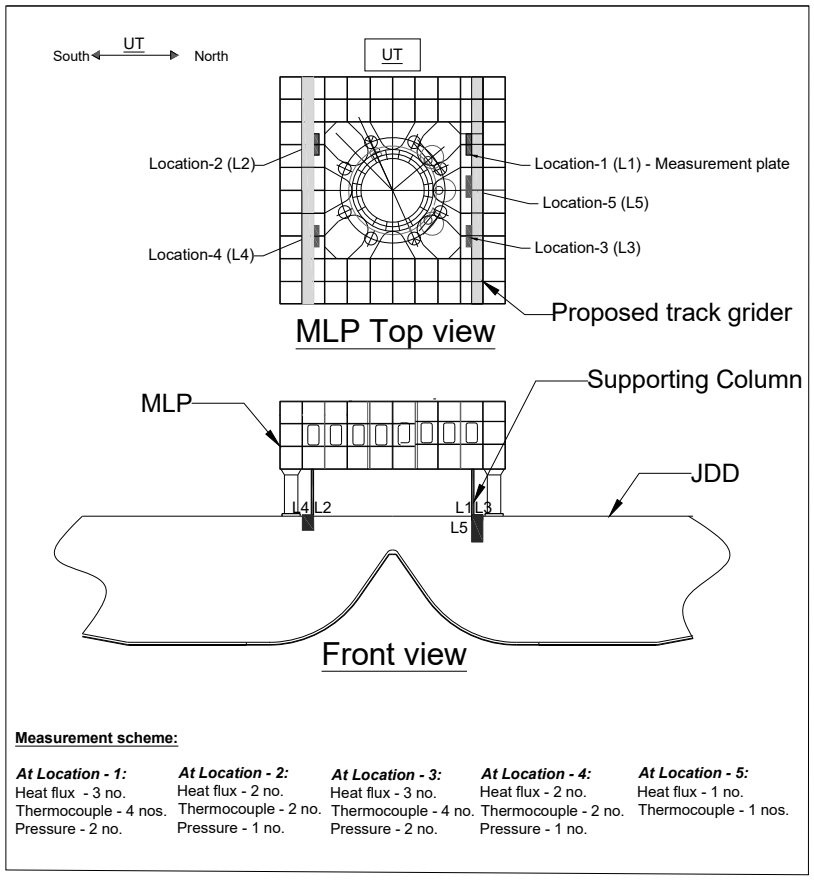

Figure 4: Sensor locations in the launch pad.

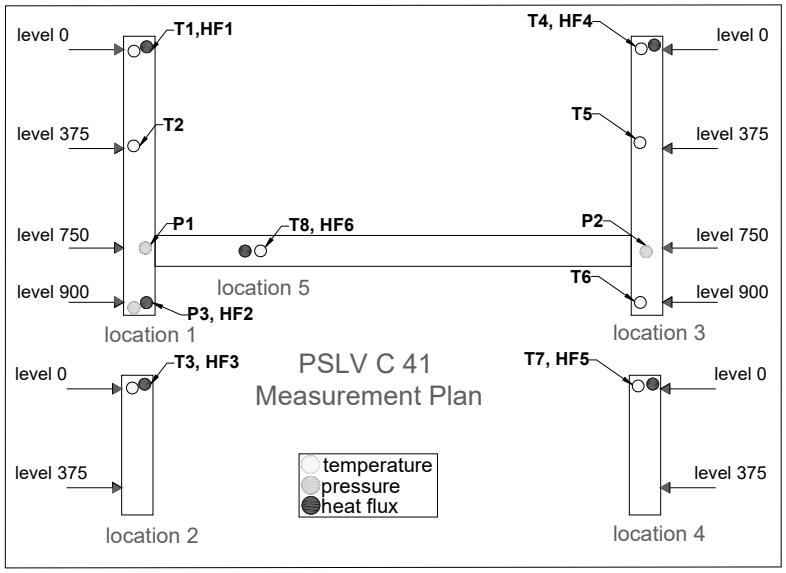

Figure 5: Sensor notations at each location of measurement

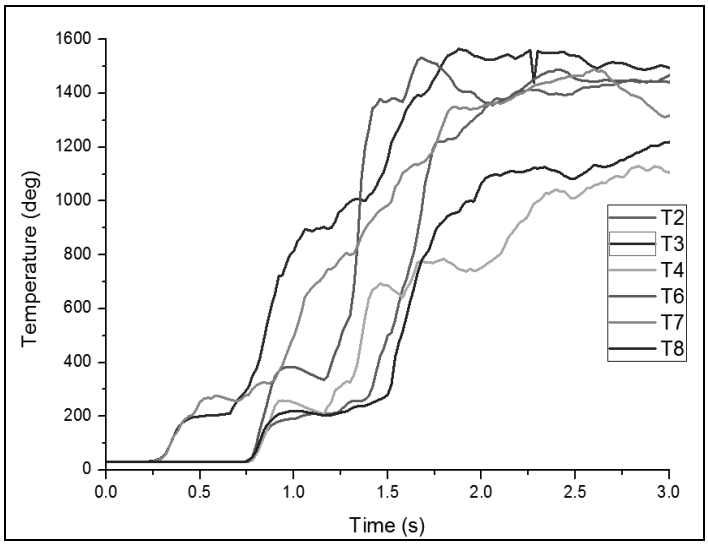

Figure 6: Temperature measured at each location

Table 2: Peak temperatures at each location

Peak temperatures values in T1 to T8 during PSLV lift-off		
Sl.no	**Location**	**Temperature – C^0**
T1	L1(level 0)	1097
T2	L1(level 375)	1447
T3	L2(level 0)	1560
T4	L3(level 0)	1229
T5	L3(level 375)	1052
T6	L3(level 900)	1530
T7	L4(level 0)	1489
T8	L5(level 750)	1222

Sensors at location T1 and T5 got saturated with in T+2seconds and are not shown in Fig.6. Similarly, peak heat flux and peak pressures measured are shown in Table 3 and Table 4.

Table 3: Peak temperatures at each location

Peak Heat Flux values in HF1 to HF8 during PSLV lift-off		
Sl.no	**Location**	**HF (W/cm^2)**
HF1	L1(level 0)	64
HF2	L1(level 900)	132
HF3	L2(level 0)	92
HF4	L3(level 0)	77
HF5	L4(level 0)	68
HF6	L5(level 750)	126

ISBN - 978-93-95038-50-8

Table 4: Peak Pressures measured at various location

Peak pressure values in P1 to P3 during PSLV C41 lift-off		
Sl.no	**Location**	**Pressure**
P1	L1(level 750)	27.9 mbar
P2	L3(level 750)	35.11 mbar
P3	L1(level 900)	19.56 mbar

5. Results and Discussions

From the cold flow experimental results, it was evident that the supersonic jet from the nozzle is not impinging on the proposed girder. From the flow visualization results, launch pad instrumentation was carried out by choosing appropriate sensors. Range of sensors was determined from the experience gained in cold flow results. Since the cold flow tests have shown that there is no direct impingement of jet on the girder, Mild Steel structure with adequate thermal protection has been designed to erect in the launch pad experiencing the thermal and jet loads during launch vehicle lift-off.

From the launch pad data, it was further evident that there is no jet impingement and the peak temperature is in the order of 1560degC. Peak heat flux is 132 W/cm2 which was measured at the lowest elevation indicating that jet interaction increases as we go deeper in to the jet deflector duct. Peak pressure measured on the girder was 35.11mbar which is again implying that there is no direct jet impingement.

6. Conclusions

Cold flow scale model experiments simulating the launch vehicle lift-off scenario and launch pad measurements were carried out in order to investigate the possible interaction of supersonic jet issued from the strap-on booster with the newly proposed rail girder beam of launch pad structure. 1:32 scale cold flow surface flow visualization technique using Titanium Dioxide powder mixed with Olive oil is used to capture the flow interaction and from the results, it is observed that no jet impingement is seen on the girder structure during lift-off; however, a slight interaction is seen at higher L/De. Further investigation using launch pad measurements helped in arriving the thermal environment on the proposed girder during PSLV lift-off. Results indicate the that the peak temperature is about 1560degC, heat flux is about 132W/cm2 and the pressure is 35.11mbar. These results conclude that proposed girder can be realized and used since hot supersonic jet from the PS0-XL jet is not impinging on the girder and creating a huge thermal load. However, adequate thermal protection scheme shall be designed to minimize the potential damage created to the girder enabling to use it for multiple launches with minimum re-work.

Acknowledgements

Authors acknowledge the support rendered by the top management of SDSC SHAR ISRO Sriharikota in conducting this work.

REFERENCES

1. Thermal Modeling of the Shuttle Solid Rocket Motors on the Launch Pad E. Mathias, R. Ahmad and H. Huppi Morton Thiokol Inc. Brigham City, UT, AlAA 89-2873
2. Design handbook for protection of launch complexes from solid propellant exhaust, march1966, NASA CR-66-11
3. Atlas II Scale Model Flame Bucket Test T. Stoer and C. Webb, General Dynamics Space Systems, San Diego, CA, AIAA-91-2168
4. Rocket Plume Impingement Heat Transfer on Plane Surfaces E. Mayer and R. Prickett, Hughes Aircraft Co., Space and Communications Group, El Segundo, CA, AIAA-86-1321
5. Launch deflector design criteria and their application to the Saturn c-1 deflector by R. L. Evans and L. Sparks George C. Marshall. Space Flight Center Huntsville, Alabama, NASA D-1275
6. Investigating Separated Shear Layers for Passive Jet Blast Deflector Cooling, Steven A. Tangen, University of Virginia, Charlottesville, VA,22904, AIAA 2006-144.
7. CFD Simulations of Launch Environments for Delta IV Vehicles at the SLC-6 Launch Pad Ari J. Majamaki and JinWook Lee the Aerospace Corporation, El Segundo, CA, 90245-4691 AIAA 2011-1236
8. Flow Field Analysis of Jet Impinging on an Inclined Flat Plate at High Plate Angles, Masato Ito, Aoyama Gakuin University, Sagamihara, Kanagawa, 229-0006, Japan.
9. Akira Oyama and Kozo Fujii, JAXA/ISAS, Sagamihara, Kanagawa, 229-8510, Japanand A. Koichi Hayashi Aoyama Gakuin University, Sagamihara, Kanagawa, 229-0006, Japan, AIAA 2004
10. The impingement of underexpanded, axisymmetric jets on perpendicular and inclined flat plates by P. J. LAM0NT AND B. L. HUNT Department of Aeronautical Engineering, University of Bristol, England, J. Fluid Mech. (1980), Vol. 100, part 3, pp. 471-611.

ISBN - 978-93-95038-50-8

Characterization of a Pressurized Convoluted Metallic Flexible Hose under Large Bending Angles for Systems Engineering of High Pressure Swiveling Thruster

B Kartik Surendra*, Sourabh Karmarkar, B Suresh Babu, Reji Joseph, Jagannathan S

Liquid Propulsion Systems Centre
Indian Space Research Organization
Thiruvananthapuram, Kerala, 695547

ABSTRACT

Metallic flexible hoses with convolutions and wire braiding are used for various of applications in the aerospace systems. One such application is for carrying a high temperature, high pressure gas for a roll control system of a core liquid stage of a launch vehicle. In this application, the flexible hose connects a fixed hot gas inlet rigid line to a swiveling thruster. The flexible hose undergoes bending in a single plane about an axis perpendicular to its length and located in between the two ends. The estimation of torque required to bend the pressurized flexible hose is needed for finalizing the design specifications of the torque motor used for swiveling the thruster. As the flexible hose is fabricated by mechanical/hydroforming process which induces plastic strain and the uncertainties associated with braiding stiffness makes accurate analytical modeling difficult. An experimental approach is adopted in this study for estimating the bending torques required for different bend angles with a specifically engineered unconventional and unique experimental set up. This study presents the results of bending tests performed on a convoluted metallic flexible hose with an internal pressure of 50 bar and assembled under stretched and un-stretched conditions for different offset distances from one of the ends. The roll thruster swivels by an angle of $\pm 50^{o}$, which subjects the flexible hose to relatively large bending angles. A nonlinear variation of bending torque with bending angle was observed in this study. When the flexible hose is assembled in an un-stretched condition, a snapping behavior is observed during bending, in which the curvature developed in one direction suddenly shifts to the other side. A significant reduction in the snapping behavior was observed upon assembly in a stretched condition. The maximum torque required for bending the flexible hose to the desired swivel angle is estimated for different configurations of the experimental setup. Torque estimated from the testsis used for selecting the torque motor and for detailed systems engineering of the roll control system.

Keywords: *Convoluted Metallic Flexible Hose, Systems Engineering, Roll Control System*

1. INTRODUCTION

Attitude control systems are an essential part of any launch vehicle, which create necessary moments as per vehicle guidance command. Roll control of a launch vehicle can be achieved via different methods depending on the configuration of stage. Here, a hot gas based roll control system is used for liquid stage of a satellite launch vehicle.

The system consists of two roll control thrusters positioned diametrically opposite and each thruster is swiveled upto 60^{o} in vertical plane to generate control force and moments.Figure 1(a) shows the configuration of the system under discussion. Hot gas for the roll control system is tapped from engine. A piping consisting of a metallic flexible hose and rigid lines transports the hot gas from engine to the fixed end of the thruster-side metallic flexible hose. The thruster-side flexible hose carries the hot gas to the swiveling thruster.

The thruster-side metallic flexible hose has a total length of 1.26 m. The swiveling axis is perpendicular to the length of the flexible hose and is located at a distance of L_2 (flexible region length) from the swiveling end. Figure 1(b) shows the swiveled configuration of the flexible hose. This distance L_2 has been referred to as the offset distance from here on. The

*Corresponding Author: E-mail: ksbilolikar@gmail.com

ISBN - 978-93-95038-50-8 https://doi.org/10.37285/bsp.sasat2023.16

hot gas in the flexible hose is under a pressure of around 50 bar and a temperature above600 K. An estimate of the maximum torque required for bending the flexible hose to the desired swivel angle is needed for the of the torque motor used for swiveling the thruster. Further, the extent of variation of bending torque with bending angle and with offset distance (L_2) is also of interest from the torque motor control perspective. These parameters are necessary to derive the design specification of torque motor.

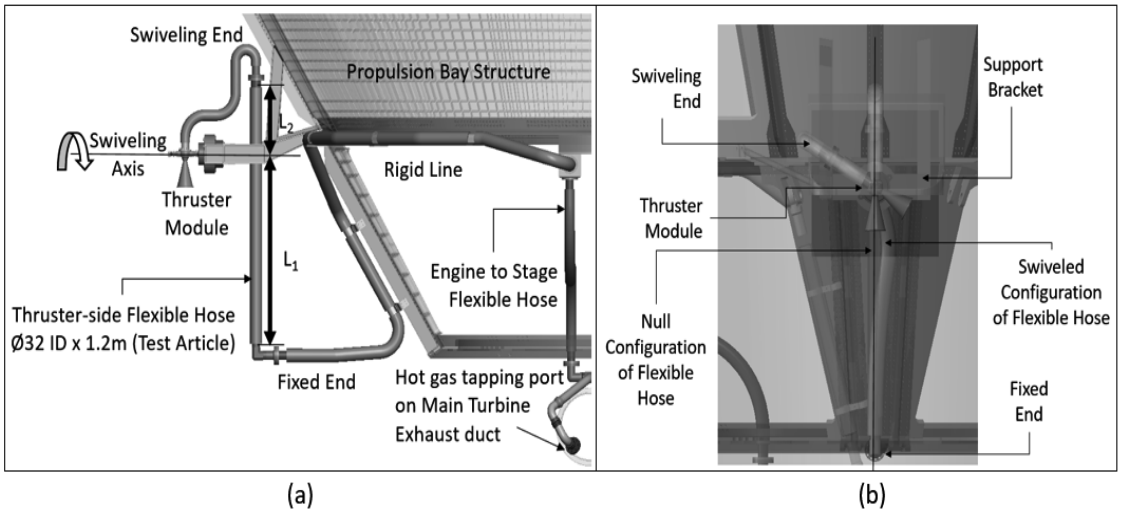

Figure 1: System Configuration

Figure 2 shows the prototype of theconvoluted metallic flexible hose made with SS321 and SS wire branding. The flexiblehose is fabricated by hydro or mechanical forming of SS304L sheets. Multiple braids of SS wiresare wrapped around the convoluted hose to provide axial strength against internal pressure. Deformation of convoluted portion under lateral loads imparts flexing action to the flexible hose assembly. The bending stiffness or in other words the torque required to bend the flexible hose depends on assembly configuration, offset distance L_2, and internal pressure.

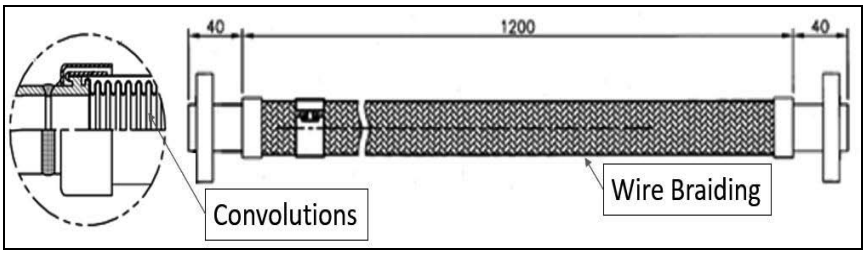

Figure 2: Convoluted Metallic Flexible Hose with Wire Braiding

Analytical estimation of bending torque requires mathematically modeling the kinematic and dynamic behavior of hose using finite element analysis techniques. Tsukimori in [1] presents a simplified theoretical modeling of creep behavior of bellows. Further, Tsukimori in [1] verifiestheoretical results with the analysis results obtained by FEM.Bechtin [2]provides a history of the development of bellows analysis methods and discusses directions requiring further development. Fatigue testing of bellows has been discussed by

ISBN - 978-93-95038-50-8

Kobatake et al. in [3]. Kobatake et al. in [3] confirmed the applicability of an empirical equation for estimatingthe fatigue life from their analysis. Failure tests and finite element analysis (FEA) of the bellows structure were performed by Ando et al. in [4]. Ando et al.in [4] conclude that it is difficult to calculate final bellow structure shapes obtained in tests by implicit analysis. Sharma &Obaid in [6] present the FEM study on metal expansion bellows under axial and transverse loads. With the help of this analysis,the study confirms the safety of the design under applied loading. Anderson in [7] presents charts for simplified calculations for designing convoluted bellows.

Huang & Zhang in [5] discuss simulations and experimental studies on axial stiffness of the braided corrugated hose. The study finds good agreement between experimental data and simulations. This study can be used as a reference for modeling the braided corrugated hose. Paramasivan in [8] discusses the modeling of steel reinforced rubber flexible hoses. The study mainly focuses on modeling of helically wounded reinforcements. The estimation of bending stiffness through analytical approaches requires defining the material properties. A metallic flexible hose is fabricated by mechanical/hydroforming process, which induces plastic strain.

Hence, it is required to estimate the properties through coupon level testing of convoluted sections. The non-linearity in material property due to plastic behavior poses challenges in modelling the dynamics of flexible hose using FE analysis.

Further, the braiding on the convoluted part controls the axial strength of the hose. The braiding process being sensitive to workmanship and procedure followed, can lead to uncertainties in the initial condition (under equilibrium) of the hose.The FE model must account for the parameters like slackness of braiding and initial profile of convolution, which cannot be quantified and modeled precisely. Hence, the uncertainties associated with manufacturingprocess incur gross approximations in analytical modeling of the convoluted metallic flexible hose.Considering these factors, an experimental approach is adopted in this study for estimating the bending torques required for different bend angles. A specific, unconventional, and unique experimental setup has also been engineered for this purpose. Next, the configuration of experimental setup is briefly explained, followed by assembly of the flexible hose in different conditions, effect of offset distance from swiveling axis, and the effect of internal pressure on maximum bending torque.

2. EXPERIMENTAL SETUP

Figure 3 shows the configuration of test fixture engineered for carrying out the flexible hose bending test. The test fixture is designed such that it replicates the hose mounting configuration in actual flight stage. Fixed end of the flexible hose is attached at the top support plate in the test fixture, and the swiveling end is attached to the bottom support plate. Further, the tests have been conducted at room temperature, since the strength of the material degrades with temperature and hence, the results obtained from the room temperature tests will be conservative. The bottom support plate swivels about an axis which represented the thruster swivel axis. The offset distance (L_2) of the free end of flexible hose from swivel axis is set by an adjustable link.

ISBN - 978-93-95038-50-8

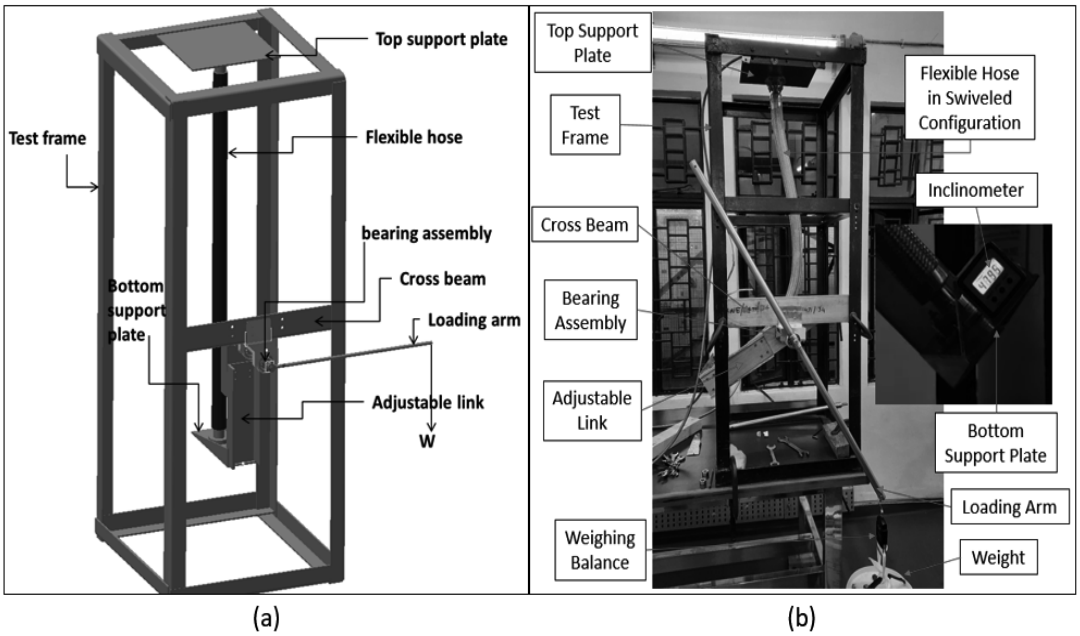

Figure 3: Configuration of Test Fixture

Change in the position of cross beam and length of the adjustable link allow for accommodating different offset distances. Ashaft connects the adjustable link and defines the axis of swiveling. A bearing assembly supports this shaft.The torque is applied by hanging a weight at the end of the loading arm. Figure 3(b) shows the realized experimental setup. A set of known weights at the end of the loading arm. The flexible hose is pressurized with gaseous N_2 at 50 bar.The weight put at the end of the loading arm is weighed using a weighing balance.The bend angle ( ) is measured by an inclinometer mounted on the bottom support plate.

The torque (T_{ss}) applied due to the weight of loading arm, adjustable link, and bottom support plate was estimated by doing a trial without connecting the flexible hose. Hence, the net torque required to bend the flexible hose is given as:

$$T_{total} = (m_{load} \cdot g \cdot L_{arm}) \cdot \cos(\quad , \qquad \therefore T_{hose} = T_{total} - T_{ss}$$

3. EFFECT OF FLEXIBLE HOSE ASSEMBLY CONDITION

In the first configuration, the swiveling end of the flexible hose was assembled to the bottom support plate without pressurization (referred to as the assembly in free condition). Upon pressurization up to 2 bar, the flexible hose undergoes dilation of about 14 mm. The dilation in length is minimal upon subsequent pressurization up to 50 bar (total dilation 15 mm, refer Figure 4(a)).The axial dilation of hose is mainly due to slackness in braiding. For accommodating this additional length in the assembled configuration, the flexible hose develops a curvature at null position. Figure 4(b) shows this effect. Because of this curvature, a snapping behavior is observed, as shown in Figure 5.

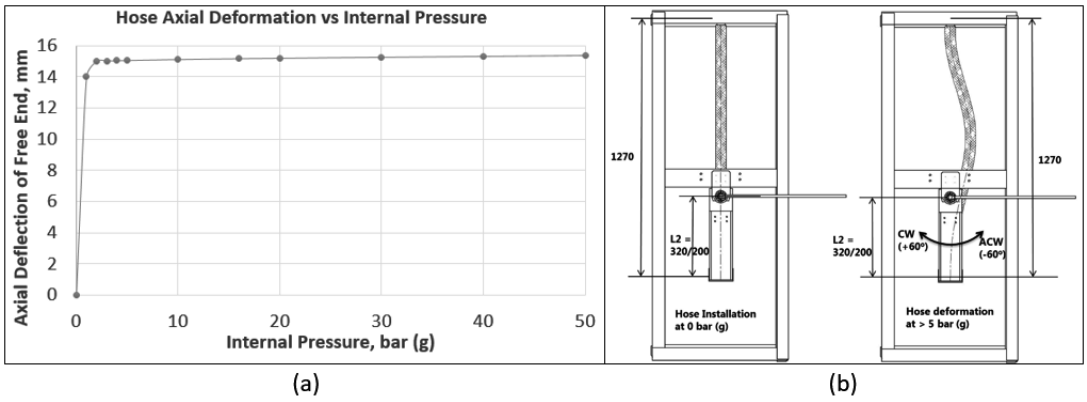

Figure 4: Dilation of Flexible Hose with Internal Pressure

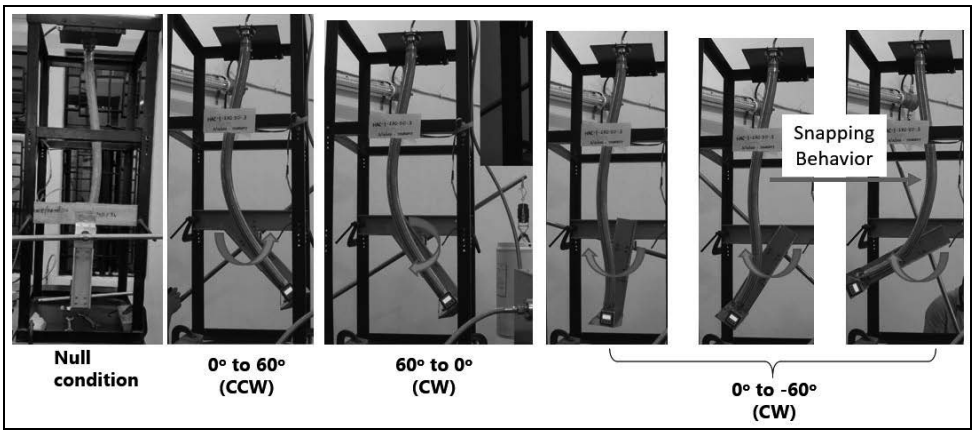

Figure 5: Snapping Behavior of the Flexible Hose

Implications of this effect is increased bending torque and non-uniform & non-linear variation of bending torque with bending angle. The torque and the dynamic characteristics of the hose are different for +60° (CW) bending vs -60° (CCW) bending, refer Figure 6.

When the hose is swiveled from 0° position to -60° position in CCW direction. The shape or the curved profile acquired by flexible hose is not in equilibrium for all bend angles. For small bend angles (up to 25° – 30°), a linear variation of torque with angular deformation (swivel angle) is observed. However, for bend angles between 30-40°, non-linear and abrupt change in torque vs swivel angle is observed in the tests. This attributed to change in geometric profile of the hose (i.e. the curvature of hose due to increase in length after pressurization). The curved shape of the hose is kinematically unstable between bend angles 30-40° for CCW bending, as shown in Figure 5. In this behavior, the curvature developed inside the flexible hose in one direction suddenly shifts to the other side during bending. This leads to a sudden drop in bending torque for increasing bend angle. Figure 6(a) shows this effect for the given assembly condition.

ISBN - 978-93-95038-50-8

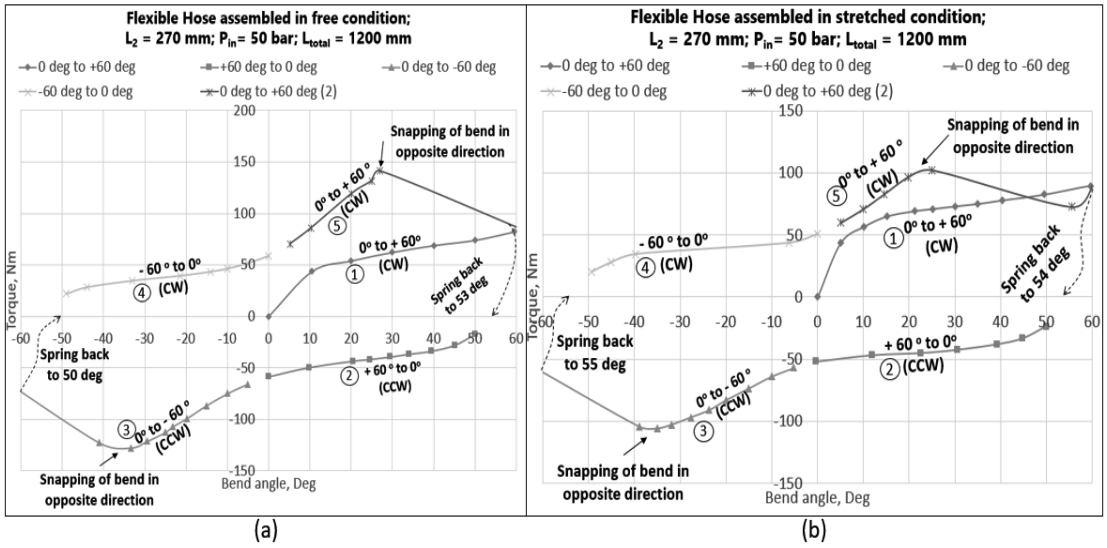

Figure 6: Variation of Bending Torque with Bend Angle for L_2 = 270 mm

In another configuration, the hose was installed after pressurizing it to 5 bar (a) (referred to as the assembly in stretched condition). The increase in hose length is accommodated by adjusting the cross beam, such that the hose is straight and vertical in null position after assembly. The subsequent dilation in the length upon pressurization up to 50 bar was minimal, and hence the curvature developed in the null condition was relatively lower. Figure 6(b) shows the variation of bending torque with bend angle for this configuration with flexible hose assembly in stretched condition. The maximum bending torque in the stretched condition (100 N.m) was considerably lower than the maximum bending torque observed in the free condition (140 N.m). This difference is attributed to the relatively lower development of initial curvature upon pressurizing the flexible hose, and as a result, the reduced snapping behavior.

4. EFFECT OF OFFSET DISTANCE FROM SWIVELING AXIS

The sensitivity of flexible hose bending torque to the offset distance has been studied by conducting further tests with a reduced offset distance of 150 mm.The flight configuration of support bracket, bottom fixed end, etc. were also revised and the flexible region length was reduced to 960 mm.A clamp was devised to help simulate the flexible hose of reduced length.Further, cyclic tests were also performed to understand the repeatability of the flexible hose behavior. Figure 7 shows the variation of bending torque with bend angle for assembly of the flexible hose in both free conditionand stretched condition for a reduced offset of 150 mm.In this case, the maximum bending torque observed for assembly of the flexible hose in the stretched condition was similar to the one observed for an offset of 270 mm. However, there is a significant reduction in the snapping behavior.

ISBN - 978-93-95038-50-8

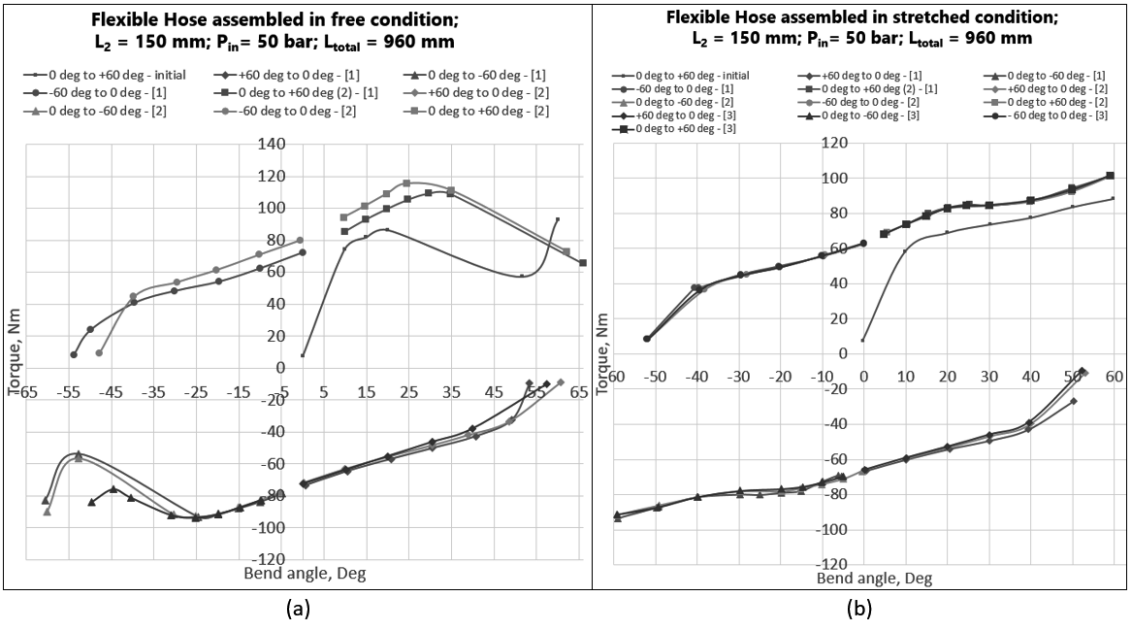

Figure 7: Variation of Bending Torque with Bend Angle for L_2 = 150 mm

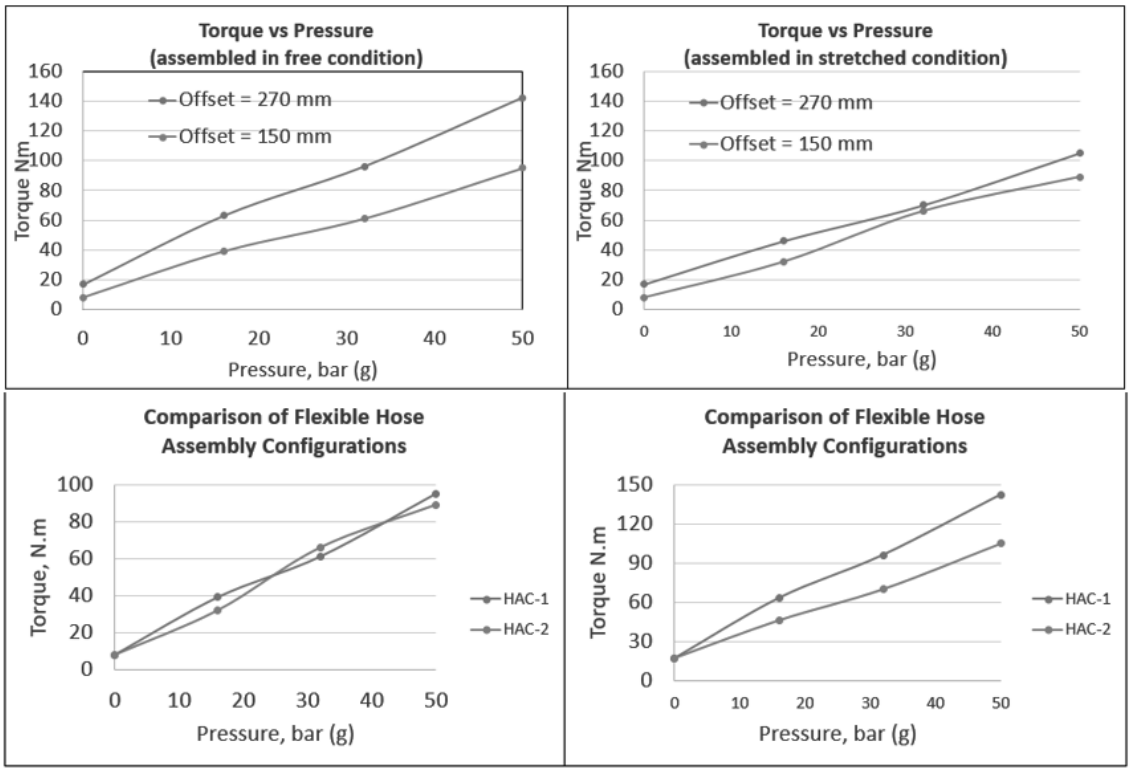

Figure 8: Variation of Maximum Bending Torque with Internal Pressure

ISBN - 978-93-95038-50-8

5. EFFECT OF INTERNAL PRESSURE

Further tests were conducted with hose pressurized to internal pressure of 16, 32, 50 bar. Figure 8 shows the variation of maximum bending torque with internal pressure for both the offset distances (L2 = 270 mm and 150 mm). [NOTE: HAC: Hose Assembly Configuration, HAC-1: Assembly in free condition, HAC-2: assembly in stretched condition]

A significant increase in maximum bending torque is observed with increase in internal pressure. The difference in magnitudes of maximum bending torques is higher for assembly of the flexible hose in free condition. Further, the magnitudes of maximum bending torques are lower for the assembly of flexible hose in stretched condition.

6. OBSERVATIONS AND DISCUSSIONS

The peak torque (140 N.m) observed for assembly of the flexible hose in free condition for an offset of 270 mm and total flexible region length of 1200 mm was maximum among all the test cases. The peak torque for this offset distance reduced significantly upon assembly in the stretched condition. Some improvement in the snapping behavior was also observed because of this modification. Changing the offset distance to 150 mm with reduction in total flexible region length to 960 mm offered a slight increase in the peak torque. However, assembly in the stretched condition in this case, led to reduction in peak torque and a significant improvement in the snapping behavior. Table 1 summarizes the major observations made in all the different tests.

Table 1: Results for Flexible Hose Bending Tests for the Internal Pressure of 50 bar

Sr. No.	Total Flexible Length [mm]	Offset Distance (L_2) [mm]	Assembly Condition of the Flexible Hose	Peak Torque [N.m]	Snapping Behavior
1	1200	270	Free Condition	≈ 140	Significant
2	1200	270	Stretched Condition	≈ 100	Reduced
3	960	150	Free Condition	≈ 120	Considerable
4	960	150	Stretched Condition	≈ 100	Significantly Reduced

7. CONCLUSIONS

A specific, unconventional, and unique experimental setup was engineered and realized to experimentally verify the maximum bending torque requirement. This result was important for finalizing the design specifications of the torque motor used for swiveling the thruster. Number of experiments were carried outfor studying the effect of assembling the flexible hose in different conditions, effect of offset distance from swiveling axis, and the effect of internal pressure on maximum bending torque.

Based on the observations made from the test data, the offset distance of 150 mm with a total flexible region length of 960 mm, and a flexible hose assembly in the stretched condition was chosen as the desired configuration. This configuration requires considerably

ISBN - 978-93-95038-50-8

lower bending torque and offers almost linear variation of bending torque with bend angle. The major conclusions derived from the tests are summarized below:

(a) A significant increase in maximum bending torque is observed with increase in internal pressure. The difference in magnitudes of maximum bending torques is higher for assembly of the flexible hose in free condition.

(b) The maximum bending torques observed for an offset of 150 mm were lower than values for an offset of 270 mm, if we negate the change in total length. Further, a significant reduction in the snapping behavior was observed for an offset of 150 mm.

(c) The magnitudes of maximum bending torques are lower for the assembly of flexible hose in stretched condition as compared to the assembly in free condition.

ACKNOWLEDGEMENTS

Authors are grateful to the fabrication workshop, integration teams, and pneumatic testing labs in LPSC, ISRO for their support in completing this study.

REFERENCES

1. 1. KazuyukiTsukimori, “Theoretical Modeling of Creep Behavior of Bellows and Some Applications”, Journal ofPressure Vessel Technology, Transactions of ASME,May 2001, Vol. 123,page no. 179 to 190
2. C. BechtIV, “Predicting Bellows Response byNumerical and TheoreticalMethods”, Journal ofPressure Vessel Technology, Transactions of ASME,August1986, Vol. 108,page no.334 to 341
3. K. Kobatake, T. Tsukada, S. Takahashi, M. Akatsu, Y. Ikemoto, O. Baba, “Elevated Temperature Fatipi Tests andInelastic Stress Analysis of Bellows”, Journal ofPressureVessel Technology, Transactions of ASME, August1975,page no.223 to 229
4. Masanori Ando, Hiroki Yada, Kuzuyuki Tsukimori, Masakazu Ichimiya, YoshinariAnoda, “Experimental Study on the Deformation and Failure of the Bellows Structure Beyond the Designed Internal Pressure”, Journal ofPressure Vessel Technology,Transactions of ASME,December2017,page no.061201-1 to 061201-12
5. Dacheng Huang, Jianarun Zhang, “Numerical Simulation and Experimental Study on Axial Stiffness and Stress Deformation of the BraidedCorrugated Hose”, Applied Science,20 May 2021, 11, 4709
6. Shubham Sharma, Ahmed J. Obaid, “Design and Analysis of Metal Expansion bellows under Axial and Transverse loadsusing CATIA V5 R21 software” IOP Conference Series Materials Science and Engineering, April 2021,DOI: 10.1088/1757-899X/1145/1/012054
7. W. F. Anderson, Analysis of Stresses in Bellows,United States Atomic Energy Commission, NAA-SR-4527(Pt. I),15 October 1964.
8. Shankar Paramasivan, Modeling of Steel Reinforced Flexible Hoses, Fraunhofer Chalmers Centre, Department of Industrial and Materials Science Chalmers, University of Technology, Gothenburg, Sweden, 2019. (Master’sThesis).

Development of Shock Test Fixture for a Heavy Rocket Valve

Renjith James*, Surya Mani Tripathi, B. Sathis Kumar, A. Alex

Liquid Propulsion Systems Centre, ISRO
Trivandrum, Kerala, 695547
renjith.james@outlook.com

ABSTRACT

This article presents the technical challenges faced during the shock test of 84kg cryogenic valve for a liquid rocket engine and the counter measures implemented to tackle the issue. Aerospace valves are generally subjected to shock test in three orthogonal directional axes (x, y & z) as part of qualification test program to simulate the sudden accelerations occurring during transportation. The main challenge was posed due to high mass (153kg) and asymmetry of the Equipment Under Test (EUT) with respect to centre of gravity (CG) of the valve. The shock level for the test is 50g force in semi-sinusoidal waveform for duration of 10millisecond. The CG of EUT is located using 3D CAD model. The CG offset varied from 37mm to 94mm from shaker axis depending on mounting plane (XY, YZ & XZ) due to asymmetry of the EUT. The large mass, offset of CG from the vertical axis and the shock level called for a higher capacity shaker with a large displacement withstanding higher overturn moment. To counter this issue, a Shock Test Fixture (STF) is designed to keep the CG of EUT within a radius of 10mm from the axis of the available shaker of 290kN capacity. The STF is developed keeping the cumulative mass of EUT within the shaker limit of 230kg and acts as an intermediate test fixture between EUT and shaker table. The shock test of EUT is conducted successfully for the first time in the 290kN shaker using the newly developed STF. This approach shows that similar design methodology can be followed for the optimum utilization of available resources in an economical way

Keywords: *Cryogenic Valve, Shock Test, Centre of Gravity, Shaker*

1. INTRODUCTION

Liquid rocket valves are subjected to environmental test such as vibration, thermal and humidity test and the performance of the hardware is evaluated by conducting valve level functional tests. The vibration test for qualification hardware consists of random, sine and shock test. Random vibrations are the result of a number of events occurring by chance and may be characterized by any frequency spectrum [1]. Sine vibration testing involves subjecting the EUT to a swept sine input over a frequency range. Mechanical shock is a sudden, non-periodic disturbance occurring when environmental accelerations are applied for short but definite period of time [1].The different parts of a electrodynamic shaker is detailed in [2]. Testing of a component for any kind of vibration involves mounting it on a shaker with the help of an intermediate element called a Fixture [3].The fixture transmits the forces produced by shaker table to EUT. The most common material used for fixture fabrication is Aluminium alloy [3].

Generally, aerospace valves are subjected to vibration test in all three orthogonal axes. However, in cases of symmetric valves, the vibration tests are limited to only two axes, one in lateral direction and other in longitudinal direction. The EUT described in this article includes a cryogenic valve of 84kg and a box type fixture. This cryogenic valve is asymmetric in shape and hence the vibration tests are performed along all three orthogonal axes. The specification of the cryogenic valve is given in Table-1.The overall size and weight of the cryogenic valve and the multiple axes vibration requirement called for the development of a box type fixture. The EUT including cryogenic valve and box type fixture discussed in this paper is shown in Figure 1.

* Corresponding author: E-mail: renjith.james@outlook.com

Table 1: Specification of Cryogenic Valve

No.	Parameter	Spec.
1	Fluid medium	Liquid Oxygen (LOX)
2	LOX flow rate, nominal (kg/s)	443
3	Fluid temperature, nominal (K)	117.3
4	Operating pressure (MPa)	45.6
5	Command fluid	Ambient GHe
6	Overall size of valve (mm)	460x381x300

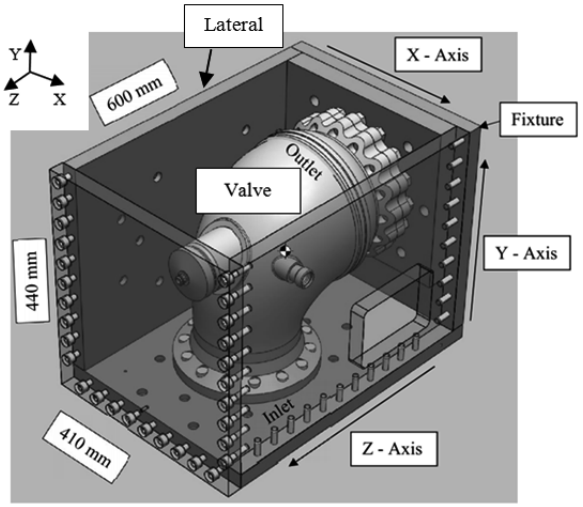

Figure 1: 3D model of EUT

1.1. SINE AND RANDOM VIBRATION TEST

The test specification of sine vibration test and random vibration test is given in Table-2 and Table-3 respectively.

Table 2: Sinusoidal Vibration Test Level

Frequency, Hz	Z-Axis	X & Y-Axis	Sweep rate
10-16	20 mm DA	12 mm DA	2 Octaves/min
16-100	10g	6g	

Table 3: Random Vibration Test Level

Frequency (Hz)	PSD (g^2/Hz)	Acceleration (g_{rms})	Duration (sec)	Axes
20	0.002	13.5	120	All three orthogonal axes
60	0.002			
250	0.138			
1000	0.138			
2000	0.034			

The overturn moment of EUT estimated for sine and random vibration tests are 1415Nm and 2703Nm against shaker capacity of 1765Nm. Additional counter masses are used accordingly to limit the overturn moment within the maximum limit of the available 160kN shaker as shown in Figure 2. As the overturn moment of random vibration test is higher compared to sine vibration test, the counter masses are estimated for the maximum requirement case of random vibration level. The details of counter mass estimated, is given in Table-4. The resultant overturn moment estimated is within the maximum capacity of shaker. As the force requirement of EUT including armature mass in sine and random vibration tests are lower (28.5kN and 54kN respectively) compared to the shock test level (229kN), the sine and random vibration tests were conducted initially with the box type fixture in 160kN shaker. The responses of pre and post-test resonance survey are comparable which ensures the mechanical integrity of EUT. The frequencies of peak responses in the resonance survey are observed within the range of 156Hz to 488Hz.

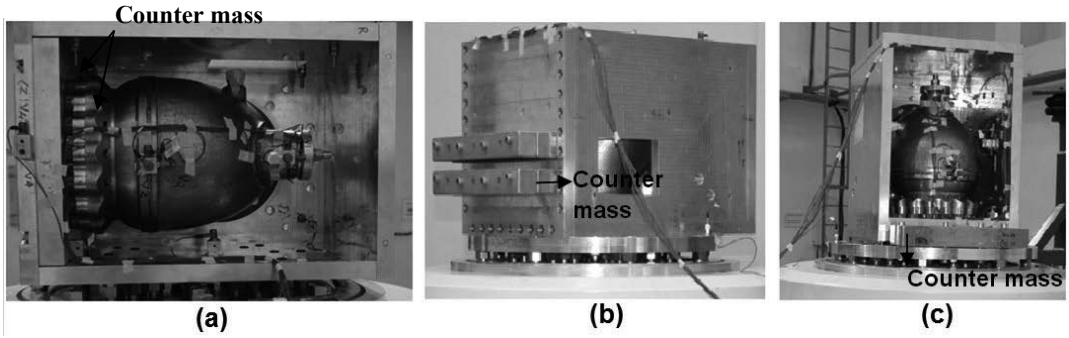

Figure 2: EUT mounted on shaker table for Sine and Random vibration test along (a) X-Axis, (b) Y-Axis and (c) Z-Axis.

Table 4: Details of counter mass used in sine and random vibration test along each axis

Vibration direction	CG offset (mm)	Over Turn moment (Nm)	Counter mass used	Resultant overturn moment after using counter mass (Nm)
X-Axis	36.9	1057	Nil	1057
Y-Axis	94.35	2703	30kg@300mm&180°	1017
Z-Axis	68.35	1958	8.2 kg@215mm&180° 8.2kg@275mm&180°	1206

1.2. SHOCK TEST

As part of general load capacity checks before the test, the overturn moment of EUT is estimated for the Shock test for 160kN shaker. The maximum turning moment of EUT for 50g shock test is 7080Nm and is above the overturn moment capacity of 160kN shaker. As a result, the feasibility study for conducting shock test in another higher capacity shaker of force rating 290kN is carried out. Towards this, a new STF was designed and realized from Aluminium alloy AA2219-T87 plate which can cater for the shock testing along all the three axes and for meeting the interface requirements of the shaker and EUT. The first section of the paper explains the design procedure followed for the development of STF. A comparison of natural frequency of STF between analytical and finite element analysis method are presented to validate the finite element model. The lowest natural frequency of STF is

estimated and sufficient margin is available to avoid resonance with EUT. Finally, the cryogenic valve was subjected to shock test using the newly developed STF and the performance of the cryogenic valve post shock test is verified by conducting functional tests.

2. DESIGN PROCEDURE

The major parameters considered for designing the STF is given below.

i. EUT
   a) Mass of EUT = 153kg
   b) Overall size of EUT = Cuboid of size 600mm x440mm x410mm
   c) Mounting holes = Minimum number of mounting holes in EUT required for shock test is finalised based on the estimate given below.

Mass of component	=	153kg
Shock level	=	50g
Size of bolt	=	M12
Total force experienced by bolts	=	153x50x9.81
	=	75047N
Total force experienced by each bolt	=	75047/6
	=	12508N

Considering higher load transfer, the bolt selected is A286 (1100MPa Class). The Factor of Safety (FOS) for the fasteners is estimated and is given in Table-5.

Table 5: Estimation of FOS for fastener

S.No.	Parameter	Value
1	Yield Strength, YS (MPa)	827
2	Tensile area, A (mm^2)	84.3
3	Load (Max) capacity of each bolt, Fmax = YS x A	69716
4	Nut Factor, k	0.16
5	Torque, T (N-m)	60^{+10}
6	Load due to torque, Ft = T/(k x d) , (N)	36458
7	Percentage of external load transfer	38%
8	External load due to vibration, Fv2, (N)	12508
9	Total load, F_{TOT} = Ft + 0.38 x Fv2, (N)	41211
10	FOS = Fmax/F_{TOT}	1.69

Based on the estimation, 6nos. of M12 bolts are sufficient to withstand the shock load.

ii. Specification of shaker
   a) Force rating of Shaker = 290kN
   b) Overturn moment of Shaker = 10kNm. In order to keep the overturn moment of EUT well within the shaker limit of 10kNm, the CG offset of EUT from the centre is required to be kept minimum. The maximum limit for CG offset is finalized as 10mm to ensure safe operation of shaker.
   c) PCD of mounting holes in shaker table = 8nos. of M12x1.75-6H holes are available in the shaker table at PCDs Ø203.2mm, Ø406.4mm, Ø558.8mm and Ø711.2mm and one number at the centre.

ISBN - 978-93-95038-50-8

iii. Material for STF fabrication = The material selected for the fabrication of STF is aluminium alloy AA2219-T87.

iv. Assembly sequence: The assembly sequence of EUT is given below.

a) Mounting STF to shaker table using 33nos. of M12x1.75 bolts.

b) Mounting EUT to STF using M12x1.25 bolts in orientations as per shock test direction.

2.1 DESIGN OF STF

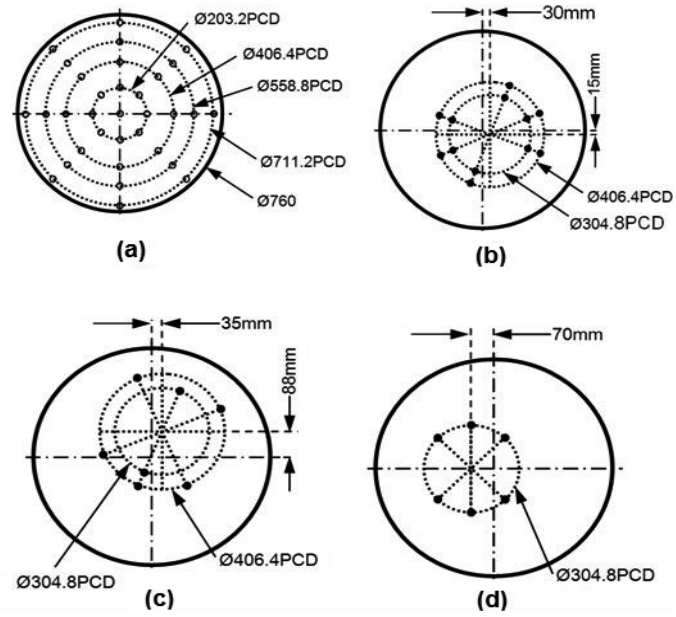

Figure 3: PCD and hole location in STF for (a) fastening to shaker table, (b) shock test along X-axis, (c) shock test along Y-axis, (d) shock test along Z-axis.

The outer diameter of STF is selected as Ø760mm based on envelope size of shaker table. The thickness of plate selected is 33mm considering the available plate size. 8Nos. of Ø13mm through holes with Ø31.5mm counterbore to a depth of 18mm at PCDs shown in Figure 3(a) is provided in STF to mount it to shaker table. The details of PCD in box type fixture are given in Table-6. In order to fasten box type fixture to STF, being an aluminium alloy, thread inserts are installed in STF. The locations of thread inserts in STF are established by ensuring the CG offset is within 10mm from shaker axis. Towards this, the centre of PCDs for thread inserts is shifted from the geometrical centre of STF.

Table 6: Details of PCD in box type fixture

Vibration direction	Mounting side in Box type fixture	PCD of holes in mounting side	No. of bolts per PCD
X-Axis	Lateral side	Ø304.8 & Ø406.4	6
Y-Axis	Inlet Side	Ø304.8	2
		Ø406.4	5
Z-Axis	Outlet side	Ø304.8	6

The mounting hole features shown in Figure 3 are superimposed on a single plate to configure STF. The 3D model of EUT assembled to STF is shown in Figure 4.

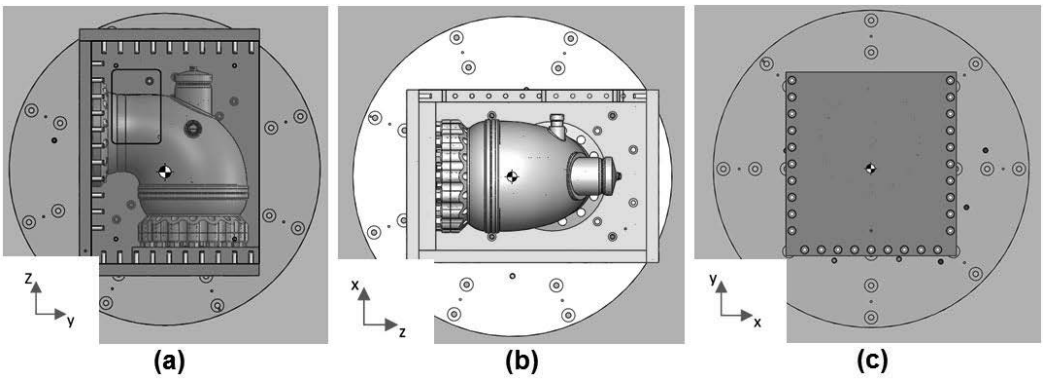

Figure 4: 3D model of EUT mounted to STF for shock test along (a) X-axis (b) Y axis (c) Z axis.

Table 7: CG offset of EUT with STF

Direction of Vibration	G offset of EUT from Shaker axis after mounting on new STF (mm)
XX	7.10
YY	1.90
ZZ	1.86

The new CG offset of EUT mounted on STF estimated using 3D model is given in Table-7 and is within the requirement of 10mm. The CG offset values in Table-7 is finalized as the attempts made to further reduce the offset in CG resulted in overlapping of thread insert hole with the counter bore. The mass of STF estimated using 3D CAD model is 40kg. The overturn moment with the maximum estimated offset of 7.1mm is 0.682kNm and is within shaker specification of 10kNm. The force rating estimated for 290kN shaker with EUT along with armature, fasteners and STF is 229kN, which is within the shaker specification. The factor of safety of fasteners for mounting STF to shaker table is estimated to be 1.85.

3. DESIGN VERIFICATION

3.1. MODAL ANALYSIS

The natural frequency of newly designed STF for clamped condition along the contour is estimated by FEA and compared with analytical result to validate the finite element model. The natural frequency of the first vibration mode of a round plate clamped along the contour is given by the Equation (1) [5]:

$$f = \frac{10.21}{R^2 \times 2\pi}\sqrt{\frac{D}{\rho \times h}} = 575Hz \quad (1)$$

where, the density $\rho = 2840kg/m^3$, thickness of material h = 0.033m, radius of circular STF R = 0.38m, Flexural stiffness of the plate $D = Eh^3/12(1-\nu^2)$, Young's modulus E = 0.73E+011Pa and Poisson's ratio $\nu = 0.33$ (UNS A92219).

The fundamental frequency estimated by FEA is 551.68Hz and is very close to the value obtained by analytical method. Further, modal analysis of STF is conducted by setting boundary condition as fixed geometry at 33Nos. of mounting holes in STF and the result is given in Table 8. The different mode shapes of STF are shown in Figure 5.

Table 8: Modes of STF

Mode	Frequency (Hz)
1	1655.1
2	1728.3
3	1729.4
4	1909.3
5	1909.5

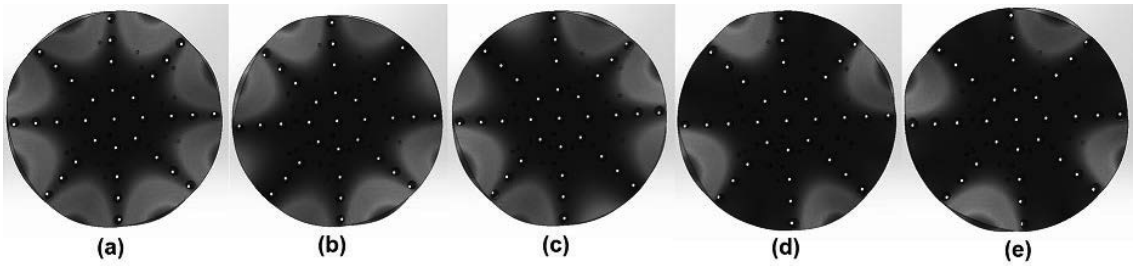

Figure 5: (a) First mode (b) Second mode (c) Third mode (d) Fourth mode (e) Fifth mode

The lowest frequency of STF is higher than the frequencies of peak responses of EUT in resonance survey and hence the design is safe.

4. EXPERIMENT AND DISCUSSION

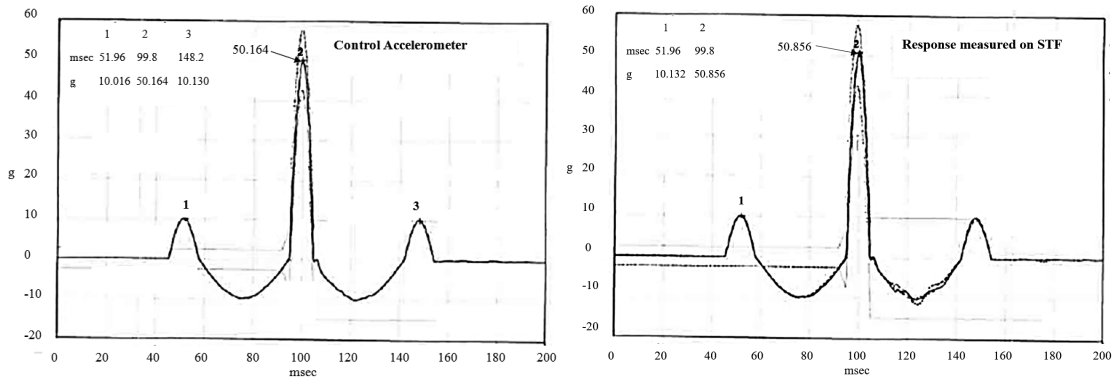

Figure 6: Validation test result

Before carrying out the full level 50g shock test on EUT, a validation test on newly fabricated STF is conducted. STF was mounted on the shaker table by using 33 Nos. of

M12x1.75 of 75mm length bolts and 70Nm torque was applied. Validation test to simulate the standalone performance of STF in shock test was carried out by starting with -18dB level. The shock level is increased in steps of 3dB until 50g is achieved. The plot of validation test at 50g shock level is given in Figure 6. The response measured on STF showed good match with control signal. EUT is then mounted on STF after the validation test.

4.1. SHOCK TEST OF EUT AND RESULT

As the shock test of this magnitude on such a large EUT is planned for the first time in the 290kN shaker, the test is conducted along all three orthogonal axes by starting from a lower level of -18dB. The shock level is then increased in steps of 3dB until 0dB to achieve the full level. The condition of EUT was checked after each shock and found satisfactory. The shock levels achieved is given in Table-9.

Table 9: Shock Test Result

Level	Peak Acceleration Achieved (g)		
	Test-1 (Z Axis)	Test-2 (Y Axis)	Test-3 (X-Axis)
-18dB	6.4	6.529	6.3
-15dB	8.92	8.879	8.936
-12dB	12.55	12.5	12.72
-9dB	17.67	17.721	17.68
-6dB	24.8	24.956	24.882
-3dB	35.31	35.307	36.344
0dB	49.89	49.75	50.217

The achieved shock levels are within the specification of 50g (+ 0 dB/ -3 dB). Post shock test health check of shaker is evaluated and found normal. The fasteners used for mounting was checked post shock test and are found to be in tight condition. Also, the performance of the cryogenic valve post shock test was verified by conducting functional test. Various functional tests include seat leak test, minimum command pressure to start open the valve and external leak test. The performance of the cryogenic valve in post shock functional test is satisfactory.

5. CONCLUSION

Design of STF is primarily controlled by various factors such as overall size and weight of EUT, shaker capacity, CG offset, natural frequency of EUT etc. A STF to meet the test requirement of an 84kg asymmetric cryogenic valve is designed and realized. The large mass, offset of CG distance from the vertical axis and the shock level called for a higher capacity shaker with a large displacement withstanding higher overturn moment. The major constraint of CG offset is addressed by adjusting the location of thread inserts suitably in STF using CAD software. The STF is designed to keep the CG of EUT within a radius of 10mm from the axis of the available shaker of 290kN capacity. The STF is developed keeping the cumulative mass of EUT and STF within the shaker limit of 230kg (excluding armature mass) and it acts as an intermediate test fixture between EUT and shaker table. Modal analysis is conducted on newly designed STF to verify the design. STF mounted on shaker is initially subjected to 50g shock test and the responses are verified. Shock test is initiated by subjecting EUT with STF to lower shock levels. This helped in gaining confidence for

ISBN - 978-93-95038-50-8

proceeding to higher shock levels by gradually increasing the levels. The shock test of EUT is conducted successfully to 50g level for the first time in the shaker using the newly developed STF. The fasteners are found to be intact after the shock test, which proves that the torque applied is adequate. Also, the performance of the shaker and cryogenic valve was satisfactory post shock test. This approach shows that similar design methodology can be followed for the optimum utilization of available resources in an economical way.

ACKNOWLEDGEMENTS

The authors wish to acknowledge the team at ISDTF, VSSC and ISITE, URSC of ISRO for extending the test facilities to carry out the vibration test.

REFERENCES

1. "Aerospace Fluid Component Designers Handbook", Volume II, Revision D, February 1970, Air Force Rocket Propulsion Laboratory. pp. 15.7.1-15.7.3.
2. Everaldo de Barros and Carlos d'Andrade Souto, "Evaluation of a Vibration Test Fixture", International Journal of Acoustics and Vibration, Vol. 22, No. 3, 2017. pp. 348-352.
3. Anjali Reddy, Hamsini K, "Design and Development of Vibration Testing Fixtures", International Journal of Students' Research In Technology & Management, Vol 4 (1) Jan-Feb 2016. pp. 8-11.
4. Srivatsa E, Rahul Sanjay Gidaveer, Sachin N, Sujay Komal Patil, Anil Kumar K, Ekanthappa J, "Design and Analysis of Vibration Test Fixture for 6.2kW Siemens[R] Motor", International Journal of Innovative Research in Science, Engineering and Technology, e-ISSN:2319-8753, p-ISSN:2320-6710, Vol. 9, Issue 5, May 2020.
5. S. Timoshenko, Vibration Problems in Engineering, July 1937. pp. 423-430.

Design and Development of Sealing Mechanism for Gaseous Medium Cryogenic Safety Valve for ISRO Launch Vehicle Application

Arun Baby[1*], Gaurav Sharma[2], Sunil S.[3], D Venkittaraman[4] and A Alex[5]

[1]Scientist-'SD', [2]Scientist-'SF', [3]Division Head
RDD/CRDG/CSC/LPSC/ISRO, Valiamala/Trivandrum, India – 695547.
[4]Group Director-CRDG/CSC/LPSC/ISRO, Valiamala/Trivandrum, Kerala, India – 695547.
[5]Deputy Director-CSC/LPSC/ISRO, Valiamala/Trivandrum, Kerala, India – 695547.

ABSTRACT

Safety valves are most commonly used in aerospace, oil and chemical industry to prevent over pressurization of systems leading to loss of man, material and machine. Usage of cryogenic valves is very common in various launch vehicles worldwide as well as within ISRO. In aerospace application, safety valves are used to prevent over pressurization of either propellant tanks or other subsystem's like command system, roll control system and/or orbit control and stabilisation systems.

Inverted operation relief valves offer advantage of relatively higher sealing stress at operating condition in comparison to direct operation relief valves. Leakage observations in relief valves are very common and also a primary cause of failure. In contrast to pneumatically operated ON/OFF valves, seat stress in relief valves are limited and further reduces close to operating conditions.

Mechanism of sealing in relief valves could be either hard on hard or soft on hard type of sealing. Owing to better leak tightness, soft on hard type of sealing is mostly preferred for cryogenic gaseous application. Soft materials like polycarbonate, Teflon &Kel-F has good sealing characteristics, whereas the mechanical strength of these soft materials is inferior to metals and cannot be used as structural member inside valves. Lesser mechanical strength of these non-metals requires sufficient metallic support to increase structural integrity of valve seats. Soft seats are inserted into these metallic poppets after dipping in liquid nitrogen to achieve required amount of dimensional shrink followed by seat pressing and crimping using special purpose dies. Specially crimped soft seats by plastic deformation of metals helps in retaining soft seats inside metallic poppet. Ductile materials like Aluminum Bronze and AISI 321 are commonly used as poppet materials.

The process of poppet sub assembly crimping is a highly skilled operation and carried out after ensuring low temperature clearances, mating point radius/chamfer and smooth edges for die travel. This paper discusses the crimping of a cryogenic safety valve poppet sub-assembly with soft seat as polycarbonate and metallic poppet made up of Aluminum Bronze. Observations during crimping and issues related to ineffective crimping along with NDT evidence are discussed in detail. Crimping process qualification and advanced NDT screening of every crimped poppet subassembly is also presented in this paper. A comparison of load requirement during crimping by analytical approach against UTM load applied is made and a good match is observed.

Keywords: *Crimping, Safety Valve, Cryogenic, Plastic Deformation*

1. INTRODUCTION

Safety relief valves are commonly used in high pressure systems to safeguard system from over pressurization. Leak tightness of relief valve at operating conditions is a critical parameter in the design especially in aerospace as gap between operating pressure and relief valve full opening pressure is very narrow due to mass constraints in flight stages. Leak tightness of valve is a function of type of seating, surface finish of the sealing surface and seat stress. Due to design constraints, seat stress in relief valves are limited and reduces close to operating conditions. Soft on hard type of sealing is mostly preferred for cryogenic gaseous applications. To provide structural integrity of seat, soft seat is embedded into a metallic body. Although soft seat will arrest primary leakage a possibility of secondary leakage occurs through the joint between structural metallic part and soft material. One of the

*Corresponding Author: E-mail: Arunbaby_86@yahoo.com

process to arrest secondary leak path is crimping in which metal lip is bend onto a soft seat to arrest secondary leak path. This paper discusses about observations and issues faced during crimping of a relief valve proto hardware poppet sub assemblyin detail.

2. LITERATURE REVIEW

Extensive research has been conducted in tube drawing process. Fundamental equations for tube drawing was developed by G. Sachs et al [1].In his study, tube drawing equation with a moving mandrel was solved for both cold-drawing and hot-drawing of thin-walled tubing through a stationary die. An analytical model using upper bound solution for tube drawing process was developed by Um et al [2]. Based on his studies many finite element models were developed by researchers. Numerical modeling of thin walled stainless steel 316L tubes were done by M. Palengatet al [3]. Effects of processing parameters on drawing stress, maximum reduction and optimal die angle were analyzed by D.W. Zhao et al [4] by using an analytical solution by strain rate vector inner product integration. Validation of finite element model for tube sinking w. r. t. drawing force and wall thickness was conducted by Maciej Pietrzyk et al [5]. An elasto-plastic large deformation analysis of ironing process was conducted by You-Min Huang et al [6] and found good agreement with load displacement relation of experiment and simulation values. Various literatures are available on tube drawing/sinking process however specific published literature on crimping of metallic poppet for soft seat retention is not available to the author's knowledge.

3. PROBLEM DEFINITION

In cryogenic stages, desired stage working and performances are obtained by actuating ON/OFF type pneumatic valves in a predefined sequence. These ON/OFF type pneumatic valves are actuated with command gas. In order to reduce the envelope of gas bottles, command gas is stored at high pressure in stages. This high pressure gas is regulated to desired command pressure using a pressure regulator and supplied to pneumatic valves. In one of ISRO's launch vehicle, gaseous helium stored at cryogenic temperature in gas bottles is used as command gas. Regulated pressure of $50^{\pm 3}$ bar is supplied to pneumatic valves via command module. In order to prevent inadvertent pressure rise at downstream of command module, cryogenic relief valve is installed in command line. Relief valve is spring loaded mechanical valve with a designed set pressure. When the system pressure reaches its upper bound pressure which is also the cracking pressure of relief valve, then relief valve vents excess pressure to ambient and restores system back to its operating regime.

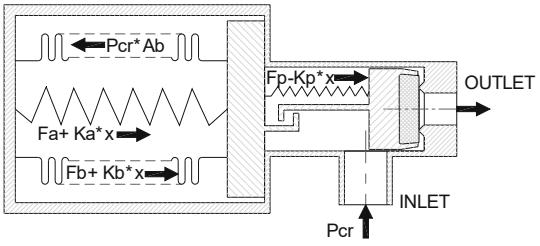

Figure 1: Working schematic of a typical Inverted operation pressure relief valve

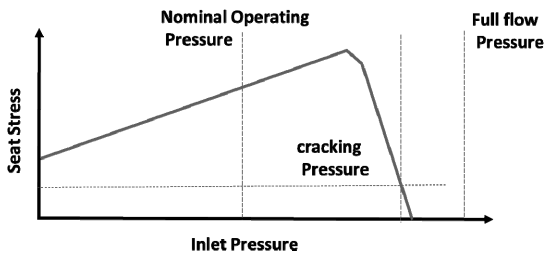

Figure 2: Variation of seat stress of inverted operation relief valve against inlet pressure

Figure 1. shows the working schematic of an inverted operation relief valve. A similar relief valve is under development at ISRO for one of upcoming launch vehicle. There are two helical compression springs in this configuration as shown in Figure 1. The first spring is a poppet spring which provides initial seat stress for seat and another one is reference spring which decides cracking and full flow pressure. The seat stress which controls the leak rate through the valve increases in inverted operation relief valve with increase in inlet pressure. Variations of seat stress against inlet pressure is shown in Figure 2. Functional checks of relief valve are carried out at room temperature and also at cryogenic temperature. Functional checks for a relief valve include determination of Cracking pressure, Full flow pressure and Reseal pressure which is depicted in Figure 3.

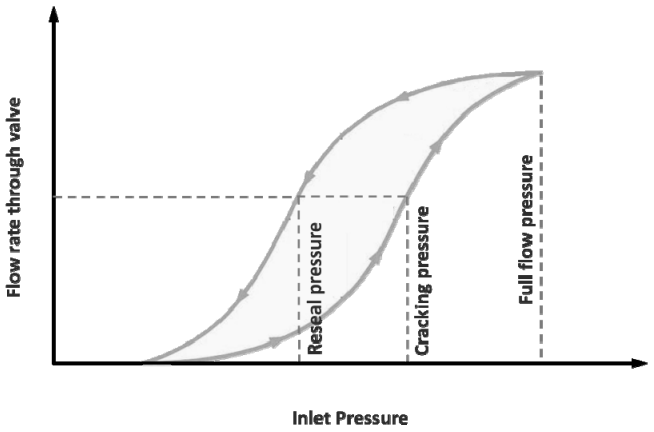

Figure 3: Cyclic functional Test pressure of typical relief valve

Cracking pressure is referred to an inlet pressure at which relief valve leakage is equal to a 0.5 sccs measured via inverted jar method in water displacement. Figure 4 shows test setup for measuring cracking and reseal pressure of relief valve. Gaseous helium is regulated to desired pressure and supplied to inlet of valve. Outlet of valve was connected to a leak tube and valve leak rate is measured using inverted jar method.

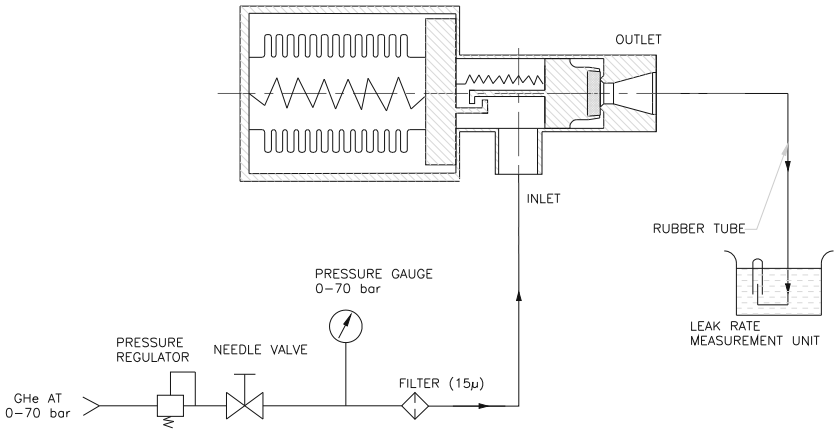

Figure 4: Test setup for measuring cracking pressure ad reseal pressure of relief vale

ISBN - 978-93-95038-50-8

Full flow pressure is defined as the inlet pressure at specified mass flow rate is discharged through valve. Reseal pressure is pressure defined as inlet pressure at which flow rate through valve is reduced to a value equal to 0.5 sccs when the inlet pressure is reduced from full flow pressure. A configuration of sealing area (poppet and seat) of valve is shown in Figure 5.

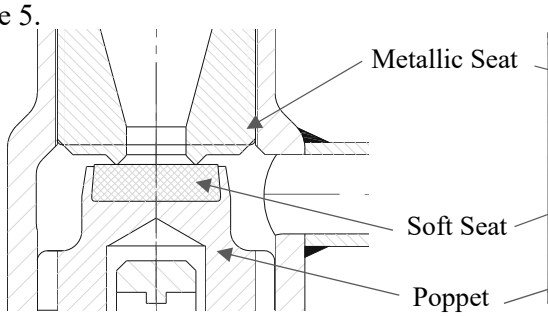

Figure 5: Configuration of Seat

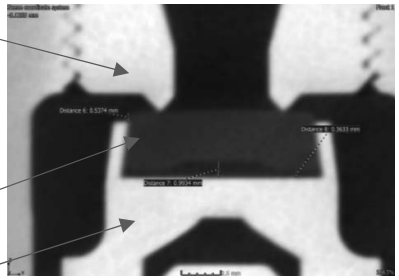

Figure 6: CT image of Seat after low temperature test

During proto hardware development, multiple cyclic actuations of relief valve is conducted, i.e. Cracking pressure to full flow pressure and then to reseal pressure. Cyclic actuations tests were conducted at ambient condition and cryogenic condition. For assessing the health of valve, a repeat health check of valve at room temperature is carried out and observed that cracking pressure and full flow pressure of the valve is changed. Another hardware was tested to the same condition and found increase in cracking pressure. In order to find the root cause of problem, CT scan of hardware was taken and is shown in Figure 6. It was revealed that polycarbonate seat had bulged up leading to change in the poppet spring Initial Load. This happened due to improper soft seat pressing against metallic poppet, leading to gas entry during cryogenic test followed by expansion of same entrapped gas during ambient testing. This lead to soft seat bulging and change in cracking and full flow pressure. CT scan image of valve clearly depicts a bulging of polycarbonate seat. In order to rectify this issue in prototype hardware, mechanical seat shall be sufficiently pressed against soft seat so that no secondary leakage path is available for the gas to enter. The process of bending the metal lip for soft seat retention to obtain a leak tight joint is termed as crimping.

4. RESEARCH METHODOLOGY

4.1. PROCESS OF CRIMPING

Aluminum Bronze material is selected as the poppet material for soft seat retention owing toits higher ductility, compatibility with cryogenic medium, self-lubricating capability and requirement of dissimilar metals for sliding joints. Material of seat is selected as polycarbonate which has excellent sealing characteristics at ambient and cryogenic temperature. Seat is designed to have an interference fit of 200-286 µm than corresponding cavity inside metallic poppet in ambient condition. Polycarbonate seat is immersed in liquid nitrogen medium to shrink so that it can be inserted inside metallic poppet. After temperature stabilization,fit between polycarbonate seat and poppet changes to clearance fit and is smoothly inserted inside poppet as shown in Figure 7. After polycarbonate seat is inserted, the metal lip of aluminum bronze is deformed using a special purpose die as shown in figure die as shown in Figure 8.

ISBN - 978-93-95038-50-8

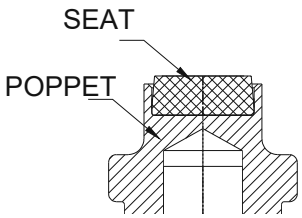

Figure 7: Seat and Poppet

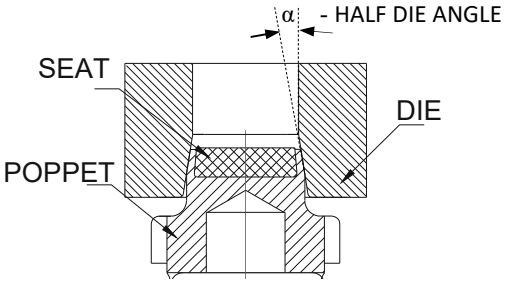

Figure 8: :Schematic representation of crimping process

The major important parameters of crimping process are the angle of crimping, surface finish of die, the die travel distance and alignment of die w. r. to poppet. Die angle is a critical parameter in determining how much the metal is pressed against polycarbonate seat. Initial angle was provided on the polycarbonate seat to ensure smooth insertion and easier bending of metallic poppet. Die angle should be more than the seat angle on polycarbonate to create a positive leak tight joint. Polycarbonate seat was designed with semi angle of 5 degree. Inorder to obtain a positive joint leak tightness final angle of metal lip after crimping should be more than that of polycarbonate seat. The semi angle of die was designed with an inner semi angle of 10º degree in order to obtain 9±1º on the final crimped poppet. Surface finish of die is important as better surface finish can reduce friction between die and poppet at the time of pressing and requires lesser load for crimping. Improper alignment of die w r to poppet can cause non uniform loading of poppet which in turn cause secondary leak path. Die travel distance is controlled to limit the amount of deflection of poppet on to soft seat so that metal will not pierce inside soft material. The plastic deformation of poppet and seat make the valve a leak tight joint.

4.2. ANALYTICAL SOLUTION

Governing equations are derived using theory of plastic deformation. Following are the assumptions made for analytical validation.

- Materials are isentropic and homogenous and free from defect
- The deformation of die, loading pin and housing are neglected and considered rigid bodies
- Tube sinking equations are used because of its similarity to crimping process.
- Volume is conserved before and after crimping.
- Resistance offered by polycarbonate seat is neglected as it can flow easily under application of heavy loads.

For analysis, the metal part is considered as a tube of fixed diameter drawn through a die. Crimping process is considered analogous to tube sinking process. The difference is that die moves forward and deforms the metal tube in crimping while in tube sinking the tube is drawn through a die.

Drawing stress in tube drawing is given by [7] and are shown in equation (1).

$$\sigma = y' \left(\frac{1+B}{B}\right)\left(1 - \left(\frac{d_f}{d_o}\right)^B\right) \quad (1)$$

$$B = \left(\frac{\mu_1 + \mu_2}{\tan\alpha - \tan\beta}\right) \tag{2}$$

an elastoplastic model of Aluminum bronze was used for the analysis

$$\sigma = k\ \varepsilon^n \tag{3}$$

y' mean flow stress is given by

$$y^f = \frac{k\varepsilon^n}{1+n} \tag{4}$$

where, = Tube drawing stress

= Coefficient of friction between die and poppet

= Coefficient of friction between poppet and inner mandrel = 0

=Half Die angle

=Half mandrel angle = 0

=Final Area of Tube

=Final Area of Tube

4.3. EXPERIMENTAL VALIDATION AND CRIMPING

For experimental validation of analytical solution, six poppets were realized with Aluminum bronze material(C63200) and seat was realized with polycarbonate material. The outer diameter of crimping lip is 15 mm and inner diameter is 13 mm as shown in Figure 9. Crimping die is made up with a harder material (SS MDN 59). A fixture was designed to hold poppet and guide the die inside as shown in figure 10. A stopper was added to prevent bulging of polycarbonate seat during crimping process. Loads are transferred to die using loading pins. Load is applied to the loading pin using a universal testing machine. This subassembly fixture i.e. along with poppet and seat is mounted in UTM and load is applied at a controlled speed of 1mm/ min. A load cell of 5T was attached to UTM Which gives the load vs deflection of die.

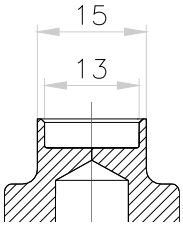

Figure 9: Cross section of poppet

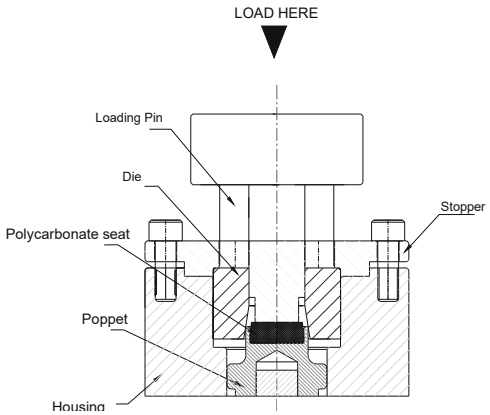

Figure 10: Schematic representation of experimental setup

The maximum travelling distance of die is limited by the mechanical stopper available at the bottom of Housing. This is done to safeguard poppet from over bending. A sudden rise in load can be observed when the die touches bottom mechanical stopper as the load will be transferred to housing. To obtain uniform surface and angle on poppet after pressing die was rotated by 180º and process of loading was repeated.

5. RESULTS AND DISCUSSIONS

Crimping fixture is loaded in UTM machine and crimping load is applied gradually at a controlled rate of 1mm per minute. A limit of 2000 kg for the load and a 3.5 mm limit for the deflection were set as an emergency stop for the UTM. The resulting load vs deflection graph is shown in Figure 11. The crimping commences with gradual increase in the deflection with increase in the load applied. Then a sudden increase in load is observed as the die makes contact with the mechanical stopper. Once die makes contact with mechanical stop,load is retained at the same level for an additional 5 minutes for stabilization and to minimize the effect of spring back. Subsequently, the load is gradually withdrawn. In order to obtain a uniform crimping and reduce the effect of misalignment of die, the crimping procedure is repeated by rotating the die by 180º. Figure 12 shows the load vs deflection graph for re-crimping. Table 1 below shows the consolidated crimping load in each pass and resultant crimping angle.

Load required for crimping of soft seat is calculated using formula given in eqn. (1). The coefficient of friction between die and aluminum bronze poppet (= 0.45. Half die angle =10º. Mean flow stress y' =318.2 MPa considering an average strain of 10% during cold working is assumed for the analysis. Total crimping load is calculated by multiplying initial area with drawing stress given in eqn. (1).

Table 1: Comparison of experimental Crimping load against theoretical crimping load

Sl No	Poppet No	Calculated Load (Kgf) Min.	Applied Load in UTM (Kgf)	Die Travel in first crimping (mm)	Load applied in second crimping(Kgf)	Die Travel in second Crimping (mm)	Achieved angle
1	Poppet 1	581.75	756.00	2.44	580.00	0.77	8º40'
2	Poppet 2	595.82	792.00	2.75	700.00	0.76	8º40'
3	Poppet 3	557.12	756.00	2.81	632.00	0.83	8º30'
4	Poppet 4	548.59	816.00	2.82	704.00	0.80	8º40'
5	Poppet 5	554.09	772.00	2.74	710.00	0.80	8º40'
6	Poppet 6	541.83	560.00	2.73	464.00	0.76	8º30'

ISBN - 978-93-95038-50-8

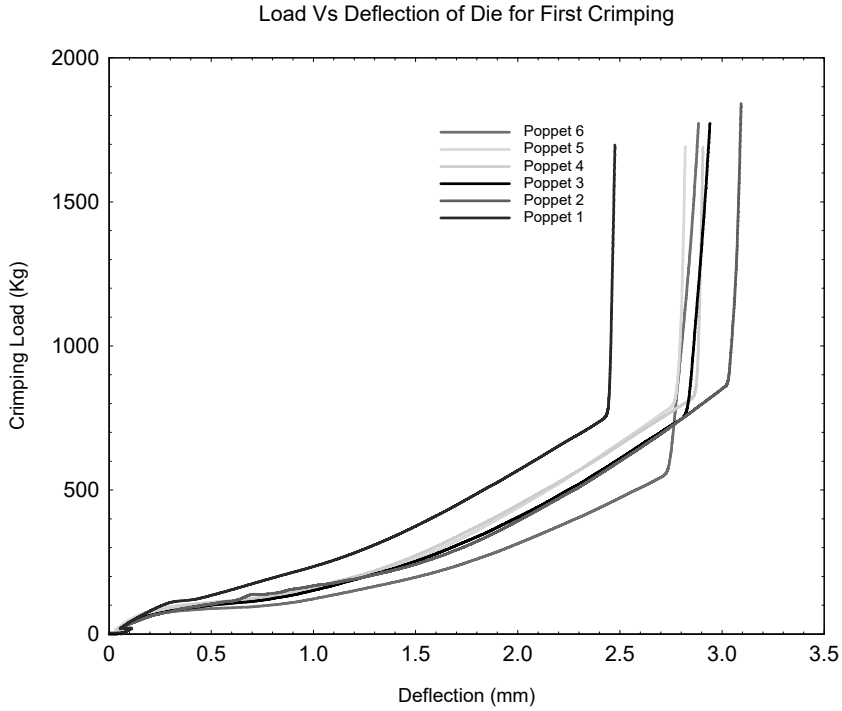

Figure 11: Load vs deflection of die in first crimping.

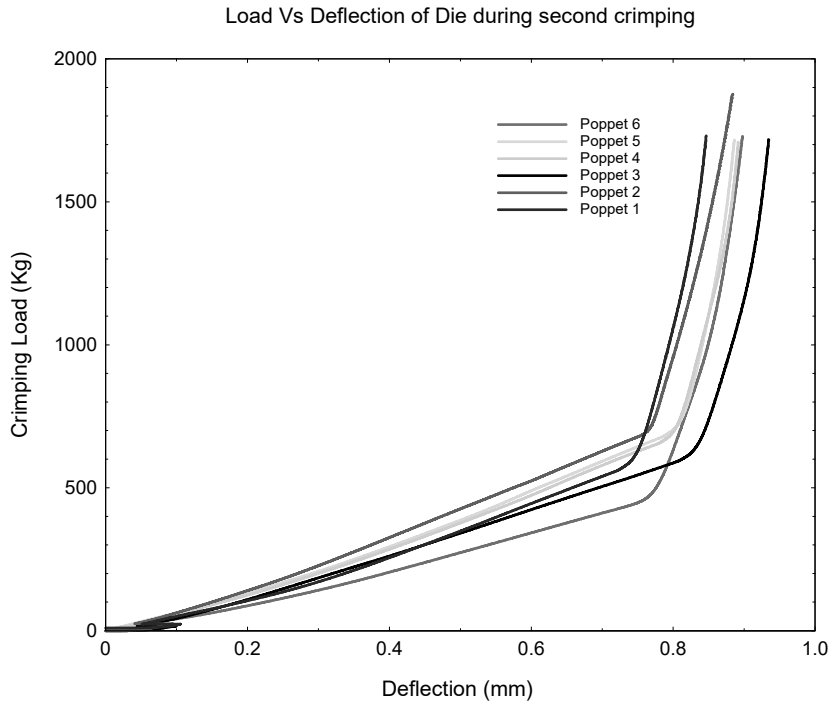

Figure 12: Load vs deflection of die in second crimping.

Table 1 shows the load applied at crimping is more than calculated load. During first crimping the applied load was found to be more than 31% of calculated average load.

Reasons could be due to nonlinearity of materials, friction between die and metallic poppet or geometric misalignment of poppet and die. The error was found to be reduced to 12% during second crimping. Average crimping angle achieved is 8º30' against expected value of 9. This is due to spring back effect. Angle provided in polycarbonate seat is 5 degree. So always a positive compression is ensured in polycarbonate seat by metal lip tocreate a leak tight joint.

To test leak tight joint each poppet was tested at low temperature and ambient condition for cracking pressure, full flow pressure and reseal pressure. CT scan image of poppet and seat was taken before and after test and is shown in Figure 13. It is evident from CT scan image that no bulging or gap at bottom side of seat was noticed. Also no bulging of soft seat was found on all six poppet subassemblies.

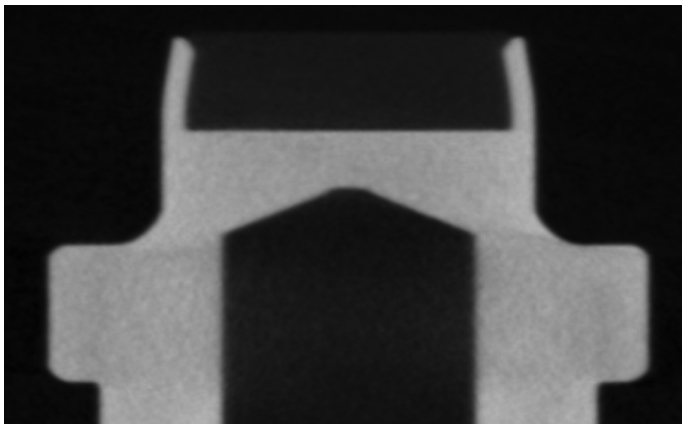

Figure 13: CT image of newly crimped poppet and seat after low temperature test

6. CONCLUSIONS

This paper provides information about design considerations and issues faced during crimping process of a cryogenic safety valve poppet subassembly for soft seat retention. A comparison of load requirement during crimping by analytical approach against UTM applied load is presented. Reasons for difference from analytical to experimental test is understood and listed.

ACKNOWLEDGEMENTS

Authors would like to thank CATF Team-Component Assembly and Testing Facility, Liquid Propulsion System Center for the support in conducting experiments, Nondestructive Testing division of Quality Control Group,LPSC for their support in conducting CT scan and analysis on observations based on CT images.

REFERENCES

1. Sachs, G., Lubahn, J. D., and Tracy, D. P. (March 8, 2021). "Drawing Thin-Walled Tubing With a Moving Mandrel Through a Single Stationary Die." ASME. *J. Appl. Mech*. December 1944; 11(4): A199–A210. https://doi.org/10.1115/1.4009393

2. Kyung-Keun Um, Dong Nyung Lee," An upper bound solution of tube drawing" Journal of Materials Processing TechnologyVolume 63, Issues 1–3, January 1997, Pages 43-48, https://doi.org/10.1016/S0924-0136(96)02597-6.
3. Muriel Palengat, Grégory Chagnon, Denis Favier, Hervé Louche, Camille Linardon, et al.. Cold drawing of 316L stainless steel thin-walled tubes: experiments and finite element analysis. International Journal of Mechanical Sciences, 2013, 70, pp.69-78. ff10.1016/j.ijmecsci.2013.02.003ff. ffhal-00936527f
4. D.W. Zhao, H.J. Du, G.J. Wang, X.H. Liu, G.D. Wang, An analytical solution for tube sinking by strain rate vector inner-product integration, Journal of Materials Processing Technology, Volume 209, Issue 1,2009, Pages 408-415,ISSN 0924-0136,https://doi.org/10.1016/j.jmatprotec.2008.02.011.
5. Maciej Pietrzyk, Lucjan Sadok, Validation of the finite-element model of the tube-sinking process, Journal of Materials Processing Technology, Volume 22, Issue 1,1990,Pages 65-73,ISSN 0924-0136,https://doi.org/10.1016/0924-0136(90)90142-H.
6. You-Min Huang, Yuung-Hwa Lu, Jia-Wine Chan, An elasto-plastic finite element and experimental study of the ironing process, Journal of Materials Processing Technology, Volume 26, Issue 1, 1991, Pages 53-80, ISSN 0924-0136, https://doi.org/10.1016/0924-0136(91)90006-Z.
7. Dieter, G.E., "Mechanical metallurgy", 1988, SI metric edition, McGraw-Hill,pp.532

Multifractal Detrended Fluctuation Analysis for Onset of Combustion Instability in Liquid Rocket Engines

Varghese Mathew Thannickal*[1], T. John Tharakan[1], S. R. Chakravarthy[2]

[1]Propulsion Research Group
Liquid Propulsion Systems Centre
Thiruvananthapuram, Kerala, 695547

[2]National Centre for Combustion Research and Development & Department of Aerospace Engineering
Indian Institute of Technology- Madras
Chennai, Tamil Nadu, 600036
Email: src@ae.iitm.ac.in

ABSTRACT

Combustion instability is a potentially destructive phenomenon that leads to time and cost overruns in a rocket engine development project. Active control in open loop or closed loop configurations is being investigated to suppress combustion instability. The active control strategies can be made more effective if there is a forewarning of impending instability. In this work, multifractal detrended fluctuation analysis (MFDFA) is examined as a technique to provide forewarning of instability in liquid engines. The method is based on the decomposition of the chamber pressure data of the engine into singularity exponents and dimensions at different fractal orders. These parameters can be parametrically combined to generate the fractal spectrum. The fractal spectrum has a definite shape characterized by its height, width, differential height and apex location. The evolution of the multifractal spectrum characteristics is known to yield information on the onset of instability based on lab level experiments. The applicability of MFDFA to investigate the onset of instability in full-scale engines assessed in this work. Typical earth storable and cryogenic engines are used as case studies.

Keywords: *Multifractal detrended fluctuation analysis, multifractal spectrum, spectral characteristics*

1. INTRODUCTION

Combustion instability is a potentially destructive phenomenon that leads to time and cost overruns in a rocket engine development project. It is characterized by high frequency pressure fluctuations that can increase vibration and thermal loading on the combustion chamber. In extreme cases, the increased loading can result in failure of the engine. Conventionally, it is controlled by passive means wherein slots, resonators and liners are used to damp out the instability. Active control is also being investigated wherein the instability is controlled in open loop or closed loop configurations. Active control strategies are most effective if coupled with some sort of forewarning of the impending instability. This is because instability sets in very rapidly, within a few milliseconds to a few seconds. By the time the control system reacts, it may be too late to mitigate the deleterious effects of the instability. It would be desirable if the onset of instability can be anticipated before it happens. This gives sufficient time for corrective action to be taken. In this work, a technique based on the analysis of the fractal spectrum of chamber pressure oscillations is investigated to anticipate the combustion instability.

2. LITERATURE REVIEW

Combustion instability is highly nonlinear in nature. A stable combustion system exhibits aperiodic low amplitude pressure fluctuations known as combustion noise. On the other hand, combustion instability is characterized by high amplitude periodic oscillations in chamber pressure. As the system transitions from stability to instability, intermittency is observed

*Corresponding Author: Email: varghesemathewthannickal@lpsc.gov.in

wherein the system behaves in a quasi-periodic manner. The transition from combustion noise to combustion instability can be inferred from nonlinear time series analysis of the pressure perturbations [1].

The concept of fractals can be used to carry out nonlinear time series analysis for the onset of combustion instability. A fractal is an object whose geometry cannot be expressed by an integer dimension but it is rather a fractional quantity [2]. The fractional dimension of a fractal is due to its self-similar nature i.e., its properties repeat at smaller and smaller scales. Most objects in nature such as contours of coastlines, branching of the circulatory system, combustion oscillations and turbulence can be described by fractals [3].

A common measure of a fractal is the Hurst exponent [4]. An analysis of the time series chamber pressure data of an unstable combustion system reveals that it is multifractal. The time series has multiple fractal components each of which has a different Hurst exponent depending on the amplitude of the perturbations [5-7].

To adequately capture the behavior of multifractal time series it is more appropriate to generalize the definition of the Hurst exponent. Using the concept of structure functions [8] the generalized Hurst exponents can be obtained using multi-fractal detrended fluctuation analysis (MFDFA) [9-11]. The onset of combustion instability has been correlated to the loss of multifractality. The Hurst exponent is found to have a decreasing trend prior to the onset of instability [12-14].

3. PROBLEM DEFINITION

The generalized Hurst exponents can be Legendre transformed and expressed as a two-dimensional curve which typically has the shape of an inverted U. This multifractal spectrum is broad in the case of combustion noise, becomes narrower during intermittency and finally contracts to almost a spot during combustion instability [12]. In the process, the location of the apex of the multifractal spectrum shifts to the right. The variation in the shape and location of the multifractal spectrum forms the basis the present work.

MFDFA has been applied to a laboratory combustor [12] and a model liquid rocket combustor [14]. It is found that the variation of Hurst exponents of different orders are good indicators of the onset of instability. However, there is very little literature on the application of MFDFA to full-scale engines, which is the purpose of the present work.

4. RESEARCH METHODOLOGY

To estimate the generalized Hurst exponents, the time series of chamber pressure, *P(t)*, is first mean adjusted and then cumulated over i intervals to get a deviated series x_i:

$$x_i = \sum_{t=1}^{i} \left(P(t) - \overline{P} \right) \tag{1}$$

The deviated series is then separated into m_w non-overlapping segments of equal width w where m_w is an integer. To measure the multifractal nature of the fractal spectrum, structure functions, S_w^q, of order q and span w, can then be obtained from the deviated series as:

$$S_w^q = \left(\frac{1}{m_w} \sum_{i=1}^{m_w} \left(\sqrt{\frac{1}{w}} \sum_{j=1}^{w} \left(y_j(t) - \overline{y}_i \right)^2 \right)^q \right)^{\frac{1}{q}} \tag{2}$$

ISBN - 978-93-95038-50-8

Here, $\bar{y_i}$ is a local polynomial fit to the deviate series y_i. The Hurst exponent of order q, H^q, is obtained from the log-log plot of S_w^q, by taking its slope in the linear regime, for a range of span sizes w. Applying a Legendre transformation, the spectrum of singularities, $f(\alpha)$, is obtained:

$$\tau_q = qH_q - 1 \tag{3}$$

$$\alpha = \frac{\partial \tau_q}{\partial q} \tag{4}$$

$$f(\alpha) = q\alpha - \tau \tag{5}$$

α is also called the singularity exponent while $f(\alpha)$ is called the singularity dimension. The multifractal spectrum is a plot of $f(\alpha)$ vs. α as seen in Fig. 1.

A typical multifractal spectrum is shown in Fig. 1. It has an inverted-U shape with a right limb and a left limb. The spectrum is not necessarily symmetric. The parameters used to describe the spectrum are named as the spectral characteristics and are indicated in the figure. Here the mean spectrum height is the average of the singularity dimensions of the ends of the limbs. In this work, attention is focused on the apex location and spectrum width.

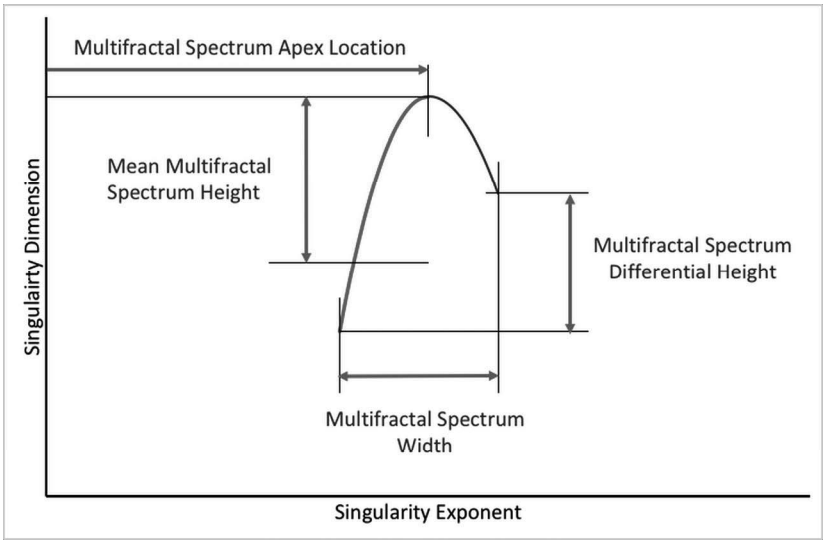

Figure 1: Multifractal spectrum with spectral characteristics

A MATLAB code is written to calculate the structure functions and thereby the multifractal spectrum. Reference [11] presents the results for three test cases viz. monofractal, multifractal and white noise signals. The present code was used to simulate these cases and the algorithm was validated.

5. RESULTS AND FISCUSSIONS

MFDFA is applied to three liquid rocket engines of ISRO. The details of the engines are given in Table 1.

Table 1: Liquid engines analysed by MFDFA

SN	Designation	Propellant combination	Type of injector	Nominal chamber pressure	Nominal mixture ratio
1	High thrust earth storable engine (HTEE)	UDMH/N_2O_4	Doublet impinging	60 bar	1.7
2	Low thrust earth storable engine (LTEE)	MMH/MON	Triplet impinging	8 bar	1.7
3	Cryogenic engine (CE)	LH_2/LOX	Swirl coaxial	60 bar	5

5.1. ONSET OF COMBUSTION INSTABILITY IN A HIGH THRUST EARTH STORABLE ENGINE

Six tests of the high thrust earth storable engine were chosen for the study comprising of both short duration and long duration tests. No instability was observed in any of these tests based on FFT analysis, but MFDFA is used to examine the potential for development of instability. In each case, the multifractal spectral characteristics are determined in the start transient and a period thereafter. The results for all the tests are similar and are illustrated with reference to the hot test designated as HTEET. Salient spectral characteristics of HTEET are given in Fig. 2.

The apex location remains above 0.7 and does not show any tendency to approach zero. This clearly confirms that there is no instability as it does not approach zero. It can be inferred that the fluctuations observed are combustion noise. This is corroborated by the fact that the spectrum does not contract as time progresses, since the width also does not approach zero. Using MFDFA, it is thus conclusively established that there is no tendency to instability in the high thrust earth storable engine tests considered.

5.2. ONSET OF COMBUSTION INSTABILITY IN A LOW THRUST EARTH STORABLE ENGINE

The onset of combustion instability in a low thrust earth storable engine is now investigated. Two tests are considered, which are designated as LTEET1 and LTEET2. In these tests, signatures of instability were observed based on FFT analysis. This can be probed further by examining the spectral characteristics at higher ranges of scale (Fig. 3). Lower scale ranges are found not to yield information pertaining to instability but rather to combustion noise.

From Fig. 3a, it is seen that the apex location shows a downward trend at 0.5s. The apex location dips from 1.4 at 0.5s to almost 0.1 when the instability manifests at 3.2s. There is a forewarning of instability of about 2.7s if the apex location is appropriately considered. Prior to the instability, the width has a value of 0.5 on average, which decreases to about 0.25 when it sets in. The greater change in apex location during the onset of instability indicates that it is a more parameter definitive for establishing tendency for instability as compared to the width.

ISBN - 978-93-95038-50-8

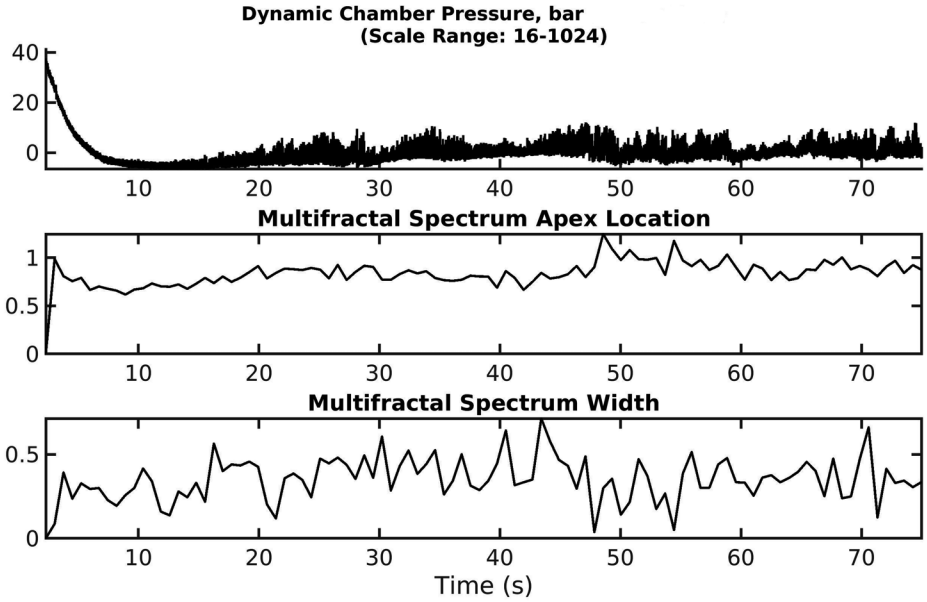

Figure 2: Apex location and width of multifractal spectrum of high thrust earth storable engine

In the case of LTEET2 (Fig. 3b), the FFT analysis shows a distinct dominant frequency. The apex location remains in the vicinity of 1 after 0.7s, which would indicate that the phenomenon is pronounced combustion noise and not instability. The behaviour of the width is more or less similar in both LTEET1 and LTEET2, being in the vicinity of 0.25 on average. The lateral contraction of the spectrum is thus not seen in the contrasting cases. This again indicates that the apex location is a key parameter from the point of view of the multifractal analysis of the onset of instability.

5.3 ONSET OF COMBUSTION INSTABILITY IN A CRYOGENIC ENGINE

A cryogenic engine has experienced instability issues in multiple instances. Two unstable tests were analysed by the present methodology. They are designated as CET1 and CET2. The former is a standalone test of the thrust chamber while the latter is a full engine test.

Both experienced catastrophic instability leading to failure of the hardware. The salient spectral characteristics for the two cases are given in Fig.4. Fig. 4a reveals a classic instability between 2.7s and 8.3s. The plotted spectral characteristics attain values very close to zero. Similarly, the initial 7s in the CET2 test are subjected to MFDFA. Again, it shows a classic instability as seen by examining the spectral characteristics (Fig. 4b). The spectral characteristics dip to zero at 5.6s. There is hardly any forewarning of the impending instability, with respect to the apex location and width, for both tests of the cryogenic engine considered. The spectral characteristics respond at or after the initiation of the exponentially growing pressure perturbations. This contrasts with the significant forewarning obtained in the LTEET1 test. It suggests that the more reactive the propellant combination, the less effective MFDFA becomes in anticipating instability.

Interestingly, after 6.8s, when the dynamic pressure trace in CET2 (Fig. 4b) shows increasing amplitude of oscillations, there seems to be a change in the nature of the instability. The spectral characteristics start to deviate from zero. This may be due to some unknown nonlinear effect that causes non-periodicity in the oscillations.

ISBN - 978-93-95038-50-8

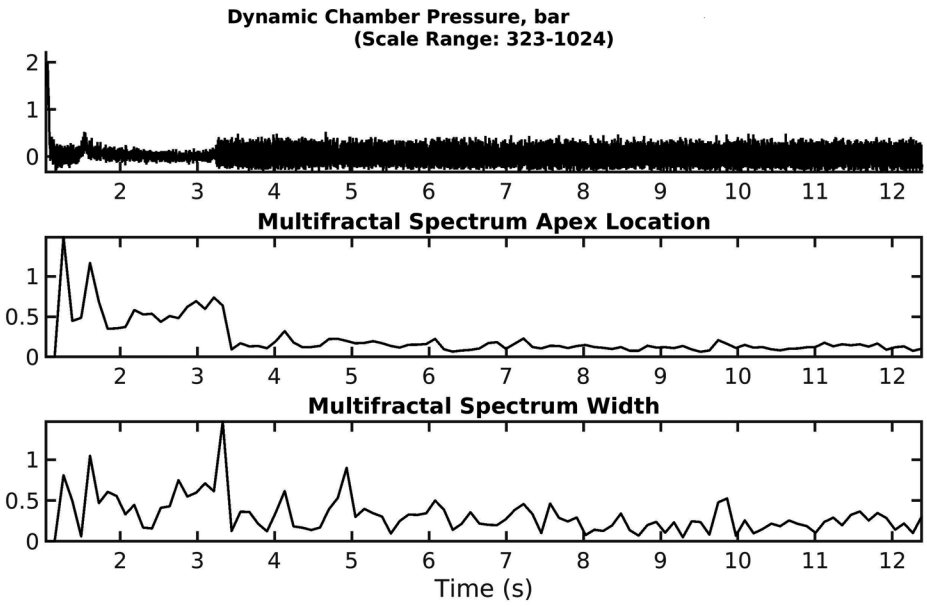

(a)

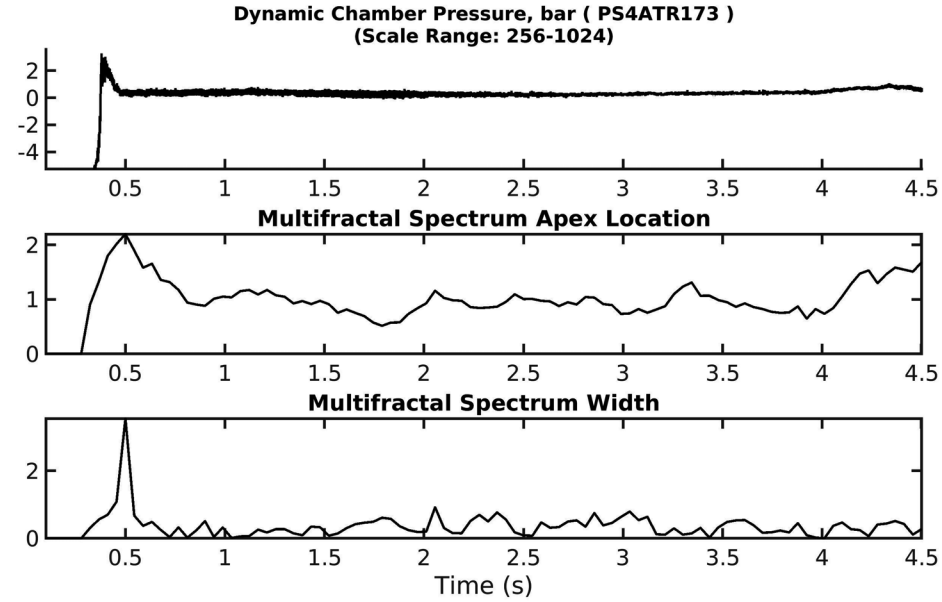

(b)

Figure 3: Apex location and width of multifractal spectrum (a) LTEET1 (b) LTEET2

6. CONCLUSIONS

The onset of combustion instability in typical liquid rocket engines was investigated using the technique of multifractal detrended fluctuation analysis. The multifractal spectrum of the chamber pressure oscillations was determined. The variation of two spectral characteristics viz. apex location and width is investigated is this work. Across all the engine tests, the apex location is the primary spectral characteristic with regard to the anticipation of the onset of instability and the width plays a secondary role.

ISBN - 978-93-95038-50-8

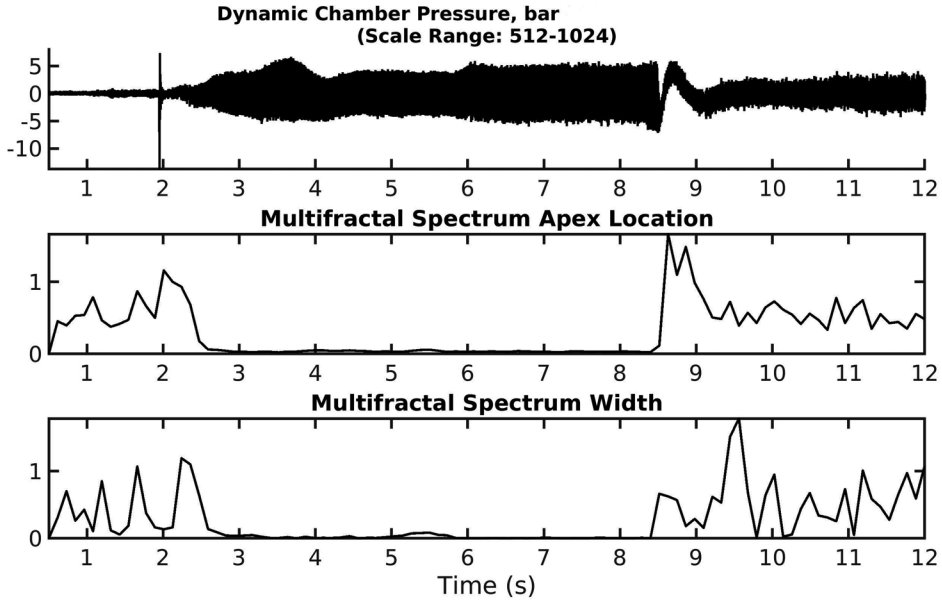

(a)

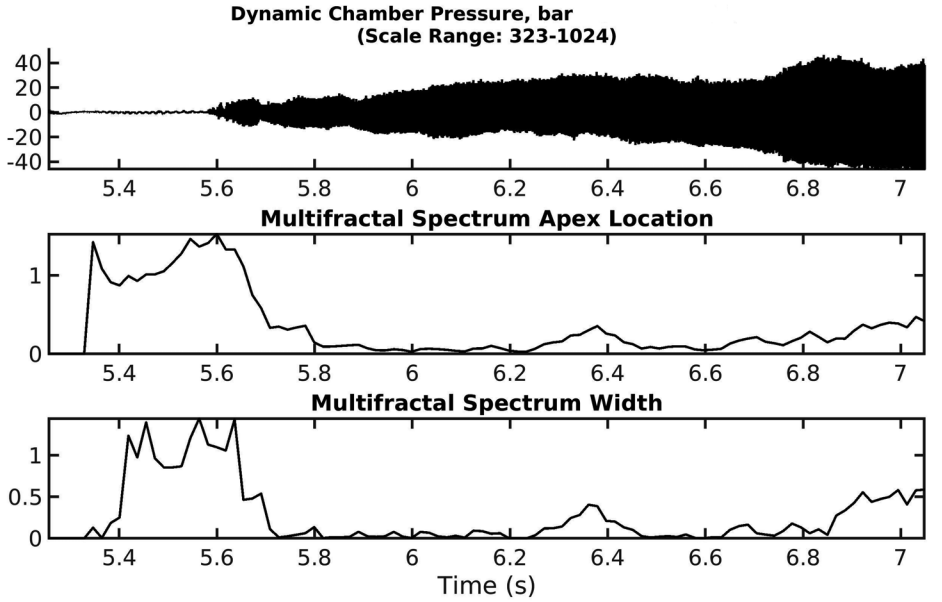

(b)

Figure 4: Apex location and differential height of multifractal spectrum (a) CET1 (b) CET2

The high thrust earth storable engine is found to be stable with no tendency to instability. The low thrust earth storable engine instability was captured in one case but in the other case, the signature is of combustion noise. Classic instability is observed in the unstable tests of the cryogenic engine prior to catastrophic failure. There are indications of a different mechanism for combustion oscillations in CET2 using MFDFA that is not immediately apparent from the pressure trace.

The forewarning time for the onset of instability tends to be almost nil for the hydrogen-oxygen propellant combination. This may be attributed to the high reactivity of the hydrogen-oxygen system.

ISBN - 978-93-95038-50-8

The variation in multifractal spectral characteristics can be used to configure an expert system to trigger a combustion controller before, at, or shortly after the moment of inception of instability. This can prevent expensive loss of hardware. However, further optimization of the MFDFA algorithm is needed to ensure robustness of the active control system.

REFERENCES

1. Kabiraj, L. and Sujith, R. I, "Nonlinear self-excited thermoacoustic oscillations: intermittency and flame blowout". J. Fluid Mech., 2012, Vol. 713, pp. 376-397: doi:10.1017/jfm.2012.463
2. Mandelbrot, and Benoit B., "The fractal geometry of nature, W.H. Freeman, New York, 1983.
3. Mandelbrot, B., "How long is the coast of Britain? Statistical self-similarity and fractional dimension", Science, New Series, 1967, Vol. 156, issue 3775, pp. 636-638. doi:10.1126/science.156.3775.636
4. Hurst, H. E, "Long-term storage capacity of reservoirs". Trans. Am. Soc. Civil Engrs., 1951, Vol. 116, pp. 770–808: doi:10.1061/TACEAT.0006518
5. Frisch, U. and Parisi, G. On the singularity structure of fully developed turbulence in Turbulence and Predictability in Geophysical Fluid Dynamics, North-Holland, 1985. pp. 84-86.
6. Meneveau, C. and Sreenivasan, K., "The multifractal nature of turbulent energy dissipation", J. Fluid Mech., 1991, Vol. 224, pp. 429-484. doi:10.1017/S0022112091001830
7. Gotoda H., Amano M., Miyano T., Ikawa, T., Maki, K. and Tachibana, S, "Characterisation of complexities in combustion instability in a lean premixed gas-turbine model combustor", Chaos, 2012, Vol. 22, issue 4, 043128: doi:10.1063/1.4766589
8. Kolmogorov, A. N, "Dissipation of energy in the locally isotropic turbulence". Dokl. Akad. Nauk SSSR, 1941, Vol. 32, pp. 16–18 (in Russian). Translated into English by Kolmogorov, A. N, Proceedings: Mathematical and Physical Sciences, Vol. 434, issue 1890, Turbulence and Stochastic Process: Kolmogorov's Ideas 50 Years On (Jul. 8, 1991), pp. 15–17.
9. Kantelhardt, J. W., Zschneiger, S.A., Koscielny-Bunde, E., Havlin, S., Bunde, A., and Stanley, H. E, "Multifractal detrended fluctuation analysis of nonstationary time series", 2002, Physica A, Vol. 316, issues 1-4, pp. 87-114. doi:10.1016/S0378-4371(02)01383-3
10. Kantelhardt, J. W. 2011, Fractal and multifractal time series in Mathematics of Complexity and Dynamical Systems,.Springer, 2011. pp. 463–487
11. Ihlen, E. A, "Introduction to multifractal detrended fluctuation analysis in Matlab", Front. Physiol., 2012, Vol. 3, 141: doi:10.3389/fphys.2012.00141
12. Nair, V. and Sujith R. I, "Multifractality in combustion noise: predicting an impending combustion instability", 2014, J. Fluid Mech. Vol. 747, pp. 635-655. doi:10.1017/jfm.2014.171
13. Sujith R. I. and Unni V. R," Complex system approach to investigate and mitigate thermoacoustic instability in turbulent combustors", Phys. Fluids, 2020, Vol. 32, 061401. doi:10.1063/5.0003702
14. Kasthuri, P., Pavithran, I. Pawar, S.A., Sujith, R.I., Gejji, R., and Anderson, W, "Dynamical systems approach to study thermoacoustic transitions in a liquid rocket combustor", Chaos, 2019, Vol. 29, issue 10, 103115. doi:10.1063/1.5120429

Reflection and Review of Fuel Delivery Systems

Sadan Kanchanapalli* and Ramanathan Subramanian

Department of Mechanical Engineering
Maturi Venkata Subba Rao Engineering College (A)
Hyderabad, Telangana, 501510.
Email: sadan.kanchanapalli@gmail.com; ramanathan_mech@mvsrec.edu.in

ABSTRACT

In attempting to keep up with emissions and efficiency forces, the fuel method employed in contemporary automobiles has changed a lot over the past few decades. Fuel solution has been in for decades, and electronic fuel injection was applied widely on European automobiles beginning in 1980s. Today, all automobiles in the world have fuel injection schemes in place for emission control. This paper compares the different fuel delivery systems, explains the working and types of fuel delivery systems currently in use in automobiles and discusses some problems present in the current fuel delivery systems.

Keywords: *fuel efficiency, fuel injection, emissions, fuel delivery systems, performance characteristics.*

1. INTRODUCTION

In the present world, efforts for achieving maximum energy conversion efficiency are being attempted. One of the focus areas in this regard is the design of efficient fuel delivery systems. There has been a transition from carburetors to electronic fuel injection systems in all modern vehicles. The major reason for this transition is the reduction in carbon emissions and higher energy conversion efficiency.

2. CONCEPT OF FUEL INJECTION SYSTEMS

It is the introduction of fuel to the combustion chamber by means of an injector. This is a very crucial step as there should be proper mixing of fuel and air so that the combustion proceeds accurately. After this, the normal cycle of the engine continues. A variety of sensors and controllers were used in the development of electronic fuel injection systems. Together, these electronic components can detect changes, and the main system calculates the correct quantity of fuel required to improve engine performance based on a "map" that is stored of the best settings for a particular set of conditions. This characteristic was absent in mechanical fuel injectors, which gave rise to the electronic fuel injection system. Also fuel injectors do a dual job, they supply fuel as well as do fuel metering. [1]

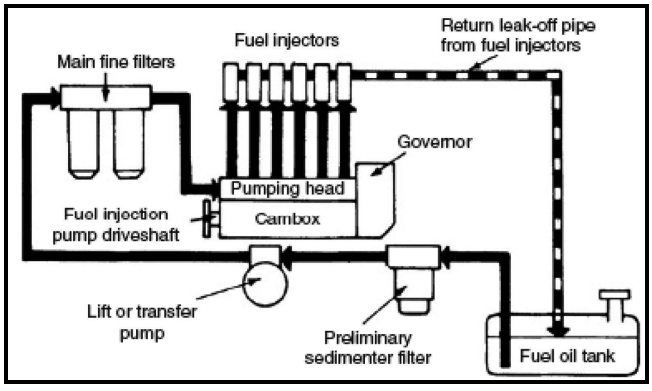

Figure 1: Simple representation of diesel engine fuel injection system

Corresponding Author: Email: sadan.kanchanapalli@gmail.com

The construction of a simple fuel injection type fuel delivery system has been given in Fig.1. [2]

3. TYPES OF FUEL INJECTION SYSTEMS

3.1 Mechanical Fuel Injection Systems

3.1.1. Air injection system

Also known as blast injection system, in this type of injection, the fuel is propelled by using compressed air. It needs an additional compression system for the injection system to work. This causes an increase in the overall weight of the engine, making it more inefficient and reducing brake power output. This system is rarely used these days due to engine weight complications. [5]

3.1.2 Solid injection system:

Also known as airless mechanical injection system, unlike in air injection, liquid fuel is directly injected into the cylinder without the use of an additional compression system. This system is further classified into four different types of injection systems.

- Individual pump and nozzle system,
- Unit injector system,
- Common rail system,
- Distributor system. [2]

3.2 Injection in SI Engine

Fuel injection systems are common in CI engines but not so much in SI engines. Presently gasoline injection systems are becoming more mainstream in SI engines due to the following drawbacks of carburetion. [2]

- Non uniform distribution of the air-fuel mixture in combustion chambers of multi-cylinder engines. [2]
- Loss of Volumetric efficiency. [2]

A gasoline injection system eliminates all these complications. The injection of fuel into an SI engine can be done by the following methods.

a. Direct injection of fuel into the cylinder
b. injection of fuel close to the intake valve
c. injection of fuel into the intake manifold. [2]

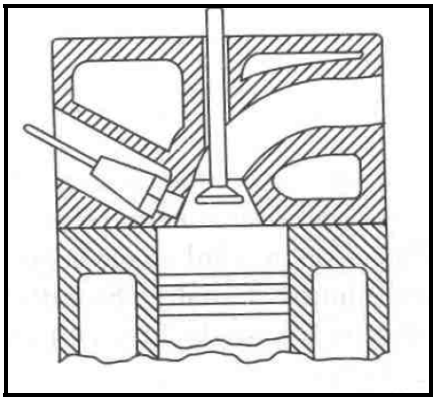

Figure 2(a): Direct injection into the cylinder

ISBN - 978-93-95038-50-8

Figs. 2(a), 2(b) and 2(c) represent the cross-sectional view of Direct injection of fuel into the cylinder, injection of fuel close to the intake valve and injection of fuel into the intake manifold respectively. [2]

3.2.1. Continuous injection systems:

This system includes a rotary pump. The system injects the fuel through a nozzle located in the intake manifold immediately down the throttle plate. The timing and duration of the injection of fuel is determined by the ECU of the engine. [2]

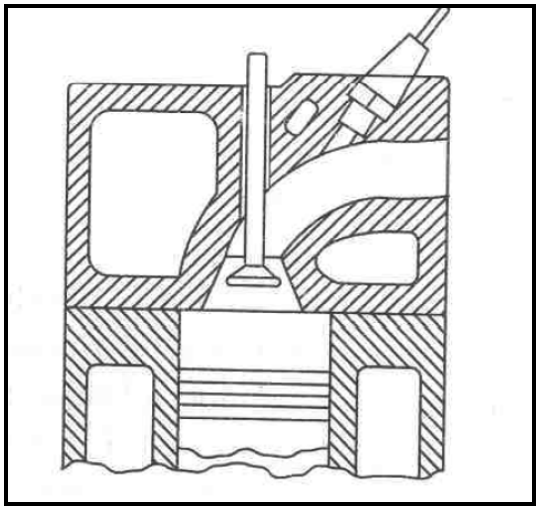

Figure 2(b): Injection of fuel close to the intake valve

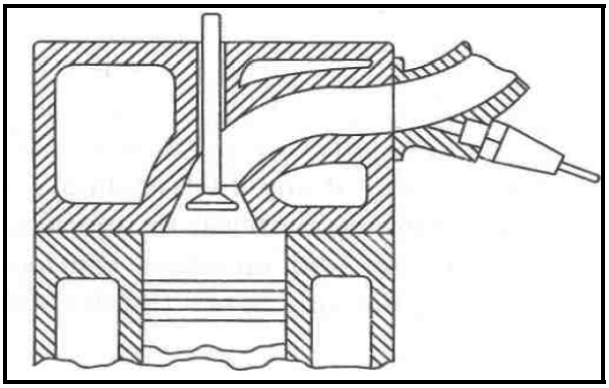

Figure 2(c): Injection of fuel into the intake manifold

3.2.2. Timed injection systems:

This system has a fuel supply pump which sends fuel at a low pressure. An injection pump and a nozzle are the other parts of this injection system. The nozzle injects the fuel into the combustion chamber or the intake manifold at very high pressures. Timed injection systems inject fuel during the early part of the intake stroke. [2]

ISBN - 978-93-95038-50-8

3.3. Electronic Fuel Injection Systems

Modern injection systems use a lot of sophisticated electronic systems which include engine sensors, a computer, and solenoid operates fuel injectors to meter and inject the right amount of fuel into the combustion chambers. These systems called electronic fuel injection (EFI) use electrical and electronic devices to monitor and control engine-operation. An electronic control unit (ECU) uses stored data to operate the injectors and other engine related systems. [2]

3.3.1. Advantages of EFI

- It enhances the volumetric efficiency of the engine.
- Wetting of the manifold is eliminated due to direct fuel injection into the cylinder.
- Good atomization of fuel even when starting the engine makes it easier to start the engine.
- Less knocking occurs due to good atomization of the fuel.
- Forming ice on the throttle plate is eliminated.
- Fuels with low volatile nature can also be used as distribution is not dependent on vaporization of the fuel. [7]

3.3.2. Disadvantages of EFI

- The maintenance cost of EFIs is very high.
- It is very difficult to service the components.
- Malfunctioning of electronic equipment is high.[2]

The fig.3 represents a simple block diagram of an electronic fuel injection system.[7]

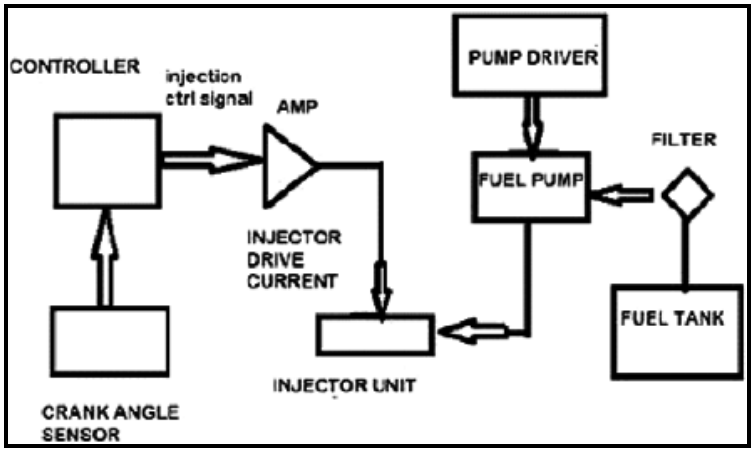

Figure 3: Block diagram of an EFI

3.4. Multi-Point Fuel Injection (MPFI) System

The main purpose of the MPFI system is to supply a proper ratio of the air-fuel mixture of gasoline and air to the combustion chamber. This system works under two basic arrangements, they are.

a. Port injection
b. Throttle body injection [8]

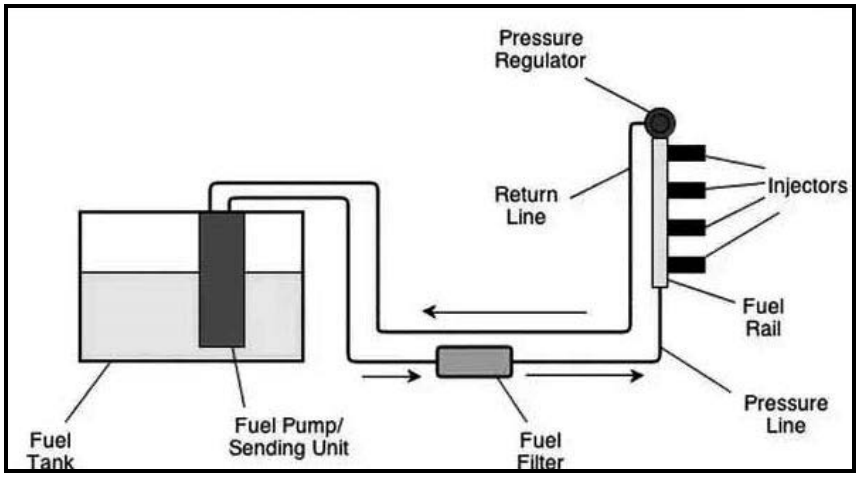

Figure 4: Multi-Point Fuel injection system

Fig. 4 represents the construction of Multi-Point Fuel injection type fuel delivery system.[9]

3.4.1. Central Port Injection System

Instead of using the central throttle body, General Motors created an 'in-between' method called central port fuel injection (CPFI), which uses tubes from a central injector to spray fuel at each intake port. However, all ports are simultaneously continually fed with fuel, which is not ideal. The standard multi-port injection system is very similar to this technology. The injector(s) are centrally located in the intake manifold plenum assembly as opposed to being placed at each intake manifold port. [4]

3.5. Comparision of Different Fuel Delivery Systems

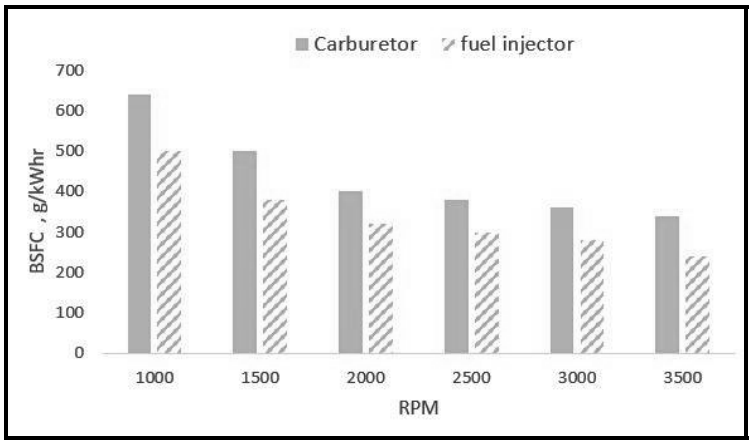

Figure 5: Variation of BSFC with respect to RPM in carburettor and EFI

Fig. 5 compares the BSFC of an engine with respect to the RPM of the engine. [6]
It is observed that the BSFC of the carburetor type of fuel delivery system is around 30-40% higher than that of the fuel injection type fuel delivery system.

ISBN - 978-93-95038-50-8

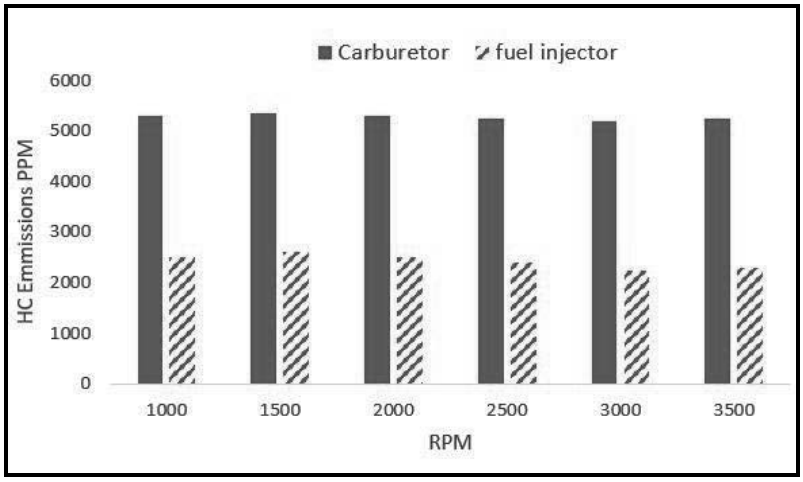

Figure 6: Variation of HC Emission with carburettor and fuel-injector

Fig. 6 compares the HC emission of an engine with respect to the RPM of the engine. [6] It is observed that the HC emissions of the carburettor type of fuel delivery system are 50-60% higher than that of the fuel injection type fuel delivery system.

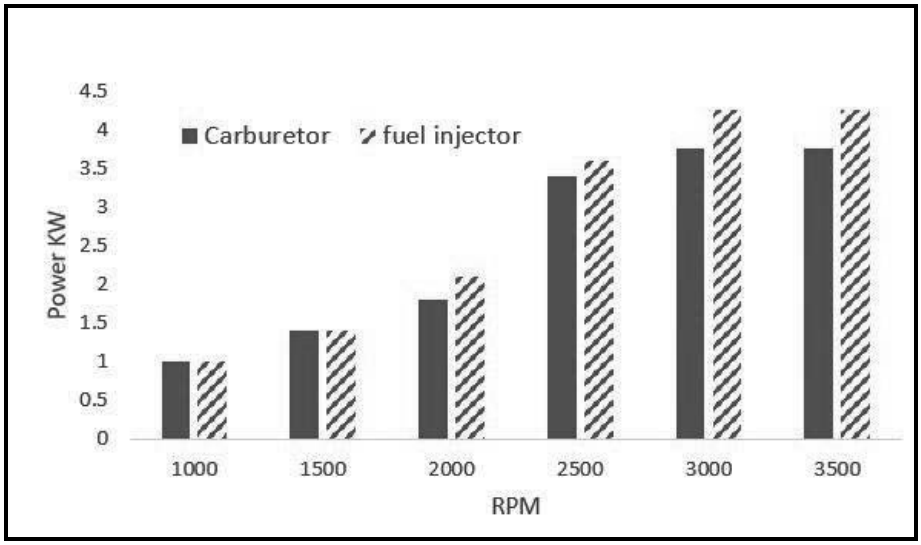

Figure 7: Variation of RPM with respective to power

Fig. 7 compares the output power of an engine with respect to the RPM of the engine. [6] It is observed that the power generated by the carburettor type of fuel delivery system is on average 8-12% lower than that of the fuel injection type fuel delivery system.

ISBN - 978-93-95038-50-8

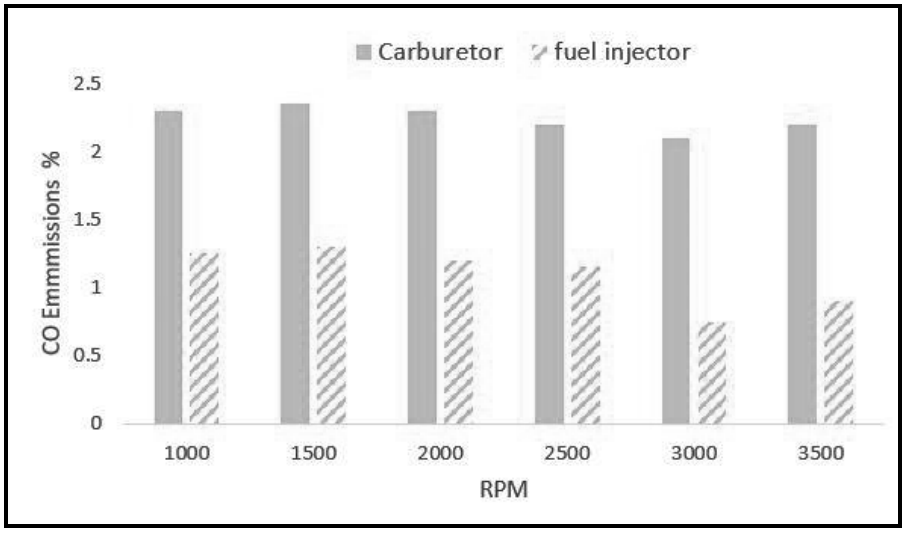

Figure 8: Variation of CO emission with respective to RPM

Fig. 8 compares the CO emissions of an engine with respect to the RPM of the engine. [6] It is observed that the CO emissions of the carburettor type of fuel delivery system are 80-120% higher than that of the fuel injection type fuel delivery system.

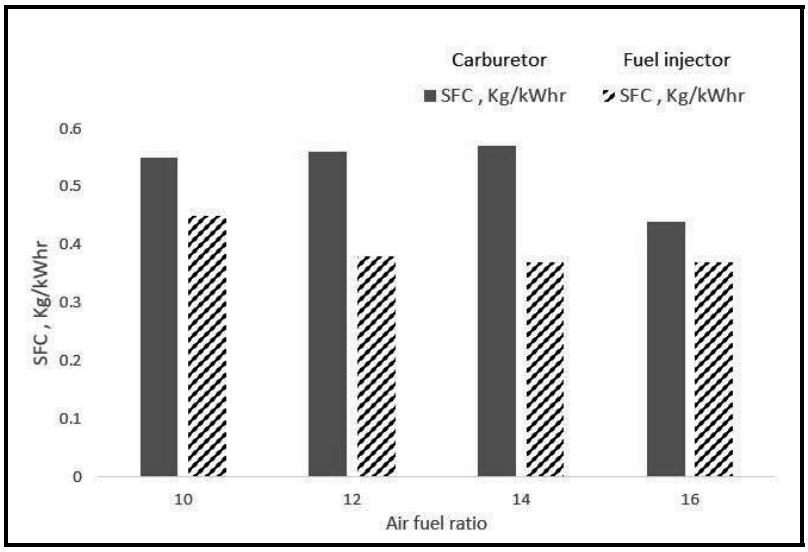

Figure 9: Difference in Specific Fuel Consumption (SFC) with respect to Air-Fuel ratio.

Fig. 9 compares the SFC of an engine with respect to the air fuel ratio input to the engine. [6]. It is observed that the SFC of the carburettor type of fuel delivery system is on average 20-50% higher than that of the fuel injection type fuel delivery system.

- Typically, gasoline engines for two-wheelers use carburettors. Even if we attain optimal performance, it is always difficult to monitor the intake of air-fuel mixture into the cylinder chamber. Due to this, there have been more exhaust emissions and the engine does not last long. Since fuel injection systems accurately determine the intake air-fuel mixture and have lower emission levels while maintaining consistent engine performance, they became more popular and good carburettor alternatives. The difference between direct injection and port injection can be determined depending on

ISBN - 978-93-95038-50-8

where the fuel injection is positioned. Direct Injection is more efficient in terms of combustion, improved fuel economy, and reduced emissions.

- Placement of fuel injection can tell the differences between a port injection and direct injection, the latter is more efficient in terms of combustion, increases fuel economy and lowers emissions. The only drawback with Gasoline Direct Injection (GDI) is that it develops a form of a deposit from oil and dirt particles that are blasted from the crankcase ventilation in the opposite direction and deposit on the walls of the inlet valve opening and the inlet valve's backside.
- A single-point injection system is a modified carburettor that optimizes the customer's driving performance while simultaneously reducing exhaust emissions.
- The development of a multi-point injection system allows the air-fuel combination to be precisely injected at a chosen location within the cylinder chamber, increasing fuel efficiency without wasting any and further lowering emissions compared to single-point injection. [6]

3.6. Why EFI are better than MFI

EFI is efficient and offers the control versatility needed for the optimum overall engine performance. EFI offers superior pollution control. The usage of an EFI system enhances atomization, which results in significant increase in the quality of the combustion of fuel. [12]

The two fundamental improvements are:

1. Reduced response time to rapidly changing inputs, e.g., rapid throttle movements.
2. Delivery of an accurate and equal mass of fuel to each cylinder of the engine, dramatically improving the cylinder-to-cylinder distribution of the engine. [12]

3.7. Performance Comparision for Single Point Fuel Injection (SPFI) and Multi Point Fuel Injection (MPFI)

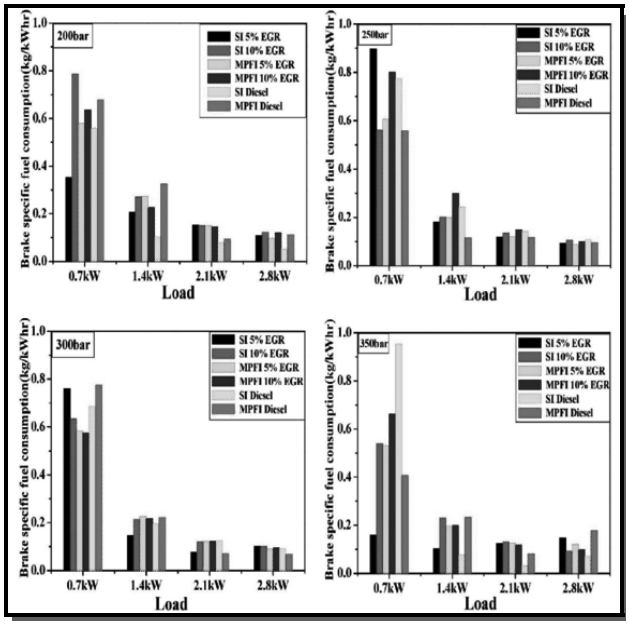

Figure 10: BSFC of SI* (SPFI) and MPFI diesel combustion at varying injection pressures for different EGR conditions.

Fig. 10 compares the BSFC of an engine with the load on the engine at different Injection Pressures. [10]

It is observed that the BSFC of the MPFI System is lower at 250-300 bar Injection Pressure but at lower injection pressure of 200 bar, but SI* (SPFI) at a higher injection pressure of 350 bar at higher power loads with very low BSFC compared to MPFI.

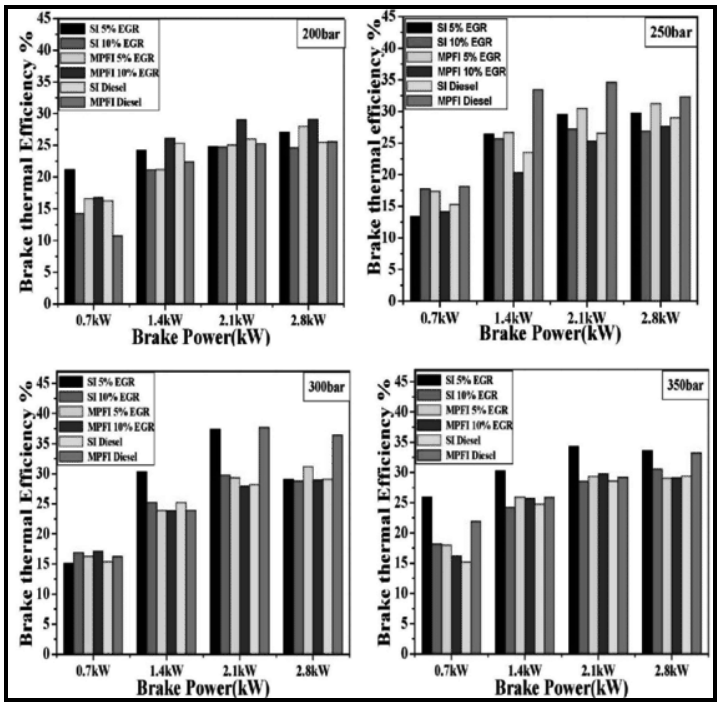

Figure 11: Brake thermal Efficiency of SI* (SPFI) and MPFI diesel combustion at varying injection pressures for different EGR conditions.

Fig. 11 compares the BTE of an engine with the Load on the engine at different Injection Pressures. [10]

It's observed that the BTE of the MPFI System is higher on average when compared to the SI* system.

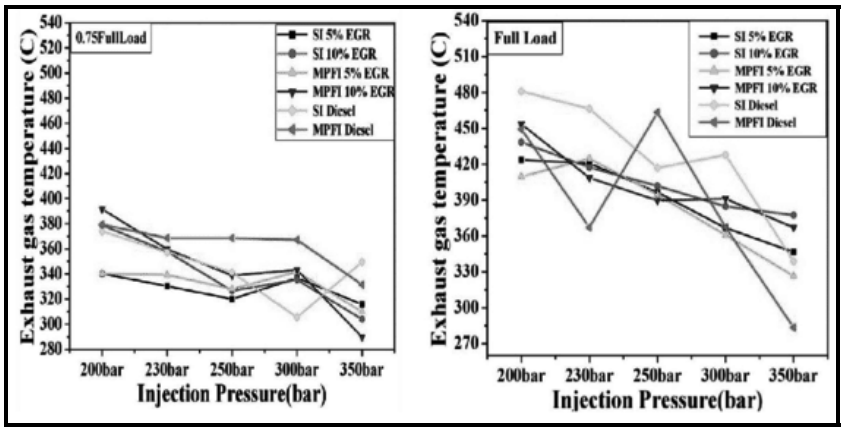

Figure 12: Exhaust gas temperature of SI* and MPFI diesel combustion at varying injection pressures for different EGR conditions.

ISBN - 978-93-95038-50-8

Fig. 12 compares the Exhaust Gas Temperature of an engine with the Injection Pressure. It is observed that the Exhaust gas temperature is an anomaly against injection pressure. [10]

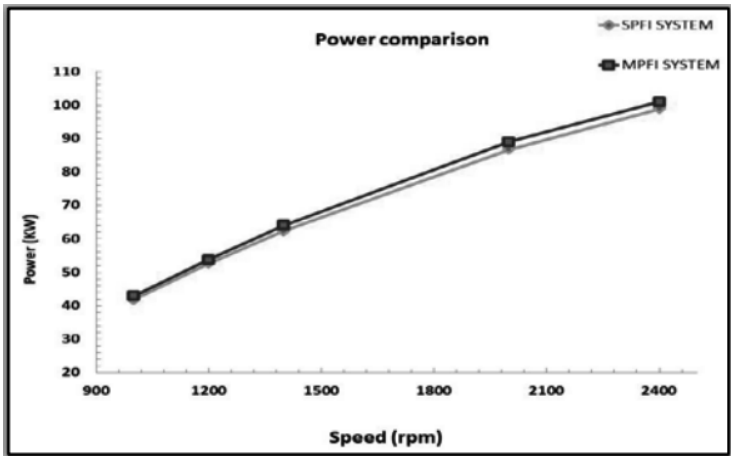

Figure 13: Power Comparison of SPFI and MPFI Systems

Fig. 13 compares the Power of an engine with the RPM of the engine. [10]

It is observed that the MPFI system delivers 3-5% higher power for the same speed compared to that of SPFI system with the same engine characteristics.

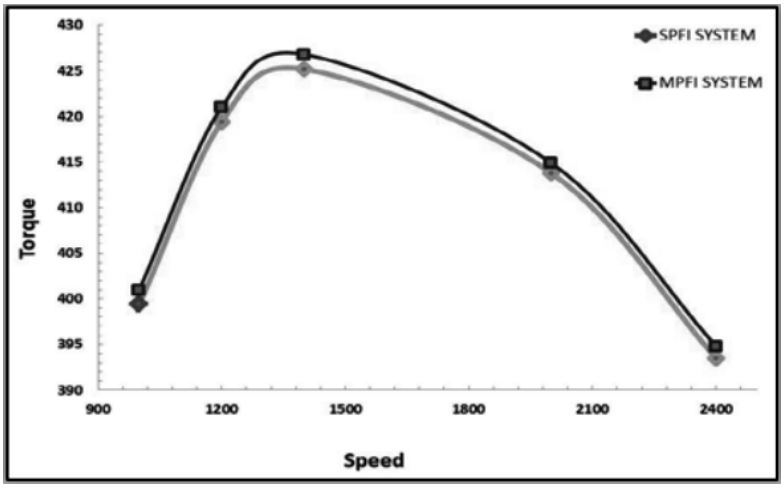

Figure 14: Torque comparison of SPFI and MPFI Systems

Fig. 14 compares the Torque output of an engine with the RPM of the engine. [11]

It is observed that the MPFI system delivers 0.5-0.7% higher torque for the same speed compared to that of SPFI system with the same engine characteristics.

3.8. Problems with Current Fuel Delivery Systems

1. The issue with this system is that because the timing is still mechanically determined by the camshaft and the injection is done into the inlet valve, some fuel does not get into the combustion chamber when the inlet valve opens. This issue affects not only this system but every other system that has been studied in the past. This is since all of them use indirect injection systems.

ISBN - 978-93-95038-50-8

2. Other issues with indirect injection include spontaneous ignition, that also affects electronic injection systems using indirect injection commonly. Therefore, the Multipoint Injection System with Direct Injection was designed to tackle these issues.
3. A direct injection engine's downsides are its complexity and price. Because direct injection systems handle fuel at much greater pressures than indirect injection systems, and because the injectors themselves must be able to withstand the heat and pressure of combustion inside the cylinder, direct injection systems are more expensive to build. [14]

4. Results and Discussions

Table 1: Subjective comparison of characteristics of different fuel delivery systems

Fuel Delivery System	Maintenance Cost	Ease of Manufacturing	Fuel Efficiency	Emissions	SFC
Carburettor	Lower	Easy	Lower	Higher	Higher
SPFI	Higher	Complicated	Higher than Carburettor	Lower than Carburettor	Lower than Carburettor
MPFI	Higher	Complicated	Higher than SFI	Lower than SFI	Lower than SFI
EFI	Higher	Complicated	Higher than MPFI	Lower than MPFI	Lower than MPFI

Table 1 compares the maintenance, ease of manufacturing, fuel efficiency and their emissions of different fuel delivery systems. It is observed that though the carburettor has lower fuel efficiency and higher emissions, it is still widely used in two-wheeler vehicles for its ease of manufacturing and low maintenance cost. Fuel Injection type fuel delivery systems are widely used in LCVs and HCVs as they have lower emissions and higher fuel efficiency even though they are complicated to manufacture and have higher maintenance than that of a regular carburettor type fuel delivery system.

5. Conclusions

With the increase in emissions, the quest for more efficient technologies is more prominent. Systems such as common rail systems are highly used for more efficiency. Injection of fuels at high pressure into the combustion chamber is going to be a lot more efficient. These systems are going to increase efficiency a lot and help in the control of emissions and in maintaining emission standards. If the above factors discussed in table 1 are addressed, there can be considerable improvement in fuel delivery systems, energy conversion efficiency and reduction in cost.

6. Acknowledgments

Valuable guidance and support from Mr. Miskin Ravi Kumar from the Mechanical Engineering Department and Mr. R. Pranav from Automobile Engineering Department of MVSREC are gratefully acknowledged.

7. REFERENCES

1. Shreyansi Gupta, Anuj Patidar, "A Review on Fuel Injection System", International Research Journal of Engineering and Technology (IRJET) Volume 07 Issue: 08 , August 2020. <https://www.irjet.net/archives/V7/i8/IRJET-V7I858.pdf>
2. V Ganesan, "Textbook of Internal Combustion Engines Fourth Edition" , 4th Edition (2012) , Tata McGraw Hill Education Private Limited, New Delhi, India.
3. Mustaffa, Hamizan. (2016). Mechanical System Design, Development of Fuel Injection System on Single Cylinder Internal Combustion.
4. Malleboyena Mastanaiah, "PERFORMANCE OF ELECTRONIC FUEL INJECTION SYSTEM USING COMPRESSOR AND CONTROLLER": IJAERS/Vol.II/ Issue III/April-June., 2013/57-59
5. Sundar , "The Classification of Injection system | Types of Injection Systems" published on 7 April , 2019. <https://extrudesign.com/classification-of-injection-system/>
6. K Venkata Mohan Krishna Reddy *et al* 2021 *IOP Conf. Ser.: Mater. Sci. Eng.* **1116** 012073 **DOI:** 10.1088/1757-899X/1116/1/012073
7. Performance and emission of a single cylinder di diesel engine operating on various parameters using diestrol at EFI system - Scientific Figure on ResearchGate. Available from: https://www.researchgate.net/figure/Block-diagram-of-Electronic-Fuel-Injection-EFI-system_fig1_305720375
8. Rini , "Electronic Fuel Injection System (EFI) – Architecture, Types, Applications" <https://electricalfundablog.com/electronic-fuel-injection-system-efi/>
9. InnovationDiscoveries, 20 January, 2021. <https://innovationdiscoveries.space/what-is-multiple-point-fuel-injectionmpfi/>
10. Edara, Gautam & Murthy, Y.V.V. & Nayar, Jayashri & Ramesh, Merigala & Srinivas, Paleti. (2019). Combustion analysis of modified light duty diesel engine under high pressure split injections with cooled EGR. Engineering Science and Technology, an International Journal. 22. 10.1016/j.jestch.2019.01.013. Gawali, S V; Dadas, K N. Annals of the Faculty of Engineering Hunedoara; Hunedoara Vol. 19, Iss. 3, (Aug 2021): 69-72.
11. Gopal Sahu, R. K. K. P. K. S. (2015). A Study on Advance Electronic Fuel Injection System. *International Journal of Scientific Research and Management*, *3*(10), 3608–3613. Retrieved from <https://www.ijsrm.in/index.php/ijsrm/article/view/268>
12. Pham, Van Viet & Thiep, Cao. (2019). A brief review of technology solutions on fuel injection system of diesel engine to increase the power and reduce environmental pollution. Journal of Mechanical Engineering Research and Developments. 42. 01-09. 10.26480/jmerd.01.2019.01.09.
13. Multipoint Fuel Injection System Ishant Gupta, Shweta Kandari, Arvind Rajput, Mohd Asif, Anand Singh Department of Mechanical Engineering Dronacharya College of Engineering Mahamaya Technical University, Noida : International Journal of Engineering Research & Technology (IJERT) Vol. 2 Issue 11, November - 2013 ISSN: 2278-0181
14. N D Petrea and C Bujoreanu 2018 IOP Conf. Ser.: Mater. Sci. Eng. 444 042020
15. Mustaffa, Hamizan & Abu Hassan, Muhammad & Masri, Muhammad & Bin Rusli, Muhammad & Mohamad, Fathi. (2016). DEVELOPMENT OF FUEL INJECTION SYSTEM ON SINGLE CYLINDER INTERNAL COMBUSTION ENGINE. 10.13140/RG.2.1.3071.3201.

Realization of Integrated Data Acquisition for Testing of Human Rated GAGANYAAN Vikas Engine

Priya Esther*, Vineeth Marella, Ethamukkala Bala Krishna, Vinoth B, Gilbert Chandra and Murugananda Bhaskaran

[1]Sci/Engr SE, [2]Sci/Engr SD, Sr, [3]Tech Asst, [4]Deputy Manager, [5]Manager and [6]Dy. Director
ISRO Propulsion Complex, ISRO, Mahendragiri, Tirunelveli, Tamilnadu, Pin-627133, India
Email: priyaesther@iprc.gov.in / vineeth@iprc.gov.in

ABSTRACT

The L110 VIKAS engine certification testing for the Gaganyaan program, comprised of three long duration qualification tests and four short-duration off nominal tests. The Test Article (The GAGANYAAN Vikas Engine) measurement system comprises of Process Measurements namely Pressure, Temperature, Strain, Speed, and Vibration. Erstwhile Test Article measurement system used individual Signal Conditioning Amplifiers, Excitation Power supplies, and the Data Acquisition system using The PCI Extension for Instrumentation (PXI- Data Acquisition system)

The revamping of the Test Article Measurement System in the Principal Test Stand control centre - was carried out by inducting the state-of art Integrated Data Acquisition systems (IDAS) with inbuilt excitation modules, Sigma delta ADCs thereby replacing the old signal conditioning modules and excitation modules. The induction of the IDAS was pivotal in ensuring accurate and precise measurements required in the GAGANYAAN ground testing. The paper elucidates the arduous Testing of the IDAS and the various Hot Test results of the GAGANYAAN Engine Test Series.

1. INTRODUCTION

"That's one small step for a man, one giant leap for the mankind", is what is Neil Armstrong quoted on his team landing on the moon. India from its humble beginnings of ISRO has come a long way in competing with the space faring club and to prove its mettle, it has launched the ambitious GAGANYAAN program with an aim of launching Humans into the space. As a part of qualifying the various subsystems of the Human Rated Rocket, major Engines, crew modules were tested in IPRC, Mahendragiri. Being the maiden attempt of ISRO, in launching Humans in the space, extra precautions and module testing and qualification tests are carried for various stages of the Rocket.

As a part of the qualification program of GAGAYAAN, the High Thrust VIKAS engine was tested in the High Pressure mode to ensure the margin availability and to satisfy the SMC box criteria. Testing of complex system includes various aspects of engineering, like testing of the Propulsion system, control system, electromechanical actuators (EMA) with quadruple redundancy.

As part of the L110 VIKAS engine certification testing for GAGANYAAN program, three long duration qualification tests and four short duration off nominal tests were planned based on SMC-S-025 standard as tabulated below.

The various parameters of the Human Rated GANYAAN VIKAS Engine consist of measurements like pressure, temperature, vibration, heat flux and acoustic measurements. Precision, accuracy and a High CMRR were critical in the test data measurements and the inaccuracy for the Pressure measurement chain is maintained within 1% of the Full scale including the sensor error of 0.7% for the 21 NA sensors used.

*Corresponding author: E-mail: priyaesther@iprc.gov.in

Test	Hardware	Pc, bar	MR	Duration	Criterion
HS - 1	H/W1	58.5	1.7	1.2x T_{nom} = 240s	• 1.2x T_{nom} on 4 engines. [HT3, HS-1, HS-2, HS-3 will meet the requirement]
HS – 2	H/W2	58.5	1.7	1.2x T_{nom} = 240s	
HS – 3	H/W3	58.5	1.7	1.2x T_{nom} = 240s	
HS – 4	H/W4	60.2 bar (+2%)	1.768 (+4%)	25	Thrust and MR margin demonstration with margin of 2%
HS – 5		56.80 bar (-2%)	1.632 (-4%)	25	
HS – 6		60.2 bar (+2%)	1.632 (-4%)	25	
HS - 7		56.80 bar (-2%)	1.768 (+4%)	25	

Figure 1: The various Hot Tests in the GAAGNYAAN program

Figure 2: The VIKAS Hot Test in the GAAGNYAAN program

2. TEST ARTICLE MEASUREMENT AND DATA ACQUISITION SYSTEM

The Principal Test Stand being one of the oldest Control centre's of ISRO, the erstwhile Test article measurement system comprised of independent signal conditioning modules, separate excitation source and the data was acquired in the PXI system.

GAGANYAAN test requirements were critical and to ensure the required accuracy class, the state of art Integrated Data Acquisition System in which the sensor excitation, signal conditioning unit, and Data Acquisition System are incorporated into a single chassis was inducted and elaborate tests were carried out. The total channel capacity of the IDAS is 260 channels.

Figure 3: The Integrated Data Acquisition system (IDAS)

IDAS comprised of pressure, temperature, vibration, modules of make Dewesoft. The various systems of Dewesoft module were synchronized by the proprietary IRIG-B

ISBN - 978-93-95038-50-8

synchronization scheme and were grounded to a separate Instrumentation ground system which is maintained at 1 ohm Ground resistance which is achieved by using special grounding Techniques.

The merits of the IDAS were that it has new technologies like dual Core Sigma Delta ADC (High Dynamic: up to 160 dB, new technology), has a CMRR of 110 dB, good excitation stability and the excitation accuracy is ±0.05 %, and has isolation voltage of 1000 V rms. The input impedance is 10 Mohm. The modules generates the excitation required for the 21 NA pressure sensors (upto 15 V, 40 mA can be provided by the IDAS).

The sampling rate can also varied from 100 samples per second to 200 kS/s as per the need. The filter settings can also be defined as per the requirement and Digital Filter: Upto 8 pole Bessel/Butterworth/Chebyshev low pass filters are configurable through the software

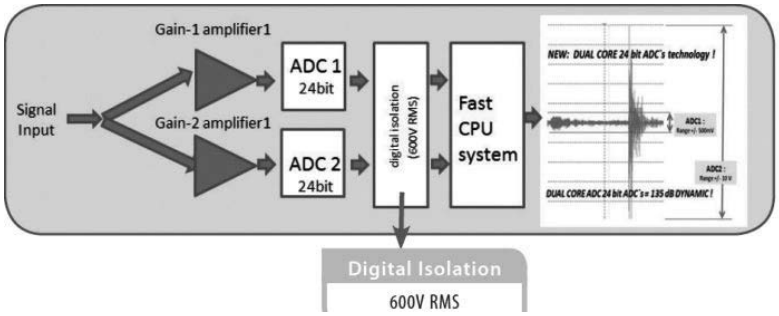

Figure 4: The Dual Core ADC of the (IDAS)

DUAL CORE ADC technology (Fig iii) always gives the full possible measuring range, because the signal is measured with a high and a low gain at the same time. The data acquisition modules are isolated (Fig 2) between themselves and the main board.

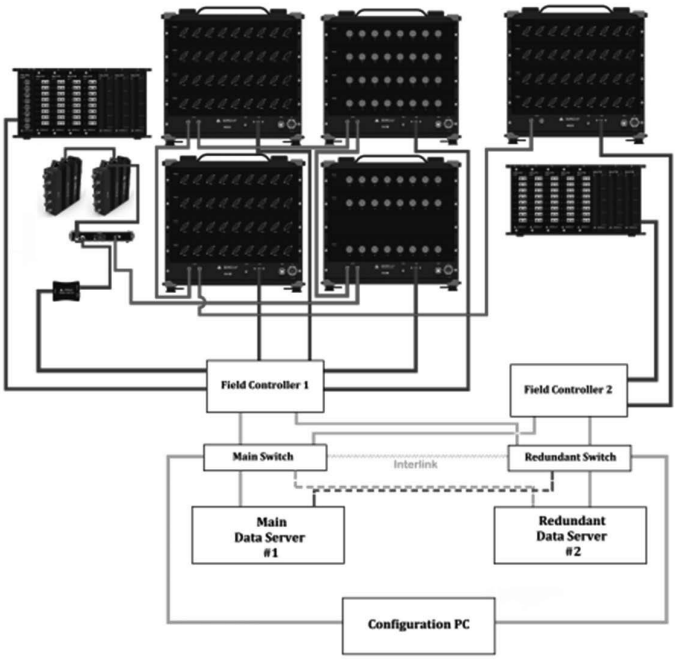

Figure 5: The configuration of the IDAS

ISBN - 978-93-95038-50-8

3. PRESSURE MEASUREMENT SYTEM

Pressure measurement is crucial as it directly relates to performance of Engine and also the Chamber Pressure is also an Abort parameter. Chamber pressure of engines is one of the critical measurement aspects, as it will be used to calculate thrust, analyze performance stability. In the GAGNYAAN engine tests, 4 numbers of Chamber pressure measurements were taken to ensure the redundancy in the measurements.

The following figures show the chamber pressure plots of the 4 tests in which the margin variation of the Chamber pressure and the mixture ratio were varied.

In all the conditions of MR variation and the Chamber Pressure variations, the engine was stable.

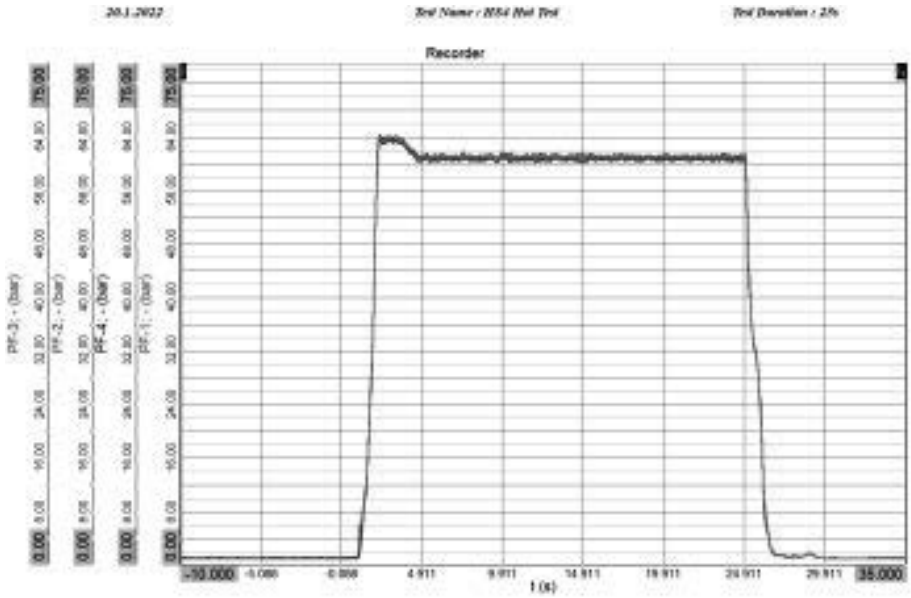

Figure 6 HS4 Chamber Pressure

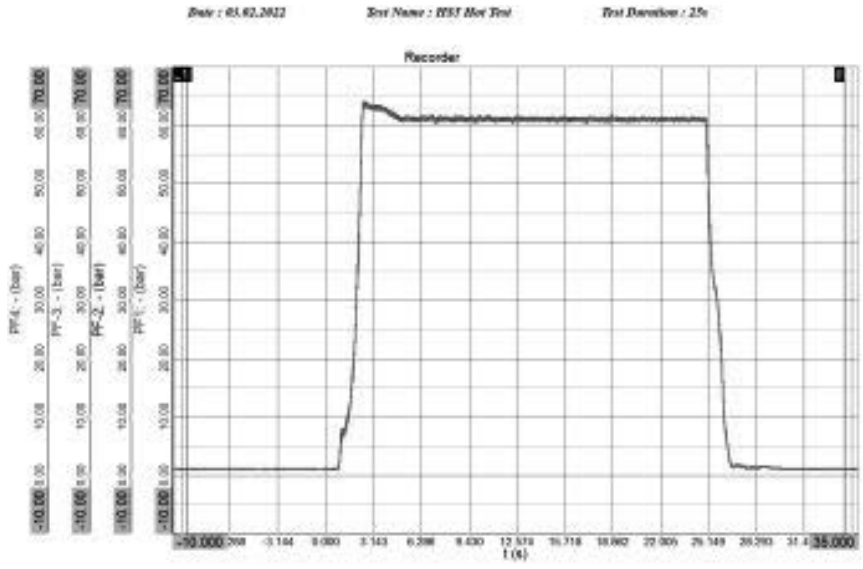

Figure 7 HS5 Chamber Pressure

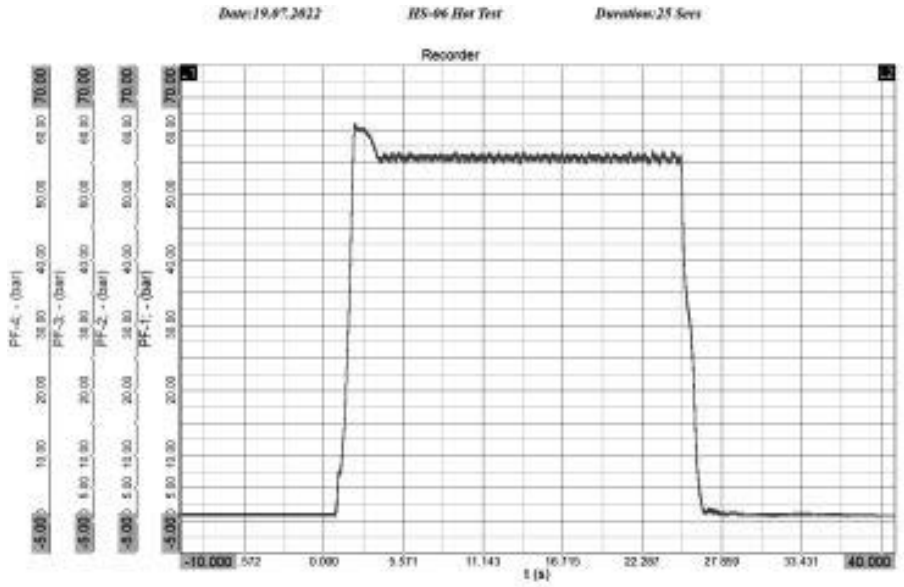

Figure 8 HS6 Chamber Pressure

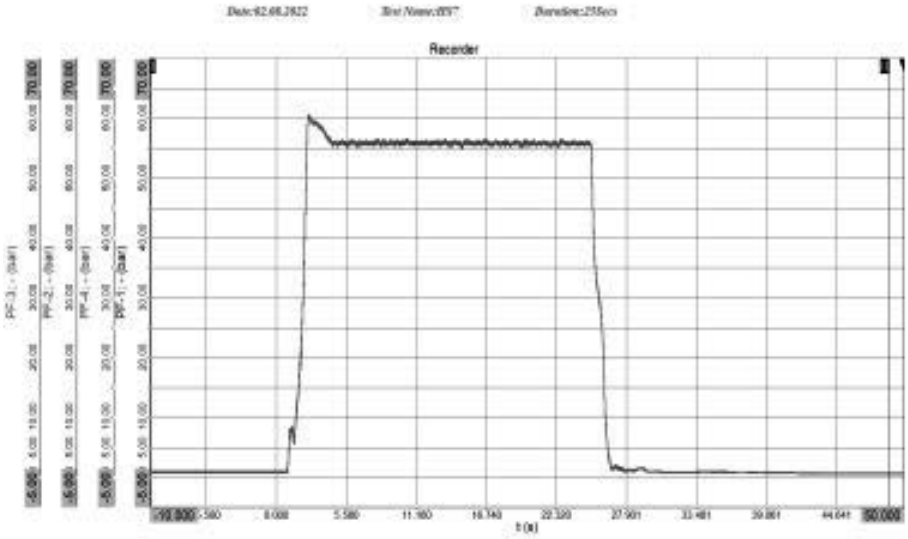

Figure 9 HS7 Chamber Pressure

4. TEMPERATURE MEASUREMENT SYSTEM

The Temperature across various parts of the engine namely the Thrust Chamber, Throat, Gas generator, etc are measured using K type thermocouple and the Data Acquisition system of make Dewsoft and IOLITE module is used for acquiring the data at 100 Samples per second.

The IOLITE Module has a real time controller and has additional add-on feature of storing the Data in the module.

The throat back wall Temperature TCH3A, B, C, TCH4 A, B, C and TCH 5A, B, C measurements are critical ins ascertaining the health of the throat. In the event of gas entry because of throat peel off, a sudden raise in the Temperatures 3A, 4A and 5 A will be observed.

ISBN - 978-93-95038-50-8

Similarly, Temperatures in the Gas Generator (GG) namely TGAT (Inlet Temperature) and TGST (Outlet Temperature) are crucial parameters and also are abort parameters. In the GAGANYAAN Engines, the redundancy of TGAT and TGST is ensured by having two measurements (TGAT1, 2 and TGST1, 2) respectively.

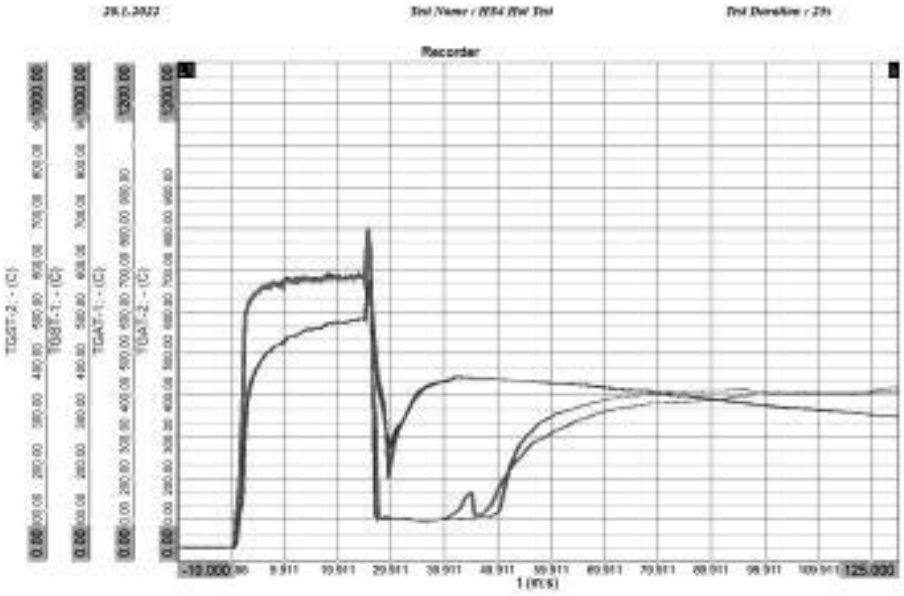

Figure 10 The Gas Generator Temperatures

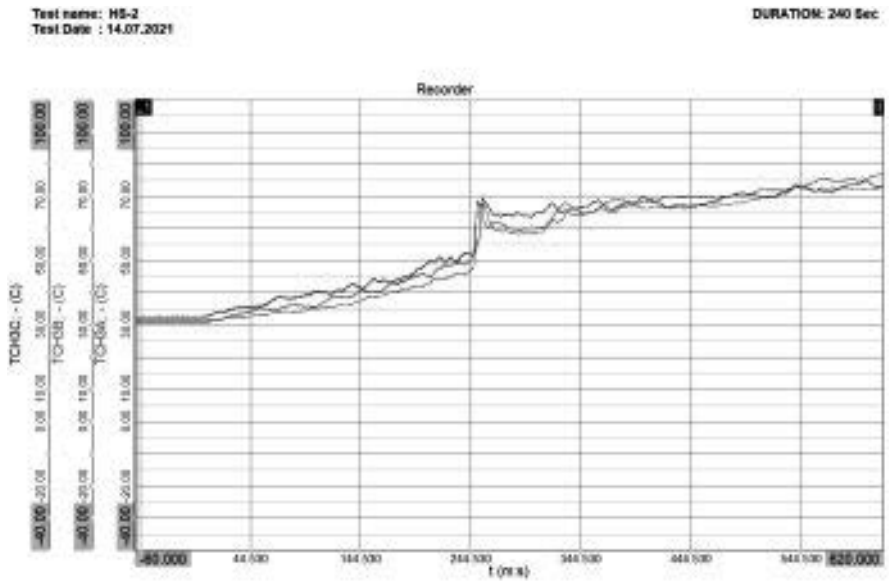

Figure 11 The Temperature plot for Long duration Test of 240 seconds

5. VIBRATION MEASUREMENT SYSTEM

The Vibration measurement of 32 channels with inbuilt excitation of 24 V was realized for ICP sensors mounted on the Engine at critical locations like the Turbo pump N204 side, UH25 side, Water Pump, Injection cover etc. The data of the vibration is acquired at 50kS/s and the post processing is done with MATLAB 3D FFT plots in which the various frequencies that are excited during the Hot Test can be studied.

ISBN - 978-93-95038-50-8

Amplitudes of critical frequencies in dynamic chamber pressure measurement and injector cover vibration are within the acceptable level indicating stability of the engine at the tested off nominal condition.

In the injector acceptance testing of the VIKAS engines, the dynamic pressure of the Engine is also measured and ensured that it is within the specification of 0.5%

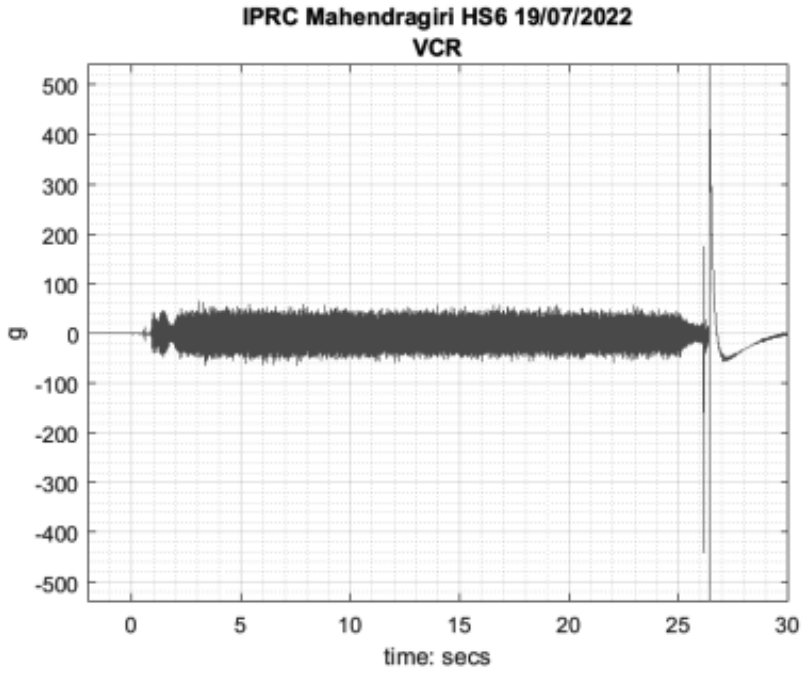

Figure 12 Injection Cover Vibration plot

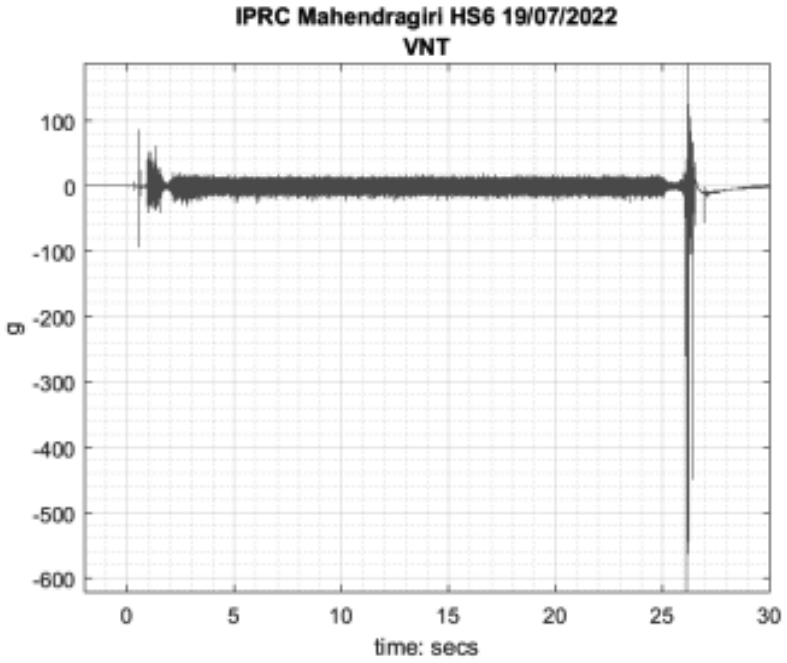

Figure 13 N pump Vibrations

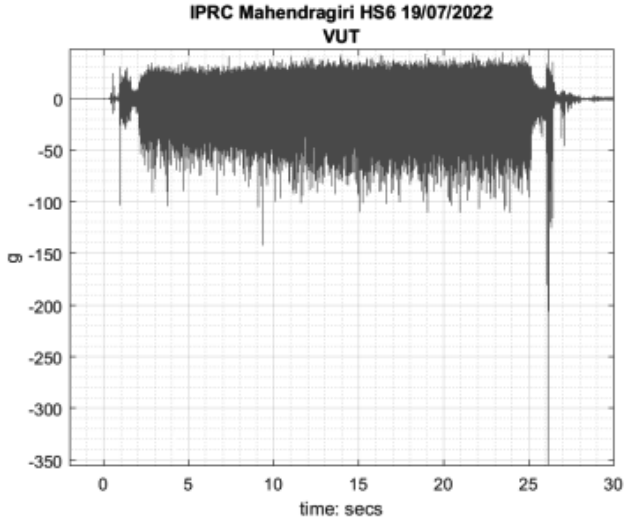

Figure 14 U pump Vibrations

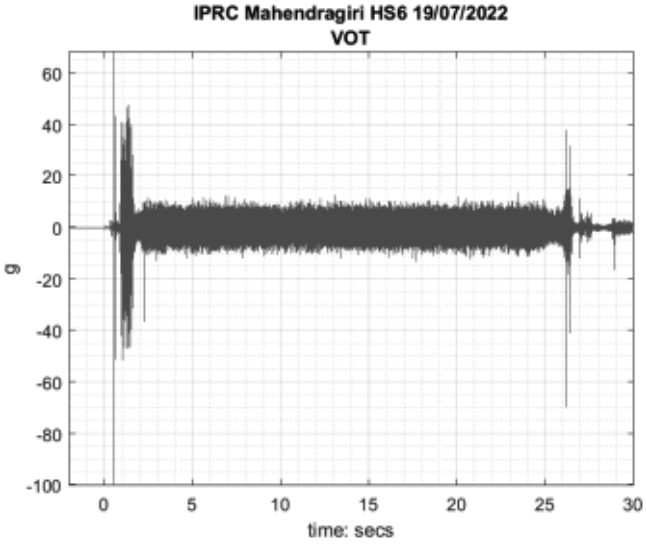

Figure 15 Water pump Vibrations

6. TESTS DONE FOR COMMISIONING THE IDAS

Various tests were carried out to assess the IDAS system and validate for inducting it for the hot test. Following tests are carried out.

Sl No	Name of Test	Sl No	Name of Test
1.1	Input Accuracy	1.2	Linearity
2.1	Gain accuracy	2.2	Gain linearity
3.1	CMRR	3.2	Cross talk
4.1	Filter response	4.2	Input noise
5.1	Input saturation	5.2	Stability
6.1	Signal delay between AI to AO	6.2	Time accuracy
7.1	Analog output availability check	7.2	Data display check

A few test procedures are elaborated below:

ISBN - 978-93-95038-50-8

6.1 INPUT ACCURACY

- Input accuracy test is carried out to determine the input accuracy of channels.
- This is done by feeding DC voltage signals in steps from high precision calibrated DC source (Yokogawa GS200) to selected channels; this input data is acquired by the system and accuracy is calculated.
- To ensure precision of the source, a 6-digit Digital Multi-meter is used to measure source output. This test is done for several input ranges.

6.2 LINEARITY

It is the proportionality between the input and measurement of the instrument. It is critical that the device has a linear response. The procedure followed:-

- DC inputs are fed to the randomly selected channels (in linear steps) from a high precision DC calibrator.
- The inputs are measured using a six and a half digit digital multi-meter (DMM).
- This is done for different input ranges (±1V & ±10V) of the module.
- The linearity is calculated and results are tabulated below.

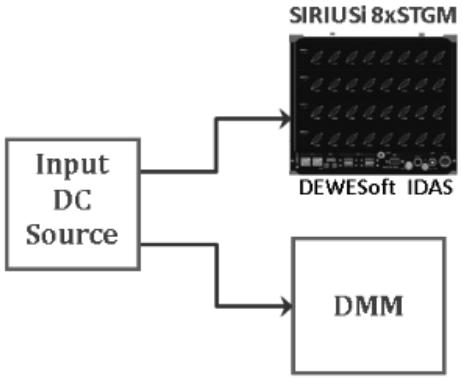

Figure 16

6.3 GAIN ACCURACY

The Sirius STGM module does not have multiple input gains. It only has unity gain with different input ranges viz. 10mV, 100 mV, 1V & 10V. Gain accuracy is measured for selected channels for different input ranges.

- Input, based on selected range, is fed using Yokogawa DC source to the selected channels.
- Applied input is acquired in IDAS and also measured using 61/2 digit multi-meter (DMM).
- Gain accuracy is calculated using following formula;
  - Gain =Input acquired by IDAS/input measured by DMM.
  - Input Gain accuracy= (1-Gain)*100.
- Gain accuracy is measured for all four input ranges.

ISBN - 978-93-95038-50-8

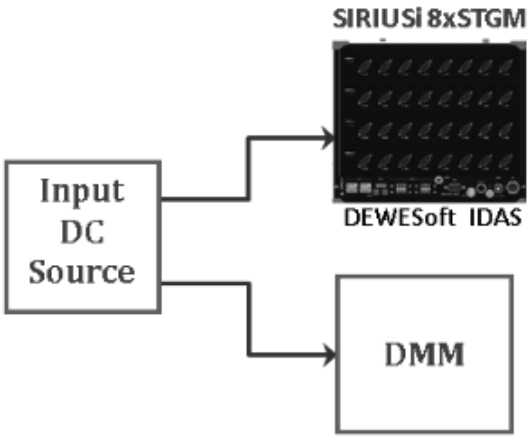

Figure 17

6.4 COMMON MODE REJECTION RATION (CMRR)

CMRR is the metric used to quantify the ability of differential amplifier to reject the common mode voltage signals. It is essential that the device has a high CMRR. This facilitates the rejection of any interference noise in the measurement chain. The detailed test procedure is described below:

- This includes measurement of two gains i.e. Common Gain & differential gain.
- For this two DC sources of same make and model are used to feed input.
- The positive terminals of both the DC sources are connected to two differential input terminals of the amplifier, whereas the negative terminals of both sources are shorted together and connected to the input ground terminal.
- Using both the sources differential and common voltage inputs are fed to the IDAS system. DMM is used to accurately measure the input.
- Following formulae are used to measure the CMRR.
- -Common mode gain (Ac) =IDAS reading/Common mode input.
- -Differential gain (Ad) =IDAS reading/Differential input.
- -CMRR=20log (Ad/Ac).
- CMRR is measured for all the input ranges.

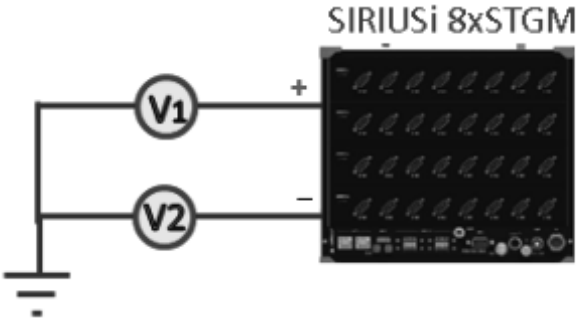

Figure 18 Block diagram of CMRR differential mode

ISBN - 978-93-95038-50-8

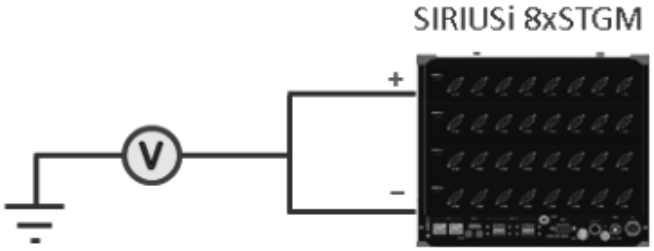

Figure 19 Block diagram of CMRR common mode

6.5 CROSSTALK

Crosstalk is a phenomenon in which a signal fed to a channel gets interfered with the signal in the adjacent channel. The signal cross talk between channels should always be very small for precise measurement. Procedure described below is followed to calculate cross talk:

- Two adjacent channels are selected from each STGM slice module.
- AC signals of different frequencies (100 Hz, 500 Hz, 1 kHz, 2 kHz & 5 kHz) are fed to a channel.
- A DC signal (1V) is fed to the adjacent channels.
- FFT is calculated for the adjacent channel to measure the amount of cross talk.
- Plots are annexed.

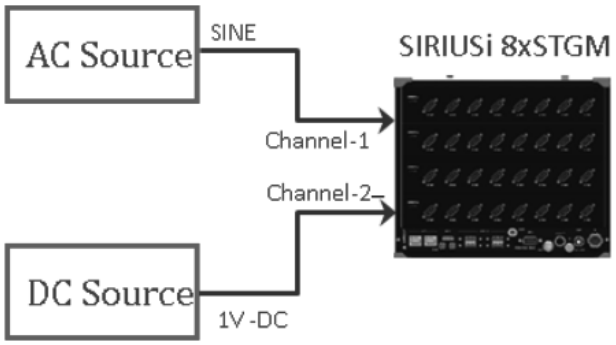

Figure 20 Block diagram of cross talk

6.6 FILTER CHARACTERISTICS

One of the key characteristics of a filter is its' roll-off rate. Roll-off rate is the steepness of filter transmission function with respect to frequency in the transition band between the pass band and the stop band. It depends on the order of the filter used. Ideal roll-off rate of 1st order filter is 20dB/decade. The roll-off rate becomes sharper with increase in the order of the filter. The procedure followed is:

- Roll-off rate is measured for Butterworth filter of different orders (2nd, 4th, 6th & 8th) for a cut-off frequency of 100Hz.
- For this, a channel is selected and configured with the required filter.

ISBN - 978-93-95038-50-8

- And AC sine signals of 10Vpp and different frequencies () are fed as input.
- Roll-off rate: 20log (w2/w1) is used to calculate the roll-off rate where w1 is filter output response at cut-off frequency and w2 is filter output response at 10 times the cut-off frequency.
- The filter output responses are measured from the FFT.

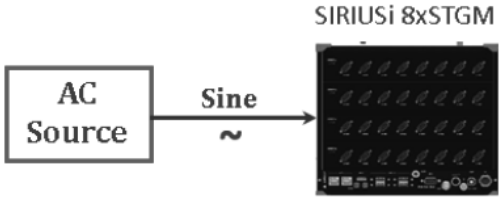

Figure 21 Block diagram of filter

6.7 INPUT NOISE CHECK

In every measurement channel, inherent noise exists and it should be very low. To check the input noise of the system, input terminals are shorted with 1kohm resistor and data is acquired for different sampling rates (100Hz, 1 kHz and 5 kHz).

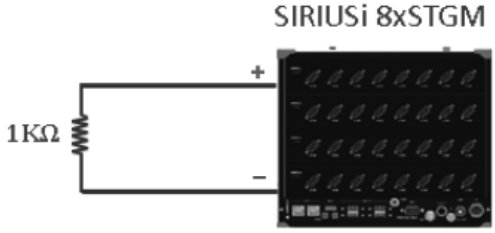

Figure 22 Block diagram of noise

6.8 INPUT SATURATION

In every measurement channel, inherent noise exists and it should be very low. To check the input noise of the system, input terminals are shorted with 1kohm resistor and data is acquired for different sampling rates (100Hz, 1 kHz and 5 kHz).

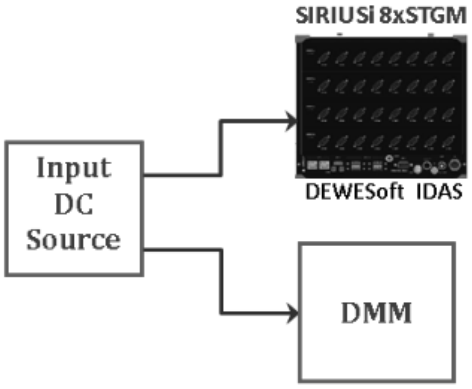

Figure 23 Block diagram of input saturation

7. COMMAND SYSTEM

Instrumentation system realization includes an important command transmission from command system to remote control valves, either its independent valves for line operation or engine valves for opening of fuel and oxidizer lines. There are two primary ways to implement command system. First is manual command system. In this one can operate each control valve manually by operating from mimic console running on the remote PC using PLC (Programmable logic controllers). Entire set of command is programmed in PLC for auto operation. Then command is relayed through PLC, which in turn gives requisite power to field relay, power required to energize valves is connected through electro-magnetic. Command system is used to implement abort system for auto abort in case of abrupt rise of any of the critical measurement or logic of critical measurements. During the command process function all the commands have worked as planned and auto sequence has executed the sequence of operations.

8. CONCLUSION

The GAGANYAAN Hot Testing was successfully carried out and precise measurements with the inaccuracy less than 1 % were achieved for all 260 channels with the robust IDAS. The vibration measurements for critical measurements like the Injector cover and the Turbo pump measurements were well within the specified limits.

The IDAS realization, though quite a challenge, paved way for the successful Hot Testing of ISRO's GAGANYAAN VIKAS Engines.

The overall efficacy of the Test article measurement chain has significantly improved with the compact modules with better CMRR, and individual ADC thereby eliminating the cross talk and improving the overall signal conditioning performance.

REFERENCES

1. Report On Test And Evaluation Of Integrated Data Acquisition System (IDAS) For PTS Instrumentation
2. PXI-Based Architecture for Real-Time Data Acquisition and Distributed Dynamic Data Processing. E. Barrera, M. Ruiz, S. López, D. Machón, and J. Vega
3. Low Cost Ground Test Equipment for Atmospheric Rocket Flights Using Embedded Systems. O. O. Babayomi, C. A. Osheku, M. A. L. Adetoro, A. Okon, and A. O. Opasina Centre for Space Transport and Propulsion, Epe, Lagos National Space Research and Development Agency (NASRDA) Federal Ministry of Science and Technology, FCT, Abuja, Nigeria Email: babayomi@ieee.org
4. DAQ: Software Architecture for Data Acquisition in Sounding Rockets. Mohammad Ahmad, Thanh Tran, Heidi Nichols, Jessica N. Bowles-Martinez Jet Propulsion Laboratory, California Institute of Technology Pasadena, CA 91009 818-458-0709 mohammad.ahmad@jpl.nasa.gov
5. Overview of Combustion Instabilities in Liquid Rocket Engines - Coupling Mechanisms & Control Techniques. John W. Bennewitz∗ and Robert A. Frederick† University of Alabama-Huntsville Propulsion Research Center, Huntsville, AL, 35899.
6. Performance Report On Gaganyaan Of fnominal Hs (4, 5, 6, 7) Test GY-IPRC-HRLV-L110-TR-091-22;R0

7. Performance Report On Gaganyaan Injector Acceptance Test Series (Hsi-2 Series)GY-IPRC-HRLV-L110-TR-090-22;R0/1
8. Development Of A Low Cost Data Acquisition System For The Space Shuttle Solid Rocket Booster ProgramDavid Pinkleton, Reusable Space Systems, Boeing North American Inc., Huntsville, Alabama

ISBN - 978-93-95038-50-8

Roll Damping Analysis of Crew Escape Vehicle with Grid Fins at Subsonic and Transonic Mach Numbers

M Jathaveda*, Kunal Garg, P Balasubramanian, Harish A and G Vidya

FMTD/ADSG, AERO, VSSC, India
ACMD/ADSG, AERO, VSSC, India.
WTDD/WTG, AERO, VSSC, India
MTech, DIAT, Pune, India
Email: (g_vidya@vssc.gov.in)

ABSTRACT

Crew Escape Vehicle (CEV) is a man rated vehicle, which is used to eject the crew module from main rocket in an emergency situation so that the crew can be saved. Grid fins are employed in this vehicle for aerodynamic stabilization. Aerodynamic characterization is quite crucial for mission simulation and studies. Static and dynamic aerodynamic coefficients govern aerodynamic behavior among which roll damping derivative represents aerodynamic damping due to roll motion. Roll damping derivatives are obtained from wind tunnel tests for range of Mach numbers but sparse data is available due to cost overhead hence CFD has been employed for same. Forced oscillation technique using CFD++ software has been validated for Basic Finner configuration and same has been applied for CEV in current studies. Roll damping derivative are obtained for CEV and compared with wind tunnel results. Current studies have been carried out for subsonic and transonic Mach number but can be extended to supersonic Mach number.

Keywords: *Crew Escape Vehicle, Wind tunnel, Roll damping, Subsonic, Transonic, CFD*

1. INTRODUCTION

Stability characteristics of a launch vehicle depend on factors like angle of attack, Mach number, body rate, etc. Determining the stability of a Crew Escape Vehicle (CEV) [1] itself is a challenging process due to its complex flow field associated with the complex geometry. CEV is designed to take away crew module from the launch vehicle during the failure at the launch pad or at high altitude. CEV ejects the crew module into the intended trajectory such that the module is taken far away from the accident site. This study is done for various Mach Numbers at subsonic and transonic flow regimes. The static stability parameters can be estimated from either wind tunnel or CFD methods, whereas the dynamic stability parameters have been estimated from wind tunnel testing, in general. Owing to the advancement in CFD solvers, now CFD can be efficiently applied to determine the damping derivatives and hence been used in current study. Forced oscillation technique [2] has been employed in CFD framework to obtain roll damping derivative for CEV. The method has been also applied on Basic Finner [3] configuration and compared with wind tunnel test data for validation.

2. LITERATURE REVIEW

C Babu et al., 2018 [1] studied aerodynamic characteristics of crew escape vehicle with grid fin at subsonic to low supersonic Mach numbers. This study gives basic understanding about the nature of the vehicle in various Mach numbers. Also this study focuses on the contribution of the grid fins on the normal force. From the results it could be observed that there is an increase in normal force while approaching sonic speed. Solver details for the current study are based on this research.

James De Spirito and Karen R Heavey, 2004 [2] undertook CFD computations of Magnus Moment and Roll Damping Moment of a Spinning Projectile. The primary objective of the study was to determine the parameters necessary for estimating the Magnus moments and roll damping on a spin-

*Corresponding author: E-mail: kvkprasad@shar.gov.in

stabilized projectile. This study gives us information that steady state CFD with appropriated source terms is adequate to calculate roll damping. This paper suggests k-ε turbulence model for better convergence of aerodynamic characteristics in steady simulation.

H Sundaramurthy, 2012 [3] carried out wind tunnel testing in NAL for Basic Finner configuration at subsonic and transonic regime for roll damping measurements. The test was conducted for various roll rates and a linear plot was obtained between rolling moment and the roll rate. The results of the study suggested that C_{lp} is invariant with roll rate. This research serves us with the data for the validation of the current methodology with the Basic Finner.

3. PROBLEM FORMULATION

Equations of motion for a flight are derived from a body-fixed coordinate system. The nose of the vehicle is chosen for the ease of calculation. Right-handed coordinate system is used as the convention.

As shown in Figure. 1 the coordinates are defined below

x axis is in the symmetry plane pointed inward of the vehicle from nose to base.

y axis is perpendicular to the x axis and points upward.

z axis is mutually perpendicular to x-axis and y-axis.

Rolling is a rotation of the body about the x-axis and the counter-clock wise rotation is assumed to be positive. A system is said to be stable when the disturbance encountered is damped by the vehicle. Damping is the resistance offered by the aerodynamics of the vehicle or any other active mechanisms to a disturbance. Roll damping is the force caused on the lifting surface of the flight to counter the rolling moment produced during the flight. Roll damping derivative is a function of the roll rate.

$$C_{l_p} = \frac{dC_l}{dp} \qquad \text{.....(1)}$$

$$p = \frac{\bar{p}d}{2V} \qquad \text{.....(2)}$$

4. METHODOLOGY

4.1 FORCED OSCILLATION TECHNIQUE

Forced oscillation technique involves forced movement of rigid body under freestream flow which results in transient aerodynamic coefficients. The coefficient history is a function of static and dynamic aerodynamic coefficient and mathematical procedure used to derive same is explained in CFD++ manual [4]. For roll damping computation the body is forced to rotate about x-axis, using coordinate frame rotation. In this mode the momentum equations are augmented with a source term to account for the rotating frame of reference [4]. This allows undertaking this roll simulation using steady state simulation reducing computation burden without compromising the accuracy and same is also highlighted in literature [2]. The roll damping derivative is defined below in Equation 3

$$C_{l_p} = \frac{C_{l,2} - C_{l,1}}{p_2 - p_1} \qquad \text{.....(3)}$$

where 1,2 represents the two different states.

The above equation is further simplified by assuming that rolling moment is zero for zero roll rate.

$$C_{l_p} = \frac{C_l}{p} \quad \text{.....(4)}$$

If the roll is not linear then a rate dependent or a local definition like Equation 3 should be used for estimating the roll damping of the system.

4.2 *COMPUTATIONAL APPROACH*

4.2.1 *CONFIGURATION USED FOR CFD SIMULATION*

The configuration used in the study consists of a nosecone followed by a cylinder, flare and large cylinder within which the crew module is placed. Grid fins are placed at the aft of the CES to provide longitudinal stability. Internal design of the grid fins is lattice structure with blunted wedge as leading edge as shown in Figure. 1. Total vehicle length is of 3.9 times of larger cylinder diameter (D), the nosecone angle is 20° and flare angle is 31°. The arrangement of the grid fin is shown in Figure. 1 [1]

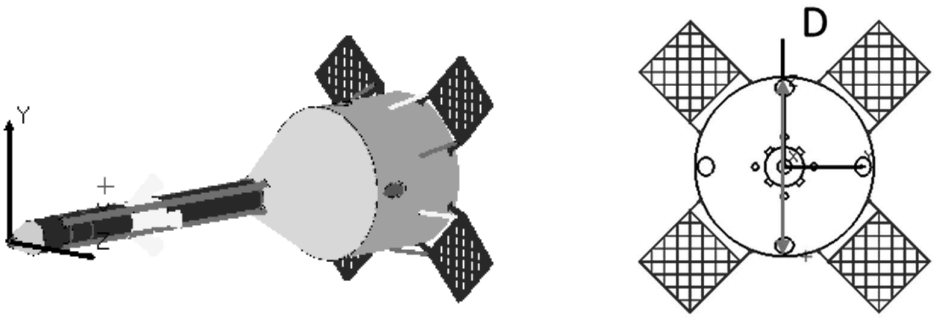

Figure 1: Configuration used for CFD simulation and the grid fins[1].

4.2.2 *GRID AND SOLVER DETAILS*

ICEM CFD is the commercial software used to generate the computational grid for CEV which is detailed in the study [1]. Volume mesh is generated around with surface triangulation. Mesh is resolved to solve the boundary layer flow by extruding the triangular prism from the wall. Farfield domains and the study configuration are shown with their respective boundary conditions in Figure. 2.

The domain of the control volume is 25D in all directions. In the entire volume there are 15.5million cells which include the 3.5 million near the wall and 12 million tetrahedral. CFD++ software is used to simulate the flow conditions. Compressible Perfect Gas solver with Realizable k-ε [2] turbulence model is utilized to solve the turbulence.

Grid motion/rotation along the X axis is invoked in the steady state solution to obtain the roll damping. The rate of rotation is kept same as that used in the wind tunnel tests. The input rate is referred from the available wind tunnel data.

ISBN - 978-93-95038-50-8

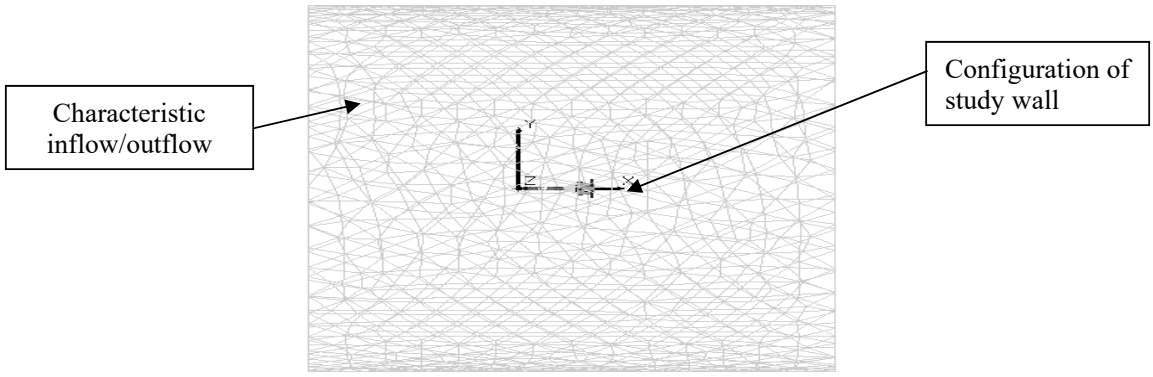

Figure 2: View of computational domain and boundary conditions [1]

4.2.3 *VALIDATION*

In general practice a simple model is chosen to validate a new method. This model is a calibration model. It is found that Basic Finner is found to be a widely accepted calibration model by the Supersonic Tunnel Association and AGARD [3]. These models were extensively tested on wind tunnels for various Mach numbers. Hence the Basic Finner configuration is used for validating our current analysis. Configuration of the Basic Finner consists of four rectangular fins on a cone body with the L/D of 10 as shown in Figures. 3 and 4.

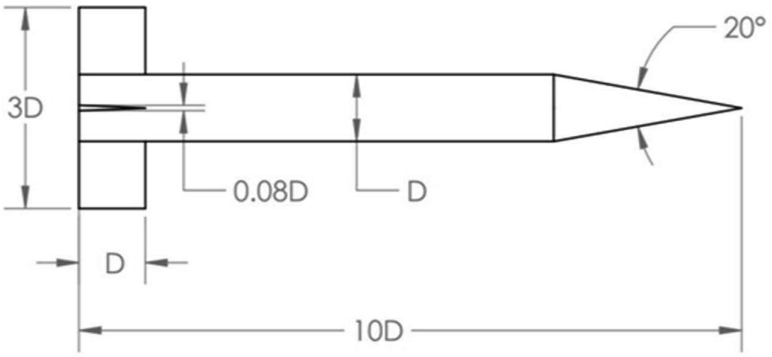

Figure 3: 2-dimensional view of the Basic Finner [3]

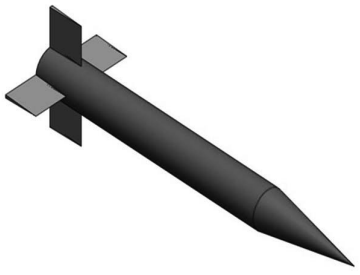

Figure 4: 3-Dimensional view of the model used for validation

Pointwise software has been used for generating mesh for Basic Finner. Volume mesh is generated with quad dominated surface and mesh is resolved to the boundary layer. Spherical domain of diameter 18.0 is used. The entire volume contains 19.47 million cells with 0.16 million cells surface mesh. The view of the domain and the grid are shown in Figures 5 and 6.

ISBN - 978-93-95038-50-8

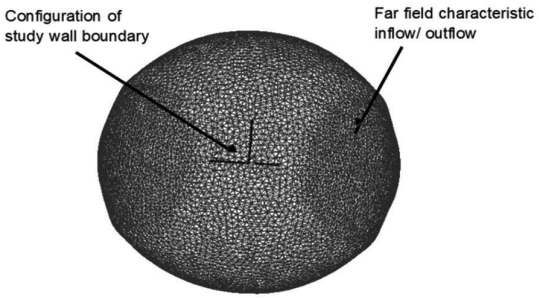

Figure 5: View of computational domain and boundary conditions

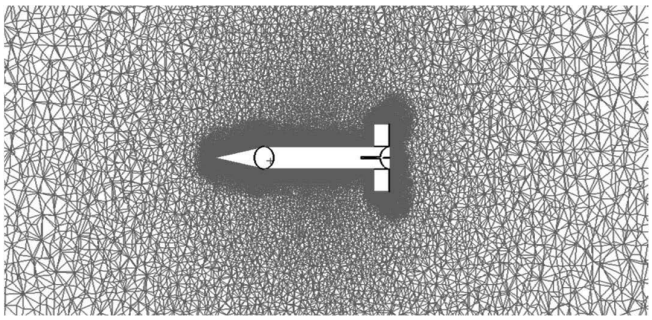

Figure 6: Grid in symmetry plane

The same solver setting is used as the above for Mach Numbers 0.5, 0.7 and 0.8 with zero incidence angles.

5. WIND TUNNEL TESTING

Measurement of C_{lp} through experiments requires a special purpose roll damping rig which was developed and validated during by NAL [3]. This rig employs the steady roll technique in which the model is rotated at a series of constant roll rates using a motor and the measurements of rolling moment on the model and its roll rate are made. The model is mounted on a single component low capacity rolling moment balance fixed at the upstream end of the sting, which in turn is supported on a pair of ball bearings. Figure. 7 shows the Basic Finner in the wind tunnel. Tests have been carried out in the wind tunnel for the series of subsonic and transonic Mach numbers. The same conditions are used for CFD simulations.

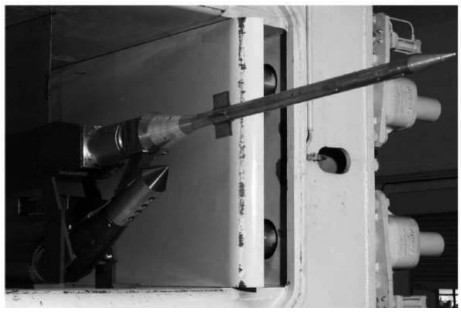

Figure 7: Basic Finner model in wind tunnel

ISBN - 978-93-95038-50-8

6. RESULTS

6.1 *VALIDATION USING BASIC FINNER*

Forced oscillation technique is validated for Basic Finner for Mach Numbers 0.5, 0.7 and 0.8. Reference frame is rolled at the rate of 103 rad/s with $\Theta = 0°$ for all Mach number as per the literature. As shown in Figure. 8, the results compare within 5% with the literature data across all Mach Numbers. These results validate the method and hence the same technique is employed for CEV.

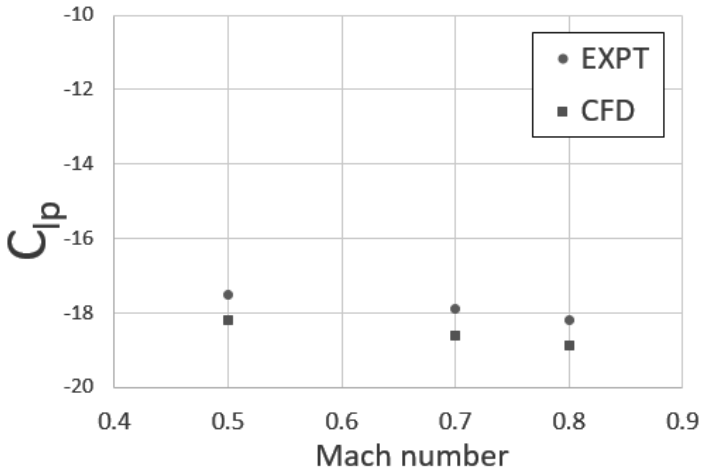

Figure 8: Comparison between computational and experimental results

6.2 *CEV CONFIGURATION*

Steady state simulation is carried out for 1000 iterations and then steady roll simulation is carried out for further 2000 iterations. Roll damping analysis is carried out at Mach numbers of 0.49, 0.71 and 0.8 for CEV configuration at angle of attack of 0° and -5°. The residual of mass, momentum, energy, turbulent kinetic energy and turbulent dissipation are shown in Figure. 9 at M = 0.71, the residual falls below 10^{-3}. Figure. 10 shows the convergence of normal force at M = 0.49, $\Theta = 0^{\circ}$.

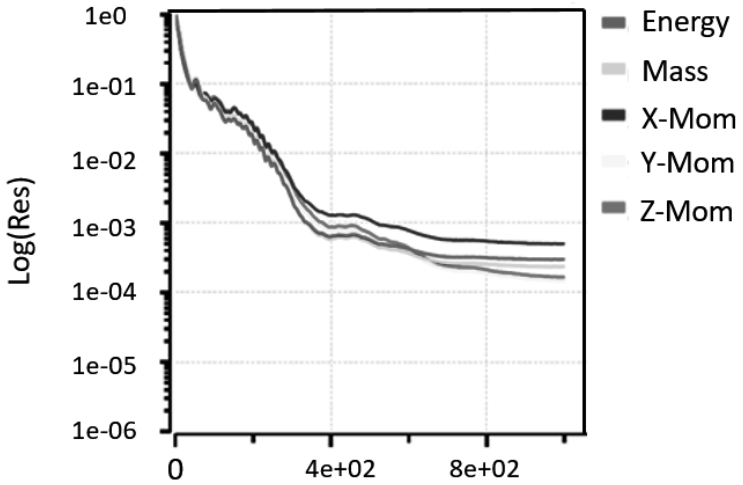

Figure 9: Convergence history for steady state at M=0.71 $\Theta = 0^{\circ}$ for CEV

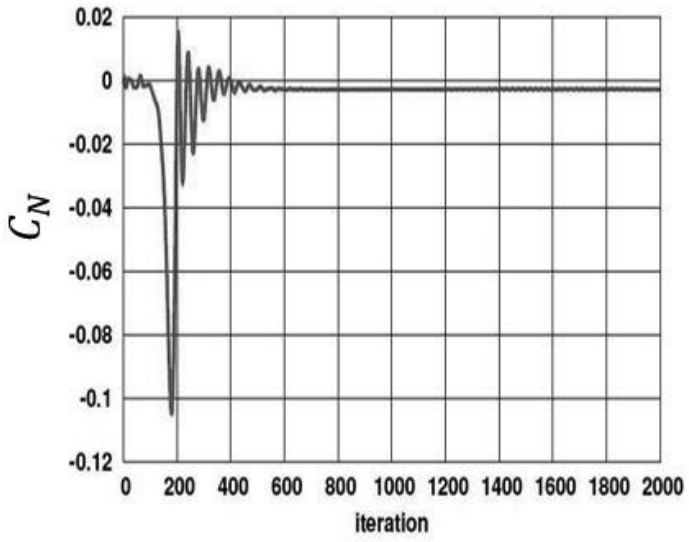

Figure 10: Convergence history of Normal force at M=0.49 Θ = 0° for CEV

The angle of attack of 0° and -5° are considered for the simulations. Figure. 11 shows the Mach palette at M=0.8 & Θ= -5° for the CEV in steady roll simulation. Expansion of flow at cone-cylinder junction leads to increase in Mach number which can be seen in palette. Also expansion region is visible at the nozzle cowlings. Large base flow is formed at the end due to aft body large diameter. Grid fin cells form a convergent-divergent section, resulting in acceleration of flow through the grid fins. Thus even though free stream Mach number is low transonic. the local Mach number through the pockets of the grid fins will tend to supersonic which is depicted in Figure. 11. Variation of the roll damping data with the Mach number and angle of attack along with its comparison with wind tunnel are shown in the Figure. 12. From the results it is evident that CFD data has a better match with wind tunnel data for angle of attack -5° and for angle of attack 0° there is a reasonable match across Mach numbers except 0.8. CEV comparison with wind tunnel data is not as good as Basic Finner validation case which is attributed to the lower value of loads for lattice grid fin as compared to planar fin. Also the grid fin flow resolution is being investigated to understand the sensitivity to modelling and mesh.

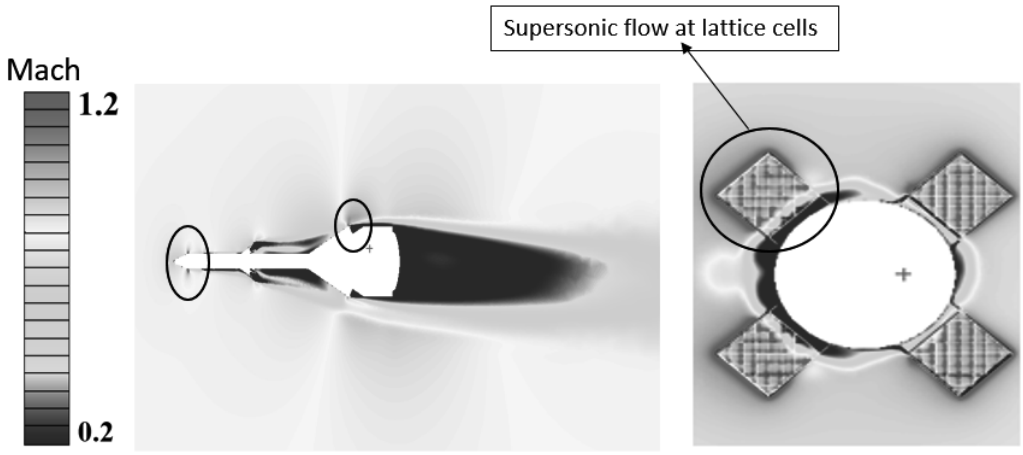

Figure 11: Mach Palette in steady roll case M=0.8 &Θ= -5°for CEV

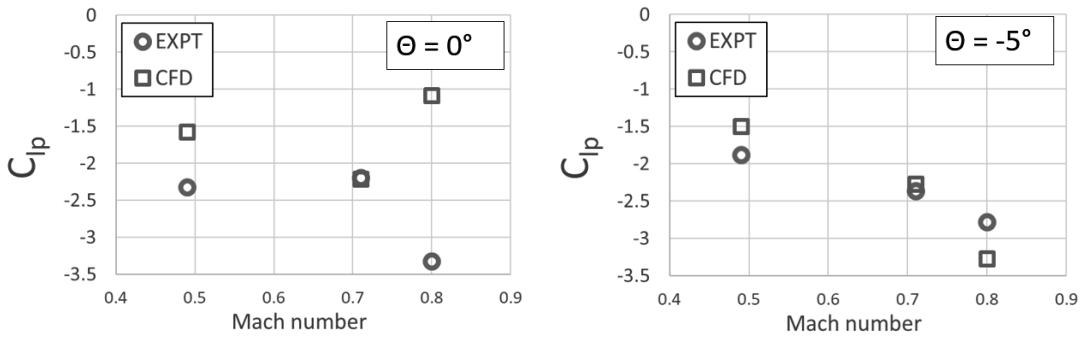

Figure 12: C_{lp} variation with Mach number at Θ=0˚&-5˚ for CEV

7. CONCLUSIONS

Roll damping derivative of Crew Escape Vehicle (CEV) is carried out using forced oscillation technique employing coordinate frame rotation source term in CFD++ framework. The method is validated using Basic Finner model against NAL wind tunnel data. Simulations are carried out for the Mach numbers of M=0.5, 0.7 and 0.8. The results compare within 5% with the literature data across all Mach Numbers. Roll damping coefficient of a CEV is computed using the same methodology as in Basic Finner for Mach numbers of 0.49, 0.71 and 0.8 for Θ= 0° & -5°. From the results it is evident that CFD data has a better match with wind tunnel data for angle of attack -5° and for angle of attack 0° there is a good match across Mach numbers except 0.8. Grid fins have a major contribution to the roll damping characteristics of the vehicle. Flow resolution in and around grid fins is identified as major reason of mismatch which will be addressed in future studies.

.

ACKNOWLEDGEMENT

We thank Babu C Sci/Eng SF, HSFC for providing us with the mesh for the current work.

NOMENCLATURE

C_p	=	Coefficient of Pressure	
C_l	=	Coefficient of rolling moments	
C_{lp}	=	Roll damping coefficient	
C_N	=	Normal Force coefficient	
d	=	Base diameter of the reference vehicle	(m)
L	=	Length of the reference vehicle	(m)
M	=	Mach number	
$\bar{p}$	=	Roll Rate	(radians/s)
p	=	Non-dimensional roll rate	
P	=	Pressure	(Pa)
Θ	=	Angle of attack	(degree, °)

REFERENCES

1. C Babu, G Vidya, Dipankar Das, M M Patil, V Ashok, “Aerodynamic characteristics of crew escape vehicle with grid fins at subsonic to low supersonic Mach numbers”, SAROD, November-December 2018
2. James De Spirito, Karen R. Heavey,“CFD Computation of Magnus Moment and Roll Damping Moment of a Spinning Projectile”, AIAA Atmospheric Flight Mechanics Conference and Exhibit, Providence, RI,16-19 August 2004
3. H.Sundaramurthy ,“Subsonic and Transonic Roll Damping Measurements on Basic Finner”, AIAA Vol19-1,23, May 2012
4. CFD++ User Manual v20.1

ISBN - 978-93-95038-50-8

Synthetic Aperture Radar Data Quality Characterization and Calibration Analysis of EOS-04

S. Sri Sudha*, S. Jaya Bharathi, S. Hari Priya and B. Santhisree

National Remote Sensing Centre, Indian Space Research Organisation, Dept. of Space, Govt. of India
srisudha_s@nrsc.gov.in

Abstract

EOS4 satellite is launched on 14th Feb 2022 by PSLV C-52 in sun Synchronous polar Orbit of 529Km. This paper presents the data products quality evaluation of Earth Observation Satellite -04 in terms of Geometric and Radiometric aspects by using Data Quality Evaluation Software Modules. Geometric and Radiometric Quality Parameters were estimated periodically using Level-1 and Level-2 data products of Strip Map and ScanSAR Imaging modes. The parameters like Background to Peak Ratio (BPRatio), Integrated Side Lobe ratio (ISLR), Peak to Side Lobe ratio (PSLR), Radar Cross Section (RCS) of the Corner Reflector (CR) and geometric resolution are computed and validated against the specification periodically using Level-1 Single Look Complex data to validate the SAR- antenna performance. The parameters like sigma naught, speckle index, radiometric resolution, signal-to-noise ratio are computed over Amazon forest to monitor and validate the radiometric stability using Level-1 Single Look Complex products. For the estimation of Polarimetric Quality Parameters, the Level-1 Single Look Complex Datasets acquired over Cal-Val sites is used.

Keywords: EOS04, Calibration, StripMap, ScanSAR, geometric and radiometric parameters

1. INTRODUCTION

EOS04 /RISAT-1A is a C-Band SAR launched by ISRO on 14th Feb 2022 by PSLV C-52 in sun Synchronous polar Orbit of 529Km. It is a Radar Imaging Satellite designed to provide high quality images under all weather conditions for applications such as Agriculture, Forestry & Plantations, Soil Moisture & Hydrology and Flood mapping. EOS04 operates over 4 identified modes -Fine Resolution Stripmap (FRS-1/FRS-2), Medium Resolution ScanSAR MRS Mode-(6 beams /8 Beams), Coarser Resolution ScanSAR CRS Mode (12 beams), n-beam ScanSAR mode and High-Resolution Spot Mode. Data is acquired in various Transmit/Receive Polarization combinations as Single, Dual, Quad and Hybrid Circular Modes. Data processing is carried out to generate Level-1 -SLC and Ground Range, Level-2 - Geo-Referenced Map-Projected and Level-1C and Level-3A polarimetric products for dissemination to users.

In order to maintain, data interoperability and to substantiate time- series measurements, the Data Quality Parameters are evaluated on a continual basis and at regular time lined intervals. This paper presents the data products quality evaluation of Earth Observation Satellite -04 in terms of Geometric and Radiometric aspects by using Data Quality Evaluation Software Modules. Geometric and Radiometric Quality Parameters were estimated periodically using Level-1 and Level-2 data products of Strip Map and ScanSAR Imaging modes. For the estimation of Polarimetric Quality Parameters, the Level-1 Single Look Complex Datasets acquired over Cal-Val sites is used.

Geometric quality of Standard Geo reference products were assessed for relative location accuracy (with Carto Ortho reference image for FRS1/FRS2 modes, with LISS3/L8 reference for MRS/CRS modes), maximum error budget could be within 30m. Absolute Geometric accuracy (with CR deployment), Calibration parameters are analyzed time to time with various deployments of CRs at different Geographic locations for FRS1 and MRS modes. Systematic data collection for 3 cycles is assessed for mosaickability at different latitudes,

*Corresponding author: E-mail: srisudha_s @nrsc.gov.in

spatial consistency and radiometric response consistency for pseudo invariant targets. Sigma naught response is studied for various targets across different incidence angles and Gamma naught response on the Uniform target 'Amazon' for radiometric fidelity across the swath pixels. The Raw data analysis is more critical and important, the data being microwave, I and Q channel amplitude and phase imbalance is studied and established and continuing to monitor over many strips. The temperature at payload junctions is important to monitor based in which image quality varies. Designated junction temperatures are being monitored for every data collection against specific threshold. Internal calibration data is analysed for replica response consistency and noise data analyzed for the amplitudes across different Calibration passes as well as with the Lab data.
In the subsequent chapters details are provided for each quality parameter along with the quantifiable numbers.

2. EOS04 GEOMETRIC DATA QUALITY

In SAR imagery, geometric correction is a crucial step due to the very characteristic of the SAR imaging geometry. It depends upon local relief, imaging direction etc. Geometric quality evaluation was done on the Level-2 Enhanced Geo-referenced products generated in the Data Processsing chain. These products are primarily corrected for SAR imaging geometry like layover, foreshortening, range ambiguity, sensor viewing direction and imaging node. These products were acquired in different acquisition modes, incidence angles, different orbit and attitude source and different terrains. The parameters which are evaluated from geometric quality evaluation are location accuracy, scale and internal distortion.

Product Evaluation is carried out using Carto1- Ortho (2.5m) data and LISS3 data as reference which has spatial accuracy specification of 15m RMSE with 90% confidence.

2.1 *LOCATION ACCURACY*

This parameter is estimated by identifying dense well distributed points in target image (data product) and reference image (Carto1-2.5m Ortho) along the azimuth and range directions. Mean-Along, Mean-Across, RMSE Along and across, radial error, CE90 are derived from these points. It is computed by estimating mean differences between the coordinates of points obtained from reference image and points obtained from SAR image.

Fig 2.1.1 shows the location accuracy of FRS-1 mode data. From this figure it is observed that most of the samples taken are within 30m specification. Fig 2.1.2 shows the location accuracy of MRS mode data. From this figure it shows that 53% of the samples are within < 30m accuracy and 6% of the products are in 80-100m accuracy is with orbit source is SPS-PB. Fig 2.1.3 shows the location accuracy of CRS products and all products are within specification. Some samples are out of specification range which may be attributed to the preliminary orbit source.

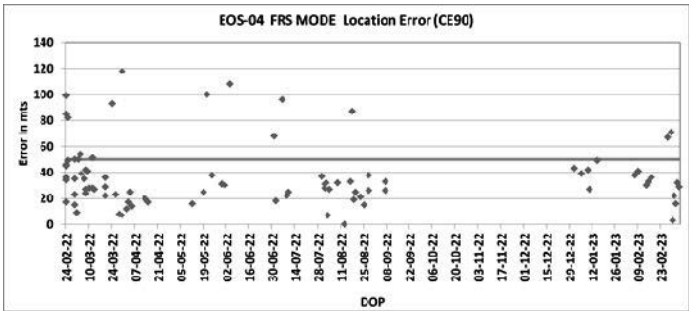

Figure 1: Location accuracy of FRS-1 mode data

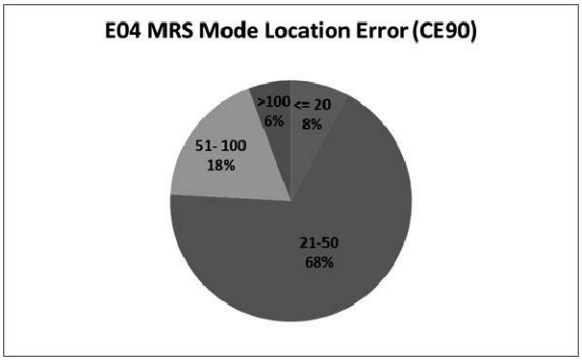

Figure 2: Location accuracy of MRS mode data

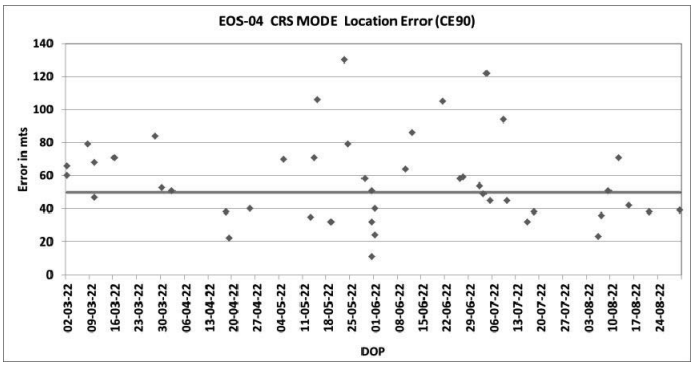

Figure 3: Location accuracy of CRS mode data

2.2 *SCALE*

Scale denotes the distance covered on ground corresponding to a pixel in the given image. It is calculated by taking mean of ratio of distance on reference image to target image for all identified control points on the product, all possible combinations of control-point pairs are considered for distance computation. This value of scale is compared with output resolution of the product and percentage variation is computed.
For all modes like FRS, MRS&CRS products scale was computed for all the modes and is found to be as expected.

2.3 *INTERNAL DISTORTION*

Variation of location error within the scene is described as internal distortion. It is estimated by from the variation in relative between points within the processed image and the reference image. It states the stability of the satellite. It will be more if the disturbance of platform is high during imaging.
For EOS-4 products for all the modes with respect to terrain there is not much variations observed and found to be as expected.

3. RADIOMETRIC AND IMAGE DATA QUALITY

Overall interpretability of a SAR image is based on the image data quality. The radar measures the intensity of the reflected signal at each resolution cell in the image. The intensity depends on the transmitted power, antenna gain, distance between the scattered and the radar, and geometry, roughness, and material properties of the object being imaged.

ISBN - 978-93-95038-50-8

Radiometric data quality evaluation is done on. Sigma-naught, speckle index, radiometric solution and NESZ are the some of the metrics calculated on the Single Look Complex/Multi Look Ground data product generated using the data acquired EOS-04 satellite in various modes, beam and polarization to the quality of the radar image.
These values are provided to the mission and DP team for further analysis and fine tuning of some sensor parameters.

3.1 *SIGMA-NAUGHT*

Sigma-naught (σ°) is one of the important parameterswhich is estimated from the SAR image which gives the estimate of energy of the backscatter signal returned from the target area of interest. Table 1 shows the sigma0 values received over Amazon forest for FRS-1 and MRS mode data. Values are as expected for all polarizations over Amazon Forest.

Table 1 Sigma0 over Amazon Forest

Polarization	Sigma0 (dB)	
	FRS-1	MRS
HH	-7.08	-7.45
VV	-6.69	-8.50
HV	-14.13	-13.38
VH	-13.89	-13.78
RH	-8.71	-7.53
RV	-8.49	-7.36

3.2 *SPECKLE INDEX*

Speckle is caused by the reflection of the radar signal from multiple objects (scatterers) that are distributed within a resolution cell. The sum of the contribution from all the scatterers results in variation in the intensity of the measured signal in adjacent resolution cells. This variability in image intensity, called speckle, limits the radiometric resolution of a SAR sensor. Speckle index is computed as the normalized variance of the signal intensity in the image of a homogeneous target.Speckle index over low SNR region is 1 for others the values are in the range 0.5-0.8.

3.3 *RADIOMETRIC RESOLUTION*

Radiometric resolution is a metric that describes the ability of a sensor to discriminate between two objects that have similar radar cross sections (i.e., that are radiometrically similar). Radiometric resolution depends on the measured signal to noise ratio and the number of independent looks from which the pixel was formed. This parameter is evaluated on the uniform distributed target and is measured in dB.
Radiometric resolution of all modes (FRS-1, FRS-2, MRS and CRS) and all polarizations are observed to be 1.9dB.

3.4 *NOISE EQUIVALENT SIGMA ZERO*

he ability to make out objects against the inherent noise generated by the sensor, NESZ is a metric that informs about the system noise level in a SAR image. NESZ is usually provided as a log-scale quantity in dB, and more negative values indicate better image quality. For instance, calm lakes are highly reflective targets in the side-looking geometry and allow the characterization of the noise level of the sensor.

ISBN - 978-93-95038-50-8

NE Sigma0 of

- MRS mode (in dB) : -20 (HH/VV) and -25 (HV/VH)
- CRS mode (in dB) : -25 (HH/VV) and -26 (HV/VH)
- FRS mode (in dB) : Less than the Specification

4. EXTERNAL CALIBRATION AND DATA QUALITY

SAR Radiometric calibration is necessary to allow a valid conversion of the observed pixel intensity into a physical relevant unit, e.g., radar cross section (RCS). Therefore, the whole SAR system has to be calibrated and various geometric and radiometric corrections have to be applied. The internal calibration compensates gain and phase variations of the instrument which may occur due to different temperatures and ensures the specified radiometric stability of the instrument over time. The antenna pointing is important to apply proper antenna pattern correction during SAR data processing, which defines the relative radiometric accuracy within a SAR image. Absolute external radiometric calibration is done applied finally using ground truth measurements.

Both Internal and External calibration data need to be monitored periodically in order to ensure the quality of the calibrated products. Sensor performance is initially assessed the quality of the on-board calibration data and later evaluating the calibrated data product by analyzing reference targets on ground such as point targets like corner reflectors with well-known RCS and extended homogeneous site such as Amazon forest region.

For the external calibration of EOS-04 satellite, calibration site is established as a part at IMGEOS located at Shadnagar and SAC ground site Ahmedabad. This site consists of square trihedral/dihedral and triangular trihedral corner reflectors. Each target is aligned by schedule in the expected line-of-sight direction for a satellite overpass for both ascending and descending orbits. In order to estimate the absolute radiometric accuracy of a SAR system, the RCS values of reference targets are derived from SAR images and compared with the theoretical RCS of these targets. Impulse response is the most important factor, to characterize these components of SAR image quality. The key impulse response parameters in both range and azimuth are Impulse response width, height, phase for complex data and the properties of its side lobe. The RCS of a point target is estimated from SLC data for the Stripmap mode and Multi-look Ground Range product for the Scansar mode product of all EOS-04 by analyzing its impulse response function. If was found the difference between the theoretical RCS and estimated RCS is less than 1dB.

Peak Side Lobe Ratio -PSLR: It describes the power resolution between the main lobe and side lobe. If a SAR system has a poor PSLR, the side lobe of a strong target will be is classified as false targets. It is derived by estimating the ratio of the highest side lobe power to the peak power in the main lobe.

Integrated Side Lobe Ratio (ISLR) describes the extent to which energy is spread around the main lobe. If a SAR system has a poor ISLR, the response from a sufficiently strong target will submerge several weak targets and result in misclassification (loss of detection). ISLR is computed by the ratio of integrated energy of the side lobes to the integrated energy of the main lobe.

From Fig: 4.1.1 PSLR varies from -17dB to -23dB in range direction and -16dB to -22dB in azimuth direction for the corner reflectors deployed at Shadnagar and SAC ground, Ahmedabad. ISLR varies from -13dB to -18 dB in range and -12dB to -18dB in azimuth.

ISBN - 978-93-95038-50-8

Fig: 4.1.2 shows an example of Corner reflector deployed at Shadnagar, SAC ground and Bopal Campus Ahmadabad.

Extended target analysis is carried out on the Amazon forest data. The expected gamma naught range from CEOS reference is -4dB to -7dB. The achieved sigma naught, gamma naught and beta naught values for FRS1 and MRS modes are in variation of a 2dB in HH, HV, VH and VV polarization and 4dB variation is observed in RH and RV polarization from near range to far range for FRS1 mode data. Variation is well within 2dB in Gamma0 for all polarization for MRS mode data.

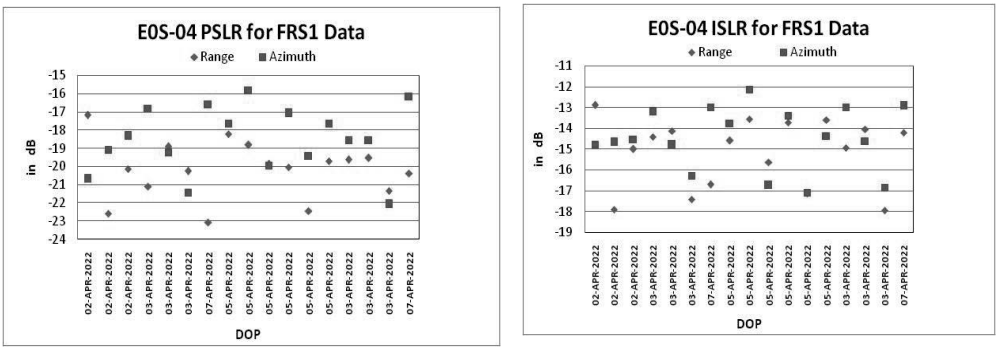

Figure 4: PSLR and ISLR of Corner reflector

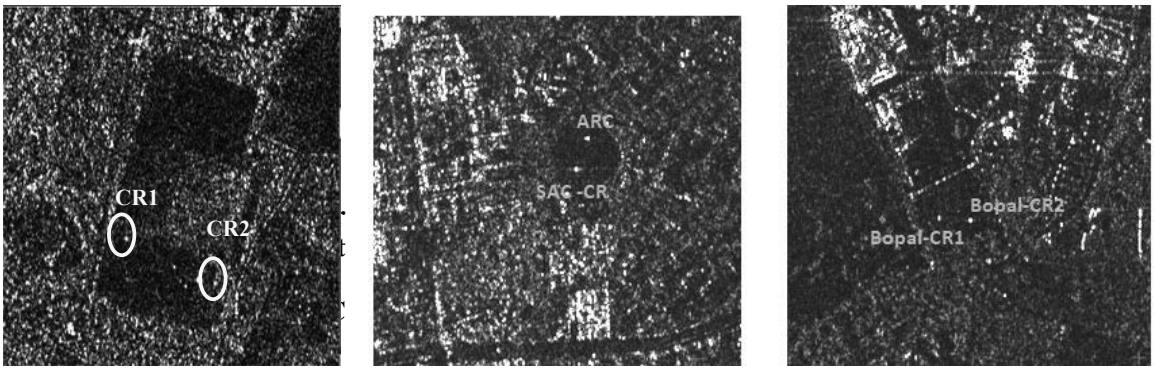

Figure 5: Impulse Response function of Corner reflectors at IMGEOS, SAC ground

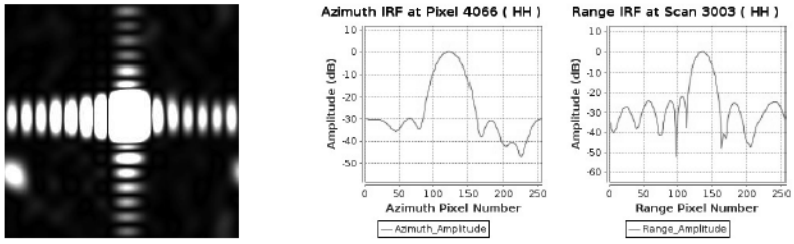

5. POLARIMETRIC DATA QUALITY

A Polarimetric SAR system measures the scattering information of the surface of observation with microwaves emitted in Dual/Hybrid / Full Quad polarization architecture. The number of output data channels depends on the transmit /receive polarization configuration**.** The design of the radar results in single look complex (SLC) imagery

ISBN - 978-93-95038-50-8

structured in the range and azimuth directions.
Using in-house developed software, the Level-1 SLC data is ingested for generating the hybrid polarimetric parameters pertaining to the data quality. Key parameters like Relative Channel Phase, Degree of Polarization, Degree of Circular Polarization, Ellipticity are generated for the Calibration site over Ahmedabad, Gujarat.

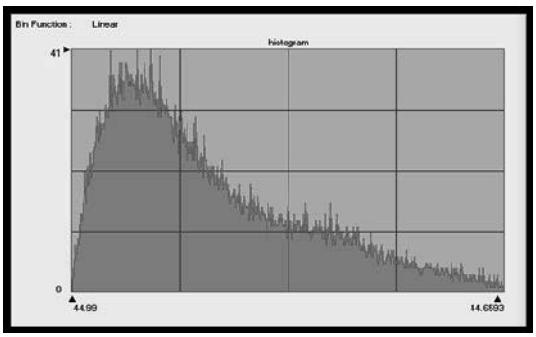

Figure 6: Ellipticity Parameter Plot

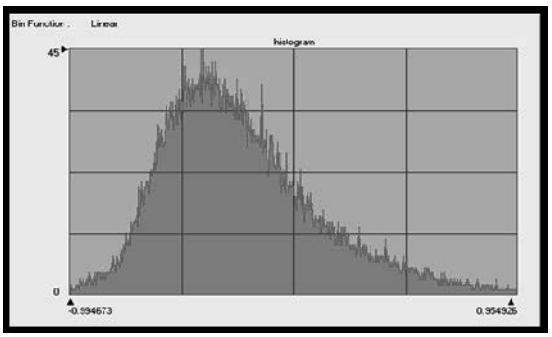

Degree of Circular Polarization (DoCP) Plot

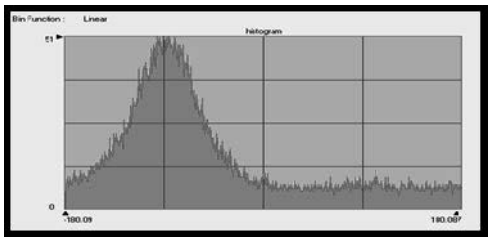

The Relative Phase Plot (delta)

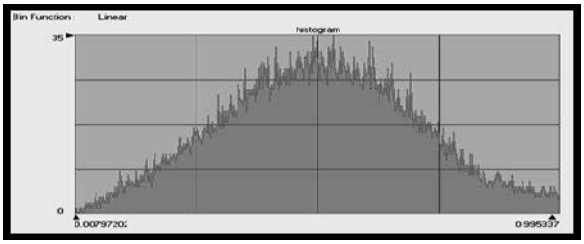

The Degree of Polarization (m factor)

The channel relative phase for hybrid polarimetric data is found to vary between -180 to +180. The Ellipticity factor is found to vary between +44.65 to -44.99 deg which is as per the nominal values.

The degree of polarization is found to vary typically in the range of 0.008 to +0.995. Nominal Range of values is 0 to 1 depending on the target polarimetric scattering. These parameters are crucial for polarimetric target decomposition and scattering mechanism analysis

6. RESULTS AND DISCUSSIONS

The EOS04 Data Products are continually evaluated as per DQE norms and procedures and the following results are summarized as follows.

6.1 *ACHIEVED PLATFORM STABILITY*

- After ground processing achieved product accuracy better than 50m.
- As the designated Orbit source is SPS-RT, In case of SPS-PB, few cases lead to poor location error.
- Target accuracy: 2km (Azimuth Direction)

6.2 *ACHIEVED RADIOMETRIC STABILITY*

- FRS1/FRS2/MRS/CRS modes all polarisations data products are analysed.

ISBN - 978-93-95038-50-8

- Near to Far range response difference is better than 1.5 dB (over Amazon)
- Absolute radiometric accuracy about 1dB.
- Scalloping issues in ScanSAR mode at low SNR regions.
- Sigma naught spurious values in Low SNR regions(crossing NE Sigma Naught with noise cal data corrections)

The achieved geometric,radiometric and polarimetric quality specifications of the various imaging modes is summarised in the following table:

Table 2: Data Quality Parameters

S.No	Quality Parameter	Imaging Mode			
		FRS-1	MRS	CRS	FRS-2
1	Spatial Accuracy (in m)	50	Better than 70	Better than 60	16
2	PSLR Range/Azimuth (in dB)	-20.1 / -18.4	-19.7 / -16.5	-	-
3	ISLR Range /Azimuth (in dB)	-15.1 / -14.5	-14.2 / -11.2	-	-
4	Radiometric Resolution (in dB)	1.9	1.9	1.9	2.2
5	Radiometric Accuracy (in dB)	1.23	0.68	-	-
6	Noise Equivalent Sigma Naught (in dB)	-19	-20	-25	-18
7.	Degree Of Pol(Hybrid Pol)	0 to 1	0 to 1	0.09 to 1	0 to 1
8.	Relative Phase (Hybrid Pol)	-180 to +180 deg	-	-	-

7. CONCLUSIONS

The EOS-04 data products at various imaging modes like FRS-1, MRS and CRS have been evaluated for the geometric, radiometric and polarimetric parameterization. The Geometric accuracy is found to be sustained for most of the cases. The radiometric quality parameters corresponding to distributed and standard point targets have been evaluated and found to be as per the data product specifications. As EOS-04 offers Full Polarimetric and Hybrid Polarimetric Data Products, the crucial polarimetric parameters are found to be in conformance for the Transmit Receive Channels.

ACKNOWLEDGEMENT

The Authors express their sincere thanks to Director, NRSC for guiding us with his technical expertise and encouragement. We express our deep gratitude to Deputy Director, DPA Mission and Project teams for the technical guidance in realizing data acquisition and processing. We also express our thanks to SAC DP and DQE teams for the incessant work in order to realize and maintain the data specifications.

REFERENCES

1. EOS-04 Data Format Specifications Document-Space Application Centre, ISRO
2. J. van Zyl, C. F. Burnette, H. A. Zebker, A. Freeman, and J. Holt, "Polcal user's manual," Jet Propulsion Laboratory, Tech. Rep., August 1992.
3. A. Freeman, Y. Shen, and C. Werner, "Polarimetric SAR calibration experiment using active radar calibrators," Geoscience and Remote Sensing, IEEE Transactions on, vol. 28, no. 2, pp. 224 –240, March 1990.
4. A. Freeman, "SAR calibration: an overview," Geoscience and Remote Sensing, IEEE Transactions on, vol. 30, no. 6, pp. 1107 –1121, November 1992.

ISBN - 978-93-95038-50-8

Emitter Geolocation from Near-Space Platform Using 3D TDOA

Suman Agrawal*

Directorate of Special Projects (DSP), DRDO, Hyderabad, TS, 500069
Email: suman.agrawal@dsplab.in

ABSTRACT

The space between the maximum altitude at which a modern plane can fly and the minimum altitude at which a satellite can operate is known to as near space. A free balloon, an airship, and an unmanned aerial (UAV) vehicle are some of the aircraft in the near space. The near-space platform has the ability to identify far-off emitters in a large area due to its unique feature of having a large coverage area, full-time, and large-scaled. Near-space has drawn a lot of attention recently since it is below the ionosphere and doesn't experience ionospheric scintillations, which can significantly degrade RF communications and navigation performance. The focus of this paper is to compute geolocation in various scenarios. Geolocation is computed in two dimension (2D) using hybrid AOA/TDOA/FDOA measurements from ground/ship-based sensors at varying emitter distances and geolocation accuracy is calculated using Root Mean Square Error (RMSE) and Circular Error of Probability (CEP_{50}). Further, geolocation is computed in three dimension (3D) using TDOA measurements from ground/ship-based sensors at varying emitter altitudes and geolocation accuracy is computed in terms of total joint covariance matrix (Standard Deviation) from all receivers. The results of above geolocation accuracy are compared with geolocation from near-space based sensors placed at varying altitudes while the emitter is placed on ground/ship-based platform using 3D TDOA measurements. TDOA measurements are obtained by cross-correlating the signal received at all the sensors. The performance for all the scenarios are demonstrated through modeling and simulations. Experimental results in varied scenarios and specifically near-space platforms will help in designing of systems as per the required accuracy and in future visualizing the accuracies from space-based platforms.

Keywords: *3D TDOA, Near-space platforms, root mean square error, CEP_{50}*

1. INTRODUCTION

In recent years, research has focused on the geolocation of an emitter from electromagnetic emissions, which is largely employed in reconnaissance, surveillance, and intelligence gathering. In the fields of aeronautics and astronautics [1] [2], near-space [3] [4] has emerged as a new research hotspot. Figure 1 shows the near space platform comprising of planes, ballons and UAVs.

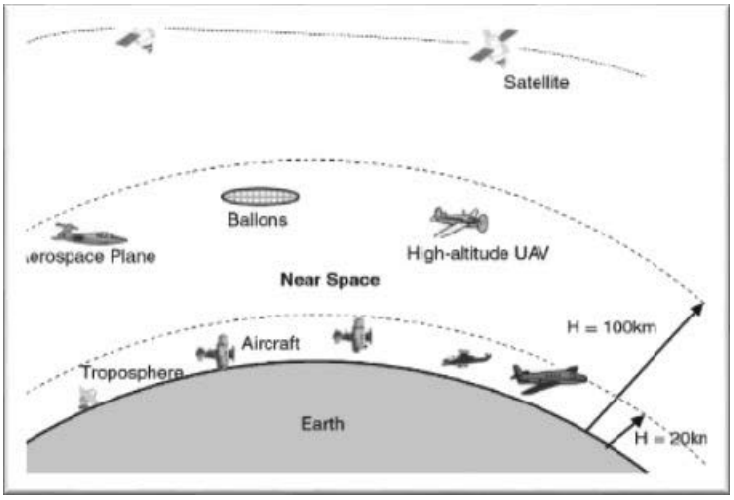

Figure 1: Near-Space Platforms

*Corresponding author: E-mail: suman.agrawal@dsplab.in

The use of near-space for global high-speed hits, communication, alarming, battlefield observation, and other purposes is possible [5] [6]. A number of localization algorithms, including Angle-Of-Arrival (AOA), Frequency-Difference-Of-Arrival (FDOA), Time-Difference-Of-Arrival (TDOA), and Received Signal Strength Indication (RSSI) have been developed [7][8][9] in the past. Geolocation methods like TDOA, FDOA, AOA, or RSSI depend on the positioning scenario and each has its own benefits and drawbacks for a certain positioning application. The TDOA positioning technique offers great location accuracy, but it demands precise sensor synchronisation, and in 3D at least four receivers are needed to produce the intersection of hyperboloids. For geolocation on the plane, AOA measurement only needs two receiving sensors, and it operates without synchronisation between them. Nevertheless, the precision of the measurement degrades with distance. The RSSI technique of geolocation operates by gauging the signal strength received from emitters. Although RSSI has the advantage of being straightforward and easy to install, its location accuracy is poor because of the built-in exponential decrease of received power when the emitter is far from the sensor.

The TDOA geolocation method makes use of receivers placed on platforms that are ground-based, ship-based, or close to space. By analysing signal arrival time measurements at four or more stations, the TDOA approach locates a 3D target. A master station collects the measurements from the many stations and processes them. Radar and communication emitters can be geolocated via a network of receivers that have a GPS receiver and an advanced military support sensor. A receiver's position and time of arrival are transmitted to a fusion center when an electronic sensor on board detects the leading edge of an electromagnetic (EM) pulse coming from that receiver. Cross-correlation is used to determine the time difference of arrivals, which is used to deduce the position of the emitter, using the measurements that each receiver in the network has gathered.

In the past, a number of solution methods that address the TDOA problem have appeared in the literature. Li J et.al in [10] [11] have presented geolocation by space-air-ground integrated network using TDOA measurements but does not give qualitative results using the parameter root mean square error. The observations are limited by heights in [12], which offers an altitude constrained source localisation utilising Time Difference of Arrival, FDOA, and differential Doppler rate. The methods of joint TDOA and FDOA localization, passive DOA multiple sensor networks for mobile targets, and multiple sources are presented in [13], [14] and [15] respectively. However, they do not take into account receivers mounted on multiplatform devices, which can be stationary or mobile, and the method is computationally intensive.

Three scenarios for estimating the position of an emitter using TDOA are presented in this research. The first involves estimating 2-D source location for a ground-based source using hybrid AOA/TDOA/FDOA readings from ground-based and ship-based sensors at various emitter distances. The second is to locate an emitter using 3D TDOA measurements, placed on near-space platform, at varying altitudes from the receivers placed on ground/ship-based platforms. The third is to locate an emitter placed on ground/ship-based platform from receivers placed on near-space based platforms at varying altitudes using 3D TDOA measurements. Numerical results based on multiple receivers are presented depicting the geolocation accuracy in emitter-receiver geometry scenarios using both 2D and 3D technique of measurements. In the following paper, Section 2 covers signal characteristics measured by the receivers, followed by TDOA geolocation technique in Section 3. Section 4 gives mathematical description of Geolocation Principle. Section 5 gives performance metrics. Section 6 and Section 7 covers Simulation Scenarios and Simulation Results respectively followed by Conclusions in Section 8.

ISBN - 978-93-95038-50-8

2. EMITTING SIGNAL CHARACTERISTICS MEASURED BY RECEIVERS

The key parameters of any emitting source signal that is mostly received by a receiver are its time of arrival (TOA), pulse amplitude, pulse width, radio frequency (RF), and angle of arrival (AOA). Moreover, frequency modulation is a metric that can be utilised to pinpoint a specific emitter and to ascertain the chirp rate or phase coding of a signal. Signals with pulse lengths longer than a few hundred microseconds are known as Continuous Wave (CW) signals. The leading edge of the pulse's internal clock is used to reference TDOA measurements. Pulse descriptor words are the name given to variables measured on a single intercept (PDW). In the parameter space, the PDW are a collection of vectors. For achieving de-interleaving mostly RF and AOA as parameters are used. To estimate the pulse repetition interval, considerations include PW and difference in time of arrival (TOA) (PRI). The carrier frequency and chirp rate are both important parameters if the signal is phase coded. Thus the characteristics of the emitting signal can be represented as

$$S_{i=}\left[AOA_i \quad f_i \quad PW_i \quad TOA_i \quad PA_i\right], \qquad \text{…..(1)}$$

for $i = 1,....,n$ where n pulses are present.

3. TDOA GEOLOCATION TECHNIQUE

For the purpose of weapon targeting and situational awareness, geolocation of emitters from ground-based, ship-based, aerial, or space-based platforms is a crucial function. AOA measurements taken from several different sites are triangulated to establish the location of an emitter using this simple geolocation approach. Both the frequency difference of arrival (FDOA) and time difference of arrival (TDOA) provides accurate estimates of source location. One TDOA measurement from two aerial platforms can be used to determine the emitter position, which is known as the location where a cone contacts the earth's surface. A second measurement between a third aerial platform and one of the initial two aerial platforms can be used to pinpoint the position of the emitter. This technique needs a precise knowledge of the distance between the flying platforms in order to synchronise the TDOA measurements. While a cesium clock typically provides great time precision, GPS can be utilised to position the platforms accurately. The TDOA calculates the difference between the signal's arrival times at two different places. Several TDOA measurements are available when there are more than two receivers. There are only a few receivers or platforms that can be used to solve the emitter geolocation problem utilising UAVs. When the source is on the earth's surface minimum of three UAVs are required for geolocation and the fourth one is required in case the source altitude is not known.

4. GEOLOCATION PRINCIPLE

Let the emitter position be denoted by $X(x, y, z)$ and that of the receivers by $X(x_0, y_0, z_0)$ and $X(x_0, y_0, z_0), i = 1, 2, 3.$ Taking first station with associated receivers as S_1, range equation for TDOA can be written as

$$\begin{cases} r_0 = \left((x-x_0)^2+(y-y_0)^2+(z-z_0)^2\right)^{1/2} \\ r_i = \left((x-x_0)^2+(y-y_0)^2+(z-z_0)^2\right)^{1/2}, i=1,2,4 \\ r_{i0} = r_i - r_0 = ct_{io} \end{cases} \quad \text{.....(2)}$$

where r_i is the range between emitter and receiver X_i, r_{io} is the range difference between the receiver X_i and the associated master station X_0. t_{io} Indicates the corresponding time difference of r_{io}. c is the speed of the light.

Equation (2) can be transformed into

$$\begin{aligned} &(x_0-x_i)x+(y_0-y_i)y+(z_0-z_i)z \\ &=(c^2t_{i0}^2+x_0^2+y_0^2+z_0^2-x_i^2-y_i^2-z_i^2)/2+ct_{i0}r_0 \end{aligned}, \ i=1,2,4 \quad \text{.....(3)}$$

Equation (3) can be written in the matrix form as

$$AX = b \quad \text{.....(4)}$$

where

$$A=\begin{bmatrix} x-x_1 & y-y_1 & z-z_1 \\ x-x_2 & y-y_2 & z-z_2 \\ x-x_4 & y-y_4 & z-z_4 \end{bmatrix}, X=\begin{bmatrix} x \\ y \\ z \end{bmatrix}$$

$$b=\begin{bmatrix} (c^2t_{10}^2+x_0^2+y_0^2+z_0^2-x_1^2-y_1^2-z_1^2)/2+ct_{10}r_0 \\ (c^2t_{20}^2+x_0^2+y_0^2+z_0^2-x_2^2-y_2^2-z_2^2)/2+ct_{20}r_0 \\ (c^2t_{30}^2+x_0^2+y_0^2+z_0^2-x_4^2-y_4^2-z_4^2)/2+ct_{40}r_0 \end{bmatrix}$$

If matrix A is full rank, regard r_0 as a constant value, we can get the intermediate value of emitter location with r_0 as below:

$$X = A^{-1}b \quad \text{.....(5)}$$

Substitute (5) in (2), we get a monadic quadratic equation with r_0 as below:

$$m_1r_0^2 + m_2r_0 + m_3 = 0 \quad \text{.....(6)}$$

Form (6) we can get

$$r_0 = \frac{-m_2 \pm \sqrt{m_2^2 - 4m_1m_3}}{2m_1} \quad \text{.....(7)}$$

when $m_1 > 0, m_2 < 0,$ and $m_2 - 4m_1m_3 > 0,$ (7) gives two positive value. Eliminating location ambiguity is necessary since only one of them is true and the other is untrue. The estimated position of the emitter can be derived by changing (5) with the right one. Location principle of subsystems S_2, S_3 works the same as S_1.

ISBN - 978-93-95038-50-8

5. PERFORMANCE METRICS

Qualitative analysis is done using standard deviation measured between the estimated and true emitter location. Generally, covariance matrix $\text{cov}(A)$ for any variable can be expressed as

$$\text{cov}(A) = E\left[\left(A-\hat{A}\right)\left(A-\hat{A}\right)^{T}\right] \quad \text{.....(8)}$$

In matrix form it can be expressed in form of variances $\sigma_x, \sigma_y, \sigma_z$ along x, y, z axis and correlation coefficient $\rho_{xy}, \rho_{yz}, \rho_{zx}$ between the respective receivers

$$\text{cov}(A) = C_{UU} = \begin{bmatrix} \sigma_x^2 & \rho_{xy}\sigma_x\sigma_y & \rho_{xz}\sigma_x\sigma_z \\ \rho_{xy}\sigma_x\sigma_y & \sigma_y^2 & \rho_{yz}\sigma_y\sigma_z \\ \rho_{xz}\sigma_x\sigma_z & \rho_{yz}\sigma_y\sigma_z & \sigma_z^2 \end{bmatrix} \quad \text{.....(9)}$$

If x, y, z are uncorrelated, then $\rho_{xy} = \rho_{yz} = \rho_{zx} = 0$. Equation (9) reduces to

$$\text{cov}(A) = C_{UU} = \begin{bmatrix} \sigma_x^2 & 0 & 0 \\ 0 & \sigma_y^2 & 0 \\ 0 & 0 & \sigma_z^2 \end{bmatrix} \quad \text{.....(10)}$$

Total standard deviation can be expressed as

$$\sigma_{total} = \sqrt{\sigma_x^2 + \sigma_y^2 + \sigma_z^2} \quad \text{.....(11)}$$

Physically this is interpreted as confidence ellipsoid along the orthogonal position axis.

6. SIMULATION SCENARIOS

Simulations are carried out using MATLAB tool kit and the various scenarios are descrided in detail. In scenario 1, geolocation is computed in two dimension (2D) using hybrid AOA/TDOA/FDOA measurements from ground/ship-based sensors at varying emitter distances. Data is received from emitters placed at locations (10,10) km, (15,15) km and (20,20) km by a pair of receivers placed at (2.5,0.5) km and (0.5,0) km. Geolocation accuracy is computed in terms of Root Mean Square Error (RMSE) and Circular Error of Probability (CEP_{50}). It is assumed that environmental errors and non-line-of-sight errors follow Gaussian distribution and the signal propagates with the speed of light.

In scenario 2, 3D TDOA geolocation is computed using measurements from n sensors, n=1,2,3,4,5 placed on ground/ship based, emitter is varied in altitudes i.e at (10,10,10) km, (15,15,15) km and (20,20,20) km. For each emitter positions, geolocation accuracy is computed in terms of total joint covariance matrix (Standard Deviation) from all receivers. In scenario 3, geolocation is computed using 3D TDOA measurements from near-space based n sensors, n=1,2,3,4,5 in form of, for example unmanned aerial vehicle and placed at an altitude of 10 km, 15 km and 20 km while the emitter is placed on ground/ship-based platform at (1,1,1) km. During simulations it is assumed that the error in the noise is having normal distribution with zero mean and in independent. Code is run for 700 times following

ISBN - 978-93-95038-50-8

Monte Carlo simulations as the total standard deviations reaches stable value after 700 iterations. and results are presented validate the effectiveness of the proposed method.

7. SIMULATION RESULTS

Table 1. shows the results for scenario 1 with geolocation accuracy computed using 2D hybrid methods. Table 2 shows the results for scenario 2 and 3 with geolocation accuracy computed using 3D TDOA method. It can be seen that RMSE of 1800 m, and CEP_{50} of 1220 m is obtained using 2D hybrid measurements at 20 km distance of emitter from receiver. In 3D scenario, measurements are taken using 3D TDOA, geolocation accuracy of 6 m is obtained when emitter is placed at an altitude of 20 km from the receiver, an d an accuracy of 16 m is obtained when data is collected from receivers placed at an altitude of 20 km (near-space platform) from the emitter placed on ground/ship based platforms. Geolocation accuracy using 3D TDOA three scenarios at 20 km is shown in Figure 1(a) and 1(b).

Table 1: Geolocation using 2D TDOA

Emitter on ground/ship-based platforms at varying distances from the receiver (placed on ground/ship-based platforms)			
Scenario 1	10 km	15 km	20 km
RMSE (m)	390	960	1800
CEP_{50} (m)	270	660	1220

Table 2: Geolocation using 3D TDOA measurements

Emitter on near-space platforms at varying altitudes from the receivers (placed on ground/ship-based platforms)			
Scenario 2	10 km	15 km	20 km
Geolocation accuracy Standard Deviation (m)	4.3565	5.2424	6.2061
Receivers placed on near-space platforms at varying altitudes from the emitter (placed on ground/ship-based platforms)			
Scenario 3	10 km	15 km	20 km
Geolocation accuracy Standard Deviation (m)	7.0626	11.4617	16.8820

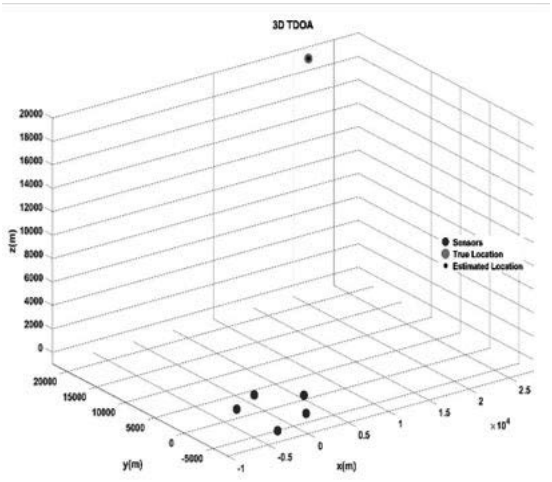

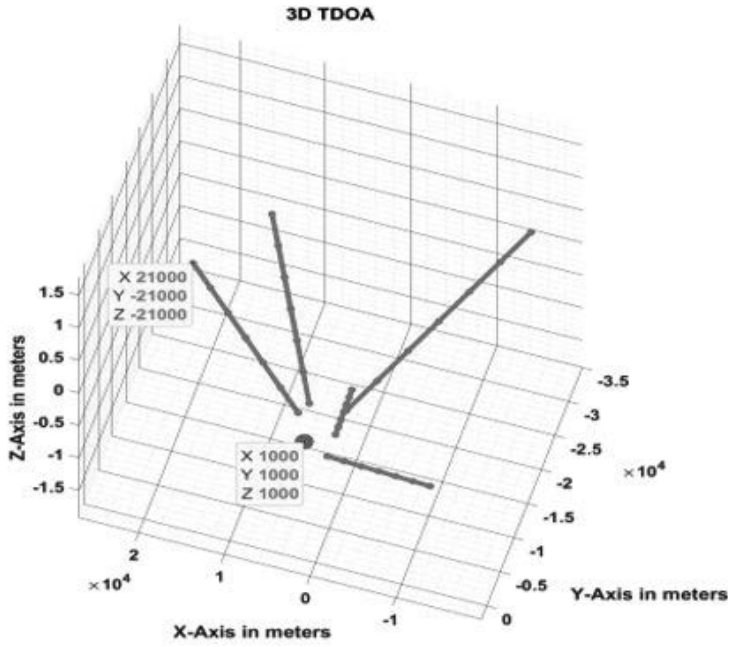

Figure 2(a) and 1(b) for geolocation accuracy for scenario 2 and 3

8. CONCLUSION

Geolocation from near-space platform using 3D TDOA technique have gained significance in past several years as it paves way for understanding geolocation accuracies from space-based platforms. In this paper, geolocation using 2D hybrid methods and geolocation using 3D TDOA is presented in all combinations of varying both emitter and receiver positions and altitudes and comparative measurements are tabulated. In 2D methods, simulation results have been presented using RMSE and CEP50, whereas for 3D TDOA, simulation results have been presented using measured Standard Deviation. In due course of time, simulation results from space-based platforms will be presented using 3D TDOA. Results are in accordance with the theoretical developments and they validate the effectiveness of the proposed method.

REFERENCES

1. Liu X, Yang T, Chen H, Qiu TZ. Research on roadside unit-assisted cooperative positioning method for a connected vehicle environment. Transportation research record. 2022 Jan;2676(1):78-90.
2. Khalaf-Allah M. Emitter Location with Azimuth and Elevation Measurements Using a Single Aerial Platform for Electronic Support Missions. Sensors. 2021 Jun 8;21(12):3946.
3. Sathyan T, Sinha A, Kirubarajan T. Passive geolocation and tracking of an unknown number of emitters. IEEE Transactions on Aerospace and Electronic Systems. 2006 Jun 19;42(2):740-50.
4. Dunham J, Simmons J, Shapero S. Analytic Emitter Geolocation and Filtering via Time Difference of Arrival. In2019 IEEE Aerospace Conference 2019 Mar 2 (pp. 1-11). IEEE.
5. Zhao K, Song J, Ai S, Xu X, Liu Y. Active fault-tolerant control for near-space

hypersonic vehicles. Aerospace. 2022 Apr 25;9(5):237.

6. Hu J, Li Y, Chen W, Gao C, Gao J, Zhang Y, Qiu Z. Performance characteristics of GaInP/InGaAs/Ge triple-junction photovoltaic panels for near-space vehicles via ground experiments. Applied Energy. 2022 Nov 15; 326:119826.
7. Pei Y, Li X, Guo F. Geolocation of a known-altitude moving source using TDOA and FDOA in the presence of altitude error. Digital Signal Processing. 2022 Dec 1; 132:103798.
8. Khalaf-Allah M. Emitter Location Using Frequency Difference of Arrival Measurements Only. Sensors. 2022 Dec 9;22(24):9642.
9. O'Donoughue N. Practical Geolocation for Electronic Warfare Using MATLAB. Artech House; 2022 Jun 30.
10. Li J, Lv S, Jin Y, Wang C, Liu Y, Liao S. Geolocation and Tracking by TDOA Measurements Based on Space–Air–Ground Integrated Network. Remote Sensing. 2023 Jan;15(1):44.
11. Li J, Lv S, Liu Y, Zhang K, Yang L, He Y. Performance analysis for space-air-ground integrated passive localization using TDOA measurements. In2022 IEEE International Conference on Unmanned Systems (ICUS) 2022 Oct 28 (pp. 199-203). IEEE.
12. Ma F, Liu ZM, Yang L, Guo F. Altitude constrained source localization using TDOA, FDOA and differential Doppler rate. Digital Signal Processing. 2022 Apr 30; 123:103385.
13. Zhan D, Wang S, Cai S, Zheng H, Xu W. Acoustic localization with multi-layer isogradient sound speed profile using TDOA and FDOA. Frontiers of Information Technology & Electronic Engineering. 2023 Jan;24(1):164-75.
14. Chen CB, Lo TY, Chang JY, Huang SP, Tsai WT, Liou CY, Mao SG. Precision Enhancement of Wireless Localization System Using Passive DOA Multiple Sensor Network for Moving Target. Sensors. 2022 Oct 6;22(19):7563.
15. Ko YH, Bu SC, Lee CS, Lim JW, Chae JH. Closed-form based 3D Localization for Multiple Signal Sources. Journal of Advanced Navigation Technology. 2022;26(2):78-84.

ISBN - 978-93-95038-50-8

Performance Observation of IRNSS in Terms of Receiver Geometry and Position Accuracy Over Hyderabad Region

R. Anil Kumar* and P. Naveen Kumar

Department of ECE, University College of Engineering,
Osmania University, Hyderabad, Telangana, 500007
Email: anilramavath@osmania.ac.in, drnaveenkumar@osmania.ac.in

ABSTRACT

The Indian Regional Navigation Satellite System (IRNSS) is a satellite navigation system developed by the Indian Space Research Organization (ISRO), using the frequencies of the L5 and S1 bands. The IRNSS system is independent of GPS. It is used for position, velocity and timing (PVT) services over the Indian region and surrounding coverage area of 1500 km. The positional accuracy of IRNSS system suffers from many sources of errors. To achieve better accuracy, combination of different navigation systems is required. This paper presents the detailed analysis of IRNSS satellite visibility, dilution of precision (DOP) and signal strength under open sky. The effect of satellite geometry on position accuracy and performance of IRNSS is presented. From the results, it is observed that the combined IRNSS/GPS hybrid mode of operation of dual frequency receiver measurements gives better accuracy compare to hybrid mode of operation using single frequency measurements.

Keywords: *DOP, GLONASS, GPS, IRNSS*

1. INTRODUCTION

A navigation system developed by ISRO is IRNSS. India will be able to track the NavIC/IRNSS satellites with a precision of 10 meters as it combines three geostationary satellites (GEO) and four geosynchronous satellites (GSO). IRNSS satellites broadcast the signals in carrier frequencies of 1176.45 MHz (F1) and 2492.08 MHz (F2), respectively, in the L5 band (1164.45–1188.45 MHz) and S band (2483.5–2500 MHz) [2]. A system such as the IRNSS has been proposed by the Indian government to provide positioning services for disaster management, navigation services for aircraft landing in CAT-1 cases, and precision surveying over the subcontinent and 1500 km in the surrounding area [1]. In the upcoming years, Internet of Things (IoT) will be an exciting technology that will connect devices together through internet. IRNSS will be fundamental for Indian navigation in the future, which can be integrated with IoT for access anywhere, anytime, and allow data back-ups and mobile assistance to be provided via IRNSS. There are a number of factors that can influence the positioning accuracy of such a system, including the geometry used, receiving the signal takes longer than expected due to the ionosphere and troposphere, multipath, Doppler Effect, clock drift, and receiver noise. Positional inaccuracies/miscalculations may arise as a result of these effects. The majority of these errors are caused by atmospheric refraction, multipath, and refraction due to atmospheric layers can be modelled, and the resulting error, namely "User Equivalent Range Error" (UERE), can be estimated based on algorithms described in the literature.

Due to the interdependence of UERE and satellite reception, positioning accuracy is determined by GNSS satellite-receiver geometry needs to be investigated as a factor in positioning accuracy. Geometric dilution of precision (GDOP) refers to how the satellites are viewed from the perspective of a GNSS receiver with regard to the satellite's spatial location. If the receiver is not able to see all satellites, the optimum-4 satellites can be used to compute the GDOP. To select the most suitable satellites from all the visible satellites at an instant, Jao et al. proposed the use of optimum interpolative networks based on neural networks. Neural

*Corresponding author: E-mail: anilramavath@osmania.ac.in

network-based approaches allow for efficient evaluation of all satellite sets without matrix inversion, thus reducing computational complexity. Without complexity matrix inversion, Mosavi proposed a "genetic algorithm" (GA) to compute GPS GDOP. The study presented by Wu et al. used SVR to approximate GPS GDOP. This method was compared with Artificial Neural Networks and genetic programming as regression methods. In a two-dimensional environment, Sharp et al. analyzed GDOP in order to determine accuracy for target tracking, which is very relevant to sports applications both indoors and outdoors [1]. In an effort to predict GDOP at a point in time, Lohani and Kumar used LiDAR data to forecast the GDOP in the presence of trees. GDOP was examined for different configurations by Srilatha Indira Dutt et al., the entire view is used instead of the optimal four satellites, which simplifies the selection process. In this paper we analyze data due to the IRNSS and GPS constellations. With the help of the IRNSS and GPS constellations, the satellite–receiver geometry is explored here to obtain a more accurate GDOP, with which the accuracy of positioning can be improved. It has been found that the GPS and IRNSS constellations with their combined satellite-receiver geometry give the best GDOP. For a typical day of 22nd January 2022, the data is obtained from IGS dual frequency receiver and Navlan IG3 single frequency receiver which are placed at AGRL, Department of ECE, UCE, OU station, Hyderabad, (Latitude/Longitude:17.4078^0 N/78.5178^{0}E) was used for the proposed study.

2. GEOMETRIC DILUTION OF PRECISION (GDOP)

Any navigation system's ability to estimate position accurately is measured by its accuracy of position estimation. As the signal propagates from satellite to receiver, many factors, including refraction in the atmosphere, multipath errors, satellite clock errors, and satellite geometry, influence the accuracy of the positioning solution. By measuring geometric dilution of precision (GDOP), we can determine the impact of satellite-receiver geometry on measurement error and positioning error. GDOP is a GPS Precision quality that measures the multiplicative effect of satellite-receiver geometry on positioning error and measurement error. The GDOP can be computed by considering pseudorange equations of all the satellites in view or the best and/or most reliable satellites of all the satellites visible. A pseudorange measurement of all visible satellites is used to compute the GDOP instead of selecting the four best satellites, which is very complicated and time consuming. Linearize with receiver position the pseudorange equations for n >= 4 satellites. The pseudorange equations for n number of satellites is shown in Equation 1 [1].

$$\begin{bmatrix}\Delta_{prn1}\\ \Delta_{prn2}\\ \Delta_{prn3}\\ \cdot\\ \cdot\\ \cdot\\ \Delta_{prnn}\end{bmatrix}=\begin{bmatrix} g_{11} & g_{12} & g_{13} & 1\\ g_{21} & g_{22} & g_{23} & 1\\ g_{31} & g_{32} & \cdot & 1\\ & & \cdot & \\ & & \cdot & \\ g_{n1} & g_{n2} & g_{n3} & 1\end{bmatrix}\begin{bmatrix}\Delta_{UX}\\ \Delta_{UY}\\ \Delta_{UZ}\\ C\Delta_b\end{bmatrix}+\begin{bmatrix}\varepsilon_1\\ \varepsilon_2\\ \varepsilon_3\\ \cdot\\ \cdot\\ \cdot\\ \varepsilon_n\end{bmatrix} \quad \text{…..(1)}$$

The general form of equation 1 is $P_r = G * U + \varepsilon$, where G is the n x 4 geometry matrix, an indicator of the satellite's direction cosine, U is the user position, in addition to measurement noise, ε accounts for unmodeled effects, such as selection and multipath. Equation 1 can be written in linear least squares approximation as shown in equation 2 [1].

$$\Delta U = (G^T G)^{-1} G^T \Delta P_r \quad \text{…..(2)}$$

GDOP is calculated using equation 3[1].

$$\text{GDOP} = \sqrt{Trace(G^T G)^{-1}} \quad \text{…..(3)}$$

GPS positioning accuracy is often measured by GDOP, which is a multiplication of the measurement error of the system. The accuracy is given by

Accuracy of position = UERE * GDOP …..(4)

The UERE provides the root sum square of a variety of errors and biases. The accepted range of DOP values is shown in table 1.

Table 1: Range of DOP [1]

Range of DOP Value	Rating
1	Ideal
2-4	Excellent
4-6	Good
6-8	Moderate
8-20	Fair
20-50	Poor

2.1 IRNSS VISIBILITY OVER THE SERVICE REGION

Any GNSS system is considered to be available as long as the signal can be received in a specific region, and the number of satellites visible from any point therein can be measured. Simulation of the NavIC satellite visibility patterns is used to generate the service region's visibility patterns for 5^0 elevation masks over a day using the method discussed earlier. There are always at least 5 NavIC satellites visible over the whole landmass of India, except for a small area in the extreme north. Satellites broadcast signals continuously. There is no difference in the strength of satellite broadcast signals. Due to path loss from free-space and interference in the transmission path, the user receives discontinuous and varying-quality signals from satellites. A GNSS satellite transmitting to a receiver will encounter a different environment depending on the user's location. The distance and the interference along this path will vary as well. Due to autocorrelation function errors in the code tracking loop, ranging error increases when received signal power is significantly below specified levels. Integer ambiguity is a problem with carrier-phase measurements, and pseudorange measurements are more precise. Centimetre-level positioning can be attained by resolving the integer ambiguity [1]. Sometimes, however, GNSS receivers are not able to generate carrier-phase measurements because a GPS signal has been temporarily blocked from latching onto the carrier. The satellite signal can be interfered with by radio interference, Ionospheric disturbances, or obstructions such as buildings and trees. Signal lock loss has been associated with high receiver dynamics. Receiver lock on satellite signals must be periodically recalculated if the receiver loses its connection to the satellite [2]. The carrier-phase measurement will be discontinuous or jumpy if the integer ambiguity changes for a satellite. Loss of satellite signals is indicated by a cycle slip in GNSS receivers. In order to calculate the new ambiguity value, receivers should allocate extra time. This results in decreased availability. In order to provide precise positioning, it can be helpful to analyse the satellite signal continuity for a given user. This study investigates the sensitivity to IRNSS and GPS signals. The following table compares IRNSS and GPS signal strength and continuity. Signal strength and quality are determined by the carrier-to-noise ratio (C/N_0). In the front-end of a receiver, the C/N_0 output indicates satellite tracking status and quality, as well as whether there is any noise.

3. METHODOLOGY

Analyzing real-time L5 and S-Band data allows us to study the quality of NavIC solutions. GNSS/NavIC users would find the latter to be of interest due to its capability to provide

ISBN - 978-93-95038-50-8

positional information. In the central NavIC service area, the quality of NavIC position solutions is evaluated in single and dual frequency operation in L5+S and GPS L1bands. An L5+S of IRNSS and GPSL1 band antenna of IGS dual frequency receiver is mounted on the roof top AGRL, Department of ECE, University College of Engineering, Osmania University. L5 of IRNSS, L1 of GPS and L1 of GLONASS, Navlan IG3 single frequency receiver, antenna is also placed on the same roof top. The 24 hours data is recorded from both the receivers. Based on the geodetic coordinate system position solutions are transformed into an East-North-Up (ENU) coordinate system. Next, the precision parameters for the solutions, namely 2DRMS, CEP, SEP, and MRSE are computed with the formulae given below using the RMS of East error (σ_x), RMS of North error (σ_y), and the RMS of Up error (σ_z) [3].

$$2DRMS = 2\sqrt{\sigma_x^2 + \sigma_y^2} \quad \text{.....(5)}$$

$$\text{CEP} = 0.62\sigma_x + 0.56\,\sigma_y; \text{ for } \frac{\sigma_x}{\sigma_y} > 0.3 \quad \text{.....(6)}$$

$$\text{SEP} = 0.51(\sigma_x + \sigma_y + \sigma_z) \quad \text{.....(7)}$$

$$\text{MRSE} = \sqrt{\sigma_x^2 + \sigma_y^2 + \sigma_z^2} \quad \text{.....(8)}$$

4. Results and Discussion

DOP values are estimated using two different types of receivers (single and dual frequency) using all available satellites of GPS, GLONASS and IRNSS (single frequency receiver) and GPS+IRNSS (dual frequency receiver). Figure (1-2) show the computed DOP values due to single frequency receiver and dual frequency receiver for a typical day of 22nd January, 2022.

The PDOP of obtained data from single and dual frequency receivers are shown in table 2 and table 3, it is observed that the maximum PDOP value of single frequency multi-constellation (GPS+GLONASS+IRNSS) receiver is 1.60 and the minimum PDOP is 1. Whereas for IGS dual frequency (GPS+IRNSS) receiver it is 2.623 and 1.184 respectively. The variation in PDOP value of both the receivers due to number of satellites in view are more for single frequency receiver. The maximum GDOP due to dual frequency receiver data is 3.346 and minimum value is 1.3.

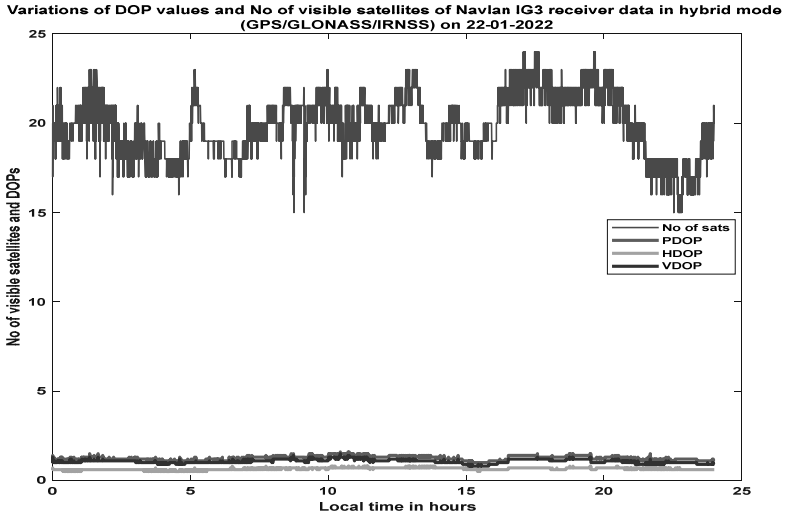

Figure 1: Number of visible satellites and DOP values of Navlan IG3 single frequency multi-constellation (GPS+GLONASS+IRNSS) receiver on 22-01-2022

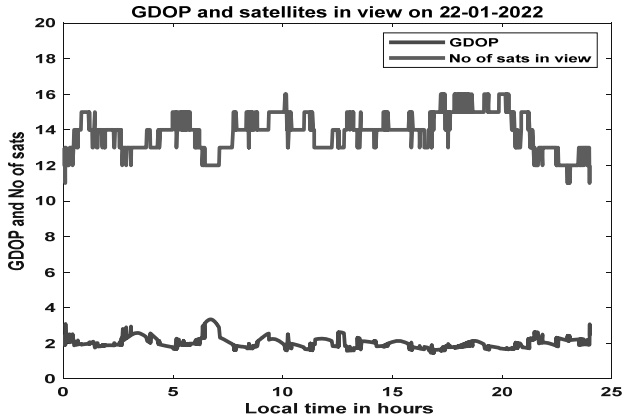

Figure 2: GDOP computed using GPS+IRNSS hybrid mode using dual frequency receiver

Figure 3 shows the C/N_0 variations of IRNSS L5 signal on 22-01-2022. The IRNSS signal strength is more than 45 dB-Hz for all the PRNs. The maximum and minimum values of signal strength is shown in table 4.

Table 2: Precision parameters of single frequency receiver in hybrid mode (GPS+GLONASS+IRNSS) on 22-01-2022

S. No	Minimum PDOP	Maximum PDOP	Mean PDOP
1	1.00	1.60	1.2328

Table 3: Precision parameters of dual frequency receiver in hybrid mode (GPS+IRNSS) on 22-01-2022

S. No	Minimum		Maximum		Mean	
	GDOP	PDOP	GDOP	PDOP	GDOP	PDOP
1	1.3	1.1848	3.346	2.6239	2.0297	1.6315

Table 4: C/N_0 variations of IRNSS using single frequency receiver data on 22-01-2022

	Max. C/N_0 in dB-Hz					Min. C/N_0 in dB-Hz				
PRN No.	**97**	**98**	**99**	**101**	**105**	**97**	**98**	**99**	**101**	**105**
C/N_0	47	52	51	45	48	32	34	41	29	33

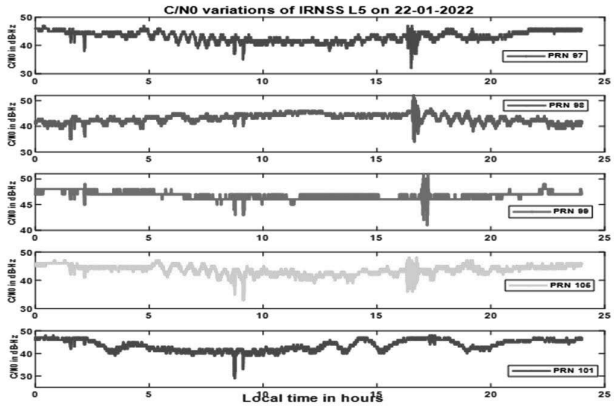

Figure 3: C/N0 variations of all IRNSS PRNs using single frequency receiver data on 22-01-2022

The maximum and minimum C/N_0 values for GLONASS system is noted in table 5 using single frequency receiver. The maximum and minimum C/N_0 values of IRNSS and GPS systems using dual frequency receiver are shown in table 6 and 7 respectively.

Table 5: Variations in C/N_0 of GLONASS using single frequency receiver data on 22-01-2022

	GLONASS PRN Number											
	65	**66**	**67**	**68**	**68**	**70**	**71**	**72**	**75**	**76**	**77**	**78**
Max. C/N0 (dB-Hz)	48	48	46	43	47	50	50	50	46	44	47	44
Min. C/N0 (dB-Hz)	40	28	29	22	37	31	33	35	38	9	40	28

Table 6: Variations in C/N_0 of IRNSS L5 and S BAND using dual frequency receiver on 22-01-2022

	IRNSS L5 band									
	Max. C/N_0					**Min. C/N_0**				
PRN No.	**2**	**3**	**4**	**6**	**9**	**2**	**3**	**4**	**6**	**9**
C/N0 in dB-Hz	53	53	50	50	52	32	43	40	33	40
	IRNSS L5 band									
	Max. C/N_0					**Min. C/N_0**				
PRN No.	**2**	**3**	**4**	**6**	**9**	**2**	**3**	**4**	**6**	**9**
C/N0 in dB-Hz	46	46	43	43	47	36	37	36	36	36

Table 7: Variations in C/N0 of GPS L1 band using dual frequency receiver on 22-01-2022

	GPS C/N_0 (dB-Hz)							
PRN No.	**1**	**2**	**3**	**4**	**5**	**6**	**7**	**10**
Max.	49	50	51	49	48	51	48	48
Min.	22	21	20	21	20	19	20	23

From table 8, the position accuracy of IRNSS is measured in terms of 2DRMS, CEP, SEP and MRSE. In case of single frequency (SF) receiver placed at AGRL, Department of ECE, UCE, OU station, the position accuracy is 5.3423 m (2DRMS), 2.0459 m (CEP), 2.4371 m (SEP) and 2.9464 m (MRSE). Where for the dual frequency receiver the accuracy is 2.666 m (2DRMS), 1.0483 m (CEP), 1.3096 m (SEP) and 1.5362 m (MRSE) are noted. Therefore, the positioning accuracy of SF receiver on 22nd January, 2022 deviated by 50% in 2DRMS, 49% in CEP, 46% in SEP and 48% in MRSE. In this study it is observed that the DF receiver measurements in hybrid mode gives better accuracy compared to SF receiver in hybrid mode. Inspite of inclusion of one more Global constellation in the SF receiver, the performance of DF receiver is much better in the order of above said percentage, when compared to SF receiver, in terms of GDOP and position accuracy

Table 8: Positional accuracy of SF and DF measurements on 22-01-2022

S. No.	**Receiver type**	**CEP (m)**	**SEP (m)**	**2DRMS (m)**	**MRSE (m)**
1	**SF receiver**	2.0459	2.4371	5.3423	2.9464
2	**DF receiver**	1.0483	1.3096	2.666	1.5362

ISBN - 978-93-95038-50-8

5. CONCLUSION

In this paper, performance of IRNSS system is studied in terms of signal strength, DOP, east, north and up errors and positional accuracy using SF receiver and DF receiver over the low latitude Hyderabad station. Initially, the precision parameters of SF receiver is measured and compared with precision parameters of DF receiver. It is observed that the GDOP is better for DF receiver in hybrid mode. Secondly, the position accuracy is measured in terms of 2DRMS, CEP and SEP. 2DRMS is improved by 50%, CEP is improved by 49% and SEP is improved by 46% due to the DF receiver hybrid mode. In terms of root mean square error (MRSE), the error is improved by 48% compare to SF receiver in hybrid mode. So that, by the results, this paper concludes that the DF receiver in hybrid mode gives the better accuracy. Inspite of inclusion of one more Global constellation in the SF receiver, the performance of DF receiver is much better in the order of above said percentage, when compared to SF receiver, in terms of GDOP and position accuracy.

REFERENCES

1. Ch. Rajasekhar, V. B. S. Srilatha Indira Dutt, G.Sasibhushana Rao, "Investigation of Best Satellite–Receiver Geometry to Improve Positioning Accuracy Using GPS and IRNSS Combined Constellation over Hyderabad Region", Wireless Personal Communications, 2015.
2. Sukabya Dan, Atanu Santra, Somnath Mahato, Anindya Bose, "NavIC performance over the service region: availability and solution quality", Sādhanā, 2020.
3. Devadas Kuna, Dr. P. Naveen Kumar, R. Anil Kumar “Positioning Parameters for Standalone and Hybrid Modes of the Indian NavIC Systems: Preliminary Analysis”, International Conference on Emerging Trends in Engineering (ICETE), 22-23 March 2019, University College of Engineering, Osmania University, Hyderabad.
4. K. M. Gayathri, N. Thangadurai. "Chapter 63 Study and Analysis of IRNSS/NavIC Signals for Atmospheric Effects near Bangalore Region", Springer Science and Business Media LLC, 2020.
5. Mehul V. Desai, Shweta N. Shah. "Chapter 18 Analysis of Ionospheric Correction Approach for IRNSS/NavIC System Based on IoT Platform", Springer Science and Business Media LLC, 2018.
6. Mehul V. Desai & Shweta N. Shah “Case Study: Performance Observation of NavIC Ionodelay and Positioning Accuracy”, IETE Technical Review, DOI: 10.1080/ 02564602.2020.1723445.
7. M. V. Desai, and S. N. Shah, “An observational review on influence of intense geo-magnetic storm on positional accuracy of NavIC/IRNSS system”, IETE Tech. Rev., pp. 1–15, 2019. DOI:10.1080/ 02564602 .2019.1599739.

Fault Management of Guidance and Control System for Aerospace Vehicles

M. Reshma Gopal[1*], O. R. Ashwin Chandar[1] and P. Koti Lakshmi[2]

[1]Scientist, ASL, DRDO,
[2]Professor, Department of ECE, UCEOU
Hyderabad, Telangana
Email: reshmagopal471@gmail.com

ABSTRACT

Aerospace vehicles generally are safety-critical systems and they rely on sophisticated control systems. For an aerospace system to be fully reliable and highly safe, it requires to have the features of fault detection and diagnosis. In case of malfunction of the control actuators or sensors or other components, a conventional feedback control design may not meet the system requirement and may cause catastrophic failure. It therefore becomes a necessity to design fault tolerating control system design to improve the reliability of the system and maintain the overall system stability. The fault tolerance is achieved by fault detection and diagnosis and isolation of the fault. After the fault is recognized, the reconfiguration is carried out by means of redundancy on-board and the flight operation is continued. This paper gives the design of highly reliable flight control systems by employing fault detection and reconfiguration on-board by hardware and analytical redundancy techniques.

Keywords: *Fault Management, Flight Control System, Redundancy Management*

1. INTRODUCTION

An aerospace system consists of the on-board systems which have embedded systems for high computation, data processing, decision making and on-board command generation based on the physical environmental conditions. However, it is critical for the on-board systems to be highly reliable systems even in case of the harsh environmental conditions and with the real-time constraints. The impact of any fault in a component of a sub-system would lead to either degradation in the actual performance or overall system failure. In most of the failures, after the post flight analysis it comes out clear that though the fault in the system/ component could not be avoided but still would have been tolerated or mitigated by means of fault tolerant logics. The Fault tolerant mechanisms are designed to either reconfigure the system with the redundant sensor information or continue with the same sensor information but mitigate and have a graceful degradation in performance that may not cause heavy economical and human loss. This in turn increases the safety and reliability aspects of any aerospace system.

Design of a Fault Tolerant Flight Control System involves Detection of the Fault & Isolation from the main control loop with reconfigurable Control law, Design of Redundancy scheme to ensure non- degraded performance even under failure and to increase the overall reliability of the system.

2. LITERATURE REVIEW

FAULT ASSESSMENT& RISK IDENTIFICATION

Fault assessment refers to the systematic approach to evaluate the fault in a complex engineered system. The risk associated with each fault can be characterized by the Magnitude

* Corresponding author: E-mail: reshmagopal471@gmail.com

of the consequence that the fault can cause and Probability with which the fault may occur in the system causing adverse consequences. The Low Matrix index[10] is given to the unlikely faults and high index to the most frequent faults in a system. A fault that is frequent in nature and is critical and catastrophic becomes the highest risk for the system. This matrix index defines the area of concern in a system and aids in the decision to go ahead with either redundancy or fault tolerant mechanisms.

FLIGHT CONTROL SYSTEM

Failure of Flight Control system [3] can occur due to fault in either in components, structure, sensors or control actuation system. These faults change the control system dynamic behavior and cause instability thereby leading to structural damage. Sensor faults or incorrect reading would lead to incorrect decision on-board and failure of the system. In addition, when the failure of the sensor is catastrophic, it is always recommended to use redundant sensors and the sensor values can be taken based on the voting logics. However, with the increase in the number of sensors the cost of the system also increases. So, it is advised to analyze the trade-off between the cost and reliability and its effect of the sensor on the system and decide. Faults in actuation system would be categorized as either saturated value or struck at a random value. Either of the fault would lead to the loss of control action, as the actuator would not respond to the input given to it. Redundancy in actuation systems to achieve fault tolerance is often not preferred due to their high prices and large size and mass.

FAULT TOLERANT FLIGHT CONTROL

Fault Tolerant Control (FTC) [1] strategies can be categorized as passive and active approaches. In case of passive approach, Control law is designed to cater for stability in case of fault as well as fault free condition. For the control law to handle both the situations with or without degradation, it has to be very robust. In case of active approach, the fault detection and diagnosis information are required for the control reconfiguration. After the control is reconfigured, on-board decision-making would resume the mission activities without any intervention from the ground. Fault Tolerant Flight Control (FTFC) can be achieved by Fault Detection and Isolation (FDI) scheme followed by Re-configuration of control.

FDI Techniques are helpful to recognize the fault early in the system before it causes irreversible damage to the system. FDI Techniques [8] are generally categorized as Model-based approaches and Data-driven approaches. Model based FDI approaches are widely used and are more economical. Examples of Model based approaches are Kalman based approach, Parity-space approach or Observer-based approach. In these schemes, state estimation techniques are used that have mathematical models of the plants that are based on linear system theory. So, the techniques mostly depend on the accuracy and precision with which the system is modelled. Data driven based FDI approaches use Fuzzy logic, Artificial Neural Network (ANN) and Genetic Algorithm (GA) based approaches for detection of the fault in the system. These approaches provide more reliable results than the model-based approach.

Reconfiguration of the control law[9] is the important aspect of the fault tolerant control where the fault diagnosis is used to restructure the control loop and adapt the controller to the faulty system. Several techniques of Control structure modification, Real-time redesign or real-time search and optimization techniques of control loop and gain scheduling can be used for fault treatment.

ISBN - 978-93-95038-50-8

3. PROBLEM DEFINITION

The aim of the project is to make the aerospace system more reliable. A way to offer increased reliability and safety is by means of a fault-tolerant flight control (FTFC) system design by means of redundancy physically or analytically and reconfiguration of autopilot design as shown in Figure 1.

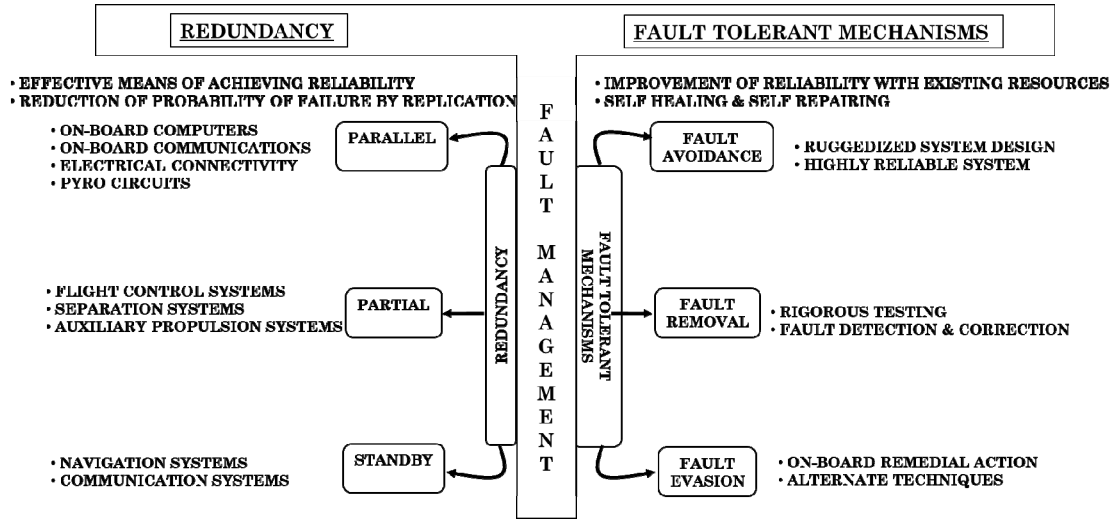

Figure 1: Fault Management

4. IMPLEMENTATION METHODOLOGY

The fault tolerance is achieved by detection and isolation followed by the reconfiguration. The implementation of the fault tolerance is as follows.

(i) Identification of fault in the actuation / sensor output based on the observer inputs.

(ii) Isolation of the fault from the control loop.

(iii) Switchover to redundant navigation sensor.

(iv) Reconfigure control law to take corrective measures.

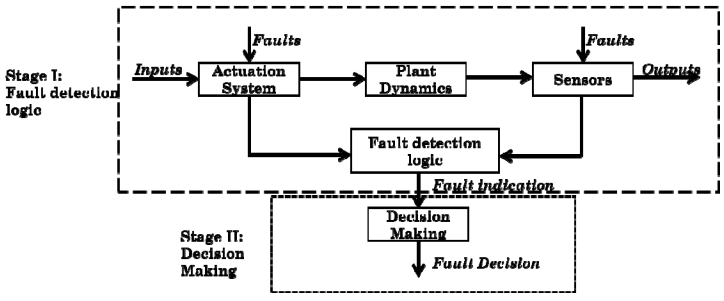

Figure 2: Fault Detection and Isolation

Stage I: Algorithm contains logic to check the values from actuator and sensor and decide fault based on the fault detection logic.

Stage-II: Decision rule is applied based on the fault detected and the control law is modified accordingly.

SENSOR FAULT TOLERANCE

Failures in navigation sensor may be due to sensor failure, processor failure, electronics failure, and communication bus failure or processor hang conditions. If there is any anomaly in the values of sensor data for consecutive 10 samples, then the corresponding sensor is isolated and the data is obtained from the corresponding redundant sensor.

Table 1: Sensor Fault Identification & Mitigation

	Failure Nodes		Action at Main Board	Action at Standby Board	Implications
1	RLG-Sensor Package	Ax, Ay, Az, Gx, Gy, Gz	Single Sensor Failure : Corresponding MEMS Sensor Data to be considered More than one Sensor Failure: Switch-over to MEMS	Single Sensor Failure : Corresponding MEMS Sensor Data to be considered More than one Sensor Failure: Switch-over to MEMS	Navigation with MEMS Sensor Package
2	MEMs-Sensor Package	Ax, Ay, Az, Gx, Gy, Gz	No Action	No Action	Navigation with RLG Sensor package only
3	GPS RX with Main Board		No Action	No Action	Navigation with RLG Sensor Package without GPS
4	GPS RX with Standby Board		No Action	No Action	Nil

ACTUATOR FAULT TOLERANCE

The system considered is a Flex Nozzle Control (FNC) system for a Solid Rocket Motor Propelled Aerospace vehicle. This FNC provides control in Pitch & Yaw plane by vectoring the main thrust from the rocket motor. FNC has two sensors called Main Sensor in the Actuator and Mirror sensor diametrically opposite to that of the main sensor.

The reason for having two sensors is to differentiate the common mode deflection, which may be caused due to the change in the internal chamber pressure and the actual deflection due to the control commands from autopilot.

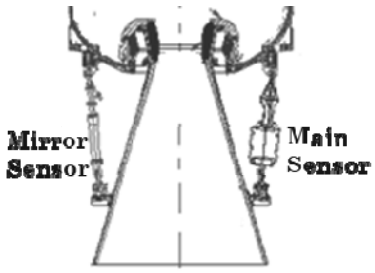

Figure 3: Typical Flex Nozzle Control System

In an ideal condition, the Main and Mirror sensor are expected to give similar deflection outputs. The differential mode signal will be given as controller feedback. The common mode and the differential mode signals can be calculated as per the equations below.

ISBN - 978-93-95038-50-8

$$Cmd_C = \frac{FB_{Main} + FB_{Mirror}}{2} \quad \text{..... Equation 1}$$

$$Cmd_D = \frac{FB_{Main} - FB_{Mirror}}{2} \quad \text{..... Equation 2}$$

One of the common modes of Failure is that of the malfunction of the mirror image sensors. Fault identification logic is designed to identify the malfunction of LVDT Sensors and to isolate from the controller feedback loop. Once the malfunction is identified, then the particular sensor is isolated from the controller feedback loop. However, for proper functioning of controller, at least one sensor is required. However, this sensor cannot handle the differentiation between common mode and differential mode signals. Therefore, an additional input such as Rocket Motor Chamber pressure (P_c), which is monitored is considered for autopilot gain scheduling.

RECONFIGURABLE AUTOPILOT

An autopilot is a closed loop system inside the main guidance subsystem that ensures that the vehicle achieves accelerations as commanded and maintains stability. Autopilot employs gain-scheduling techniques due to variation of velocity and altitude and the thrust, thereby scheduling the gains as a function of Mach number or Dynamic Pressure. The vehicle attitude information is obtained from the Inertial navigation system. Attitude errors are computed by knowing the desired attitude and sensed vehicle attitude and the error is fed to the control actuators. The Control system stabilizes the vehicle and executes the guidance commands to maneuver the vehicle in the desired trajectory. This is the most classical technique used in flight control system.

In reconfiguration based on the prior designed failure modes, the control filter changes are stored in the flight control system memory and when the fault is detected, the control filters are modified. With the recent trend of digital flight control systems, along with the gain scheduling modifications, control filter coefficients and time constants are modified.

5. RESULTS AND DISCUSSIONS

Being Time critical events, the objective of the testing is to see whether the failure is handled and the stand-by system takes over within the time frame to execute the next event.

SENSOR FAULT TOLERANCE

All Single node failure scenarios are designed based on Redundancy Management Scheme.

Failure scenarios include Data validity not OK, Data freezing and Bus Failure/Silence.

Test Methodology

The testing of the redundancy logics is carried out using the Zync SoC board, which consists of a Dual core processor making it suitable for the implementation of redundant navigation configuration. The requirements of the system are mapped to the implementation, a traceability matrix is prepared to introduce failures in the system, and the failures are introduced at critical time events.

ISBN - 978-93-95038-50-8

Table 2: Requirement Traceability Matrix

Requirement ID	Test Condition	Test Case ID
1	Single Sensor Failure of RNAV-IMU (any one sensor failure among Ax, Ay, Az, Gx, Gy, Gz)	Test Case 1
2	More than one Sensor Failure of RNAV-IMU (Any one sensor failure among Ax, Ay, Az, Gx, Gy, Gz)	Test Case 2
3	Single /Multiple Sensor Failure of MEMS-IMU (Any one sensor failure among Ax, Ay, Az, Gx, Gy, Gz)	Test Case 3
4	GPS+GLONASS RX link failure with Main Board	Test Case 4
5	GPS+GLONASS RX link failure with Standby Board	Test Case 5

TEST RESULTS

Based on the traceability matrix the result of the test case with single sensor failure is presented below as shown in Table 3.

Table 3: Test Case-1 Results & Analysis

Requirement Details				
Requirement ID	**Failure Node**	**Action at OBC (M)**	**Action at OBC (S)**	**Mission Implication**
1	Single Sensor Failure of RNAV-IMU	Corresponding MEMS sensor data to be considered for Navigation	Corresponding MEMS sensor data to be considered for Navigation	Navigation with one MEMs sensors and all other RNAV sensors
Test Case Details				
Test Case Id	Aim	Test condition at OBC (M)	Test condition at OBC (S)	Observed Result
TC-1	To verify the switchover condition when data validity for Sensor data is Not OK in both OBC (M) & OBC(S) at the same time.	Sensor data set as NOT OK	Sensor data set as NOT OK	OBC (M) continued to execute further events.
Test Result Analysis & Remarks				
OBC (M) continued with the execution of further events. Data of failed RINS sensor will be replaced with the MINGS sensor data. Navigation with one MINGS sensor and other two with RINS sensor will not have much implication on positional accuracies provided GPS data is available				

ISBN - 978-93-95038-50-8

ACTUATOR FAULT TOLERANCE

PRE-FLIGHT ESTIMATIONS

In an ideal case, for a Control Command to flex nozzle control, feedback is available from both Main and mirror image sensors as shown in Figure 4.

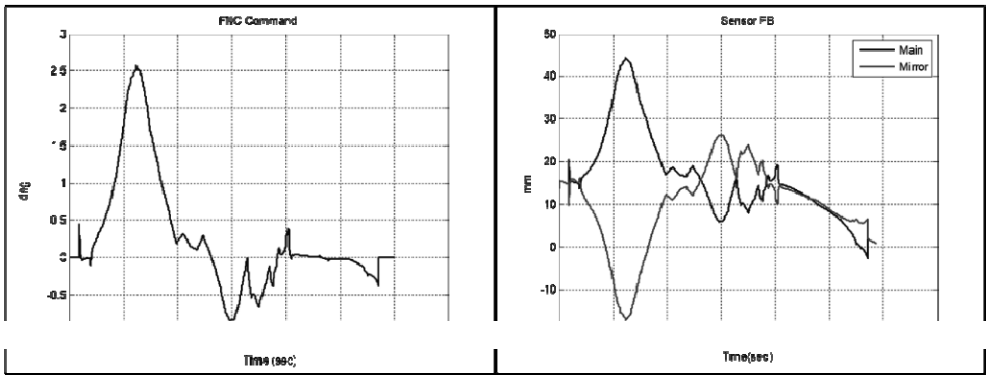

Figure 4: FNC Command & Feedback from Main and Mirror image sensors

The Actuator common mode signal is measured on ground for the system as a function of Chamber Pressure and the data is stored on-board. The Chamber Pressure data and the corresponding common mode deflection stored on-board are shown in Figure 5.

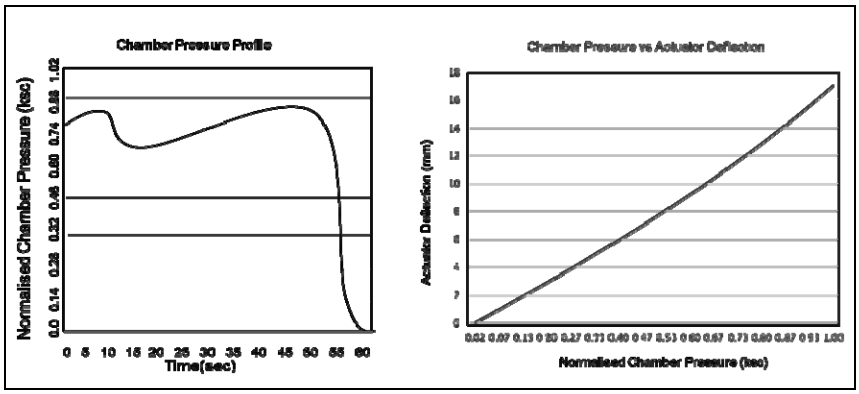

Figure 5: Chamber Pressure and Common Mode Actuator Deflection w.r.t Chamber Pressure

On-board fault identification and parameter estimation

The mirror image sensor (FB_{Mirror}) is declared faulty based on the fault check conditions and is isolated from the control loop. FB_{Mirror} can be declared faulty based on

$$\frac{d(FB_{Mirror})}{dt} \neq \frac{d(FB_{Main})}{dt} \quad \text{for 3 consecutive cycles}$$

In case of failure of the mirror image sensor, the FNC feedback value is available only from the main sensor and different output is obtained from the mirror sensor. The mirror image sensor output is calculated back from the stored Common mode signal and the Main sensor feedback signal.

$FB_{Mirror} = 2*Cmd_C - FB_{Main}$ ……. Equation 1

RECONFIGURATION OF AUTOPILOT

The reconfiguration of an autopilot is to be tested in a closed loop performance with the vehicle dynamics to understand and analyse the behavior of the system. The reconfiguration in autopilot is tested in the 6-DoF simulation test bed by means of injection of fault in the system and see the behavior of the autopilot whether the vehicle is controllable even in the fault condition.

TEST RESULTS

In case of a sensor failure, the sensor is declared faulty and isolated from the control loop. The Control autopilot is then reconfigured for the redundant sensor configuration and the vehicle is controlled back. The results of the 6-Dof simulation under fault condition are shown in Figure 6.

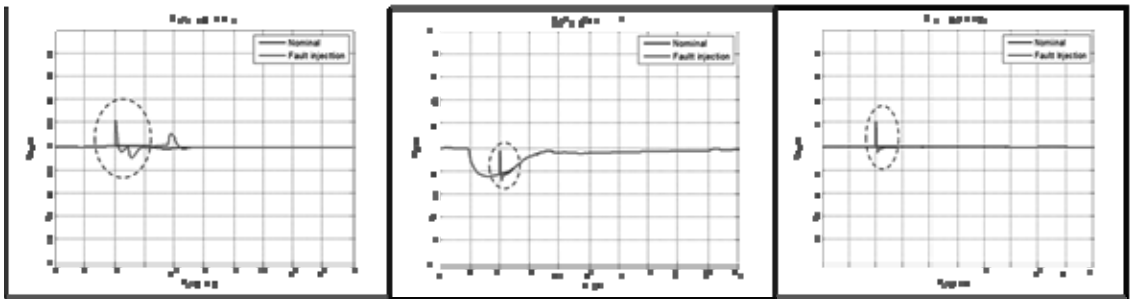

Figure 6: Comparison of Body Rates in faulty and fault free conditions

From the body rates it is evident that the autopilot is able to reconfigure the control gains in case of fault and the vehicle is controllable.

RELIABILITY ANALYSIS

In the design and development of the aerospace systems, due to the requirement of mission success even under the extreme unpredictable conditions, the reliability and safety[4] is to be considered as the top most priority. Monte-Carlo simulation method can be used to generate random numbers using mathematical models and link these numbers to the events. Monte-Carlo simulation is carried out with the 6-DoF simulation models and the failure of each system or sub-system failures are modelled in the system. Control failures would be modelled as Struck at faults. Struck at zero, struck at last command, struck at saturation are the various failure modes. The simulation is carried out with these failure modes at various instances of time and the performance of the system under all these conditions is evaluated.

SUMMARY & CONCLUSION

This Fault Management in Guidance and Control System for Aerospace vehicles can be achieved through fault identification, isolation and reconfiguration. Once the fault is identified in the system, the isolation of the sub-system from the main loop is necessary to prevent further damage to the system. And the fault mitigation is carried out by means of

sub-system redundancy and further with the reconfiguration of the system. The fault management techniques have been developed for the multiple modes of failure in an aerospace vehicle and the performance of the system with implementation of this fault tolerant techniques have been studied under various conditions. The results have been presented and analyzed. The results show that these techniques can be effective in under faulty conditions. Few of these techniques have been tested in real time implementation and the computational loads incurred by the on-board computer. All these results have proved excellent performance of the system.

REFERENCES

1. BN Suresh, Failure Detection management in Launch Vehicle Avionics, Proceedings of IEEE International Conference on Industrial Technology 2000, 2000 pp.718-722 vol.2
2. D.R. Kiran, Chapter 26 - Failure Modes and Effects, Total Quality Management, Butterworth-Heinemann, 2017, Pages 373-389, ISBN 9780128110355, https://doi.org/10.1016/B978-0-12-811035-5.00026-X.
3. Verhaegen, M., Kanev, S., Hallouzi, R., Jones, C., Maciejowski, J., Smail, H. (2010). Fault Tolerant Flight Control - A Survey. In: Edwards, C., Lombaerts, T., Smaili, H. (eds) Fault Tolerant Flight Control. Lecture Notes in Control and Information Sciences, vol 399. Springer, Berlin, Heidelberg. https://doi.org/10.1007/978-3-642-11690-2_2
4. J H Wensley and D.D. Uhrich, Reliability and Cost Considerations for Launch Vehicle Avionics, 9th IEEE/AIAA/NASA Conference on Digital Avionics Systems, 1990, pp 117-124
5. Hyunsang park, Youdankim, Adaptive Fault Tolerant Flight Control for Input Redundant Systems Using a Nonlinear Reference Model, IEEE transactions on aerospace and electronic systems vol. 57, no. 5 October 2021
6. M.Thirumarimurugan, N.Bagyalakshmi, P.Paarkavi, Comparison Of Fault Detection And Isolation Methods: A Review, IEEE
7. C. Edwards et al. (Eds.): Fault Tolerant Flight Control, LNCIS 399, pp. 47–89
8. Ali Zolghadri , David Henry, J´erˆomeCieslak Denis Efimov, Philippe Goupil, Fault Diagnosis and Fault-Tolerant Control and Guidance for Aerospace Vehicles, From Theory to Application
9. Hajiyev Chingiz/ CaliskanFikret, Fault Diagnosis and Reconfiguration in Flight Control Systems
10. https://en.wikipedia.org/wiki/Risk_matrix

Immunotronics Inspired Novel Self Repairing Finite State Machine for RISC-V based Processor

Deepanjali.S[1*], Noor Mahammad[1], Balasubramanian.P[2] and G Venkat Reddy[2]

[1]Indian Institute of Information Technology, Design, and Manufacturing, Kancheepuram,
[2]Research Centre Imarat, DRDO, Hyderabad

ABSTRACT

RISC-V processor is an open-source Instruction-set architecture (ISA), used to implement soft-core processors or System-on- Chip (SoC) in multiple FPGA and embedded systems. The increasing reduction in the size of these devices has increased the probability of upsets towards radiation environments. These errors are called Single Event Upset (SEU) which can cause functional failures in mission-critical components like control circuits. Hence reliability through self- healing mechanisms has become an essential characteristic of digital systems. Motivations from the human system to resist the invasion of harmful foreign bodies have been incorporated into the field of fault-tolerant electronics under the research area called Immunotronics. Our proposed system introduces self-repairing capabilities for the RISC-V control circuit through Immunotronics. The results are summarized as a proof-of- concept to verify the SEU-Tolerance.

Keywords: *Fault-Recovery, Immunization, Bio-Inspired fault-tolerance,SEUMitigation*

1. INTRODUCTION

The RISC-V Instruction SET architecture is used in multiple processors to execute 32/64-bit instruction in five stages as shown in Fig 1. The Instruction is fetched from the Instruction memory consisting of two main sections such as opcode, and operand address of registers containing the source value, and destination address. The Instruction decoding logic is the main control unit of the Processor whose functionality is described using a behavior model called Finite State Machine (FSM) as shown in fig 2.

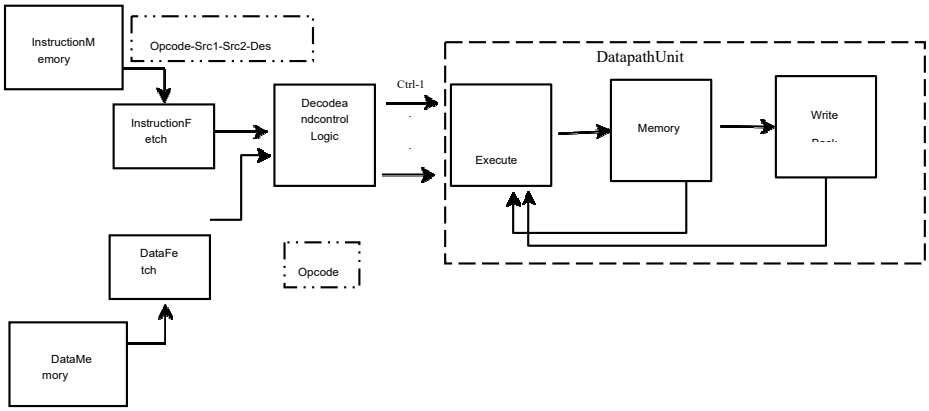

Figure 1: RISC-V Processor Design Phases

*Corresponding Author: E-mail: cs21d0001@iiitdm.ac.in,noor@iiitdm.ac.in

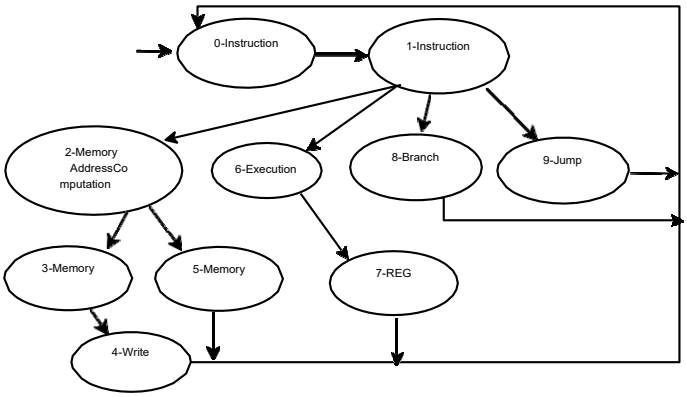

Figure 2: Behaviour Model: Finite State Machine of RISC-V Processor Control circuit
Immunotronic: RISC-V Processor

The FSM contains in total of ten states numbered from State 0-9 as shown in Table 2. Each input state on accepting the opcode from the decode unit transits to the output state. The details of the Opcode are given in table 1. At each outputstate, respective control signals such as ALUSRC A, PCWrite, RegA, MemRead, Memwrite, etc. are signaled as 1 and communicated to the Data path unit such as ALU and Memory for further execution. On occurrence of SEU in the FSM of the control logic functional error or unknown state transition can happen. For instance, Consider the Instruction Decode Stage where Stage 1 accepts the input opcode 0-000000 (Branch-if-equal) and reaches state 7-Branch completion. IF SEU happens in the second Bit from LSB then the operation related to state 9-Jump completion is performed releasing an erroneous control signal to the data path elements.

Table 1: Opcode and its corresponding Instruction

Opcode	OP0	OP1	OP2	OP3	OP4	OP5	Instruction
35	1	0	0	0	1	1	R-Type
43	1	0	1	0	1	1	j
0	0	0	0	0	0	0	Branch if Equal
4	0	0	0	1	0	0	Load Word
2	0	0	0	0	1	0	Store Word

Table 2: FSM Table of RISC-V Processor Control Circuit

States	Input State	Opcode						Output state
		OP0	OP1	OP2	OP3	OP4	OP5	
0	0000	x	x	x	x	x	x	0001
1	0001	1	0	0	0	1	1	0010
1	0001	1	0	1	0	1	1	0010
1	0001	0	0	0	0	0	0	0110
1	0001	0	0	0	1	0	0	1000
1	0001	0	0	0	0	1	0	1001
2	0010	1	0	1	0	1	1	0011
2	0010	x	x	x	x	x	x	0101
3	0011	x	x	x	x	x	x	0100
4	0100	x	x	x	x	x	x	0000
5	0101	x	x	x	x	x	x	0000
6	0110	x	x	x	x	x	x	0111
7	0111	x	x	x	x	x	x	0000
8	1000	x	x	x	x	x	x	0000
9	1001	x	x	x	x	x	x	0000

ISBN - 978-93-95038-50-8

Hence self-healing mechanisms are required for Decoding and Control logic shown in Fig 1. The traditional approach chosen for dealing with the SEU tolerance is generally Hardware redundancy or Information redundancy where the control logic is replicated three times with Voting logic or FSM state encodings are added with redundant data encoding respectively. In both these cases area and power increase as the redundancy rate increases. In a lightweight and cost-effective digital system redundancy is not appreciable. Hence a bio- inspired system-level self-repairing concept motivated by a complex Immune system found in organisms is adopted in our proposed system.

2. BIO-INSPIRED FAULT TOLERANCE

The Bio-Inspired Fault tolerant system is a concurrent, online system that per- forms Fault detection, minimization, and recovery procedures. For the past four decades, this field has been used in multiple STEM domains. But only for a few years, the implementation of these concepts are incorporated in real-time systems. In general bio-inspired system mimics the adaptability, Learning, and self-organizing nature found in different organisms. The living organism's tendency to sense and adapt to nature is the core concept that motivates bio-inspired systems [10]. These systems are influenced by the evolving nature of organisms to produce a better population in different phases of life is mimicked in electronics called as Evolvable Hardware [7,8,9]. The organism's multicellular development from a primary cell and the nature of cell replacement is adopted in Embryonic [4,5,6]. Similarly, the learning characteristics of the organism to fight and survive harmful foreign invasions are studied under Immunotronics. In general, the multilayered nature such as Physical, Psychological, innate, and acquired protection such as skin, acidity, Macrophages, and Cell-mediated immunity found in living organ- isms is adapted to electronics such as Physical enclosure, Temperature control, Triple modular redundancy, and Immunotronics respectively.

In our proposal, the fourth area of bio-inspired electronics is explored and implemented. The immune cells (T-cells) in the human system possess a memory that is used to detect harmful/Non-harmful organisms. This acquired immunity is mapped to FSM correct/incorrect transition in the error-detection process. In the memory of the human immune system called as T-cell the gene are formed together to create Antibodies. Similarly, for Fault tolerance electronics, the Error Recovery component creates admissible conditions that are required for the appropriate functioning of the electronic circuit. The gestation learning performed by T-cells is achieved in FSM fault tolerance during the training stage and clonal detection is mapped to negative selection-based recognition of acceptable conditions in fault-tolerant electronics.

3. RELATED WORKS

The works of [1] have introduced the immunological aspect of hardware fault tolerance. The introductory implementation proceeded with XCV300 FPGA. The FSM of the basic 0-10 counter circuit is designed along with immune cell modules. The proposed system is verified for stuck-at-Faults by holding the state at its current value. The latched value of the states is set to either 0 or 1 for stuck-at-fault effects and a comparison value is provided with an Ok signal if the match is found. The authors of this work have considered the self/non-self-differentiation of faulty states for future work. The future work of the previous paper was continued in [2]. The noteworthy exception as mentioned by the author is to avoid distributed nature of FSM fault tolerance. The proposed work achieved a continuous and autonomous

implementation of fault tolerance in the same counter circuit with self/non-self-differentiation. The generation of tolerance conditions is one of the major requirements for the Immunization cycle. In this work, [3] a symbiotic evolution is used to generate the tolerance condition or otherwise termed antibodies. The conditions are generated usingsymbiotic evolution for decade counter and MCNC benchmark FSM circuits and compared with standard genetic algorithm generation.

4. PROPOSED DESIGN PHASES OF FSM IMMUNIZATION

The design phases for absolute fault Detection and recovery are illustrated for RISC-V processor, Although the design phases are generic to any FSM model of the hardware circuit. The hardware circuit represented in behaviour model of FSM is considered for Logic-Under-test for Immunization. The FSMs in general indicate the admissible state transition as shown in Fig 2. During any possible in- put given to the circuit, the FSM is considered reliable when states transit to only allowed output state represented in Table 2. The transitions from any individual state to another than an admissible state are considered as faulty operation of the control circuit. For RISC-V control circuit the fundamental function includes accepting the opcode and input state and transiting to output state. With respect to state transition table 2 and Table 1 there are 10 states each representing the operation performed on instruction based on the opcode of the instruction received. Hence the antibodies for RISC-V FSM are constructed using INPUT STATE / OPCODE / Output STATE / CONTROL Signals. For Instance, 0000/xxxxxx/0001/0000010010 represents that 0000 (Input State- Instruction Fetch) on receiving opcode of any combination 0's and 1's reaches 0001 (Output State-Instruction Decode) and signals control signal Decode, InsMemRead and DataMemRead. The antibodies are constituted by generating all combinations of input state and opcode for an FSM. Hence for RISC V processor consists of fifteen admissible antibody strings each of length 4 + 6 + 4 + 10 = 24 bits. The proposed design stage for the Immunization process includes 1) Antibodies Acquisition and Generation 2) On-Line Fault Detection 3) Fault Elimination as shown in Fig 3.

4.1 ANTIBODIES ACQUISITION AND GENERATION

The objective of antibody acquisition is to create a corpus of all possible functionalities or transitions admissible for the FSM. The corpus can be generated in two ways 1) Predetermined input states available in the State transition diagram or table 2) Applying random inputs to FSM. The latter approach is similar to the human immune systematic way of coping with nature through the learning process. In both approaches fault tolerant FSM is considered for the acquisition and generation. In our proposed design corpus is created in both approaches and compared. In general, the former approach is widely used due to its simplicity, only for circuits whose admissible transition is not available, the second approach is adopted. In general, second approach is also suitable since antibodies of 200,000 count can be generated in 10Sec which is considered the training stage for the Immune cells which is performed offline prior to operation.

The negative Selection algorithm used for intrusion detection in networks is used in our proposed design to generate strings G that fail to match antibodies in at least p positions. The other bio-inspired fault tolerance system such as Evolvable hardware and embryonic verifies the presence of a valid condition of fault-free operation. On contrary, the negative selection algorithm checks the strings generated in a random corpus with the antibodies. The strings

dissimilar at p positions are removed. Hence this negative selection process is generally united with the random acquisition of corpus.

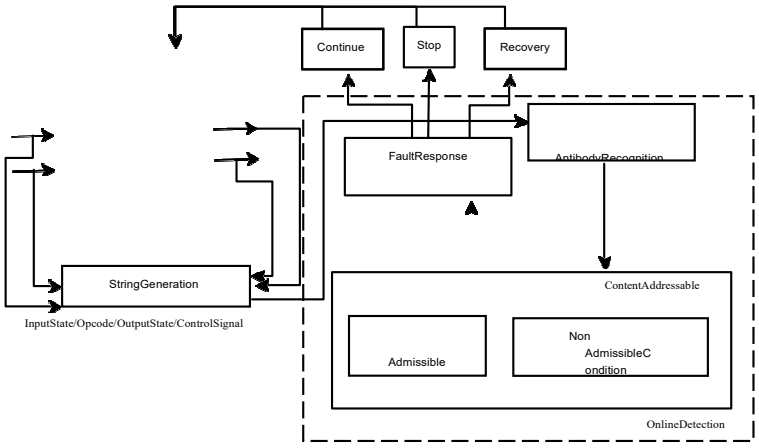

Figure 3: Block Diagram of Proposed Immunization design phases

4.2 ON-LINE FAULT DETECTION

The hardware immune system will be integrated with the FSM and perform as an interface to the hardware control logic. The detection mechanism includes main components such as the Control circuit module for fault repair - FSM of the circuit, Fault injection module which randomly injects the error in the opcode of the FSM, Under Non-Injection instance, the FSM produces a string with valid bits of input state, opcode, output state, and control signal. On fault injection, the strings dissimilar to the antibodies are generated by the FSM. A string initiation components generate the string in a format similar to the standard corpus discussed in the previous section, which is compared with the antibodies stored in the Immune cell memory. A content-addressable memory is used to store the antibodies. The indexed memory allows parallel searching and comparison for strings with the antibodies. The match is checked for p adjoining position. The comparison operation signals 1/0 representing the presence and absence of antibody match with the index of the antibody. The immune cell memory is 64-bit in length where 24 bits are used for data and the rest is used for address mask as per the requirement. The mask size and data bits are reconfigurable by the designer. The comparison is performed by window- based search. The window size is increased or decreased to ensure the found signal generation within the transition cycle of the FSM. For RISC-V detection of antibodies, 10 bits were set as the window size. The partial matching with the window method is similar human T-Cell mediated immune system. Hence the online detection of fault is performed for an FSM at every state instance. The generated string is compared with the antibodies for at least p- positions. The partial mapping allows detection to be made before the erroneous transition is made by the FSM, thereby prohibiting the wrong control signals.

4.2 FAULT ELIMINATION

The final stage of the proposed design cycle follows the fault removal stage. In many related works, complete immune system-based fault recovery solutions are not explored. In our proposed solution fault removal techniques are also motivated by the human immune

system. In the human immune system, the classic approach to be protected from outside invasion is achieved by fighting foreign bodies and neutralizing the ruinous behavior of these bodies. In the hardware system to neutralize the fault N-modular redundancy is followed. In accordance to FSM, the states can be triplicated with a voting logic. Hence the outputs from individual states are compared in the voting logic to choose the majority output, thereby faults can be tolerated when a match signal is not found. The faulty state identified by the voting logic is replaced with non-faulty in consecutive cycles. On contrary, the complete Immune-based solution would require a fault recovery procedure also to be placed in immune cell memory. For this recovery, states are also embedded in the antibodies stored in the immune cell. On the occurrence of a non-match signal, the recovery state of the current input state is performed. It is achieved in hardware tolerance by storing the recovery states in the multiplexer as a spare state. In further understanding, the anti- bodies attach with the antigen to protect from attacking normal cells. In FSM similar approach is obtained by maintaining a spare state, which requires precedent knowledge of the system operations. A complete bio-inspire fault tolerance can also be obtained by combining two other approaches such as embryonic or Evolvable hardware for fault elimination.

5. RESULTS AND DISCUSSION

As a proof of concept the RISC-V Processor's Finite state machine is implemented in the Verilog on Zynq 7000 FPGA. The Immunotronics model as represented in Fig.3 along with fault injection module is deployed in the FPGA to verify the fault recovery model. The fault injection model consists of behaviour level implementation of XOR gate to flip the bits in the input of the Finite State machine and the state encoding. The Random generator module is designed to select the input and state encoding at random cycle. In the case of RISC-V processor the opcode is the input and states 0-9 are the state encoding. When the bits of the above two fault location are selected, it is applied to XOR gate with one of its input masked to Vcc. This process of bit flip causes an erroneous transition which has to be mitigated by Immunotronics module. The proposed design is compared traditional redundancy method called Triple Modular Redundancy and Hamming distance, where each state is triplicated along with a majority voter state, to select at most correct outputs from the three states and state encoding is attached with redundant bits respectively. The error recovery rate is high in proposed system since complete error recovery is possible with no redundant bits added to the state encoding; When compared to TMR the number of core cells are less but the Flash ROM usage to store the antibodies is high.

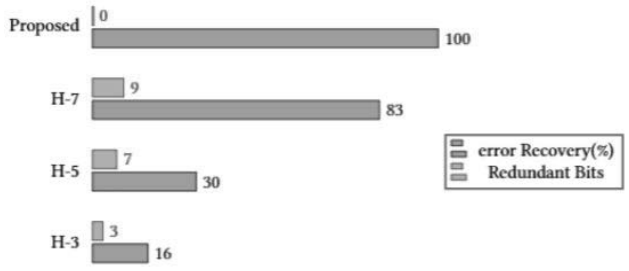

Figure 4: Comparison of error recovery in Information redundancy and Immunotronics in terms of Redundant Bits in RISC-V Processor

Table 3: Resource Utilization for TMR vs Proposed Design

	Proposed Design	TMR
Core Cell	122	145
I/O Cell	24	28
FlashROM	5Kb	0
Delay	17ms	0

6. CONCLUSION

The Fault tolerance approaches has increased requirement in designing reliable control circuit. In comparison to Redundancy based mitigation techniques the Immunotronics techniques has higher error coverage and less area utilization. The memory occupancy of Immunotronics plays huge role in hindrance of the development and real-time usage. Hence an alternative method to deploy the antibodies will be explored in our future works.

7. ACKNOWLEDGEMENTS

The author acknowledges the encouragement and support provided by Sh U Raja Babu, Outstanding Scientist & Director RCI and his team to continue and pursue the research activity.

REFERENCES

1. "Immunotronics: Hardware fault tolerance inspired by the immune system". In: Evolvable Systems: From Biology to Hardware: Third International Conference, ICES 2000 Edinburgh, Scotland, UK, April 17–19, 2000 Proceedings 3. Springer. 2000, pp. 11–20.
2. "Immunotronics-novel finite-state-machine architectures with built- in self-test using self-nonself differentiation". In: IEEE Transactions on Evolutionary Computation 6.3 (2002), pp. 227–238.
3. Sanghyung Lee et al. "A new immunotronic approach to hardware fault detection using symbiotic evolution". In: Artificial Intelligence and Knowledge Engineering Applications: A Bioinspired Approach: First International Work-Conference on the Interplay Between Natu- ral and Artificial Computation, IWINAC 2005, Las Palmas, Canary Islands, Spain, June 15-18, 2005, Proceedings, Part II 1. Springer. 2005, pp. 133–142.
4. Tyrrell, A., 2004. Embryonics and Immunotronics: Biologically Inspired Computer Science Systems. Computation in Cells and Tissues: Perspectives and Tools of Thought, pp.93-116.
5. Mange, D., Sipper, M., Stauffer, A. and Tempesti, G., 2000. Toward robust integrated circuits: The embryonics approach. Proceedings of the IEEE, 88(4), pp.516-543.
6. Mange, D., Sanchez, E., Stauffer, A., Tempesti, G., Marchal, P. and Piguet, C., 1998. Embryonics: A new methodology for designing field-programmable gate arrays with self-repair and self-replicating properties. IEEE Transactions on Very Large Scale Integration (VLSI) Systems, 6(3), pp.387-399.
7. Kalganova, T., 2000, July. Bidirectional incremental evolution in extrinsic evolvable hardware. In Proceedings. The Second NASA/DoD Workshop on Evolvable Hardware (pp. 65-74). IEEE.
8. Greensted, A.J. and Tyrrell, A.M., 2007. Extrinsic evolvable hardware on the RISA architecture. In Evolvable Systems: From Biology to Hardware: 7th International Conference, ICES 2007, Wuhan, China, September 21-23, 2007 Proceedings 7 (pp. 244-255). Springer Berlin Heidelberg.
9. Haddow, P.C. and Tyrrell, A.M., 2011. Challenges of evolvable hardware: past, present and the path to a promising future. Genetic Programming and Evolvable Machines, 12, pp.183-215.
10. Moreno, J.M., Thoma, Y. and Sanchez, E., 2006, June. Poetic: A Hardware Prototyping Platform With Bioinspired Capabilities. In Proceedings of the International Conference Mixed Design of Integrated Circuits and System, 2006. MIXDES 2006. (pp. 363-368). IEEE.

Electro Cardiogram (ECG) Monitoring using Internet of Things and Predict Future in Advance using Artificial Intelligence

G. Sasikala*, G. Satya Krishna

ECE dept, Vel Tech Rangarajan Sagunthala R&D Institute of Science and Technology, Chennai, India

Abstract

An IoT Based Electro cardiogram monitoring system will continue monitor the patient health condition related to heart and update immediately if any abnormality found in the patient health viz Wi-Fi to things peak application in mobile phone. The doctor located at remote location will monitor the situation accordingly and take appropriate decision, so that life time of the patient will be increased. In addition to it we may predict the health condition in advance using artificial intelligence. Based on patient health data we may produce trainee set and compare it with test set to estimate the variation in the health status and based on variation observed it may alert the doctor to indicate the early deterioration of patient health condition, so that we may arrest the growth of disease in advance. Here we are using ECG sensor to take the patient health data and it will be processed using Arduino board, Arduino microcontroller will compare the patient ECG with threshold limits, if it crosses lower or upper value it may alert the doctor. After processing it will transfer data to smart phone using Wi-Fi. Patient data will be continuously logged and it will be taken as trainee set and compared it with available test set to estimate the patient health condition in advance.

Keywords: ECG Sensor, ARDUINO UNO, WI - FI

1. INTRODUCTION

Now a days the number of heart patients were increased due to various reasons viz change in food habits and timings, nature of food and lack of nutrition in food. Here we are acquiring patient health information using ECG sensor and processed using Arduino microcontroller board and transmit using internet of things. We can predict the future health condition of patient in advance using artificial intelligence. So that many of heart patients may continuously check their health status by their own.

2. LITERATURE REVIEW

Health monitoring system using LPC2138 microcontroller was realized by srushti jagtap et al [1]. This paper collected using various sensors and processed using LPC2138 microcontroller and it will be displayed ON normal LCD screen

Development of an IoT based health monitoring system for e-health was realized by Md julhas Hossain et al [2]. This paper explained how to update the important health parameters and validate data.

Intelligent health monitoring system was realized by rishi kumar et al [3]. This paper explained how the sensor data will be read and processed by Arduino supported Wi-Fi enabled node MCU controller.

Analysis of IoT based health monitoring system using ARM7 was realized by Tejaswi et al [4]. This paper demonstrated that the patient parameters were transmitted over the IoT and finally it was displayed on UART and LCD.

Patient E-health monitoring system on ARM7 – LPC2148 microcontroller and GSM was realized by Priyanka A J et al [5]. This paper realized that the sensors were connected to LPC2148 and transmit information using GSM modem to doctor.

Smart and automatic health monitoring of patient using wireless sensor network was realized by Asha G Hagargund et al [6]. This paper demonstrated that the patient carries a batch of body sensors to collect their physiological parameters using Arduino and wireless sensor network.

Real time patient monitoring system based on internet of things was realized by mohammad salah Uddin et al [7]. This paper proposed an intelligent patient monitoring system to monitor the patient's health condition automatically through sensors based connected networks.

Intelligent patient monitoring system based on PLC with microcontroller was realized by umera banu et al [8]. This paper focuses on power line communication for transferring the patient parameters.

Zigbee based patient monitoring: Early detection of Alzheimer disease was realized by Shailesh V et al [9]. This paper proposes a ZigBee based home patient monitoring system which helps in early detection of Alzheimer disease. The location and movement patterns of a patient will be tracked and recorded with the help of short-range ZigBee communications.

Cloud based intelligent healthcare monitoring system was realized by Mr. Khyamling A. Parane et al [10]. This paper proposed a system consisting of a computing device and a number of sensors mounted on patient body.

Smart health care monitoring using wearable sensors was realized by Rishikesh D. borse et al [11]. This paper explores machine learning approach for continuously acquiring data using smart wearable sensors. The goal of this project was to provide early warnings of patient abnormally to doctor located in remote place.

Smart secure system for human health monitoring was realized by Nikhil Nair et al [12]. This paper demonstrated that the sensors were acquire the patient data and was processed using Raspberry pi and sent over the cloud to record keeping and transmitting patient information to doctor located faraway from patient.

Wearable sensors-based activity recognition for smart human health care using IoT was realized by Ning Hu et al [13]. This proposed an IoT and black chain-based health care monitoring system for human activity recognition via monitoring vital signals collected from wearable sensors remotely.

Enhanced IoT assisted wearable data analytics for patient monitoring and health care system was realized by Jaishankar et al [14]. The sensor data was collected here sent to cloud for storage and analysis for patient health, based on emergency the operator located at remote place generates emergency alerts to concerned doctor.

Adaptive vital signals monitoring system based on early warning score approach in smart hospital context was realized by et al [15]. This paper proposed early score approach, based on patient data it generated score related to risk content of patient. Finally, we are generating this paper with 4 sections. Section [1] is giving introduction and clear idea about topic. Section [2] covers literature survey. Section [3] covers basic block diagram and tables related to software logic. Section [4] covers methodology followed here to generate messages to alert the doctor. Section [5] covers results and analysis. Section [6] references.

ISBN - 978-93-95038-50-8

3. BLOCK DIAGRAM

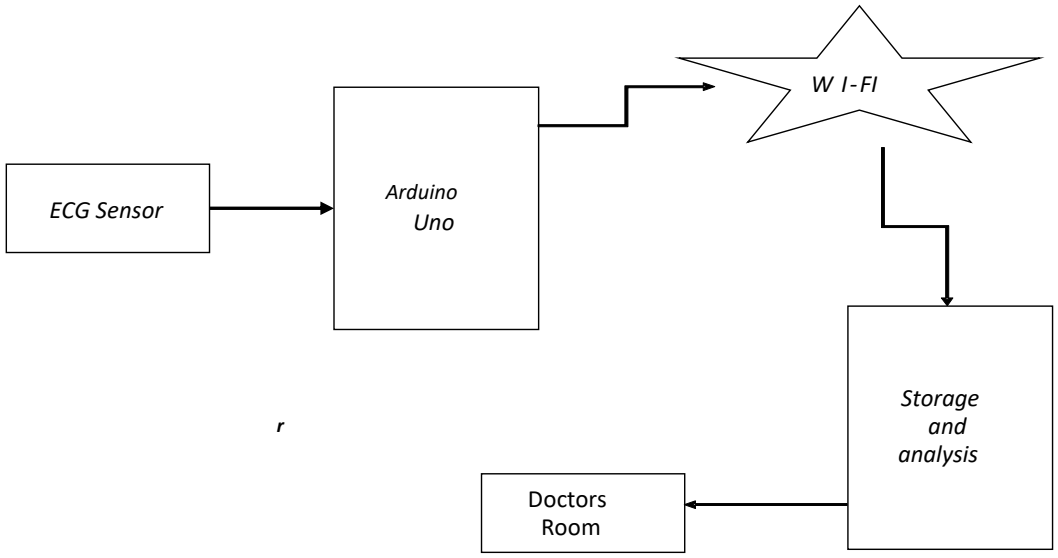

Figure 1: Block Diagram

4. METHODOLOGY

This paper proposed a method for measuring patient health condition by taking electro cardiogram (ECG) and it can compare the data with threshold lower and upper limits, if any abnormality is there it will identify and give the alert to the doctor. This processing will be done by Arduino microcontroller board using embedded c language. The data will be sent to smart phone mobile application thing speak viz Wi-Fi.

ECG sensor (AD8232)

ECG Sensor is used to measure heart functioning of the patient using 3 leads.

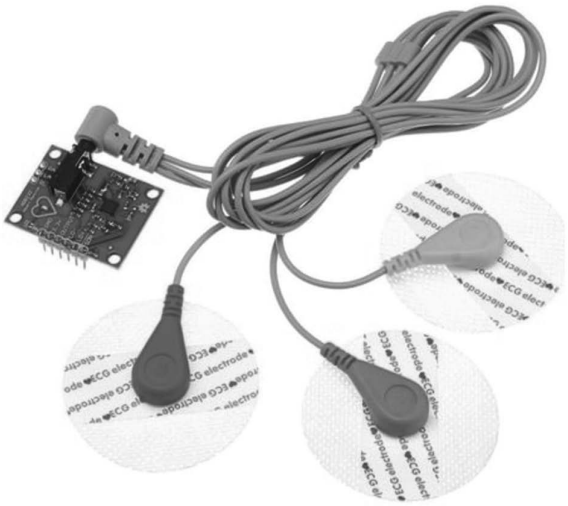

Figure 2: ECG Sensor

Board Label	Pin Function	Arduino Connection
GND	Ground	**GND**
3.3v	3.3v Power Supply	**3.3v**
OUTPUT	Output Signal	**A0**
LO-	Leads-off Detect -	**11**
LO+	Leads-off Detect +	**10**
SDN	Shutdown	**Not used**

Figure 3: ECG Sensor with terminals

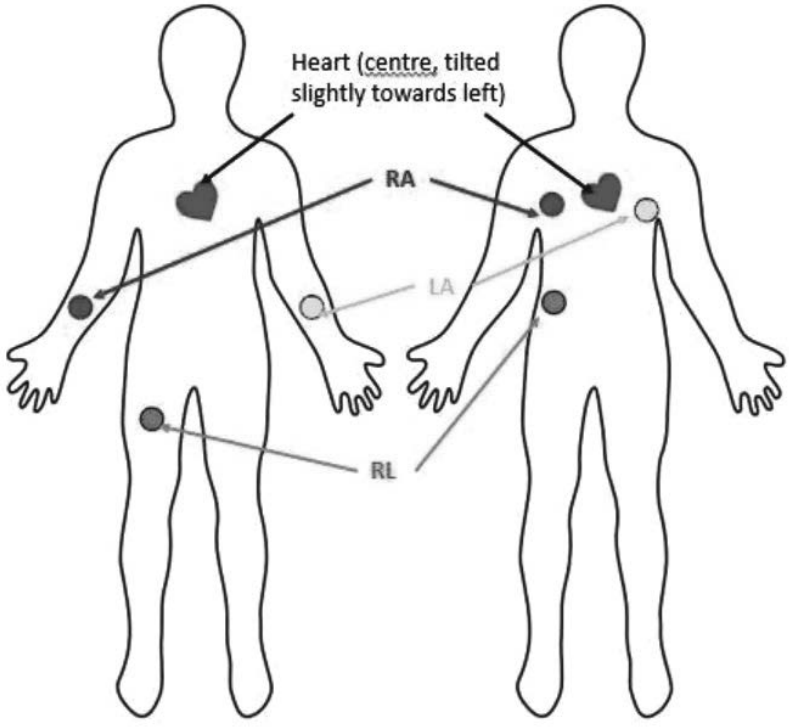

Figure 4: Lead position during measurement

Table 1: Lead Position during measurement

Electrode name	Electrode colour	Location
RA	Red	Right Arm
LA	Yellow	Left Arm
RL	Green	Right Leg

Threshold:

Table 2: Threshold Values

Heart rate	49 to 100bpm for men 55 to 108bpm for women
P Wave duration	81 to 130ms for men 84 to 130ms for women
PR Interval	119 to 210ms for men 120 to 202ms for women
QRS duration	74 to 110ms for men 78 to 114ms for women

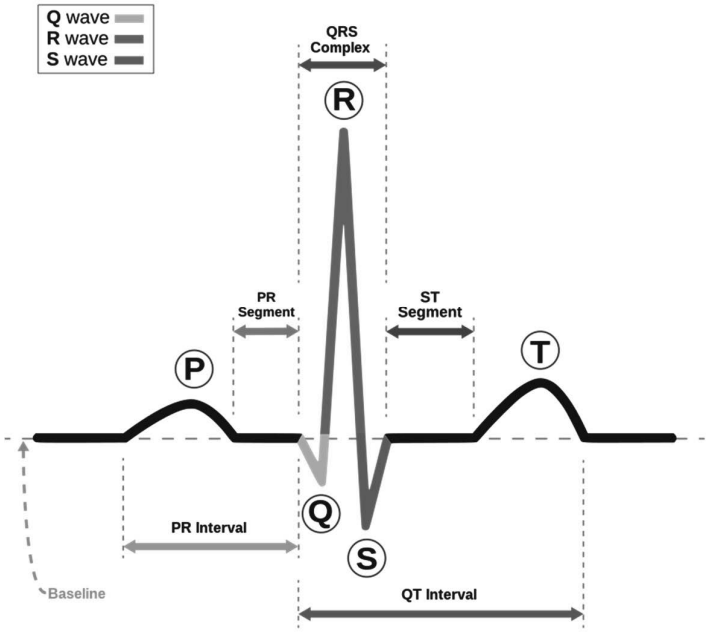

Figure 5: Single ECG wave

ISBN - 978-93-95038-50-8

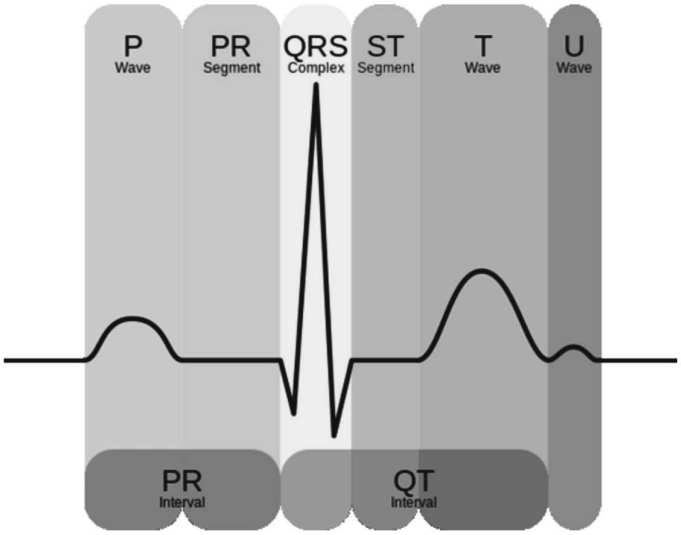

Figure 6: Detailed view of Single ECG wave

Each interval has an optimal value range, and deviation from that might be linked to a particular disease. Here are the main parts of an ECG signal.

1. P wave - It is the trailing wave on the left of the QRS complex.
2. QRS complex - It is an impulse generated by ventricular contraction.
3. T wave - It is a leading wave right to the QRS complex.
4. U wave - It is not always observed due to its low peak value.

There are many other features as well, but these are the main ones. Based on the shapes of the above features, their interval as well as the interval between them, we can diagnose a lot of cardiac diseases and irregularities. For example:

- Irregular heartbeat or absence of P-wave: It might Atrial Fibrillation
- Resting Heart Rate of more than 100: It might Tachyarrhythmia
- Tachyarrhythmia and delta wave: Wolf-Parkinson-White or WPW syndrome
- Sawtooth P wave: It means Atrial flutter
- Depression of ST-segment: it might indicate Ischemia
- Elevation of ST-segment: it might indicate myocardial Infarction

Hence, ECGs are extremely important for a cardiologist or any doctor for that matter.

Arduino Uno

Arduino Uno board is a microcontroller device based on ATmega328P. It contains 14 digital I/O Pins in which six can be used as PWM O/Ps and other six can be used as analog/Ps.

ISBN - 978-93-95038-50-8

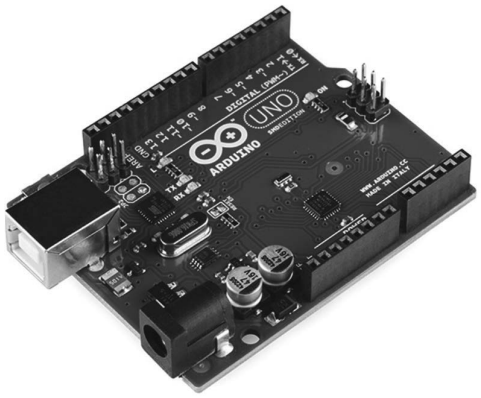

Figure 7: Arduino Uno

Thing Speak:

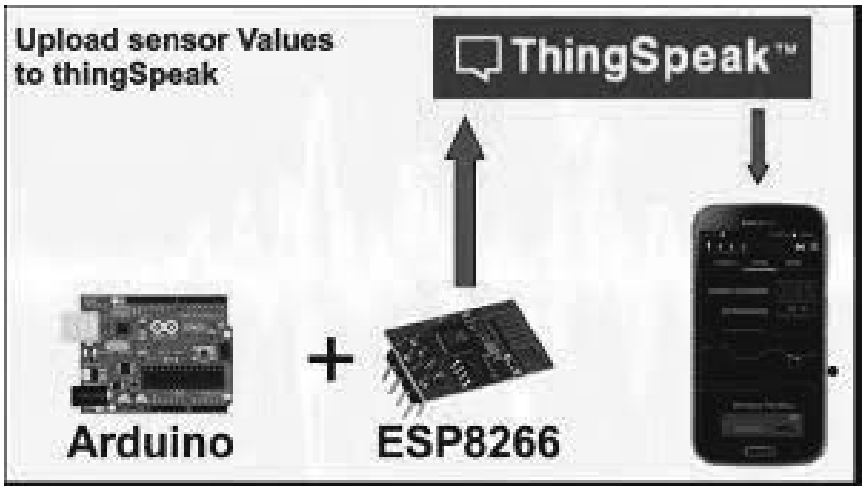

Figure 8: Data Transfer using ESP8266 to Things peak application

Figure 9: Data Plot in Things peak application

Flow Chart:

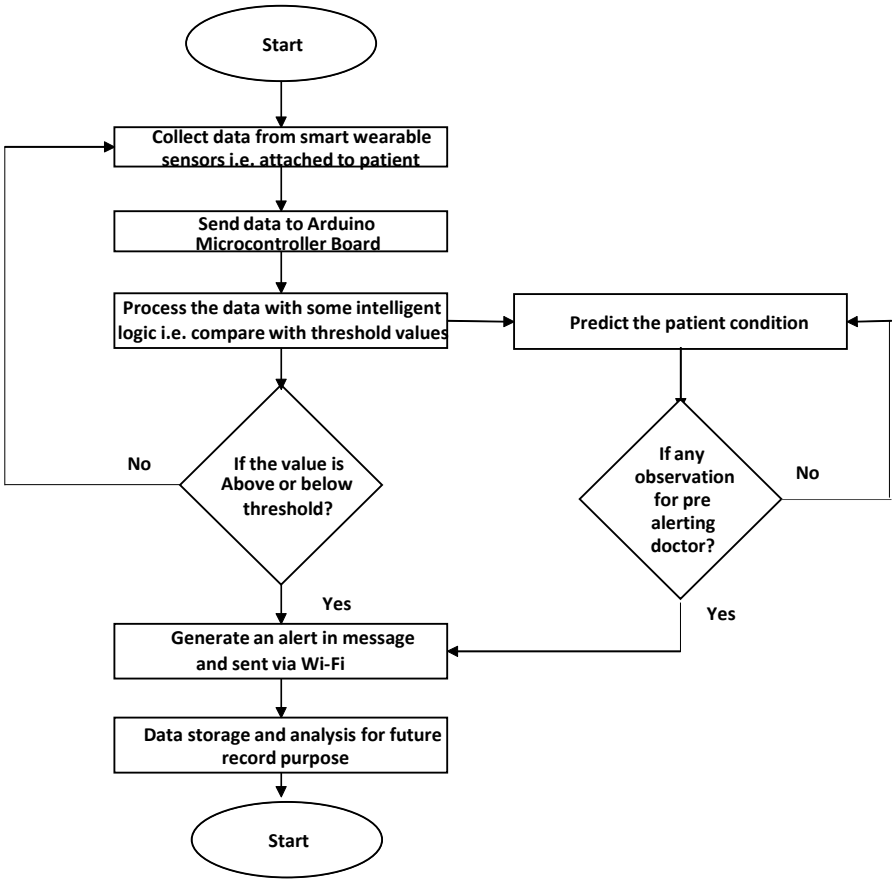

Figure 10: Flow Chart

5. RESULT AND ANALYSIS

Figure 11: Serial Plotter in Arduino software

6. CONCLUSION

The Electro cardiogram (ECG) monitoring system was realized using various smart wearable ECG sensor with Arduino board. The Arduino board was processing data using software written in embedded C language. The processed data sent Over Wi-Fi network for storage and analysis of patient data monitored by doctor located faraway from patient. This type of health care facilities requires in now a day due to increase number of patients and due to lack of health care facilities at rural areas.

REFERENCES

1. Srushti Jagtap, Aryan Gupta, Gaurav Tawde.: 'Health monitoring system using LPC2148 microcontroller'. Journal of emerging technologies and innovative research (JETIR). JETIR.ORG ISSN:2349-5162| ESTD Year:2014|Monthly Issue.
2. Md Julhas Hossain, Md Ambadul Bari and Mohammad Monirujjaman Khan, "Development of IoT Based Health Monitoring system for e-Health", CCWC | 978-1-6654-83003-2/22@2022 IEEE | DOI:10.1109/CCWC54503.2022.9720825.
3. Rishi Kumar, Akshit Vashistha, Anshuman Asthana, Aishwarya Srivastava, Sanjeev KR, Saini," Intelligent health monitoring system", International Research Journal of Engineering and Technology (IRJET)Volume: 08 Issue: 07 | July 2021.
4. Bhashipangu Tejaswi, Dasari Ramesh, "Analysis of IoT based health monitoring system using ARM7", AIJREAS VOLUME5, ISSUE 01(2020, JAN) (ISSN-2455-6300) ONLINE ANVESHANA'S INTERNATIONAL JOURNAL OF RESEARCH IN ENGINEERING AND APPLIED SCIENCES.
5. Priyanka A J, Dr. N. Manja Naik, "Patient E-Health monitoring system on ARM7-LPC2148 microcontroller and GSM", International Journal for Research in Engineering Application & Management (IJREAM) ISSN:2454-9150Vol-05, Issue-03, June 2019.
6. Prof Asha G Hagargund, Aman Srivastav, Chandan Kumar Nayak, Mausam Kumar Singh, " Smart and automatic health monitoring of patient using wireless sensor network", IEEE-43488, 9th ICCCNT 2018.
7. Mohammad salah Uddin, Jannat Binta Allam,"Real time monitoring system based on Internet of things", 2017 4th ICAEE.
8. Umera banu, Dr G.M Patil, Dr, Rukar Fatima, "Intelligent patient monitoring system based on PLC with microcontroller", International Journal of Innovative Research in Science, Engineering and Technology (An ISO 3297: 2007 Certified Organization) Vol. 5, Issue 6, June 2016.
9. Shailesh V. Kumbhar, Asha Durafe," Zigbee based patient monitoring: Early detection of Alzheimer disease", @ 2015 IJEDR | Volume 3, Issue 2 | ISSN: 2321-9939.
10. Mr. Khyamling A. Parane, Mr Naveenkumar C patil, Mr. Shivananda R. poojara, Mr . Tejaskumar S.Kamble,"Cloud based Intelligent Healthcare Monitoring system", 978-1-4799-2900-9/14@2014 IEEE.
11. 11Rishikesh D. Bose, Pratik S. Bankar, Dnyaneshwar K. Bhosale, Prasad V. Gadekar," Smart Health care Monitoring using wearable sensors", IERJ, Volume2, Issue 9. Page 3338-3341,2017 ISSN 2395-1621.
12. 12 Nikhil Nair R, Kiran K A," Smart secure system for human health monitoring", International conference on Intelligent Computing and Control systems.
13. 1Narendra Kumar, Alok Aggrawal and Nidhi Gupta," wearable sensors for remote healthcare monitoring system", International Journal of Engineering Trends and Technology-Volume 3 Issue1 -2012.
14. 1Enhanced IoT-Assisted wearable data analytics for patient monitoring and healthcare systems", ICACCS, DOI: 10.1109/ICACCS54159.2022.9785016.
15. Imen Ben Ida,Moez Balti, Sondes, Jemai,"Adaptive vital signs monitoring system based on early warning score approach in smart hospital survey context", IET smart cities, DOI:10/1049

Real Time Face Recognition System using Jetson Nano

Vaddi Chandra Sekhar*, D Penchalaiah, G Naresh Kumar, Abhijit Bhattacharyya
Defense Research and Development Laboratory
Hyderabad, Telangana, 500058
Email: vcsekhar.drdl@gov.in

ABSTRACT

This work aims to deploy an accurate face recognition system on a low cost, portable and reliable hardware. Nvidia Jetson Nano is a small size, portable and powerful computer to run Neural Networks. It uses an integrated 128-core Maxwell GPU for parallelization. The total power consumed by the device is less than 10 watts. Face recognition system consists of 2 steps, Face detection and Identification. Multi-Task Cascaded Convolutional Neural Networks (MTCNN) Model has been used for Face detection and VGG-Face has been used for Face Identification. The network is trained on VGG-Face dataset which consists of 2.6 million face images of 2,622 people. The system has achieved real time performance of upto 4 fps with an accuracy of 97.6% on Labeled Faces in the Wild (LFW) dataset.

Keywords: *Face Recognition, MTCNN, VGG-Face, Jetson Nano, TensorRT*

1. INTRODUCTION

A Face recognition system confirms the identity of an individual using their facial features. Facial recognition technology is in the limelight today more than ever, COVID-19 pandemic and several other diseases spread through contact from contaminated surfaces. Hence classical biometric systems based on password typing and fingerprints are unsafe especially in large spaces like offices, educational institutions etc. Face recognition technology is preferred in such cases because of its non-contact nature. Furthermore, facial recognition algorithms have very high accuracy rates and have very fast processing speeds. Significant advances in face recognition have occurred because of Artificial Intelligence technologies [1], previous research interests were mainly focused on face recognition under controlled conditions where simple classical approaches provided excellent performance. But with emergence of Deep Learning, the focus of research is on unconstrained conditions as it offers strong robustness against the numerous variations that can alter the recognition process

To run these Deep Learning based Face recognition algorithms a low cost, portable, low power powerful hardware is required, the hardware has to be affordable yet powerful enough to yield high throughput. For this task we have chosen Nvidia Jetson Nano as the hardware for our Face recognition system. NVIDIA Jetson Nano Developer Kit is [2] a small, powerful computer that runs multiple neural networks in parallel, it has a power consumption of less than 10 watts.

2. LITERATURE REVIEW

A large part of the literature in face recognition is focused on the development of algorithms that can accurately recognize faces. Some of the most widely used algorithms include Principal Component Analysis (PCA) [3], Linear Discriminant Analysis (LDA), and Fisherface [4], among others. More recent algorithms, such as Convolutional Neural Networks (CNNs) [5], have also shown promising results in face recognition.

The performance of face recognition algorithms is often evaluated using benchmark datasets, such as the Labeled Faces in the Wild (LFW) [6] dataset and the MegaFace dataset

* Corresponding author: E-mail: vcsekhar.drdl@gov.in

[7]. The evaluation metrics used for face recognition include recognition accuracy, processing time, and sensitivity to variations such as pose, illumination, and expression.

Jetson Nano has been shown to have real-time performance for face recognition, making it a popular choice for use in various applications. For example, in the study [8] the authors demonstrated the real-time performance of a face recognition system implemented on Jetson Nano. Several studies have compared the performance of Jetson Nano with other platforms for face recognition. For example, in the study [9] the authors compare the performance of Raspberry Pi and Jetson Nano for face recognition using various algorithms. They found that Jetson Nano outperformed Raspberry Pi in terms of recognition accuracy and processing speed. Jetson Nano has been integrated with various technologies to enhance its performance for face recognition. For example, in the study [10], the authors integrate Jetson Nano with OpenCV to improve the performance of a face recognition system. They found that the integration improved the accuracy of the system and reduced the processing time. These findings suggest that Jetson Nano is a promising platform for face recognition, with real-time performance and good accuracy. However, further optimization and improvement of algorithms is needed to overcome the limitations of Jetson Nano.

3. RESEARCH METHODOLOGY

Figure 1: Research Methodology

Facial recognition process typically involves the following steps: Capture and Pre-processing, Face Detection, Feature Extraction and Comparison.

Capture and Pre-processing: The first step is to capture an image or video of the person's face. The image or video is then pre-processed. This can involve cropping the image, converting it to grayscale, and normalizing the brightness and contrast.

Face Detection: Face detection is a computer technology used to identify and locate human faces in digital images or video frames. Face detection algorithms typically starts by searching for high-level features, such as eyes, noses, and mouths, and then uses these features to identify faces. The algorithm will then localize it by drawing a bounding box around the face. This can be done using techniques such as Haar cascades [11], HOG features [12], or deep learning-based object detectors.

Feature Extraction: Next, the facial features are extracted and represented as a set of numerical values, known as a feature vector. This can involve detecting facial landmarks, such as the corners of the eyes, mouth, and jaw line, and measuring their relative positions and distances.

Comparison: The extracted feature vector is then compared to a database of known faces, and the algorithm attempts to find a match. The comparison step typically involves calculating a similarity score between the input feature vector and each face in the database.

ISBN - 978-93-95038-50-8

4. PROPOSED METHOD

4.1 FACE DETECTION USING MTCNN:

The Multi-task Cascaded Convolutional Networks (MTCNN) [13] is a popular deep learning framework used for face detection, alignment, and recognition. The method is based on cascaded neural networks, which are trained to perform several tasks in a sequence, allowing for a hierarchical and efficient approach. For the face detection task, MTCNN uses a multi-stage architecture to achieve high accuracy and speed.

In the first stage, a Proposal Network (P-Net) is used to generate candidate face boxes by proposing windows in the image. In the second stage, a Refine Network (R-Net) is used to further refine the face boxes and reject non-face regions. Finally, an Output Network (O-Net) is used to perform a face alignment and output a facial landmark points. These landmark points are then used to align the face and extract the face region from the image.

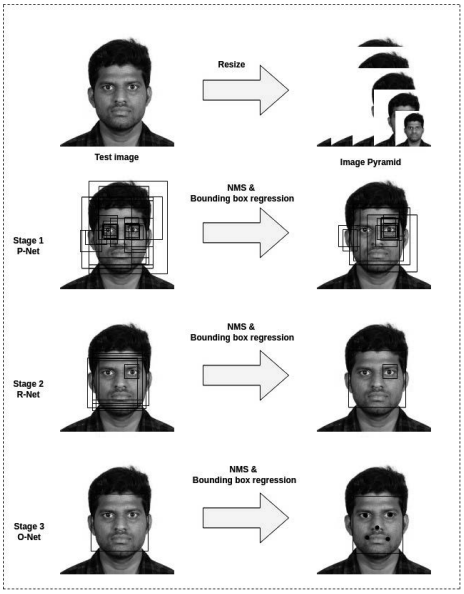

Figure 2: Face detection using MTCCN

The MTCNN framework has proven to be effective in a variety of real-world applications and has achieved high accuracy and efficiency in comparison to other traditional face detection methods. On the popular WIDERFACE dataset [14], MTCNN has been reported to have an accuracy of over 97%. In our work, MTCNN will be used to perform the initial face detection and alignment, allowing for the subsequent use of deep learning models for face recognition.

Figure 3: Face detection even when the person is not looking at camera

ISBN - 978-93-95038-50-8

4.2 VGG-FACE NETWORK

*Visual Geometric Group (*VGG)-Face [15] is a deep neural network architecture that has been trained to identify faces in digital images and videos. It is built on the VGGNet architecture, which is a deep convolutional neural network that has been proven to be very effective for image recognition tasks.

The VGG-Face architecture has been trained on 2.6 million face images of 2,622 people. It is capable of extracting rich and complex features from an image, which can be used to classify the faces of individuals. The VGG-Face architecture has been evaluated on several benchmark datasets and has achieved impressive accuracy rates, outperforming many other popular face recognition models.

For example, it has achieved an accuracy of over 97% on the Labeled Faces in the Wild (LFW) dataset, which is a benchmark dataset for face recognition algorithms. This high accuracy rate makes VGG-Face a strong choice for face recognition applications, such as facial recognition systems, face verification systems, and biometric authentication systems.

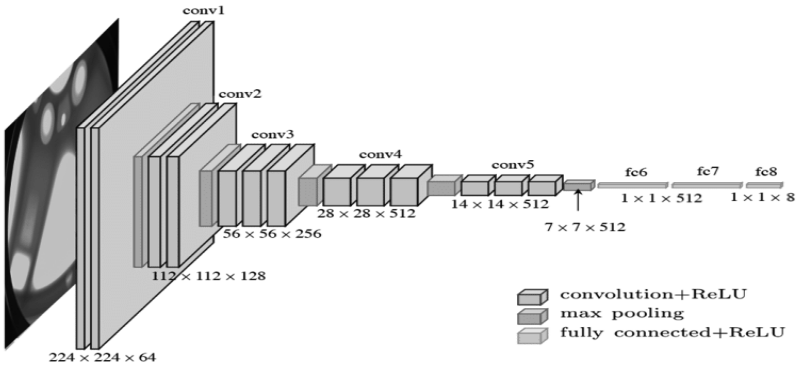

Figure 4: VGGNET ARCHITECTURE

5. RESULTS AND DISCUSSIONS

Figure shows the experimental setup used. A low-cost webcam is used to capture the images. Jetson Nano 2 GB is used to run the MTCNN and VGG-Face models. These models are accelerated to give high throughput by using NVIDIA TensorRT libraries.

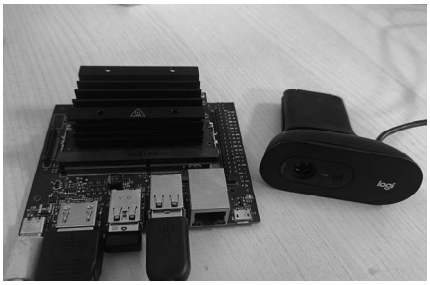

Figure. 5: Experimental Setup

ISBN - 978-93-95038-50-8

It was seen that the Face recognition system was able to detect and classify the persons successfully under partial mask scenarios also. The accuracy of facial recognition remained unaffected under different conditions such as lightning, and the distance from the camera.

Figure 6: Face detected even with partial Mask.

6. CONCLUSIONS

A cost effective and accurate Face recognition system has been developed by using Deep Learning models available in literature. We were able to get real time performance on a very low-cost hardware by utilizing the NVIDIA TensorRT optimization libraries. We successfully demonstrated the model's efficiency even with partial mask scenarios. Although this system has limitations for very large user database as the Jetson nano has limited processing power, memory and storage capacity. More powerful alternatives are in development by NVIDIA to provide low cost and highly powerful GPU edge systems, and these need to be tested in future.

ACKNOWLEDGEMENTS

The authors express their sincere gratitude to Shri Boda Nehru, Sc 'C' DRDO for helping them throughout this work.

The authors express their sincere gratitude to Shri Mallikarjun B, RA, DRDO for helping them throughout this work.

The authors express their sincere gratitude to Shri K Dinesh, KL University for helping them while writing this publication.

REFERENCES

1. Adjabi, Insaf, et al. "Past, present, and future of face recognition: A review." Electronics 9.8 (2020): 1188.
2. Cass, Stephen. "Nvidia makes it easy to embed AI: The Jetson nano packs a lot of machine-learning power into DIY projects-[Hands on]." IEEE Spectrum 57.7 (2020): 14-16.
3. Moon, Hyeonjoon, and P. Jonathon Phillips. "Computational and performance aspects of PCA-based face-recognition algorithms." Perception 30.3 (2001): 303-321.
4. Anggo, Mustamin, and La Arapu. "Face recognition using fisherface method." Journal of Physics: Conference Series. Vol. 1028. No. 1. IOP Publishing, 2018.
5. Lawrence, Steve, et al. "Face recognition: A convolutional neural-network approach." IEEE transactions on neural networks 8.1 (1997): 98-113.

6. Gary B. Huang, Manu Ramesh, Tamara Berg, and Erik Learned-Miller. Labeled Faces in the Wild: A Database for Studying Face Recognition in Unconstrained Environments. University of Massachusetts, Amherst, Technical Report 07-49, October, 2007.
7. Kemelmacher-Shlizerman, Ira, et al. "The megaface benchmark: 1 million faces for recognition at scale." Proceedings of the IEEE conference on computer vision and pattern recognition. 2016.
8. Lindner, Tymoteusz, et al. "Face recognition system based on a single-board computer." 2020 International Conference Mechatronic Systems and Materials (MSM). IEEE, 2020.
9. Süzen, Ahmet Ali, Burhan Duman, and Betül Şen. "Benchmark analysis of jetson tx2, jetson nano and raspberry pi using deep-cnn." 2020 International Congress on Human-Computer Interaction, Optimization and Robotic Applications (HORA). IEEE, 2020.
10. Sati, Vishwani, et al. "Face detection and recognition, face emotion recognition through NVIDIA Jetson Nano." Ambient Intelligence–Software and Applications: 11th International Symposium on Ambient Intelligence. Springer International Publishing, 2021.
11. Padilla, Rafael, C. F. F. Costa Filho, and M. G. F. Costa. "Evaluation of haar cascade classifiers designed for face detection." World Academy of Science, Engineering and Technology 64 (2012): 362-365.
12. Mahajan, J. A., and A. N. Paithane. "Face detection on distorted images by using quality HOG features." 2017 International Conference on Inventive Communication and Computational Technologies (ICICCT). IEEE, 2017.
13. Zhang, Kaipeng, et al. "Joint face detection and alignment using multitask cascaded convolutional networks." IEEE signal processing letters 23.10 (2016): 1499-1503.
14. Yang, Shuo, et al. “Wider face: A face detection benchmark.” Proceedings of the IEEE conference on computer vision and pattern recognition. 2016.
15. O. M. Parkhi, A. Vedaldi, and A. Zisserman, "Deep face recognition," in British Machine Vision Conference, 2015, p. 6.

ISBN - 978-93-95038-50-8

SAR Image based Target Detection & Identification using Deep Learning Model YOLOv7

B Nehru[1]*, Vaddi Chandra Sekhar, A Naresh, D Penchalaiah, Abhijit Bhattacharya

Department
DRDL
Email: nehrurgukt8@gmail.com

ABSTRACT

In this paper we have implemented a Real Time ship Target Detection on SAR Imagery Using deep learning model. Ship detection is crucial to neutralize marine targets during combat scenario. SAR images operate in all-weather conditions and all-day and independent of range. SAR imagery-based surveillance technology is particularly well suited for marine surveillance. An Open-source SAR-ship dataset (HRSID) along with custom dataset is used for detection and identification. The existing AI based methods of detection (two stage object detectors) have proposed regions followed by extraction of features. The speed of the process for these methods is slow for real-time applications. Hence one stage detector, YOLOv7 with 415 convolution layers is used for the application which will overcome constraints of the previous methods. Mean Average Precision (mAP) of 78% @ 0.5 IOU is achieved for test HRSID dataset and custom dataset. NVIDIA GPU (RTX A4000) hardware is used for the training. The inference time of 8.2 milliseconds is achieved on NVIDIA RTX A4000 GPU. Hence YOLOv7 is suitable for real time detection of military targets on SAR images.

Keywords: *IOU, Convolution networks, SAR, mAP*

1. INTRODUCTION

Radar is used in military applications for remote sensing, target detection, guidance and global positioning [1]. Radar has a limitation of physical dimension of aperture [2]. SAR (Synthetic Aperture Radar) is a technique to overcome the physical limitation of radar by using signal processing. SAR is able to illuminate wide area for 24x7 in any weather condition with wide look angles. So, it is very useful for military applications where detection of objects is important for situational awareness.

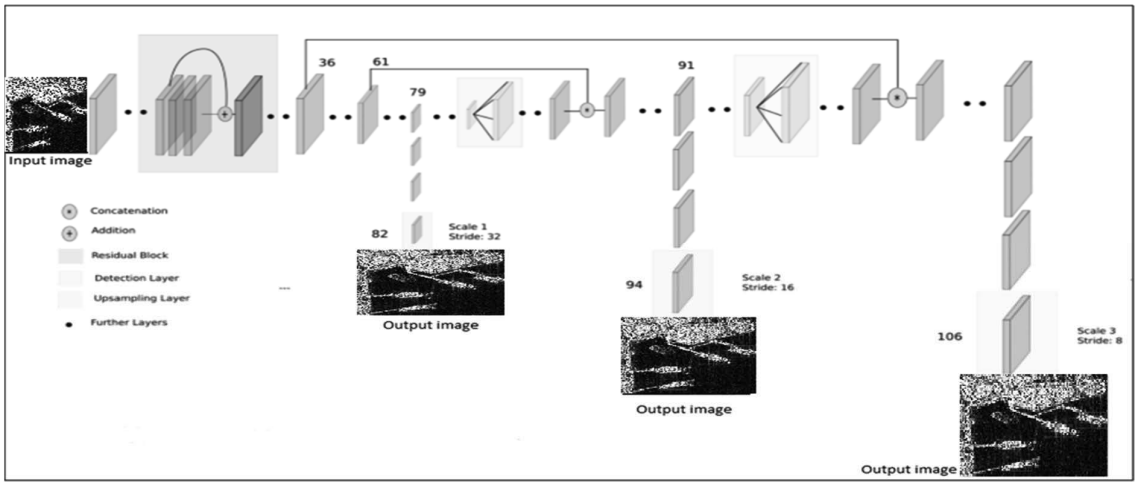

Figure 1: One stage detector of YOLOv7

[1] Corresponding author: E-mail: nehrurgukt8@gmail.com

For detection of objects on SAR imagery, YOLOv7 convolutional network is used. YOLOv7 [3] is single stage detector where detection and identification of objects is done in one pipeline, so it is suitable for real time applications compared to two stage detectors. Architecture of one stage detector is show in Figure 1. YOLOv7 can be trained on custom dataset without pre-trained weights. Aim of this paper is to detect ship target from SAR images. Open source dataset HRSID (High resolution SAR image dataset) along with custom dataset of 800x800 pixels size images is used for training the model. Convolutional neural network (CNN) is deep, feed-forward neural network for identifying objects from visual images. CNN includes convolutional layer, fully-connected layers (Dense layer) and pooling layer. In existing two stages CNN models' regions are proposed and then given for the classifier for detection of object, which makes them slow. YOLOv7 outperforms the older versions of YOLO in speed (prediction & training) and accuracy. The training & inferencing of YOLOv7 is done on NVIDIA RTX A4000 GPU.

2. LITERATURE SURVEY

A single stage detector model, YOLOv7 is used for detection of ships on SAR images. Wang et. Al proposed yolov7 algorithm. They architecture of YOLOv7, combines the strengths of Scaled-YOLOv4 and EfficientDet-D7 models to achieve high accuracy and fast performance. They have proposed the trainable bag-of-freebies method to enhance the accuracy of object detection. Vo et. al [4] used CeyMo Road Marking dataset for detection and identification road markings. They have experimented and evaluated performance of the different object detection models and algorithms. They could find out that YOLOv7 performed better compared to other methods and it is current best method for effective detection and identification of road markings for their road marking dataset. Liu et. Al [5] investigated to build a robust and fast model for estimation of vehicle distance. Synthesized theoretical insights in the context of odometry and based on proposed conceptual framework YOLOv7 is customized. In this research, KITTI data set is used for distance estimation using their attention model along with YOLOv7, YOLOv7 is used for the first time. Gallo et. al [6] performed deep object detection using real case dataset of crop weeds captured from uav images. The YOLOv7-based object detection model performed better compared to the existing two-stage detectors (RCNN, FRCNN) and single-stage (YOLOv5, YOLOv4) in terms of detection accuracy. YOLOv7 achieved better results compared to YOLOv5 in terms of the mAP score using the LB dataset. L Jin et al [7] proposed a real-time fault diagnosis model of PV modules for integrated energy systems to overcome the complexity of infrared images of PV array based on YOLOv7. They have shown that compared to SSD [8] and Faster-RCNN [9] target object detection algorithms YOLOv7 has a faster image processing speed.

3. ARCHITECTURE OVERVIEW

YOLOv7 (You Only Look Once version 7) is a state-of-the-art object detection algorithm that uses deep learning to detect objects in images and video. The block diagram is shown in figure (2). The architecture is an improvement over its predecessor YOLOv5 [10], and is based on a combination of the Scaled-YOLOv4 [11] and EfficientDet-D7 models.

YOLOv7 has following key features in its architecture:

Backbone network: YOLOv7 uses the CSPDarkNet53 as its backbone network, which is a lighter and faster version of the DarkNet architecture. The CSPDarkNet53 includes cross-stage partial connections, which allow for better feature propagation and optimization.

ISBN - 978-93-95038-50-8

Neck network: YOLOv7 uses the SPP-PANet as its neck network, which includes a Spatial Pyramid Pooling (SPP) module and a Path Aggregation Network (PAN). The SPP module allows for detection of objects at different scales, while the PANet module aggregates feature maps from different levels to improve object detection accuracy.

Head network: YOLOv7 uses the YOLOv4-Lite as its head network, which includes a series of convolutional layers followed by a detection layer. The detection layer uses anchor boxes and class probabilities to generate object detection predictions.

Training strategy: YOLOv7 uses a combination of supervised and unsupervised learning strategies, including data augmentation, mix up training, and self-training. The model is trained on large-scale datasets such as COCO [12], Pascal VOC [13], and ImageNet [14].

Overall, the YOLOv7 architecture is designed for fast and accurate object detection, with a focus on optimizing the performance of the backbone, neck, and head networks. It achieves state-of-the-art results on object detection benchmarks such as COCO and KITTI, making it a popular choice for various applications such as autonomous driving, surveillance, and robotics.

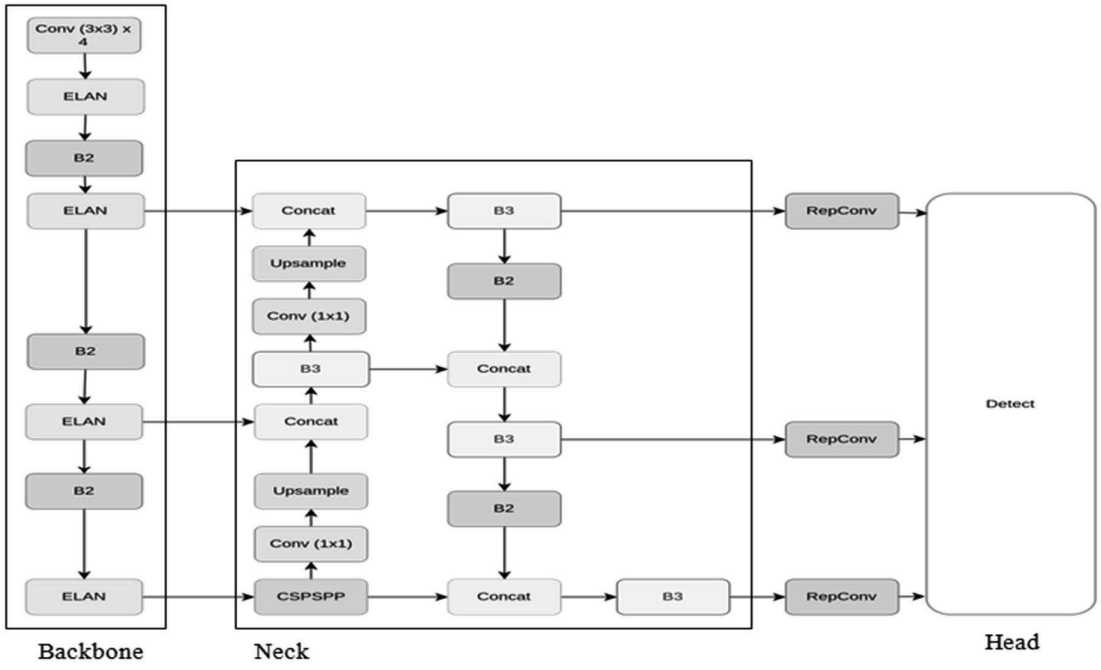

Figure 2: YOLOv7 Architecture

4. Real Time Target Detection for SAR Imagery

Dataset

HRSID open dataset & custom dataset is used for training. During training, 3000 images are used for training, 1647 images are used for validation and 300 images are used for testing. The following are the few images from dataset.

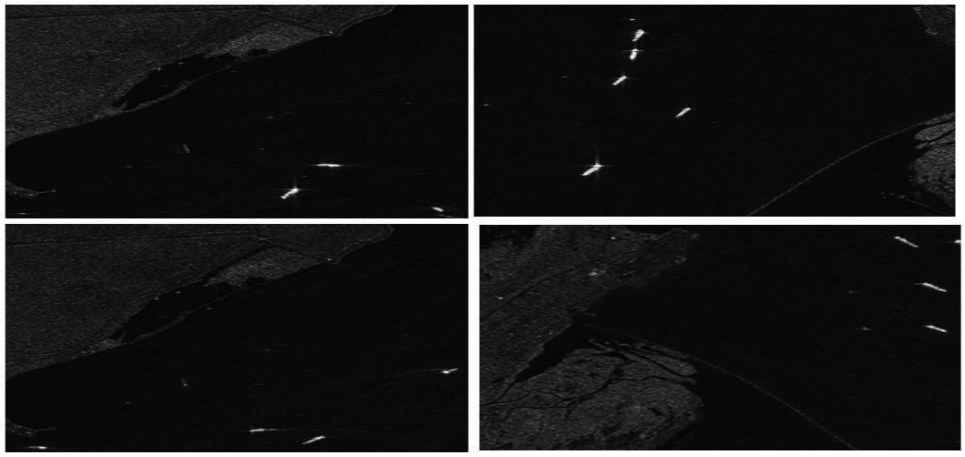

Figure 3: Images from SAR-ship dataset

DATASET ANNOTATION

Dataset is annotated in YOLO Format. In YOLO format center coordinates and width and height which represent bounding box for each object in an image. LabelImg, which is graphical user interface tool is used for annotating SAR images of ship. YOLO format contains, center coordinates, length and width of bounding boxes.

5. EXPERIMENTAL RESULTS

DETECTION PERFORMANCE ANALYSIS OF THE YOLOV7 MODEL

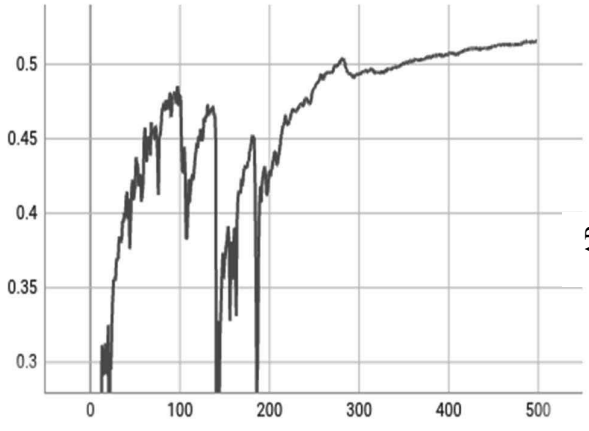

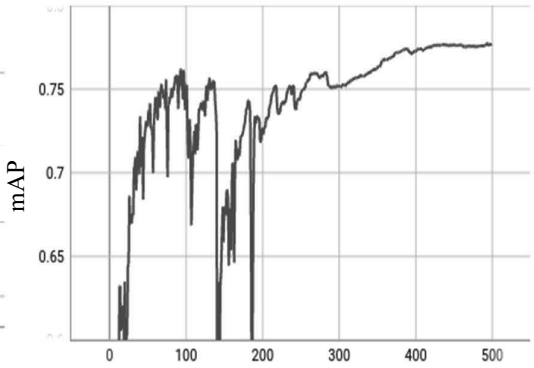

Fig.4 (a) mAP@ IOU 0.5 Epochs Fig.4 (b) mAP@ IOU 0.5-0.95 Epochs

Ship target detection and identification is carried out on NVIDIA RTX A4000 on Ubuntu 20.04 of Linux operating system. NVIDIA GPU has GPU memory 16GB, 6144 Cuda cores. The model performance is measured in terms of mean Average Precision (mAP). The model achieved 0.78 mean average precision (mAP) with validation dataset of size 800 x 800 as depicted in figure 3. An mAP @ IOU 0.5 indicates mean average precision at IOU of 0.5. Model is trained for 500 epochs with mini-batch size of 8. Training took around 11 hours on RTX A4000 GPU. Figure 4(a) shows mAP at 0.5 IOU with respect to number of epochs. The model gets properly trained nearly after 500 epochs. Figure 4(b) shows mAP of 0.52 in the range of IOU varying from 0.5 to 0.95 indicating the accuracy of localizing and detecting targets at higher IOUs.

Table 1 Result with one stage detector: YOLOv7

Image Input Size	mAP@0.5	Recall@0.5	Precision@0.5	Prediction time
608 x 608	78%	0.7	0.85	8.2ms

Table 1 shows the performance parameters of YOLOv7 model on ship target dataset. 800X800 image is re-scaled to 608X608 by YOLOv7 model.

YOLOv7 vs YOLOv4: Both YOLOv7 & YOLOv4 models are trained on NVIDIA RTX A4000 GPU with HRSID and custom dataset of ship with 3000 training, 1647 validation and 300 testing images. The training time for YOLOv7 and YOLOv4 is around 16 & 11 hours respectively for 500 epochs. YOLOv7 takes less training time compared YOLOv4. mAP@0.5 and inference time of YOLOv4 are 57.9% and 11.6 ms respectively. mAP@0.5 and inference time of YOLOv7 are 78% and 8.2 ms respectively.

TESTING OF THE MODEL WITH TEST IMAGES

Figure 5 shows the detected targets on few images of test dataset. Ships detected are enclosed in bounding boxes along with confidence score. The size of input images given to the prediction model is 800 x 800 pixels. The model re-scales image to 608X608.

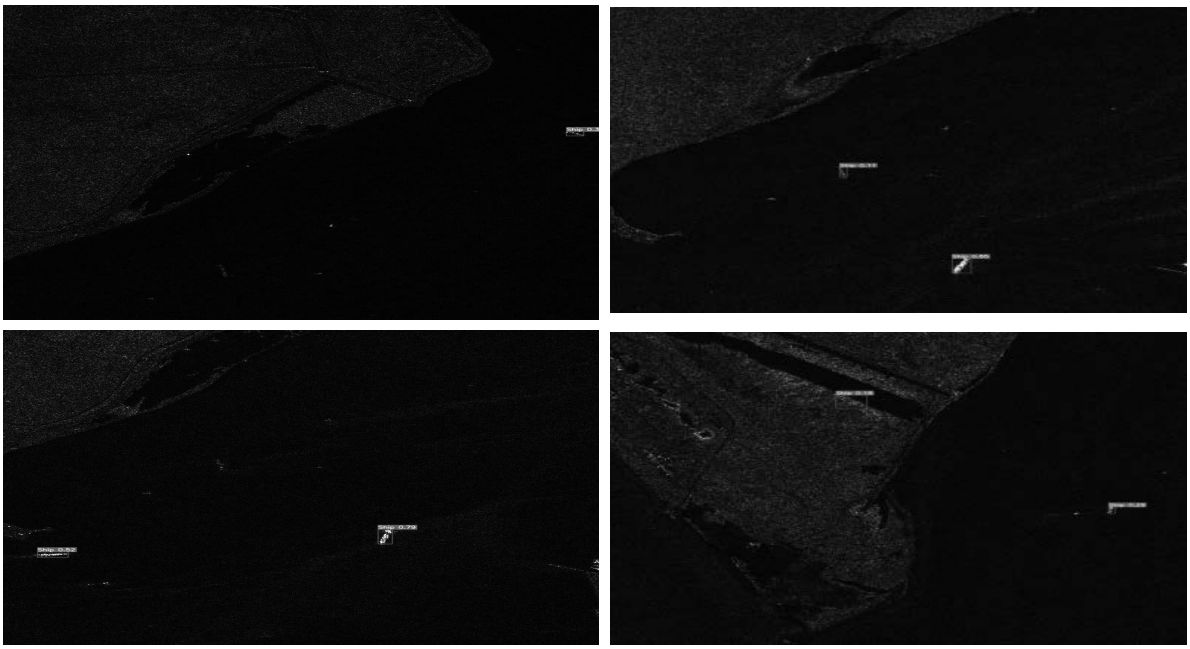

Figure 5: Detection of ships on test images (Detected ships localized with rectangular boxes)

6. CONCLUSION

In this paper, we have implemented a Real Time Target Detection on SAR images. SAR images cover large area for all day and for all weather conditions compared to optical images. YOLOV7 model is used for training and inference as it is superior over other YOLO versions in terms of accuracy and speed. Training is done with open source HRSID & custom dataset of ship as target. 78% of, mAP achieved with 0.5 IOU and inference time of model is 8.2 ms.

ISBN - 978-93-95038-50-8

The model is trained on NIVIDA RTX A4000 GPU. Training time for 500 epochs is approximately 11 hours

There is a room for improvement in accuracy by varying CNN layers, prediction time may be minimized further on SAR by using better dataset and fine tuning of the model. YOLOv7 has good performance over YOLOv4 in terms of mAP and inference and training time. YOLOv7 can be trained on custom dataset without pre-trained weights. mAP further can be improved by training for more number of epochs and using better dataset. This model helps in detection of multiple targets in real time.

REFERENCES

1. El-Rabbany, Ahmed. Introduction to GPS: the global positioning system. Artech house, 2002.
2. Buck, G., and J. Gustincic. "Resolution limitations of a finite aperture." IEEE Transactions on Antennas and Propagation 15.3 (1967): 376-381.
3. Wang, Chien-Yao, Alexey Bochkovskiy, and Hong-Yuan Mark Liao. "YOLOv7: Trainable bag-of-freebies sets new state-of-the-art for real-time object detectors." arXiv preprint arXiv:2207.02696 (2022).
4. Vo, Nguyen D., et al. "Empirical Study of the Performance of Object Detection Methods on Road Marking Dataset." 2022 RIVF International Conference on Computing and Communication Technologies (RIVF). IEEE, 2022.
5. Liu, Xiaoxu, and Wei Qi Yan. "Vehicle-Related Distance Estimation Using Customized YOLOv7." Image and Vision Computing: 37th International Conference, IVCNZ 2022, Auckland, New Zealand, November 24–25, 2022, Revised Selected Papers. Cham: Springer Nature Switzerland, 2023.
6. Gallo, Ignazio, et al. "Deep Object Detection of Crop Weeds: Performance of YOLOv7 on a Real Case Dataset from UAV Images." Remote Sensing 15.2 (2023): 539.
7. Jin, Lu, et al. "Real-time Fault Diagnosis of Photovoltaic Modules for Integrated Energy Systems Based on YOLOv7." (2023).
8. Liu, Wei, et al. "Ssd: Single shot multibox detector." Computer Vision–ECCV 2016: 14th European Conference, Amsterdam, The Netherlands, October 11–14, 2016, Proceedings, Part I 14. Springer International Publishing, 2016.
9. Girshick, Ross. "Fast r-cnn." Proceedings of the IEEE international conference on computer vision. 2015.
10. Thuan, Do. "Evolution of Yolo algorithm and Yolov5: The State-of-the-Art object detention algorithm." (2021).
11. Wang, Chien-Yao, Alexey Bochkovskiy, and Hong-Yuan Mark Liao. "Scaled-yolov4: Scaling cross stage partial network." Proceedings of the IEEE/cvf conference on computer vision and pattern recognition. 2021.
12. Lin, Tsung-Yi, et al. "Microsoft coco: Common objects in context." Computer Vision–ECCV 2014: 13th European Conference, Zurich, Switzerland, September 6-12, 2014, Proceedings, Part V 13. Springer International Publishing, 2014.
13. Hoiem, Derek, Santosh K. Divvala, and James H. Hays. "Pascal VOC 2008 challenge." World Literature Today 24 (2009).
14. Deng, Jia, et al. "Imagenet: A large-scale hierarchical image database." 2009 IEEE conference on computer vision and pattern recognition. Ieee, 2009.

ISBN - 978-93-95038-50-8

Adversarial Machine Learning Problems: Threats and Attacks

Revathi Lavanya Baggam[1*], V. Valli Kumari[2], Gowri Shankar Wuriti[3]

[*]Research Scholar, Andhra University College of Engineering, Waltair
[2]Professor, Andhra University College of Engineering, Waltair
[3]Scientist & Technology Director, ASL, DRDO, Hyderabad

ABSTRACT

Machine Learning is being extensively used in many wide range applications, as it shows cases its technical breakthroughs. It also has proved its success by handling complex scenarios and exhibited its capabilities very close to humans or even much beyond the human ability. But, the research in recent times even prove that machine learning models are being much more helpless to various kinds of attacks, which in turn are compromising its security aspects of the models and their applications. However, these types of attacks are cautious due to their unexpected behavior of deep learning methods. In this survey, a systematic analysis of the security issues of ML majorly focusing on the existing set of attacks on ML systems, and their related defenses or the secure learning approaches and the evaluation techniques. Inspite of keenly focusing on only one type of approach or attack, this paper details about the various phases of machine learning security starting from training phase to the testing phase. Initially, this paper explains about the machine learning in the existence of the adversaries present, and the reasons behind why the machine learning can be easily attacked is analyzed. Later, the aspects with respective to machine learning security are classified into majorly five sets namely: backdoors present in the training set; theft to model; poisoning the training set; sensitive training data recovery; adversarial example attacks. Also, the threat models, various approaches to attack and the defense methods are analyzed.

Keywords: *Poisoning attacks, backdoor attacks, adversarial examples, Artificial intelligence security*

1. INTRODUCTION

In the recent years' machine learning has its wide share in many sectors like driverless cars, natural language processing, smart healthcare, NLP and image classification. In image classification sector the speed and accuracy of the machine learning is extensively exceeding the humans. In some of the applications like malicious program detection, spam filtering for e.g., machine learning enables the security aspects and its capability.

But recent study proves that machine learning algorithms are being easily prone to threat to security. Some of the security threats like:

i. Poisoning the training data results in reduction of the model accuracy or may even lead to many other error-specific attacks.
ii. Risky circumstances for the system can also be brought on by backdoors in the training data.
iii. The adversarial example, which is a well-designed disturbance in the test input, may cause the model to act incorrectly.
iv. Some of the attacks like model stealing attack, membership inference attack and model inversion attack may result in stealing the parameters of the model or even retrieve some very sensitive training data.

However, threat to machine learning security may lead to severe consequences like safety and security of some of the typical applications like smart healthcare, autonomous driving etc.

In recent times there have been a large amount of research are going on safety of deep learning algorithms like:

[1]*Corresponding author : Email: Revathi Lavanya Baggam

Szegedy et al. [1] focused on the threat of hostile examples, whereas the security of machine learning is not a new concept [3]. The previously stated work by Dalvi et al.[4] [5] focused on the adversarial machine learning with respective to non-deep machine learning techniques in relation to PDF malware exposure, intrusion detection etc. [3]. These previously attacks are said to be as the evasion attacks, and some other as poisoning attacks.

Motivated by the above issues, this paper presents the comprehensive survey about the security of machine learning.

In 2010, Barreno et al. [6] examined the evasion techniques against non-deep learning systems and concentrated on spam filter. Akthar et. al. [7] surveyed adversaries in the field of computer vision. Yuan et al. [8] reviewed about adversaries in deep learning and they discussed the various adversary example generation methods and discussed its countermeasure too. Riazi et.al [9] discussed regarding privacy protection techniques with respective to cryptographic primitives. All the above reviews mainly focus on only adversarial attack. Biggio et.al [3] majorly focused into the evasion and poison attacks, as they reviewed the wild patterns in adversarial machine learning over a decade which includes the earlier non-deep and recent develop deep learning techniques in computer vision and cyber security sectors. Lie et al. [10] surveyed about the assessment and data security. Papernot et al. [11] have described three security aspects that are availability, honesty, and confidentiality, and also they discussed the defenses with respect to the robustness, accountability and privacy [11].

The major difference of this paper to the previous survey papers is this paper:

1. Properly explains about the entire machine learning security starting restraining phase to the testing phase, including entire categories of attacks.
2. Majorly focuses on five sets of attacks namely: backdoors present in the training set; theft to model; poisoning the training set; sensitive training data recovery; adversarial example attacks.
3. Direction to future research on machine learning security is presented which includes the privacy preserving machine learning methods, along with attacks in real physical conditions.

The paper is organized as follows: Section II contains the behavior of machine learning in the presence of adversary. In Section III the threat models along with the approach of attack is reviewed. Section III discusses about the evaluation techniques. The future direction on security of machine learning is discussed in Section IV. Section V concludes the paper.

2. Behaviour of Machine Learning Model in Presence of Adversary

2.1. Overview of machine learning

There are mainly two stages of a machine learning system: (1) training phase, which helps the algorithm to learn from the training data to develop a model with the parameters (2) Testing phase. The trained model is then applied to a specific assignment, like classification to provide predicted level value for the input data. The machine learning algorithms have been broadly divided into a set of two division: (a) N algorithms (b) non-NN algorithms. The abbreviation NN is used to depict the Deep Neural Networks (DNN), Convolutional Neural Network (CNN), Recurrent Neural Network (RNN) and Neural Network (NN) algorithms have found to be majority of contribution in recent years by increasing the performance of machine learning systems. Non-NN algorithms represent the machine learning algorithms like SVM (Support Vector Machine), Naïve-Bayes, etc. A machine learning algorithm usually consists of the

following attributes, data holder, system and the clients. But in the case of adversarial model where attackers too are present.

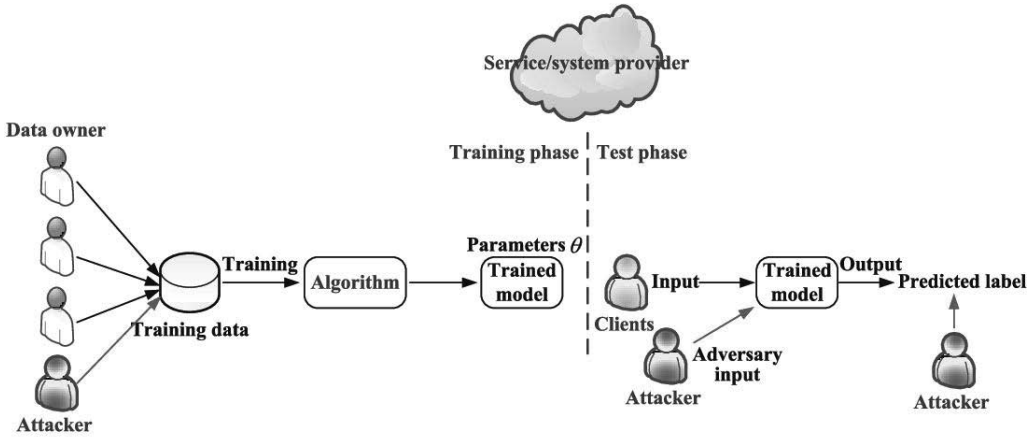

Figure 1: Overview of machine learning systems, which illustrates the two phases, the learning algorithms, and different entities

From the diagram, the data owners are the owners of the huge training data which is private. The service provider builds the algorithm, trains the model, and then uses it to carry out a job or offer a service. The clientele make advantage of the services. An attacker in this scenario may be a system user, either internal or foreign, who has a strong desire to learn more about the other entities.

2.2. WHY IS MACHINE LEARNING ATTACKED?

In training phase, huge training data along with its computational complexity; the training procedure is leading to: 1) to outsource the training procedure [12]; 2) the third parties lending the pre-trained models which are the intellectual properties (IP), are integrated; 3) a huge chunk of data that lack any data validations and are obtained from unreliable third parties. These are bring new security threats to system. Also the machine-earning-as a-service are used intensively , where the present model the machine learning model which is works on the server/cloud, as clients are able to analyzed through prediction of APIs. This huge data is of great commercial and confidential too, which is the major target for attackers. Good fellow et al. [2] pointed linear DNN in high dimensional space causes adversarial attack which is being vulnerable too. Studies [1], [8] incomplete training data is one of the reasons these adversarial example attacks. Yeom et al. [13] studied that overfitting is one of the reasons for the attacker to implement membership inference attacks.

3. ATTACKS ON ML

The security threats are broadly classified into five: 1) Backdoors present in the training set; 2) Theft to model; 3) Poisoning the training set; 4) Sensitive training data recovery; 5) adversarial example attacks

ISBN - 978-93-95038-50-8

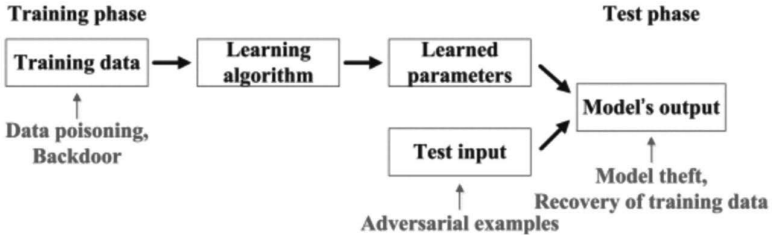

Figure 2: Attacks on Machine Learning

3.1. BACKDOORS PRESENT IN TRAINING SET

The approaches suggested by the previous surveys is as follows:

BadNet [12]; PLMs [32]; Attack on deep learning [33]; Attack on CNNs [34] [35]; Attack on federated learning [36]. These approaches follow a working mechanism of adding well-designed signals of backdoor to the clean data and also to manipulate the parameters of the model directly. Due to this the target model is able to misclassify the backdoor instances. The advantage of these approaches is that they are stealthy and do not affect the model's performance, but they need to participate in the process of training or they need to re-train the model which is the major drawback of this.

The below diagram explains how an attacker can hide the backdoor in the training data or in a pre-trained model.

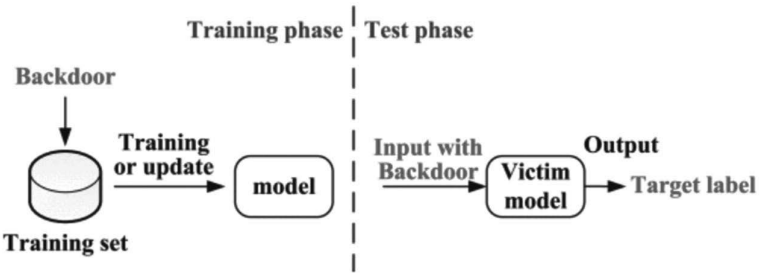

Figure 3: Backdoor attacks

3.2. MODEL THEFT

The recent research has proved that by observing the output label and confidence levels the adversaries can steal the machine learning models, which is also known as model extraction attack or model stealing attack.

Some of the researchers have surveyed the attacks and the approaches are as follows:

1. Tramer et al. [63]; Shi et al. [64] and Chandrasekharan et al. [65] have proposed an approach that uses the working mechanism of extraction through prediction APIs and also to train a model which is similar to that of the target model, and to use an active learning technique [65]. This is effective in generating a model which is very similar to that of the target model and so helpful in extracting the model parameters without the knowledge of the target model. But the target model needs to be queried very frequently which is a drawback of this approach.
2. Wang and Gong [66] have suggested to calculate the hyperparamters by solving the linear equations. This is effective in to steal the hyperparameters of the models and is also suitable to be applied to various machine learning algorithms, but this requires the information about the training set and the target algorithm too.

ISBN - 978-93-95038-50-8

3. Milli et al. [67] proposed that the query gradients of a model to be chosen inputs and the heuristic model reconstruction, which is effective to reconstruct the target model. This is more efficient when compared to querying the labels, but this incurs too much of computational cost and this only capable of evaluating on a two-layer NN.

3.3. POISONING THE TRAINING SET

Some of the researchers have proposed some of the training set poisoning approaches which have been broadly classified as below:

Some of the researchers have proposed some of the training set poisoning approaches which have been broadly classified as below:

Targeting non-NN models

A. Anomaly detection or security detection application: This target system or model uses the approach of poisoning PC-subspace based anomalies detection [14] as well as chronic poisoning against IDS [15]. This model follows the poisoning the training data of the model working mechanism with an effect to reduce the performance of the anomaly detection algorithms. The advantages of this target system is this is very simple and effective on several training models [15]. This target system too has some disadvantages which is that it is non-generic [14] and it is long-term slow poisoning and complicated to implement.

B. Biometric recognition systems: This target system follows the approach of poisoning PCA based face recognition systems [16], and poisoning face templates [17]. This target system follows the mechanism of submitting a set of fake faces and claiming to be the victim. The effect of this type of target system is to replace the victim's template in the system. The advantage of this model is that it is stealthily and gradually. This model requires the information about the target system or about the victim.

C. SVM: This model follows the approach of poisoning the SVM approach and uses the strategy of gradient ascent which is based about the optimal solution of SVM. This has an effect of misleading the clustering algorithms. The main advantage of this model is, it uses the optimized formulation and it can also be kernalized too, but it needs the full information/knowledge about the algorithm and also about the training too which is the major drawback of this approach.

D. Clustering algorithms: This model follows the approach of poisoning the clustering data [19] and also poisoning the behavioral of malware clustering [20]. Mainly the poisoning attack is based out of the distance between the clusters which is its working mechanism. This showcases the effect of misleading the clustering algorithms. This is very generic to the clustering algorithms which is its major advantage, of course it requires the whole sum information about the target algorithm which is this model's drawback.

E. Machine learning algorithms or processing methods: The model follows the approach of poisoning the feature selection [21], as well poisoning the collaborative filtering [22] and also poisoning the regression learning [23]. This model follows the optimized based or statistical based poisoning attack approach. It misleads the feature selection algorithms, as well the collaborative filtering system or the linear regression one, but it is very powerful and effective that adds as an advantage to this model. But this is non-generic and hugely requires the information/data about the target system.

F. Online learning or data sanitization defenses: There are two proposed approaches in this model:

- The first approach follows to poison the breaks data sanitization defenses [24], and works on optimizing the poisoning attacks. This approach is effective in bypassing the data sanitization defenses and it is strong and effective under the defenses which is an advantage of this approach. This incurs too much of overhead on computations.
- The second approach follows poisoning the online data [25] [26] and it follows the mechanism of optimizing the poisoning attacks likewise the first approach. This mainly effects the performance of online learning in reducing the same, helps to work for the online learning scenarios which is its advantage. This approach too incurs too much of overhead on computations like the first one.

Targeting NN models:

The below approaches have been proposed:

- Generative poisoning against NN [27] follows the working mechanism of poisoning attack based out of Generative Adversarial Networks(GAN). This approach effects the accuracy of the NN model by reducing the same. This majorly generates the poisoning data quickly, but it requires too many interactions with the model very frequently.
- The second approach is poisoning of deep learning algorithms by optimizing the back gradient [28]. This follows the mechanism of optimizing the poison attacks, which effects the healthcare systems, recommender systems as well the crowd sensing systems by misleading them. We will be able to apply the poisoning attacks towards the practical applications and scenarios which is these approaches major advantage, but this requires too much of information with respective to target system.

Specific applications oriented:

This majorly follows the approach of poisoning the healthcare systems [29] as well poisoning the graph based recommendation system [30] and also poisoning the crowd sensing systems [31]. The approaches follow the functionality of optimizing the poisoning attacks and effectively misleads the systems of healthcare, recommender and crowd sensing. These helpful in applying the poisoning attacks to most of the practical applications as well as scenarios, but this too needs too much of information/knowledge with related to the target system.

3.4. ADVERSARIAL EXAMPLE ATTACKS

Researchers have proposed few of the below approaches to the adversarial example attacks:

Earlier evasion attacks on non-NN models:

- Targets like game theory can be handled with the approach of classifying adversarial [4] by the mechanism of modifying the features which show a great impact on the detector, due to this approach on this type of targets the malicious instances cannot be detected by the detector. This greatly evades the detection of security related applications, but this needs the information of feature extraction algorithm.
- The approach of adversarial learning [40] through reverse engineering the classifier follows the working approach of modifying the features which are having the greatest impact on the detector, due to wchih the malicious instances cannot be detected by the detector. This avoids in detecting pf the security related applications, but this needs great knowledge about the feature extraction algorithm.
- The approach suggests by Nelson et.al [5] for spam filtering follows the mechanism of modifying the features which are having the greatest impact on the detector, because of which instances which are malicious cannot be dected by the detector. This needs too much of

information about the feature xtraction algorithm, but helps in evading the detection of the security related applications.

- Stochastic search –based attack [44] and the Evade-HC [45] approach for malware detection(black-box) works using the heuristic search-based method as well as the stochastic search- based method. Eventhough the malicious instances cannot be detected by the detector, but this requires too many iterations and feedback from the system. This is very generic and does not requires any information about the systems.
- The approach to attacka linear classifier [43] which targets the android malware detection follows the mechanism of modifying the features that have the great impact on the detector which is effective in not detecting the malicious instances. This completely evades the concept of detecting the security related applications but requires data about the algorithm of feature extraction.

Adversarial example attacks on NN models: The approaches of Intriguing properties of NN[1], FGSM[2], BIM[3], JSMA[47] and One-pixel attack[48], Carlini and Wagner[49][50], Universal perturbations[51], Malware classification[52], Face recognition[53] which are targeted to first work of adversarial examples on NN, one-step/one-shot methods, take multiple small steps iteratively, perturbing only a few pixels, high-confidence adversarial examples, universal adversarial perturbations, targeting deep learning based security detection and inbiometric authentication systems follow the mechanism of optimization-based or gradient-based adversarial example attacks. This is effective in misleading the model and also this cannot be completely perceived by human-being. This do not require any information about the feature extraction algorithm of the system and also the perturbations are very small and imperceptible too. But these attacks may have a chance of failing in the real world.

In real world conditions the approaches like road sign recognition attack [54], cellphone camera attack [46], face recognition attack [46],3D objects attack [55] follow the method of simulating the physical properties of the adversarial examples generation. These are effective in attacking the physical conditions successfully and are very robust to any physical condition. But the perturbations are high and conspicuous.

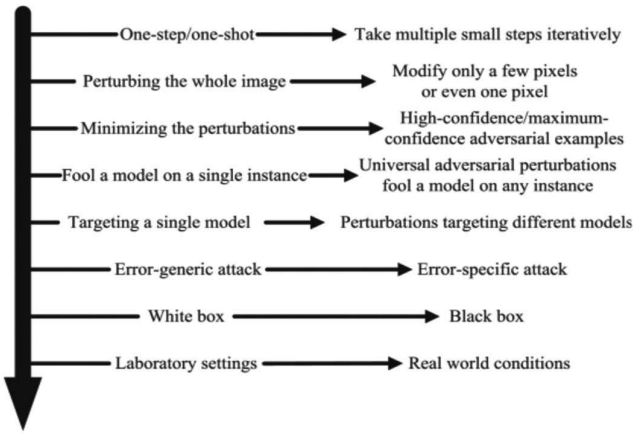

Figure 4: Pipeline of adversarial example attacks in deep learning algorithms

4. FUTURE DIRECTION OF SECURITY THREAT

There are have been numerous of security attacks on machine learning algorithms but the effect of these attacks under real physical conditions are the current research topics

ISBN - 978-93-95038-50-8

Also in recent years the machine learning algorithms privacy has gained much focus, so the deep learning needs to answer the issue of privacy protection, along with this the cryptographic primitive – based ML approaches efficiency too needs to be improved.

5. CONCLUSION

Current manuscript provides information about the proposed approaches by various researchers about the attacks on machine learning algorithms. Machine learning algorithms facing a wide variety of security threats all though its phases, as new security threats are continuously emerging. Studies prove that adversarial and poisoning examples can be generalized among various different machine learning models. This transferability can be helpful for the attacks to be successful in black-box scenarios.

REFERENCES

1. C. Szegedy, W. Zaremba, I. Sutskever, J. Bruna, D. Erhan, I. J. Goodfellow, and R. Fergus, ‘‘Intriguing properties of neural networks,’’ in Proc. 2nd Int. Conf. Learn. Represent., Apr. 2014, pp. 1–10.
2. I. J. Goodfellow, J. Shlens, and C. Szegedy, ‘‘Explaining and harnessing adversarial examples,’’ in Proc. Int. Conf. Learn. Representations, Mar. 2015, pp. 1–11.
3. B. Biggio and F. Roli, ‘‘Wild patterns: Ten years after the rise of adversarial machine learning,’’ Pattern Recognit., vol. 84, pp. 317–331, Dec. 2018.
4. N. N. Dalvi, P. M. Domingos, Mausam, S. K. Sanghai, and D. Verma, ‘‘Adversarial classification,’’ in Proc. 10th ACM SIGKDD Int. Conf. Knowl. Discov. Data Min., Aug. 2004, pp. 99–108.
5. B. Nelson, M. Barreno, F. J. Chi, A. D. Joseph, B. I. P. Rubinstein, U. Saini, C. A. Sutton, J. D. Tygar, and K. Xia, ‘‘Exploiting machine learning to subvert your spam filter,’’ in Proc. USENIX Workshop Large-Scale Exploit. Emerg. Threat., Apr. 2008, pp. 1–9.
6. M. Barreno, B. Nelson, A. D. Joseph, and J. D. Tygar, ‘‘The security of machine learning,’’ Mach. Learn., vol. 81, no. 2, pp. 121–148, Nov. 2010.
7. N. Akhtar and A. S. Mian, ‘‘Threat of adversarial attacks on deep learning in computer vision: A survey,’’ IEEE Access, vol. 6, pp. 14410–14430, Jul. 2018.
8. X. Yuan, P. He, Q. Zhu, and X. Li, ‘‘Adversarial examples: Attacks and defenses for deep learning,’’ IEEE Trans. Neural Netw. Learn. Syst., vol. 30, no. 9, pp. 2805–2824, Sep. 2019.
9. M. S. Riazi and F. Koushanfar, ‘‘Privacy-preserving deep learning and inference,’’ in Proc. Int. Conf. Comput.-Aided Design ICCAD, Nov. 2018, pp. 1–4.
10. Q. Liu, P. Li, W. Zhao, W. Cai, S. Yu, and V. C. M. Leung, ‘‘A survey on security threats and defensive techniques of machine learning: A data driven view,’’ IEEE Access, vol. 6, pp. 12103–12117, 2018.
11. N. Papernot, P. D. McDaniel, A. Sinha, and M. P. Wellman, ‘‘SoK: Security and privacy in machine learning,’’ in Proc. IEEE Eur. Symp. Secur. Privacy (EuroS&P), Apr. 2018, pp. 399–414.
12. T. Gu, B. Dolan-Gavitt, and S. Garg, ‘‘BadNets: Identifying vulnerabilities in the machine learning model supply chain,’’ 2017, arXiv:1708.06733. [Online]. Available: http://arxiv.org/abs/1708.06733
13. S. Yeom, I. Giacomelli, M. Fredrikson, and S. Jha, ‘‘Privacy risk in machine learning: Analyzing the connection to overfitting,’’ in Proc. IEEE 31st Comput. Secur. Found. Symp. (CSF), Jul. 2018, pp. 268–282.
14. B. I. P. Rubinstein, B. Nelson, L. Huang, A. D. Joseph, S. Lau, S. Rao, N. Taft, and J. D. Tygar, ‘‘ANTIDOTE: Understanding and defending against poisoning of anomaly detectors,’’ in Proc. 9th ACM SIGCOMM Conf. Internet Meas. Conf. (IMC), Nov. 2009, pp. 1–14.
15. P. Li, Q. Liu, W. Zhao, D. Wang, and S. Wang, ‘‘Chronic poisoning against machine learning based IDSs using edge pattern detection,’’ in Proc. IEEE Int. Conf. Commun. (ICC), May 2018, pp. 1–7.
16. B. Biggio, G. Fumera, F. Roli, and L. Didaci, ‘‘Poisoning adaptive bio-metric systems,’’ in Proc. Int. Workshops Stat. Tech. Pattern Recognit. Struct. Synt. Pattern Recognit., Nov. 2012, pp. 417–425.
17. B. Biggio, L. Didaci, G. Fumera, and F. Roli, ‘‘Poisoning attacks to com-promise face templates,’’ in Proc. Int. Conf. Biometrics (ICB), Jun. 2013, pp. 1–7.

18. B. Biggio, B. Nelson, and P. Laskov, ''Poisoning attacks against support vector machines,'' in Proc. 29th Int. Conf. Mach. Learn., Jun. 2012, pp. 1467–1474.
19. B. Biggio, I. Pillai, S. R. Bulò, D. Ariu, M. Pelillo, and F. Roli, ''Is data clustering in adversarial settings secure?'' in Proc. ACM Workshop Artif. Intell. Secur. AISec, Nov. 2013, pp. 87–98.
20. B. Biggio, K. Rieck, D. Ariu, C. Wressnegger, I. Corona, G. Giacinto, and F. Roli, ''Poisoning behavioral malware clustering,'' in Proc. Workshop Artif. Intell. Secur. Workshop AISec, Nov. 2014, pp. 27–36.
21. H. Xiao, B. Biggio, G. Brown, G. Fumera, C. Eckert, and F. Roli, ''Is feature selection secure against training data poisoning,'' in Proc. 32nd Int. Conf. Mach. Learn., Jul. 2015, pp. 1689–1698.
22. B. Li, Y. Wang, A. Singh, and Y. Vorobeychik, ''Data poisoning attacks on factorization-based collaborative filtering,'' in Proc. Annu Conf. Neural Inf. Proc. Syst., Dec. 2016, pp. 1885–1893.
23. M. Jagielski, A. Oprea, B. Biggio, C. Liu, C. Nita-Rotaru, and B. Li, ''Manipulating machine learning: Poisoning attacks and countermeasures for regression learning,'' in Proc. IEEE Symp. Secur. Privacy (SP), May 2018, pp. 19–35. P. W. Koh, J. Steinhardt, and P. Liang, ''Stronger data poisoning attacks break data sanitization defenses,'' 2018, arXiv:1811.00741. [Online]. Available: http://arxiv.org/abs/1811.00741
24. Y. Wang and K. Chaudhuri, ''Data poisoning attacks against online learning,'' 2018, arXiv:1808.08994. [Online]. Available: http://arxiv.org/abs/1808.08994
25. X. Zhang, X. Zhu, and L. Lessard, ''Online data poisoning attack,'' 2019, arXiv:1903.01666. [Online]. Available: http://arxiv.org/abs/1903.01666
26. C. Yang, Q. Wu, H. Li, and Y. Chen, ''Generative poisoning attack method against neural networks,'' 2017, arXiv:1703.01340. [Online]. Available: http://arxiv.org/abs/1703.01340
27. L. Muñoz-González, B. Biggio, A. Demontis, A. Paudice, V. Wongrassamee, E. C. Lupu, and F. Roli, ''Towards poisoning of deep learning algorithms with back-gradient optimization,'' in Proc. 10th ACM Workshop Artif. Intell. Secur. AISec, 2017, pp. 27–38.
28. M. Mozaffari-Kermani, S. Sur-Kolay, A. Raghunathan, and N. K. Jha, ''Systematic poisoning attacks on and defenses for machine learning in healthcare,'' IEEE J. Biomed. Health Informat., vol. 19, no. 6, pp. 1893–1905, Nov. 2015.
29. M. Fang, G. Yang, N. Z. Gong, and J. Liu, ''Poisoning attacks to graph-based recommender systems,'' in Proc. 34th Annu. Comput. Secur. Appl. Conf., Dec. 2018, pp. 381–392.
30. C. Miao, Q. Li, H. Xiao, W. Jiang, M. Huai, and L. Su, ''Towards data poisoning attacks in crowd sensing systems,'' in Proc. 18th ACM Int. Symp. Mobile Ad Hoc Netw. Comput. - Mobihoc, Jun. 2018, pp. 111–120.
31. Y. Ji, X. Zhang, and T. Wang, ''Backdoor attacks against learning sys-tems,'' in Proc. IEEE Conf. Commun. Netw. Secur. (CNS), Oct. 2017, pp. 1–9.
32. X. Chen, C. Liu, B. Li, K. Lu, and D. Song, ''Targeted backdoor attacks on deep learning systems using data poisoning,'' 2017, arXiv:1712.05526. [Online]. Available: http://arxiv.org/abs/1712.05526
33. C. Liao, H. Zhong, A. C. Squicciarini, S. Zhu, and D. J. Miller, ''Backdoor embedding in convolutional neural network models via invisible pertur-bation,'' 2018, arXiv:1808.10307. [Online]. Available: http://arxiv.org/abs/1808.10307 VOLUME 8, 2020 74739
34. A. Kurakin, I. J. Goodfellow, and S. Bengio, ''Adversarial examples in the physical world,'' in Proc. Int. Conf. Learn. Represent. (ICLR) Workshop, Feb. 2017, pp. 1–14.
35. N. Carlini and D. A. Wagner, ''Towards evaluating the robustness of neural networks,'' in Proc. IEEE Symp. Secur. Privacy (SP), May 2017, pp. 39–57.
36. N. Carlini and D. A. Wagner, ''Adversarial examples are not easily detected: Bypassing ten detection methods,'' in Proc. 10th ACM Workshop Artif. Intell. Secur. (AISec), 2017, pp. 3–14.
37. S. Moosavi-Dezfooli, A. Fawzi, O. Fawzi, and P. Frossard, ''Universal adversarial perturbations,'' in Proc. IEEE Conf. Comput. Vis. Pattern Recognit. (CVPR), Jul. 2017, pp. 86–94.
38. K. Grosse, N. Papernot, P. Manoharan, M. Backes, and P. D. McDaniel, ''Adversarial examples for malware detection,'' in Proc. 22nd Eur. Symp. Res. Comput. Secur., Sep. 2017, pp. 62–79.
39. M. Sharif, S. Bhagavatula, L. Bauer, and M. K. Reiter, ''Accessorize to a crime: Real and stealthy attacks on State-of-the-Art face recognition,'' in Proc. ACM SIGSAC Conf. Comput. Commun. Secur. CCS, 2016, pp. 1528–1540.

40. K. Eykholt, I. Evtimov, E. Fernandes, B. Li, A. Rahmati, C. Xiao, A. Prakash, T. Kohno, and D. Song, ‘‘Robust physical-world attacks on deep learning visual classification,’’ in Proc. IEEE/CVF Conf. Comput. Vis. Pattern Recognit., Jun. 2018, pp. 1625–1634.
41. A. Athalye, L. Engstrom, A. Ilyas, and K. Kwok, ‘‘Synthesizing robust adversarial examples,’’ in Proc. 35th Int. Conf. Mach. Learn., Jul. 2018, pp. 284–293

Artificial Intelligence based Electronic Warfare Systems: A Review

Kiran Garje[1]*
DLRL, DRDO,
Hyderabad, Telangana, 500060
kiran.kumar.dlrl@gov.in

ABSTRACT

Electronic Warfare is one of the most important aspects of modern era Wars. Control of the spectrum, attack on adversary or obstruct the enemy assault using Electromagnetic spectrum are some of functions achieved as part of this warfare. Upcoming trends in AI indicate that, evolving EW technology will have a revolutionizing influence on Armed Forces. AI based algorithms can be very productive in various fields of EW viz. signal processing for recognition and classification of targets, revelation of Jammers and its characteristics for evolving suitable anti-jamming algorithms as well as satellite signal monitoring and interception. Autonomous operation of EW systems can also be realized using AI based approach. This paper gives an insight on different aspects of EW, the usage of AI in EW systems and different techniques that have been incorporated in conventional and Satellite based systems.

Keywords: *Electronic Warfare, Satellite Communication, Artificial Intelligence, Learning*

I. INTRODUCTION

Current-era Armed Forces rely on various developing technologies for effective usages of EW spectrum to get the edge over adversaries. EW system helps in monitoring and securing the RF spectrum to gather the intelligence and nullify the enemy targets electronically. In spite of having vast improvement in war fighting capability because of deployment of EW systems, Armed forces continue to face hurdles in optimal resources management and effective decision support. AI based system are expected to narrow the gap between expected war-fighting capability and existing skills.

AI based system for EW applications are being considered for tactical deployment. Essential reasons for AI being used in EW applications are management and analysis of huge data, decision support, situational awareness, visualization of conflict zones/threats, and counter measures based on approximate responses. This paper describes various traits of EW, it's building blocks, and relevant technologies of current EW systems, as well as AI usage for decision making in war zones.

II. ELECTRONIC WARFARE

EW is basically use of RF spectrum to intercept, identify, analyse, monitor and deceive/neutralize adversary's electronic systems while protecting own assets upon such attacks. These technologies are mainly targeted for communication systems and RADARs which are extensively being used by Armed Forces. Three major areas come under EW viz. Electronic Support (ES), Attack (EA) and Protection (EP). ES techniques are targeted for monitoring, intercepting, and analysing possible adversaries. Similarly, EA based techniques are mainly focussed on Deception/Jamming to protect against DoS attack for EW spectrum within our territory whereas EP techniques are emphasized on protecting own assets while using RF spectrum whereas. Overall EW system architecture which includes functions such as ES, EA & EP is shown in Fig 1.

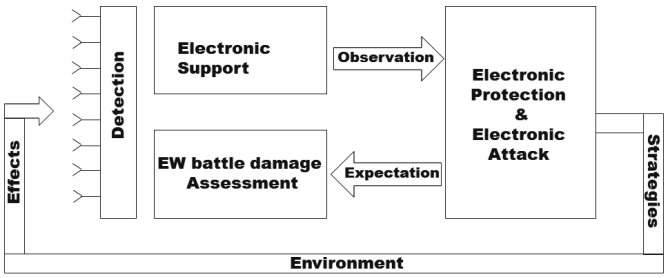

Figure 1: Functions of EW in System Architecture [1]

[1] Corresponding author: E-mail: kiran.kumar.dlrl@gov.in

A. Problems faced by existing EW Systems

1. Typically, systems operate over BW of at least 2-3 octaves. It may perform RADAR, EW Radiometric and communication functions necessary for survival of a platform at assigned frequency. Many EW systems have issues such as multiband antenna, multiplexors, LNAs, transmitters, which are required to operate over targeted broad BW (typically multi-band).
2. Problems related to a system that performs a wide range of EW functions when threat vary dynamically and prime power available is limited.
3. The requirement may arise due to exercise of Jammers in spatial and frequency domain simultaneously.
4. Modern day SDRs & cognitive RADARs employ dynamism which poses a challenge for characterization.
5. Complex target parameter estimation such as classification, intra-pulse analysis, decoding, processing of real-time data streams etc.
6. In communication systems, Several challenges are being faced by designers in satellite communication area although it provides better coverage and quality of communication. Typically, LEO satellites have bare minimum on-board resources and travel fast because of low altitude bring intense dynamics to network access which demand suitable handoff management between satellites.
7. Various other issues of EW systems based on satellite communication also need to be focussed such as Multi-Input-Multi-Output (MIMO) system [2], Network of Remote Things [3], Inter-Satellite Communication [4], Quality of Service [5] and Physical Space Security [6] etc.

B. Role of AI in EW Systems

EW applications fall in two major types of groups/categories viz. strategic level and tactical for various operations of War. The strategic level application of AI consists of functions such as order of wars/battles, assignment to Armed Forces, War Strategy and decisions, scale and escalation of War, intelligence gathering, information interpretation, scope and nature of battle, deployment of Armed Forces and Assets. The Tactical level applications of AI consists of aspects related to short-term objectives, immediate planning, removing immediate uncertainties and preparation for War etc.

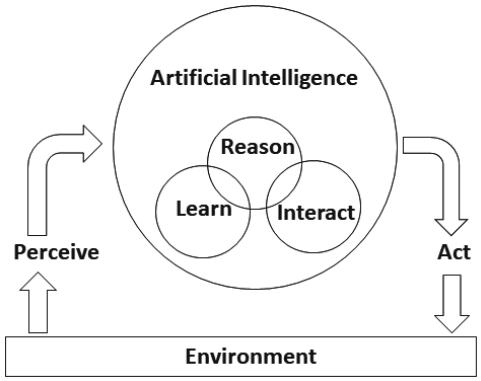

Figure 2: AI perspective EW Systems [1]

Usage of AI in EW systems is responsible for paradigm shift in utilization and protection of EM spectrum. AI based approach is main driving force to make EW systems more effective and autonomous [7]. Because of huge requirement to automate the EW systems, AI techniques are being explored to get value addition along with basic EW capabilities such as assistance in decision making, analysis of big data, simultaneous processing and identification of multiple targets and graphical simulations for war-games etc. Also, AI is useful in Threat analysis, intelligence gathering and logistic support. AI perspective of EW system is shown in Fig 2. EW system perceives threat using AI to learn, reason and interact with EM Environment and formulate the counter measures.

Various aspects of EW systems which includes Pre-Mission, ES, EA & EP as well as Electronic Battle Management and Data Management are shown in Fig. 3. The add-on AI functions such as mission planning, resource allocation, decision assistance, characterization, classification, data fusion, intent recognition, scheduling and coordination play complementary role in enhancing the overall capabilities of EW systems

C. AI Model Selection

AI consist of various sub-fields; each in-turn may have multiple approaches. The learning in AI technique can be supervised, unsupervised or reinforcement based. It can be deeper or shallow learning. Typically, with common notion it is presumed that deep learning is superior to shallow learning, which is actually the case except computer vision problem. The DL techniques demand higher computational resources and huge dataset which are not always present. Moreover, supervised learning is a better approach when complete labelled dataset is present. However, this may not be possible always since data can be costly, challenging, unavailable or even may be extremely difficult to get. Different work functions of AI useful for EW capabilities are listed in Table 1.

Table 1: AI Functions in EW world [1]

Sl. No.	AI Term	EW term
1	Situational Assessment	Electronic Support (ES)
2	Decision Making	Electronic Protection and Attack (ES & EP) Electronic Battle Management (EBM)
3	Executive Monitoring	Electronic Battle Damage Assessment (EBDA) Effects analysis
4	Learning	EW Reprogramming (Data & Software)

Similarly, it is easy for unsupervised learning/RL based algorithm to find hidden pattern in non-labelled data. Hence, unsupervised learning is a good technique to extract the information from given dataset, whereas reinforced learning is better for decision making jobs. Therefore, the AI algorithm should be chosen based on characteristics of problem, amount and quality of data, computational resources and time limitations etc.

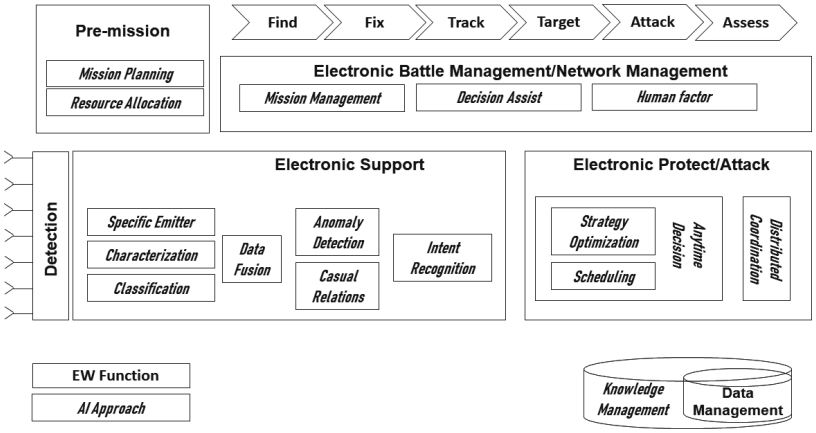

Figure 3: AI perspective EW Systems [1]

AI system needs to be trained on datasets for effective outputs. Typically, Artificial Neural Network (ANN) based systems require huge data to train the algorithm sothat effective weights are adjusted to meet the requirements. Similarly, self-learning algorithms keep adapting to the new environment and adjust weights continuously.

D. AI based EW system at Strategic level

1. Surveillance, Intelligence, and Reconnaissance (ISR) capability is extremely important to get multi-domain situational awareness with available data. AI can analyse huge data in real time to give better perspective for dynamic War situation. Additionally, AI can assist the operator in making the decision to analyse, identify and attack the target with best resource management.

ISBN - 978-93-95038-50-8

2. AI is useful in formulating War strategies, battlefield simulation and train Armed Forces to War-games, and improve navigation system for effective target acquisition, tracking, identification and validation.
3. AI steered exploration, mapping and systematic hacking of enemy computer network to collect information for War tactics.

E. AI based EW system at Tactical level

1. AI in Unmanned Air/Underwater Vehicles: AI enhanced navigation system helps to find the target path for UAV, Underwater Unmanned Vehicle in enemy territory. AI powered Vehicles/Drones may carryout advanced war tactics and adapt to enemy war strategies to exploit on field opportunities.
2. AI based systems for collection, interpretation and analysis: Various information as a part of military war is gathered from different systems such as electronics intelligence, signal intelligence, and communication intelligence etc. Data collected from these systems need careful scrutiny and analysis to conclude the relevant interpretations.

III. Review of AI applications

A) AI for EW perspective usages

Different AI techniques are being used in EW systems such as Convolutional Neural Network (CNN), Deep Learning and Neuro-computing etc., which helps in acquisition of surrounding acquaintance.

a. AI is very much useful in automatic detection and classification of modulation for RADAR EW, Communication EW and Data Processing & Analysis. AI algorithms such as SVM and Bayesian are discussed in [8] to extract various attributes of monitored signal using Time and Frequency analysis, DFT and Autocorrelation. Anti-Jamming method against Intelligent Jamming using Reinforcement Learning based AI technique has been discussed in [9].
b. A scheme based on Deep Learning has been proposed for selection of antenna for Cognitive RADAR systems [10]. Identification of Jammers and determination of attack characteristics are presented in [11]. The Jammer being used for software defined radio is identified using Deep CNN and Deep RNN techniques.
c. A novel AI based algorithm using probability moment and approximate Entropy is being used for RADAR signal classification [12].
d. Typically, ESM receivers need to process huge amount of real time data, hence a compressive sensing (CS) technique can be employed to reduce computational cost. Various algorithms such as Artificial Neural Network (ANN), Decision Tree (DT), Naïve Bayes (NB) [13], are used for classification of 5 different antenna scan types. Compressive Sensing based ESM receivers need a handful of compressively obtained data to detect and locate the targets.
e. A ESM Receiver system has been discussed in [13] to evaluate Doppler angels of enemy targets whose details are not known using Sparse Bayesian Learning (SBL) algorithm. A novel approach to carry out Cyber Electronic Warfare (CEW) tasks for target identification using Deep Reinforced Learning has been discussed in [14]. The approach briefly discusses about mitigation techniques for spatial sparsity, obstructive, partly obstructive surroundings and continuous actions required for cognitive/self-learning EW systems.
f. Channel Modelling, and remote sensing application make use of Support Vector Regression.
g. Channel modelling, Satellite Telemetry, Network Traffic Prediction, Interference Management and Remote Sensing make use of Decision Tree based AI technique.
h. Remote Sensing, Channel modelling, Inter-Satellite Hand-off Management, Unknown Signal Detection and Identification using CNN.
i. Satellite Telemetry, Anti-Jamming, Satellite Hand-off Management use RNN based AI algorithm.
j. Auto-Encoder based AI Technique has been used for Signal Interference Management.
k. Anti-Jamming, Satellite Beam Hopping, Interference Management and Energy Management may use Reinforcement Learning.

B) AI for Satellite Communication perspective usages

AI is being used extensively for satellite-based systems for various functions such as Beam Hopping, Anti-Jamming, Network Traffic Prediction, Channel Modelling and Carrier Signal Detection.

i. Beam Hopping*:* The resources at satellite are scarce and expensive, hence need optimal resource usage and time sharing. Traditional satellites system has multi beam configuration and there may be mismatch in resources

available and demand at any given time, since there may be uniform distribution of resources across each beam. So, high demand spot beam may have higher waiting period to complete the communication. Similarly, for better utilization of multi-beam communication satellite system, flexible resource allocation based on demand needs to be employed for better service to larger coverage area. It has been observed that, Beam Hopping is an effective technique to cater non-uniform and volatile traffic request at any given time [15,16]. In this technique satellite highlights (activates) few narrow beams within a broad regional beam based on traffic demand. The narrow spot beams are selected in time variant manner to cater the traffic requirements. Hence the critical tasks in such system are to select the narrow beam dynamically and amount of time till the beam remains activated.

A generic AI based approach on Genetic Algorithm has been proposed by Angeletti et al [17] for selection of beam in BH system. It has also shown that BH scheme reduce the number of Transponder transmission amplifiers for Terabits/sec speed satellites. An iterative technique with combination of BH scheme and spectrum assignment to optimally use offered network capability under the traffic demand and power limitations [18].

Hu et al [19] has proposed DRL based approach to optimally use system throughput with different transmission delay in a multi-beam satellite system using on Markov Decision Process (MDP) model. This approach makes use of long-term accumulation reward optimization and has shown the reduction in transmission delay by 52.2%. Similarly, it has increased the system throughput by 11.4% compared to conventional algorithms. A novel approach which is combination of optimization and end-to-end learning for best selection in Beam Hopping system using fully connected Neural Network has been employed [51]. The self-learning pre-trained algorithm has been used to estimate feature vectors to select useful data in a large search space.

ii. Anti-Jamming: Satellites utilized in military communication system need to be reliable and secure. Hence, anti-jamming capabilities are necessary. Various types of attacks are possible which may limit or disrupt the communication entirely. Considering this, frequency hopping, and spread spectrum technique are frequently being used in satellite based tactical communication systems [20,21]. Bae et al [23] used Frequency Hopped Frequency Division Multiple Access using hop-dehop transponder. Conventional anti-jamming techniques cannot counter intelligent jamming techniques based on self-correcting attack methodology which monitor the enemy signals and continue learning. In this context, [24,25] proposed self-adjusting, Smart Jammer to vary the jamming power and channel number. Lec et al [26] used a long term-short term Memory Network based on Reinforced Neural Network (RNN) to learn the time domain aspects of the signal. A reduction in overall synchronization time in FH-FDMA situation has been demonstrated in [26].

A novel approach using RL in mobile communication terminals can work seamlessly without need to know about jamming or model for radio channel in the dynamically changing scenario [27]. A learning technique to counter smart Jamming using space based anti-jamming approach for Internet of Satellites (IoS) application has been demonstrated by Han et al[28]. He has also combined Reinforced Learning and Game Theory algorithm to demonstrate the usage of Deep Learning to deal with huge decision space generated by virtue of dynamics of IoS as well as interplay between satellites and Intelligent Jamming surrounding.

iii. Network Traffic Prediction: Predicting traffic in a network is a pre-emptive approach to ensure reliable and good quality communication. Various aspects of satellite communication such as Traffic Congestion Control, Dynamic Channel Allocation and Management, Dynamic Routing Control, Network Planning and Security can be managed effectively using such predictions [29]. Many of scholars have predicted network traffic for satellite and terrestrial networks using various technique such as Auto-Regressive Moving Average (ARMA) [30]. Neural Network based approach has been proposed by Katris and Daskalaki [31], whereas a combination on Neural Network with differential evolution has been used by Pan et al [32] for internet traffic prediction. A least square SVM technique using classification and Regression analysis has been used for prediction [33]. Similarly, Liu and Li [34] have used principle component analysis to get smaller set of input dimensions using Regression Neural Network and achieve better accuracy in prediction with reduced training period. Distributed routing for LEO satellites has been discussed by Na et al [35] to predict the traffic in the network. Another researcher [36] used Extreme Machine Learning to predict the traffic congestion before routing.

iv. Channel Modelling: It is a mathematical illustration of communication channel behaviour used for wireless signal propagation, which is usually the impulse response represented in Time/Frequency domain. Typically, a channel has various impediments such as noise, interference and path loss along with shadowing etc.

True real channel models are essential to evaluate and understand the performance of communication system considering various vulnerabilities for reliable operation. These models may be useful to predict the signal propagation which would be useful in pre-deployment phase and to best utilize the coverage and channel capacity. A stochastic model [37] has been used for wireless communication to estimate channel parameters.

Researchers have used Machine Learning approaches such as SVM [38,39], Neural network [40] & Decision Tree [41] to predict path-loss for given media.

Ates et al [42] used Deep CNN algorithm to estimate channel parameters and variance in shadowing to get the path loss exponent. Thrane et al [43] used Deep Learning model on satellite photographs along with other parameters to predict Reference Signal Received Power (RSRP) at specific locations. Additionally, Ahmadien et al [44] proposed Deep Learning approach to predict the path loss using satellites' 2D images having generalized data.

v. Carrier Signal Detection: Typically, in wireless communication signal is processed by means of modulation, encoding and encryption etc. to optimally use the channel BW. Each of the above-mentioned function need to be performed over signal to extract the plain message. Algorithm to detect carrier signal based on Threshold values which require human mediation has been proposed by [45]. Another researcher Kim et al [47] discussed the use of slope tracing-based approach to investigate signal based on various parameters such as amplitude, signal slope, deflection width and distance between consecutive deflections.

Morozov and Ovchinnikov [48] made use of fully connected Neural Network for detection of carrier signal. Similarly Yuan el al[49] used Deep Learning algorithm to differentiate signal blind detection in wideband. A fully Convolutional Network based model has been proposed by Huang et al[50] to identify the signal in broadband power spectrum.

IV. CONCLUSION

Current era Armed Forces need systems that use highly robust and adaptable EW systems with feedback to adjust rapidly against EM surrounding because of innovation in digital technology. EW systems based on AI are very much important considering above scenario. Automation of EW systems have become possibility with use of AI which may improve situational awareness and make decision making more trustworthy. Considering this, an AI based EW system may become more effective in recognizing the enemy radar & communication emitters so as to investigate the lethality of the threat and use suitable counter strategy to destroy the hostile EW threat. The usage of AI has shown huge improvements in various EW and satellite communication systems such as RADAR operation in multi threat scenario, Threat classification, ESM, Anti-Jamming, and Radio design etc.

The paper gives a brief assessment of EW's fundamental aspects, problems faced by current systems and the importance of AI techniques in modern EW including satellite systems. Future work in EW should focus on application of AI to accomplish more efficient, secure, trustworthy, and better-quality communication systems.

REFERENCES

1. [1] Cognitive EW: An AI Approach by Haigh and Andrusenko [Artech House 2021].
2. [2] P. D. Arapoglou, K. Liolis, M. Bertinelli, A.Panagopoulos, P. Cottis, and R. De Gaudenzi, "MIMO over satellite: A review", *IEEE Communication Survey Tutorials*, vol. 13, no. 1, pp. 27–51, 2011.
3. [3] M. De Sanctis, E. Cianca, G. Araniti, I. Bisio, and R. Prasad, "Satellite communications supporting internet of remote things", *IEEE Int. Things J.* , vol. 3, no. 1,pp. 113–123, 2016.
4. [4] R. Radhakrishnan, W. W. Edmonson, F. Afghah, R. M.Rodriguez-Osorio, F. Pinto, and S. C. Burleigh, "Survey of inter-satellite communication for small satellite systems: Physical layer to network layer view", *IEEE Communication Survey Tutorials*, vol. 18, no. 4, pp. 2442–2473, 2016.
5. [5] C. Niephaus, M. Kretschmer, and G. Ghinea, "QoS provisioning in converged satellite and terrestrial networks: A survey of the state-of-the-art", *IEEE Communication Survey Tutorials*, vol. 18, no. 4, pp. 2415–2441, 2016.
6. [6] B. Li, Z. S. Fei, C. Q. Zhou, and Y. Zhang, Physical layer security in space information networks: A survey, IEEE Int. Things J., vol. 7, no. 1, pp. 33–52, 2020.
7. [7] J. R. Allen and G. Massolo, "The Global Race for Technological Superiority-Discover the Security Implications", Milan, Italy: Ledizioni, 2019.
8. [8] F. Wang, S. Huang, H. Wang, and C. Yang, "Automatic modulation classification exploiting hybrid machine learning network," Math. Problems Eng., vol. 2018, pp. 1_14, Dec. 2018, doi: 10.1155/2018/6152010.

9. [9] Y. Li, X. Wang, D. Liu, Q. Guo, X. Liu, J. Zhang, and Y. Xu, "On the performance of deep reinforcement learning-based anti-jamming method confronting intelligent jammer,"Appl. Sci., vol. 9, no. 7, pp. 3161_3176, 2019.
10. [10] A. M. Elbir, K. V. Mishra, and Y. C. Eldar, "Cognitive radar antenna selection via deep learning," 2018, arXiv:1802.09736. [Online]. Available: http://arxiv.org/abs/1802.09736.
11. [11] S. Gecgel, C. Goztepe, and G. K. Kurt, "Jammer detection based on artificial neural networks: A measurement study", in Proc. ACM Workshop Wireless Secur. Mach. Learn. (WiseML), 2019, pp. 43_48.
12. [12] C. M. Jeong, Y. G. Jung, and S. J. Lee, "Neural network-based radar signal classification system using probability moment and ApEn," Soft Comput., vol. 22, no. 13, pp. 4205_4219, Jul. 2018.
13. [13] S. Salari, I.-M. Kim, F. Chan, and S. Rajan, "Blind compressive-sensing- based electronic warfare receiver," IEEE Trans. Aerosp. Electron. Syst., vol. 53, no. 4, pp. 2014_2030, Aug. 2017.
14. [14] S. You, M. Diao, and L. Gao, "Deep reinforcement learning for tar- get searching in cognitive electronic warfare," IEEE Access, vol. 7, pp. 37432_37447, 2019, doi: 10.1109/ACCESS.2019.2905649.
15. [15] M. Á. Vázquez, A. Pérez-Neira, D. Christopoulos, S. Chatzinotas, B. Ottersten, P.-D. Arapoglou, A. Ginesi, and G. Taricco, "Precoding in multibeam satellite communications: Present and future challenges", IEEE Wireless Communications, vol. 23, no. 6, pp. 88–95, 2016.
16. [16] A. Freedman, D. Rainish, and Y. Gat, "Beam hopping how to make it possible, in Proc. Ka and Broadband" Communication Conference, Bologna, Italy, 2015, p. 6.
17. [17] P. Angeletti, D. F. Prim, and R. Rinaldo, "Beam hopping in multi-beam broadband satellite systems: System performance and payload architecture analysis", 24th AIAA Int. Communications Satellite Systems Conf., San Diego, CA, USA, 2006, p. 5376.
18. [18] J. Lei and M. Á. Vázquez-Castro, "Multibeam satellite frequency/time duality study and capacity optimization", J. Communication Network, vol. 13, no. 5, pp. 472–480, 2011.
19. [19] X. Hu, S. J. Liu, Y. P. Wang, L. X. Xu, Y. C. Zhang, C. Wang, and W. D. Wang, "Deep reinforcement learning based beam hopping algorithm in multibeam satellite systems", IET Communication, vol. 13, no. 16, pp. 2485–2491, 2019.
20. [20] M. K. Simon, J. K. Omura, R. A. Scholtz, and B. K. Levitt, "Spread Spectrum Communications Handbook", Electronic Edition. New York, NY, USA: McGraw-Hill,2002.
21. [21] D. Torrieri, Principles of Spread-Spectrum Communication Systems. Berlin, Germany: Springer, 2015.
22. [23] S. Bae, S. Kim, and J. Kim, "Efficient frequency-hopping synchronization for satellite communications using dehop-rehop transponders", IEEE Trans. Aerosp. Electron. Syst., vol. 52, no. 1, pp. 261–274, 2016.
23. [24] F. Q. Yao, L. L. Jia, Y. M. Sun, Y. H. Xu, S. Feng, and Y. G. Zhu, "A hierarchical learning approach to anti-jamming channel selection strategies", Wirel. Netw., vol. 25, no. 1, pp. 201–213, 2019.
24. [25] L. Xiao, D. H. Jiang, D. J. Xu, H. Z. Zhu, Y. Y. Zhang, and H. V. Poor, "Two-dimensional antijamming mobile communication based on reinforcement learning," IEEE Trans. Veh. Technol., vol. 67, no. 10, pp. 9499–9512, 2018.
25. [26] S. Lee, S. Kim, M. Seo, and D. Har, "Synchronization of frequency hopping by LSTM network for satellite communication system," IEEE Communication Lett. , vol. 23, no. 11, pp. 2054–2058, 2019.
26. [27] L. Xiao, D. H. Jiang, D. J. Xu, H. Z. Zhu, Y. Y. Zhang,and H. V. Poor, "Two-dimensional antijamming mobile communication based on reinforcement learning," IEEE Trans. Veh. Technol., vol. 67, no. 10, pp. 9499–9512, 2018.
27. [28] C. Han, L. Y. Huo, X. H. Tong, H. C. Wang, and X. Liu, "Spatial anti-jamming scheme for internet of satellites based on the deep reinforcement learning and stackelberg game," IEEE Trans. Veh. Technol., vol. 69, no. 5, pp. 5331–5342, 2020.
28. [29] Y. X. Bie, L. Z. Wang, Y. Tian, and Z. Hu, "A combined forecasting model for satellite network self-similar traffic," IEEE Access, vol. 7, pp. 152004–152013, 2019.
29. [30] D. Yan and L. Y. Wang, "TPDR: Traffic prediction based dynamic routing for LEO&GEO satellite networks," 2015 IEEE 5th Int. Conference Electronics Information and Emergency Communication, Beijing, China, 2015, pp. 104–107.
30. [31] C. Katris and S. Daskalaki, "Comparing forecasting approaches for internet traffic," Expert Syst. Appl., vol. 42, no. 21, pp. 8172–8183, 2015.

31. [32] X. Q. Pan, W. S. Zhou, Y. Lu, and N. Sun, "Prediction of network traffic of smart cities based on DE-BP neural network," IEEE Access, vol. 7, pp. 55807–55816, 2019.
32. [33] J. X. Liu and Z. H. Jia, "Telecommunication traffic prediction based on improved LSSVM", Int. J. Pattern Recognition Artificial Intelligence, vol. 32, no. 3, p. 1850007, 2018.
33. [34] Z. L. Liu and X. Li, "Short-term traffic forecasting based on principal component analysis and a generalized regression neural network for satellite networks," J. China Univ. Posts Telecommunication, vol. 25, no. 1, pp. 15–28, 36, 2018.
34. [35] Z. Na, Z. Pan, X. Liu, Z. A. Deng, Z. H. Gao, and Q. Guo, "Distributed routing strategy based on machine learning for LEO satellite network," Wireless Communication Mobile Comput., vol. 2018, p. 3026405, 2018.
35. [36] G. B. Huang, Q. Y. Zhu, and C. K. Siew, "Extreme learning machine: a new learning scheme of feedforward neural networks," 2004 IEEE Int. Joint Conf. Neural Networks (IEEE Cat. No.04CH37541), Budapest, Hungary, 2004, pp. 985–990.
36. [37] C. X. Wang, J. Bian, J. Sun, W. S. Zhang, and M. G. Zhang, "A survey of 5G channel measurements and models," IEEE Communication Survey Tutorials, vol. 20, no. 4, pp. 3142–3168, 2018.
37. [38] M. Piacentini and F. Rinaldi, "Path loss prediction in urban environment using learning machines and dimensionality reduction techniques," Comput. Manag. Sci., vol. 8, no. 4, pp. 371–385, 2011.
38. [39] M. Uccellari, F. Facchini, M. Sola, E. Sirignano, G. M. Vitetta, A. Barbieri, and S. Tondelli, "On the use of support vector machines for the prediction of propagation losses in smart metering systems," 2016 IEEE 26th Int. Workshop on Machine Learning for Signal Processing (MLSP), Vietri sul Mare, Italy, 2016, pp. 1–6.
39. [40] S. P. Sotiroudis, S. K. Goudos, K. A. Gotsis, K. Siakavara, and J. N. Sahalos, "Application of a composite differential evolution algorithm in optimal neural network design for propagation path-loss prediction in mobile communication systems," IEEE Antennas Wirel. Propag. Lett., vol. 12, pp. 364–367, 2013.
40. [41] C. A. Oroza, Z. R. Zhang, T. Watteyne, and S. D. Glaser, "A machine-learning-based connectivity model for complex terrain large-scale low-power wireless deployments," IEEE Trans. Cogn. Commun. Netw., vol. 3, no. 4, pp. 576–584, 2017.
41. [42] H. F. Ates, S. M. Hashir, T. Baykas, and B. K. Gunturk, "Path loss exponent and shadowing factor prediction from satellite images using deep learning," IEEE Access, vol. 7, pp. 101366–101375, 2019.
42. [43] J. Thrane, D. Zibar, and H. L. Christiansen, "Model-aided deep learning method for path loss prediction in mobile communication systems at 2.6 GHz," IEEE Access, vol. 8, pp. 7925–7936, 2020.
43. [44] O. Ahmadien, H. F. Ates, T. Baykas, and B. K. Gunturk, "Predicting path loss distribution of an area from satellite images using deep learning," IEEE Access, vol. 8, pp. 64982–64991, 2020.
44. [45] P. Henttu and S. Aromaa, "Consecutive mean excision algorithm," IEEE 7th Int. Symposium Spread Spectrum Techniques and Applications, Prague, Czech Republic, 2002, pp. 450–454.
45. [46] J. Kim, M. Kim, I. Won, S. Yang, K. Lee, and W. Huh, "A biomedical signal segmentation algorithm for event detection based on slope tracing," 2009 Annual Int. Conf. IEEE Engineering in Medicine and Biology Society, Minneapolis, USA, 2009, pp. 1889–1892.
46. [47] K. R. Chowdhary, "Natural language processing, in Fundamentals of Artificial Intelligence," K. R. Chowdhary, ed. Springer, 2020, pp. 603–649.
47. [48] O. Morozov and P. Ovchinnikov, "Neural network detection of MSK signals," 2009 IEEE 13th Digital Signal Processing Workshop and 5th IEEE Signal Processing Education Workshop, Marco Island, FL, USA, 2009, pp. 594–596.
48. [49] T. Yairi, T. Tagawa, and N. Takata, "Telemetry monitoring by dimensionality reduction and learning hidden Markov model," presented at Int. Symp. Artificial Intelligence, Robotics and Automation in Space, Turin, Italy, 2012.
49. [50] H. Huang, J. Q. Li, J. Wang, and H. Wang, "FCN-based carrier signal detection in broadband power spectrum," IEEE Access, vol. 8, pp. 113042–113051, 2020.
50. [51] L. Lei, E. Lagunas, Y. X. Yuan, M. G. Kibria, S. Chatzinotas, and B. Ottersten, "Beam illumination pattern design in satellite networks: Learning and optimization for efficient beam hopping," IEEE Access, vol. 8,pp. 136655‑136667, 2020.

Efficient Biometric Service Protocol for Cloud Services

SwathiGowroju*, S. Sai Satyanarayana Reddy[2], V. Swathi[3], R. Srinija[4],
P. Rishika[5], K Naveen Reddy[6]

1Associate Professor, Sreyas Institute of Engineering and Technology
2Professor, Sreyas Institute of Engineering and Technology
3,4,5,6 Sreyas Institute of Engineering and Technology

Email: swathigowroju@sreyas.ac.in

ABSTRACT

Cloud services will be ones that can be accessed from a scattered cloud stockpiling worker rather than an on-site server. These measured systems are operated by an outsider and allow users online access to PC resources like systems administration or research. Cloud computing is used to store data on cloud workers and to distribute processing resources across the Internet. Due to the pooling of resources, security and data insurance have become a crucial area of concern in cloud computing. Cloud service providers use server farms that are affected by information spillage to store and keep customer data. It has been noted that several techniques have prioritised data protection while ignoring privacy in the execution. Authentication helps to safeguard and confirm a recipient's identity. We also offer a practical method for creating a session key between two interacting parties that makes use of two biometric models for secure message delivery. Finally, thorough tests and a comparison analysis were used to determine the validity and usefulness of the suggested remedy. Index Terms: Session key, cloud service access, biometric-based security, and authentication.

Keywords: *Bio-Metrics, Fingerprint, Authentication, Cloud*

1. INTRODUCTION

In current world, cloud services are typical. However, providing safe access to cloud services is not a simple effort, and establishing reliable authentication, authorization, and access accounting is a never-ending problem, both operationally and from a research standpoint. In the literature, a variety of authentication methods have been put forth, including ones based on Kerberos, OAuth, and OpenID technologies. These protocols often aim to create a secure delegated access mechanism between two communicative entities linked in a distributed system. These guidelines are predicated on the fundamental premise that the distant server a trustworthy network entity is in charge of authentication. In particular, a user must first register with a distant server. This is required to guarantee the owner's consent. When a user attempts to visit a server, the distant server verifies their identity. The server is also authenticated by the user and the user. Once if both checks are completed successfully, the user receives using a remote server to access the services.

The fact that the user's credentials are kept on the authentication server, where they can be stolen and (mis)used to obtain unauthorised access to numerous services, is a major drawback of the current authentication techniques. Additionally, present techniques often employ symmetric key cryptography, which necessitates the sharing of a number of cryptographic keys throughout the authentication process, to ensure safe and quick communication. The authentication protocols are burdened by this tactic. The flaws found in the published protocols [1-11] are evidence that designing secure and effective authentication protocols is difficult.

We thus aim to provide a reliable and effective authentication technique in this work. We'll start out by offering an alternative to the typical password-based authentication method.

ISBN - 978-93-95038-50-8 https://doi.org/10.37285/bsp.sasat2023.33

Corresponding author: Email: swathigowroju@sreyas.ac.in

Then, without using any shared or pre-loaded information, we show how to create secure communication between the parties participating in the authentication protocol.

According to the suggested method, a user's fingerprint image serves as a secret credential. We create a private key from the fingerprint picture, which is then used to covertly store the user's credentials in an authentication server database. In the authentication step, we take a fresh picture of the user's biometric fingerprint, create the private key, and then encrypt the biometric information as a query. The authentication server receives the biometric data that has been queried and compares it to the data that has been stored there. The user is now prepared to access his or her service from the chosen server after successfully completing the authentication process. Mutual authentication utilising a short-term session key has been suggested between the user and authentication server as well as between the user and service server in order to achieve secure access to the service server. We describe an efficient and reliable method to create the session key using two fingerprint data. For message authenticity purposes, a biometric-based message authenticator is also created.

The essential contributions and advantages of the proposed strategy are outlined below.

1. A practical method for sending a user's biometric information to an authentication server through unencrypted network channels is given.
2. We provide a method for creating an irreversible fingerprint image straight from a revocable private key. The private key and a direct representation of the user's biometric information don't need to be kept anywhere.
3. By eliminating the need for the user's credentials to be kept on the authentication server, we overcome the drawback of conventional techniques.
4. We provide a unique technique for creating session keys.
5. Each entity needs some preloaded information in a typical authentication system, which adds overhead.

2. LITERATURE REVIEW

For security reasons, it is necessary that neither the client nor the server understand anything about the database or the requested biometry and the results of the matching procedure. The proposed protocol by Barni et al. [1] uses homomorphic encryption as the primary cryptographic primitive and adopts a multi-party computing strategy. Finger code, a specific encoding of fingerprint pictures, is used to reduce protocol complexity as minimal as feasible. Our main solution is a generic identification protocol and it allows to select and report all the enrolled identities whose distance to the user's finger code is under a given threshold, in contrast to previous works on privacy-preserving biometric identification that concentrate on choosing the best matching identity in the database.

It is a difficult task to implement closest neighbor request over encrypted data in the cloud while safely resisting the collusion of cloud server and query consumers. CloudBI-II has recently been proposed by Evans et al. [2] to facilitate closest neighbor queries on encrypted cloud data and is advertised as secure even when cloud servers conspire with certain untrusted query consumers. In this research, we suggest an effective attack strategy that predicts Cloud BI-II will expose the collusion attack's difference routes. The process of searching a pre-established biometric database for a matching record for an inquiring

ISBN - 978-93-95038-50-8

biometric attribute obtained from an unknown subject of interest is known as biometric identification (BI). Cloud computing, which offers many conveniences but also raises new privacy problems, has lately helped with this. Wang et al. [3] recently introduced two cloud-aided BI strategies that aim to protect privacy in ESORICS '15. In order to expose the security flaws in these two systems, we suggest various intricately designed attacks in this work. Theoretical analysis is provided to support our suggested assaults, and it shows that using such attacks, the cloud server may precisely deduce the external database and the identification request.

Furthermore, we demonstrate how the difference vector disclosure will lead to a major privacy violation and achieve a successful attack strategy to undermine CloudBI-II. That is, CloudBI-II is unable to provide the security that was promised. The proposed strategy can quickly retrieve the original data from the encrypted data set in CloudBI-II proposed by Zhu et al. [4] through theoretical analysis and laboratory assessment. Finally, we offer an improved system that effectively counters the collusion attack.

A password-based user authentication system for wireless networks of sensors was created by Jiang et al. [7] (WSNs). This kind of authentication uses both a smart card and a password, making it a two-factor method. An authorized user registers or reregisters with the trusted gateway node during the user signup process (GW N). The appropriate credentials are subsequently saved on a smart card that the GW N then provides. Additionally, all of the deployed sensor nodes register with the GW N using a secure channel and receive their corresponding secret credentials. During the login and verification phases, the GW N assists a genuine user in authenticating with a chosen sensor node using the pre-loaded credentials.

Other user authenticated based consensus strategies were put out by Turkanovic et al. [8]. However, the system developed by Turkanovic et al. [8] is vulnerable to assaults such as contactless payment theft, guessing offline login credentials, user impersonating, offline identification guessing, and sensor network impersonation [6]. A smart card-based user identification system that protects user privacy and employs hashing operations for biometric verification was created by Park et al. [9]. The plan, however, is vulnerable to denial-of-service (DoS) assaults [10].

A biometric-based user verified key agreement system was created by Pan et al. [5] for safe access to services offered by Internet of Things (IoT) devices. Despite using lightweight operations, this technique is not immune to DoS assaults since it employs the perceptual hashing (bio hashing) procedure rather than the fuzzy extractor used by [12]. This is largely due to the fact that the bio hashing approach seldom ever generates a particular feature BH(BIOi) from the physiological biometric BIOUi of an authorized user Ui at various input times, despite the fact that it may minimise output error [12]. There were several biometric applications developed by Gowroju et al. [16-21] that deals with security related applications efficiently using pupil of the person.

We may access shared configurable resources like memory, network, servers, services, and apps using the cloud-based solution instantly, conveniently, and from any place. Due to the numerous advantages that cloud platforms provide, many businesses are transferring and integrating their identity verification management systems there. Compared to on-premises biometric solutions, cloud biometrics are simpler to implement. Cloud-based biometrics solutions may be quickly integrated with any current online or desktop application via API integration.

ISBN - 978-93-95038-50-8

4. RESEARCH METHODOLOGY

We provide a reliable and privacy-preserving biometric identification system that can withstand a cloud and user-launched collusion assault. Our primary contributions, namely, may be summed up as follows: We analyses the biometric identification system and demonstrate its shortcomings and security flaws when exposed to the suggested level-3 attack. In particular, we show that the attacker may decode all users' biometric features by collaborating with the cloud to obtain their secret keys. We introduce a brand-new, effective biometric identification system that protects user privacy. The extensive security study demonstrates that the suggested approach is capable of achieving the necessary level of privacy protection. In particular, our system can withstand the suggested attack and is secure under the biometric identification outsourcing model as shown in Figure 1.

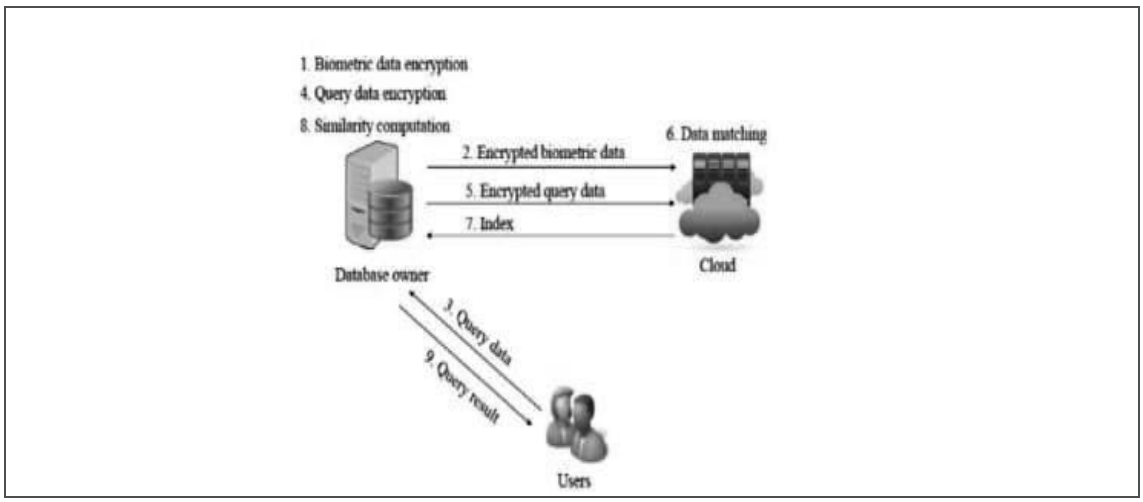

Figure 1: Architecture of Proposed system

In this study, we adhere to the widely used "Dolev-Yao (DY) threat model" [13]. The DY model allows an adversary, say A, to edit, remove, or even insert fake information into the messages as they are being sent. Communications exchanged while network elements are in communication. As a result, under the DY model, the network entities communicate with one another over a public channel. We also assume that while the authentication servers (AS) and resource servers (RS) are semi-trusted network entities, the clients are not. If low-entropy passwords are used in a password-based authentication scheme, password guessing attacks are possible. On the other hand, a brute-force attempt to guess biometric data in a biometric-based authentication method is computationally impossible. A, may, however, carry out further possible attacks, including replay, man-in-the-middle, privileged insider, denial-of-service, biometric data guessing, stolen smart card, and password guessing assaults (for password-based authentication schemes). Additionally, A has the ability to alter both stolen and previously stored biometric data.

When C receives a receive request, it first checks the received DB and remote DB to make sure the message is genuine. When the message is verified, C and remote server utilise session server for access to services. In this manner, C can use a service provided by RS. Figure. 2 depicts a summary of the messages sent and received during the user authentication phase of the proposed approach.

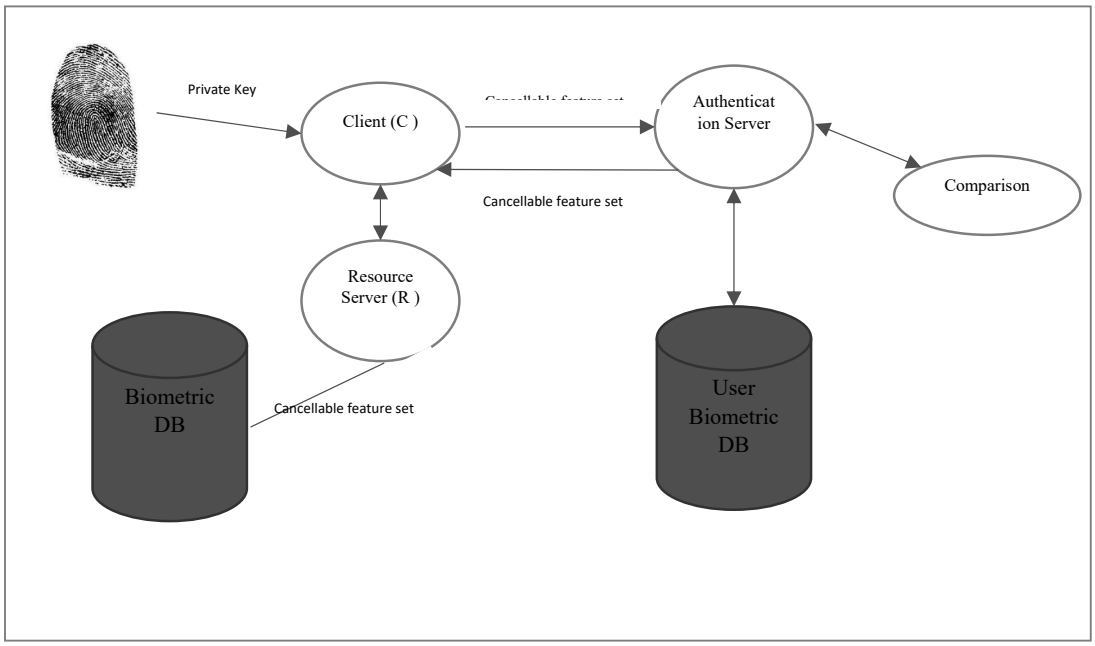

Figure 2: Authentication Mechanism

We extract every detail point from a user's fingerprint picture that has been taken. We initially align the fingerprint picture to improve feature extraction accuracy. We choose the consistent region from this fingerprint image that has been aligned. The fingerprint region, which has a high likelihood of appearing in any fingerprint picture that is recorded, can be described as the consistent region. To extract the minute points, we choose this constant region. We suggest using a horizontal segment to pick a group of minute points from the consistent region. A tiny portion of the consistent region, which has the most minute points, is represented by the horizontal segment. We choose these little details to create a codeword from the convolution coding's Trellis diagram.

This codeword shall be known as BioCode can then be used to create a private key, abbreviated Keyc. as Keyr is a random number, and Keyc = H(BioCode ⋈ Keyr) H is an application-generated standard hash produced by C. function and./ (for instance, Secure Hash Algorithm (SHA-1) [14]). is a one-way transformation of the two input parameters. It is much simpler to calculate in the forward direction, but not in a reverse fashion. Another option is SHA-256. [14] to make the suggested method very secure.

Proposed system uses publicly available dataset from [15]. A biometric fingerprint database called Sokoto Coventry Fingerprint Dataset (SOCOFing) was created with academic research in mind. 6,000 fingerprint photos from 600 African people make up SOCOFing, which also includes synthetically changed copies with three distinct levels of alteration for obliteration, central rotation, and z-cut. SOCOFing also includes labels for gender, hand, and finger names. The sample images from the dataset are shown in Table 1.

ISBN - 978-93-95038-50-8

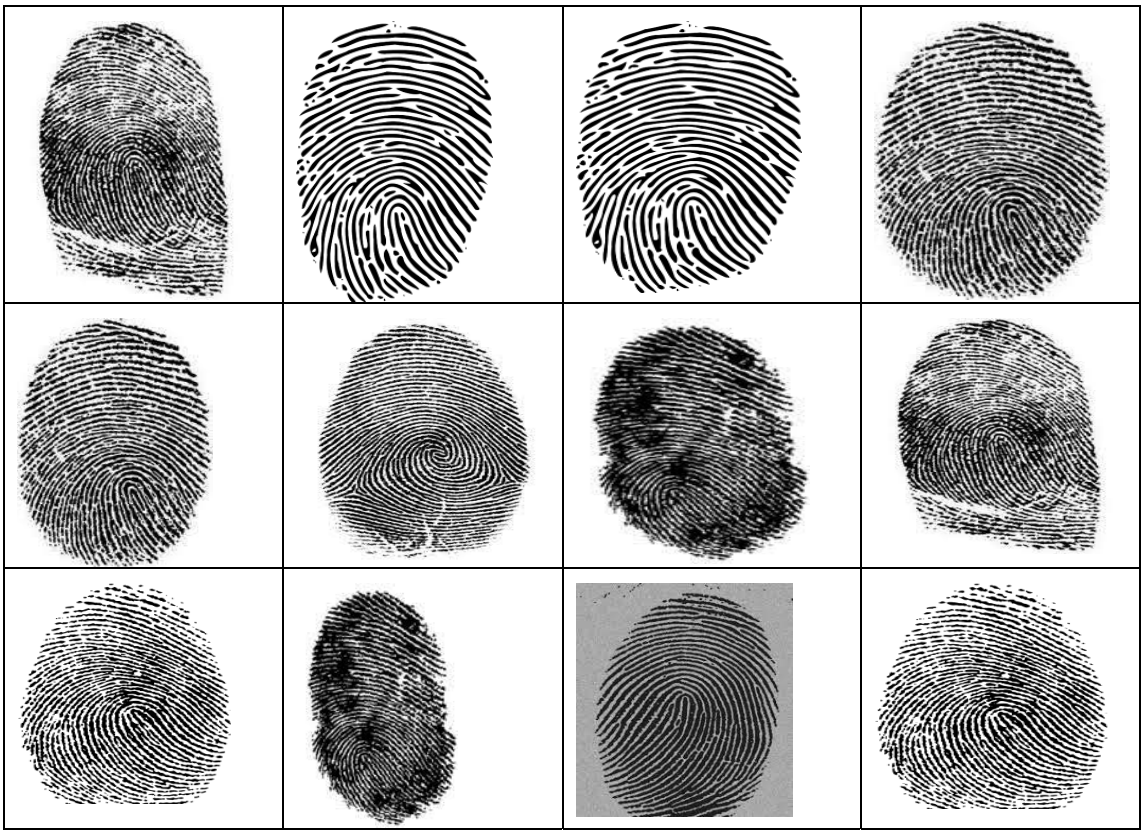

5. RESULTS AND DISCUSSIONS

In the proposed approach, we consider a fingerprint image of a user as a secret credential. From the fingerprint image, we generate a private key that is used to enroll the user's credential secretly in the database of an authentication server. Before registering into the application, it runs the PreCalcu procedure, and both C and AS have their current session keys, say K. C then does the following. The application of C records a fresh fingerprint picture of C, let's say Ireg. From Ireg, we take minutiae points and create minutiae pairs. We initially partition Ireg into a number of little square blocks in order to produce a pair of minutiae points (Figure.3). We go around each block in Ireg, creating pairs of minutiae points by taking into account that each minutiae point belongs to each block and that all minutiae points belong to its eight linked neighboring blocks. By moving through each block one at a time, we may create pairs of minute points. We determine the Euclidean lengths and angles of each of the obtained straight lines. Figure: shows the home page of authentication server.

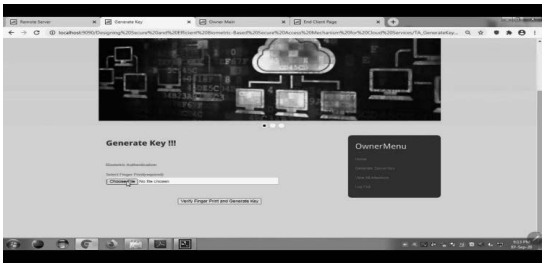

Figure 3: Authentication Server

In the authentication phase, we capture a new biometric fingerprint image of the user, and subsequently generate the private key and encrypt the biometric data as a query. This queried biometric data is then transmitted to the authentication server for matching with the stored data as shown in Figure 4. Once the user is authenticated successfully, he/she is ready to access his/her service from the desired server.

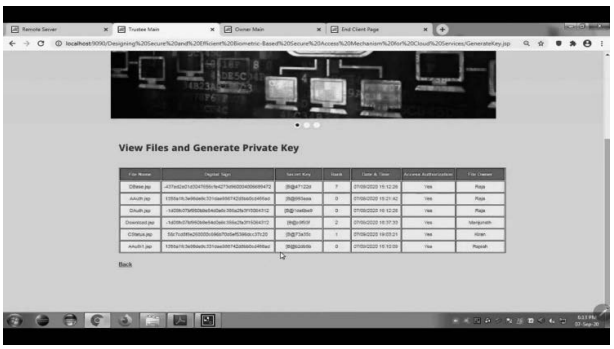

Figure 4: Generated key for individual user

To obtain secure access authentication mutually, between the user and authentication server, and also between the user and service server have been proposed using a session key as shown in Figure: 5. Using two fingerprint data, we present a fast and robust approach to generate the session key. First, we will be visiting the home page of the designing secure and efficient biometric based secure access. In this page we will be having cloud, owner, and user. In the home page when we click on the owner. This is the owner login page and we can login in to it by using password and username. If the owner is new, he /she can register by clicking on register as shown in Figure 6. once the owner is logged in, he/she will be asked for biometric finger print.

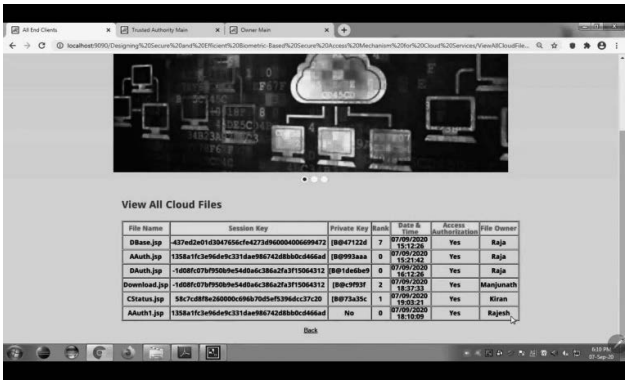

Figure 5: Access authentication of individual user

This is the owner main page where we can upload the images. In the upload images we need enter the title that we are going to upload and biometric image name that going to upload and you can add the biometric description to that image if needed. This is the user page where we can upload the images. In the upload images we need enter the title that we are going to upload and biometric image name that going to upload and you can add the biometric description to that image if needed. We need to put the biometric fingerprint to

login. This is the user main page as shown in Figure: 7 where we need to enter the keyword to search what the owner had uploaded.

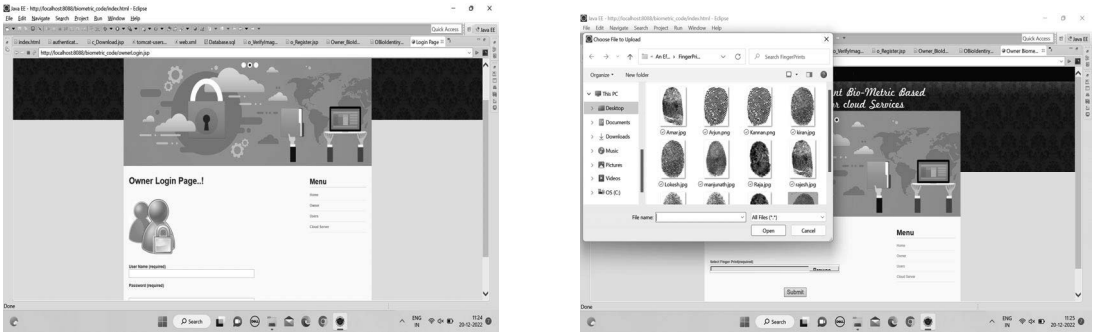

Figure 6: Login page and process of uploading finger print

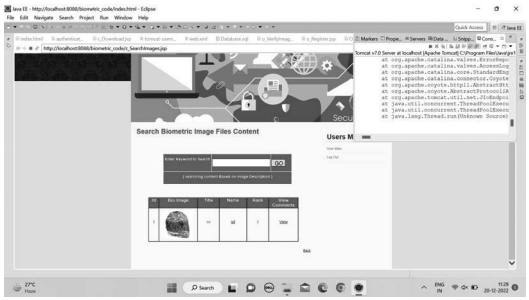

Figure 7: View of user

We create minutiae pairings by taking into account a core point and each minutiae point that is a part of the eight blocks that surround the identified core point (Figure. 3(b)). In a similar manner, we choose each minute point from the eight linked blocks that surround the block where the delta point is discovered (Figure. 8). We determine the Euclidean distances and angles for each pair produced using the core point and delta point. The delta point on a friction ridge is the location at or closest to the point of divergence of two type lines and is regarded to be a pattern of a fingerprint in biometrics and fingerprint scanning. when we tap on the name we will be getting to enter the file name and then we need to generate a private key. So that we can download the content that has been sent by owner.

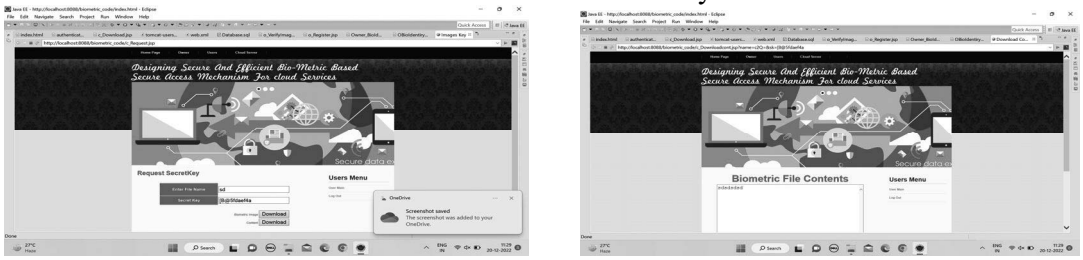

Figure 8: Biometric content viewer

This cloud server page. We just need to login. There is no need to register. It analyses owners list, users list, etc. These are the contents of the cloud server. Cloud can also see the

owner bio image files in the cloud services. Cloud can view owner and user as shown in Figure: 9.

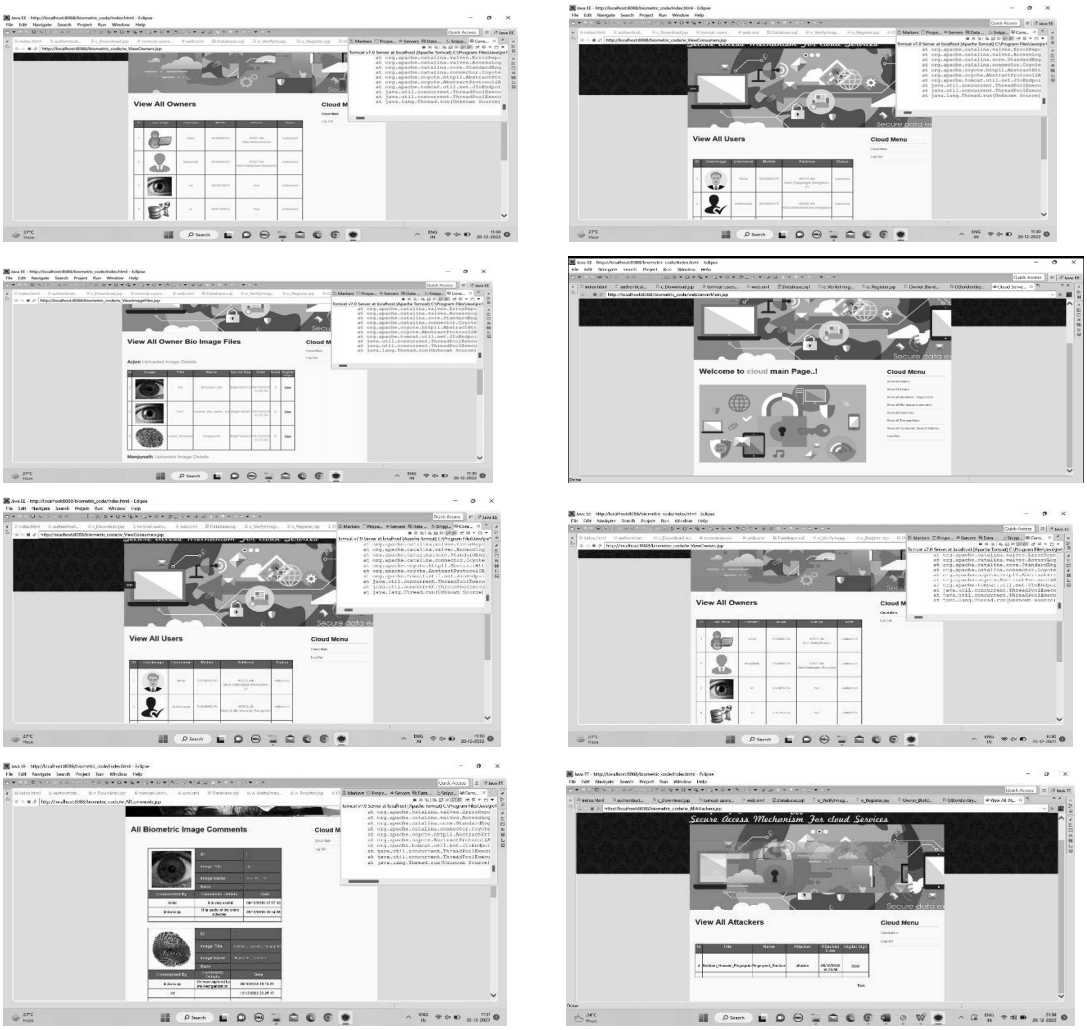

Figure 9: Cloud view of existing users

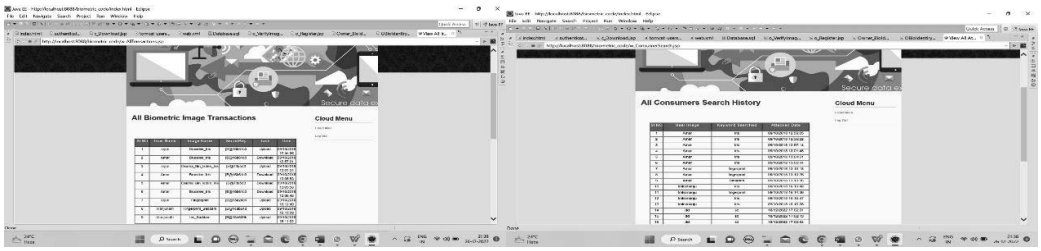

Figure 10: Admin view of the proposed system

If an adversary A has the biometric data of a legitimate user, may they utilise it to get secret information. This is due to the tampering attacks against stolen and stored biometric information (i.e., session key). A privileged-insider attack occurs when a trusted user acts as a privileged insider within the company to steal a registered user's secret credentials during registration, then makes an effort to utilise those stolen credentials. In the replay attack, A

tries to record the communications that are sent and then deceive another legal entity by using the information again when the two parties are communicating as shown in Figure:10.

A might try to update, edit, or delete the message contents that were sent to the receivers under the man-in-the-middle attack by listening in on communications between the entities.

If an attacker A with a stolen or lost smart card belonging to a registered user can extract all the credentials from its memory using power analysis techniques [14], they will next try to determine the user's secret credentials. An event that prevents a system or network from carrying out its anticipated functionality, such as resource depletion, is referred to as a denial-of-service (DoS) assault. In an impersonation attack, the adversary pretends to be the sender so that the receiver thinks the communication has come from a trustworthy source. If a password-based system is employed, adversary A could utilise eavesdropped communications, data kept in the system, and/or a user's smart device to attempt to guess a lawful user's password as shown in Figure: 11 (in either an online or offline mode).

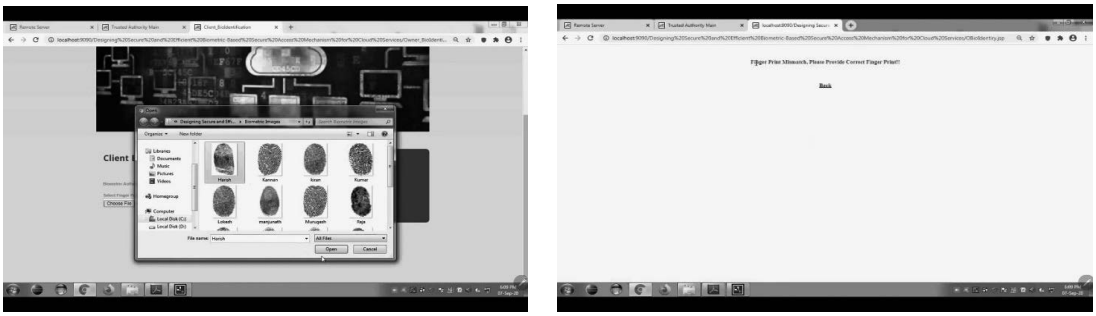

Figure 11: Attacker view of the proposed system

It has been found that the proposed system offers improved security for the biometric template maintained on the server, as well as user-generated private keys. Additionally, in contrast to current technology. It does not require a password or smart card for authentication techniques. The proposed system offers validity and strength for practical deployment in real-world applications as a consequence.

6. CONCLUSIONS

The growing use of biometrics demonstrates that it offers distinct benefits over traditional password and token-based security systems (e.g., on Android and iOS devices). In this research, we present an authentication method based on biometrics for users attempting to access services and computing resources from a distance. Our suggested method makes it feasible to build a private key from a fingerprint biometric reveal since it is able to do so with 95.12% accuracy. There is no need to communicate any prior information when utilizing the session key creation method, we suggest using two biometric data. Our strategy is more resistant to various known attacks when compared to other authentication methods of a similar nature.

ACKNOWLEDGEMENTS

This guideline and template are modified and tailored for SASAT-2023.

REFERENCES

1. Barni, Mauro, Tiziano Bianchi, Dario Catalano, Mario Di Raimondo, Ruggero Donida Labati, Pierluigi Failla, Dario Fiore et al. "Privacy-preserving fingercode authentication." In *Proceedings of the 12th ACM workshop on Multimedia and security*, pp. 231-240. 2010.
2. Evans, David, Yan Huang, Jonathan Katz, and Lior Malka. "Efficient privacy-preserving biometric identification." In *Proceedings of the 17th conference Network and Distributed System Security Symposium, NDSS*, vol. 68, pp. 90-98. 2011.
3. Wang, Lizhe, Jie Tao, Marcel Kunze, Alvaro Canales Castellanos, David Kramer, and Wolfgang Karl. "Scientific cloud computing: Early definition and experience." In *2008 10th ieee international conference on high performance computing and communications*, pp. 825-830. Ieee, 2008.
4. Zhu, Youwen, Yue Zhang, Xingxin Li, Hongyang Yan, and Jing Li. "Improved collusion-resisting secure nearest neighbor query over encrypted data in cloud." *Concurrency and Computation: Practice and Experience* 31, no. 21 (2019): e4681.
5. Pan, Shiran, Shen Yan, and Wen-Tao Zhu. "Security analysis on privacy-preserving cloud aided biometric identification schemes." In *Australasian Conference on Information Security and Privacy*, pp. 446-453. Springer, Cham, 2016.
6. W. E. Burr, D. F. Dodson, E. M. Newton, R. A. Perlner, W. T. Polk, S. Gupta, and E. A. Nabbus, "NIST Special Publication 800- 63-2: Electronic Authentication Guideline," 2013, National Institute of Standards and Technology (NIST), U.S. Department of Commerce. Accessed on July 2019.
7. Q. Jiang, J. Ma, X. Lu, and Y. Tian, "An efficient two-factor user authentication scheme with unlinkability for wireless sensor networks," Peer-to-Peer Networking and Applications, vol. 8, no. 6, pp. 1070–1081, 2015.
8. M. Turkanovic, B. Brumen, and M. Holbl, "A novel user authentication and key agreement scheme for heterogeneous ad hoc wireless sensor networks, based on the internet of things notion," Ad Hoc Networks, vol. 20, pp. 96 – 112, 2014.
9. M. Park, H. Kim, and S. Lee, "Privacy Preserving Biometric-Based User Authentication Protocol Using Smart Cards," in *17th International Conference on Computational Science and Engineering*, Chengdu, China, 2014, pp. 1541–1544.
10. P. K. Dhillon and S. Kalra, "A lightweight biometrics based remote user authentication scheme for IoT services," *Journal of Information Security and Applications*, vol. 34, pp. 255 – 270, 2017.
11. M. Turkanovic and M. Holbl, "An improved dynamic password-based user authentication scheme for hierarchical wireless sensor networks," *Elektronika Ir Elektrotechnika*, vol. 19, no. 6, pp. 109 – 116, 2013
12. C.-C. Chang and N.-T. Nguyen, "An Untraceable Biometric-Based Multi-server Authenticated Key Agreement Protocol with Revocation," *Wireless Personal Communications*, vol. 90, no. 4, pp. 1695–1715, 2016.
13. D. Dolev and A. C. Yao, "On the security of public key protocols," *IEEE Transactions on Information Theory*, vol. 29, no. 2, pp. 198–208, 1983.
14. "Secure Hash Standard," FIPS PUB 180-1, National Institute of Standards and Technology (NIST), U.S. Department of Commerce, April 1995. http://nvlpubs.nist.gov/nistpubs/FIPS/NIST.FIPS.180-4.pdf. Accessed on January 2019.
15. Gowroju, Swathi, and Sandeep Kumar. "Robust Deep Learning Technique: U-Net Architecture for Pupil Segmentation." *In 2020 11th IEEE Annual Information Technology, Electronics and Mobile Communication Conference (IEMCON)*, pp. 0609-0613. IEEE, 2020.
16. Swathi, Aarti, and Sandeep Kumar. "A smart application to detect pupil for the small dataset with low illumination." *Innovations in Systems and Software Engineering* (2021): 1-15.
17. Swathi, Aarti, and Sandeep Kumar. "Review on Pupil Segmentation Using CNN-Region of Interest." In *Intelligent Communication and Automation Systems, pp. 157-168. CRC Press*, 2021.
18. Gowroju Swathi, Aarti and Sandeep Kumar. "Robust Pupil Segmentation using UNET and Morphological Image Processing." In 2021 *International Mobile, Intelligent, and Ubiquitous Computing Conference (MIUCC)*, pp. 105-109. IEEE, 2021.

19. Swathi, S. Kumar, V. S. T, S. Rani, A. Jain and R. K. M.V.N.M, "Emotion Classification using Feature Extraction of Facial Expression," 2022 2nd *International Conference on Technological Advancements in Computational Sciences* (ICTACS), 2022, pp. 283-288, doi: 10.1109/ICTACS56270.2022.9988544.
20. Swathi Gowroju, Sandeep Kumar, Aarti, Anshu Ghimire, "Deep Neural Network for Accurate Age Group Prediction through Pupil Using the Optimized UNet Model", *Mathematical Problems in Engineering*, vol. 2022, Article ID 7813701, 24 pages, 2022. https://doi.org/10.1155/2022/7813701

Transfer-learning Enhanced Physics Informed- Neural-Networks for Burgers' Equation with High Reynolds' Number

Nishant Kumar[1*], Manish Kr. Tiwari[2*], P.S Gurugubelli[1],

Anil Kumar[2], M. Raghavendra Rao[2]

[1]Birla Institute of Technology & Science, Pilani, Hyderabad
[2]Advanced Systems Laboratory, DRDO, Hyderabad

ABSTRACT

We have attempted to solve Burgers' equation with Physics Informed Neural Networks (PINNs) using transfer learning to address the difficulties in solving the equation with high Reynolds number, that is, low values of kinematic viscosity. The obtained solutions are compared with benchmark results from classical numerical methods, and it is found that they are in close agreement. PINNs are also shown to accurately model physical behaviour at low viscosities Transfer learning is shown to be a great enhancement, particularly for low values of viscosity.

Keywords: *Burger's Equation, PINN, Transfer Learning, Reynolds Number*

1. INTRODUCTION

Partial Differential Equations (PDEs) and Ordinary Differential Equations (ODEs) have gained large popularity, due both to their mathematical and practical significance. Some of the most important PDEs that describe physical phenomena include the Navier-Stokes, the Euler's equations, the heat equation, and Schrodinger's equation. Because it is often difficult or impossible to obtain the analytic or exact solutions for these PDEs, there has been much interest in methods for obtaining numerical solutions. Finite difference methods, finite element analysis, finite volume analysis, and spectral methods are some of the schemes employed to obtain the solution of these problems.

Another group of powerful computational methods that have gained prominence over the past three decades are machine learning techniques. The field of deep learning has particularly taken off following the Deep Learning Revolution. However, these methods are data-driven, generally rendering them unsuitable for applications where obtaining data might be difficult or expensive.

There has only recently been a surge of interest at the intersections of PDEs and machine learning, especially with the advent of frameworks such as "Physics Informed Neural Networks". What is known as Scientific Machine Learning has gained prominence, and continued to expand developing frameworks such as Universal Differential Equations [1]. Many libraries for the same have also been developed, such as TensorDiffEq [2], DeepXDE [3], SciANN [4], and more. Apart from these, Julia has emerged as a prominent programming language for the implementations of these models as well as development of interfaces to facilitate such frameworks [5]. Physics Informed Neural Networks (or PINNs) were formally introduced by [6]. Although the idea of solving differential equations utilizing neural networks had originated much earlier [7], the interest in the subject was spurred by this work.

Despite significant interest in PINNs, and Burger's equation being a central benchmark in its research, there have not yet been any studies evaluating PINNs on some common set of

* Corresponding author: E-mail: nishantkumar490@gmail.com

problems widely used in the study of numerical methods. This would also entail evaluating the performance of PINNs at very low viscosities, which most numerical methods find difficult to capture and remains an active area of research. The following study hopes to contribute to that. In addition, it also provides great evidence of the usefulness of transfer learning in the context of PINNs.

The study is organised as follows. Section 2 details the methodology, including the architecture of PINNs, the structure of Burger's equation, and transfer learning. Section 3 summarises our results with a brief discussion. Section 4 concludes our paper, while Section 5 describes the challenges and future work.

2. METHODOLOGY

The fundamental idea of PINNs can be encapsulated by what is known as the "Universal Approximation Theorem". In various formulations, the theorem states that neural networks, of enough breadth and/or depth, are capable of arbitrarily approximating any real valued function [8] [9]. PINN utilizes the power of automatic differentiation, through the same technique that backpropagation is carried out, and approximates the hidden solution of a differential equation.

This is done through formulating the loss equation to reduce the residual of the Partial Differential Equation, along with the given Initial and Boundary Conditions of the problem. In formal terms, given the PDE:

$$f(x,t,u,u_x,u_t,\ldots,\lambda)=0 \quad x\ \epsilon\ \Omega,\ t\ \epsilon[0,T]$$

with the Initial Condition:

$$u(x,t_0)=g_0(x) \quad x\ \epsilon\ \Omega$$

and the Boundary Conditions:

$$u(x,t)\ =g_\Gamma(t) \quad x\ \epsilon\ \Gamma,\ t\ \epsilon\ [0,T]$$

The loss function can be formulated as

$$Loss\ =\ Loss_f + Loss_{BC} + Loss_{IC}$$

With the availability of data, an additional loss term for data can also be added.

PINNs have some distinct advantages over classical numerical methods. First, PINNs is a meshless method, and helps avoid the complex mesh generation involved in the classical computational methods. In addition to this, any available data from experimental or other computational sources can seamlessly be integrated into this framework. PINNs also provide a greater opportunity for exploring inverse or "ill posed" problems, as they can also be investigated using essentially the exact same framework.

Despite these perks, computational costs remain a major obstacle in the implementation of PINNs [10] [11]. One of the techniques whose power can be leveraged against this is transfer learning: transferring the knowledge of one task to other similar tasks. In this case, tackling various kinds of boundary conditions and parameters can be done through this technique. Despite many of the works highlighting the importance of transfer learning in this context [11], this area has been relatively underexplored in literature. We attempt to investigate the effects of transfer learning on the convergence of models with differing parameters and

ICs/BCs, taking into consideration a well-known benchmark of the PINNs: Burger's equation.

Burger's equation is a simplified form of the Navier-Stokes, without the pressure gradient term. The equation is as follows:

$$u_t + uu_x = \nu u_{xx} \tag{1}$$

where v is the kinematic viscosity.

The Burgers' equation has a wide range of applications, from modeling of turbulence to cosmology. It is especially useful for testing of numerical schemes [12]. Indeed, Burgers' equation has widely been used as a benchmark for PINN studies [6]. The analytic solution to this equation is available, and is given by the Hopf-Cole [13] transformation as follows:

$$u = -2\nu\frac{\theta_x}{\theta}$$

This transformation converts the original Burger's equation to a form of the heat equation. By separation of variables method, an analytic solution can be reached. For the boundary conditions,

$$\mathrm{u}(0,\mathrm{t}) = \mathrm{u}(1,\mathrm{t}) = 0$$

And the initial conditions,

$$\mathrm{u}(\mathrm{x},0) = \mathrm{f}(\mathrm{x})$$

The solution is given by,

$$u(x,t) = \frac{2\pi\nu\sum_{m=1}^{\infty} mA_m \sin(m\pi x)\exp(-m^2\pi^2 t\nu)}{A_0 + \sum_{m=1}^{\infty} A_m \cos(m\pi x)\exp(-m^2\pi^2 t\nu)} \tag{2}$$

Where,

$$A_m = 2\int_0^1 \cos(\mathrm{m}\pi\mathrm{x})\exp\{-\frac{1}{2\nu}\int_0^x f(x')\,\mathrm{d}x')\}\,dx$$

$$A_0 = \int_0^1 exp\left\{-\frac{1}{2\nu}\int_0^x f(x')dx'\right\}dx \tag{3}$$

Despite the availability of analytic solutions, for many problems especially for lower values of viscosity (i.e., higher Reynolds number) this infinite series does not converge well [14]. Hence, numerical methods are required to compute solutions. Many such schemes have been developed over the years. [15] present an explicit and exact-explicit finite difference method. A finite element method is provided by [16]. Galerkin methods remain popular for solving these kinds of problems [17]. Recently, wavelet-based solutions have also shown success in this regard [18] [19].

We propose PINN as another method for solving particularly challenging versions of the Burgers' equation. In this approach, we employ transfer learning as a critical technique to

enhance the capability of neural networks. Additionally, this helps evaluate the effectiveness of transfer learning methods in PINNs more generally, since Burgers' equation is an essential benchmark for any numerical computational technique.

Transfer learning is characterized by transferring knowledge across domains. Various techniques are used such as parameter sharing, feature-based strategy, model-based regularization, etc. [20]. Parameter sharing and fine tuning are well-regarded strategies in image processing and natural language processing tasks [21] [22]. In this method, parameters are initialized based on a benchmark network (eg. ImageNet) and the last few layers of the network are "fine-tuned" for a specific task, rather than building a network from scratch. This is based on the idea that the early layers of the network capture generalities, while the later layers get more specific.

In PINNs, these methods can be used for enhancing the learning of related sets of equations. The use of transfer learning can significantly boost the ability to solve problems with differing parameters, initial and boundary conditions.

There has been some research into the aspect of transfer learning in the context of PINNs. A key study was conducted by Desai et al, who trained networks on six families of differential equations: First order ODEs, Second-order ODEs, Coupled linear oscillators, Nonlinear oscillators, Poisson and Schrodinger's. They concluded that PINNs have the ability to learn from as few as three sets of parameters, and can then perform one-shot approximations of closely related sets of parameters with high accuracy.

Burgers' equation poses some unique problems. Modeling flows with lower levels of viscosity, or higher Reynolds number remains a challenge as this often results in formation of shock waves near boundary layers. There is also a well-established set of boundary conditions that are not as closely related as those considered by [23]. Transfer learning can thus provide a deeper advantage for these less viscous flows, whose solutions it is otherwise difficult to converge.

3. RESULTS AND DISCUSSION

We consider two problems with distinct boundary conditions for a few values of viscosity, and we train PINNs with a depth of 5 hidden layers, and a width of 20 neurons per layer based on the governing equations of these problems. We use Adam optimizer with a training rate of 5xE-4 for all the networks, but we may adjust the learning rate during training depending on the specific requirements. We compare the values with some classical numerical methods reported in various studies.

3.1. PROBLEM 1

We consider Equation (1) with the following boundary and initial conditions:

$$\begin{aligned} u(0,t) &= u(1,t) = 0, \qquad t > 0 \\ u(x,0) &= \sin(\pi x), \qquad 0 \le x \le 1 \end{aligned} \tag{4}$$

The solution from equation (3) becomes:

$$A_m = 2\int_0^1 \cos(m\pi x)\exp\left(\frac{1}{-2\pi\nu}(1-cos(m\pi x))\right)\mathrm{d}x$$

$$A_0 = \int_0^1 \exp\left(\frac{1}{-2\pi\nu}(1-cos(\pi x))\right)\mathrm{d}x \tag{5}$$

Table 1 Solution for Problem 1 at v=0.1 and v=0.01.

x	t	v=0.1				v=0.01			
		Ref. [16]	**Ref. [18]**	**Present**	**Exact**	**Ref. [16]**	**Ref. [18]**	**Present**	**Exact**
0.25	0.4	0.31429	0.30889	0.30866	0.30889	0.34244	0.34191	0.34191	0.34191
	0.6	0.24373	0.24075	0.24076	0.24074	0.26905	0.26896	0.26887	0.26896
	0.8	0.19758	0.19569	0.19586	0.19568	0.22145	0.22148	0.22141	0.22148
	1.0	0.16391	0.16258	0.16260	0.16256	0.18813	0.18820	0.18815	0.18819
0.5	0.4	0.57636	0.56963	0.56955	0.56963	0.67152	0.66069	0.66083	0.66071
	0.6	0.45169	0.44724	0.44711	0.44721	0.53406	0.52942	0.52948	0.52942
	0.8	0.36245	0.35927	0.35924	0.35924	0.44143	0.43914	0.43917	0.43194
	1.0	0.29437	0.29195	0.29191	0.29192	0.37568	0.37443	0.37447	0.27442
0.75	0.4	0.62592	0.62537	0.62552	0.62544	0.94675	0.91023	0.91019	0.91026
	0.6	0.49034	0.48718	0.48706	0.48721	0.78474	0.76723	0.76714	0.76724
	0.8	0.37713	0.37391	0.37389	0.37392	0.65659	0.64740	0.64751	0.64740
	1.0	0.29016	0.28747	0.28758	0.28747	0.56135	0.55606	0.55609	0.55605

The collocation points are taken from an equispaced 100x100 grid on the domain $0\leq x\leq 1$, $0\leq t\leq 1$. PINNs are trained for values v=0.1 and v=0.01.

The network trained with v=0.01 is then used for transfer learning of v=0.004. Only the last two layers are fine-tuned and the rest of the network is frozen. In the last few iterations, the model is "opened", i.e., all the weights are updated. This provides a heavy advantage in the convergence of the network as can be seen in Fig 1. Further, networks for viscosity values 0.001 and 0.0001 are also trained through this transfer-learning enhanced method.

ISBN - 978-93-95038-50-8

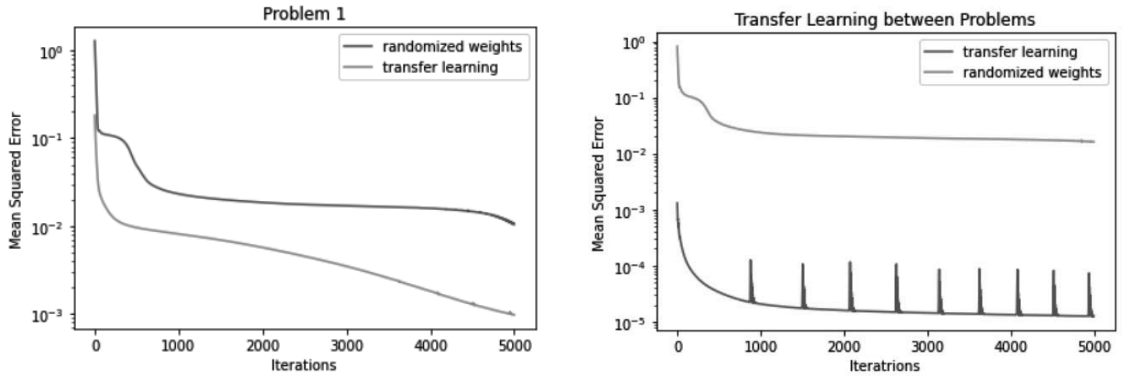

(a) (b)

Figure 1: Transfer learning. (a) shows transfer learning between two values of viscosity. Comparison of Problem 1 at v=0.004 between fine-tuning a pre-trained model on v=0.01 vs. training from randomly initialized weights. (b) shows transfer learning between Problem 1 and Problem 2 at v=0.004.

Table 2 Solution for Problem 1 and Problem 2 at v=0.004

x	t	PROBLEM 1			PROBLEM 2		
		Ref. [18]	Present	Exact	Ref. [18]	Present	Exact
0.25	1	0.18891	0.18936	0.18891	0.19640	0.19682	0.19641
	5	0.04696	0.04625	0.04697	0.04744	0.04671	0.04747
	10	0.02422	0.02414	0.02421	0.02434	0.02417	0.02434
	15	0.01632	0.01575	0.01631	0.01637	0.015503	0.01637
0.5	1	0.37598	0.37588	0.37596	0.38850	0.38849	0.038846
	5	0.09394	0.09369	0.09393	0.09491	0.09451	0.09491
	10	0.04843	0.04819	0.04843	0.04868	0.04822	0.04870
	15	0.03259	0.03234	0.03259	0.03271	0.03236	0.03270
0.75	1	0.55883	0.55848	0.55881	0.57320	0.57271	0.57315
	5	0.14089	0.14076	0.14089	0.14225	0.14205	0.14225
	10	0.07221	0.07161	0.07220	0.07258	0.071830	0.07257
	15	0.04678	0.04702	0.04677	0.04697	0.04719	0.04695

ISBN - 978-93-95038-50-8

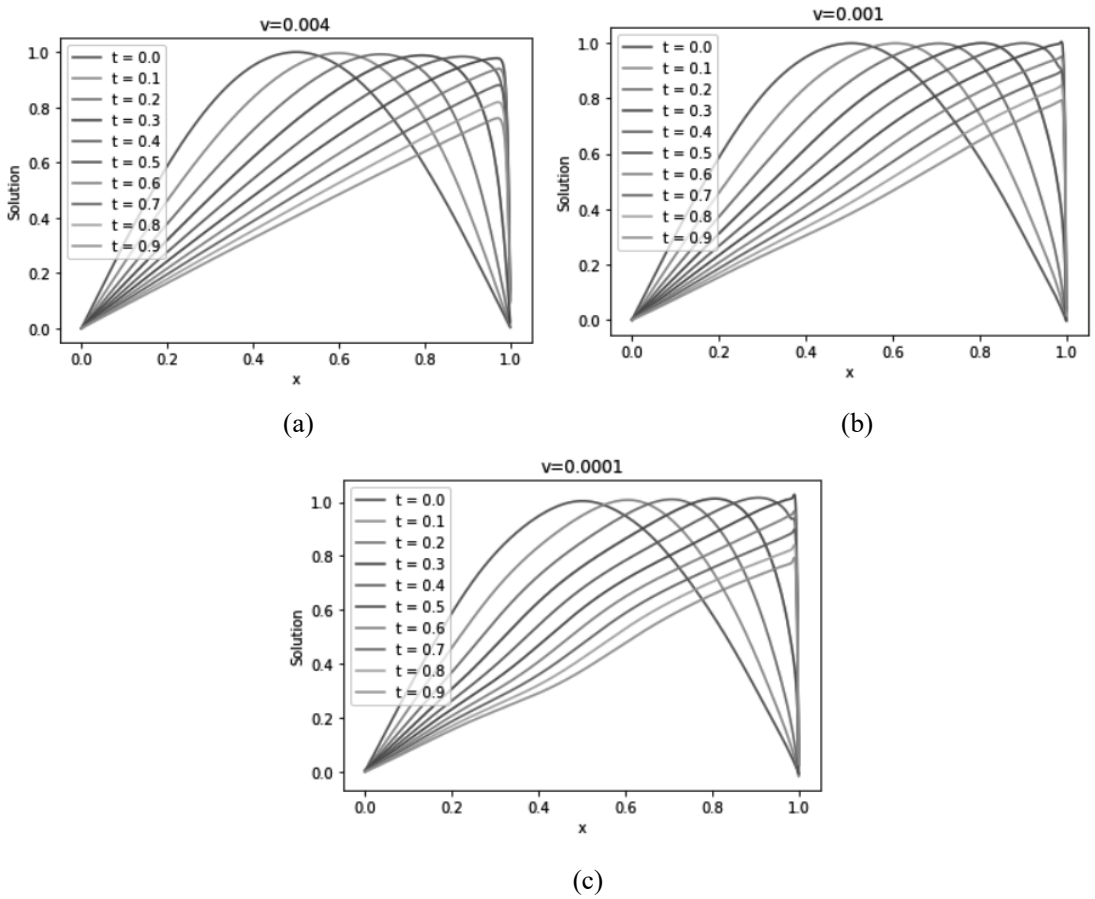

(a) (b)

(c)

Figure 2: Solutions for Problem 1 at different values of viscosity. PINNs have the ability to quite accurately model physical behaviour at high Reynolds numbers.

3.2. PROBLEM 2

We consider Equation (1) with the following boundary and initial conditions:

$$\begin{aligned} u(0,t) &= u(1,t) = 0, \qquad t > 0 \\ u(x,0) &= 4x(1-x), \qquad 0 \le x \le 1 \end{aligned} \tag{6}$$

The solution from equation (3) becomes:

$$A_m = 2\int_0^1 \cos(m\pi x)\exp\left(\frac{1}{-3\nu}\left(3x^2 - 2x^3\right)\right)\mathrm{d}x$$

$$A_0 = \int_0^1 \exp\left(\frac{1}{-3\nu}\left(3x^2 - 2x^3\right)\right)\mathrm{d}x \tag{7}$$

The collocation points are taken from an equispaced 100x100 grid on the domain 0≤x≤1, 0≤t≤1. PINNs from Problem 1 of equal viscosity are taken and trained with the governing equations. The comparison of the present method with exact solutions are as follows:

Table 3 Solution for Problem 2 at v=0.1 and v=0.01.

x	t	v=0.1				v=0.01		
		Ref. [16]	Ref. [18]	Present	Exact	Ref. [18]	Present	Exact
0.25	0.4	0.32679	0.31752	0.31740	0.31752	0.36225	0.36219	0.36226
	0.6	0.25117	0.24615	0.24620	0.24614	0.28204	0.28189	0.28204
	0.8	0.20270	0.19957	0.19963	0.19956	0.23045	0.23031	0.23045
	1.0	0.16780	0.16561	0.16552	0.16560	0.19469	0.19452	0.19469
0.5	0.4	0.59661	0.58454	0.58444	0.58454	0.68364	0.68380	0.68368
	0.6	0.46581	0.45800	0.45799	0.45798	0.54831	0.54835	0.54832
	0.8	0.37293	0.36744	0.36733	0.36740	0.45371	0.45372	0.45371
	1.0	0.30253	0.29838	0.29838	0.29834	0.38568	0.38570	0.38568
0.75	0.4	0.64680	0.64556	0.64564	0.64562	0.92044	0.92037	0.92050
	0.6	0.50852	0.50265	0.50263	0.50268	0.78297	0.78276	0.78299
	0.8	0.39117	0.38532	0.38533	0.38534	0.66272	0.66279	0.66272
	1.0	0.30066	0.29585	0.29583	0.29586	0.56932	0.56934	0.56932

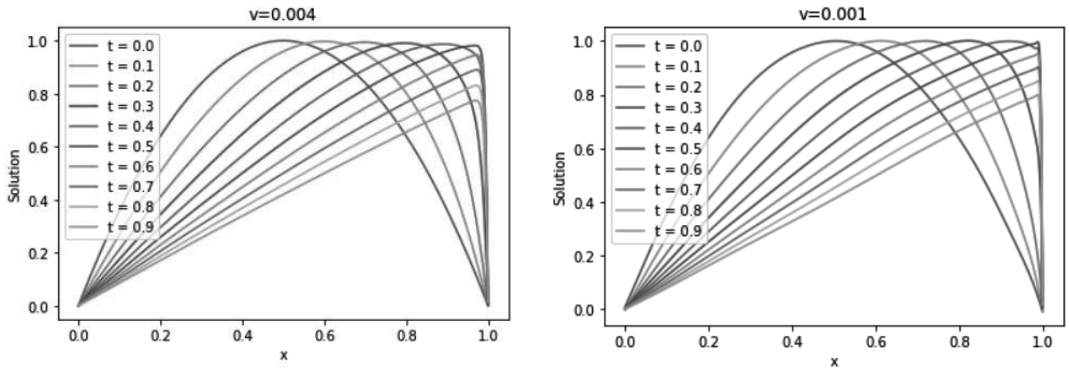

(a) (b)

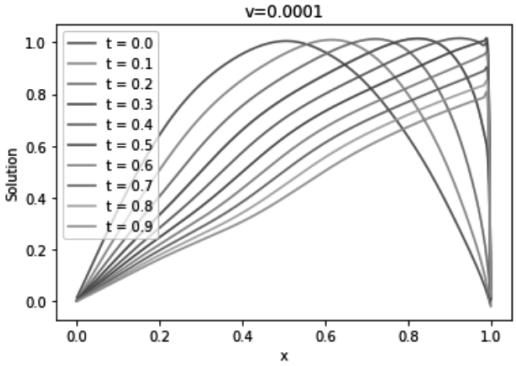

(c)

Figure 3 Solution for Problem 2 at different values of viscosity.

4. CONCLUSION

We investigate the ability of Physics Informed Neural Networks to approximate solution to Burgers' equation at lower values of viscosity, i.e., high Reynolds numbers. While PINNs can model higher viscosities with great accuracy, it encounters difficulties at lower viscosities. We attempt to overcome this problem by using transfer learning enhanced techniques. We have found that transfer learning and fine tuning are greatly advantageous to these problems. The PINNs are made to solve two problems and the results are compared to exact solutions and some benchmark data from classical numerical methods. The solution is found to be in agreement with them.

5. CHALLENGES AND FUTURE WORK

While PINNs have shown the capability of approximating solution for Burgers' equation for a large range of values of kinematic viscosity within the same framework, there are many challenges in this area. The accuracy, as well as computational cost, worsens for much lower values of viscosity. Some possible methods of mitigation can include weighing the loss functions. These could either be hyper parameters or self-adaptive weights. Sampling of collocation points is also an extremely important aspect and deserves attention on its own. The usual hyper parameter tuning can also greatly improve the performance of PINNs.

REFERENCES

1. Rackauckas, Christopher, et al. "Universal differential equations for scientific machine learning." arXiv preprint arXiv:2001.04385 (2020).
2. McClenny, Levi D., Mulugeta A. Haile, and Ulisses M. Braga-Neto. "TensorDiffEq: scalable multi-GPU forward and inverse solvers for physics informed neural networks." arXiv preprint arXiv:2103.16034 (2021).
3. Lu, Lu, et al. "DeepXDE: A deep learning library for solving differential equations." SIAM review 63.1 (2021): 208-228.
4. Haghighat, Ehsan, and Ruben Juanes. "SciANN: A Keras/TensorFlow wrapper for scientific computations and physics-informed deep learning using artificial neural networks." Computer Methods in Applied Mechanics and Engineering 373 (2021): 113552.

5. Ranocha, Hendrik, et al. "Adaptive numerical simulations with Trixi. jl: A case study of Julia for scientific computing." arXiv preprint arXiv:2108.06476 (2021).
6. Raissi, Maziar, Paris Perdikaris, and George E. Karniadakis. "Physics-informed neural networks: A deep learning framework for solving forward and inverse problems involving nonlinear partial differential equations." Journal of Computational physics 378 (2019): 686-707.
7. Lagaris, Isaac E., Aristidis Likas, and Dimitrios I. Fotiadis. "Artificial neural networks for solving ordinary and partial differential equations." IEEE transactions on neural networks 9.5 (1998): 987-1000.
8. Hornik, Kurt. "Approximation capabilities of multilayer feedforward networks." Neural networks 4.2 (1991): 251-257.
9. Kidger, Patrick, and Terry Lyons. "Universal approximation with deep narrow networks." Conference on learning theory. PMLR, 2020.
10. Chuang, Pi-Yueh, and Lorena A. Barba. "Experience report of physics-informed neural networks in fluid simulations: pitfalls and frustration." arXiv preprint arXiv:2205.14249 (2022).
11. Rezaei, Shahed, et al. "A mixed formulation for physics-informed neural networks as a potential solver for engineering problems in heterogeneous domains: comparison with finite element method." Computer Methods in Applied Mechanics and Engineering 401 (2022): 115616.
12. Bonkile, Mayur P., et al. "A systematic literature review of Burgers' equation with recent advances." Pramana 90 (2018): 1-21.
13. Cole, Julian D. "On a quasi-linear parabolic equation occurring in aerodynamics." Quarterly of applied mathematics 9.3 (1951): 225-236.
14. Zhang, D. S., et al. "Burgers' equation with high Reynolds number." Physics of Fluids 9.6 (1997): 1853-1855.
15. Kutluay, S. E. L. Ç. U. K., A. R. Bahadir, and A. Özdeş. "Numerical solution of one-dimensional Burgers equation: explicit and exact-explicit finite difference methods." Journal of computational and applied mathematics 103.2 (1999): 251-261.
16. Öziş, T., E. N. Aksan, and A. Özdeş. "A finite element approach for solution of Burgers' equation." *Applied Mathematics and Computation* 139.2-3 (2003): 417-428.
17. Soliman, A. A. "A Galerkin solution for Burgers' equation using cubic B-spline finite elements." *Abstract and Applied Analysis*. Vol. 2012. Hindawi, 2012.
18. Jiwari, Ram. "A hybrid numerical scheme for the numerical solution of the Burgers' equation." *Computer Physics Communications* 188 (2015): 59-67.
19. Liu, XiaoJing, et al. "Wavelet solutions of Burgers' equation with high Reynolds numbers." *Science China Technological Sciences* 57 (2014): 1285-1292.
20. Zhuang, Fuzhen, et al. "A comprehensive survey on transfer learning." *Proceedings of the IEEE* 109.1 (2020): 43-76.
21. Guo, Yunhui, et al. "Spottune: transfer learning through adaptive fine-tuning." *Proceedings of the IEEE/CVF conference on computer vision and pattern recognition*. 2019.
22. Houlsby, Neil, et al. "Parameter-efficient transfer learning for NLP." *International Conference on Machine Learning*. PMLR, 2019.
23. Desai, Shaan, et al. "One-shot transfer learning of physics-informed neural networks." *arXiv preprint arXiv:2110.11286* (2021).

Driver Drowsiness Monitoring System using Visual Behaviour and Machine Learning

Ambika Sahitya Batchu*[*], Madhuvani Patnam, Goutham Karnati

Electronics and Communication Engineering
Hyderabad, Telangana, 500039

abisahi2002@gmail.com, madhuvanikashyap@gmail.com, karnatigoutham26@gmail.com

ABSTRACT

One of the leading factors in traffic accidents and fatalities is drowsy driving. Hence, identifying driver weariness and related symptoms is a current research subject. The majority of traditional approaches are either vehicle-, behavior-, or physiological-based. Some approaches necessitate costly sensors and data processing, while others are obtrusive and distracting to the driver. The result of this work is the development of real-time, low-cost technology that can identify drowsy driving. A webcam records the video in the designed system, and utilizing image processing algorithms, the driver's face is recognized in each frame. Following the computation of the eye aspect ratio, mouth opening ratio, drowsiness is determined by adaptive thresholding based on the location of facial landmarks on the identified face. Moreover, offline implementations of machine learning algorithms have been made. Based on support vector machine classification, it was found that the sensitivity was 95.58% and the specificity was 100%.

Keywords: *drowsy driving, detection of drowsiness, eye aspect ratio, mouth opening ratio*

1. INTRODUCTION

One of the main factors contributing to fatalities in traffic accidents is drowsy driving. Long-distance bus drivers, nighttime bus drivers, and truck drivers who operate for extended periods of time are particularly prone to this issue. In every country, passengers' most frightening nightmare is a drowsy driver. Many people are hurt or killed in traffic accidents each year as a result of driver drowsiness. Thus, due to its enormous practical relevance, the detection of driver weariness and its indication are significant study areas. Three modules make up the fundamental sleepiness detection system: the acquisition system, the processing system, and the warning system. In this instance, the frontal face of the driver is collected on camera by the acquisition system and sent to the processing block for online analysis to identify tiredness. The alert system will give the driver a warning or alarm if drowsiness is detected.

Drowsy driving detection techniques are often divided into three categories: vehicle-based, behavioral-based, and physiological-based. In the vehicle-based approach, many variables, such as steering wheel movement, brake or accelerator pattern, vehicle speed, lateral acceleration, and lane position deviations, are continuously tracked. Driver drowsiness is deemed to exist when any abnormal change in these parameters is discovered. Due to the sensors' lack of attachment to the driver, this measurement is non-intrusive. With a behavioral-based method, drowsiness is identified by analyzing the driver's visual behaviour, such as eye blinking, eye closing, yawning, head bending, etc. Given that only a basic camera is needed to identify these traits, this assessment is also non-intrusive. The degree of sleepiness or weariness is determined by physiological signals such as heartbeat, pulse rate, Electrocardiogram (ECG), Electooculogram (EOG), and Electroencephalogram (EEG).

This measurement is intrusive since the driver will be distracted by the sensors that are attached to him or her. The cost and size of the system will increase as more sensors are used.

[*] Corresponding author: E-mail: abisahi2002@gmail.com,

Nonetheless, adding more parameters or features could improve the system's accuracy. These elements push us to create a low-cost, accurate real-time driver sleepiness detection system. So, in order to make the system portable and low-cost, we have presented a webcam-based system to identify driver weariness solely from the face image utilizing image processing and machine learning algorithms.

2. THE PROPOSED SYSTEM

In Fig.A block diagram of the driver drowsiness monitoring system is shown. The footage is initially captured with a webcam. To get a clear shot of the face of the driver, the camera will be placed in front of him or her. To create 2-D images, the video's frames are removed. Histogram of oriented gradients (HOG) and linear support vector machine (SVM) for object detection are used to identify faces in the frames. Face detection is followed by the marking of facial landmarks on the photos, such as the locations of the eyes, nose, and mouth. A determination of the driver's tiredness is made utilising machine learning and variables such as eye aspect ratio, mouth opening ratio, and head posture. These variables are measured from the driver's facial landmarks. In the event of drowsiness, a warning alarm will be sounded to warn the driver. Below, each block's specifics are described.

The development a non-intrusive system that can detect human fatigue and alert quickly is the idea of the project. Drivers who do not regularly stop on long distances are highly vulnerable to drowsiness, which they often do not recognize early enough. According to the research conducted by the expert, approximately one-quarter of all grave motorway accidents are attributed to sleep-paced drivers in need of rest. They can be prevented by taking the effort to get enough sleep before driving, drink coffee or energy drink, or have a rest when the signs of drowsiness occur. Complex approaches, such as EEG and ECG, are used to detect drowsiness popularly. This method is very accurate for measuring, but contact metering needs to be used, and driver fatigue and drowsiness monitor are subject to many restrictions. Therefore, driving in real-time is not comfortable. This document provides a method by measuring the eye closing rate and yawning for the detection of drowsiness signs among drivers.

This system monitors the driver's eyes with a camera, and we can detect driver fatigue symptoms early enough by developing an algorithm that avoids sleep. This project will therefore assist in detecting driver fatigue in advance and alarms and pop-up warning output. In addition, a warning is manually disabled instead of automatically.

A driving simulation system is driven by a participant in the video, and a webcam takes place in front of the driving system is designed for the identification of the face of the video image. The aim to use the face area so that eyes and mouth can be detected in the face area. Once the face is found, the eyes and the simulator. The video is recorded with the webcam to see the change from awake to sleepy.

The eye and mouth detection parameters are generated inside the face image. The video will be transformed into frames per second. The eyes and mouth can be located from there. Once the eyes have been located, the eyes are opened or closed by measuring the intensity changes in the eye area. If the eyes are found to be closed for 4 consecutive frames, the driver is confirmed to be drowsy.

ISBN - 978-93-95038-50-8

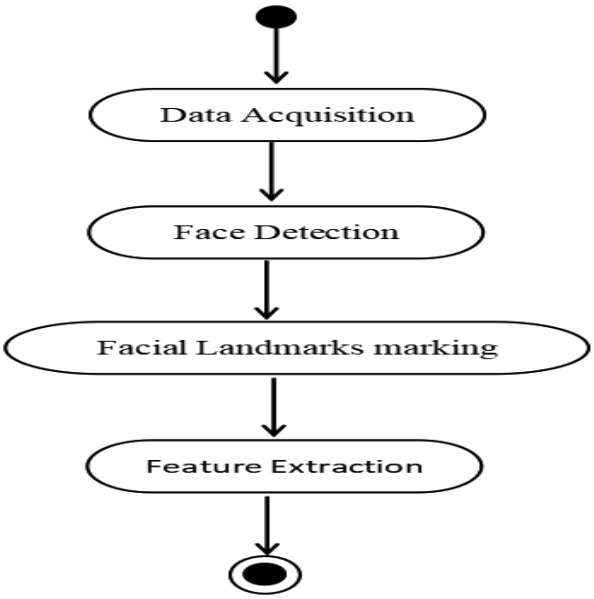

Figure 1: The block diagram of detection of drowsiness

A. DATA ACQUISITION

Sony CMU-BR300 camera is used to record the video, and a laptop is used to extract and process the individual frames. These 2D images are subjected to image processing methods after the frames have been extracted. At this time, artificial driver data has been produced. In order to participate in this experiment, participants are instructed to gaze at the webcam while yawning, sighing, and blinking occasionally. The video is recorded for thirty minutes.

B. FACE DETECTION

Faces are initially found after frames have been extracted. There are many face detection algorithms available online. In this study, the linear SVM algorithm is used in conjunction with the histogram of oriented gradients (HOG). This method computes HOG descriptors on positive samples of a fixed window size obtained from the images. Thereafter, identical-sized negative samples of the desired object to be detected (in this case, a human face) are taken, and HOG descriptors are computed. Often, there are far more negative samples than positive samples. A linear SVM is trained for the classification job after the characteristics of both classes are obtained. Intensive data mining is used to increase the SVM's accuracy. The classifier is evaluated on the labelled data in this technique after training, and the false positive sample feature values are used once more for training. The classifier computes the output for each window point for the test picture after translating the fixed-size window over the image. Ultimately, the recognized face is identified as the largest value output, and a bounding box is formed around the face. This non-maximum suppression step eliminates bounding boxes that are unnecessary and overlap each other.

C. FACIAL LANDMARKS MARKING

The next objective is to locate various facial features, such as the corners of the lips and eyes, the tip of the nose, and so on. This is after the face has been detected. Prior to that, the facial photos should be normalized to lessen the impact of camera distance, uneven lighting, and changing image resolution. The face image is therefore scaled down to 500 pixels in width and made into a grayscale image. An ensemble of regression trees is used to estimate landmark positions on the face from a sparse selection of pixel intensities after picture normalization. The

sum of square error loss is improved through gradient boosting learning in this method. To find various structures, several priors are employed. Using this technique, the boundary points for the eyes, mouth, and the central line of the nose are marked. Table I lists the number of points for each boundary point. Figure B displays facial landmarks. The detected landmarks needing additional processing are indicated by red pointers.

Table 1 Points of Facial Landmarks

Facial Landmarks	
Parts	***Points***
Right eye	[37-42]
Left eye	[43-48]
Mouth	[49-68]

Figure 2 : Facial Landmark Points

D. FEATURE EXTRACTION

The characteristics are computed as follows after identifying the facial landmarks.

Eye aspect proportion (EAR): The ratio of the eye's height to its width, as determined by the eye corner points, is known as the eye aspect ratio and is given as below

$$EAR = \frac{||(p_2 - p_6)|| + ||(p_3 - p_5)||}{2||(p_1 - p_4)||} \quad (1)$$

Equation 1 : Eye Aspect Ratio

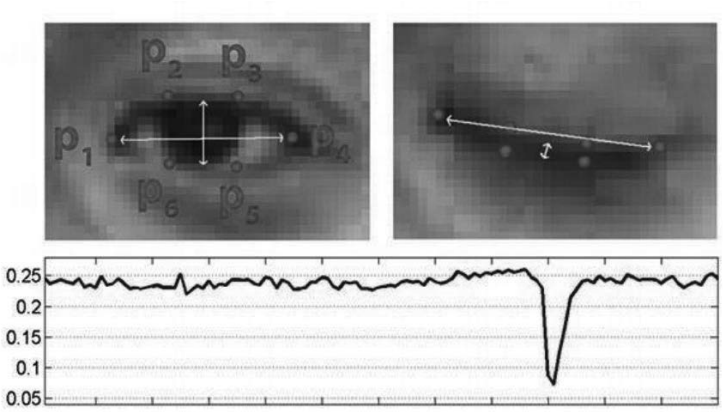

Figure 3: Top-left: A visualization of eye landmarks when then the eye is open.

Top-right: Eye landmarks when the eye is closed.

Bottom: Plotting the eye aspect ratio over time. The dip in the eye aspect ratio indicates a blink.

Mouth opening ratio (MOR): MOR is a parameter used to identify yawning while drowsy. It is calculated similarly to EAR as,

$$MOR = \frac{||(p_2 - p_8)|| + ||(p_3 - p_7)|| + ||(p_4 - p_6)||}{3||(p_1 - p_5)||} \quad 2$$

Equation 2 : Mouth Opening Ratio

E. CLASSIFICATION

The following challenge is to identify sleepiness in the extracted frames after computing all three features. First, adaptive threshold is taken into account for categorization. Later, to categorize the data, machine learning methods are employed. It is assumed that the driver is fully awake at the start of computing the threshold values for each feature. The setup process is at this point. The EAR values for the first 24 frames are recorded during the setup process. The hard threshold for EAR is the average of 20 maximum values out of these 24 initial face-containing frames. The higher numbers are taken into account to ensure that there are no instances of eye closure. If the test result falls below this cutoff, drowsiness (or eye closure) is identified. This initial configuration for each person will lessen this effect because eye size might differ from person to person. Similar to this, the threshold for MOR is determined empirically from the observations because the mouth might not be fully open in the initial frames (setup phase). Yawn (i.e., drowsiness) is recognized if the test value exceeds this threshold. By measuring the angle the head makes with regard to the vertical axis in terms of the ratio of projected nose lengths, the head bending feature may be used. NLR typically ranges from 0.9 to 1.1 for the normal upright position of the head and it rises or falls when the head bends down or up while drowsy. Assuming there is no head bending, the average nose length is calculated as the average of the nose lengths throughout setup. The system is tested after the threshold values have been calculated. If at least one feature in a test frame indicates drowsiness, the system will recognise it.

This threshold is based on the previous 75 frames, which makes it more realistic. The system will indicate drowsiness detection and sound an alarm if at least 70 frames satisfy the

sleepiness criterion for at least one characteristic. Another single threshold value that initially depends on the EAR threshold value is computed in order to make this threshold adaptive. The average of the 150 maximum values from among the 300 frames in the setup phase is used to calculate EAR values. The threshold is then obtained by subtracting the offset from the average value, which is determined heuristically. When EAR falls below this level, driver safety is put in jeopardy. With each yawn and head bend, this EAR threshold value rises slightly till a certain point. Because each yawn and head bending occurs over a number of frames, the yawning and head bending of succeeding frames are treated as a single event and are only added once to the adaptive threshold. If the EAR value in a test frame is below this adaptive threshold value, drowsiness is identified and the driver is alerted. The device may occasionally fail to detect the face when the head is too low as a result of bending. In this case, the previous three frames are taken into account, and if there was any head bending in those three frames, a sleepiness alarm will be displayed.

3. RESULTS AND DISCUSSIONS

With the generated data, the suggested system has been created and tested. For additional processing and categorization of the internet video streaming, the webcam is connected to the laptop. The feature values are then saved for later statistical analysis and classification.

Figure 4 displays one frame from the usual or waking condition.

For this frame, the feature values are

EAR = 0.35 MOR = 0.38

Figure 4: Normal or awake state with facial landmarks

Figure 5: Drowsiness detected by the system due to (a) eye closing, (b) yawn, (c) head bending.

4. CONCLUSIONS

A low-cost, real-time driver drowsiness monitoring system based on visual behaviour and machine learning has been proposed in this work. Here, streaming video from a webcam is used to compute aspects of visual behaviour such eye aspect ratio, mouth opening ratio. A real-time method for detecting driver intoxication has been created using adaptive thresholding. With the generated synthetic data, the built system performs precisely. The feature values are then saved, and machine learning methods are applied to classify the data.

REFERENCES

Journal Article

1. 1.M. Karchani, A. Mazloumi, G. N. Saraji, A. Nahvi, K. S. Haghighi, B. M. Abadi, A. R. Foroshani, A. Niknezhad, “The Steps of Proposed Drowsiness Detection System Design based on Image Processing in Simulator Driving”, International Research Journal of Applied and Basic Sciences, vol. 9(6), pp 878-887, 2015.
2. Book/Monograph
3. Richard O. Duda, Peter E. Hart, David G. Stork, “Pattern Classification”, Wiley student edition.
4. A chapter from a Book

5. 3.K. T. Chui, K. F. Tsang, H. R. Chi, B. W. K. Ling, and C. K. Wu, “An accurate ECG based transportation safety drowsiness detection scheme,” 343IEEE Transactions on Industrial Informatics, vol. 12, no. 4, pp. 1438- 1452, Aug. 2016.
6. Conference Paper
7. W. B. Horng, C. Y. Chen, Y. Chang, C. H. Fan, “Driver Fatigue Detection based on Eye Tracking and Dynamic Template Matching”, IEEE International Conference on Networking,, Sensing and Control, Taipei, Taiwan, March 21-23, 2004.
8. V. Kazemi and J. Sullivan; "One millisecond face alignment with an ensemble of regression trees", IEEE Conf. on Computer Vision and Pattern Recognition, 23-28 June, 2014, Columbus, OH, USA.
9. 6.W. L. Ou, M. H. Shih, C. W. Chang, X. H. Yu, C. P. Fan, "Intelligent Video-Based Drowsy Driver Detection System under Various Illuminations and Embedded Software Implementation", 2015
10. international Conf. on Consumer Electronics - Taiwan, 2015.

Design and Implementation of Private Cloud Infrastructure based on OpenStack for Strategic Organizations

M. Swapna*[1], Devanahalli Sunil Archana
Research Centre Imarat (RCI), Hyderabad- 500 069, India
E-mail: swapna@rcilab.in, sunil.archana@rcilab.in*

ABSTRACT

Cloud technologies have become indispensable part of organizations today. As an evolving paradigm for anytime, anywhere, cost effective computing, cloud computing has attracted huge attention among academics and industry. Many commercial companies are providing public cloud solutions through internet. In public clouds, control over the entire cloud infrastructure and the data hosted on it remains with the company providing cloud solution. However, government and defense organizations require that control over the cloud infrastructure and the hosted data is retained with them. Hence private clouds are more suitable for strategic organizations.

This paper discusses design choices and challenges involved in implementing an Open Stack based private cloud system for an organization and customizing it for developing strategic applications while saving recurrent costs and also providing data security. It also focuses on automating the entire deployment with minimal manual work. As a case study for PaaS, deep learning frameworks have been provided on cloud for training deep learning models.

Keywords*: Open Source clouds**, OpenStack, Private Cloud, Design of private Cloud*

1. INTRODUCTION

Cloud Computing provides a shared pool of computing resources (storage, network, memory and CPU) to users using cloud enabling technology called virtualization. This gives users a perception that they have access to unlimited computing resources.

The National Institute of Standards and Technology (NIST) [1] definition of cloud computing describes it as a “model for enabling ubiquitous, convenient, on-demand network access to a shared pool of configurable computing resources (e.g., networks, servers, storage, applications and services) that can be rapidly provisioned and released with minimal management effort or service provider interaction”. This model is composed of three service models namely, Infrastructure as a Service (IaaS), Platform as a Service (PaaS) and Software as a Service (SaaS). It elaborates on IaaS as "The capability provided to the consumer is to provision processing, storage, networks, and other fundamental computing resources where the consumer is able to deploy and run arbitrary software, which can include operating systems and applications “. The control sphere of consumer here is over operating systems, storage and applications deployed. Management of cloud infrastructure is out of customer control sphere. In PaaS model, consumer is provided with programming framework, such as programming language, libraries, tools to build and develop applications. Consumer control sphere is within deployed applications and over configuration settings of development environment. Management of underlying infrastructure and operating system is out of consumer control sphere. In SaaS model, consumer is provided access to applications running on cloud infrastructure. The control sphere of consumer is over application configuration settings. Management of underlying infrastructure, operating system or development environment is out of consumer control sphere.

The IaaS cloud architecture consists of different layers as shown in Figure 1. The resource pool consists of all physical hardware. Hypervisor runs natively on physical hardware and

[1]Corresponding author: E-mail: swapna@rcilab.in

enables sharing of resources of physical hardware among of multiple virtual machines hosted on physical hardware. IaaS software runs on hypervisor and controls pool of storage, compute and network resources. Most of the open source cloud solutions support IaaS service model.

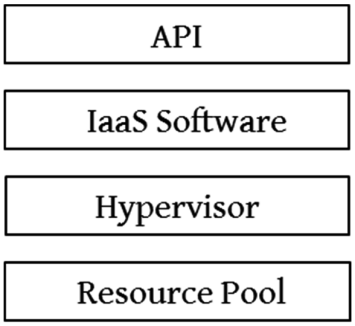

Figure 1: Different layers of OpenStack IaaS Cloud [2]

The paper is structured as follows. Section 2 points to literature review of existing open source cloud solutions. Section 3 formulates the problem definition and section 4 explains the setup of private cloud computing system and its deployment plan. Section 5 presents discussion on important design aspects. Section 6 presents challenges faced during the implementation, remedies and case study of hosting deep learning frameworks on cloud for application development and finally section 7 provides conclusions and future work.

2. LITERATURE REVIEW

Five major implementations of Open-Source cloud solutions for IaaS namely OpenStack, CloudStack, OpenNebula, Eucalyptus and Nimbus dominate the market. TheoLynn et. al presents comprehensive overview of features of these top five open source frameworks and their comparative analysis based on 19 criteria [3]. OpenStack was chosen for our deployment keeping in mind, its modular architecture, wide adoption, community support, free access to source code, developer documentation and its suitability to private deployments.

OpenStack is free and open-source software for deploying Infrastructure as a Service (IaaS). The technology behind OpenStack consists of a series of interrelated projects delivering various services for cloud infrastructure solution. Each OpenStack service provides one or more endpoints through which user can access resources and perform operations. Some of the important services of OpenStack are compute service, image service, object storage, identity service, networking service, block storage, orchestration service, accounting service, bare metal service and dashboard service. Compute service is provided by **Nova**. Nova manages life cycle of virtual machines, from spin up to termination of virtual machines. Image service is provided by **Glance.** It provides a repository of VM images and snapshots. Object storage is provided by **Swift.** Identity service is handled by **Keystone**. It manages authentication, authorization and OpenStack service information. It provides means to access various OpenStack services by different users. Networking service is provided by **Neutron**. It manages networks and IP addresses. Block storage i.e. persistent block level storage devices for use by VM are provided by **Cinder.** Orchestration service is provided by **Heat.** Heat provides an orchestration engine to launch group of machines, networks and other resources based on templates. A heat template is used to describe infrastructure resources (servers, volume, users) for an application in text file. Account of user's usage of different components of OpenStack

ISBN - 978-93-95038-50-8

is provided by **Ceilometer**. **Ironic** provides bare metal service where instances of physical hardware can be spawned. All of these services can be managed though a web based dashboard service called **Horizon** or through APIs or through command line interface. Horizon provides a web based UI for users and administrators. Interaction between these services is illustrated in Figure 2. We have used Kernel Virtual Machine (KVM) hypervisor in our cloud deployment. Choice of KVM hypervisor is based on two reasons:

(i) It is default hypervisor for OpenStack and widely adopted hypervisor in the OpenStack community.

(ii) It is feature complete and free from license charges and restrictions.

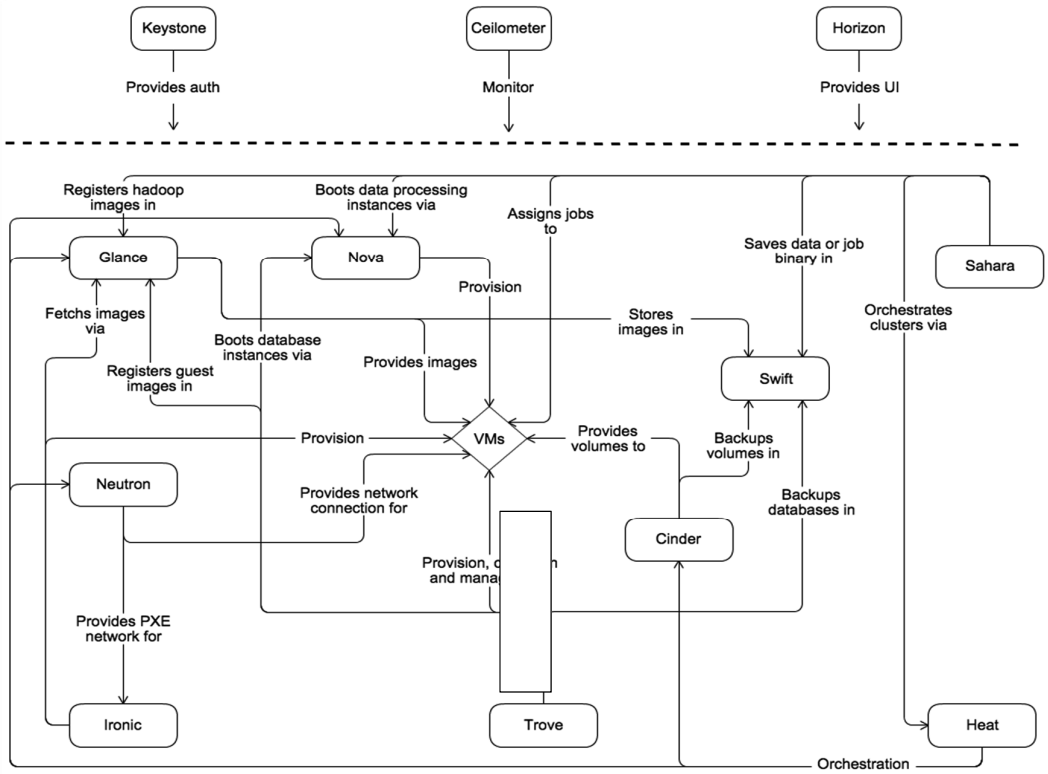

Figure 2: OpenStack core services interaction. (Source: docs.openstack.org) [4]

3. PROBLEM DEFINITION

The goal of this work is to design a scalable architecture for private cloud and implement a private cloud solution aiming at maximum automation and minimal amount of manual work. The Storage solution of the private cloud should provide for redundancy and also data security.

4. METHODOLOGY

4.1. SETTING UP THE PRIVATE CLOUD

OpenStack based private cloud computing system was installed on group of servers mounted on two racks in lab environment. The hardware used for the setup consists of 22 high performance dell power edge servers. The servers are deployed in the following fashion.

I. Three servers as controller nodes, running all sub-services except nova-compute.

II. Sixteen servers as compute nodes which run nova-compute.

III. Three servers as storage nodes with ceph storage cluster configured.

Each compute and controller server has 20 cores, 128 GB RAM and attached 4TB hard disk. Each storage server has 8 cores, 256GB RAM, 9×4TB hard disk. Each server has 4 Network Interface Cards (NICs). Servers are connected using 1 Gigabit ethernet switch for cloud management and 10 Gigabit ethernet switch for VM traffic. All compute nodes are mounted on single rack. Controller nodes, storage nodes and switches are mounted on the second rack. Figure 2 shows distribution of OpenStack services across different nodes.

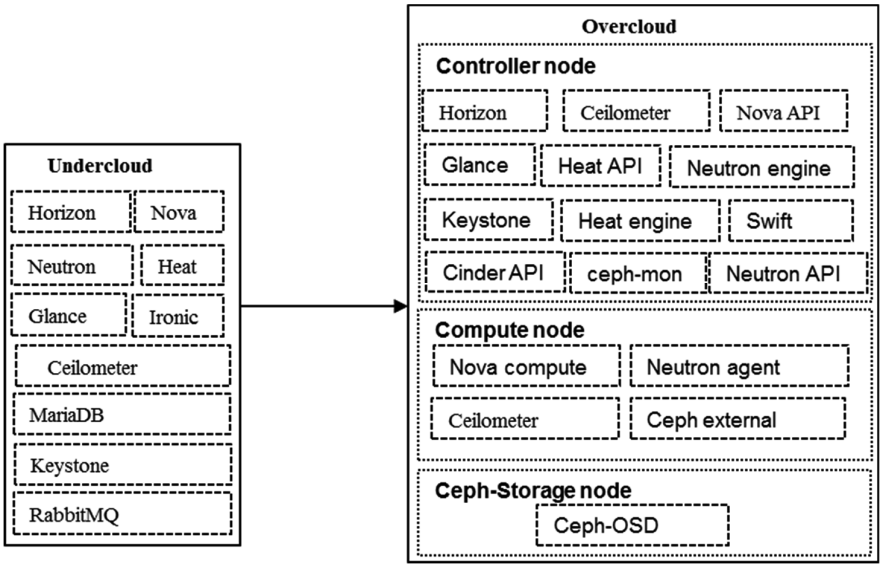

Figure 3: OpenStack Services deployment overview

4.2. DEPLOYMENT PLAN

TripleO (OpenStack On OpenStack) was used to deploy OpenStack. TripleO is a tool to install and manage OpenStack cloud using OpenStack's own services building on Nova, Neutron and Heat. Its aim is to install, test, manage and update it's overcloud servers. Deployment of OpenStack has been done in two steps: Undercloud deployment and overcloud deployment. Undercloud or director is a single node OpenStack installation deployed on virtual machine. This contains necessary OpenStack components to deploy and manage overcloud or OpenStack cloud. Undercloud and Overcloud deployments are elaborated in subsequent subsections. Figure 3 shows services deployment in overcloud and undercloud. Figure 4 shows architecture of the designed cloud computing system.

Table 1: Specification of workstation hosting director and services VM

Processor	x86_64
Cores	20
Threads	2
Virtualization	KVM
Memory	256GB
Disk	4TB

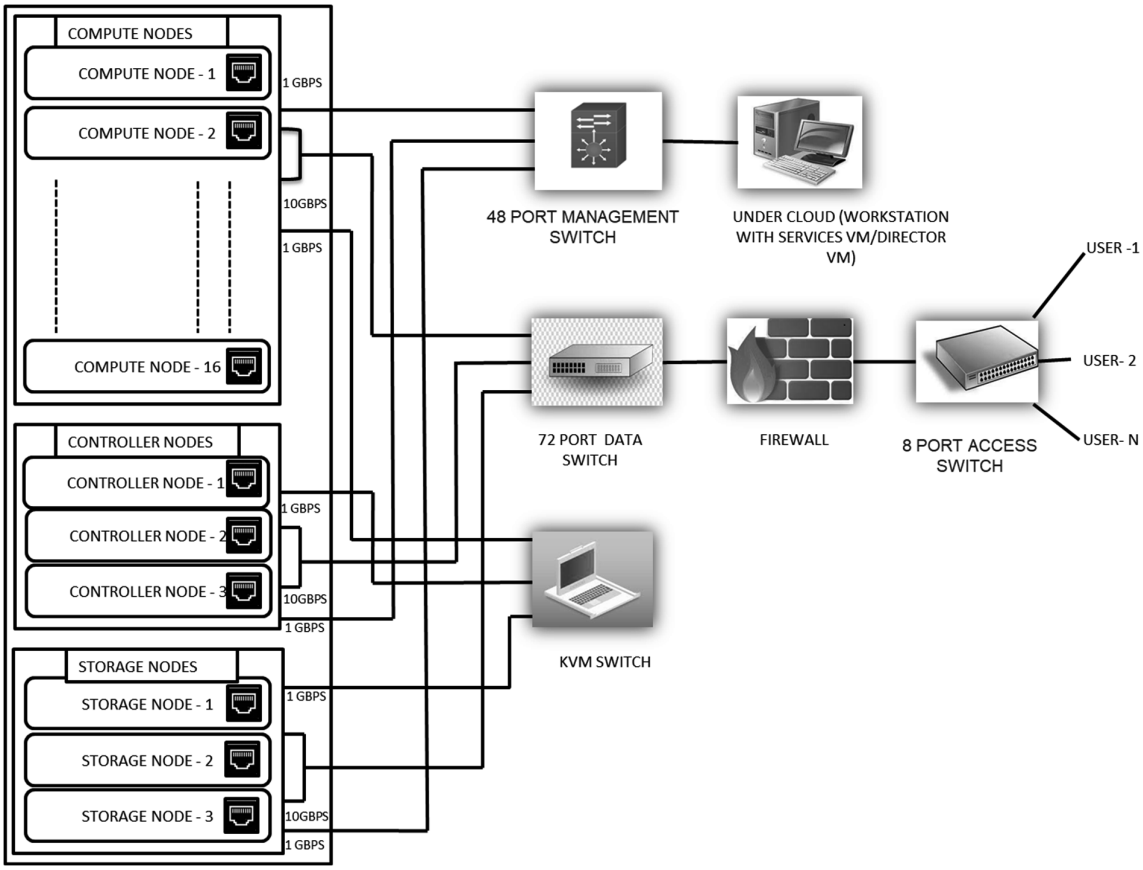

Figure 4: OpenStack based Private Cloud Architecture

4.3. UNDERCLOUD DEPLOYMENT

A dedicated workstation (specification in Table 1) was used for deploying undercloud.

Two Virtual machines (VMs) were installed on this workstation. First VM (specification in Table 2) hosts DHCP, NTP and DNS services. Second VM (specification in Table 3) hosts director. Director and services were chosen to be hosted in virtual machines as they can be cloned for backup. In the director VM, TripleO client was installed. Upon successful installation of TripleO client, undercloud.conf file was generated. Configuration parameters of undercloud were edited and updated in undercloud.conf. After this, undercloud was installed using the command - openstack undercloud install. Successful installation of undercloud created two files named stackrc.conf and password.conf. This completed Undercloud deployment. Overcloud disk images are downloaded from internet and placed in local repository before commencing overcloud deployment.

Table 2 Specification for services VM

Host CPU	1
Memory	1024MB
Disk Storage	20GB

Table 3 Specification for director VM

Host CPU	10
Memory	24576MB
Storage	100GB

4.4. OVERCLOUD DEPLOYMENT

Deployment of overcloud comprises the following steps – registration, introspection, profile tagging, preparation of configuration files and deployment.

- Registration: Overcloud servers were registered in undercloud. Intelligent platform Management Interface (IPMI) related information like IDRAC IP address, username, password, MAC of PXE enabled interface of each server were specified in instackenv.json. Importing this json file completed registration.
- Introspection: Inspection of hardware nodes was done by running introspection agent though PXE. This agent fetched hardware properties of nodes and stored in local database. This information was used in profiling tags.
- Profile tagging: Each node was tagged into specific profiles – control, compute or ceph according to roles chosen for nodes.
- Deployment files were prepared using configuration files. TripleO client provided generic YAML configuration files. Entries in these files were edited to describe environment of overcloud according to the architecture. The environmental files used were *network*-environment.yaml, network-isolation.yaml, roles.yaml, layout.yaml, storage-environent.yaml, network-isolation.yaml and node-info.yaml.
- Deployment: Overcloud deployment was commenced using command - openstack overcloud deploy. Each round of deployment took 3 to 4 hours. After 8 weeks of rigorous installations, consulting and following up on forums, installation was concluded.

5. DISCUSSION ON DESIGN CHOICES

OpenStack based private cloud deployment as discussed in section 4 was mostly automated after a minimal amount of manual work including physical racking, interconnect, MAC-to-IP assignment and power configuration [5]. Our focus was on key design issues as they are hard to modify post deployment. Designing a cloud involves selecting hardware, hypervisor, cloud software and operating system, configuring storage and network interfaces. Rationale behind selection of KVM as hypervisor and OpenStack as cloud software has been discussed in Introduction section. This section sheds light on other design issues.

To ensure symmetry in hardware and its configurations of the physical nodes, servers with same hardware specification were chosen. This symmetry offers following advantages:

(i) Managing spare servers is easy as we are storing only one type of server and replacing of nodes is easy in case of node failures.

(ii) Troubleshooting of software issues are simplified as error terminology remains same throughout complete cloud system.

ISBN - 978-93-95038-50-8

By default, all servers had single redundant array of independent (RAID) disk. Owing to this, in case of any controller node failure, risk of cloud system failing is high. To mitigate this, 4TB disk was added and configured as RAID2 in all controller nodes.

OpenStack uses concept of isolated networks to host specific network traffic type i.e. different network traffic type traverses through different isolated networks (mentioned in Table 4). Ideally each network required one network interface. We have more isolated networks (six) and less network interface cards (four). To remedy this, Virtual Local Area Networks (VLAN) were used. 5 VLANs were configured (as shown in Table 5) to efficiently use available interfaces. Isolated networks were assigned as follows: One physical 1G network port was assigned for IPMI and provisioning network. One network port was assigned for VLAN20 (Internal API) as VMs communicate with higher bandwidth. Two 10G network ports are bonded using Link Aggregation Control Protocol (LACP). LACP offers aggregation, failover and load balancing. This bonded interface was assigned to VLAN30, VLAN40, VLAN50 and VLAN60.

Table 4 Isolated networks in OpenStack

Isolated Network	Role	Connection
Intelligent Platform Management Interface (IPMI)	Power management	Controller, compute and ceph storage
Provisioning	Undercloud control plane for deployment and management	Controller, compute and ceph storage
External API	Public OpenStack API, Access Horizon and floating IPs	controller, compute and undercloud
Storage network	Access to storage resources from compute and controller nodes	Controller, compute and ceph storage
Internal API	OpenStack Internal API, Access and RPC between OpenStack components	Controller, compute and ceph storage
Storage management network	Replication and ceph-backend services.	Controller, ceph storage
Tenant network		Controller, compute

ISBN - 978-93-95038-50-8

Table 5 VLAN and network assignments

VLAN No.	Isolated Network
VLAN20	Internal network API
VLAN30	Storage management Network
VLAN40	Storage Network
VLAN50	Tenant network
VLAN60	External API network

6. IMPLEMENTATION CHALLENGES AND RESULTS

Implementation of cloud deployment comprises of downloading required packages and images, registration of nodes, introspection, profile tagging, preparation of configuration files, installing packages on all nodes simultaneously, and troubleshooting errors.

OpenStack's RDO packages of Pike[2] were used for deployment. OpenStack has placed its Redhat Package Manager (RPM) on ftp server. This RPM changes rapidly because of large contributing community and frequent updates. Use of incompatible packages causes deployment to err. To resolve this, we have prepared local satellite repository, where we downloaded all required packages once and used this as satellite repository for deployment.

Troubleshooting of errors during different stages of deployment required technical expertise on OpenStack. OpenStack has many components which are strongly related. Determining which component failed was difficult and time consuming. For example, common error "No valid host found" was encountered during overcloud deployment phase. Enabling debug or verbose did not give much information on what caused the error. There were many possible scenarios causing this error such as IPMI validation, provisioning state, monitoring compute services, identifying mismatch in properties of nodes and assigned flavors.

During the deployment, failure of even a single node to load boot images from PXE booting leads to failure of complete deployment, resulting in longer deployment time. Therefore, first eight compute nodes were deployed along with controller nodes and storage nodes. The remaining eight compute nodes were added to scale out the cloud by updating heat template.

The deployed cloud could provide IaaS, PaaS as service. As case study deep learning frameworks were provided on a virtual machine to train DL models. The benefit of providing deep learning framework on cloud is that large datasets can be used to train the models. The Qcow2[3] image of the VM was uploaded to Glance service of cloud. A user could login into the cloud and spawn the machine learning VM readily. As a case study

[2] Pike is the 16th release of OpenStack: open source infrastructure software

[3] Qcow2 stands for QEMU copy on write. It is a file format for disk images.

ISBN - 978-93-95038-50-8

7. Conclusions and Future Work

This paper presents setting up of multi-node OpenStack cloud and discusses design choices made while setting up private cloud for strategic organization. It also presents a case of providing deep learning frameworks on cloud. The future work will be to deploy container as a service, applications as a service, security analysis of this cloud and work on framework to enhance security of the private cloud.

Acknowledgements

This activity would not have been initiated without encouragement of late Dr. Manuj Sharma, Scientist G, DRDO. I am deeply thankful to him for proving valuable insights on architecture design and overall supervision.

References

1. Mell,P. and Grance,T. (2011), The NIST Definition of Cloud Computing, Special Publication(NIST SP), National Institute of Standards and Technology, Gaithersburg, MD, [online], https://doi.org/10.6028/NIST.SP.800-145 (Accessed Febraury 9,2023)
2. Hans Lindgren, Performance management for Cloud Services: Implementation and Evaluation of Schedulers for OpenStack. Kungliga Tekniska Hgskolan, Stockholm, 2013, page 10.
3. TheoLynn, Graham Hunt, David Corcoran, John Morrison, Philip Healy. “A Comparative Study of Current Open-Source Infrastructure as a Service frameworks”. In Proceedings of the 5th International Conference on Cloud Computing and Services Science – Volume 1: CLOSER, ISBN 978-989-758-104-5, pages 95-104. DOI: 10.5220/0005423300950104
4. OpenStack docs: Conceptual architecture.https://docs.openstack.org/ocata/admin-guide/common/get-started-conceptual-architecture.html.
5. Tom Fifield, Diane Fleming, Anne Gentle, Lorin Hochstein, Jonathan Proulx, Everett Toews, Joe Topjian. OpenStack Operations guide. Oreilly, 2014.

Design of High Speed Drive System for Rocket Subsystem Tests

Deepak Dinesh*, Arun Kumar S, Remya KP, Harikumar K, Unnikrishnan Nair P, N. Jayan, Jose Paul

LPSC, ISRO, Trivandrum, Kerala 695547

ABSTRACT

A high-speed drive system driven by a radial turbine was designed for testing high speed seals and bearings for rocket engine turbopump. The drive system uses angular contact ceramic ball bearing pairs with high speed capability for supporting the rotor and is lubricated using oil mist lubrication method. The radial turbine design was carried out by 1-D mean line method, to match the output of the available air supply from a screw compressor. The preliminary design of the radial turbine was analysed using CFD with CFX software. Structural analysis was performed using ANSYS to ensure that stresses are benign at the operating conditions. Rotordynamic analysis of the rotating system was carried out with in-house FORTRAN code and Campbell diagrams obtained showed that sub-critical operation was achieved. The hardware was realised at in house fabrication facility and balancing of the rotating system was carried out to achieve minimum unbalance levels. The facility realization required for the drive involved integrating procured pneumatically operated valves and sensors with necessary instrumentation to the fabricated feed lines and test bed. The testing of the high-speed drive was performed by remote operation and the test parameters were logged using a data acquisition system. The testing carried out achieved the targeted speed of greater than 60,000 rpm. Test Data showed minimal temperature rise at the bearing location and large margins for the valve openings, suggesting that even higher speeds are feasible. Post-test observation revealed good health of the hardware.

Keywords: *High speed drive, radial turbine, testing*

1. INTRODUCTION

A high-speed drive system capable of achieving speed greater than 60,000 rpm for carrying out high speed tests on bearings and seals was developed in LPSC. Here system engineering concept takes significance, due to the multi-disciplinary branches of engineering analysis has to be applied for the design acceptance. Preliminary design using analytical methods followed by modelling, CFD, structural and validation testing was rendered towards the product development.

2. LITERATURE REVIEW

The preliminary design of radial inflow turbines is discussed in [1]. A non-dimensional design is developed based on the initial specification of the turbine pressure ratio and the stage efficiency. The inlet velocity triangle is defined by radial blades with an incidence flow selected for minimum inlet Mach number. The relative exit Mach number was used for the design of the exhaust guide vanes. The relative velocity ratio is then specified to define the outlet velocity triangle. The rotor non-dimensional geometry is now worked out based on the assumed efficiency of the stator. The design is optimized by adding various loss models like curvature, tip leakage etc.

The design procedure in [2] followed a solution of equations for speed parameter, flow angles, blade width ratio, mass flow parameter using a constrained optimization algorithm. A computer program was written to optimize the axial length of the rotor by minimizing the

* Corresponding author: E-mail: dd28686@gmail.com

loss of stagnation pressure. This also gave the hub and shroud contours of the rotor. The nozzle-less casing was designed using the equations of mass flow rate, energy, and angular momentum, where isentropic free vortex flow was assumed.

Detailed measurements of the flow in a procured radial turbine were performed in [3], where details measurements were made at volute inlet, volute exit, rotor exit and diffuser exit. 2 to 4% of the inlet stagnation pressure was lost from volute inlet to impeller inlet, and the swirl angle was a function of the velocity ratio. The diffuser effectiveness was very low at 0.2 to 0.4. Rotor efficiency peak was observed at an incidence of -40°, and at a reaction of 0.6-0.65 with U/C_0 of 0.7.

The design and testing of a very high-speed radial turbine for a rocket turbopump is described in [4]. The design features a vaneless volute, an unshrouded rotor, and an exhaust with guide vanes to reduce swirl losses. The turbine has only 7 primary parts, with cast housings. Testing with GH2 at 35% rated power level met the targeted efficiency.

Radial turbine tip clearance flow was studied in [5]. Flow visualization was performed with ammonia injection, and static pressure measurements were performed on the blade surface at the gap region. Additionally, static pressure was measured in the rotor casing. The flow in the gap was also measured using hot wire traverse. The tip gap mass flow was much lower for the radial turbine case compared to the axial turbine for the same gap, due to the "scraping" effect of the flow.

An experimental comparative study of oil mist lubricated all steel and hybrid ball bearing performance was made in [6]. The measured friction torque was lower for hybrid ball bearings for the high-speed range. The centrifugal loads on ceramic balls were lower compared to steel balls due to lower density. Consequently, the contact loads and frictional forces were lower in hybrid ball bearings.

The performance of hybrid ball bearings for turbocharger applications at speeds up to 120,000 rpm was evaluated in [7]. Comparisons with all steel and floating bush bearings were also made. Oil jet lubrication was used. The frictional loss in hybrid bearings was 30% lower than floating bush bearings. Hybrid ball bearings did not seize even at 10% of the oil feed amount of where the steel ball bearings seized and under 5% of oil feed amount where bush bearings seized. Hence anti-seizure performance was superior to them.

The advantages of hybrid ball bearings over steel ball bearings were discussed in [8]. Hybrid ball bearings are electrically non-conducting, highly wear resistant, and have a high bearing stiffness and long service life. Hybrid bearings have lower coefficient of thermal expansion which results in more stability over temperature change and wear rate of hybrid bearings under contaminated lubrication is comparably very low than steel bearings which makes it suitable for high speed rotating machines because of low friction.

The performance of hybrid and steel ball bearings with oil-mist lubrication for sensitivity with different oil viscosity, oil flow, mist supply pipe length etc was studied in [9]. It was found that hybrid bearings had lower temperature rise compared to steel bearings for all operating conditions. The optimum length of pipe of 1.5m and oil viscosity of 100 cSt gave the lowest temperature rise for both ceramic and steel bearings.

ISBN - 978-93-95038-50-8

3. DESIGN, ANALYSIS AND MANUFACTURING PROCESS

3.1. CONFIGURATION

A radial turbine rotor powered by compressed air is supported on hybrid ball bearings in a housing cooled with an oil mist spray. Figure 1 shows the schematic of the high-speed drive. It consists of a radial turbine rotor mounted on a shaft. The shaft is in turn supported on two pairs of angular contact hybrid ball bearings. During operation, these bearings are cooled using an oil mist which is sprayed on the bearings through the mist injector (Fig. 1). A mist generator uses compressed air to generate mist using oil stored in its reservoir. The mist is admitted to the high-speed drive through plastic tubes. The drive system owes its high-speed capability to these angular contact ball bearings.

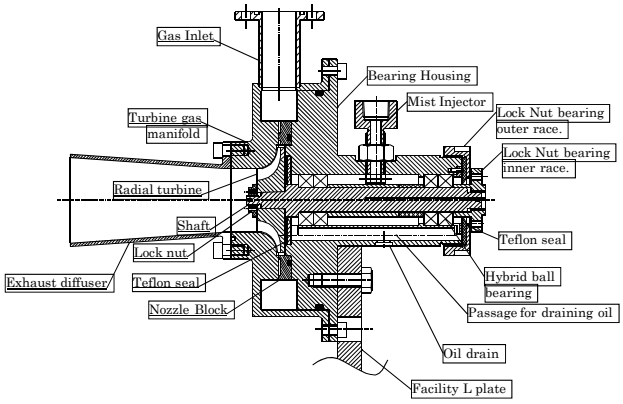

Figure 1: Schematic of high speed drive

Figure 2 shows the schematic of the test facility established for running the high-speed drive. It consists of a diesel engine powered screw compressor which can deliver compressed air at 200 g/s at 11 bar. Compressed air from the screw compressor is admitted to the turbine inlet manifold through a 1" SS pipe. Flow is controlled by a control valve in the line. Emergency shut off of the high-speed drive can be done by an electro-pneumatic valve. Flow rate through the turbine is monitored using a flow meter in the line.

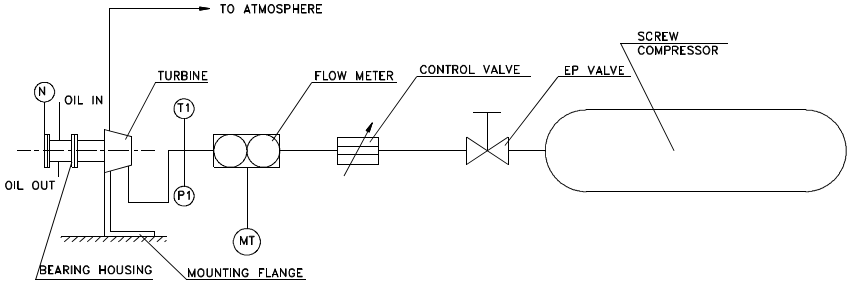

Figure 2: Schematic of the test facility for carrying out high speed test

3.2. DESIGN DETAILS

3.2.1. DESIGN OF RADIAL TURBINE

The design inputs for the rotor are given in Table 1.

Table 1: Design inputs for the rotor

Parameter	Value
Working fluid	Air
Inlet total gas pressure (P_0), bar	10
Inlet total gas temperature (T_0), K	335
Overall turbine pressure ratio (PR)	10
Speed of rotation of the rotor (N), rpm	100,000
Mass flow rate (m), g/s	200

CFD analysis of the design was carried out. Flow pattern across the turbine was smooth, with no abrupt changes in fluid variables (Fig. 3).

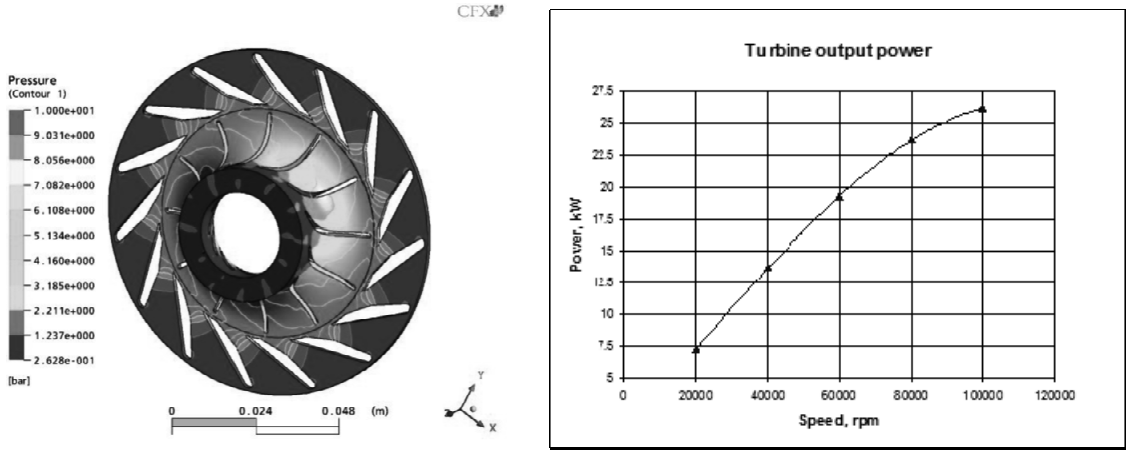

Figure 3: CFD analysis of the radial turbine

Configuration of turbine rotor arrived after detailed design is given in Fig. 4.

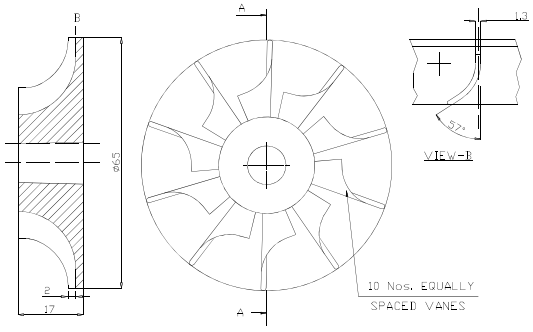

Figure 4: Configuration of turbine rotor

Structural analysis of turbine rotor was carried out for estimating the safe operating speed. Turbine rotor was made of D16T aluminum alloy. Mechanical properties of the turbine rotor are given in Table 2.

ISBN - 978-93-95038-50-8

Table 2: Mechanical properties of materials at RT

Sl No	Part Name	Material	Young's modulus	Poisson's ratio	YS	UTS	%el
1	Rotor	D16T	70,000	0.33	265	470	10

Results of the FEM analysis carried out using ANSYS are given in Table 3. Assuming a factor of safety of 4 on uniform elongation of 5%, the failure speed of the rotor was estimated as 1,17,500 rpm.

Table 3: Summary of stress analysis

Parameter	Value
Axial deformation (mm)	-0.27
Radial deformation (mm)	0.02
Axial stress (N/mm^2)	-33
Radial stress (N/mm^2)	65
Hoop stress (N/mm^2)	177
von Mises stress (N/mm^2)	170

3.2.2. DESIGN OF SHAFT/BEARING SYSTEM

A detailed rotor dynamic analysis of the rotor is also carried out to estimate the critical speeds of the rotating system. The FEM analysis of the rotating system is carried out by considering each element as a Timoshenko beam element (Fig. 5). Turbine rotor, sleeves on shaft OD and lock nut are considered point masses. The shaft material is SS 202, turbines rotor is D16T aluminum alloy, lock nut for bearing inner race for locked bearing is Ti6Al4V (Titanium alloy) and other rotating elements are made of SS321 stainless steel. Rotordynamic analysis was carried out using in-house developed rotordynamics code in FORTRAN.

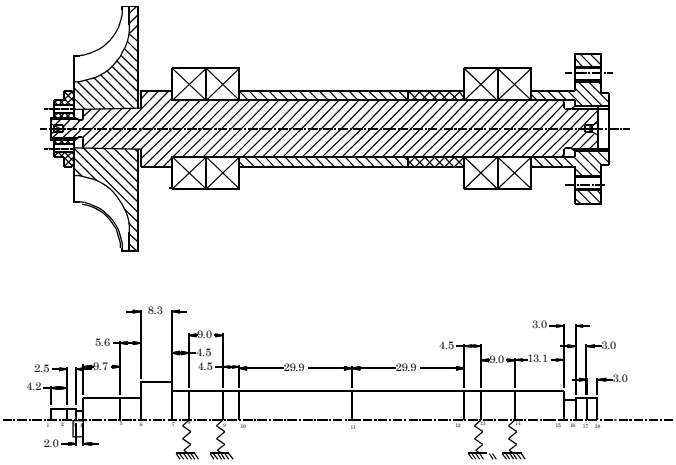

Figure 5: Finite element model for carrying out rotor dynamic analysis

The Campbell diagram (Fig. 6) shows that the first critical speed for the rotating system is 1,40,000 rpm whereas the second critical speed is 1,58,000 rpm.

ISBN - 978-93-95038-50-8

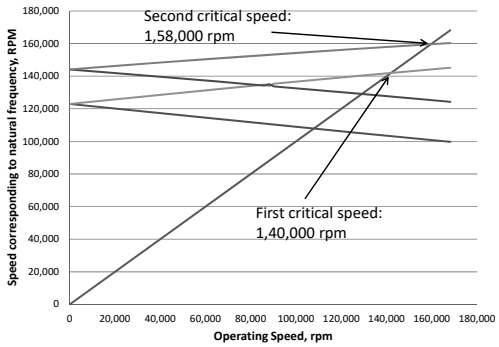

Figure 6: Campbell diagram for rotordynamic analysis

3.3. MANUFACTURING OF PARTS

Test rig elements including rotor, shaft, nozzle block, casing and bearing housing were realized in-house (Fig. 7). Other items like valves and bearings were procured (Fig. 8).

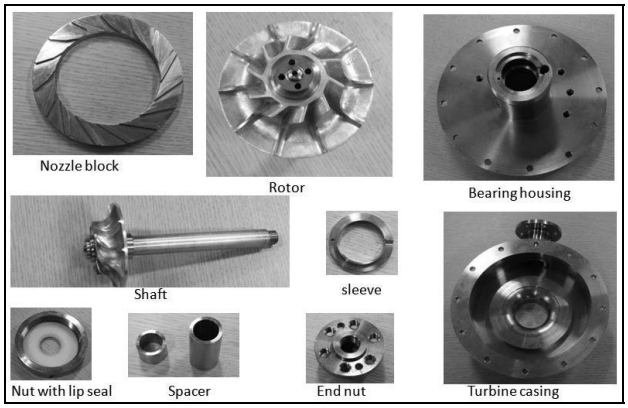

Figure 7: Test rig elements realized

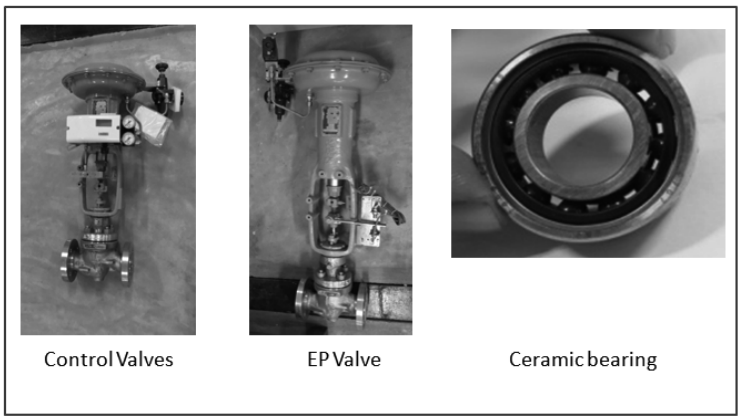

Figure 8: Procured items for high speed drive

3.4 TESTING

3.4.1. BALANCING OF THE ROTATING ASSEMBLY

Balancing is a crucial activity for system operating at very high speeds. Two plane balancing was carried out at 2800 rpm, to achieve a turbine side unbalance of 0.25 g.mm and 0.192 g.mm on the nut side. Here, balancing is done at low speeds as the turbine operates below its first critical speed.

3.4.2. TESTING

The photograph of the facility established for the test is shown in Fig. 9. The facility consists of the following elements: 1) A diesel engine driven air screw compressor (flow rate of 200 g/s at 11 bar). 2) An EP valve for stopping of the turbine. 3) A control valve to control the flow of air to the turbine. 4) A flow meter to measure 5) Temperature and pressure sensors at turbine inlet and outlet 6) Mist lubrication system to supply oil mist for cooling of hybrid ball bearings. 7) Thermocouple for measurement of bearing temperature (locked bearing). 8) Accelerometer to monitor vibration 9) Optical sensor for speed measurement 10) GN2 cylinders and associated lines for actuation of pneumatic valves.

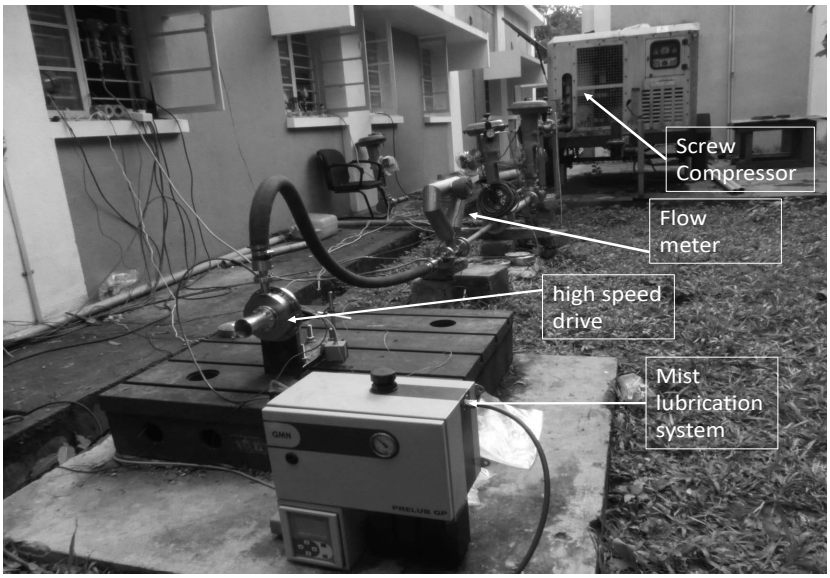

Figure 9: Facility established for testing of high speed drive

Detailed measurement plan for the test is shown in Table 4. All measurements were acquired remotely using a data acquisition system.

Table 4: Measurement plan

Parameter	Legend	Range	Nominal value	Accuracy	Sensor Type
Turbine Inlet Pressure	PTI	0-15 bar	10 bar	±1 % FS	Absolute Pressure Transmitter
Turbine Inlet Temperature	TTI	300-360 K	335 K	± 0.5 K	TP 198-05 –Probe type RTD
Surface temperature of	TBI	300-360 K	335 K	± 2.5 K	K type

ISBN - 978-93-95038-50-8

Table 4 *contd…*

locked bearing					thermocouple
Parameter	**Legend**	**Range**	**Nominal value**	**Accuracy**	**Sensor Type**
Turbine speed	STI	0-125,000 rpm	100,000 rpm	0.5 % rdg	Optical speed
Turbine Inlet flow	FTI	0-250 g/s	200 g/s	0.5 % rdg	Mass flow meter
Vibration measurements	VBX, VBY	± 100 g	20 grms	± 5 % rdg	CE 252

4. RESULTS AND DISCUSSIONS

4.1. TEST PROCEDURE

The high-speed drive was assembled as per the schematic shown in Fig. 1. The test article was mounted on the test bed. The facility elements were connected as per schematic shown in Fig. 2. Instrumentation of the facility was performed and data acquisition was set up. Facility valves, namely the EP value and control valves were kept in the closed position. The mist lubrication system was turned on. The diesel air screw compressor was used to supply air at the required pressure. The EP valve was opened, following which the control valve was opened gradually in small steps and the speed was monitored. The control valve was opened slowly to reach the target speed of 60000 rpm and the speed was maintained for 10s. To stop the test, the EP valve was closed to stop air supply to the turbine. The mist lubrication system was then switched off, and finally, the screw compressor was switched off.

4.2 TEST RESULTS

The turbine speed reached close to 60,000 rpm at 106s. The speed was maintained up to 119s for a duration of 13s. The speed was achieved for no load conditions at turbine inlet pressure of 1.37 bar and flow rate of 18.5 g/s. The rise in bearing temperature was gradual and well within the safe limits. A total temperature rise of 7K was observed. The operating power level was estimated based on the pressure ratio and mass flow rate. The efficiency of the turbine could not be estimated as no torque measurement or power absorbing devices were available for this speed. Vibration levels were found to be benign throughout the test.

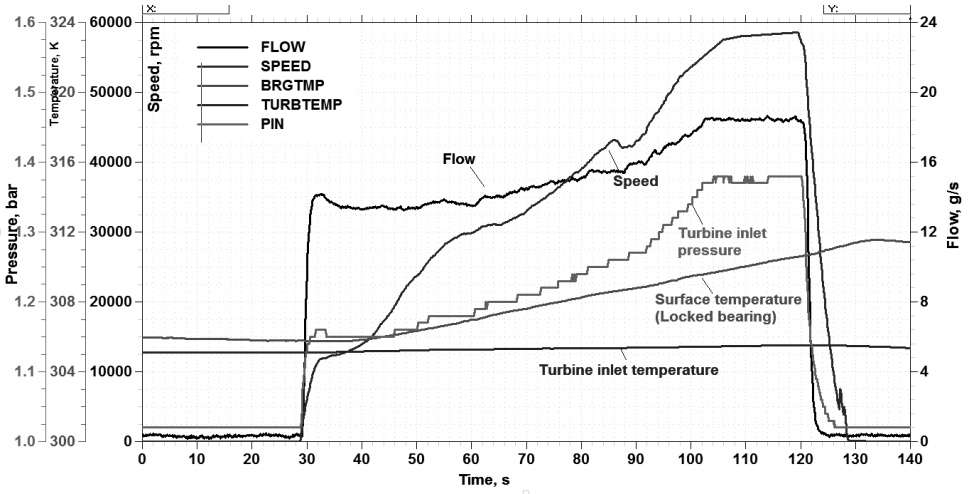

Figure 10: Test results

5. CONCLUSIONS

Design, modeling, analysis and realization of the radial turbine including bearing housing, shaft and lubrication system were completed. Facility realization and instrumentation was also carried out. Finally testing of the high-speed drive system was carried out at 60,000 rpm. This drive system can be used for high speed testing of seals and bearings, towards future programmes.

This project gave hands on experience in developing a new drive system with high speed capability and its associated test facility. The design of the radial turbine was carried out for the first time in LPSC. And for the first time the concept of mist lubrication was implemented for a drive system.

ACKNOWLEDGEMENTS

The support provided by the team at TPL is hereby acknowledged.

REFERENCES

1. Whitfield, A, “Preliminary design of radial inflow turbines”, Transactions of the ASME, Vol. 112, pp. 50-57, 1990.
2. Ebaid, MSY; Bhinder, FS & Khdairi, GH, “A unified approach for designing a radial flow gas turbine”, Trans. of the ASME, 2003, Vol. 125, pp. 598-606.
3. Japikse, D “Characteristics of a radial inflow turbine with internal component measurements” Proceedings of the ASME Turbo Expo 2000.
4. Rodriguez, JL, “Design and test of a radial inflow turbine for an advanced liquid hydrogen turbopump”, AIAA 2000-2679.
5. Dambach, R; Hodson, HP & Huntsman, I, “An experimental study of tip clearance flow in a radial inflow turbine”, Trans. of the ASME, 1999, Vol. 121, pp. 644-650.
6. Paleu, V; Cretu, S & Nelias,D, “Friction moment in oil and kerosene mist lubricated all steel and hybrid ball bearings”, 16th International Colloquium Tribology, 2008
7. Tanimoto, K; Kajihara, K &Yanai, K, “Performance of Hybrid ball bearings for turbochargers”, Koyo Engineering Journal English Edition No. 157E (2000).
8. Singh,V& Pandey,PK, “Advancement of ceramic bearings and its applications”, JEITR, November 2018.
9. Jiang, S & Mao, H “Investigation of high-speed rolling bearing temperature rise with oil-air lubrication”, Journal of Tribology, April 2011, Vol 133.

High Resolution Spectral Analysis of Pressure Oscillations in Large Segmented Solid Rocket Motors

Kali Prasad KVASN*, Sankaran S and Anuj Nigam

[1]Dy. Manager, GTF&RDF, TO, [2]Chief General Manager,
SMP&ETF, SDSC SHAR, Sriharikota, Tirupati Dt, AP-524124
[3]Student, Department of Aerospace Engineering, Indian Institute of Technology Madras, Chennai, 600036

ABSTRACT

In the present work various methods of Spectral Analysis are analysed and implemented to get high resolution spectrogram results to find frequencies of pressure oscillation varying with time for a Large Segmented Solid Rocket Motor. The analysis was conducted using MATLAB software package R2022a. Validation of the implemented code has been made using a theoretical signal which was generated using MATLAB program to closely resemble the variation in frequency and amplitude to Large segmented solid rocket motor pressure signal data. Pressure Oscillations in Large Segmented Solid Rocket Motors are caused by vortex shedding at frontal thermal protections (inhibitors) and acoustic response upon from impingement of vortices on surfaces like other inhibitors or rocket motor nozzle. This coupling along with change in internal diameter of rocket motor due to fuel-grain burning causes continuous variation in frequency of pressure oscillations in motor. The conventional Fast-Fourier Transform algorithm used in spectral analysis is unable to produce high resolution results to be able to identify this continuous frequency variation in pressure oscillations.

Keywords: *Pressure Oscillations, Spectral Analysis, Solid Rocket Motor, MATLAB*

1. INTRODUCTION

Large Segmented Solid Rocket Motors like S200 are known to exhibit Pressure oscillations during flight. These in-turn lead to thrust oscillations which may lead to critical dynamic loads on the structure of the Launch Vehicle. Thus, study of mechanism of pressure oscillation in Large segmented Solid Rocket Motor and ways to mitigate and control it are of significant importance.

These pressure oscillations have been identified to arise due to periodic vortex shedding at the frontal thermal protections (inhibitor) [1]. The role of inhibitor is to restrict the fuel-grain from burning in axial direction. In large segmented solid rocket motors, the fuel-grain burns radially at high rate which after some burn time leads to inhibitors getting exposed into flow as obstruction. This flow obstruction leads to vortex shedding. The magnitude of Pressure oscillations gets amplified if the frequency of vortex shedding is close to frequency of acoustic modes of the duct. Thus, there is a coupling between vortex shedding and acoustics of rocket motor chamber when the shedding frequency matches chamber acoustic mode [1]. The mechanism behind pressure oscillations in large segmented solid rocket motor can be summarised as due to obstruction of flow inhibitors cause periodic vortex shedding, these vortices travel downstream and impinge on other inhibitors or rocket motor nozzle to generate acoustic feedback which in-turn travels upstream to the location of vortex generation and perturbs the shear layer to complete a positive feedback loop. Further as fuel-grain burns radially in large segmented solid rocket motor, this leads to increased chamber volume which reduces mean flow velocity in the chamber. This reduction in mean flow velocity leads to decrease in frequency of vortex shedding to such an extent that it decouples from the chamber acoustic mode. Reference [1] suggested that further change in volume due to fuel grain burning leads to increase in number of vortices shed which in turn causes increases in vortex shedding frequency. Once again it couples with acoustic mode as it comes close to acoustic frequency mode. This coupling-decoupling of vortex shedding and acoustics causes continuous variation of frequency of pressure oscillation in large segmented solid rocket motor with very high amplitude near acoustic modes.

ISBN - 978-93-95038-50-8 https://doi.org/10.37285/bsp.sasat2023.38

In order to investigate the presence of above-described phenomenon in Large segmented solid rocket motor and further find frequency at each time instant requires high resolution spectral analysis of pressure signal captured during working of solid rocket motor.

2. LITERATURE REVIEW

The Pressure signal obtained from large segmented solid rocket motor is non-stationary as the mean of the signal is changing with time. The oscillations in pressure are about this mean pressure signal. There are many algorithms to find power spectrum from time-domain signal but as the signal is non-stationary and rapidly varying with time, there are very limited algorithms which give accurate frequency-power results.

2.1 SHORT-TIME FOURIER TRANSFORM

Fourier transform is a method to convert time-domain signal into frequency domain information. In Short-Time Fourier Transform, a series of Fourier Transform is applied by windowing the signal by applying time shift t. The window function $w(t'-t)$ centered around t is applied to the signal $X(t')$ to get windowed signal $X(t')w(t'-t)$. Generally, the window function is square signal which gives value of signal $f(t')$ for a time window which is shifted till all the signal is covered. STFT for a signal $X(t')$ can be defined as,

$$Y(t,f) = \int_{-\infty}^{\infty} X(t') \cdot w(t'-t) \cdot e^{-2\pi i f t'} dt' \quad \ldots\ldots (1)$$

Here, $X(t')$ is Input Signal, f is frequency, t is time and $Y(t,f)$ is STFT output for signal.

This can be like wise performed for discrete signals, but the important thing here is to choose the window length which is based on the resolution trade-off [2]. For instance, if the signal has rapidly fluctuating properties, then shorter window is preferred to enable fine temporal resolution however in the case of signal with slowly fluctuating properties larger window is preferred as it gives finer frequency resolution. This trade-off is characteristic feature of STFT and there is no optimal way to choose window length.

The features of window function also affect the results of STFT, as if the window function is having non-zero value through-out then the windowed signal value is non-zero at end points which might give absurd values in frequency domain. This problem can be solved by using windowing function like Hann function which smoothly goes to zero at ends thus making the windowed signal values starting and ending with zeros with smooth increment which reduces any absurdity in frequency domain results.

But even with all the above improvements some of signal characteristics or frequencies go un-noticed due to windowing effect. The windowing effect might cause loss of signal characteristics at the ends of the window as it does not consider previously processed window to report any features of signal that were present at the end of the window [2]. This problem can be solved using constant overlapping window.

Constant overlapping window uses some amount of data from previously processed window alongside the current window. This essentially does two things: one it increases temporal resolution for same length of window and other it improves results by reporting features of signal which might be present at the ends of non-overlapping windows [2].

2.2 WIGLER-VILLE DISTRIBUTION

Wigler-Ville Distribution is Fourier transform of local Auto-correlation function [3]. Local Auto-correlation function reports if any similarity is there between any segments on left and right

and how much they overlap in characteristics. It checks the whole signal for all possible segments giving uniform weights to all segments. But to get actual local properties at an instant more importance or weight should be given to local properties or closer segments and less weight for far away segments [4]. Wigler Ville Distribution does not suffer from leakage effects as in STFT due to windowing thus gives better resolution.

$$W(t,f) = \int_{-\infty}^{+\infty} Z\left(t+\frac{\tau}{2}\right) Z^*\left(t-\frac{\tau}{2}\right) e^{-2\pi i f\tau} d\tau \quad \ldots\ldots(2)$$

Here $W(t,f)$ is wigler-ville distribution, Z and Z^* are analytical signal and its conjugate. Due to its quadratic nature, it possesses cross terms which lead to interference. A common strategy to reduce impact of interference is to introduce smooth kernel in wigler-ville distribution. This algorithm is called pseudo-Wigler Ville Distribution which uses ambiguity function which gives higher weights to near segments and lower weights to far segments [5]. However, attenuation of cross-terms by means of smoothening kernel leads to increase of time-frequency spread which reduces precision of representation.

2.3 MAXIMUM ENTROPY METHOD

In practice time series data are measured within some finite time interval and analysis assumes data outside this interval to be zero. To reduce error due to this assumption we use weighting functions like Hann functions. Maximum Entropy method provides alternative method for determining power without using this assumption. In principle method provides means of extending sampled data beyond measurement window by taking weighted sum of known data. The weighing function is called prediction error filter which is determined by minimizing the error power output from least mean square fit of measured data to get predicted data. The Method involves maximization of "Entropy" of the system with respect to the power spectrum, subject to constraints imposed by the data! In spectral analysis this application means maximizing entropy of stationary Gaussian process which is given by [6]:

$$H = \int ln\ \left(P(f)\right) \cdot df \quad \ldots\ldots(3)$$

Where P (f) is the power-spectrum which should be consistent with auto-correlation function.

To maximise the H with respect to P and with further algebraic manipulations the extremised Entropy occurs when power is given by [6]:

$$P(f) = \frac{P_m \cdot \Delta t}{|1 - \sum_{n=1}^{m} a_{mn}\, e^{-2\pi i f \Delta t}|^2} \quad \ldots\ldots(4)$$

Here $P(f)$ is the power spectrum while P_m is power output by prediction error filter of order m+1 with elements a_{mn} which can be calculated from the matrix equation given below.

$$\begin{bmatrix} R_0 & R_1 & \cdots & R_m \\ R_1 & R_0 & \cdots & R_{m-1} \\ \vdots & \vdots & \ddots & \vdots \\ R_m & R_{m-1} & \cdots & R_0 \end{bmatrix} \begin{bmatrix} 1 \\ -a_1 \\ \vdots \\ -a_m \end{bmatrix} = \begin{bmatrix} P_m \\ 0 \\ \vdots \\ 0 \end{bmatrix}$$

Figure 1: Algebraic Relations governing Auto-correlation coefficients, Prediction error filter coefficients and Error Power output [6].

Here R (k) is the measured value of auto-correlation function which is dependent of a recursive relation involving prediction-error filter as given below.

To calculate auto-correlation coefficients too, prediction error filter coefficients are required which can be determined as shown in the below example for two-order prediction error-filter [6].

$$R_k = \frac{1}{N}\sum_{i=1}^{N-k} x_i \cdot x_{i+k} \quad \ldots\ldots (5)$$

$$R_k = \sum_{i=1}^{k} R_{k-i} \cdot a_i \quad \ldots\ldots (6)$$

For instance, consider a two-point prediction filter: $[1\ a_{11}]$

Now the regressive function will scan through data and filter will predict forward terms using its preceding term and least-square fit is performed to get best value of a_{11} which minimizes error P_1 [6]. For the filter to be stable the coefficients a_{ij} should be less than unity and so to satisfy the criterion the forward power output is averaged by power output obtained by operating the filter in reverse direction.

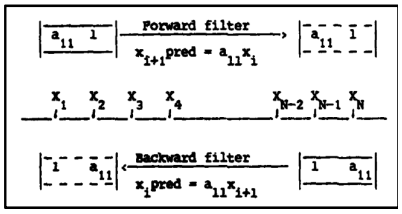

Figure 2: Prediction Error Filter [6]

Thus, by minimizing error with respect to a_{11} we get the following equation shown below [6],

$$a_{11} = \frac{2 \cdot \sum_{i=1}^{N-1} x_i \cdot x_{i+1}}{\sum_{i=1}^{N-1}({x_i}^2 + {x_{i+1}}^2)} \quad \ldots\ldots (7)$$

This implementation can be followed for higher number of poles too. Once auto-correlation coefficients are found, power can be calculated.

2.4 *CONTINUOUS WAVELET TRANSFORM*

This Algorithm computes sliding cross-correlation of signal X(t) and family of wavelets as shown below [7]:

$$Y(a,b) = \frac{1}{\sqrt{a}}\int X(t) \cdot \Psi^*\left(\frac{t-b}{a}\right) dt \quad \ldots\ldots (8)$$

Here a and b are the scales and time shifts of reference wavelet Ψ, Ψ^* is the complex conjugate of reference wavelet. The reference wavelet is also called mother wavelet. Mother wavelets are mean zero oscillatory signals which are given as input by the user. The mother wavelet is cross-correlated with the signal by stretching, dilating and traversing wavelet over it. Thus, longer wavelets are used for low frequencies to improve frequency localization at the cost of temporal localization while for the higher frequencies it works in opposite sense [7]. This algorithm achieves variable time-frequency resolution. Continuous wavelet transform gives wavelet coefficients as output which can be used to plot scalogram [8]. Scalogram is just analogous to spectrogram from short-time Fourier transform.

3. PROBLEM DEFINITION

Target of this study is to achieve very fine (almost continuous; ~0.1Hz/0.1sec) resolution in both frequency and time simultaneously and to be able to observe multiple frequencies modes at any time instant (if available) that might get activated due to fluid-acoustic coupling, find how the frequency clusters/contours vary with time.

ISBN - 978-93-95038-50-8

4. RESEARCH METHODOLOGY

4.1 *SHORT TIME-FOURIER TRANSFORM*

The hyper-parameters which are critical for high resolution results are choosing length of window as the resolution in time is equal to ratio of length of window and sampling frequency of the signal. But frequency resolution is inverse of that ratio. Thus, larger window gives better frequency resolution but worse time resolution and vice versa. This characteristic of FFT can be exploited by adding zeroes to extend window size, this is called zero-padding and it essentially gives interpolation of frequency data by adding frequency bins due to larger window size without affecting time resolution. But actually, it does not increase resolution in frequency as it is just giving interpolant values.

4.2 *WIGLER-VILLE DISTRIBUTION*

In this Algorithm the signal data was first converted to analytical signal using Hilbert transformation function in MATLAB. Hilbert Transform provides minimum phase-response as the imaginary part of the signal. Further Kernel K(n) was generated by overlaying segments of analytical signal (z) over its conjugate (z*) where n iterates from 1 to N_s (total length of signal) as shown in equation below:

$$k_n(l) = \begin{cases} z(n-l)z^*(n+l), & |l| \le min\{n, N_s - n\}, \\ 0, & |l| > min\{n, N_s - n\}. \end{cases} \quad \text{.....(9)}$$

$$K(n) = \{ k_n(-l), \dots k_n(0), \dots k_n(l)\} \quad \text{.....(10)}$$

Here l is the length of window which can be taken in exponents of 2 just like FFT. Further FFT was performed over kernel K(n) to get wigler-ville distribution which gives power spectrum. For pseudo-Wigler ville distribution, ambiguity function was taken from MATLAB in-built function to perform wigler-ville distribution algorithm in order to get power spectrum.

4.3 *MAXIMUM ENTROPY METHOD*

In this algorithm, a recursive code is used to find auto-correlation coefficients with equation 5 and 6 as shown in literature review of the algorithm. Further to get error power for every iteration using the algebraic relation shown in figure 2 we can use the following equation [6]:

$$P_m = P_{m-1} \cdot \left(1 - a_{m,m} \cdot a^*{}_{m,m}\right) \quad \text{.....(11)}$$

Here m denotes the number of iterations completed and it runs from 1 to M (total length of filter). Error Power output is initialized as [6]:

$$P_0 = \frac{1}{N} \sum_{i=1}^{N} x_i \cdot x^*{}_i \quad \text{.....(12)}$$

Here N is total length of signal, x_i and $x^*{}_i$ denote i^{th} element of signal and its conjugate respectively. The length of filter also known as poles in signal processing terms is a hyper-parameter which must be tuned to get finer results. The recursive algorithm calculates filter coefficients and error power for each iteration till it reaches user-input filter length. But selecting filter length is very difficult as too short filter will lead to smoothening of data while too high filter length will lead to splitting of peaks. From various iterations it was found during this study that filter length of 10-25 poles works good for the data encountered in Large segmented solid rocket motor.

ISBN - 978-93-95038-50-8

4.4 *CONTINUOUS WAVELET TRANSFORM*

In this Algorithm, Mother wavelet is a hyper-parameter which needs to be given as input. The characteristics of mother wavelet affect the resolution of scalogram which is generated from continuous wavelet transform. There are three pre-defined mother wavelets available in MATLAB in-built function to perform continuous wavelet Transform namely Morse wavelet, Mortlet Wavelet and Bump Wavelet. All these wavelets were analyzed in this study.

5. RESULTS AND DISCUSSIONS

Reference Signal was generated to validate all the algorithm implementations as given below:

Table 1: Characteristics of signal

Parameter	Value
Sampling Frequency (f_s)	500 Hz
Time Range	0-140 sec
Signal-to-Noise Ratio	20
Number of Frequency tracks	6

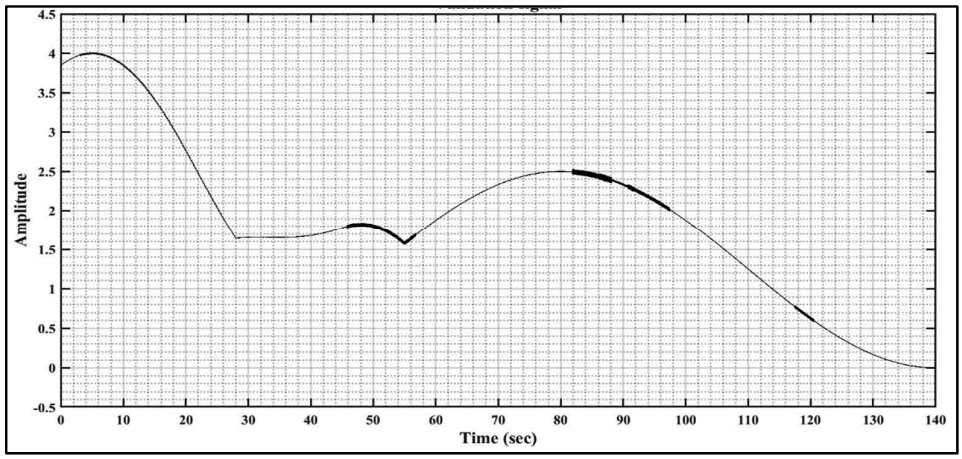

Figure 3 : Reference Signal

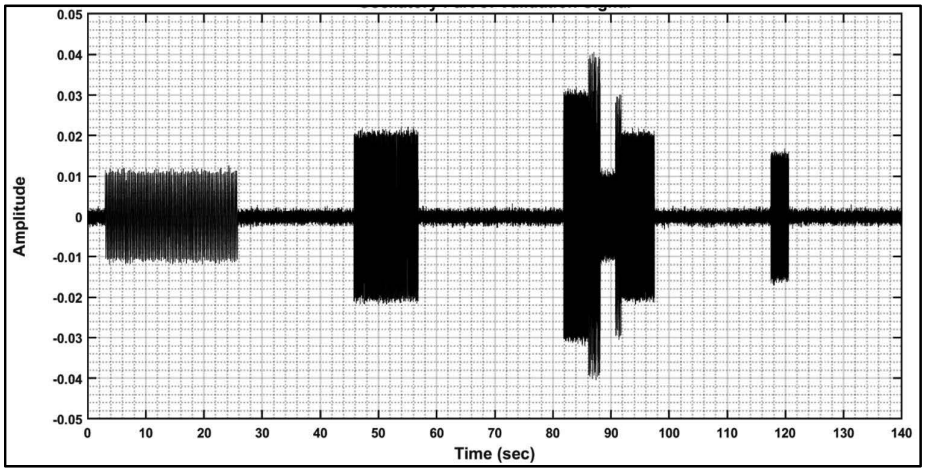

Figure 4: Oscillatory Part of Reference Signal

Mean signal is composed of two Gaussian humps (Hann function) and a quadratic function to mimic solid rocket motor pressure like behavior. Mean signal is superimposed over oscillatory signal which has 6 continuous frequency trains in different time segment to mimic solid rocket motor pressure oscillation behavior.

Table 2: Continuous Frequency tracks

Frequency track (Hz)	Time Range (sec)
5-4.5	3 - 25.8
10-9.5	45.7 - 56.9
32-31	81.8 - 88.2
37-36	86.1 - 91.6
29-30	90.6 - 97.3
65-64	117.3 - 120.4

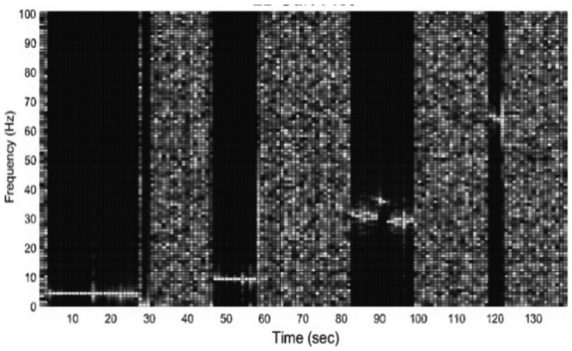

Figure 5: Spectrogram without overlap between windows using STFT

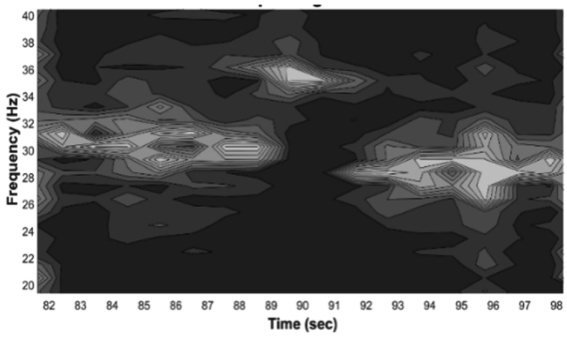

Figure 6: Spectrogram without overlap zoomed to time range of 82 -98 sec

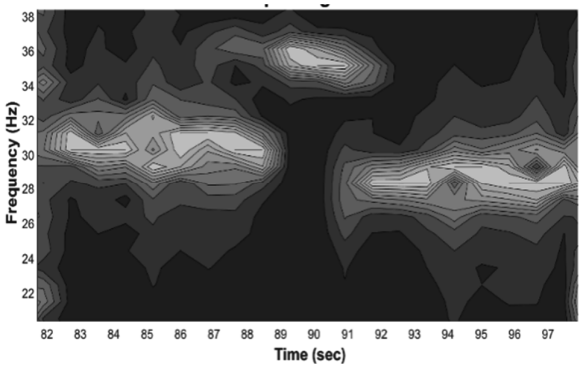

Figure 7: Spectrogram using 20% overlapping window in STFT

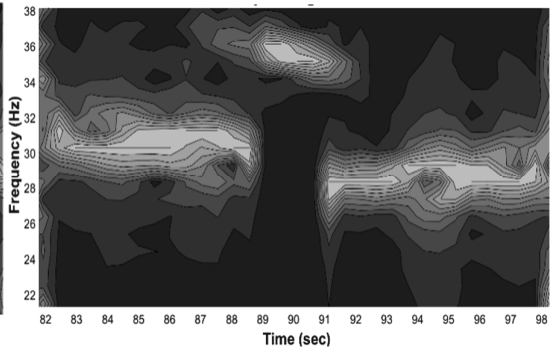

Figure 8: Spectrogram using 50% overlapping window in STFT

It is evident from figure 5 that FFT captures a lot of noise in between frequency tracks. Figure 6 is spectrogram zoomed to time range 82-98 sec as it is region of interest because of three coincident frequency tracks. Further in figure 7 and figure 8 it can be observed that using higher overlapping ratio increases the frequency resolution a bit without affecting much on temporal results. But this increases in resolution is quite low and after 50% overlap the improvement is not visible. Further results from all algorithms will be compared for this region of interest.

ISBN - 978-93-95038-50-8

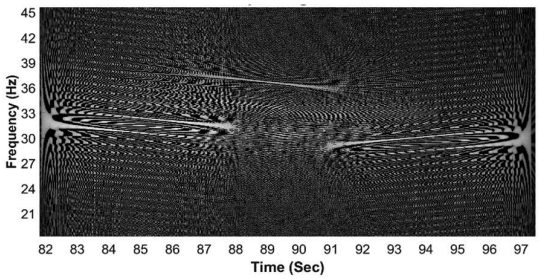

Figure 9: Power Spectrum from Wigler-Ville Distribution

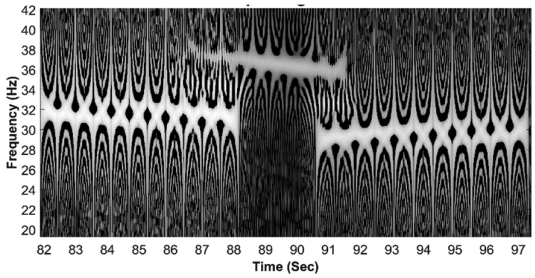

Figure 10: Power Spectrum from Pseudo Wigler-Ville Distribution

From the results of Wigler ville distribution in figure 9 it can be observed that the frequency tracks are highly resolved and overall frequency-time resolution is quite high in the spectrum but a lot of noise is captured in the power spectrum. The pseudo-Wigler ville distribution gives significant reduction in noise but it smoothens out the frequency track making resolution worse.

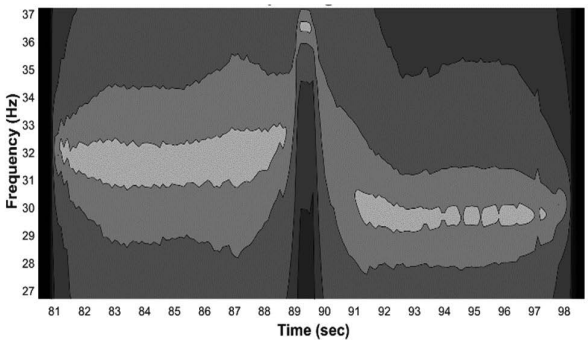

Figure 11: Power Spectrum from Maximum Entropy Method using 10 poles

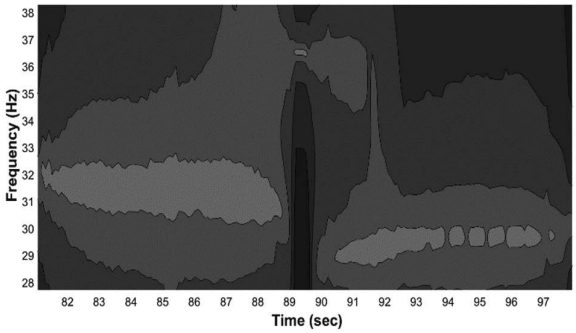

Figure 12: Power Spectrum from Maximum Entropy Method using 20 Poles

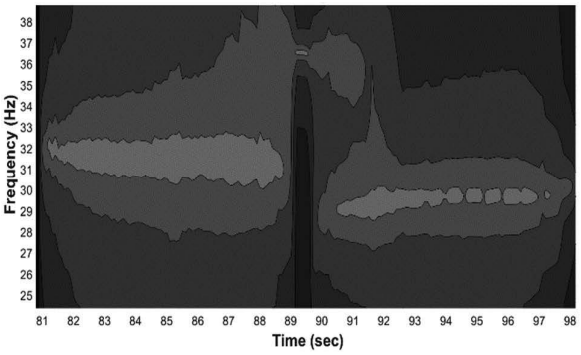

Figure 13: Power Spectrum from Maximum Entropy Method using 25 poles

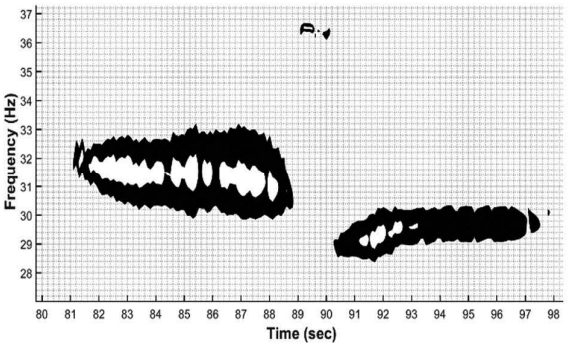

Figure 14: Filtered Power Spectrum from Maximum Entropy Method using 25 poles and filter of 6.3×10^{-4} W/Hz and 2.5×10^{-3} W/Hz

From the results of Maximum Entropy From the results of Maximum Entropy Method, it can be observed at lower poles (10 poles) in figure 11 there is some visible interference between frequency tracks. This interference is reduced as the number of poles increase. After 25 poles the peaks were showing splitting. But with this method there is some interference when frequency tracks coincide. Filtering Power spectrum gives improved results but still some frequency track is lost to interference.

ISBN - 978-93-95038-50-8

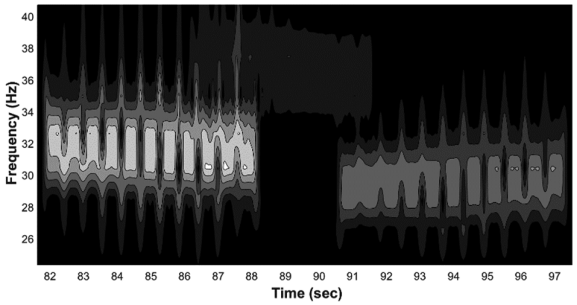

Figure 15: Scalogram from continuous wavelet transform using bump mother wavelet

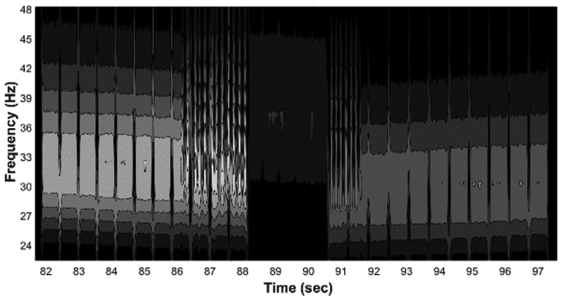

Figure 16: scalogram from continuous wavelet transform using morse mother

Scalogram obtained from Continuous wavelet Transform show high temporal resolution as the frequency tracks precisely start and stop at the time ranges which were used in signal generation as provided in table 2. From all the three wavelets used as mother wavelet, bump wavelet gives best frequency resolution but it is still quite coarse.

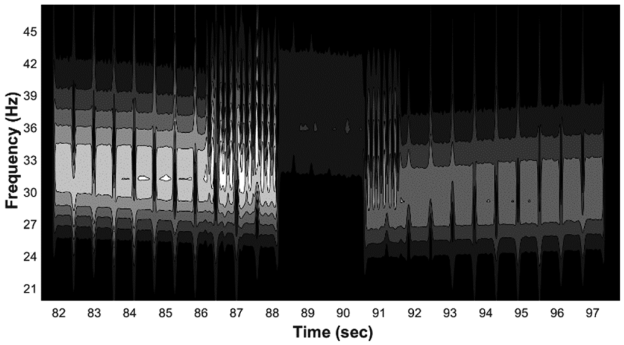

Figure 17: scalogram from continuous wavelet transform using Mortlet mother wavelet

Table 3: Comparision between Algorithms

Algorithms	Spectral Characteristics	Limitations
Short-Time Fourier transform	Power of signal	Very Coarse resolution
Wigler-Ville Distribution	Frequency and Time (even coincident frequency tracks)	Very high computational space requirement
Maximum entropy Method	Frequency and Time	Interference between coincident frequency tracks
Continuous Wavelet transform	Time	Coarse frequency resolution

6. CONCLUSIONS

From the Results it can be concluded that Wigler-Ville Distribution gives the best resolution in frequency-time but is very computationally heavy algorithm while Maximum Entropy Method also gives fine frequency-time resolution but it shows some interference when frequency tracks are coincident. Hence, Wigler-ville distribution and Maximum Entropy Method are best suitable for analysis of Large Segmented Solid Rocket Motor pressure data. But Wigler-ville can only be performed over small-time interval due to high space requirements. Thus, Maximum Entropy method can be performed over full data, and then if required, small time domain data can be analyzed further with wigler-ville distribution to get finer results.

ISBN - 978-93-95038-50-8

REFERENCES

1. K. Dotson, et.al, Vortex Shedding in a Large Solid Rocket Motor Without Inhibitors at the Segment Interfaces, Journal of Propulsion and Power Vol. 13, No. 2, March – April 1997, https://doi.org/10.2514/2.5170
2. Gröchenig, K. (2001). The Short-Time Fourier Transform. In: Foundations of Time-Frequency Analysis. Applied and Numerical Harmonic Analysis. Birkhäuser, Boston, MA. https://doi.org/10.1007/978-1-4612-0003-1_4
3. O'Toole, J., Mesbah, M., and Boashash, B. (2005). A discrete time and frequency Wigner Ville distribution: Properties and implementation. 8th International Symposium on DSP and Communication Systems, DSPCS'2005, Noosa, Queensland, Australia, 19-21 December 2005.
4. Bradford, Yang, J., & Heaton, T.H. (2005). Variations in the Dynamic Properties of Structures : The Wigner-Ville Distribution by S Case.
5. Y.S. Shin, J.J. Jeon, Pseudo Wigler-Ville Time-Frequency distribution and its applications to machinery condition monitoring, Shock and Vibration, Vol. 1, No. 1, pp. 65-76 (1993) https://doi.org/10.3233/SAV-1993-1109
6. R.W Herring, Maximum Entropy Spectral analysis and Radar signal processing, CRC report Number 1330, January 1980
7. Tary JB, Herrera RH, van der Baan M. 2018 Analysis of time-varying signals using continuous wavelet and synchrosqueezed transforms. Phil. Trans. R.Soc. A 376: 20170254. http://dx.doi.org/10.1098/rsta.2017.0254
8. Sadowsky, J.S. (1994). The continuous wavelet transforms: a tool for signal investigation and understanding.

ISBN - 978-93-95038-50-8

Predicting the Shear Properties in S-glass Epoxy Composite by Finite Element Analysis

Pullela Ramalakshmi*, Kongari Akshaya, Pinninti Ravinder Reddy

Mechanical Engineering Department
Chaitanya Bharathi Institute of Technology, Hyderabad, Telangana State, 500 075
Email: pramalakshmi_mech@cbit.ac.in

ABSTRACT

S-glass is technically significant glass fiber. It has high stiffness, strength and softening point. This fiber finds application in light weight armor. In the present work, S-glass reinforced composite is considered to examine the shear properties by finite element analysis. To examine the shear properties, the specimen mentioned in ASTM C 1425 is selected. In the standard, the sample dimension is 30 mm X 15 mm X 2 mm by maintaining the notch separation as 6mm. In the present work, shear properties will be examined at the sample thickness of 10 mm and the notch separation will be varied from 1 mm to 5 mm to understand the variation of shear properties. The shear properties examined from this work will be useful in design data considerations.

Keywords: *S- glass epoxy composite, woven fabric, FEA*

1. INTRODUCTION

S-glass (R Glass) has higher tensile strength and modulus than E glass (electrical glass), with better wet strength retention. Higher ILSS (inter laminate shear strength) and wet out properties are achieved through smaller filament diameter. S-glass (called R-glass in France) has better properties than E-glass, includinghigher thermal stability, but its higher cost has limited the extent of its use. Wallenberg and Brown [1] have recently described the properties of experimental calcium aluminates glass fibers with stiffness's as high as 180GPa. S-Glass has a typical nominal composition of SiO_2 65wt%, Al_2O_3 25wt%, MgO 10wt%. Some other materials may also be present at impurity levels.

Epoxy resins are low molecular weight pre-polymers or higher molecular weight polymers which normally contain at least two epoxide groups. The epoxide group is also sometimes referred to as a glycidyl or oxirane group. A wide range of epoxy resins are produced industrially. The raw materials for epoxy resin production are today largely petroleum derived, although some plant derived sources are now becoming commercially available.

Epoxy resins are polymeric or semi-polymeric materials, and as such rarely exist as pure substances since variable chain length results from the polymerisation reaction used to produce them. High purity grades can be produced for certain applications, e.g., using a distillation purification process. One downside of high purity liquid grades is their tendency to form crystalline solids due to their highly regular structure, which require melting to enable processing.

The equivalent weight or epoxide number is used to calculate the amount of co-reactant (hardener) to use when curing epoxy resins. Epoxies are typically cured with stoichiometric or near-stoichiometric quantities of curative to achieve maximum physical properties. As with other classes of thermoset polymer materials, blending different grades

* Corresponding author: E-mail: pramalakshmi_mech@cbit.ac.in

of epoxy resin, as well as use of additives, plasticizers or fillers is common to achieve the desired processing and/or final properties, or to reduce cost.

The demand on material performance is so great and diverse that individual materials used alone are not able to satisfy them. Composites are those materials that can satisfy the desired requirements which were unattainable by these individual ones.

2. LITERATURE REVIEW

Over years several mathematical models are developed to predict the properties of composites [2]. Failure theories were proposed by Hinton and Soden [3, 4] in 1998. Soden et al. [5] and Chamis et al. [6] theory performed well to predict the ILSS (interlaminar shear strength) for unidirectional continuous fiber reinforced polymer. Murthy and Chamis [7] and Huang et al. [8] suggested micromechanical theory illustrated in Hinton and Soden's study. Liu et al [9] observed that twenty-five-point four percent (25.4%) increase in the ILSS while adding 0.5 wt.% MWCNTs (multi walled carbon nanotubes) and 10 phr n butyl glycidyl ether for GFRC. Pullela et al [10] predicted the distribution of ILSS in neat resin and CNT reinforced carbon epoxy composite as per ASTM C1425 by experimental method for thin laminate. For 120% increase in the applied load, ILSS enhanced by 87% upon adding 1 wt.% of amine functionalized long length multi walled nanotube. For thin laminate, the average ILSS value from experimental method is observed to be 34.98 MPa and its corresponding value from ANSYS is 36.99 MPa when the applied average load is 2,892.28 N. ILSS in neat resin and CNT reinforced carbon epoxy composite [11] from experimental method as per ASTM C1425 for thin laminate is 32 MPa and 60 MPa. When the distance between the notches is such that the stress fields around the notches interact, the measured interlaminar shear strength increases.

3. PROBLEM DEFINITION

Ramalakshmi et al [10] examined S-glass epoxy composite by experimental method and finite element analysis for thin and thick laminates by maintaining the notch separation as 6 mm as per ASTM C 1425. In the present work, the notch separation will be varied from 1 mm to 5 mm and its shear properties will be examined for thick laminate at an average load of 2787 N. The boundary conditions and volume fraction of the composite mentioned in [10] will be imposed on the present problem statement.

Table 1: Recommended Dimensions for Double-Notched Compression Specimen in ASTM C 1425

Dimension	Description	Value, mm	Tolerance, mm
L	Specimen Length	30	±0.10
h	Distance between the notches	6	±0.10
w	Specimen Width	15	±0.10
d	Notch Width	0.5	±0.05
t	Specimen thickness	2	-

ISBN - 978-93-95038-50-8

Table 2: Recommended Dimensions for Double-Notched Compression Specimen in the present work

Dimension	Description	Value, mm	Tolerance, mm
L	Specimen Length	30	±0.10
h	Distance between the notches	1 to 5	±0.10
w	Specimen Width	15	±0.10
d	Notch Width	0.5	±0.05
t	Specimen thickness	10	-

4. RESEARCH METHODOLOGY

The sample size from reference [10] was 30 mm X 15 mm X 10 mm and acid digestion was conducted as per ASTM D 3171. The volume fraction of the fiber, matrix and void content was 60.8 %, 38.7% and 0.5% respectively. Table 1 shows the material properties of the composite by extended rule of mixtures [12]. Orthotropic material properties are used to develop the finite element model.

Table 3: Properties of S-glass epoxy composite

Elastic constant	Volume fraction of fiber is 60.8
E_1 (GPa)	35.72
E_2 (GPa)	35.72
E_3 (GPa)	12.86
ϑ_{12}	0.095
ϑ_{23}	0.912
ϑ_{13}	0.912
G_{12} (GPa)	4.42
G_{23} (GPa)	4.41
G_{13} (GPa)	4.41

In the present work, ANSYS finite element analysis software is used to predict the shear properties of S-glass epoxy composite. There are three modules in this software. In the preprocessor module, geometric model is generated and Shell 281 from ANSYS library [13] is selected for the generation of finite element model. Shell element has four corner nodes, four mid-side nodes. Each node has three translational and rotational degrees of freedom. Orthotropic materials properties are provided as input and finite element model is generated. The finite element model has 2149 nodes and 680 elements. In the solution module, boundary conditions mentioned in ASTM 1425 are imposed and load mentioned in reference [10] is applied. In the general post processor module, by element table the shear properties [11] of S-glass epoxy composite are predicted.

ISBN - 978-93-95038-50-8

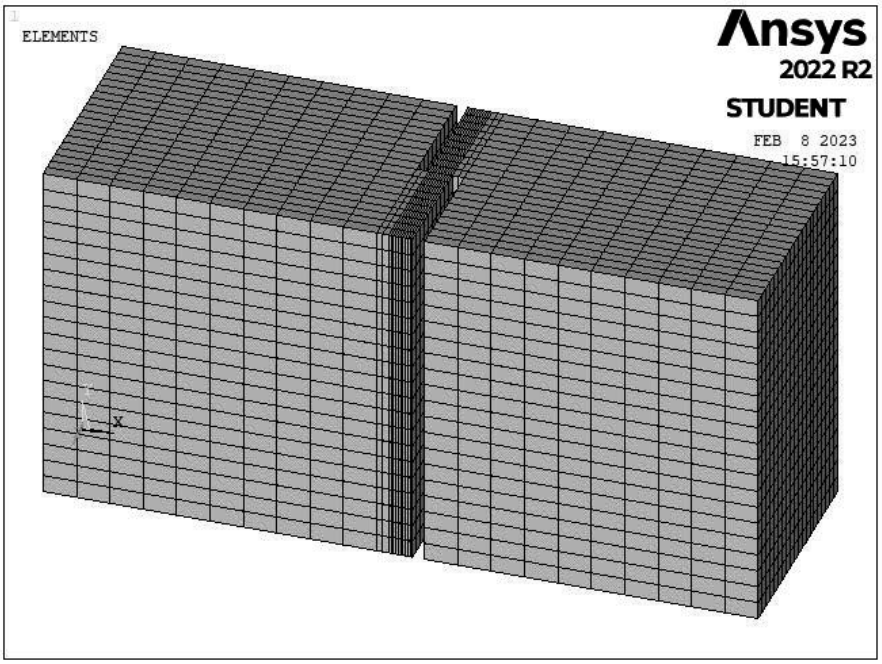

Figure 1: Finite element model of thick laminate whose sample size is 30 mm X 15 mm X 10 mm at notch separation of 1 mm.

5. Results and Discussion

In this section, the distribution of interlaminar shear strength (ILSS) and instantaneous shear modulus (ISM) in S-glass epoxy composite is presented in table 4 when the notch separation (h) is varying from 1 mm to 5mm. The plot of interlaminar shear strength at a notch separation of 1 mm is presented in figure 2 and its corresponding instantaneous shear modulus is shown in figure 3.

Table 4 Distribution of Interlaminar Shear Strength and Instantaneous Shear Modulus in S-glass epoxy composite

Sl Num	h in mm	ILSS in MPa	ISM in MPa
1	1	5.12	5.03
2	2	4.77	4.62
3	3	4.47	4.39
4	4	4.21	4.08
5	5	3.98	3.39

From table 4, it is inferred that as the notch separation increases from 1 mm to 5mm, the distribution of interlaminar shear strength and instantaneous shear modulus decreases due to weak interaction of forces between the fiber and the resin. Peak value of ILSS and ISM is noticed to be 5.12 MPa and 5.03 MPa when the notch separation is 1mm due to the strong interaction of the shear stresses among the constituents of the composite.

From figure 5.1, least value of -0.31 MPa is noticed in the thick laminate due to the resistance offered by the fiber and the matrix. At the vicinity of the notch, ILSS is varying from 4.51 MPa to 5.12 MPa due to the strong interaction of the stresses between the notches.

ISBN - 978-93-95038-50-8

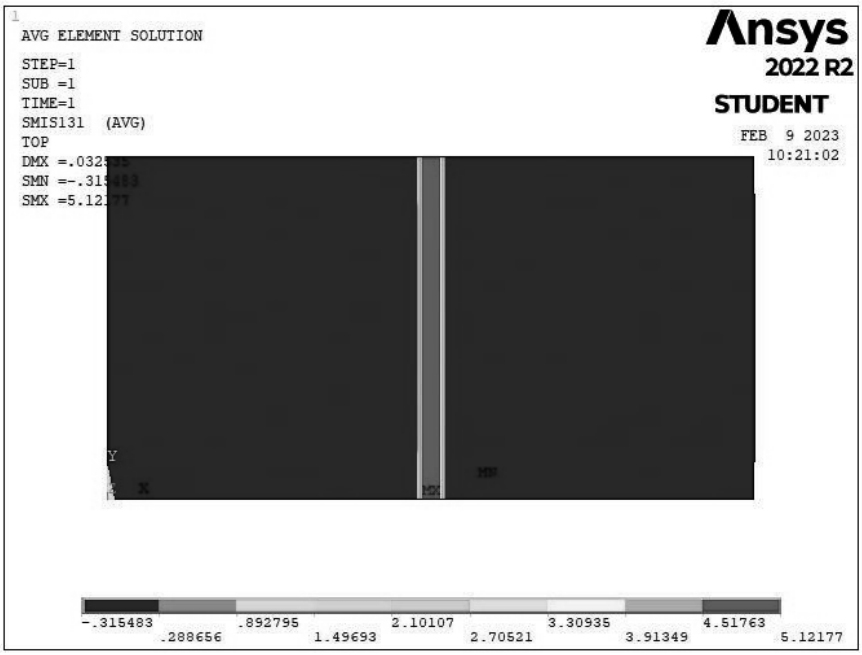

Figure 2: Distribution of Interlaminar shear strength in S-glass epoxy composite at a notch separation of 1mm

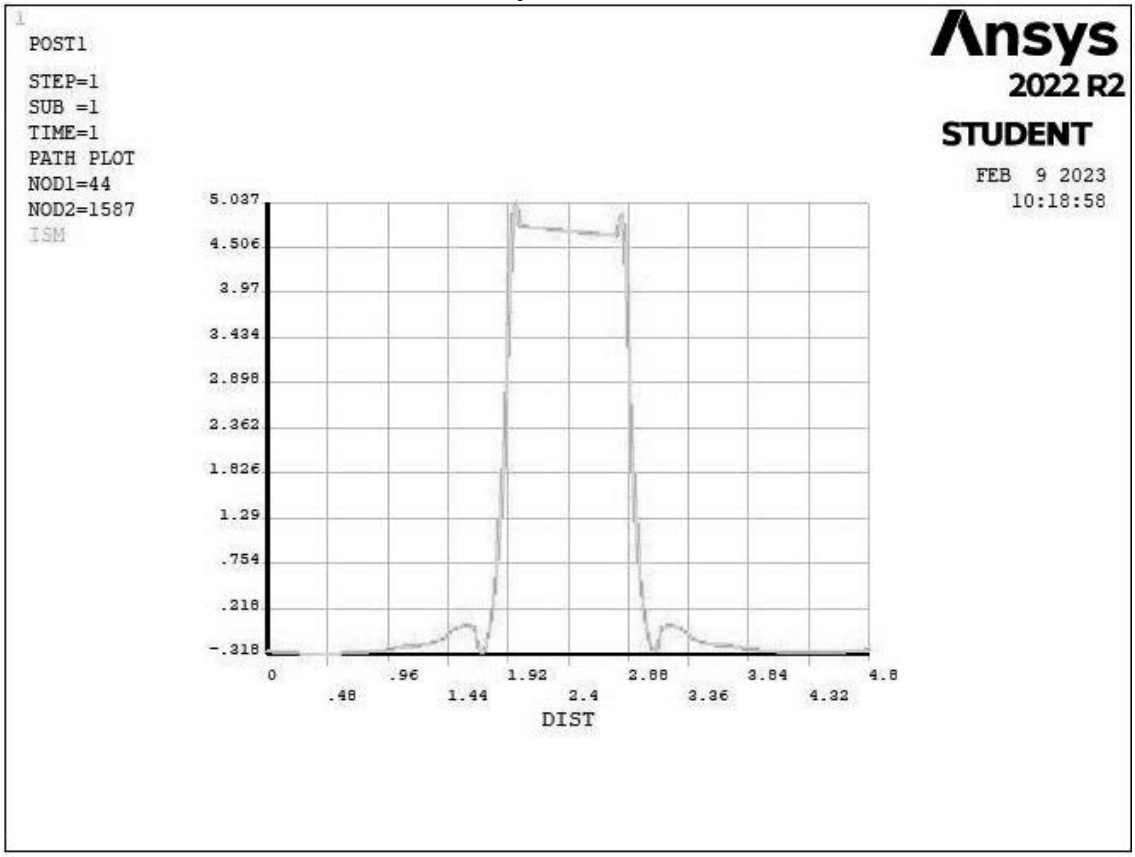

Figure 3: Instantaneous Shear Modulus in S-glass epoxy composite at a notch separation of 1 mm

ISBN - 978-93-95038-50-8

Path is plotted along the length of the specimen (DIST) with special focus on the notch separation to understand the distribution of ISM. The variation of ISM is shown in figure 5.2. When DIST is zero, minimum value of -0.31 MPa ISM is noticed and a sharp rise to 5.03 MPa is seen when DIST is 1.68 due to the strong interaction of the shear stresses between the notches. Between the notches, the variation of shear modulus is uniform and a sudden drop to -0.31 MPa is noticed due to the weak interaction of the stresses when the notches are far apart.

6. CONCLUSIONS

In the present work, instantaneous shear modulus in S-glass epoxy composite is predicted from the distribution of interlaminar shear stress and its corresponding deformation. It is concluded that when the notches are far apart, due to weak interaction of the stresses, shear properties are less. When the separation between the notches is 1mm, high values of interlaminar shear stress and instantaneous shear modulus is inferred due to the strong resistance offered by the constituents of the composite.

ACKNOWLEDGEMENTS

The authors thank Smt G Rohini Devi, Shri Anil Kumar, Dr I Srikanth and his team members of Ceramic Matrix Composite Division, HTCC at Advanced System Laboratory for their invaluable guidance provided in reference [10].

REFERENCES

1. Wallenberger and Frederick, “The effects of lithia and alumina on the viscosity and strength of commercial fibreglass and other glass compositions”, Glass Technology - European Journal of Glass Science and Technology Part A; 2011, Vol. 52, issue 4, pp. 117-126, doi : https://www.ingentaconnect.com/ content/sgt/gta/2011/00000052/00000004/art00003
2. Capello E, “Work piece damping and its effects on delamination damage in drilling thin composite laminates” , Journal of Materials Processing Technology; 2004 , Vol. 148, issue 2, pp.186-95, doi: 10.1016/S0924-0136(03)00812-4
3. Hinton, M. and Soden, P, “ Predicting Failure in Composite Laminates: The Background to the Exercise” , Composites Science and Technology; 1998, Vol. 58, issue 7, pp. 1001-10, doi: 10.1016/S0266-3538(98)00074-8
4. *P.D. Soden , M.J. Hinton , A.S. Kaddour , “Lamina properties, lay-up configurations and loading conditions for a range of fibre-reinforced composite laminates”, Composites Science and Technology;1998, Vol. 58, issue 7, pp. 1011-1022, doi.org/10.1016/S0266-3538(98)00078-5*
5. Soden P., Kaddour A., and Hinton M “Recommendations for Designers and Researchers Resulting from the World-Wide Failure Exercise”, Composites Science and Technology; 2004,Vol. 64, issue 3, pp.589-604, doi.org/10.1016/S0266-3538(03)00228-8
6. Chamis C. C, “Simplified Composite Micromechanics Equations for Strength, Fracture Toughness, Impact Resistance and Environmental Effects.” NASA Lewis Research Centre, 1984,Tech.Rep,doi https://apps.dtic.mil/sti/citations/ADA304541
7. Murthy PL, and Chamis CC “Integrated composite analyzer (Ican)- users and programmers manual” NASA Lewis Research Centre, 1986, Tech Rep, doi https://apps.dtic.mil/sti/citations/ADA301372
8. Huang Z M. “Micromechanical Prediction of Ultimate Strength of Transversely Isotropic fibrous Composites.” International Journal of Solids and Structures, 2001, Vol. 38, issue 22, pp :4147-4172, doi: 10.1016/S0020-7683(00)00268-7

9. Liu, Y., et al. “Role of Matrix Modification on Interlaminar Shear Strength of Glass Fibre/Epoxy Composites” Composites Part B: Engineering, 2012, Vol. 43,issue 1, pp. 95-98, doi: 10.1016/ j.compositesb.2011.04.037
10. P.Ramalakshmi, P.Anjani Devi, P.Ravinder Reddy, K.Yamuna and Y.Bharathi, “Estimation of interlaminar shear strength in glass epoxy composites by experimental and finite element method”, Journal of Physics:Conference Series,2019, Vol.1240,pp.1-10,doi:10.1088/1742-6596/1240/1/012027
11. P. Ramalakshmi, T Rushyanth and P. Ravinder Reddy, “Estimation of instantaneous shear modulus in neat resin and multi walled nanotube reinforced carbon epoxy composites by finite element analysis ” , Recent Advances in Computational and Experimental Mechanics , Lecture Notes in Mechanical Engineering, Springer Nature Singapore 2022, Vol – I, , pp. 97 -109, doi:10.1007/978-981-16-6738-1_8
12. Aly MF, Goda IGM, Hassan GA, “Experimental investigation of the dynamic characteristics of laminated composite beams”, International Journal of Mechanical & Mechatronics, 2010, Vol. 10, issue pp:59–68
13. ANSYS SOFTWARE R2022 Version; ANSYS HELP: Element Reference, ELEMENT LIBRARY: SHELL 281 Input data

Visualization of Spokes Mode in a Hall Effect Thruster

Souradeep Roy Choudhury*, Samvram Sahu, Vara Prasad Kella, Vikash Kumar

Liquid Propulsion Systems Centre, Indian Space Research Organization,
Thiruvananthapuram, Kerala: 695547;
National Remote Sensing Centre, Indian Space Research Organization, Hyderabad, Telengana: 500084
Email: [1]souradeep28@gmail.com, [2]samvram.iist@gmail.com, [3]varapk51@gmail.com and
[4]vikashkumar@lpsc.gov.in

ABSTRACT

The present work investigates the dynamics of rotating spokes modes in a Hall Effect Thruster (HET) also known as a Stationary Plasma Thruster (SPT). Understanding these modes is important to investigate electron transport phenomena which constitute power losses for the thruster. Furthermore, the results may be inputs to future simulation studies. In this paper, post processing technique of raw images to visualize the spoke modes is presented. Images of an 85 mm mean diameter SPT anode channel, operated at 783 W at a pressure of $3.2\ x\ 10^{-5}\ mbar$ *were acquired via a High-Speed Camera. The images so obtained were extremely saturated with the cathode intensity while the anode channel intensity was dominated by its DC component. Automated image processing techniques were then applied. In this process, the images were normalized with respect to the camera specifications and the cathode and anode were segmented from the anode channel image frames using Otsu's thresholding. The normalized and extracted regions are subjected to a string of post-processing involving normalization by mean image and removal of noise and the DC component. This resulted in an improved contrast as well as removal of saturation in the images due to the cathode, enabling one to focus exclusively on spokes modes.*

Keywords: *Hall Effect Thruster, Stationary Plasma Thruster, Rotating Spokes Mode*

1. INTRODUCTION

Hall Effect Thrusters find wide-range applications in space propulsion, starting from propulsion devices for orbit transfer [1] to deep space travel ([2], [3]), among others. In recent years, a significant volume of literature has been devoted to the simulation ([4, 5]) and diagnostics of HET's ([6, 7]), tackling several open problems along the way. However, the physics of the thrusters is still not fully understood. One such open problem is the anomalous cross-field electron transport.

In a typical HET, the magnetic field lines are parallel to the radial direction of the anode channel alongside an electric field along the axial direction emanating from the anode. Once placed in a magnetic field, a moving charge rotates about an axis normal to both the velocity as well as the magnetic field. For dimensions greater than the larmour radius, the charged particle makes a full rotation and hence can be confined by the magnetic field while for dimensions less than this length, the species would only be deflected away from their direction of motion.

In an HET, the anode channel depth is greater than the larmour radius of an electron but lesser than that of an ion. Hence, the electrons follow a helical path in the channel, their centers forming concentric arcs residing inside the channel where they remain confined. The ions, in contrast, are relatively unaffected by the magnetic field and free to be accelerated by the external electric field. This ideality is however, not always observed during operation of the thruster, which may give rise to several modes depending upon the operating conditions [8].

*Corresponding author: E-mail: souradeep28@gmail.com

Due to inhomogeneities in the magnetic field, interactions between electrons and the wall of the thruster channel [9], plasma instabilities [10] or other unknown factors, the electron density may fluctuate along the channel direction. The emergence of this additional fluctuating electric field along the channel leads to an axial drift velocity, referred to as the anomalous cross-field electron transport problem. This phenomenon would lead to power losses in the thruster operation, since the additional electron current would not contribute to the thrust but would consume power to sustain itself.

High speed imaging has been used as a nondestructive method to probe into these instabilities [11, 12]. The cross-field current density carried by the spokes modes has also been quantified using segmented anodes, establishing that in some cases, the spokes modes might even carry 50 % of the total current [13], leading to further insights from simulations and theoretical modeling of the phenomenon [14, 15].

While the universal cause for spokes modes is still unknown, it has been studied in a wide variety of operating conditions on a host of different thrusters [12 - 15], suggesting that spokes modes have a fundamental origin. While the physics is still not understood completely, all of the literature points to the increasing need for more experimentation, analysis, theoretical modeling as well as simulations to gather a greater variety of data under different operating conditions for different hardwares.

The current work is divided into six sections. Section 0 details the experimental setup and the various operating conditions used. Section 0 describes the various techniques applied to the images in order to extract useful information about the spokes modes. Section 0 elucidates the results of the experimentation and subsequent analysis. Section 0 ends with a few concluding remarks and possible future avenues in this direction.

2. Experimental Setup and Methodology

Experiments are carried in a cylindrical vacuum chamber with diameter 1.6 m and length 4 m. The chamber is equipped with pumping system consists of roughing pumps, turbo molecular pumps, cryo pumps and cryo cold heads. The pumping system can maintain the vacuum at 9.11×10^{-5} mbar with Xenon load of $3\ \mathrm{mg\ s^{-1}}$. An SPT of mean diameter 85 mm is chosen for these studies. The hardware is designed for optimized performance at 1.5 kW with 3.2 mg s^{-1} anode flow rate. However due to the facility limitations, in the present studies, the hardware was operated at a discharge voltage of 300 V, a discharge current of 2.61 A, flow rates of $30.18\ \mathrm{mg\ s^{-1}}$ and $3\ \mathrm{mg\ s^{-1}}$ for the anode and the cathode respectively. The magnets were restricted to a current of 0.7 A, with the inner magnet drawing 3.8 V while the outer magnet consumed 3.1 V. The vacuum pressure in the chamber was 3.2×10^{-5} mbar. High speed images were acquired using Phantom make V 2012 model camera in monochrome at a rate of 60000 frames per second, with a total span of 50001 frames being captured. This led to a total time span of 0.8335 seconds. The channel was captured through the direct view port from the rear doom of the vacuum chamber. Each of the images contained 384 x 288 pixels with individual pixel intensities being 10 bit integers. Although the camera specification mentions 12 bits as the depth of each pixel, the packed raw cine files use a depth of 10 bits [15] to ensure faster transfer.

3. Data Analysis and Image Processing

Reading the Images

The raw images acquired were contained in a proprietary extension, the .cine file. The file was manipulated according to the documentation [15] and the camera metadata was read,

followed by the images. An open-source file reader [17] was modified to be dynamic with respect to the input files such that parameters like the image size, the frame rate and the black and whitelevels were obtained from the metadata contained in the file itself. This enabled the modified code to be able to read arbitrary image sizes, as opposed to merely 8, 16- or 48-bit pixels in the original code, proving extremely essential for the later analysis since all the pixels in the dataset were 10 bit long and could not be read by the original syntax.

Pre-processing and Post-processing

The camera uses the 'blacklevel' and the 'whitelevel' to prevent problems like oversaturation and losing out on valuable luminosity [15] by specifying the minimum and maximum intensities detectable by the sensor respectively. Hence, pixels with intensities outside this range are faulty and unreliable. Once they are discarded, the remaining valid pixels were rescaled. Both these quantities were read from the camera setup information [15], enabling further automation.

Once the images are pre-processed, the contrast for the anode channel needs to be enhanced. Following previous literature [11] as well as introducing image-processing techniques led to improvements in the image quality as well as important insights on the physics of the process.

The first step in this process was to normalize the images, as per Equation **…..**(1).

$$I_{normalized}(\boldsymbol{r},t) = \frac{\sum_{\boldsymbol{r}',t'} I(\boldsymbol{r}',t')}{\sum_{\boldsymbol{r}'} I(\boldsymbol{r}',t)} I(\boldsymbol{r},t) \qquad \text{…..(1)}$$

where $I_{normalized}(\boldsymbol{r},t)$ is the intensity afternormalization at spatial position $\boldsymbol{r}$ and time t.

$I(\boldsymbol{r},t)$ is the intensity before normalization at spatial position $\boldsymbol{r}$ and time t.

As a result of this normalization, the mean of any image at a particular timestamp becomes constant, cancelling out the net temporal fluctuations. This uniformity in time enables the use of averaging methods for further image processing techniques wherein instead of each image, the mean image could be dealt with as a representative unit. Hence, the intensities were averaged over time to get an average profile $I_{mean}(\boldsymbol{r})$ for different spatial co-ordinates $\boldsymbol{r}$.

The thruster now appeared as a bright surface and the background was composed of relatively low intensities. The region could be geometrically segmented into a circular cathode, a ring-shaped anode and a background. Along the same lines, a threshold was required such that a mask could be formed by substituting all the pixels as 1 for being higher than the threshold and 0 otherwise.

Azimuthal symmetry of the anode channel allowed the use of global thresholding methods whereby the threshold is a constant independent of position. Amongst these, Otsu's thresholding algorithm [18] stands out in terms of simplicity and speed [19]. Once the pixels exceeding the threshold in intensity were singled out and the rest discarded, the nearest neighbors of all such surviving pixels were examined, both along the perpendicular axes as well as the diagonals. If the nearest neighbor of a surviving pixel also crossed the threshold, the two pixels would be part of a common blob. This was implemented using Connected Component Labeling [21], which builds on top of Union-Find strategies for Blob generation [22].

Implementing this led to the formation of two distinct blobs in the mean image corresponding to the cathode and the anode, along with a third blob in certain cases of high noise levels inside the anode cavity. Hence, in order to separate the anode, it was essential to

extract the parameters of each blob, including the area of the blob in terms of number of pixels covered, its centre, edge co-ordinates and so on. The anode was then characterized by the largest area, since the cathode was isolated below it and the noisy internal channel lay entirely inside its domain.

The final image processing step would be the detection of the inner and outer radii of the anode channel. To utilize the azimuthal symmetry of the system, the mean image was transformed to polar co-ordinates around the blob centre. The maximum radius was fixed as the minimal stretch of the bounding edges containing the anode blob. The angular bins were pre-defined from 0° to 360°. The pixel intensities were interpolated from pixel co-ordinates to the required grids. For faster handling of the data, the polar intensities were averaged with respect to the angular co-ordinate to obtain an averaged intensity distribution varying with radii.

For further automation, the pixels were global thresholded once more. The outer radius r_{max}, was the distance of the farthest pixel from the centre to cross the threshold while the inner radius r_{min}, would be the distance of the farthest pixel from the centre to lie below the threshold, provided it did not exceed r_{max}. However, since the overall process was dependent on a user defined radial resolution, it was necessary to check for convergence. Hence, the ratio between r_{max} and r_{min} was computed and forced to lie within a tolerance band of the actual radius ratio of the hardware, scaled down by a factor each time the limits were violated. This ensured a self-correcting feedback as well as scaling between hardware and image.

Equipped with the radii, each image was transformed to the polar basis with the radius bounded between $[r_{min}, r_{max}]$ and the convergent radial resolution. They were then converted back to the cartesian basis again for further analysis.

Analysis

The images obtained contain information only about the anode channel where the intensities fluctuate in time as well as space. However, not all such oscillations constitute rotating spokes modes which exhibit simultaneous oscillations in time as well as space. The oscillations retaining homogeneity in time are breathing modes which eclipse the weaker spokes modes. Therefore, it is essential to remove these modes for further analysis.

Hence, the circle fit images were normalized once more followed by reduction with the mean image. This led to only oscillating components surviving, being hence called AC coupled.

To focus exclusively on the channel, the anode was cropped out with the help of the edge co-ordinates obtained during anode segmentation. This led to images with reduced area, containing just the anode channel. Apart from reducing the number of pixels, it also eliminated the need for storing the channel centre coordinates, since it now lay exactly at the centre of all images.

For visualization of only the anode channel inhomogeneities, a mask was prepared such that pixels having a radius more than the outer radius and less than the inner radius were removed. These pixels were already zero pixels deemed unnecessary for visualization. The masked images were then contour plotted together in subplots with a global colorbar.

Although the images no longer contained the cathode or other sources of noise outside the anode, they still exhibited a wide range of fluctuation across different frames. This created problems while plotting different image frames together, since setting the limits of the colorbar merely by the extrema of the intensities caused a few images to be intense whereas the rest were all at the other end of the colorbar, with no attributes to distinguish them from each other.

ISBN - 978-93-95038-50-8

The colorbar limits were set at percentile values of the intensities, defined as the maximal intensity for which the cumulative probability equals the numerical value of the percentile (divided by 100). Any intensity above the maxima would then be colored the same as the colorbar maximum. This allowed the visualization of spokes modes all over the dataset.

The above process, however, was insufficient to remove the granular texture of the images. Median filtering was used wherefore each pixel, inside the bulk of the image, was placed at the centre of a rectangular window comprising of neighboring pixels. The median of this window was plotted instead of the original pixel intensity, within a bounded colorbar. This enabled clustering and removed the high degree of granularity present in the plots earlier. However, the window size, along with the percentile limits for the colorbar, had to be set based on trial and error and not automatically computed by the algorithm.

4. Results and Discussion

The parameter values are mentioned in Section 0. The rotating spokes modes seemed more probable due to the magnet currents (0.7 A) being less than the nominal value (1.3 A). For the forthcoming analysis, 20 frames were used, beginning with the first, corresponding to a time span of 0.33 seconds. The algorithm was implemented using Python 3.10 which took approximately 1 min 16.322 seconds for execution with 6 cores.

The raw data from the camera, having been pre-processed, was first visualized using contour plots with fixed and graded colorbars in grayscale, as shown in Figure 1(a). As expected, the images are highly saturated due to the cathode as well as noise, with no visible difference across frames. These images were then normalized to obtain slightly better contrast, as can be perceived from Figure 1(b).

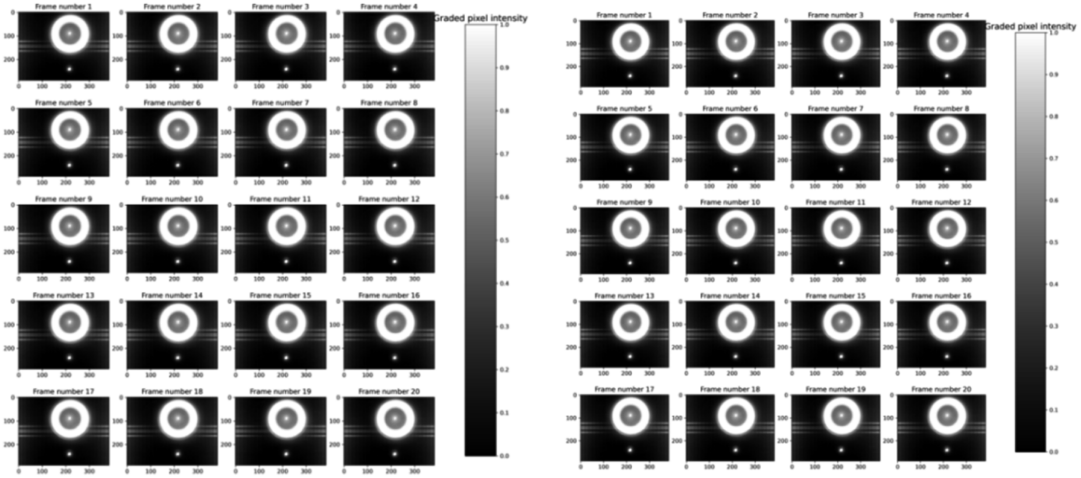

a. b.

Figure 1: (a) Camera pre-processed images, (b) Normalized images where the limits of the colorbar were kept at 10 percentile and 90 percentiles

Then the cathode was removed and the two concentric circles were fit. The initial radial resolution was 1 unit, the tolerance 0.4 and the actual radii ratio 1.5. This was processed to obtain Figure 2(a). The anode was subsequently extracted, to yield Figure 2(b).

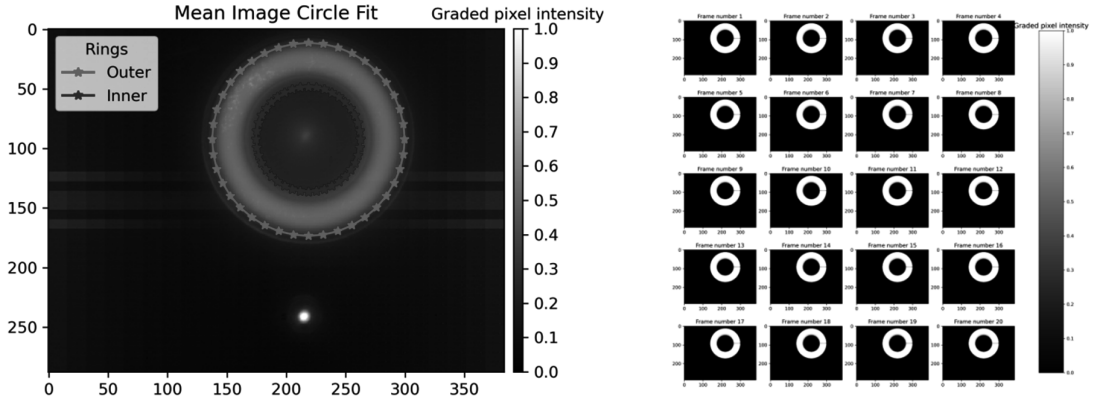

a. b.

Figure 2: (a) Fitting concentric circles on the anode channel. The colorbar was not restricted and Python default limits were not altered. (b) Cathode removal and concentric circle fitting. The colorbar limits were at 10 and 90 percentiles.

The highly saturated images were AC-coupled leading to more contrast, as shown in Figure 3(a). The colorbar was confined less than the other plots, due to the majority of pixels being zero. These cause the percentiles to be biased towards more extreme values than the usual 10 - 90 percentiles. Finally, the anode was scooped out, a mask was applied outside the channel and false color was used with a more limited colorbar due to the huge variation across the channel. The window size of five was fixed via trial and error. The final plot is shown in Figure 3(b).

The spatial inhomogeneities in the anode channel become instantly visible, with overlapping regions of high and low intensities. This set the perfect stage for visualizing the rotating spokes modes. From Figure 3(b), the spokes mode $m = 1$ is discernible, albeit not with absolute clarity. The presence of several rotating spokes modes with different temporal frequencies superimposing on each other might explain this behavior.

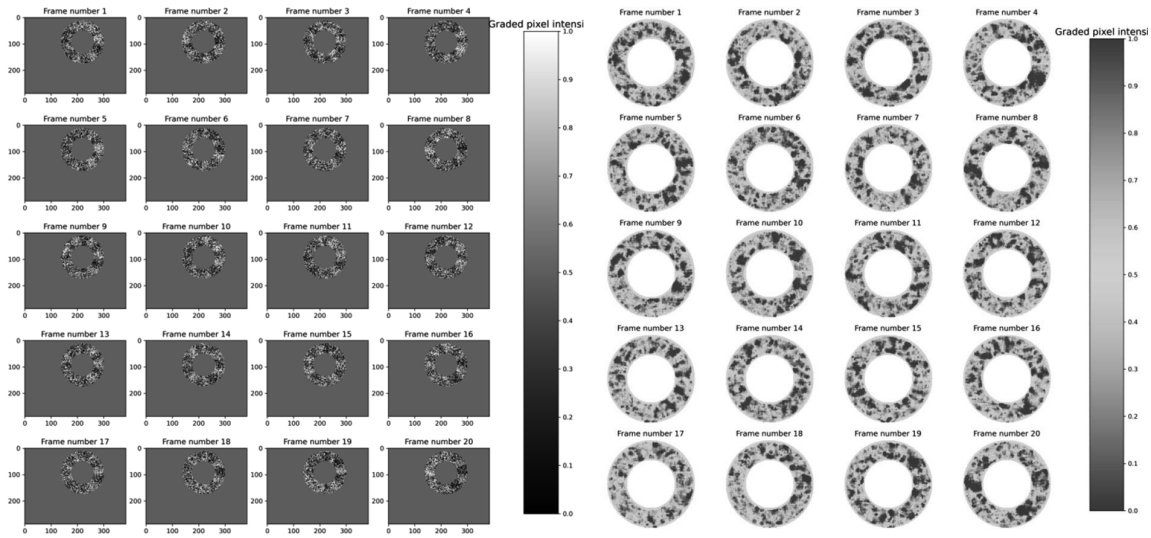

a. b.

Figure 3: (a) AC Coupled Images. The colorbar was limited between 5 and 95 percentiles. (b) Visualization of Rotating Spokes Modes. The colorbar was confined between 20 and 80 percentiles

5. CONCLUSION

The present work describes the steps leading up to the visualization of rotating spokes modes in an HET anode channel, starting from raw images. This involved various stages of image processing, with high computational complexities. Hence, automation was a necessity, facilitated by the statistical nature of the algorithm. The plots showed a prominent $m = 1$ mode mixed with other spokes modes of varying compositions.

The next step in the analysis would be to investigate the dynamics of the images via integral transforms. This might lead to quantification of temporal as well as spatial frequencies, suitable for future simulations or experimentation.

ACKNOWLEDGEMENTS

We are grateful to Liquid Propulsions Systems Centre Valiamala, Indian Space Research Organization and National Remote Sensing Center Hyderabad, Indian Space Research Organization for supporting this work.

REFERENCES

1. Gulczinski, III, Frank, and Ronald Spores. "Analysis of Hall-effect thrusters and ion engines for orbit transfer missions." *32nd Joint Propulsion Conference and Exhibit*. 1996.
2. Koppel, Christophe R., and Denis Estublier. The SMART-1 Hall effect thruster around the moon: In flight experience. 2005, p. 119. 29th International electric propulsion conference,
3. A. Bapat, P. B. Salunkhe and A. V. Patil, "Hall-Effect Thrusters for Deep-Space Missions: A Review," in *IEEE Transactions on Plasma Science*, vol. 50, no. 2, pp. 189-202, Feb. 2022, doi: 10.1109/TPS.2022.3143032.
4. Adam, J. C., et al. "Physics, simulation and diagnostics of Hall effect thrusters." *Plasma Physics and Controlled Fusion*50.12 (2008): 124041.
5. Mikellides, Ioannis G., et al. "Hall-effect thruster simulations with 2-D electron transport and hydrodynamic ions." (2009).
6. Touzeau, M., et al. "Plasma diagnostic systems for Hall-effect plasma thrusters." *Plasma Physics and Controlled Fusion* 42.12B (2000): B323.
7. Benavides, Gabriel F., et al. "Diagnostic for verifying the thrust vector requirement of the AEPS hall-effect thruster and comparison to the NEXT-c thrust vector diagnostic." *2018 Joint Propulsion Conference*. 2018.
8. Sekerak, Michael J. *Plasma oscillations and operational modes in Hall effect thrusters*. Diss. University of Michigan, 2014.
9. Morozov, A. I., and V. V. Savel'Ev. "Theory of the near-wall conductivity." *Plasma Physics Reports* 27 (2001): 570-575.
10. Bohm, David. "The characteristics of electrical discharges in magnetic fields." *Qualitative Description of the Arc Plasma in a Magnetic Field* (1949).
11. McDonald, Michael Sean. Electron transport in Hall thrusters. University of Michigan, 2012. (Dissertation).
12. Ortega, A. Guglielmi1 A. Martıín, et al. "Influence of double-stage operation on breathing oscillations and rotating spokes in the ID-HALL thruster." (2019): 33.
13. Ellison, C. L., Y. Raitses, and Nathaniel J. Fisch. "Cross-field electron transport induced by a rotating spoke in a cylindrical Hall thruster." *Physics of Plasmas* 19.1 (2012): 013503.
14. Matyash, K., et al. "Rotating spoke instabilities in a wall-less Hall thruster: Simulations." *Plasma Sources Science and Technology* 28.4 (2019): 044002

15. Mansour, A. R., and K. Hara. "Full fluid moment modeling of rotating spokes in Penning-type configuration." *Plasma Sources Science and Technology* 31.5 (2022): 055012.
16. Vision Research. “Cine File Format” https://phantomhighspeed.my.salesforce-sites.com/servlet/fileField?id=0BE1N000000kD2i
17. Light, Adam D. (2013) “pyCine” https://github.com/adamdlight/pyCine
18. N. Otsu, "A Threshold Selection Method from Gray-Level Histograms," in IEEE Transactions on Systems, Man, and Cybernetics, vol. 9, no. 1, pp. 62-66, Jan. 1979, doi: 10.1109/TSMC.1979.4310076.
19. Perez, A. and Gonzalez, R. C. "An Iterative Thresholding Algorithm for Image Segmentation," in IEEE Transactions on Pattern Analysis and Machine Intelligence, vol. PAMI-9, no. 6, pp. 742-751, Nov. 1987, doi: 10.1109/TPAMI.1987.4767981
20. Liao, P-S., Chen, T-S. and Chung, P-C., “A fast algorithm for multilevel thresholding”, Journal of Information Science and Engineering 17 (5): 713-727, 2001
21. Kensheng Wu, Ekow Otoo and Arie Shoshani, “Optimizing connected component labeling algorithms”, Paper LBNL-56864, 2005, Lawrence Berkeley National Laboratory (University of California)
22. Christophe Fiorio and Jens Gustedt, “Two linear time Union-Find strategies for image processing”, Theoretical Computer Science 154 (1996), pp. 165-181.

ISBN - 978-93-95038-50-8

Experimental Study of Magnetic Field Effects on SPT Performance

Vara Prasad K*, Umesh R Kadhane, M Rafi, Anish A and Anooja S

Department of Space
[1]Liquid Propulsion Systems Centre, [2]Indian Space Science and Technology,
Thiruvananthapuram, Kerala, 695547
Email: k_varaprasad@lpsc.gov.in

ABSTRACT

Stationary Plasma Thrusters (SPT), also known as Hall Effect Thrusters (HET) are one of the matured electric propulsion thrusters used by different space agencies for spacecraft orbit raising and NSSK operations. Higher I_{sp} and higher reliability offered by these thrusters make them standout in this category. ISRO has taken steps to develop SPTs of various power levels to cater the Indian space programme. Magnetic field profile is the heart of these SPTs, which will confine the electrons for better ionization of propellant and helps in creating strong electric field to accelerate the charged ions. The magnetic field strength affects the ceramic liner erosion which in turn determines the life of the thruster. In this study, the effects of magnetic field on thruster performance are examined experimentally. The SPT used in these experiments is a 85mm mean diameter thruster operated at 700W discharge power. The test facility used is a cylindrical vacuum chamber with 1.6m diameter and 4m length, equipped with roughing pumps, turbo molecular pump, cryo pump and Xenon cold heads. The vacuum level in the chamber during the testing of the thruster was $2.6x10^{-5}$ mbar of Xenon. Discharge current, discharge current oscillations and plasma plume profile were monitored at different magnetic fields. The magnetic field is tuned by varying the magnet coil currents. The 3D profiles of the magnetic field were measured using an automated 3D magnetic field mapper system. Discharge current oscillations are acquired through a high sampling oscilloscope and plume angle estimated based on measurements with Faraday probe. In this paper the performance of SPT in terms of discharge current oscillations and plume angle is presented with different peak magnetic field strengths from 78G to 171G. The mean discharge current, divergence angle are lower at 143G. High frequency modes are observed to be exit at 0.9A and 0.7A of coil current corresponds to magnetic field of 100G and 78G..

Keywords: *Stationary Plasma Thrusters, Electric Propulsion Thrusters, Magnetic field mapper and Plume angle*

1. INTRODUCTION

Electric propulsion thrusters have been dominant in spacecraft propulsion over last few decades. Their capability in delivering higher specific impulse makes them stand out over tradition chemical propulsion systems. Stationary Plasma Thrusters (SPT) also known as Hall Effect Thrusters (HET) is one of the matured thrusters in electric propulsion. These thrusters are widely used for orbit raising and NSSK operation and interplanetary missions by various space agencies. At present thousands of SPTs are under operational. Indian Space Research Organization has also taken initiative in developing these thrusters to cater Indian space programmes. Liquid Propulsion Systems Centre, one of the core centres of ISRO, had taken up this responsibility and developed SPTs of different power levels.

SPTs consists of a coaxial channel with anode at bottom and cathode outside the channel. The primary electrons generated by the cathode tends to move towards the anode in the channel, while the radial magnetic field produced by the combination of inner and outer magnets make them confine in the channel and produces Hall current in azimutal direction, resulting strong electric field in the channel. The propellant coming from the bottom of the channel through anode gas distributor will be ionized by electron impact ionization process

*Corresponding author: E-mail: k_varaprasad@lpsc.gov.in

and accelerated by the electric field and produces thrust.

The magnetic field plays a crucial role in confine the electrons for better propellant utilization and thrust generation. This magnetic field also produce repulsion of ions from walls of the channel by the electric field, thus reducing the channel erosion. Several theoretical and experimental work carried out on the studies of magnetic field effects on SPT performance. [1-4]

In this work, magnetic field effects on the SPT performance are studied through discharge parameters, discharge current oscillations and divergence angle.

2. EXPERIMENTAL SET-UP

Experiments are carried in a cylindrical vacuum chamber with diameter 1.6m and length 4m. The chamber is equipped with pumping system consists of roughing pumps, turbo molecular pumps, cryo pumps and cryo cold heads. The pumping system is maintaining the vacuum at 2.6×10^{-5} mbar with Xenon flow rate of 3.0 mg/s. SPT of mean diameter 85 mm is chosen for these studies. This hardware is designed for optimizes performance of 1.5kW with 3.2mg/s anode flow rate. However due to the facility limitations, in the present studies, the hardware is operated with ~700W at 300V discharge voltage and anode flow rate of 3mg/s. The magnetic field strength is varied in these studies by varying magnet coil current.

2.1 *MAGNETIC CIRCUIT*

The magnetic field in the SPT is generated using combination of one inner magnet, four outer magnets magnetic circuit. The typical magnetic field profile simulate with ANSYS Maxwell software is given in Figure. The magnetic field is strong near the exit of the thruster channel and rapidly decreases towards the anode and slowly decreases towards the outside. The relation between discharge voltage, channel width, maximum radial magnetic field and other parameters of SPT is given by [5],

$$\frac{\sqrt{U_d}}{wB_{rmax}} \cong \sqrt{\frac{\nu_{iz}}{\nu_e}} \sqrt{\frac{e}{M}} \frac{1}{K_W(e^{\langle\alpha\rangle L^*_{ac}} - 1)} \quad (1)$$

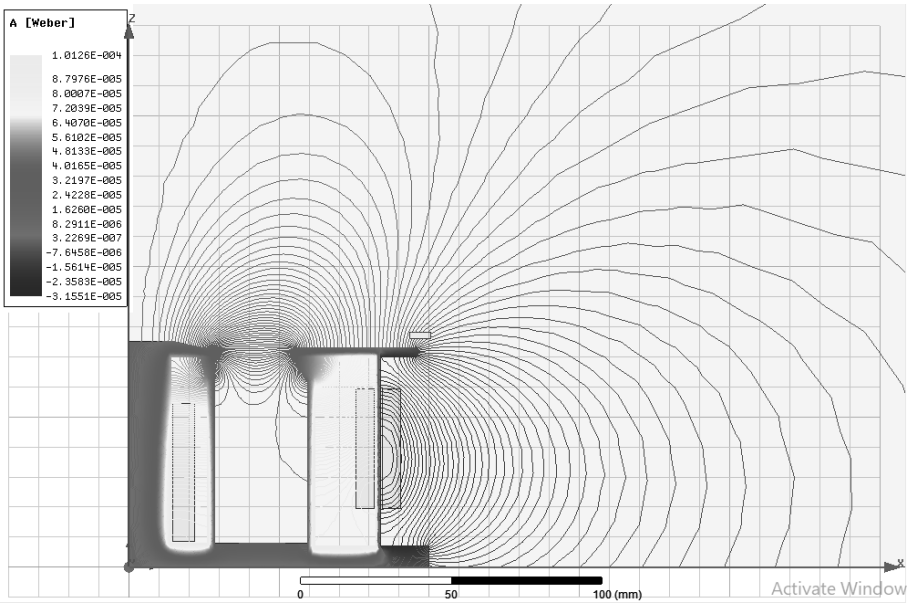

Figure 1: Axi-symmetric magnetic field simulation in the SPT

2.2 *FARADAY PROBE*

A nude Faraday probe consists of a collector and gaurd ring is used in these experiments to measure the ion current density in the plume of the thruster. The collector has diameter of 10mm. The collector and gaurd ring are biased externally with -15V to collect the saturated ion current and repel the electron current. Potential drop across the shunt resister of 1kΩ measured using digital oscilloscope to estimate the probe current. The probe is installed on a rotating C-arm of radius 50cm to measure the ion current density in the plume at different angles. The divergence angle is estimated with charge weighted average method [6-8]

2.3 *DISCHARGE CURRENT OSCILLATIONS*

Discharge voltage is applied between anode and cathode using commercial power supply. A filter circuit is place between thruster and power supply to protect the power supply from discharge current oscillations. The voltage across a 1Ω resistor is acquired through scope for measuring discharge current oscillations with a high sampling rate of 500KSa/s.

3. EXPERIMENTAL RESULTS AND DISCUSSIONS

Magnetic field profiles are measured with 3D automated magnetic field profiler, which is specially designed for 3D mapping of magnetic fields. The radial profile long the channel for 1.3A magnet current is as shown in Figure 1 (left) with bottom to top indicates anode to exit of the channel. The center line in the plot indicates the center line of the channel and horizontal line is the exit of the channel. The line profile along the center of the channel is shown in Figure 2 (right). The magnetic field is highest at the exit and almost reaches to zero gauss towards the anode. The center line magnetic field profiles with different magnet current are given in Figure 4. The magnetic field is highest for 1.6A of magnet coil current and decreases as decrease in the coil current as given in Table 1.

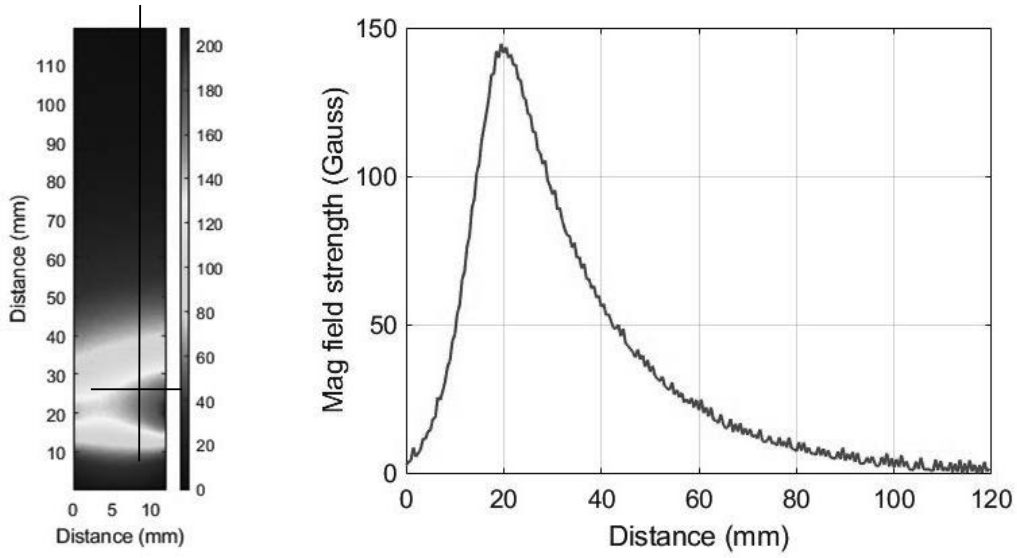

Figure 1: Radial magnetic field (Gauss) profile along the channel (left); Magnetic field line profile along the center line of the channel for 1.3A magnet current (right)

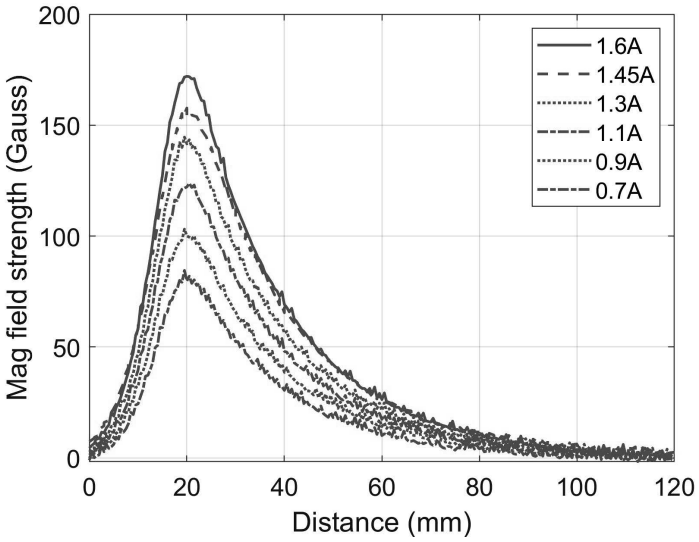

Figure 2: Magnetic field profile along the center of the channel

Table 1: Peak magnetic field strength with respect to coil current

S.No.	Magnet coil current	Peak Magnetic field strength (Gauss)
1.	1.6	171
2.	1.45	154
3.	1.3	143
4.	1.1	121
5.	0.9	100
6.	0.7	78

Discharge current oscillations with coil current are presented in Figure 3. The frequency spectra of discharge current oscillations obtained from FFT is given in Figure 4. The mean discharge current and RMS values of AC component of discharge currents with coil current are given in Table 1. The mean discharge current is lowest at 1.4A and increases on both sides of 1.3A coil current. The RMS value of AC component of discharge current is steadily decreasing for coil current from 1.6A coil to 0.7A and significantly decreasing below 1.1A. This indicated the peak -peak oscillations are decreasing with coil current but mean discharge current increases with lower coil current. The breathing mode frequency is in the nominal range of 22 to 35kHz with the presence of harmonics. High frequency modes are present at 0.7A and 0.9A of magnet currents. This indicates the existence of different instabilities at these coil currents.

Due to the limitations in the facility, the ion current density profile was measured from -40 deg to +50 deg about the thruster axis. The data is fitted and extrapolated to -90 to +90 deg using Lorenzian fitting. The typical fitted curve of ion current density profile measured with Faraday probe is given in Figure 5. The ion current density profiles with coil current are given in Figure 6. The ion current density in the plume steadily decreases for magnet coil current from 1.6A to 0.7A, while total discharge current increases as discussed. This indicates the electron current component in the discharge current is increases with decrease in coil current. Hence electron confinement becomes weak for coil current below 1.1A. The divergence angle also increases with decrease in the coil current showing poor confinement of plume towards the lower values of coil current.

ISBN - 978-93-95038-50-8

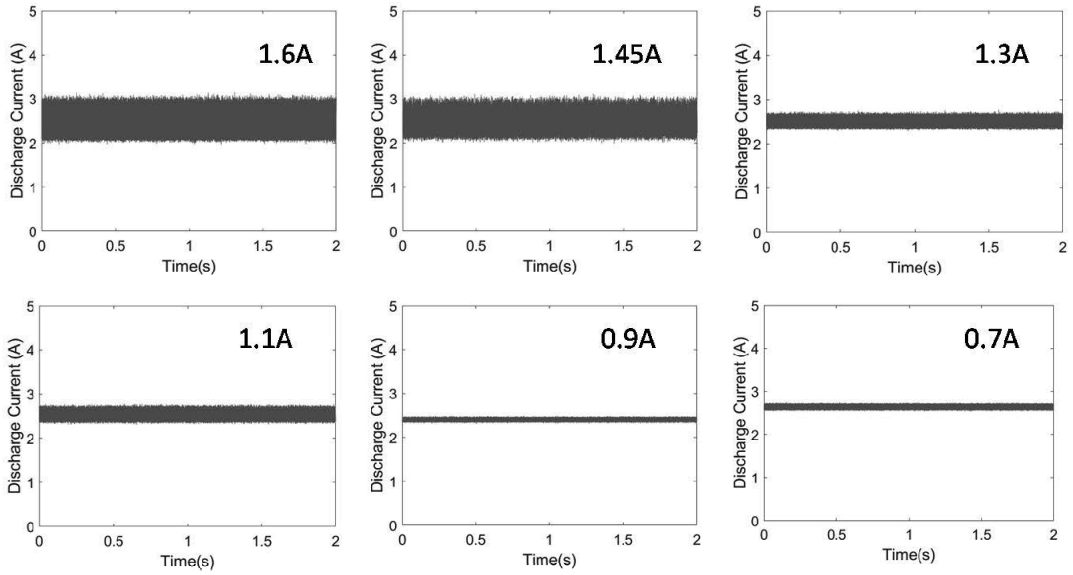

Figure 3: Discharge current oscillations with varying magnet current

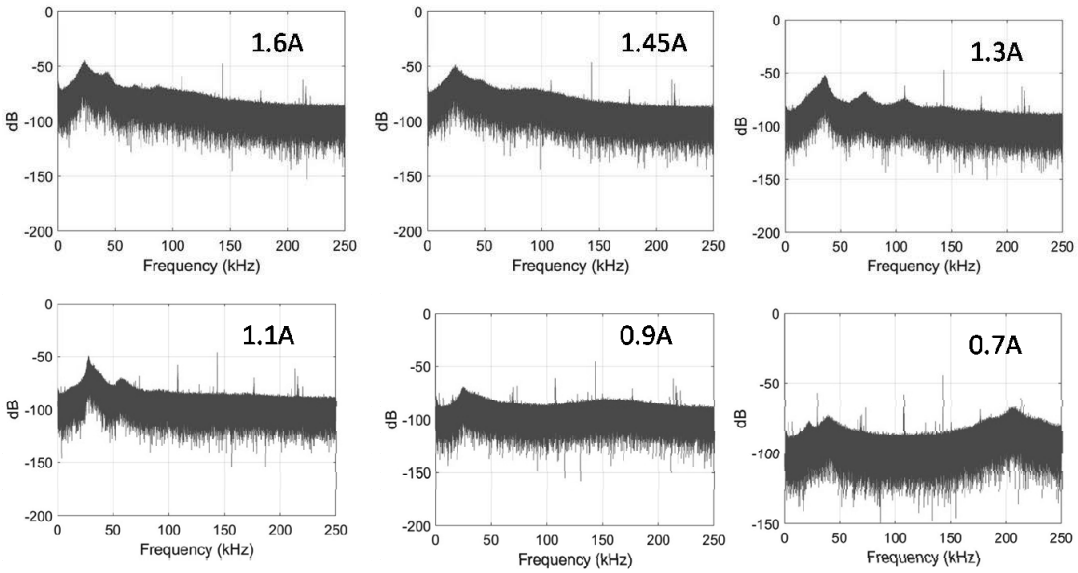

Figure 4: Frequency spectra of discharge current oscillations with magnet current

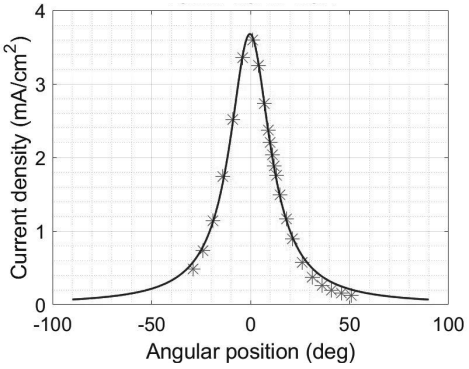

Figure 5: Ion current density profile

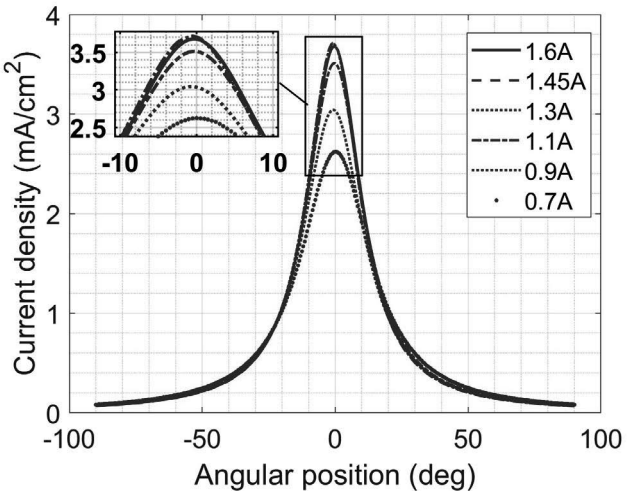

Figure 6: Ion current density profiles with different magnet currents

Table 1: Summary of results

Magnet Current (A)	Peak magnetic field strength (G)	Mean Discharge Current (A)	RMS	Frequency kHz	Divergence angle (deg)
1.6	171	2.48	0.17	23.2,45.7,69.2	39.4
1.45	154	2.47	0.12	24.6,48.7,91.4	39.3
1.3	143	2.50	0.07	35.6,72,108	39.3
1.1	121	2.52	0.07	28,57.2	39.8
0.9	100	2.40	0.02	24.7,153	40.4
0.7	78	2.63	0.03	22.2,39.7,205	41.6

5. CONCLUSIONS

The theoretical estimation of optimum magnetic field is obtained as for 300V discharge voltage for the particular hardware in study. The overall experimental results indicating the thruster performance is optimum for coil current of 1.3A corresponding to peak magnetic value of 143G. The increase in the mean discharge current, divergence angle and presence of high frequency components indicating the magnetic field strength is not adequate for the better plasma confinement below 1.1A of coil current corresponding to below 121G.

ACKNOWLEDGEMENTS

We would like to thank Shri. Shibu Mathew and Dr. Sunil Kumar S for constant support in conducting these experiments. This work performed within Liquid Propulsion Systems Centre, ISRO, Thiruvananthapuram.

REFERENCES

1. Oleg A. Gorshkov, Andrey A. Shagayda and Sergey V. Irishkov, “The Influence of the Magnetic Field Topology on Hall Thruster Performance”, AIAA, 2006, 4472.
2. Alexei I Morozov, “Electric propulsion thrusters and plasma dynamics”, IEPC, 95, 05.

3. Alberto Rossi, Frédéric Messine, Carole Henaux and Satafa Sanogo, “Parametric optimization of a Hall Effect Thruster magnetic circuit”, IEPC, 2015, 40.
4. Ioannis G. Mikellides, Ira Katz, Richard R. Hofer, and Dan M. Goebel, “Magnetic shielding of a laboratory Hall thruster .1. Theory and validation”, Journal of Applied Physics, 115, 043303, 2014.
5. M.H.Moghimi, “Physical Features and Parameters Calculations of a Hall Thruster”, IEPC, 2011, 002.
6. Daniel L. Brown, C. William Larson, Brian E. Beal and Alec D. Gallimore, “Methodology and Historical Perspective of a Hall Thruster Efficiency Analysis”, AFRL-RZ-ED-JA-2009-023
7. Daniel L. Brown and Alec D. Gallimore, “Evaluation of Plume Divergence and Facility Effects on Far-Field Faraday Probe Current Density Profiles”, IEPC, 2009,030.
8. Daniel L. Brown, Mitchell L. R. Walker, James Szabo, Wensheng Huang and John E. Foster, “Recommended Practice for Use of Faraday Probes in Electric Propulsion Testing”, Journal of Propulsion and Power, Vol 33, No.3, 2017.

ISBN - 978-93-95038-50-8

Studies to Investigate the Effect of Feed Line Orientation on Chill-Down Performance of Cryogenic Feed Lines

Venkatesh N*, Anant Singhal, Deepak Kumar Agarwal, A Salih and S Sunil Kumar

[1]Liquid Propulsion Systems Centre, Indian Space Research Organization, Valiamala
[2]Indian Institute of Space Science and Technology, Trivandrum
*Email: nvnktvpm@gmail.com

ABSTRACT

In Cryogenic Systems, chilldown of transfer or feed lines to a temperature very close to that of the cryogen is to be achieved first prior to its admission at rated flow rate for steady state operation and this is achieved by admitting the cryogen at a low flow rate. This chilldown process is very complex and is highly sensitive to parameters like feed line orientation, distribution of thermal mass associated with the system, mass flux of the cryogen, heat in-leak etc. In the present study, experiments are conceived to address the influence of feed line orientation on chilldown performance. A set-up is realised employing a foam insulated test section and experiments are conducted using Liquid Nitrogen. Tests are performed in horizontal and different upward as well as downward orientation. Chill down performance is analysed using the measured surface temperature data. It is observed to be very sensitive to feed line orientation, faster with upward inclination and slower with downward orientation. Wall heat flux is estimated using experimental data and heat flux pattern for different feed line orientation is studied. Heat flux pattern at bottom locations is observed to be not affected significantly by feed line orientation. Whereas heat flux pattern at top locations is distinctly different in tests with upward orientation. CFD simulation is also done, as a typical case, for 45^o downward inclination, using ANSYS software to capture the flow pattern and wall temperature profile. Flow structure is well captured and very good match is seen with the experimental data for the bottom wall temperature profile.

Keywords: *chilldown, inverse heat transfer technique, minimum heat flux, critical heat flux, feed line orientation.*

1. INTRODUCTION

In Cryogenic systems, feed or transfer line chilldown, is an important pre-requisite, to be achieved prior to admission of cryogen at rated condition. Time required to complete this chilldown, which is defined as "Chilldown time" is very strongly influenced by parameters like mass flux of cryogen, feed line orientation, its thermal mass, heat in-leak etc and an attempt is made here to study experimentally the effect of feed line orientation on chilldown performance.

Chilldown performance of cryogenic transfer lines has been a topic of extensive research for the last several decades since 1960s. JC Burke et al. [1] carried out experiments with horizontally held long transfer lines using Liquid Nitrogen (LN_2) to evaluate the chilldown time. Experiments were carried out by K Srinivasan et al. [2] and Durga Prasad et al. [3] with LN_2 using insulated short length test sections. It was concluded that for short transfer lines, contribution from forced convection is not significant. Experiments were performed by Jelliffee Jackson [4] to evaluate the chilldown time and heat transfer coefficient at the wall for different mass flux conditions. Chilldown time was reported to be less with higher mass flux. Influence of feed line orientation and mass flux on chilldown performance was studied by Jijo Johnson et al. [5]. Chilldown performance was reported to be improving upto 10^o upward inclination and inferior for 15^o upward inclination. Jesna Mohammmed et al. [6] studied the influence of mass flux on chilldown time and chilldown efficiency by conducting experiments with LN_2. Mass flux was reported to having a significant influence on the chill-down time and efficiency. Lingxue Jin et al. [7, 8] performed experiments using a stainless-steel test section with LAr, LOX and LN_2. Chilldown time was reported to be less with LN_2 compared to LAr.

*Corresponding author: E-mail: nvnktvpm@gmail.com

Influence of test section orientation on chilldown behaviour was studied extensively by SR Darr et al. [9,10] . Apart from horizontal and vertical directions, tests were done for different upward, and downward inclination (15^o, 30^o, 45^o and 60 ^{o}) Chilldown was reported to be slower with downward inclination of test section compared to horizontal and faster with upward inclination. Jason Hartwig et al. [11] conducted experiments with LOX and Liquid Methane using 25.4mm and 114.3mm diameter lines. Stratification was not observed in smaller diameter transfer line, whereas in tests with larger diameter line, stratification and large temperature gradients were reported between top and bottom measurements. Venkatesh N et al. [12] conducted experiments with a SS test section of 30mm inner diameter, 1mm wall thickness and 2m length, with LN_2 as test medium to study the influence of feed line orientation and mass flux on chilldown performance. Wall temperature profile and heat flux pattern for different test section orientation were compared and certain findings with respect to influence of feed line orientation on chilldown performance were broughtout. Certain observations with respect to influence of feed line orientation on critical and minimum heat flux values were also reported.

As can be seen from available literature, only limited experiments are done to visualise and understand the flow structure prevailing during chilldown. Further, studies to understand the influence of feed line orientation are scarce. It is in this context that in the present work, experiments are devised to study the influence of feed line orientation on chilldown performance.

In the present study, experiments are conducted to study the influence of feed line orientation, with test section held at different upward and downward inclination upto 45^o with respect to horizontal. Apart from this, CFD analysis using ANSYS is also done for 45^o downward orientation and results are compared with experimental data. Details of the test set-up, experiments carried out, results and findings of the present study are covered in the subsequent sections.

2. EXPERIMENTAL STUDY

A test set up is conceived with the required measurements and realised to conduct experiments and understand the influence of feed line orientation on chilldown performance. Details of the experimental set-up, measurements made, test procedure, test matrix etc. are covered in the subsequent sections.

2.1 *TEST SETUP*

A photograph of the set up employed is shown in Figure 1. The set-up consists of stainless-steel test section of 39mm inner diameter, and 1.5mm wall thickness, and 2 m length provided with 28 mm thick polyisocynurate foam insulation. During tests, LN_2 is fed to the test section from a 380 litres dewar and a calibrated orifice of diameter 2.73 mm provided at the inlet to test section is used to control the LN_2 flow rate to the test section. A 50 litre GN2 cylinder and a pressure regulator are used to pressurize the dewar and maintain the required pressure at test section inlet during the experiments. In tests with varying feed line orientation, desired orientation of test section is achieved using a pre-formed spool piece of approximately 100mm length provided at the inlet to the test section.

ISBN - 978-93-95038-50-8

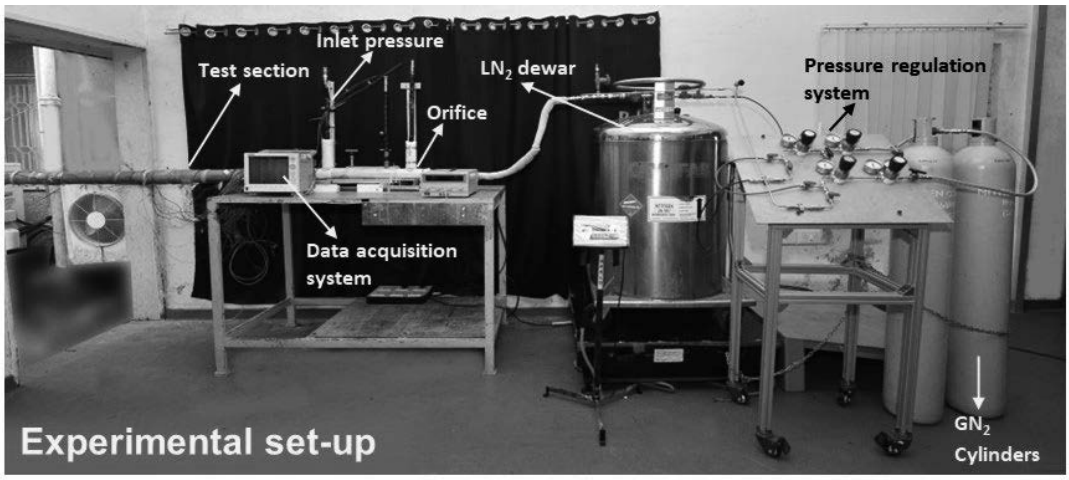

Figure 1: Photograph of test set-up

2.2 *TEST INSTRUMENTATION*

A schematic showing the details of test instrumentation is shown in Figure 2. The experimental set-up is instrumented with three pressure sensors (P1, P2 and P3), two RTDs and 8 thermocouples. Pressure sensors are of strain gauge type, 0-5bar range and have an accuracy ±0.7% of the full-scale reading. Sensor P1 measures the orifice inlet pressure, P2 the orifice outlet pressure and pressure at inlet to the test section is measured using P3. Thermocouples, 2nos. each are provided at 4 stations along the length of test section to measure the test section outer wall temperature. They are of T type and have an accuracy of ±~1.5K for the measured temperature range. Two 100Ω Platinum RTDs (TF1 and TF2) are used to measure the fluid temperature at two stations.

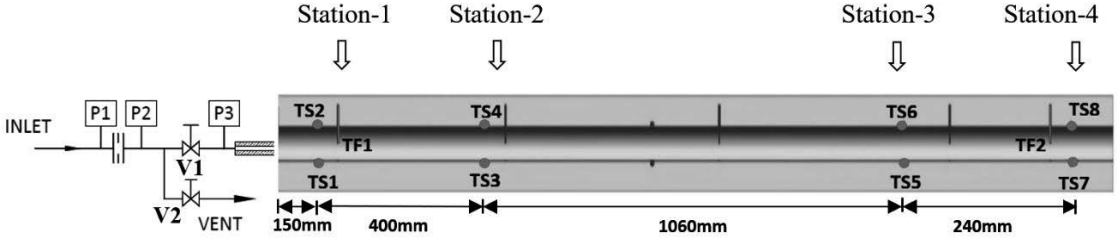

Figure 2: Instrumentation schematic for tests with varying feed line orientation

Temperature and pressure values read by these sensors are acquired using a `Yokogawa' data logger with a sampling rate of 1Hz.

2.3 *TEST MATRIX*

Nineteen tests are performed with an inlet pressure of 0.35MPa (Abs) for different test section upward and downward orientation upto 45^o with respect to horizontal and mass flux simulated during the experiments is 60 kg/m^2-s. Experiments are repeated for selected orientations to confirm repeatability.

3. EXPERIMENTAL RESULTS AND DISCUSSION

A set of nineteen experiments are carried out covering a test section orientation of horizontal position, and upward, and downward inclination of 10^o, 20^o, 30^o, and 45^o with respect to

horizontal. Wall temperature data measured during the experiments and inner wall heat flux values estimated by inverse heat flux technique are analysed in detail to understand the pattern of their variation with respect to feed line orientation. Most of the observations are in line with the ones reported by Venkatesh N et al. [12] based on experiments performed with test section of 30mm inner diameter. Salient findings of the present study are broughtout in the subsequent sections.

3.1 *WALL TEMPERATURE PROFILE*

In tests with horizontal and downward inclination, the bottom wall temperature profile shows signature of all the three boiling regimes as in pool boiling, whereas top region is cooled only by vapour. In tests with upward inclination, pattern observed in surface temperature measurement at bottom location is almost similar to tests with horizontal and downward inclination. Whereas temperature profile of top location is significantly different and shows signature of liquid wetting. The observations reported above are clearly reflected in Figure-3, wherein as a typical case, the temperature profile observed in tests with horizontal position, 45^o downward and 45^o upward orientation are shown.

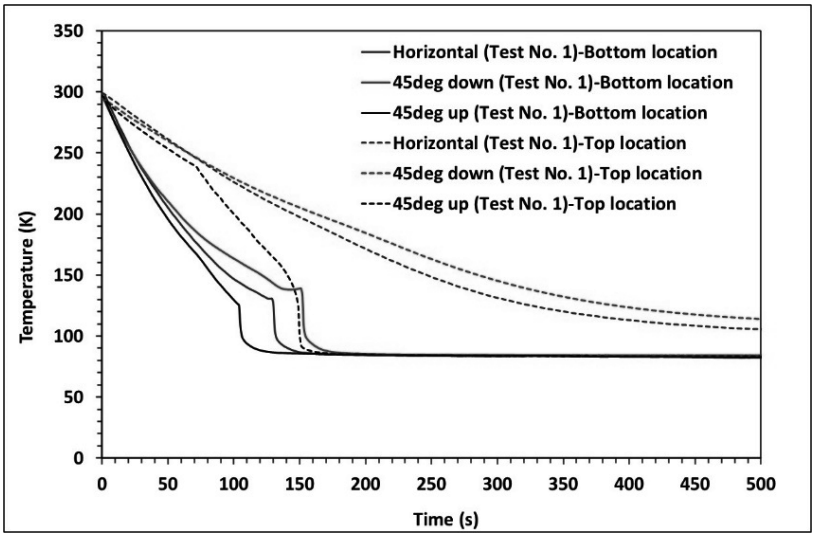

Figure 3: Temperature profile at station-3 during test in horizontal position, 45^o upward and downward orientation

Average of bottom and top temperature measurements is taken to estimate the average temperature at station 3. Profile of average temperature at Station 3, indicates that chilldown performance is inferior with downward inclination and improves significantly with upward inclination.

3.2 *HEAT FLUX COMPARISON FOR DIFFERENT ORIENTATION*

Heat flux at test section inner wall, both top and bottom locations, is estimated by Inverse Heat Transfer technique. The observations with regard to heat flux pattern are almost similar to the ones reported by Venkatesh N et al. [12]. Heat flux pattern at bottom locations are almost similar in tests with horizontal position, upward and downward inclination. whereas heat flux at top location, shows a significant jump in heat flux, when the wall superheat falls below a critical value. This is attributed to wall wetting by the liquid. As a typical case, heat flux pattern observed at bottom and top locations in station 4 during tests in horizontal, 45^o upward and downward orientation are shown in Figure-4 to substantiate the above.

ISBN - 978-93-95038-50-8

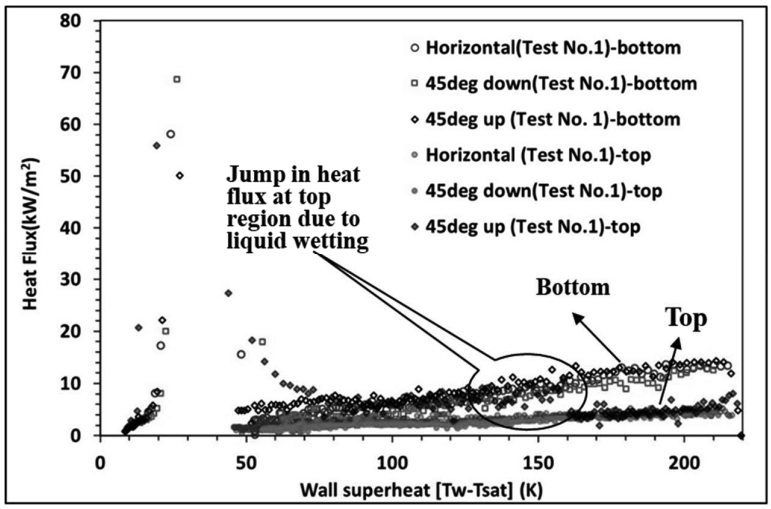

Figure 4: Heat flux pattern at bottom and top locations at Station 3 during tests in Horizontal position, 45° upward and downward orientation

Average minimum heat flux and critical heat flux are computed by taking the average of values estimated for Stations 2 and 3. Each data point in Figure 5 represents the average of critical heat flux observed at Stations 2 and 3 in a particular experiment conducted with a fixed test section orientation. Critical heat flux is found to increase with downward inclination of the test section and decrease with upward inclination. Each data point in Figure 6 represents the average of minimum heat flux observed at Stations 2 and 3 in a particular experiment done with a fixed test section orientation. Minimum heat flux is found to decrease with downward orientation of the test section, whereas reverse is the trend with upward orientation. These observations are very similar to the ones reported by Venkatesh N et al. [12] based on experiments with test section of 30mm inner diameter.

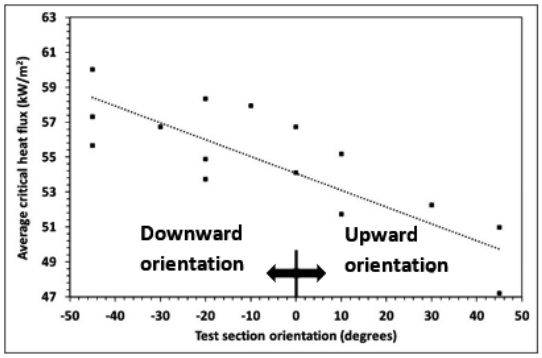

Figure 5: Comparison of average critical heat flux for different test section orientation

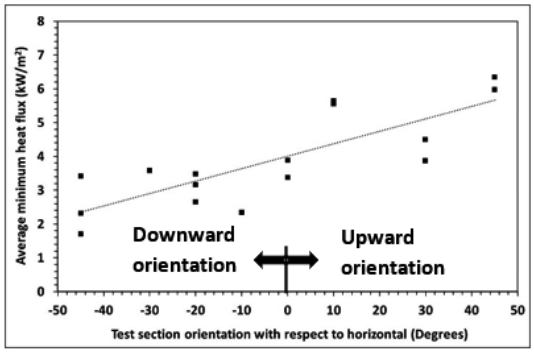

Figure 6: Comparison of average minimum heat flux for different test section orientation

4. CFD ANALYSIS

4.1 *COMPUTATIONAL DOMAIN AND BOUNDARY CONDITIONS*

The 3D computational domain of the feedline is shown in 7. The domain consists of the 2m long feedline with a small diameter line at the inlet. Foam insulation is also modeled over the feedline outerwall. The domain is meshed with hexahedral elements with finely spaced cells near the pipe inner wall to capture the flow gradients accurately. The total mesh count is 5.3lakhs with maximum skewness of 0.87.

Liquid nitrogen mass flow rate of 73.4g/s at the pipe inlet and ambient pressure of 101325Pa at the feedline outlet is specified as boundary conditions for the CFD analysis. The outer wall of the foam insulation is considered to be radiatively and convectively coupled to the ambient. The components of gravitational acceleration are specified to model the pipe oriented as 45^0 downwards. The domain is initialized with GN2 in the feedline and LN2 at 77K in the inlet pipe. The initial pressure in the domain is taken to be 101325Pa.

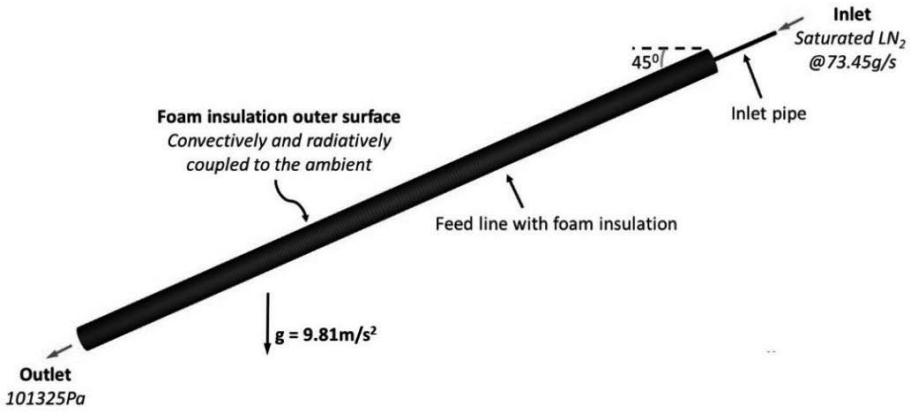

Figure 7: Computational domain of the Test section

4.2 *NUMERICAL METHODOLOGY*

The numerical simulations are carried out using ANSYS Fluent. The boiling of liquid nitrogen at the feedline wall during the chilldown process is modelled using Semi-mechanistic boiling framework in the Mixture model. The effective wall heat flux is modeled using Chen's correlation. The single-phase heat transfer coefficient is calculated from the liquid and vapor heat transfer coefficients weighted by the wetting fraction. The nucleate boiling heat transfer coefficient is calculated using the Zuber and Foster correlation given by Eq. (1) [].

$$h_{nb}=0.00122\ \frac{k_l^{0.79}c_{p_l}^{0.45}\rho_l^{0.49}}{\sigma^{0.5}\mu_l^{0.29}L^{0.24}\rho_v^{0.24}}\left(P_{sat,T_w}-P_{sat,T_{sat}}\right)^{0.75}\left(T_w-T_{sat}\right)^{0.24} \quad \text{.....(1)}$$

where the k is the thermal conductivity, Cp is the specific heat, ρ is the density, σ is the surface tension, μ is the viscosity, T_w is the wall temperature, $P_{sat,Tw}$ is the saturation pressure at wall temperature and L is the latent heat of vaporization.

The turbulence is modeled using SST k-ω turbulence model. The pressure and velocity coupling is achieved using the Pressure-Implicit with Splitting of Operators (PISO) scheme. The discretization of the governing equations was carried out using second order upwind scheme in space. First order implicit scheme was used for time marching with a time step of $1x10^{-3}$s.

The two-phase flow was modelled by solving the momentum, continuity and energy equations for the mixture and the volume fraction equation for the liquid phase. The following governing equations were solved during the simulation:

$$\frac{\partial}{\partial t}(\rho_m)+\nabla.(\rho_m \mathbf{v_m})=0 \quad \text{.....(2)}$$

where, $\mathbf{v}_m$ is the mass-averaged velocity.

ISBN - 978-93-95038-50-8

ρ_m is the mixture density and n is the number of phases. In the present simulation n=2.

$$\frac{\partial}{\partial t}\left(\rho_m \mathbf{v_m}\right) + \nabla.\left(\rho_m \mathbf{v_m} \mathbf{v_m}\right) = -\nabla p + \nabla.\left[\mu_m \left(\nabla \mathbf{v_m} + \nabla \mathbf{v_m}^T\right)\right] + \rho_m \mathbf{g} + \mathbf{F} \quad \text{.....(3)}$$

where F is a body force, and μ_m is the viscosity of the mixture,

The energy equation has the following form:

$$\frac{\partial}{\partial t}\sum_{k=1}^{n}\left(\alpha_k \rho_k E_k\right) + \nabla.\sum_{k=1}^{n}\left(\alpha_k \mathbf{v}_k \left(\rho_k E_k + p\right)\right) = \nabla.\left(k_{eff} \nabla T\right) + S_E \quad \text{.....(4)}$$

The liquid-vapor mass transfer is governed by the vapor transport equation

$$\frac{\partial}{\partial t}\left(\alpha_v \rho_v\right) + \nabla.\left(\alpha_v \rho_v \mathbf{v}_v\right) = \dot{m}_{l\to v} - \dot{m}_{v\to l} \quad \text{.....(5)}$$

where the subscripts v and l are for vapor and liquid phase respectively.

5. CFD RESULTS AND DISCUSSION

As a typical result, wall temperature profile at a distance of 1060mm from inlet is compared with the experimental results [12] in Figure 8 and void fraction contour plot is shown in Figure 9. As can be seen, very good match is seen with the experimental results. Flow regime could be well captured, with bottom wall getting cooled by the liquid and top region only by vapour. A very good match is seen for the temperature profile at the bottom, though the fall rate of top wall temperature appears to be little slower compared to experimental data. More simulations are being done for other test section orientations for a one to one comparison and better understanding of the flow physics.

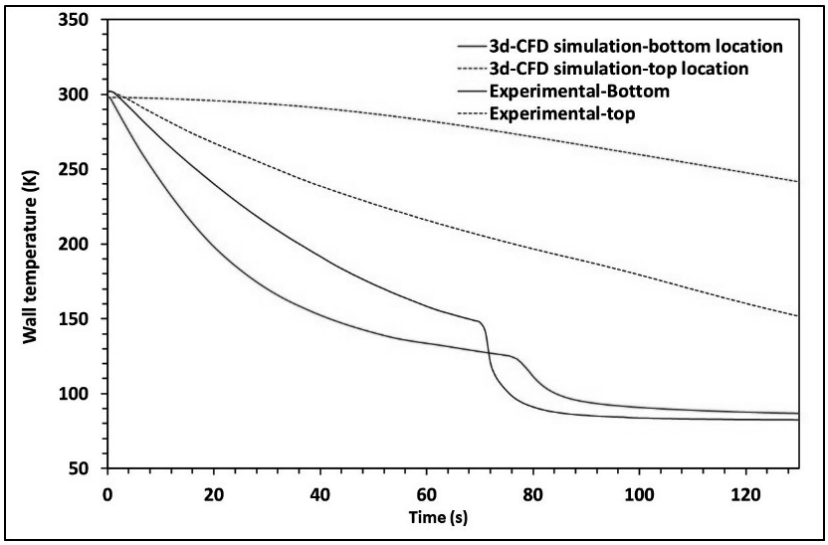

Figure 8: Comparison of wall temperature profile at 1060mm from inlet obtained through CFD analysis with experimental data

ISBN - 978-93-95038-50-8

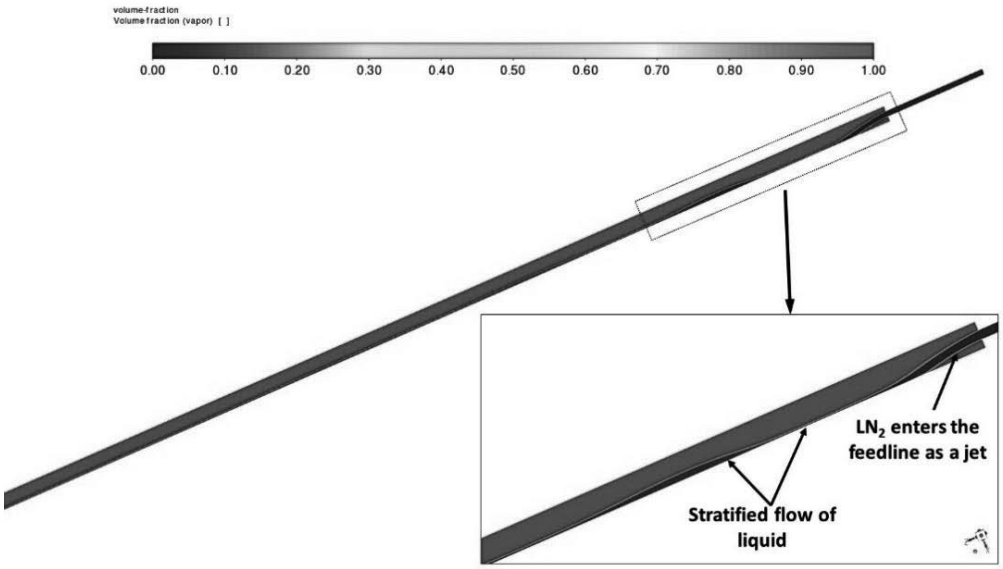

Figure 9: Void fraction contour obtained in CFD simulation

6. CONCLUSIONS

In the present study, experiments are performed employing a stainless steel test section insulated with poly-isocynurate foam using LN_2 as medium. Influence of feed line orientation on chilldown performance is studied. Major findings are:

- Bottom region goes through all the three regimes as in pool boiling in tests with horizontal and downward orientation, whereas top region is cooled only by vapour.
- In the test conditions simulated during the experiments, chilldown is slower with downward inclination compared to horizontal position, whereas chilldown improves significantly with upward orientation, mainly due to wetting of top wall by liquid.
- Pattern of variation of heat flux at bottom region of test section is not affected significantly by orientation. Heat flux pattern is significantly different for top wall, in tests with upward inclination. This is due to wetting of the top region of the test section by saturated liquid.
- Average critical heat flux values observed in the present study are higher with downward inclination and lower with upward inclination. Whereas the observation with minimum heat flux is reverse. This could be due to the flow structure prevailing in the test section and needs to be investigated further.
- CFD simulation done for 45^o downward orientation could capture the flow structure and wall temperature profile at bottom location very closely.

The findings of the present study will help to understand better the influence of feed line orientation on chilldown performance.

ACKNOWLEDGEMENT

The experimental work reported here has been carried out in Thermal laboratory under Propulsion Research Studies Entity of Liquid Propulsion Systems Centre, Indian Space Research Organisation and authors acknowledge the support provided by the staff of Thermal

Engineering lab. Authors also deeply acknowledge the support extended by Dr V Narayanan, Director, Liquid Propulsion Systems Centre and Shri. MS Suresh, Associate Director, Liquid Propulsion Systems Centre, in carrying out the research work. Authors also thank the Proto Fabrication Facility team at Liquid Propulsion Systems Centre and Insulation team at APD/VSSC for their whole hearted support in establishing the experimental set-up.

ABBREVIATION

LN_2	Liquid Nitrogen
LAr	Liquid Argon
LOX	Liquid Oxygen
GN_2	Gaseous Nitrogen
Abs	Absolute

REFERENCES

1. JC Burke, Byrnes WR, Post AH, Arthur FER, Pressurised cool down of Cryogenic Transfer lines, Advances in cryogenic Engineering, 1960; Volume 4; pages 378-394.
2. K Srinivasan, V Seshagiri Rao and MV Krishnamurthy, Analytical and experimental investigation on cooldown of short cryogenic transfer lines. Cryogenics, September 1974; pages 489-494.
3. A Durga Prasad, K Srinivasan and MV Krishna Murthy, Cooldown of foam insulated cryogenic transfer lines, Cryogenics November 1974; pages 615-617.
4. Jelliffee Jackson, Transient heat transfer during chill down, Proceedings of HT-2005 ASME summer heat transfer conference paper, USA.
5. Jijo Johnson, SR Shine, Transient cryogenic chill down process in horizontal and inclined pipes, Cryogenics 71 (2015); pages 7-17.
6. Jesna Mohammed, Abdul Mohizin, KE Reby Roy, Experimental investigations on transient cryogenic chilldown of a short horizontal copper transfer line, Indian Academy of sciences, 202045:12.
7. Lingxue Jin, Hyokjin Cho, Sangkwon Jeong, Experimental investigation on line chilldown process by Liquid Argon, Cryogenics 97 (2019); pages 31-39.
8. Lingxue Jin, Jisung Lee, Sangkwon Jeong, Investigation of heat transfer in line chilldown process with various cryogenic fluids, Int Journal of heat and mass transfer; Volume 150 (2020); 119204.
9. SR Darr, Hong Hu, N Glikin, JW Hartwig, AK Majumdar, AC Leclair, JN Chung, An experimental study on terrestrial cryogenic transfer line chill down I. Effect of mass flux, equilibrium quality, and inlet sub-cooling, International Journal of Heat and Mass transfer, (2016); pages 1225-1242.
10. SR Darr, Hong Hu, N Glikin, JW Hartwig, AK Majumdar, AC Leclair, JN Chung, An experimental study on terrestrial cryogenic transfer line chill down II. Effect of flow direction with respect to gravity and new correlation set, International Journal of Heat and Mass transfer, 103(2016); pages 1243-1260.
11. Jason Hartwig, Peter Meyerhofer, Benjamin Stiegemeier, Robert Morehead; Liquid Methane and Liquid Oxygen horizontal chilldown experiments of a 2.54 and 11.43cm transfer line; Applied thermal Engineering; 205 (2022) 118042.
12. Venkatesh N, Deepak Kumar Agarwal, A Salih and S Sunil Kumar; Chilldown of Cryogenic feed lines-An insight into the influence of feed line orientation and mass flux; Journal of Cryogenics; 130 (2023) 103644; January, 2023.

Cold Flow Characterization of Triplet Injector Head Realized Through Additive Manufacturing

Vikash Kumar*, Rafeeque T.A, Madhukumar T, and John Tharakan T

Liquid Propulsion Systems Centre, Indian Space Research Organization
Thiruvananthapuram, Kerala: 695547
Email: vikashkumar@lpsc.gov.in

ABSTRACT

Additive manufacturing is an emerging field in the area of fabrication process and being employed for the realization of rocket engine systems and subsystems. This process is comparatively cheaper and requires less lead time compared to conventional machining process. PSLV, a workhorse launch vehicle of ISRO uses a pressure fed PS4 engine for its upper stage. This engine is realized through conventional machining routes and qualified for flight so far. An attempt has been made to realize the PS4 engine through additive manufacturing route at LPSC. Injector is the major part of the engine which controls the combustion process inside the combustion chamber of rocket engine. It is imperative to realize the injector head first through additive manufacturing and checked for its cold flow performance. The present work investigates the cold flow characteristics of PS4 triplet injector head realized through additive manufacturing. PS4 injector consists of 45 nos of triplet injector elements, injecting oxidizer through the two angular impinging orifices and fuel through the central orifice. There are also 36 nos of fuel film cooling elements placed at the periphery of the injector face angled at 45°. Cold flow characteristics were evaluated for both oxidizer and fuel flow paths at the rated flow rates. Experiments were also conducted at different pressure drops to evaluate the coefficient of discharge for both oxidizer and fuel orifices. Impinging patterns of the oxidizer flow path was also visualized through photographic method.

Keywords: *Triplet Injector head, Additive manufacturing, Coefficient of discharge*

1. INTRODUCTION

The combustion chamber is the most important part of any liquid rocket engine, gas turbine engine or automobile engine. In case of liquid rocket engine, propellants are injected in atomised form through injector inside the combustion chamber. The characteristics of the injector decides the efficacy of thrust chamber which in turn decides the performance of the liquid rocket engine. Injector should meter the correct proportions of the propellants, atomise it in the form of droplets and distribute these in correct proportions inside the combustion chamber in order to achieve stable combustion. Different types of injectors are used in liquid rocket engine such as impinging jet injectors, swirl coaxial injectors, shear coaxial injectors etc. Impinging type of injectors is commonly used with oxygen hydrocarbon and storable propellants. These injectors can be classified into doublet impinging and triplet impinging types [1]. PSLV, a workhorse launch vehicle of ISRO uses a pressure fed PS4 engine for its upper stage. This engine uses impinging type of injectors. PS4 injector head consists of 45 nos of triplet injector elements, injecting oxidizer through the two angular impinging orifices and fuel through the central orifice. There are also 36 nos of fuel film cooling elements placed at the periphery of the injector face angled at 45°. This engine is realized through conventional machining routes and qualified for flight test so far. An attempt has been made to realize the PS4 engine through additive manufacturing route at LPSC.

Additive manufacturing is an emerging field in the area of fabrication process and being employed for the realization of rocket engine systems and subsystems. This process is comparatively cheaper and requires less lead time compared to conventional machining

*Corresponding author: E-mail: vikashkumar@lpsc.gov.in

process. It is imperative to realize the injector head first through additive manufacturing and checked for its cold flow performance. The present work investigates the cold flow characteristics of PS4 triplet injector head realized through additive manufacturing. Cold flow characteristics were evaluated for both oxidizer and fuel flow paths at the rated flow level. Experiments were also conducted at different pressure drops to evaluate the coefficient of discharge for both oxidizer and fuel orifices. Impinging patterns of the oxidizer flow path was also visualized through photography method.

2. LITERATURE REVIEW

Additive manufacturing is a non-conventional manufacturing process which has progressed over the last decade. Due to its inherent advantages above the conventional process, this technology is being employed for the realization of various systems or sub systems of liquid rocket engine throughout the world.

Soller et. al. [2] discussed regarding the injector development logic followed for the injectors realized through additive manufacturing. They discussed about the material characterization, single element characterization, sub scale testing and then full scale demonstrator. They used Vulcain 2 gas generator injector for the introduction of additive manufacturing on a full scale engine. They also investigated the thrust chamber injector of Vinci engine was with respect to the possibilities to apply additive manufacturing on a larger injector in addition to the Vulcain gas generator. Paul et. al. [3] provided the details of various internal programs at the NASA MSFC using additive manufacturing to develop combustion devices hardware. They informed that combustion devices component hardware ranging in size from 100 lbf to 35,000 lbf have been designed and manufactured using SLM and deposition-based additive manufacturing processes, and many of these pieces have been hot-fire tested at the NASA MSFC. The different combustion devices component hardware like thrust chamber injectors, injector components such as faceplates, regeneratively-cooled combustion chambers, regeneratively-cooled nozzles, gas generator and preburner hardware, and augmented spark igniters are fabricated using additive manufacturing method. They explained the results on the hot fire tests conducted on these subscale and large scale components. David et. al. [4] investigated the design modifications using CFD and experimentally tested a single-element liquid oxygen/kerosene swirl coaxial injector fabricated using additive manufacturing method. Reddy et. al. [5] compared the spray and liquid sheet characteristics of single element injector with different orifice shapes fabricated using additive manufacturing method. Ahn et. al. [6] investigated the cold flow characteristics of five different types of coaxial injector fabricated using additive manufacturing. They analyzed the injection pressure drop, discharge coefficient, spray pattern, breakup length, and spray angle for each injector and concluded that the shape of the oxidizer post had a significant influence on the performance of the injector. Jedesky et al. [7] investigated the effect of fabrication method and surface roughness on spray characteristics for pressure swirl atomizers. They evaluated the spray characteristics of these injectors using PDA and mechanical patternator.

Though a number of studies have been conducted for cold flow characterization of swirl injectors fabricated using additive manufacturing, there is not enough information available for impinging type of injectors. The present paper details about the cold flow characterization carried out on triplet impinging injector head manufactured using additive manufacturing.

ISBN - 978-93-95038-50-8

3. EXPERIMENTAL HARDWARE AND OBJECTIVES

A triplet injector head with film cooling orifices is realized through additive manufacturing process. The test article consists of 45 nos of triplet injector elements, injecting oxidiser through the two angular impinging orifices and fuel through the central orifice. There are also 36 nos of fuel film-cooling elements placed at the periphery of the injector face angled at 45°. The objective is to study the performance of injector manufactured through additive process. Cold flow evaluation consists of pressure drop estimation of oxidiser and fuel orifices for nominal and off-nominal flow rate, impingement pattern of doublet (oxidiser) and spray pattern of fuel orifices and measure the percentage of fuel available for film cooling of the chamber wall.

4. DESCRIPTION OF EXPERIMENTAL SETUP

The experimental setup consists of a VFD controlled multistage centrifugal pump to generate required injection pressure for the test medium stored in a run tank. Each feedline consists of perforated filter elements to limit particle size above 50microns entering test article. The mass flow rate through each flow path is independently measured using Micromotion make Coriolis mass flow meters. The injection pressure of the test medium is tapped close to inlet manifold to eliminate pressure drop in feedline and is measured using Rosemount make pressure transmitters. DM water is used as simulant fluid for characterizing the injector. Ambient pressure is assumed as 1 bar. The schematic of the setup is shown in Figure 1.

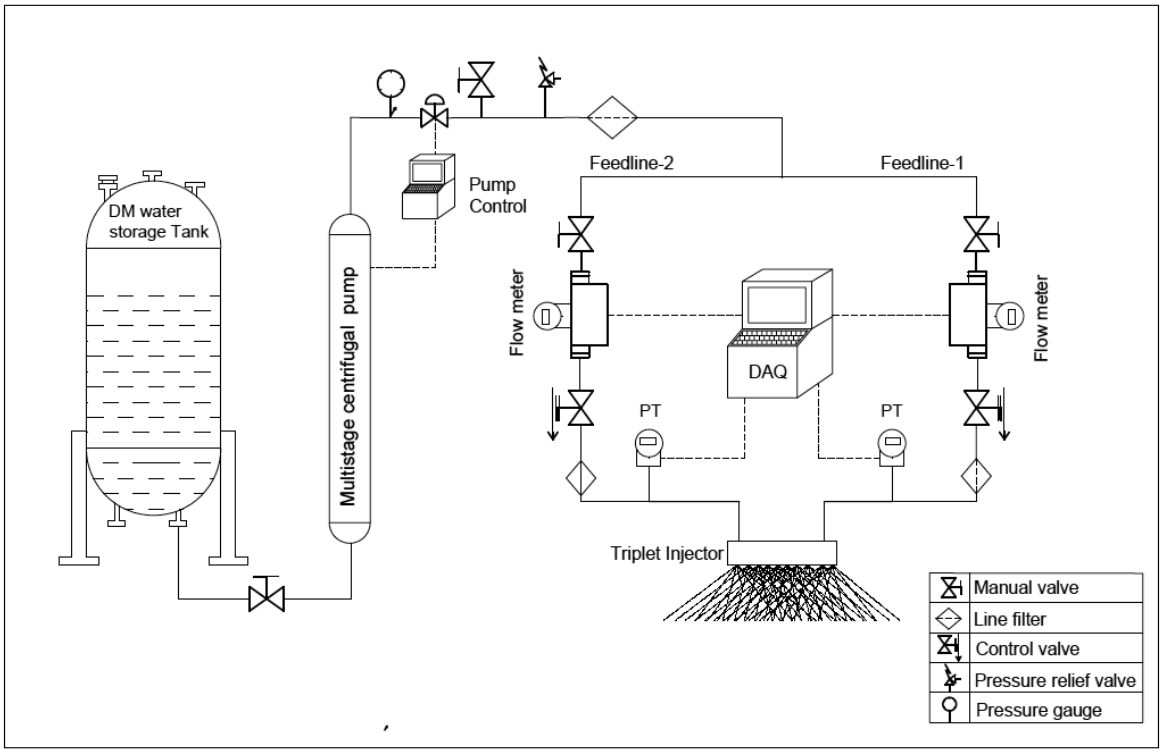

Figure 1: Schemtic of Experimental Set up

ISBN - 978-93-95038-50-8

5. MEASUREMENT METHODOLOGY

Three different fixture configurations were used to carry out the measurements depending on the parameter being investigated. Figure 2 shows the different types of fixtures used during the experiment. Fixture-1 was configured to measure pressure drop through the fuel flow path of the injector head with minimum pressure drop in fixture. This fixture configuration had shorter tube length to minimise pressure drop in line and had a projection from injector face due to which visualisation is inaccessible. Fixture-2 was used for proper visualization of spray impingement pattern. This fixture was configured to enhance visualisation by directly connecting feedlines into fuel flow manifold. Fixture-3 was used to independently measure flow available for film cooling. Oxidizer flow was not routed through fixture part as it can be directly connected to facility flange.

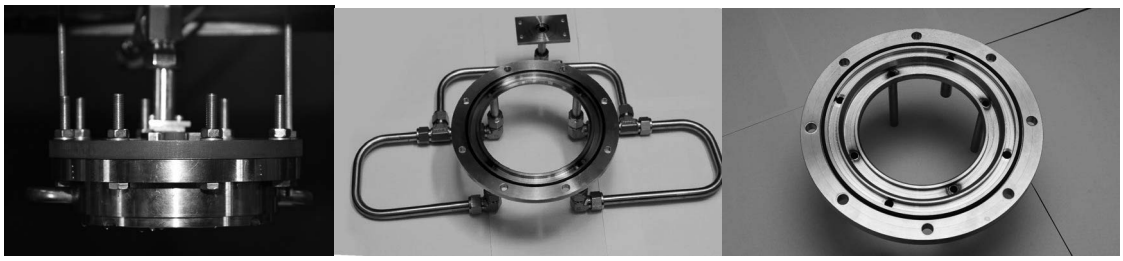

Fixture-1 Fixture-2 Fixture-3

Figure 2: Fixture configurations used during experiments

The combination of experiments conducted using different fixtures are shown in Table 1:

Table 1: Test details with fixture configuration

Sl.No.	Test details	Flow path	Fixture	Flow condition	Flow rate (g/s)
1	Flow visualisation and impingement pattern	Oxidizer	Directly mounted to facility interface	100%	1194
				50%	597
				15%	180
2		Fuel	Fixture-2	100%	1093
4	Pressure drop estimation	Oxidizer	Directly mounted to facility interface	100%	1093
				50%	597
5		Fuel	Fixture-1	100%	1093
				50%	547
6	Film cooling percentage	Fuel	Fixture-3	100%	1093
7				50%	547

ISBN - 978-93-95038-50-8

6. RESULTS AND DISCUSSION

6.1. FLOW THROUGH OXIDISER ORIFICES

Hardware was subjected to cold flow evaluation of injection through the oxidiser flow paths alone. Experiments were conducted at various pressure drops ranging from 1 bar to 6 bar and oxidiser flow rates were measured. During the experiments, the flow rate was varied in such a way that it covers the flow range from 55 % to 128 % of nominal value. The pressure drop value was also observed to be normal.

Figures 3 and 4 respectively show the variation of oxidiser mass flow rate and CdA with respect to pressure drop. It is seen from the data that the CdA decreases with increase in pressure drop. This is expected due to the contraction coefficient for orifices at higher velocities.

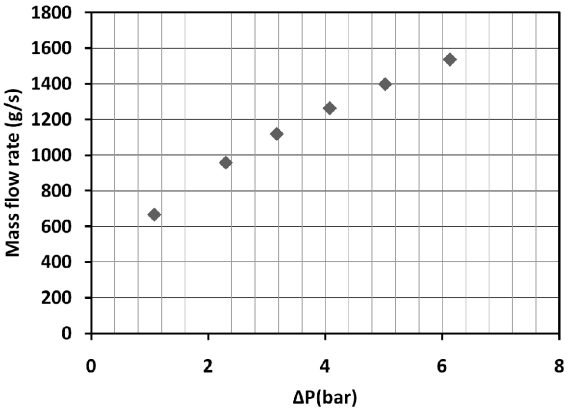

Figure 3 Mass flow rate vs. ΔP (Oxidiser orifices)

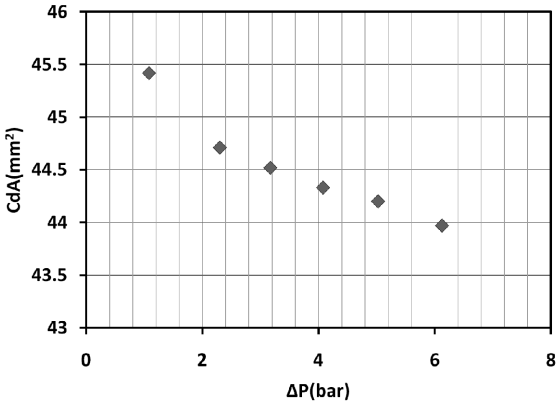

Figure 4 CdA vs. ΔP (Oxidiser orifices)

Further visualisation tests were also conducted simulating the nominal mass flow rate and off-nominal flow rate at 50% and 15 %. All orifices were visually verified for impingement pattern. These doublets were impinging at uniform distance and fan formation was also in the perpendicular direction as shown in Figure 5.

Figure 5: Impingement and fan formation of doublet oxidiser jets at 15% flow rate

ISBN - 978-93-95038-50-8

Figures 6 and 7 show the impingement pattern for 100% of flow rate and 50% of flow rate through oxidiser path respectively. Overall the cold flow performance of oxidiser flow paths realised through additive manufacturing is in line with that of conventional manufacturing.

Figure 6: Impingement at 100% flow rate

Figure 7: Impingement at 50% flow rate

6.2. FLOW THROUGH FUEL ORIFICES

Experiments were also carried out for fuel flow path (combined flow of core and film cooling) at various pressure drops ranging from 1 bar to 6 bar. During the experiments, the flow rate was varied in such a way that it covers the flow range from 57 % to 131 % of nominal value. Figures 8 and 9 show the variation of fuel mass flow rate and CdA with respect to pressure drop respectively. It is seen from the data that the CdA decreases with increase in pressure drop like oxidiser path. The reduction in CdA value is comparatively less compared to oxidiser path. This can be attributed to the difference in entry configuration of the orifices. The fuel orifices of core flow are open to a common manifold where the oxidiser doublet configuration has a U shaped cavity into which the orifices are connected with an inclination to create doublet exit jet configuration.

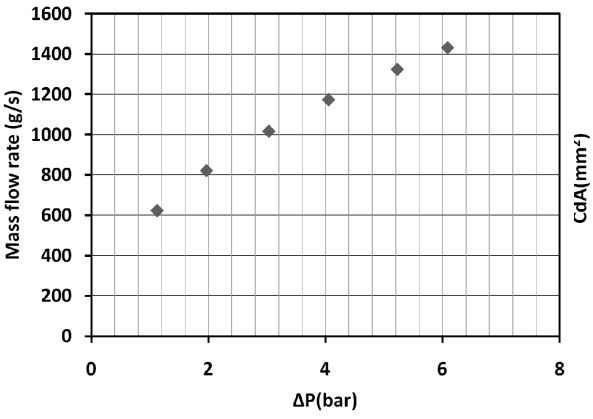

Figure 8 Mass flow rate vs. ΔP (Fuel orifices)

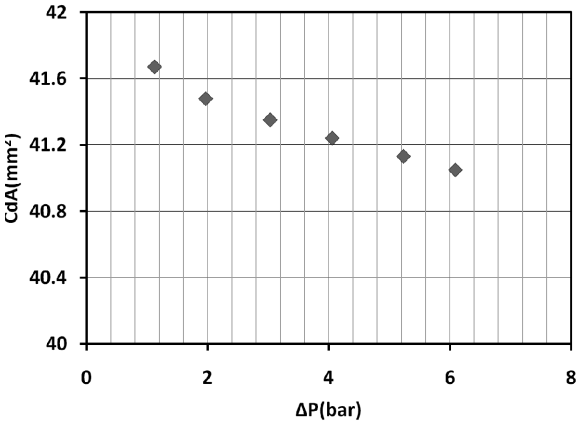

Figure 9 CdA vs. ΔP (Fuel orifices)

Further, visualisation experiments were also conducted for fuel orifices at nominal mass flow rate and at 50% of nominal value. Each fuel orifices were visually verified for individual core fuel flow jets and film cooling jets. All the orifices were having normal flow pattern and film cooling jet through radial passages were exiting. Figures 10 and 11 show the jet pattern for fuel orifices at100% of flow rate and 50% of flow rate respectively.

ISBN - 978-93-95038-50-8

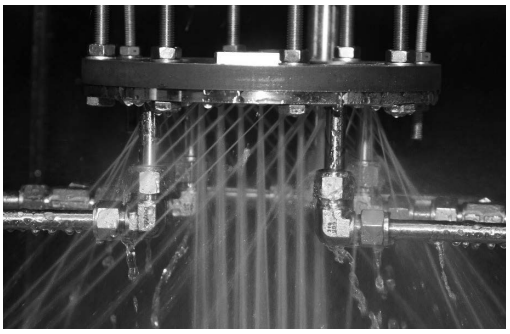

Figure 10: Fuel jet pattern at 100% flow rate

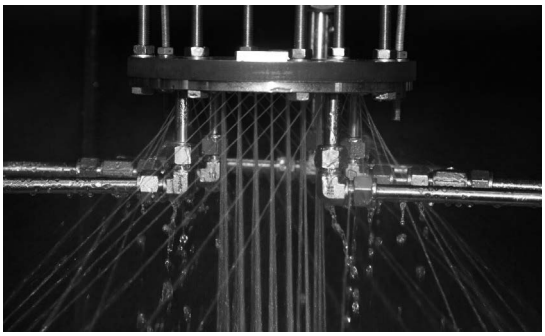

Figure 11: Fuel jet pattern at 50% flow rate

6.3. EVALUATION OF FILM COOLING PERCENTAGE

To measure the percentage of flow through film cooling orifice, flow through central orifices were isolated using Fixture-3. Flow through the core fuel orifices was collected for a specific duration and flow through the film cooling orifices were computed from the total flow rate. Film cooling percentage was measured for both nominal flow and 50 % nominal flow. Results shows reduced flow (~26-27%) through film cooling passage against the design value(~30%) at 50% flow rate and in case of nominal flow rate, reduction in percentage of film cooling by about 1% was observed compared to 50% flow rate .

7. CONCLUSIONS

Experiments were conducted for a triplet injector head manufactured through additive manufacturing for its cold flow characterization. Flow behavior of both oxidizer and fuel orifices were measured. Results indicate that pressure drops observed for both oxidizer and fuel paths are within the design specifications. Visualization experiments show that impinging pattern of oxidizer orifices and jet pattern of fuel orifices are normal. The percentage of fuel available for film cooling is marginally lower than the design specifications.

8. FUTURE WORK

Experiments are planned to evaluate the effect of surface finish and geometrical tolerances of injection orifices using triplet injector head. Experiments are also intended to evaluate its spray characteristics using high speed imaging and drop size and its distribution using Malvern Particle Sizer. Further comparative spray characterization studies of this injector is also planned with respect to triplet injector head through conventional machining process.

ACKNOWLEDGEMENTS

Authors are grateful to Liquid Propulsion Systems Centre for supporting this work.

REFERENCES

1. George P. Sutton, & Oscar Biblarz, “Rocket Propulsion Elements”, 7th Edition, John Wiley & Sons, 2001, pp 271-274

2. Soller S.; Behr R.; Beyer S.; Laithier F.; Lehmann M.; Preuss A.; & Salapete R.;“ Design and testing of liquid propellant injectors for additive manufacturing” Proceedings of the 7th EUROPEAN conference for aerospace sciences, EUCASS 2017
3. Paul Gradl.; Sandy E. Greene.;Christopher Protz.; Brad Bullard.; James Buzzell.; Chance Gracia.; Jessica Wood.; Kenneth Cooper.; James Hulka.; & Robin Osborne.; " Additive Manufacturing of Liquid Rocket Engine Combustion Devices", 54th AIAA/SAE/ASEE Joint Propulsion Conference 2018
4. David S. Morrow.; Anil P. Nair.; & R Mitchell Spearrin.; "Minimizing hydraulic losses in additively manufactured swirl coaxial injectors" AIAA Propulsion and Energy Forum, 19-22 August 2019
5. Abbavaram Revanth Reddy.; Purushothaman Nandagopalan.; Varun Sai G.; Jaya Sai P.; Harsha Narakatla.; Datta Maheshwar B.;Turkish Online Journal of Qualitative Inquiry (TOJQI), Vol 12, Issue 6, June 2021, pp76- 86
6. Ahn, J.; et al. "Injection properties according to the inner shape of the metal additive layer manufactured coaxial injectors" ***J**ournal of **A**pplied **F**luid **M**echanics*, Vol. 15, No. 4, pp. 2311-2411, 2022
7. Jedesky J. et al.; "Effect of fabrication method and surface roughness on spray characteristics for small pressure atomizers" ***J**ournal of Manufacturing Processes*, pp. 166-178, 2023

ISBN - 978-93-95038-50-8

Study on Effect of Vibration Loading of Beam Specimens on its Dynamic Characteristics

C Raja Kumaran*[1], V. Srinivasulu[2], V. Venkata Ramakrishna[3],
T. Srinivas Reddy[4], S. Sankaran[5]

[1]Engr-SD, E&HATF, [2]Technical officer C, E&HATF, [3]Dy. Manager, E&HATF,
[4]Manager, E&HATF, [5]Chief General Manager,
SMP&ETF, SDSC SHAR, Sriharikota, Tirupati Dt, AP-524124
Email: rajakumaranc@shar.gov.in, srinu.v@shar.gov.in, vvrk@shar.gov.in,
srinivasreddy.t@shar.gov.in, sankaran.s@shar.gov.in

ABSTRACT

Vibration fatigue is an important aspect to be considered during the design and development of any structure or component operating under vibration environment. Any component under fatigue may fail abruptly below the yield or ultimate point, if it reaches its end of fatigue life. Hence fatigue life estimation is very crucial for the safe operation of any structure. In the case of launch vehicle/ launch pad structures, the jet loads and acoustic loads experienced during the launch vehicle lift-off are random in nature. Fatigue life estimation under random loads are complex compared to harmonic loads. Several research works have been done in the area of health monitoring and fatigue life estimation under sinusoidal and random loading. In this work, an effort is made to understand the effect of fatigue damage on the dynamic characteristics of a simple beam structure under harmonic vibration loading and the prediction of residual life of a structure based on the change in the dynamic characteristics is proposed. Cantilever beam specimens of two different materials are considered in this study and the same were made to fail under harmonic loading for the predetermined number of cycles using an electro-dynamic shaker vibration testing setup. In this process, the variation of dynamic parameters of the test beams with the number of cycles of loading was monitored and the data is presented. Also, the initiation and propagation of crack was monitored till the damage of the beam. Hence, from the variation of natural frequency data, the residual life of the structure under study is predicted.

Keywords: *Fatigue life, natural frequency, electrodynamic shaker, strain gauge, accelerometer*

1. INTRODUCTION

Fatigue is a gradual process of local strength reduction. It is a phenomenon of damage accumulation at stress concentrations caused by fluctuating stresses and/or strains. In metals, this results in microscopic cracks. These will start to grow under continued cyclic loading until final failure occurs. The process of fatigue is essentially a process of crack growth. In general, the damage accumulation, i.e. crack growth, is slow in the early stages and at the end of fatigue life it accelerates very quickly towards failure. All engineering metals are sensitive to fatigue.

Fracture mechanics has become a perfect tool to deliver a useful methodology to compensate the inadequacies of conventional design concepts. The conventional design criteria are based on tensile strength, yield strength and buckling stress. These criteria are useful for several engineering applications, but they are insufficient when there is a crack in a structure. Hence integrity of many engineering structures is in jeopardy by the presence of these initial cracks. Even though the design may appear to be safe, but structure may fail due to aggravation of secondary cracks under same or low cyclic loads. These secondary cracks may grow either from the free surface or from the initial geometrical features such as notches. Hence it is essential to address the problem of notch under fatigue loads and

* Corresponding author: E-mail: rajakumaranc@shar.gov.in

consequent failure of the structures. Also, during the process of fatigue failure or crack growth under repeated or random loads, the dynamic properties of the structure tend to change. Monitoring the dynamic characteristics variation will be helpful in predicting the unexpected failures. In this study, the change of dynamic characteristics of a simple cantilever beam structure under harmonic vibration loading is evaluated. Also, it is proposed to predict the fatigue life of a structure from the change in dynamic characteristics.

2. LITERATURE REVIEW

The effect of fatigue life on the dynamic characteristics has been studied by various researchers. **Behzad Ahmed Zai et al [4]** proposed a methodology to predict the crack growth and fatigue life of a cantilever beam made of Acrylonitrile Butadiene Styrene (ABS) manufactured with fused deposition modelling. Three beam configurations based on length were considered and empirical relationships are formulated between the natural frequency and the crack growth. Using the experimental data, a global relation is formulated for the in-situ crack depth prediction with an error of less than 10%.

Mahantesh. Matur et al [5] studied the fatigue crack growth behaviour of an arc shaped specimen with inner surface notch. Stress intensity factor (SIF) values obtained by the numerical simulation for the single edge notch bend specimen showed a good agreement with the results obtained by photo elastic technique and hence using the same numerical simulation based finite element analysis (FEA) technique, an influence of presence of notch on the fatigue life of aluminium specimen was investigated by the numerical simulation and compared with experimental results. **Da Yu et al [8]** developed an assessment methodology based on vibration tests and finite element analysis to predict the fatigue life of designed PCB with ball grid array (BGA) package under random vibration loading.

Ed Habtou et al [9] developed a new method where the damage accumulation rate is computed in the frequency domain using Linear Elastic Fracture Mechanics (LEFM), stress intensity & the natural frequency and a finite element model was developed to predict the stress intensity and natural frequency during damage accumulation.

K Klein et al [12] investigated fatigue crack detection using modal analysis. Steel cantilever beams were subjected to repetitive cyclic stress. Periodic measurements with accelerometers, force transducers and pressure microphones recorded both the frequency response and pressure transfer functions of the specimens. The objective was to observe the changes in both vibration and acoustic variables that occurred with the presence of a fatigue crack. Shifts in natural frequency, damping and other parameters were documented as sample specimens were fatigued into cracking. From the mode shapes, it was observed that the crack's position was close to maxima of the fourth and fifth modes in both tests. The natural frequencies of the fourth and fifth modes were observed to be most affected. Likewise, the apparent damping coefficient increased for these modes.

3. PROBLEM DEFINITION

The main objective of the present work it to study the variation of natural frequency with the number of cycles of loading, when a structure is subjected to fatigue loading. The fatigue loading may be harmonic or random. This work deals with harmonic sinusoidal loads. The objective is achieved by designing a cantilever beam specimen with two different materials and subjecting it to the required strain and stress in order to make it fail at the predefined

ISBN - 978-93-95038-50-8

number of cycles of harmonic fatigue loading with stress ratio R = -1. The natural frequency variation is monitored during the fatigue loading at regular intervals till the failure of the beam. From the variation in natural frequency, it is proposed to predict the residual fatigue life of the structure.

4. EXPERIMENTAL SETUP0

4.1. PREPARATION OF BEAM SPECIMENS

In this study, beams with two different materials namely mild steel IS 2062 Grade B E250 and aluminum Al 6061 T6 are considered. The dimensions are selected appropriately for both the beams so as to achieve the required stress levels in the beam during vibration loading using electro-dynamic shaker. The edges and surfaces are prepared properly to avoid discontinuities, which may become the crack initiation point during fatigue loading. The dimensions of the aluminium and MS beams selected are 250*25*3 mm and 250*25*2 mm respectively and the beams are provided with a hole at one end for mounting the beam on the miniature electrodynamic shaker. Figure 1 shows the mild steel and aluminium beam specimens bonded with strain gauges. The strain gauges are bonded on to the beams very close to the mounting point as seen in Figure 1, where maximum stress is expected. In order to subject the beam to required stress and strains levels, so as to make it fail under fatigue for the calculated number of cycles, it is required to increase the mass at the free end of the cantilever beam. This was achieved by fixing predetermined mass blocks at the free end of the beam.

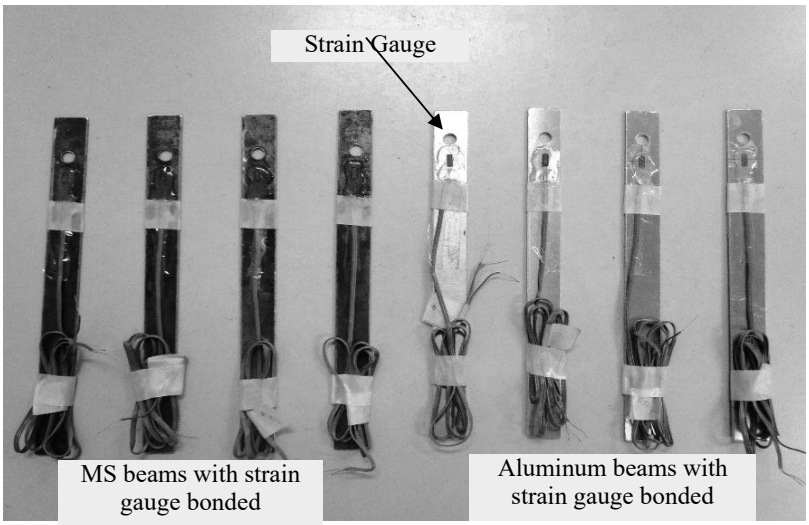

Figure 1: Mild steel & Aluminum cantilever beam specimens

4.2. TEST SETUP FOR VIBRATION LOADING AND EVALUATION OF NATURAL FREQUENCY

The experimental setup consists of a miniature electrodynamic shaker (MS 1000, Sentek dynamics), Power amplifier (Sentek Dynamics, LA 1500), tear drop accelerometers accelerometers (PCB make, Sensitivity range ~ 10mv/g, Model No 352C22), Strain gauges (FLAB-6-350-11), Strain gauge data acquisition card (National Instruments NI 9236 module), Chassis for data acquisition card (National Instruments NI cDAQ-9184), Computer with National instruments signal express software, Data acquisition system for vibration

ISBN - 978-93-95038-50-8

system (16 channel vibrunner AI810), Computer with m+p international software, Cantilever beam specimens, mounting fasteners, necessary tools and cables. The test setup is shown in figure 2. The cantilever beam specimen is mounted directly on the shaker table using suitable fasteners. A dummy mass of calculated weight is fixed on beam at the free end in order to achieve the required strain levels near the fixed end of the beam. One accelerometer is mounted on the fixed end while the other is mounted on the free end of the beam. The miniature electro-dynamic shaker is controlled by the m+p international vibrunner software through the data acquisition system and power amplifier. The same system is used to measure the vibration/acceleration levels on the beam through the accelerometers. The strain gauge data acquisition system consists of the strain gauge, NI 9236 strain gauge measurement module, NI cDAQ-9184 chassis and control computer using NI signal express software. The strain gauge is connected in quarter bridge configuration using the strain gauge measurement module. The estimation of natural frequency of the beam is carried out using the accelerometers and data acquisition system.

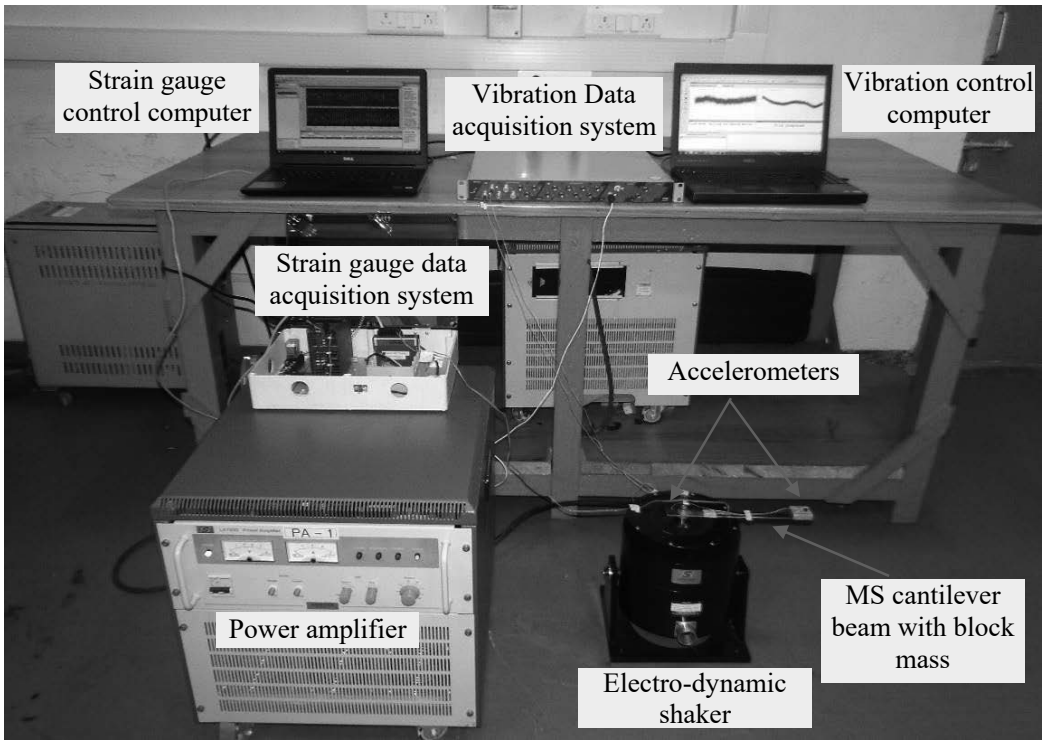

Figure 2: Experimental test setup for fatigue testing

5. TESTING METHODOLGY

In this study, the cantilever beam specimens are subjected to bending fatigue loading for the predetermined number of cycles to failure calculated using SN curve equations of mild steel [12] & Al 6061[13] and the variation in natural frequency of the beams till failure were recorded at specified intervals.

Initially, the test setup was arranged as shown in figure 2. The cantilever beam specimens bonded with strain gauge was mounted on the shaker table and the accelerometers are mounted on the beam specimen. Alignment of the beam is ensured and suitable torque was provided to the mounting bolts. After configuring the strain gauge data acquisition

system and vibration data acquisition system, a tap test was performed to determine the natural frequency of the untested beam. Figure 3 shows the frequency domain data and time domain data measured during a tap test.

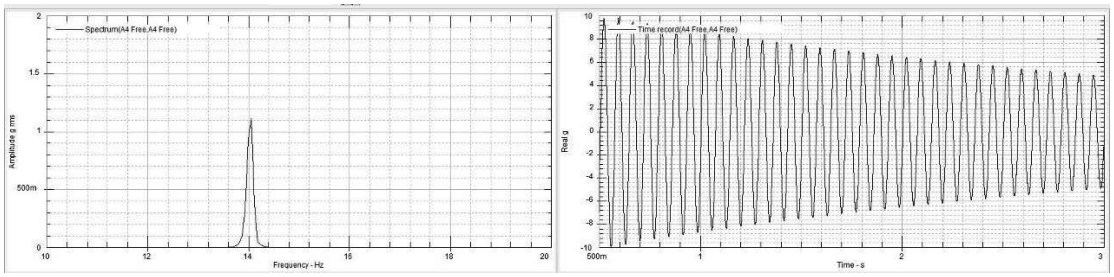

Figure 3: Tap test measurement – frequency and time domain data

From the predetermined no of cycles to failure for the selected beam specimen material, the corresponding stress was calculated using the SN curve relations available in literature. The equivalent strain for the stress calculated from SN curve relation was evaluated. After determining the natural frequency and strain, a sine dwell test is carried out for a small portion of the predetermined cycles using the miniature electro-dynamic shaker system at a frequency which is lesser and very close to the natural frequency so as to use the effect of resonance in achieving the required strain and stress at the fixed end of the cantilever beam. During the sine dwell test, the vibration levels are increased by quickly adjusting the gain in the amplifier till the calculated strain level is achieved at the strain gauge bonded near the fixed end of the beam specimen. At this strain level, the sine dwell test is carried out for the time duration corresponding to the small portion of predetermined of cycles of operation and the frequency. After the sine dwell test, tap test is carried out to determine the change in natural frequency of the beam specimen. The sine dwell test for the next few cycles of vibration loading is carried out again followed by the tap test to determine the change in natural frequency. The process is repeated until the beam specimen cracks and fails.

In this work, mild steel and aluminum beam specimens were tested considering the predetermined cycles to failure as 1,25,000 and 10,000 cycles respectively. From the SN curve relations, the equivalent strain to be subjected near the fixed end of the mild steel and aluminum cantilever beam specimens were estimated as $1.27 * 10^{-3}$ and $3.5 * 10^{-3}$ respectively. The natural frequency of the mild steel and aluminium beam specimens were close to 16 Hz and 14 Hz respectively. Four beam specimens of mild steel and aluminium were tested to check the repeatability of data.

6. RESULTS AND DISCUSSION

The mild steel and aluminium beam specimens were fatigue tested using the miniature electro-dynamic shaker system to the predetermined cycles and the change in natural frequency were recorded. Figure 4 shows the variation of natural frequency of MS cantilever beam specimen against the number of cycles. As per the plan of the MS cantilever beam specimen fatigue testing, design cycles to failure was 1,25,000 cycles for a strain value of $1.27*10^{-3}$ strains. But the actual cycles to failure was found to be around 1,80,000 cycles. A crack was observed around 1,45,000 cycles which was accompanied by a small dip in natural frequency from 16.1Hz to 15.94Hz. From then, the crack propagation was observed and further dip in natural frequency was observed. The crack propagated and grew larger

ISBN - 978-93-95038-50-8

throughout the width of the beam, at the end of 1,80,000 cycles and the corresponding value of natural frequency was found to be 13.25Hz.

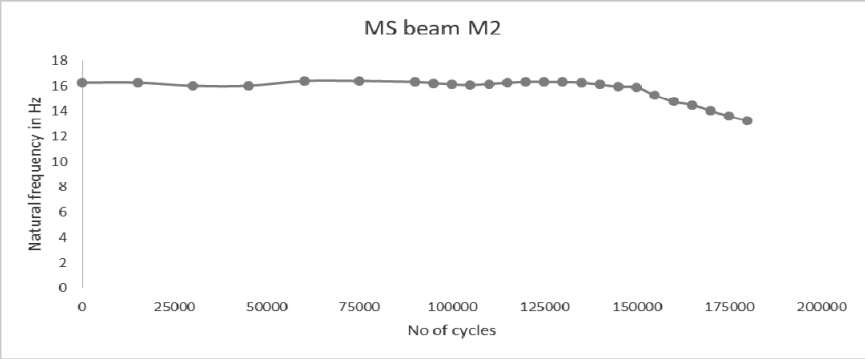

Figure 4: Natural Frequency Variation for MS Specimen

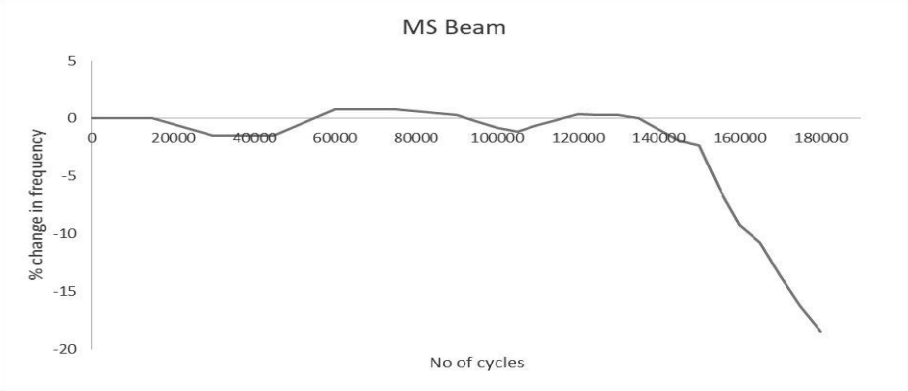

Figure 5: %Change in Frequency vs Number of Cycles for MS Beam

Figure 5 shows the % change in frequency with respect to the number of cycles. From figure 5, it can be seen that, after the natural frequency has reduced by nearly 5%, the residual life to failure is only 25000 cycles which is 13.8% of the actual life of 180000 cycles. Figure 6 shows the crack on top and bottom side of one mild steel specimen.

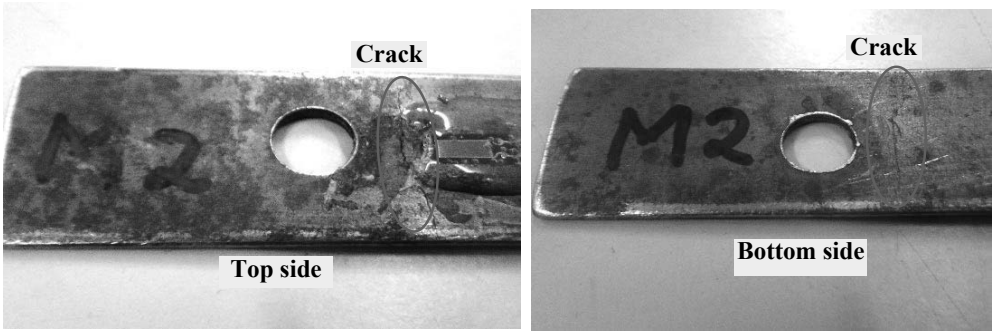

Figure 6: Crack on the top side and bottom side of MS beam

Figure 7 shows the variation of natural frequency of Al cantilever beam specimen against the number of cycles and Figure 8 shows the % change in frequency with respect to the

number of cycles. As per the plan of the Al cantilever beam specimen fatigue testing, design cycles to failure was 10,000 cycles for a strain value of $3.5*10^{-3}$ strains. But the actual cycles to failure was found to be 10093 cycles with a deviation of 1%. A crack was observed around 9250 cycles that was accompanied by a small dip in natural frequency from 14.06 to 13.82. From then, the crack propagation was observed and further dip in natural frequency was seen. Figure 8 shows that, after the natural frequency has reduced by nearly 5%, the residual life to failure is only 468 cycles which is 4.6% of the actual life of 10093 cycles. The cracks observed on the surfaces of aluminium beam is shown in Figure 9.

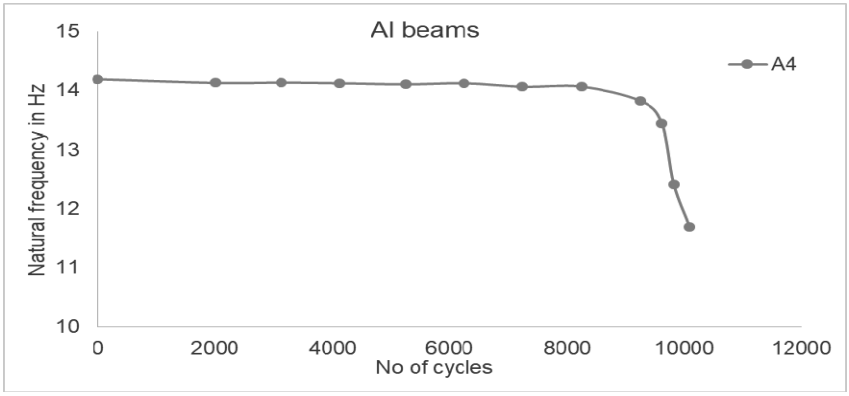

Figure 7: Natural Frequency Variation for Aluminium Specimen

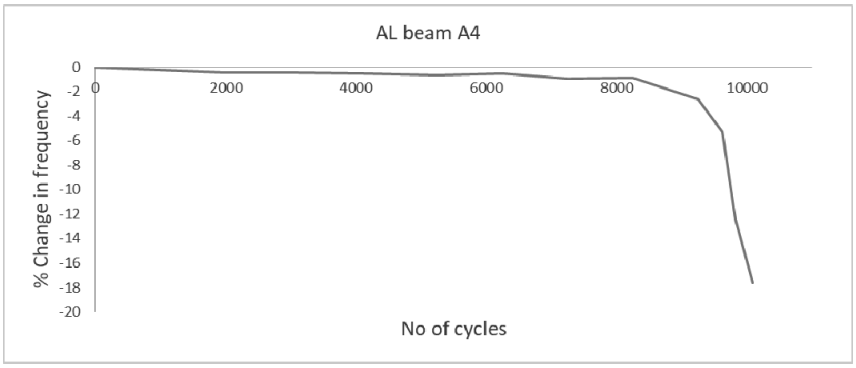

Figure 8: %Change in Frequency vs Number of Cycles for Al Beam

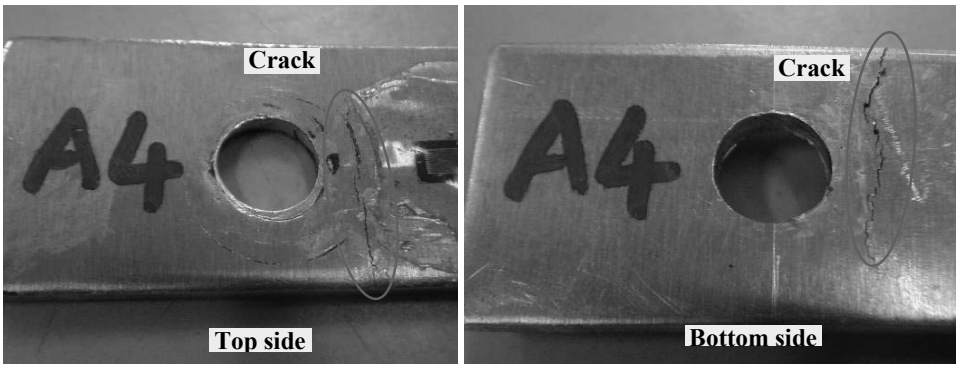

Figure 9: Crack on the top side and bottom side of Aluminium beam

The summary of the results of MS and Al beams are provided in Table 1. From the table, it can be seen that, after a reduction in natural frequency of 5% in mild steel and aluminium

beam specimens, the residual life available was found to be 25000 and 468 cycles respectively. Hence for the cantilever beams of the selected size and material with harmonic loading, the residual life can be predicted from the change in natural frequency data evaluated in this work. The change in natural frequency and residual life with the change in size and shape and type of loading has to be studied. Also the change in residual life with random loading will be studied as an extension of this work.

Table 1: Summary of MS & Al beam test results

Description	**Design life in no of cycles**	**Actual life in no of cycles**	**% variation in no of cycles**	**Residual life in cycles after reduction in natural frequency of 5%**	**Residual life in % after reduction in natural frequency of 5%**
MS IS 2062 Grade B cantilever beam	1,25,000	1,80,000	30%	25000	13.8%
Al 6061 T6 cantilever beam	10,000	10,093	1%	468	4.6%

7. CONCLUSION

The variation of natural frequency of cantilever beam specimens made of IS 2062 E250 Grade B (mild steel) and Al 6061 T6 materials with respect to the number of cycles of fatigue loading was measured. The MS beam specimen was tested for a designed fatigue life of 1,25,000 cycles while the actual cycles to failure was found to be 1,80,000 cycles which is a deviation in life of 30%. Similarly, the Al beam was tested for a designed fatigue life of 10,000 cycles while the actual cycles to failure was found to be 10093 cycles. The deviation between the design life and actual life for the MS and Al beam specimen was 30 % and 1% respectively. The deviation of actual life with respect to design life is within the deviation levels for both the materials as specified in literatures. For MS beam, after the natural frequency has reduced by nearly 5%, the residual life to failure is only 25000 cycles which is 13.8% of the actual life of 180000 cycles. For Al beam, after the natural frequency has reduced by nearly 5%, the residual life to failure is only 468 cycles which is 4.6% of the actual life of 10093 cycles. Hence, this methodology can be applied to the health monitoring of critical structures for averting unexpected failures by monitoring the variation in natural frequency during its operation and determining its residual life.

8. FUTURE SCOPE

The present work deals only with the study of variation of natural frequency under harmonic loading of plain cantilever beams with stress ratio of R = - 1. The same can be extended to beams with different stress ratios and in the presence of holes, notches, other discontinuities, etc. In this study, dimension of the beam is fixed and experiments are carried out. The present study can be carried out using beams of different sizes and different materials.

ISBN - 978-93-95038-50-8

This study can be implemented to complex structures and methodology of continuous health monitoring of critical structures can be devised to avoid unexpected failures. Harmonic load conditions are comparatively simple compared to random loads. Majority of the structures are subjected to random loads. Hence the effect of fatigue and fracture under random loads and the associated variation in the dynamic parameters can be studied. Random loads are complex in a way that, it requires techniques like rain flow counting for determining the number of cycles of loading and its amplitude and the same can be explored. The natural frequency variation in the presence of a crack and the residual life after 5% reduction of the same is calculated for a cantilever beam specimen. A methodology can be developed to correlate the cantilever beam results to any structure and predict the residual life of the same.

REFERENCES

1. Yulian kin & Krasimir zahariev: Natural frequency method (impact acoustic method) for crack defect evaluation in steel parts, American society for engineering education, 2006, page 11.953.1
2. Martin Česnik & Janko Slavič: Vibrational Fatigue and Structural Dynamics for Harmonic and Random Loads, Strojniški vestnik - Journal of Mechanical Engineering 60(2014)5, 339-348 2014, DOI:10.5545/sv-jme.2013.1831
3. M. Cesnik, J. Slavi˘c and M. Bolte˘zar: Uninterrupted and accelerated vibrational fatigue testing with simultaneous monitoring of the natural frequency and damping, Journal of Sound and Vibration, Vol. 331(2012), 5370-5382, DOI: 10.1016/j.jsv.2012.06.022
4. Behzad Ahmed Zai, Muhammad A. Khan, Sohaib Z. Khan, Muhammad Asif, Kamran A. Khan, Ahmed N. Saquib, Asif Mansoor, Majid Shahzad & Ahmed Mujtaba: Prediction of crack depth and fatigue life of an Acrylonitrile Butadiene Styrene cantilever beam using dynamic response, ORICD: 0000-0002-2584-9006
5. Mahantesh. Matur, V. Krishnan & P. Dinesh: Study On Fatigue Crack Growth Behavior Of Aluminum Alloy In The Presence Of Notch: An FEA Approach, IOSR Journal of Mechanical and Civil Engineering (IOSR-JMCE), e-ISSN: 2278-1684,p-ISSN: 2320-334X, Volume 12, Issue 5 Ver. II (Sep. - Oct. 2015), PP 68-74
6. R. R. Ambriz, G. Mesmacque, A. Ruiz, A. Amrouche, V. H. Lo´pez & N. Benseddi: Fatigue crack growth under a constant amplitude loading of Al-6061-T6 welds obtained by modified indirect electric arc technique, Science and Technology of Welding and Joining 2010 VOL 15 NO 6, Institute of Materials, Minerals and Mining, DOI 10.1179/136217110X127858895 49589
7. Seong-In Moon, Il-Je Cho and David Yoon, Fatigue life evaluation of mechanical components using vibration fatigue analysis technique. Journal of Mechanical Science and Technology 25 (3) (2011) 631~637
8. Da Yu, Abdullah Al-Yafawi, Tung T. Nguyen, Seungbae Park and Soonwan Chung, High-cycle fatigue life prediction for Pb-free BGA under random vibration loading, Microelectronics Reliability 51 (2011) 649–656
9. Ed Habtour, Mark Paulus & Abhijit Dasgupta: Modeling Approach for Predicting the Rate of Frequency Change of Notched Beam Exposed to Gaussian Random Excitation, Hindawi Publishing Corporation, Shock and Vibration, Volume 2014, Article ID 164039
10. Troy Savoie and Vit Babuška, Predicting Fatigue Failure of a Circuit Board in Random Vibration:The Reference Model, SAND2014-1768C
11. Costas Papadimitriou, Claus-Peter Fritzen, Peter Kraemer & Evangelos Ntotsios: Fatigue predictions in entire body of metallic structures from a limited number of vibration sensors using Kalman filtering, structural control and health monitoring, Struct. Control Health Monit. (2010), Published online in Wiley InterScience (www.interscience.wiley.com). DOI: 10.1002/stc.395
12. Monitoring change in modal parameters using fatigue, K Klein, JY Guigne, ASJ Swamidas
13. Julie.A.Bannantine: Fundamentals of metal fatigue analysis,
14. G.T.Yahr: Fatigue design curves for 6061-T6 Aluminium.

15. MIL Handbook MIL-HDBK-5J
16. MIL Handbook MIL-HDBK-5H
17. Paul H Wirsching, Statistical summaries of fatigue data for design purposes, GRANT NAG 3 4 1, July 1983.
18. Carol Johnston, Statistical analysis of fatigue test data, ASME 2017, OMAE 2017.

ISBN - 978-93-95038-50-8

Optimization of a Stiffened Interstage Structure of a Launch Vehicle using Differential Evolution Algorithm in Indigenous FE Software

Manash Kumar Bhadra*[1], Shachindra Nath Sharma, Partha Ajit Surve, Vinod G

Vikram Sarabhai Space Centre
Indian Space Research Organisation
Thiruvananthapuram, Kerala 695022
Email: manash.bhadra2009@gmail.com

ABSTRACT

Optimization has become synonymous to improvement in the context of design of launch vehicle structures. Problem is challenging because it not only involves multiple variable but also multiple objectives and constraints. The paper presents a method to optimize a stiffened interstage structure of a launch vehicle using differential evolution algorithm. The optimization was carried out to find the optimal number of stiffeners required and the optimal geometry of the hat stiffener that will minimize the hardware mass for specified axial compressive load, natural frequency and the strength of the material. The proposed method is implemented in finite element analysis software using Python based scripting.

Keywords: *Optimization, stiffened structures, differential evolution, finite element analysis*

1. INTRODUCTION

In the last decade Evolutionary algorithm (EA) appears as an important optimization and search technique. EA is a set of modern heuristics search method and it is a subdivision of Evolutionary Computations (EC). It is a popular problem-solving method used world-wide optimization problems because of its flexibility and robustness innate from Evolutionary Computation. In case of complex problems it can be used successfully. For a complex and multivariate function for finding the overall range or minimum or maximum, Differential Evolution (DE) which is a popular EA technique can be used. The algorithm is particularly well-suited for problems that are non-linear and have many local optima, as it is based on the idea of genetic algorithms and simulates the process of natural evolution.

The inter stage is an inevitable portion in the launch vehicle and it interconnects two stages of the vehicle. The interstage that is provided between the first stage (solid rocket motor stage) and second stage (earth storable liquid stage) is considered for study. Closely stiffened shell structure preferred over monolithic structures to increase the stiffness to withstand the structural, inertial aerodynamic loads. The closely stiffened structure comprises typically hat sections made out of metal or composite called stinger which is fastened to the skin shell. The structure is cylindrical in shape. Closely stiffened shell type construction is adopted with uniformly spaced stiffeners along the circumference. The elements of the hat namely flange side web and crown will have the crippling strength by design whereas the skin needed wrinkling strength and shear strength additionally. A typical interstage structure modelled in indigenous software is shown in figure-1. In this paper, optimal number of stiffeners required and the best geometry of the hat stiffener that will minimize the hardware mass for a typical column is determined using differential evolution algorithm. Natural frequency and the maximum value of effective stress are considered as design constraints. The proposed method is implemented in finite element software using Python based scripting. The finite element model is developed in a parametric form using Python interface and the model can be used to optimize interstage structure with different diameter and height as well.

[1] Corresponding author: E-mail: manash.bhadra2009@gmail.com

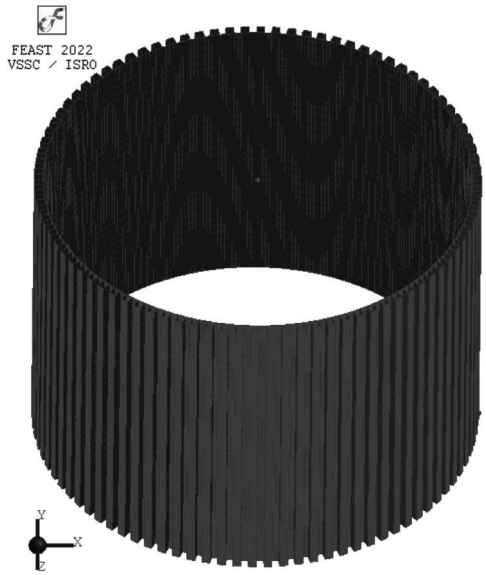

Figure 1: Typical launch vehicle interstage structure

2. LITERATURE REVIEW

Layout optimization of stiffeners in large shell structures was studied by Savine et al [1]. They proposed the extension of the stiffener element-based techniques. Stiffeners integrated to components are considered as sets of beam elements. The assembly is simulated in the ground structure which is meshed using structural elements like shells and beams. In the optimization process, the stiffener which is intrinsically a beam is represented as an equivalent framework. The components are free to move over the shell surface, without any re meshing operation in this method.

Advanced design procedures for design of metallic launch -vehicle cylinder under axial compression was studied and presented by Wagner et al [2]. They conceived the orthogrid stiffened cylinders from NASAs SBKF and demonstrated and validated in this study. Metallic launch vehicle shells with orthogrid stiffened panels were developed and verified. A design curve for the buckling load of orthogrid shells delivered typically 20% higher KDFs on average compared to the design curve for equivalent isotropic shells. The buckling factor depends on the L/R ratio which results in improved KDFs for the orthogrid short shells while relating to the empirical NASA SP-8007. An orthogrid cylinder which is having different buckling characteristics like column buckling, skin buckling and local buckling are examined during the design of actual launch-vehicle shells.

Zheng et al [3] analyzed the stiffness and critical force of a lattice cylinder theoretically by equivalent continuum method. The four failure modes for a lattice cylinder under axial compression are global buckling, two strut buckling modes (including out-of-plane strut buckling and in-plane strut buckling) and strength failure. Curves of load capacity and the failure maps revealed that the failure of large-scale lattice cylinder is generally dominated by global buckling due to the small thickness of the shell.

Vikhar and Baba [4] studied about Evolutionary Algorithms (EA). The study involves the implementation of its generic procedure and a critical summary of Evolutionary Algorithms. The merits of evolutionary algorithms over classical techniques of optimization are discussed. The various invariants of EA comprise of Genetic Programming (GP), Genetic Algorithm

ISBN - 978-93-95038-50-8

(GA), Evolutionary Programming (EP) and Evolution Strategies (ES) are also counted in this study. Various extensive refinements were focused in the area of evolutionary algorithms to solve real life problems.

Beielstein et al [5] explains how the evolutionary algorithms can be adapted to work well in dynamic or noisy optimization problems and with multiple objectives. The study outlines the state of art in evolutionary algorithms. It also presents the important nontechnical treatment of evolutionary algorithm ideas. They also presented some recent developments from theory and also attempted the tuning of the algorithms. Real-world problems connected with typical applications of evolutionary algorithms are finally shown with special emphasis on data-mining applications.

Koke et al [6] presented optimization of a grid interstage structure with unit cell approach. The capability of the unit cell in combination with the augmented lagrangian particle swarm algorithm is used to solve mixed-integer constrained optimization problems. The optimization of the grid structure is tried by only with stability constrained. The most critical factor is the local buckling of bars. The stability criteria was driven by a monolithic helix and its implementation in the unit cell because of the variable moment of inertia for the axial bars. The stiffening effect of the sandwich is the scope of the future study.

Sleight et al [7] studied about the composite structural design concepts for the pre-V interstage structure as a part of NASA's advanced composite technologies project. Structural design and analysis were performed with the help of "Hyper sizer" design sizing software and "Nastran" finite element analysis software. This study revealed that the structural weight of the closely stiffened panel design is 11% lesser compared to the honey comb sandwich design. The interstage design was shorted in length based on the detailed investigation and higher loads were enforced to reflect the current state of Ares-V within the NASA constellation program

Bagheri et al [8] developed a genetic algorithm optimization of a ring stiffened cylindrical shells for axial and radial buckling loads. The four constraints viz, fundamental frequency, structural weight, axial buckling load and radial buckling load are imposed. Optimized stiffening cylindrical shells leads to a reduced structural weight, higher natural frequencies and larger axial and radial buckling loads simultaneously. The upper and lower bounds of the design variables influenced the optimum results considerably. The axial and radial buckling loads considerably influenced by the distributions of eccentricity and spacing of the stiffeners.

Collier et al [9] studied and proved that hat stinger stiffened panels are the most effective to carry the buckling load experienced in the Ares V Heavy Launch Vehicle. Closely stiffened panel concept is 20% lighter compared to honeycomb sandwich concept. The weight savings in the hat stiffened panels overcome the weight of the ring frames, connected joints and fasteners even if ring frames are required for buckling stability. to Optimization of the closely stiffened panels are more complex than sandwich panels because of more optimization variables. However, this offers more customization and weight savings opportunities. Automated analysis tool like Hyper Sizer similar to ref-7 is needed to fully explore the design space.

Hrstka et al [10] studied the improvements of Real Coded Genetic Algorithms built on differential operators avoiding Premature Convergence. Several forms of evolutionary algorithms used for global optimization on real domains presented in the study. Real coded methods with several improvements in general exhibit better behaviour on real domains than binary algorithms. The positive impact of the differential operators due to the possibility of

ISBN - 978-93-95038-50-8

self-adaptation is demonstrated. Real encoded differential algorithm enhanced by the technology described in this study is a widespread and reliable method of solving of all proposed test problems.

Design study for structural optimization of a hat-stiffened laminated composite panel for an upper cover panel of a typical passenger bay of a blended wing body transport airplane configuration completed by Vitali et al [11]. The adequacy of a hat-stiffened composite panel for the upper cover panel is investigated and compared to a thick sandwich panel on the basis of weight. The structural optimization is framed using the panel weight as the objective function with constraints on stress and buckling. The optimization conducted with the response surfaces resulted in weight savings.

3. PROBLEM DEFINITION

A closely stiffened interstage structure of typical diameter 2000mm and height 1500mm is to be designed for an upper bound load carrying capacity of 150kN and natural frequency of 50 Hz. The maximum stress in the structure to be less than the 0.2% proof strength of Aluminum Alloy. The number and sizing of the hat stiffener is to be estimated which satisfies the above conditions.

4. RESEARCH METHODOLOGY

4.1. DIFFERENTIAL EVOLUTION

The optimization problem is framed as a search for the optimal solution in a population of candidate solutions. At each iteration, DE generates new candidate solutions by combining the existing solutions in a way that reflects the genetic variation that occurs in natural populations. The algorithm iteratively refines the population by selecting the best candidate solutions and incorporating their characteristics into the next generation. The central idea behind DE is to generate trial solutions by combining two or more existing solutions in the population. The combination process involves selecting three random solutions from the population and generating a new trial solution by adding a weighted difference of two of the selected solutions to a third solution. The new trial solution is then compared to the existing solutions in the population, and if it provides a better solution, it is added to the population for the next iteration. One of the key advantages of DE is its ability to explore a large search space effectively, making it well-suited for problems with a high number of variables and complex landscapes. The algorithm is relatively simple to implement, as it only requires a small number of user-defined parameters, and can be easily adapted to a wide range of optimization problems. In addition to its effectiveness, DE also has several other advantages. It is a robust algorithm, meaning it is insensitive to the choice of initial population and can still produce good results even when the starting population is not very well-suited to the problem. DE is also a highly parallelizable algorithm, meaning that it can be easily parallelized and run in parallel on multiple processors or GPUs to achieve fast convergence. Despite its many advantages, DE is not without limitations. One of the main drawbacks of the algorithm is that it can be sensitive to the choice of control parameters, such as the population size and the weighting factor used in the combination process. It is also important to note that DE may not always find the global range; minimum or maximum of a function, as it is possible that the algorithm may converge to a local minimum instead. Differential Evolution is a powerful optimization technique that has proven to be effective in a wide range of optimization problems. Its ability to explore a large search space, robustness to the choice of initial population, and parallelizability make it an attractive choice for researchers and

ISBN - 978-93-95038-50-8

practitioners. Despite its limitations, DE remains a valuable tool for solving complex optimization problems and continues to be widely used in a variety of fields, including engineering, finance, and biology. The different steps in a differential evolution are shown in figure-2.

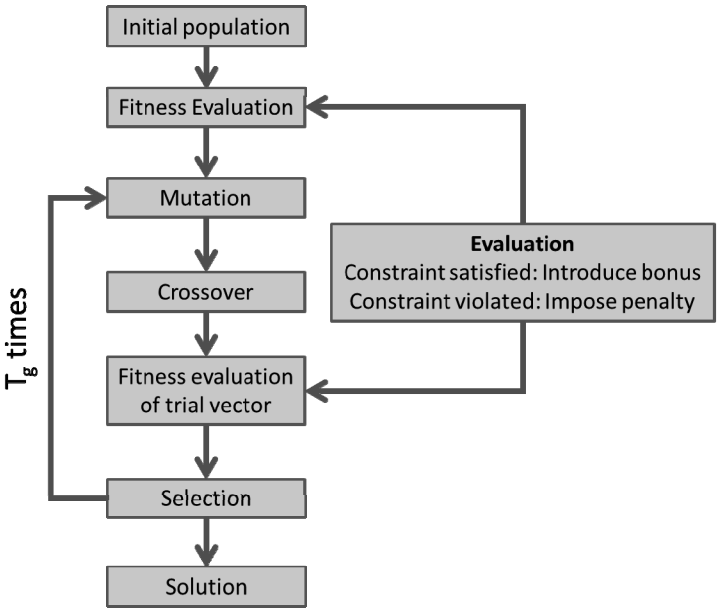

Figure 2: Flowchart of different steps in differential evolution algorithm

4.2. OPTIMIZATION DETAILS

Table 1*: Design and optimization parameters*

Design objective	Minimize the weight of the interstage structure	
DE parameters	Population size	50
	Number of generations	30
	Crossover rate	0.90
	Scaling factor	0.85
Design variables	Height of the stiffener	10mm to 100mm
	Width of the stiffener	10mm to 200mm
	No. of stiffener	12 to 120
Design Constraints	Minimum natural frequency	60 Hz
	Maximum von Mises stress	350 MPa
	Minimum buckling load	150kN
Material property	Young's Modulus	70000 MPa
	Poisson's ratio	0.3
Dimension details	Internal diameter	2000 mm
	Height	1500 mm

ISBN - 978-93-95038-50-8

Table-1 is given the design inputs used in the optimization of the closely stiffened cylinder. Linear buckling analysis has been carried out to evaluate the fitness of a particular solution. The finite element is discretized using an element size of 10mm. Mapped meshing is carried out using 3D shell elements. The constraints provided on the edge nodes at one end specified with all displacement and rotation degrees of freedom. For the nodes on the other cylindrical edge, hinged boundary condition is used. Edge load is applied axially in the model.

5. RESULTS AND DISCUSSIONS

The optimization converged for a maximum load of 196kN. The optimal numbers of circumferential stiffeners are 90. The optimal depth of the side web and width of the crown of the stiffener are 30mm and 20mm respectively. The maximum von Mises 166.7MPa. Figure-3 shows the distribution of von Mises stress.

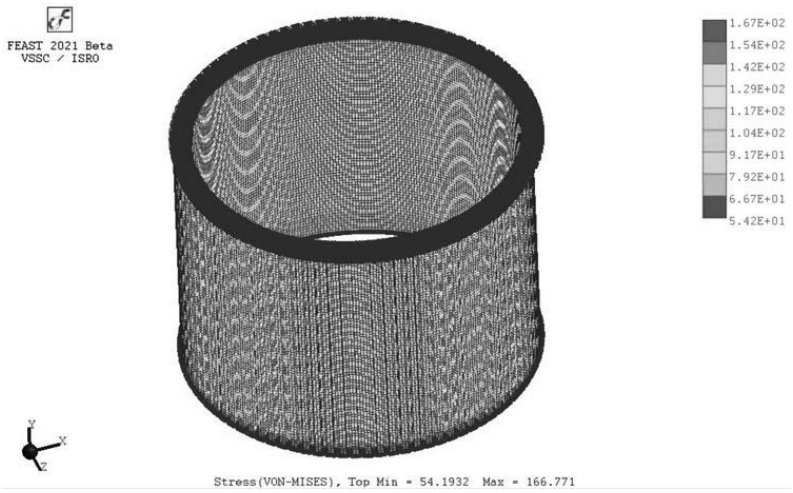

Figure 3: Distribution of von Mises stress

Figure-4 shows the variation of maximum fitness (critical buckling load in kN). The highest converged value is attained in the 15th generation and thus it justifies the number of generations considered. Evaluation of each candidate solution of the population took about 4 minutes and the total time taken for the optimization was 10 hours. The maximum displacement in mode 1 is 2.85mm and is shown in figure-5.

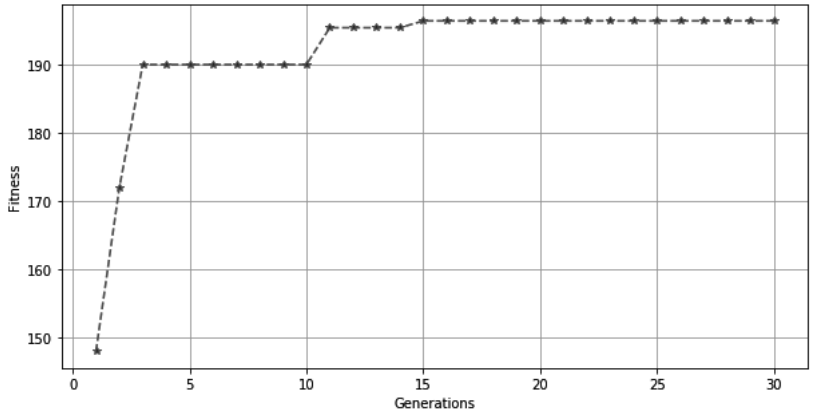

Figure 4: Variation of the fitness (critical buckling load in kN) in various generations

Figure 5: Displacement in mode-1

6. CONCLUSIONS

Differential evolution algorithm was used to find the optimal configuration of the closely stiffened panel which minimizes the mass of the interstage structure while satisfying the constraint in natural frequency and material strength. The evaluation of the candidate solution was carried out in indigenous finite element analysis software using its Python interface. The established method can be extended to find the optimal design of conical interstage structure and structures with cut-out after incorporating the required modification in the model.

ACKNOWLEDGEMENTS

The authors are grateful to Santhosh SS and Venkateswaran KP for their guidance.

REFERENCES

1. Florient Savine, Franc, Ois-Xavier, Irisarriedric Julien, Yannick Guerin.C and Angela Vincenti, “A Component-based method for the Optimization of Stiffener Layout on Large Cylindrical Rib-Stiffened Shell Structures”, Springer ,2021
2. H.N.R. Wagner, C. Huhne, S. Niemann, “Buckling of launch-vehicle cylinders under axial compression: A comparison of experimental and numerical knockdown factors”, Thin Walled Structures, 2020
3. Q Zheng, D Jiang, C Huang, Shang, X.Shang, S Ju, “Analysis of failure loads and optimal design of composite lattice cylinder under axial compression”, Composite Structures (2015)
4. Pradnya A.Vikhar and Shri Sant Gadge Baba “Evolutionary Algorithms: A Critical Review and its Future Prospects”, International Conference on Global Trends in Signal Processing, Information Computing and Communication, 2016
5. Thomas Bartz-Beielstein, Jurgen Branke Jorn Mehnen and Olaf Mersmann “Evolutionary Algorithms”, Wires Data Mining and Knowledge Discovery, June 2014
6. H. Koke, L. Weib and C. Huhne, “Effective Lightweight Design of a Rocket Interstage Ring through Mixed-Integer Optimization”, Research and Applications in Structural Engineering, Mechanics and Computation, 2013

7. David W.Sleight, Thammaiah Sreekantamurthy, Daniel N.Kosareo, Robert A.Martin and Theodore F.Johnson, “Structural design of Ares V Interstage Composite Structures”, American Society of Aeronotics and Acoustics, April 26, 2012
8. M.Bagheri, A.Jafari and M.Sadeghifar, “A Genetic Algorithm Optimization of Ring Stiffened Cylindrical Shells for Axial and Radial buckling Loads”, February 25 2011
9. Craig Collier, James Ainsworth, Phil Yarrington and Ryan Lucking, “Ares V Interstage Composite Panel Concept and Ring Frame Trade Spacing Studies”, American Institute of Aeronautics and Astronautics, 2010
10. Ondrej Hrstka and Anna Kucerova, “Improvements of Real Coded Genetic Algorithms based on differential operators preventing Premature Convergence”, Advances in Engineering Software, 2004
11. Roberto Vitali, Oung Park, Raphael T, Haftka and Bhavani V.Sankar, “Structural Optimization of a Hat Stiffened Panel Using Response Surfaces”, Journel of Aircraft”, January 2002

ISBN - 978-93-95038-50-8

Multi Optimization of Friction Stir Welding of Aluminium AA 6061 Alloy using Grey based Taguchi Method

Pranav Ravindrannair[1*], K Kishore[2], P Laxminarayana[2],
U Ashok Kumar[2], F Hayat Khan[1]

[1]Department of Automobile Engineering, MVSR Engineering College, Hyderabad, TS.
[2]Department of Mechanical Engineering, University College of Engineering Osmania University, Hyderabad, TS.
[2] Department of Mechanical Engineering, Vasavi College of Engineering, Hyderabad, TS.
Email: Pranav_auto@mvsrec.edu.in

ABSTRACT

In this paper an experimental investigation has been carried out to determine the optimal parametric setting during Friction Stir Welding (FSW) of Aluminium AA 6061 alloy. The FSW process parameters considered are welding speed, axial force and tool rotational speed whereas the quality characteristics considered are tensile strength and tensile elongation. The Taguchi method was applied in designing the experiments involved in this study to optimize the welding parameters. Following the Taguchi quality design, an L9 (3 3) orthogonal array was chosen to design the experiment. The process parameters that were taken and their levels incorporated in the array were chosen after conducting pilot experiments and also through literature survey. The significant process parameters that affect welding performance were determined by making use of Analysis of Variance (ANOVA) and the F-test values along with the experimental results obtained. By considering the significant parameters so obtained, the verification of the improvement in the quality characteristics for the FSW of Aluminium AA 6061 was done and the results obtained were found out to be an improvement over the results obtained while using the original parameters (original setup). Apart from the optimization of each process parameter taken individually, multi response optimization has also been performed on both the process parameters that have been mentioned above by making use of the Taguchi-Grey relational analysis.

Keywords: *Design of Experiments, Multi Optimization,ANOVA, Orthogonal arrays, Aluminium 6061*

1. INTRODUCTION

Friction stir welding is one of the solid state welding process where two components are rubbed together at a controlled rotational speed to induce friction. That friction is used to generate enough heat that allows both components to reach a state of plasticity, helping to generate a bond when both the components are forced together. The force is laterally applied and is termed as 'up-set' which is used to fuse the components. The bond is created when layers of plastic material from both components interwine and create new layers of combined material [1]. Friction welding can replace conventional welding and one piece construction as one of the most economical welding processes available. It also gives benefits in design, strength and cost reduction. The process can provide increased design flexibility, superior strength and significant cost savings over other conventional welding processes. Heat treatable wrought Aluminium- Magnesium-Silicon alloy AA 6061 has very good welding characteristics among high strength Aluminium alloys. These types of alloys are used extensively in pipelines, marine frames, storage tanks and aircraft applications among others. Defects in welding such as large distortion, solidification cracking, porosity and oxidation are not observed in FSW compared to several other fusion welding processes that are generally used for joining structural alloys [2,3]. In order to produce an excellent quality welded joint, it is necessary to optimize the process parameters. In the present research an experimental

* Corresponding author: E-mail: Pranav_auto@mvsrec.edu.in

investigation is done on the FSW of Aluminium AA 6061 alloy taking into account Tensile strength and tensile elongation as the quality characteristics. The experimentation process is designed using the Taguchi method where the process parameters considered are Welding speed, axial force and tool rotational speed. Multi optimization is done by making use of the Grey co relational analysis while ANOVA is made use of to determine the significance of the process parameters with respect to the outcome.

2. METHODOLOGY

In this study 6mm thick plates of 6061 Aluminium alloy was used as the base metal. The chemical composition of the alloy and its properties are shown in Table 1 and Table 2 respectively. The configuration used is of the butt type and the welding was carried out by using a vertical milling machine. The process parameters under investigation were selected based on literature survey. The respective levels were selected based on preliminary experiments. Each experiment was run thrice and the average values for the quality characteristics were taken in order to account for variance

Table 1: Chemical composition for base metal (%wt)

Material	Mg	Fe	Cu	Cr	Si	Al
6061-T6	0.8- 1.2	0.33	0.25	0.18	0.4- 0.8	Rest

Table 2: Properties of base metal

Property	Metric
Density	2.7 g/cc
Brinell Hardness	95
UTS	310 MPa
Modulus of elasticity	68.9 GPa
Poisson’s ratio	0.33
Thermal conductivity	167 W/mK

The experimental investigation is conducted with the aim of optimizing the FSW process in order to improve the above discussed quality characteristics namely Tensile strength and Tensile elongation, Several researches have been carried out by researchers showcasing the techniques involved in the selection of the optimal parametric values for Tensile strength and Tensile elongation [4,5]. Taguchi method has been widely used in the selection of the process parameters. Taguchi method makes use of Orthogonal Arrays (OAs) [6] for designing the experiments. The predominant advantage of this technique lies in its simplicity and adaptability. They provide the required information making use of only the least possible number of trials. However they still yield results which have good precision and are reproducible.

In order to determine the performance characteristics corresponding to the optimal machining parameters, a specially designed experimental methodology is imperative. A full factorial experimental design will cover all the possible arrangements possible for a particular experimental setup. However as the number of factors and levels increases, the total number of experiments also increases. Making it unviable both financially and in terms of time taken. Hence Taguchi's orthogonal arrays are made use of to reduce the number of experiments required. The experiment includes three process parameters each of three levels.

ISBN - 978-93-95038-50-8

Therefore each process parameter will contribute 2 degrees of freedom each. Therefore there are 6 degrees of freedom in total. The interaction between the parameters is neglected [6-9]. The levels of the individual process parameters/factors are given in Table 3. While selecting an Orthogonal Array it should be noted that the degrees of freedom of the Orthogonal Array must be greater than or equal to those of the process parameters. [10]. An L9 array will have 8 degrees of freedom (i.e.: 9-1=8). It has already been specified that the process parameters used here have 6 degrees of freedom. The degree of freedom for the Orthogonal Array is less than the degrees of freedom of the process parameters. Hence it is possible to use an L9 for the experiments in this study. The experimental layout for the process parameters in terms of an L9 Array is given in Table 4.

Table 3: Factors and their levels

Factor	Unit	Level 1	Level 2	Level 3
Welding speed (A)	mm/min.	60	80	100
Axial force (B)	kN	5	6	7
Tool rotational Speed (C)	RPM	900	1000	1100

Table 4: Experimental layout

Experiment No.	A	B	C
1	60	5	900
2	60	6	1000
3	60	7	1100
4	80	5	1000
5	80	6	1100
6	80	7	900
7	100	5	1100
8	100	6	900
9	100	7	1000

3. RESULTS AND DISCUSSIONS

The experiments were conducted as per the arrangement of the orthogonal array in Table 4. Three sets of experiments are conducted for each run and the average values of the quality characteristics are calculated and tabulated as shown in Table 5.

The experimental results are obtained by conducting the experiments are shown in Table 5. The results showcase the effect of the four control parameters on the 2 quality characteristics. The S/N ratios are also displayed in the same table. Once the calculations are made, the graphs for the particular control parameters at their three levels of application are plotted. For maximizing each response, the main effect plot for S/N ratio (Fig. 1 and 2) gives different factor levels as shown in Table 6.

ISBN - 978-93-95038-50-8

Table 5: Experimental results

Exp. No.	Tensile Strength (MPa)	S/N ratio for Tensile Strength (dB)	Tensile Elongation	S/N ratio for Tensile Elongation (dB)
1	154	43.7504	5.41	14.6639
2	164	44.2969	5.22	14.3534
3	170	44.6090	5.33	14.5345
4	163	44.2438	5.86	15.3580
5	171	44.6599	5.79	15.2536
6	157	43.9180	5.74	15.1782
7	168	44.5062	6.35	16.0555
8	157	43.9180	6.37	16.0828
9	165	44.3497	6.29	15.9730

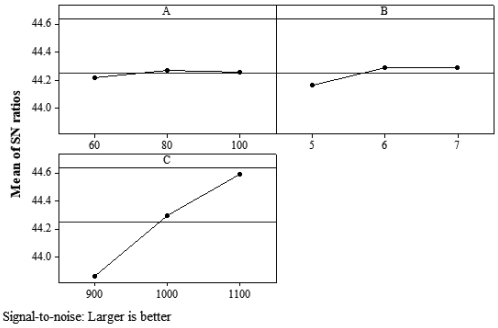

Figure 1: Main effects plot for S/N ratio of Tensile Strength

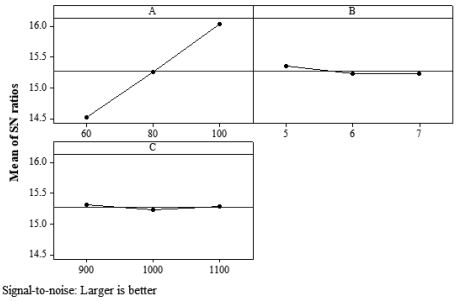

Figure 2: Main effects plot for S/N ratio of Tensile Elongation

Table 6: Optimised levels of corresponding quality characteristic

Factors	Quality characteristic	
	Tensile Strength (MPa)	Tensile elongation (%)
A	80	100
B	7	5
C	1100	900

The analysis of variance method (ANOVA) is made use of to determine the relative influence of each factor and these results are presented in Table 7 and Table 8 for tensile strength and tensile elongation respectively.

ISBN - 978-93-95038-50-8

Table 7: ANOVA for Tensile strength

Factor	DOF	SS	V	F-value	P- value
A	2	1.556	0.778	7	0.125
B	2	10.889	5.444	49	0.020
C	2	282.889	141.444	1273	0.001
Error	2	0.222	0.111		
Total	8	295.556			
$R^2 = 99.92\%$; $R^2(adj) = 99.70\%$					

Table 8: ANOVA for Tensile elongation

Source	DOF	SS	V	F-value	P- value
A	2	1.55242	0.776211	140	0.007
B	2	0.01396	0.006978	1.26	0.443
C	2	0.00389	0.001944	0.35	0.740
Error	2	0.01109	0.005544		
Total	8	1.58136			
$R^2 = 99.30\%$; $R^2(adj) = 97.20\%$					

It is clearly observed from Table 6 and Fig. 1 and Fig. 2 that optimum factors for the highest tensile strength are A_2, B_3 and C_3 and for the highest tensile elongation are A_3, B_1 and C_1 respectively. From ANOVA Table 7 and 8, it is observed that with respect to Tensile Strength, the significance of the input parameters are the tool rotation speed, axial force and welding speed with the tool rotation speed being the most significant and the welding speed being the least significant. Whereas for Tensile elongation it is observed that the welding speed is the most significant parameter and the tool rotation speed is the least significant parameter. The adequacy of the analysis is carried out using the Anderson–Darling (AD) test and results are illustrated in Fig. 3. It clearly shows that that the data obtained follows normal distribution. This developed procedure is thus suitable to explore the design.

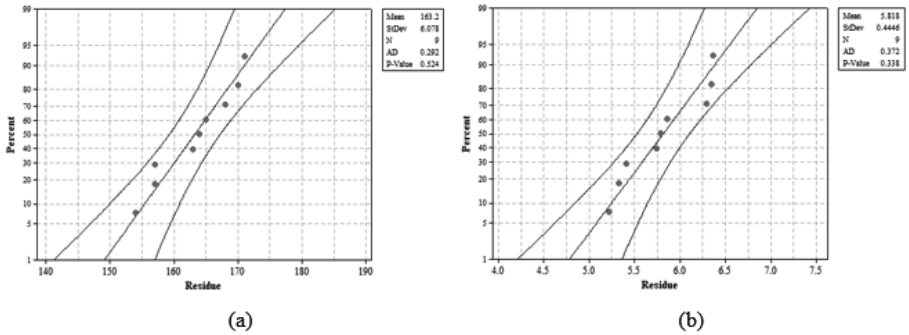

(a) (b)

Figure 3: Normal probability plot of residue at 95% of confidence: (a) Response is tensile strength and (b) Response is tensile elongation

4. MULTI OPTIMIZATION USING GREY CO-RELATION

Taguchi method cannot be used directly to optimize the multi-response problems. The data which was observed for each response using Taguchi designs can be analyzed by different methods to obtain a solution for a multi response problem. Here we attempt to

perform a multi response optimization for all three quality characteristics taken all at once. The Taguchi Grey relational analysis is used to perform this multi optimization [11,12].

The value of the grey relational grade is directly proportional to the corresponding factor combination to the optimal value. The results of grey relational grade calculations are summarized in Table 9.

Table 9: Gray relational grade

Grey relational generation			Grey relational coefficient		Grey relational grade
Exp. No.	TS	IE	TS	IE	
1	0	0.179565	0.333333	0.378663	0.355998
2	0.600833	0	0.55607	0.333333	0.444702
3	0.943988	0.104739	0.89926	0.358356	0.628808
4	0.542423	0.580869	0.522151	0.543992	0.533072
5	1	0.520511	1	0.51047	0.755235
6	0.184252	0.47695	0.380012	0.488735	0.434373
7	0.830967	0.984206	0.747348	0.969379	0.858363
8	0.184252	1	0.380012	1	0.690006
9	0.658889	0.936523	0.594452	0.887348	0.7409

Table 10: ANOVA Table for Grey Relational Grade (GRG)

Source	DF	SS	V	F	P
A	2	0.127351	0.063676	43.66	0.022
B	2	0.003432	0.001716	1.18	0.459
C	2	0.101308	0.050654	34.73	0.028
Error	2	0.002917	0.001459		
Total	8	0.235008			

5. CONFIRMATION EXPERIMENT

A confirmation experiment is executed to validate the results obtained from the aforementioned analysis. The levels of process parameters made use of for the confirmation test are given in Table 9 and the responses obtained for the levels are presented in Table 11. It is observed that the results are in good agreement with those predicted mathematically and are within expected range at 95% of confidence.

Table 11: Confirmation test results

Response	**Optimal factor combination**			**Significant factors**	**Predicted value**	**Experimental value**	**Absolute error (%)**
	A	B	C				
Tensile Strength (S/N ratio) (db)	2	3	3	B, C	44.63	44.66	0.067
Tensile Elongation (S/N ratio) (db)	3	1	1	A	16.04	16.16	0.74
GRG	3	2	3		0.763	0.831	8.2%

ISBN - 978-93-95038-50-8

6. CONCLUSIONS

An attempt was made to optimize the FSW process with respect to the selected quality characteristics. The necessary levels at which the process parameters have to be set to obtain an optimized result for the quality characteristics have been obtained. From them, we come to the following conclusions.

- For optimum Tensile strength, the recommended parametric combination is A2B3C3 where A2 is 80 mm/min, B3 is 7kN and C3 is 1100 RPM whereas for optimum tensile elongation the recommended parametric combination is A3B1C1 where A3 is 100 mm/min, B1 is 5kN and C1 is 900 RPM.
- It is observed that the Tool rotation speed is the most significant parameter that affects the Tensile strength of Aluminium 6061 followed by axial force and welding speed whereas welding speed is the most significant parameter that affects the tensile elongation of Aluminium 6061 followed by axial force and tool rotation speed.
- Multi optimization has been performed for both quality characteristics and the optimal level of the parametric arrangement is found to be A3B2C3.
- By conducting the conformational experiments we can see that the results so obtained are in close line with the theoretical models that were obtained.

REFERENCES

1. J. Stephen Leon, V. Jayakumar, Investigation of mechanical properties of aluminium 6061 alloy friction stir welding, American Journal of Mechanical Engineering and Automation, 1, (1), pp. 6-9, 2014.
2. B. Singh, P. Singhal, Kuldeep K. Saxena, Effect of transverse speed on mechanical and microstructural properties of friction stir welded aluminium AA2024-T351, Advances in Materials and Processing Technologies, 6, (3), pp. 519-529.
3. Binit Kumar, Rohit Sahu & Mukesh Mishra, Optimization of process parameter for commercially pure aluminium alloy during friction stir deformation, Advances in Materials and Processing Technologies, 2020, DOI: 10.1080/2374068X.2020.1860601.
4. M. l. Santella, T. Engstrom, D. Storjohann, T. Pan, Effects of friction stir processing on emchanical properties of cast Aluminium alloys A319 and A356, Script Materialia, 53, pp. 201 – 206, 2005.
5. Y. S. Liao, J. T. Huang, A study on the machining parameter optimization of WEDM, Journal of Material Processing Technology, 71, pp. 487- 493, 1997.
6. P. J. Ross, Taguchi techniques for quality engineering, McGraw-Hill Second Edition, New Delhi, 2005.
7. Abbas Al Refaie, Tai-His Wu, Ming-Hsien Li, An effective approach in solving the Multi-Response problem in Taguchi Method, Jordan Journal of Mechanical and Industrial Engineering, 4, (2), pp. 314-323, 2010.
8. Douglas C Montgomery, Design and Analysis of experiments, John Wiley and sons Eight Edition, Hoboken, 2013.
9. K. Krishnaiah, P. Shahabudeen, Applied Design of Experiments and Taguchi Methods, PHI Learning, New Delhi, 2012.
10. D. Chandrakar, A. Venu Gopal, Multi-Objective Optimization of Electrochemical machining of EN31 steel by Grey Relational Analysis, International Journal of Modeling and Optimization, 1, (2), pp. 113-117, 2011.
11. H. Lindman, Analysis of variance in experimental design, Springer-Verlag, New York, 1992.
12. M. I. Equbal, Azhar Equbal, M. A. Equbal, R. Pranav, Optimization of hot forging parameters using Taguchi method and grey relational analysis for AISI 1035 Steel, International Journal of Microstructure and Materials Properties, 13, (¾), pp. 198-212, 2018.

ISBN - 978-93-95038-50-8

Design & Development of Four-Wheel Steering Mechanism for Minimum Turning Radius: A Case Study of CM Transportation Trolley

V Venkateswarlu[1], Jaiteerth R Joshi[2]

Defence Research and Development Laboratory, Hyderabad, India-500 058
venkatteju123@gmail.com, joshidrdl@gmail.com

ABSTRACT

The main intent of this research is to discuss the benefits, applications, and implementation of four-wheel steering mechanism over two-wheel steering mechanism on CM Transportation trolley. Based on a review of the relevant academic journals, books, and textbooks investigation concludes that two-wheel steering is more commonly used than four-wheel steering because of its lower steering efficiency. Turning radius is decreased at low speeds, steering reaction is enhanced, and vehicle stability is maximized with four-wheel steering. Because of the limited space available in the magazines, the only feasible alternative for designing a trolley to transport canisterized missiles is to equip it with four-wheel steering. Explosion-proof prime movers are required for usage on the CM transportation trolley, which moves CM containers containing items from the magazine to the loading/unloading bay and back again. To accomplish this tighter turn, the rear wheels has to rotate counter to the front wheels which is arranged by a system composed of intermediate linkages and rotating components thus, transmits entire relative motion to the rear wheels. The design and development of the linkage mechanism and chassis frame was accomplished with the help of Creo v7, and Safety margins were determined by structural analysis performed in Ansys 21. The turning radius of the CM Transportation trolley was found to be reduced by roughly 48% when compared with a two-wheel steering system after which a prototype was built and tested with a constant radius.

Keywords*: Four Wheel Steering, Turning radius, CM transportation Trolley*

NOMENCLATURE:

C_1 = Front Axle to Instantaneous Centre Distance	T = Track Width of the vehicle
C_2 = Rear Axle to Instantaneous Centre Distance	L = Wheel Base of the vehicle
a_2 = Distance of CG from Rear Axle	δ_{if} = Front Inner Wheel Steering Angle
θ = Front Inner Wheel Steering Angle	δ_{ir} = Rear Inner Wheel Steering Angle
Ø = Front Outer Wheel Steering Angle	δ_{of} = Front Outer Wheel Steering Angle
T_f /T_r =Front/Rear Track Width	δ_{or} = Rear Outer Wheel Steering Angle

R_1 = Distance from Instantaneous Centre to Centre of the vehicle

1. INTRODUCTION

Four-wheel steering improves vehicle maneuverability and turning. With a normal two-wheel steering system, the rear wheels do not revolve in the curve, reducing steering efficiency [1]. Four-wheel steering reduces vehicle turning radius by rotating the rear wheels with the front [2]. Four-wheel steering improves active safety by stabilizing overtaking maneuvers, reducing vertical axis oscillation, reducing lateral wind sensitivity, and neutralizing cornering [3,12]. Four Wheel Steering offers cornering, high steering reaction, straight line stability, lane change, and low speed maneuverability. 4-Wheel Steering is complicated and costly despite its advantages over two-wheel steering [4,11]. Operating factors determine rear-wheel steering compared to front-wheel steering. At low speed, rear wheels steer opposite front wheels. When steering is slight at high speed, the front and rear wheels turn the same way [5-7]. Reversing the rear wheels reduces the vehicle's turning radius, making parking, low-speed cornering, and high-speed lane changes easier [8-10]. In this study, four-wheel steering is used to lower the trolley's turning radius and improve its maneuverability.

[1] Corresponding author E-mail: venkatteju123@gmail.com

2. LITERATURE REVIEW

Most vehicles use steering to regulate the movement. Figure 1 shows the steering mechanism's essential components: the steering wheel, steering column, steering rack, and vehicle wheels.

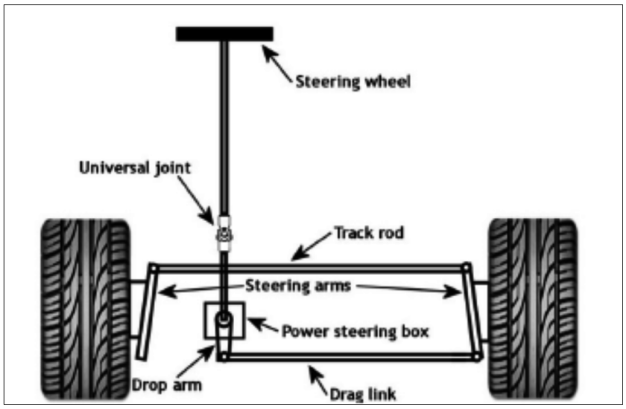

Figure 1: Main Components in Steering System [17]

Four-wheel steering, which uses all four wheels for steering, is the most effective. The intricacy of typical mechanical four-wheel steering systems makes this technology unpopular. The Honda Prelude and Nissan Skyline GT-R have four-wheel steering systems that spin the rear wheels to help the front wheels steer. These systems only guided the rear wheels by 2 or 3 degrees since they assisted the front wheels rather than steering themselves.

Modern four-wheel steering systems have completely electronic steer-by-wire systems, equal front and rear steer angles, and sensors to monitor vehicle dynamics and modify steer angles in real time. Many experimental models using these technologies have been developed and tested, but a complicated four-wheel steering model has not been produced.
Four-wheel steering has several benefits over two-wheel steering.

(a) Smaller Turns – With four-wheel steering, the vehicle can turn with a tighter radius than with two-wheel steering since the rear wheels may pivot in the opposite direction of the front wheels. This allows you to make turns without widening your turn.

(b) Good Stability – Stability helps you drive smoothly. While rounding corners or driving in the rain, a four-wheel steering system helps you manage and stabilize your car. Even in strong gusts or potholes, a straight route will keep your automobile straight.

(c) Smooth Steering – Unresponsive steering wheels are the worst. Four-wheel steering responds faster than two-wheel steering. You'll be able to steer more precisely, making driving more comfortable.

(d) Faster Lane Changes – If you often change lanes or overtake people on the road, a four-wheel steering system will help you accomplish this quickly and efficiently. With solid and steady steering control, you can change lanes faster than with a two-wheel steering system.

(e) Better Terrain Performance – Four-wheel steering is better for tougher terrains like rainy, snowy, or dirt roads. Your car won't get stuck on these terrains.

ISBN - 978-93-95038-50-8

3. APPLICATIONS OF FOUR-WHEEL STEERING

(a) Gentle curve: Rear-wheel steering on mild bends Stabilizes vehicle.

(b) Parking: To minimize the car's turning circle when parking, the driver frequently spins the wheel across a wide arc.

(c) Junctions: At a crossroads or other intersection where roads converge at 90° or tighter angles, rear-wheel counter-phase steering aligns the front and rear wheels. The car can turn effortlessly at a function.

(d) Slippery road surfaces: Rear wheel steering prevents rear end sideways slide on snow, ice, mud, and other low friction surfaces. Hence, automobiles are easier to steer.

(e) High-speed straight-line operation: While driving in a straight line at high speed, a driver often needs to make tiny steering corrections to maintain the intended direction. In phase steering of the rear wheels reduces these steering corrections.

(f) Narrow roads: On small roads with tight curves, rear-wheel counter-phase steering reduces the vehicle's turning radius, minimizing steering wheel rotation and making the vehicle simpler to turn.

(g) U-Turns: Counter-phase steering of the rear wheels allows U-turns on small highways by reducing the vehicle's turning radius.

4. CASE STUDY OF CM TRANSPORTATION TROLLEY USING FOUR WHEEL STEERING SYSTEM

A trolley is a mechanical device used to transfer weights or convey materials. Based on the application, we must choose a trolley from the market or design a new one. Due of their two-wheel steering mechanisms and wider turning radius, present trolleys are unsuitable. According to investigations of the relevant literature, the only alternative that can fulfill the requirements for mobility within magazines is a trolley with four wheels steering system. CM Transportation Trolleys have three primary sub-assemblies are Suspension System, Chassis and Steering Mechanism.

4.1. DESIGN SPECIFICATIONS

(a) Design, Development and Delivery of CM transportation Trolleys with Minimum Turing Radius available in Storage Magazines

(b) The payload carrying capacity is 1 ton

(c) Explosives Proof, Anti-Static and Shall be grounded.

(d) Low speed, Light Weight and Towing type.

(e) Easy to maintenance and Space Parts Shall be available freely outside the market.

4.2. METHODOLOGY

The design methodology of CM transportation trolley for minimum turning radius as shown in figure 2. It includes comparison of two and four-wheel steering mechanism, CAD modelling, Finite Element Analysis, Porotype development and experimental validation of design.

ISBN - 978-93-95038-50-8

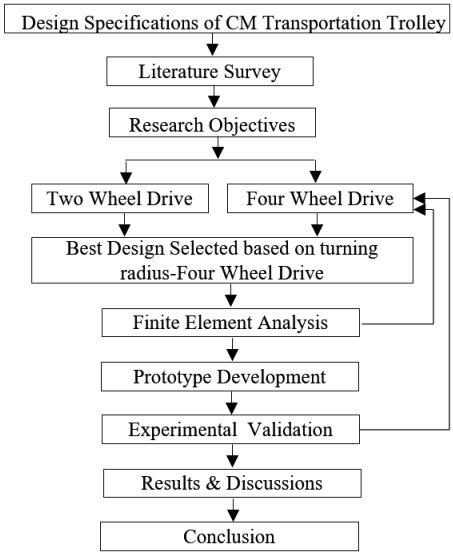

Figure 2: Design Methodology of Trolley

4.3 STEERING MECHANISM

4.3.1 ACKERMAN STEERING MECHANISM

Most four-wheeled vehicles employ four-bar linkages, often known as Ackermann-type steering mechanisms, to turn the wheels. Ackermann steering linkage is commonly seen on stiff steering axles in trucks and off-road vehicles [16]. With perfect Ackermann, the perpendicular line across the centers of all the wheels always converges on a single point, regardless of the direction in which the vehicle is being steered. The problem is that this can be hard to construct in practice with only linking objects together. While the Ackermann theory is sound for low speed movements, current automobiles do not employ pure Ackermann steering since it overlooks significant dynamic and compliant effects.

4.3.2 STEERING WHEEL CONFIGURATION

(a) Two Wheel Steer: The front wheels are free to spin in the direction of the steering wheel, while the rear wheels are locked, requiring a large turning radius to turn.

(b) Four Wheel Steer: Rear and front wheels are opposite in directions. This allows sharp turns with little turning radius at a slow speed.

(c) Crab Steer: Both front and rear wheels face the same direction during high-speed lane changes.

(d) Zero turn: The car moves in a circle of "zero radius" since the front and rear wheels are aligned as shown in figure 3.

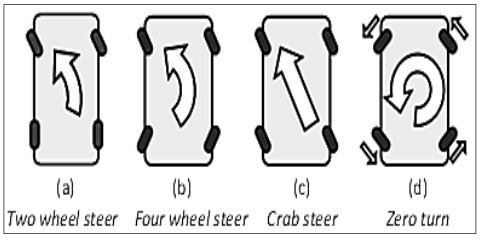

Figure 3: Types of Steering wheel configuration [6,11,17]

4.3.3 TURNING RADIUS

A vehicle's turning radius, sometimes called its turning circle, is the lowest diameter at which it can complete a full circle turn [17].

Turning circle radius = (Wheelbase/ sin (average steer angle)) — (Track width / 2)

4.3.4 CALCULATIONS TO FIND OUT TURNING RADIUS

(i) ***Two Wheel Steer Mechanism:*** From the benchmark Ackerman Steering Mechanism as shown in the figure 4, we have

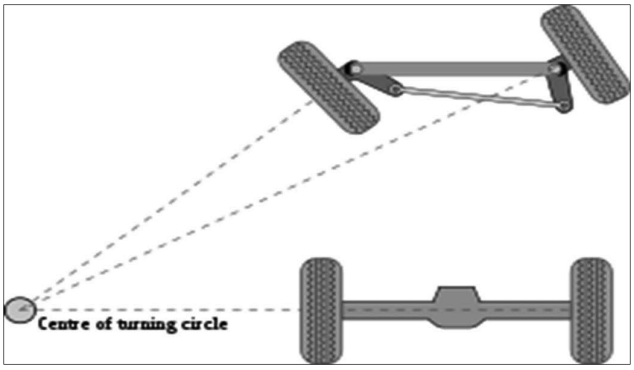

Figure 4: Two Wheel Steer [8,10,12,15]

From the figure 5 of Two-wheel steer of CM Transportation Trolley, assume front inner wheel steer angle $\delta_{if} = 30°$

$$\text{Cot } \delta_{of} - \text{Cot } \delta_{if} = T / L \quad (1)$$

$$\text{Cot } \delta_{of} = (1582 / 5000) + \text{Cot } 30°$$

$$\delta_{of} = 26.0204°$$

To find Turning Radius of two-wheel drive

we have equation

$$R^2 = a_2^2 + L^2 \times \text{Cot}^2\delta \quad (2)$$

$$\text{Cot}\,\delta = (\text{Cot } \delta_{if} + \text{Cot } \delta_{of}) / 2 \quad (3)$$

$$\text{Cot}\,\delta = 1.890251$$

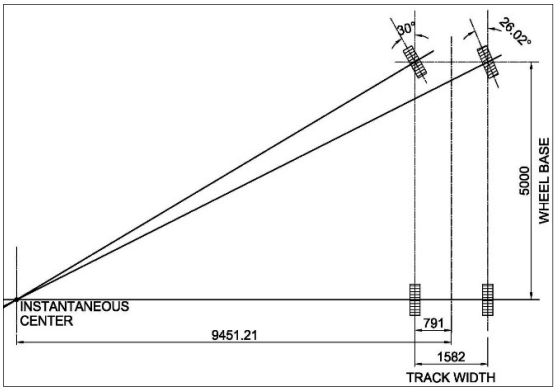

Figure 5: Two Wheel Steering in Transportation Trolley

Therefore, from equation 2, we have

$$R^2 = 2800^2 + 5000^2 \times \cot^2\delta$$

$$R = 9857.29 \text{ mm}$$

Therefore, the Turning Radius (R) of the two-wheel steering is = 9857.29 mm

(ii) ***Four Wheel Steer Mechanism:*** Four-wheel steering (4WS), sometimes termed rear-wheel or all-wheel steering, actively steers the rear wheels during turns. Four-wheel drive, which powers all four wheels, is different. It enhances handling and tightens corners.

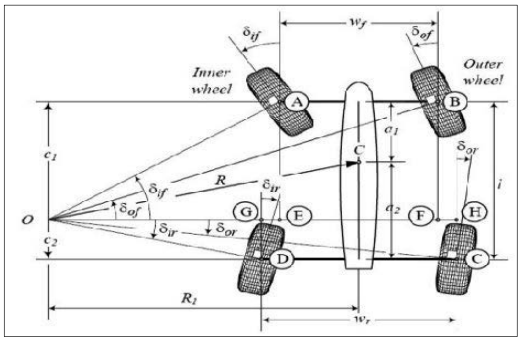

Figure 6: Steering angles position of Instantaneous Centre for Turning Radius 4.4 m [4,7,10,13,14]

From the figure 6, we know that

$$R^2 = a_2^2 + R_1^2 \quad (4)$$

From the figure 7 Four-wheel steering of CM Transportation Trolley, R_1=5121.13 mm

∴ from the eq.4, we have, $R^2 = a_2^2 + R1^2$

$$R^2 = 300^2 + 5121.13^2$$

$$R = 5129.90 \text{ mm}$$

To find the Steering Angle assume front inner wheel $\delta_{if} = 30°$

$$\text{Tan}(\delta_{if}) = C_1 / (R_1 — T_f / 2) \quad (5)$$

$$C_1 + C_2 = L \quad (6)$$

Where,

$C_1 = C_2 = 2500$, Tr = 1582, L = 5000 mm

T = 1582 mm, R_1 = 5121.13 mm, R = 5129.9 mm

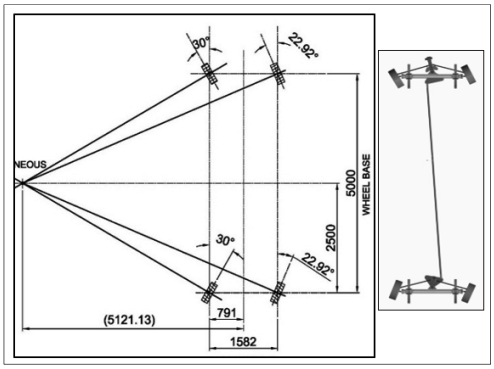

Figure 7: 4WS in CM Transportation Trolley [8]

From Eq.5, we have, $\text{Tan}(\delta_{if}) = C_1 / (R_1 - T_f / 2)$

$\therefore C_1 = 2500$ mm

From Eq.6, we have, $C_1 + C_2 = L$

$\therefore C_2 = 2500$ mm

To Find δ_{of} = Front Tyre Outer Angle

$$\text{Tan}(\delta_{of}) = C_1 / (R_1 + T_f / 2)$$

$$\delta_{of} = 22.92°$$

To Find δ_{ir} = Rear Tyre Inner Angle

$$\text{Tan}(\delta_{ir}) = C_2 / (R_1 — T_r / 2)$$

$$\delta_{ir} = 29.99°$$

To Find δ_{or} = Rear Tyre Outer Angle

$$\text{Tan}(\delta_{or}) = C_2 / (R_1 + T_r / 2)$$

$$\delta_{or} = 22.91°$$

Therefore, the Turning Radius (R) of the four-wheel steering is = 5129.90 mm

The purpose of this article is to outline plans for creating a four-wheeled trolley designed specifically for transporting CM containers. This device is used to enhance responsiveness of the steering, enhance stability during high-speed maneuvers, or reduce turning radius in low-speed situations as shown in figure 8.

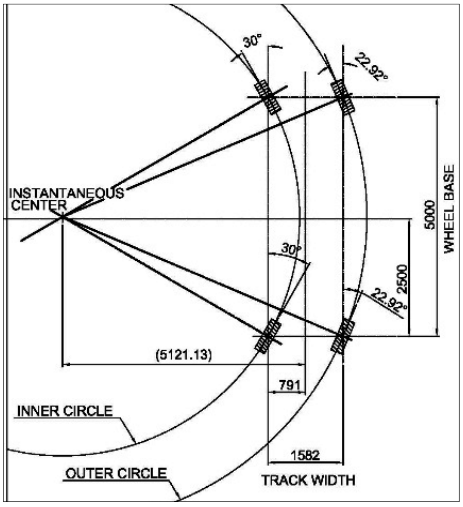

Figure 8: 4WS Turning Radius for Inner and Outer Wheels

With four-wheel steering, the rear wheels aren't always required to follow the front ones. The rear wheels may turn in the same way (same-side steering) as the front wheels, or in the opposite direction, depending on the speed of the vehicle (counter steering). Most modern four-wheel-steer vehicles may be navigated in either a counterclockwise or clockwise direction. With counter steering, a regular automobile may reduce its turning radius by a whole yard while making tight, low-speed bends. Yet, at high speeds, counter steering can make an automobile dangerously unstable, whereas same-side steering actually enhances the ride quality as shown in the figure 9.

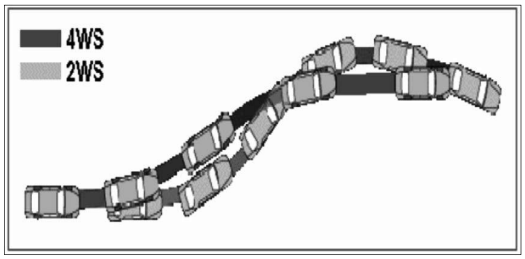

Figure 9: Wheel Steer under 2 Wheel Steer and 4 Wheel Steer [13]

4.4. DESIGN OF CM TRANSPORTATION TROLLEY

4.5. CHASSIS

The term "chassis" refers to the primary framework of a vehicle. A chassis resembles the skeleton of an organism since it is composed mostly of the supporting structure of the vehicle to which all of the other components are linked. You might say that it's the "spine" of the car, or the main support for the weight of the vehicle. Side and cross members form the chassis frame. Based on boundary conditions and loads, Finite Element Method (FEM) stress analysis determined the chassis' critical point of maximum stress. The trolley FOS is calculated from the maximum stress.

4.5.1. LADDER FRAME CHASSIS

The ladder chassis is widely regarded as one of the oldest types of automotive chassis or car chassis, and despite its age, it is the type of chassis that the vast majority of SUVs utilize even now. As depicted, it resembles a ladder with two longitudinal rail sinters joined by multiple lateral and cross bracing as shown in the figure 10 and Table 1 shows key dimensions, pay load, and other characteristics that help determine max. stress.

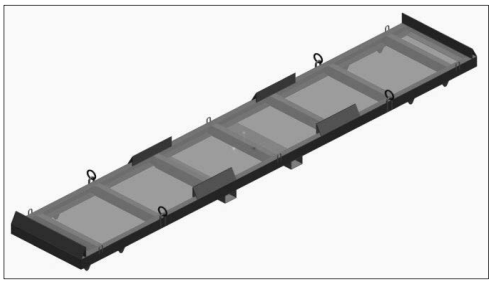

Figure 10: Chassis of Transportation Trolley

Table 1: Design Parameters of the Chassis [3,13]

Sl No.	PARAMETERS	VALUE
1.	Total Chassis length	6110 mm
2.	Width of the chassis	1080 mm
3.	Wheel base (L)	5000 mm
4.	Track width (T)	1582 mm
5.	Front over hang	365 mm
6.	Rear over hang	745 mm
7.	Ground clearance	200 mm
8.	Capacity (gvw)	5000 kg's
9.	Kerb weight	4000 kg's
10.	Pay load	1000 kg's
11.	C Channel Dimension	150H x 75W x 6.5t

ISBN - 978-93-95038-50-8

4.6. SUSPENSION SYSTEM

Spring, shock absorbers, and linkages connect a vehicle's wheels to its suspension, allowing relative motion. It helps with the vehicle's handling and braking for good active safety and driving pleasure, and it also keeps the passengers comfortable and relatively well separated from road noise, bumps, and vibrations, among other things. The suspension model is shown in the figure 11 & 12.

Figure 11: Front suspension of trolley

Figure 12: Rear suspension of trolley

4.7. FINITE ELEMENT ANALYSIS

The suspension pieces are welded to the chassis frame, and the chassis frame also serves as the support structure for the steering column and the linkage body. While designing the chassis frame, we take the length and passage dimensions of the CM container into account. The chassis structure is responsible for supporting the vehicle when it is moving, including the weight of the vehicle, the driver, and the road surface. C-Channel is used for Chassis frame. The material chosen for it is structural steel, the Ultimate Tensile Strength and the Yield Strength of the materials are 460 MPa & 250 MPa. A Payload of 1 ton is applied as a uniform pressure on chassis frames and all DOF are fixed at eight points where four-leaf springs are connected to the chassis frame. The maximum von-misses stress on chassis frame is 32.27 MPa and the deformation is 0.0056 mm as shown in the figure 13.

ISBN - 978-93-95038-50-8

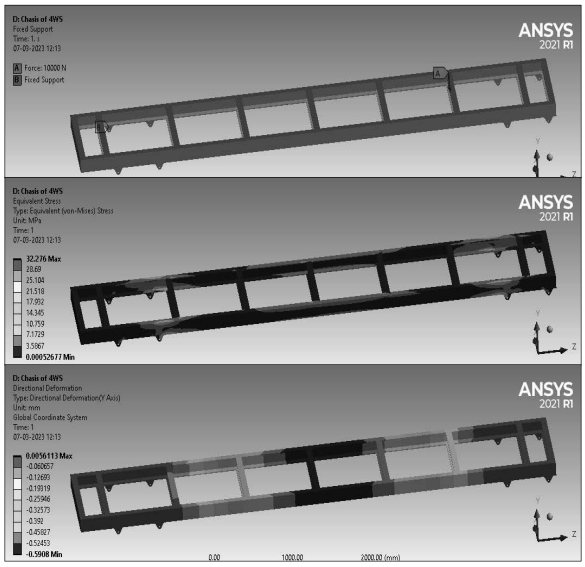

Figure 13: Applied Load & Boundary Conditions, Von-Misses Stress and Deformation along Y axis direction of Chassis

A hallow tube with four welded plates (for supporting the leaf springs) are used for axle. The material chosen for axle is alloy steel, the UTS and Yield Strength of the material is 450 MPa & 250 MPa as shown in the figure 14.

Figure 14: Applied Load & Boundary Conditions, Von-Misses Stress and Deformation along Y axis direction of Axle

Load of two tons (1 Ton of payload + 1 Ton of chassis weight) is applied on the welded plate surfaces where leaf springs are connected. Fixed boundary conditions are applied at both end portions of the axle where the hubs are connected. The maximum Von-Misses stress on axle is 24.98 MPa and the deformation is 0.0187 mm.

ISBN - 978-93-95038-50-8

A hub is designed with a hole to fix the axle both ends and two hinge joints at top and bottom molded to the Knuckle of the wheel. The material chosen for hub is cast iron, the UTS and Yield Strength of the material is 415 MPa & 276 MPa. Load of two tons (1 Ton of payload + 1 Ton of chassis weight) is applied on the two surfaces of the hub where knuckle is connected. The fixed boundary conditions are applied at the end portions of the axle where the hubs are connected. The maximum Von-Misses stress on axle is 55.98 MPa and the deformation is 0.036566 mm as shown in figure 15.

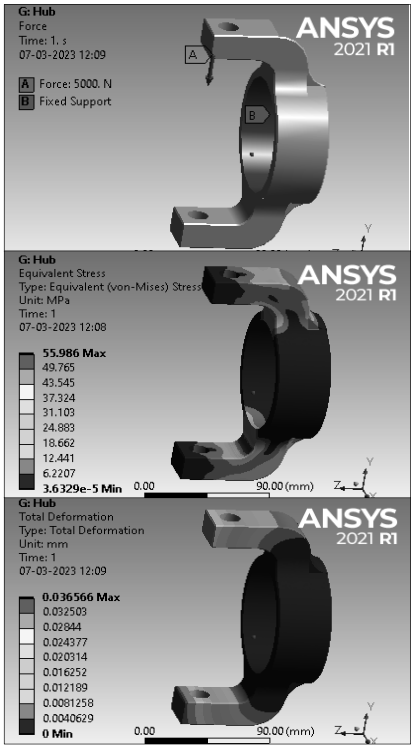

Figure 15: Applied Load & Boundary Conditions, Von-Misses Stress and Deformation of Hub

5. PROTOTYPE DEVELOPMENT

Complete CM Transportation Trolley was modeled in Creo v7 software and structural analysis was carried out using Finite Element Analysis Ansys 21 and updated CAD model based on stress analysis to maintain the factor of safety & Prototype was Developed, load test and min. Turning Radius test conducted at vendor premises and it was operated at a low speed of 15kmph with CM Container as a pay load on the Transportation trolley shown in the figure 16.

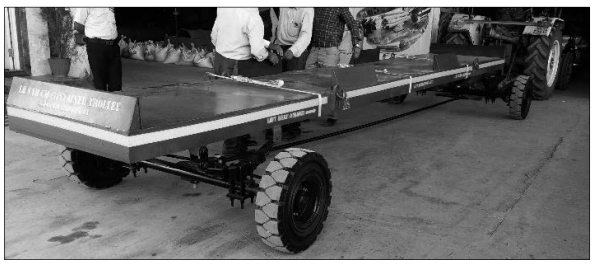

Figure 16: CM Transportation Trolley

Four-wheel steering mechanism is designed using linkages directly connected to front wheels and the rear wheels. The design is aimed to turn the front wheels at a maximum angle of 30° and the stopper is provided at an angle of 35° as to stop the over turn of the wheels. The Chassis Frame was able to withstand the entire CM Container load during its testing on the road with bumps and found satisfactory. The operating instructions of trolley is shown in the figure 17.

Figure 17: Operating instructions of CM Trolley

6. EXPERIMENTAL VALIDATION

Experiment carried out on developed prototype with payload of 1 ton at rated speed using prime-mover on the normal road and measured the minimum turning radius possible.

7. RESULTS AND DISCUSSION

Analytical and experimental results of two-wheel steer and four-wheel steer turning radii as shown in table 2. The experiment result of four-wheel steering turning radius decreased by 48% and analytically reduced by 51.26% over two-wheel steering. Four Wheel Steering has several benefits and may successfully replace two Wheel Steering Mechanism for less turning radius. Consequently, the four-wheel steering system has cornering, high steering reaction, straight-line stability, lane shifting, and low-speed maneuverability.

Table 2: Comparison minimum turning radius of Two- & Four-Wheel Steer [10, 17]

Turning Radius (R)	Two Wheel Steer	Four Wheel Steer
By Analytical	9.87 m	5.12 m
By Practical	--	5.31 m

8. CONCLUSION

Canisterized Missile (CM) Transportation trolley is designed and developed using Creo and Ansys workbench for Finite Element Analysis. Structural analysis was carried out to verify stresses and deformation of the chassis, axle, hub and all other components, the results are within the safety margins. Analytically and Graphically validated the mechanism to suit the minimum turning radius available in the Magazines. Load test was carried out on realized CM Transportation Trolley for minimum turning radius and found satisfactory. Four-wheel steering mechanism worked effectively in reducing turning radius of CM Transportation Trolley and Cleared for further production.

ISBN - 978-93-95038-50-8

ACKNOWLEDGEMENT

The authors would like to express their heartfelt thanks to the Director of the Defence Research and Development Laboratory (DRDL), Hyderabad, for granting permission to publish this study and for the assistance offered in doing of this work.

REFERENCES

1. Sachin Saxena, et al., 4 Wheel Steering Systems (4WAS). International Journal of Mechanical Engineering and Robotics Research 2014; ISSN 2278-0149 vol.1, No.1, pp. 213-218.
2. Mohan Kumar G R, et al., Design and analysis of a four-wheel steering system for a car. International Journal of Innovative Research in Technology 2021; Vol. 8, Issue 2, ISSN: 2349-6002 pp. 657-661.
3. Akash Singh Patel and Jaideep Chitransh. Design and Analysis of Tata 2518TC Truck Chassis Frame with Various Cross Sections Using CAE Tools. International Journal of Engineering Sciences & Research Technology 2016; ISSN: 2277-9655, pp. 692-714.
4. Vishnu Murali, et al., Design and Development of Four-Wheel Steering for All Terrain Vehicle (A.T.V). International Research Journal of Engineering and Technology (IRJET) 2020; e-ISSN: 2395-0056 Vol.7 Issue: 11, pp.1660-1668
5. Dhaval S, et al., Design and Fabrication of a Four-Wheel Steering System Model. Journal of Emerging Technologies and Innovative Research 2021; Vol.8, Issue 5, ISSN-2349-5162, pp. 203-210.
6. Rahil Pednekar, et al., Design and Fabrication of Four-Wheel Steering System. International Journal of Research in Engineering, Science and Management 2019; Vol.2, Issue:4, ISSN: 2581-5792, pp. 263-267.
7. P. Suresh Kumar, et al., Design and Fabrication of Four-Wheel Steering System for Efficient Transportation Systems. International Journal of Innovative Technology and Exploring Engineering (IJITEE) 2019; ISSN: 2278-3075, Vol.8, Issue:10, pp. 401-407.
8. Saket Bhishikar, et al., Design and Simulation of 4 Wheel Steering System. International Journal of Engineering and Innovative Technology (IJEIT) 2014; Vol.3, Issue:12, ISSN: 2277-3754, pp.351-367.
9. Sanket I Naik, et al., Development of Four-Wheel Steering System for a Car. International Research Journal of Engineering and Technology (IRJET) 2019; e-ISSN: 2395-0056, Vol.6, Issue:4, pp.3029-3032.
10. Siraj Mahibub Shaikh, et al., Development of four-wheel steering system. International Journal of Innovative Research in Technology 2017; Vol.3, Issue:12, ISSN: 2349-6002, pp. 68-77.
11. Afthab P Shamsudheen, et al., Four Mode Steering System for A Four-Wheel Vehicle. International Journal of Advance Research and Innovative ideas in Education 2020; Vol-6, Issue-3, ISSN(O)-2395-4396, pp. 519-525.
12. Vaibhav Jadhav, et al., Four Wheel Steering System. International Journal of Innovations in Engineering Research and Technology 2019; ISSN: 2394-3696, pp.68-72.
13. Bhavesh K. Gohil, et al., Optimization of Steering System for Four Wheel Vehicle. International Journal of Mechanical and Production Engineering 2018; ISSN(p): 2320-2092, Vol.6, Issue-8, pp.52-62.
14. V. Arvind. Optimizing the turning radius of a vehicle using symmetric four-wheel steering system. International Journal of Scientific & Engineering Research 2013; Vol.4, Issue 12, ISSN 2229-5518, pp.2177-2184.
15. Sriram M, et al., Reduction of Turning Radius Using Four Wheel Steering System. International Research Journal of Engineering and Technology (IRJET) 2021; Vol.8 Issue: 7, e-ISSN: 2395-0056, pp. 2550-2556.
16. Aayush Soni, et al., Study of Four-Wheel Steering Systems' Viability in Future Automobiles. International Journal of Engineering Applied Sciences and Technology (IJEAST) 2021; Vol. 6, Issue 2, ISSN No. 2455-2143, pp. 258-266.
17. Md. Danish Akhtar, et al., Wheel Steering System. International Journal of Engineering Research and Technology 2013; ISSN 0974-3154, Vol. 6, No. 3, pp. 393-398.

Optimization of Process Parameters in Pulsed Current GTA Welding Process on ASTM 106 Grade-B Steel Pipes using Linear Regression

G Prakasham[1], L Siva Rama Krishna[2*], J Kandasamy[3]

[1,2] Department of Mechanical Engineering, University College of Engineering,
Osmania University, Hyderabad – 500007,
[3]Maturi Venkata Subba Rao (MVSR) Engineering College, Hyderabad, Telangana, 501510
Email: sivaramakrisna.l@uceou.edu

ABSTRACT

The present research work aims to optimize the process parameters in the Pulsed Current Gas Tungsten Arc Welding (PCGTAW) process by employing the Design of Experiment (DOE) technique on ASTM 106 Grade-B Steel pipes. Taguchi method-based orthogonal array, L9 for four factors Pulse current (PC), Background Current (BC), Pulse Frequency (PF), and Pulse on time (PO) with three levels are employed. The higher the better reaction is picked to decide the ideal conditions for maximum ultimate tensile strength. The optimum values are found to be 220 A pulse current, 100 A background current, 4 Hz pulse frequency, and pulse on-time 50 %. ANOVA is implemented to gauge each factor's % contribution. The outcomes indicate that background current and pulse current are the significant process parameters to yield maximum ultimate tensile strength. Regression equations are used to model ultimate tensile strength, microhardness, and impact strength. Confirmation experiments are conducted to validate the results.

Keywords: *ASTM A106 Grade- B, Pulsed TIG welding, Taguchi, ANOVA*

1. INTRODUCTION

Many industrial applications need the use of welding, particularly when creating pipes. A specific welding method called pulsed current gas tungsten arc welding (PCGTAW) is used to join low-carbon steel products like ASTM A 106 Grade-B Steel pipes. Short, high-current pulses are used often during the welding process in PCGTAW, which enhances weld quality and minimizes thermal distortion. However, the PCGTAW process parameters, such as peak current, background current, pulse frequency, and pulse on time, have a significant impact on the quality. In this study, the ultimate tensile strength of ASTM 106 Grade-B Steel pipes produced by the PCGTAW method will be maximised by adjusting these process parameters. The Design of the Experiment (DOE) approach and the Taguchi method will be used to carry out the optimization. The study's findings will offer useful information for fabricating ASTM 106 Grade-B Steel pipes effectively and efficiently utilizing the PCGTAW method.

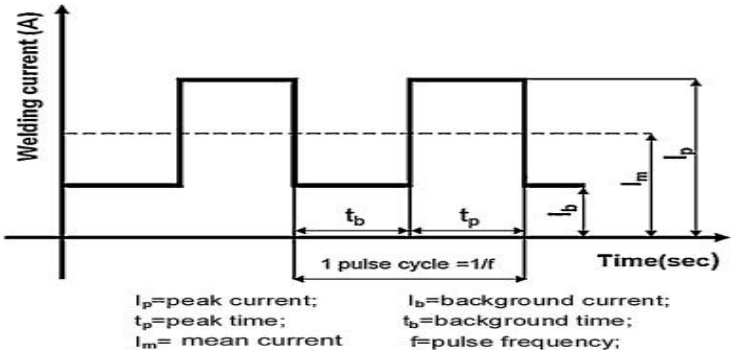

Figure 1: Pulsed TIG welding process

* Corresponding author: E-mail: sivaramakrisna.l@uceou.edu

2. LITERATURE REVIEW

Low carbon materials, like ASTM 106 Grade-B Steel pipes, are difficult to weld because of their great strength, toughness, resistance to corrosion, and ability to withstand high temperatures. Due to its enhanced weld quality and decreased thermal distortion, Pulsed Current GTA (PCGTAW) is one of the welding processes that has been widely employed for joining high-alloy materials. Due to its enhanced weld quality and decreased thermal distortion, Pulsed Current Gas Tungsten Arc Welding (PCGTAW) is one of the welding processes that has been widely employed for joining high-alloy materials.

Studies have revealed that the PCGTAW technique's process parameters have a considerable impact on weld quality. Peak current, background current, pulse frequency, and pulse on time are the most important variables. While a lower background current lowers the heat input and lessens thermal distortion, a higher peak current improves penetration and narrows the weld bead. While the pulse on time defines the length of the high-current pulse, the pulse frequency specifies how many pulses are applied every second.

Numerous researches have been conducted with the goal of enhancing the PCGTAW technique's process parameters to maximise ultimate tensile strength in high-alloy materials like ASTM 106 Grade-B Steel pipes. To determine the appropriate process parameters, this research made considerable use of the Taguchi method and the Design of Experiment (DOE) technique. Pulse Current Gas Tungsten Arc (PCGTA) welding achieves rapid solidification due to the decreased heat input, which is responsible for the fine microstructure. These pipes were linked utilizing a Tungsten Inert Gas (TIG) welding procedure with ER70S3 filler wire, with the root welded with 1.6 mm diameter wire and the finished weld with 2.5 mm filler wire. The combination of temperature cycles in the root and finish with low welding heat input results in a considerable change in the grains at the base metal as well as in the HAZ (Heat-Affected Zone). When extreme heat is utilized, the same results have not been documented [1]. Utilizing pulsed current GTA welding, ERNiCrMo-3 as a filler wire, and different junctions made of Monel 400 and AISI 316, the microstructure and mechanical characteristics of these joints are studied. Because of the thermal characteristics, the heat-affected zone is reduced and minor grain coarsening was found at the stainless steel's boundary [2]. Due to the low heat input provided to the base metal, the effects of filler metal on segregation and mechanical properties in AISI 904L material were improved, and migrated grain boundaries are visible at the weld zone of AISI 904L weldments [3]. Investigated the outcome of pulsed GTA welding on mechanical properties and microstructure, because the variation in the base and pulse current may reason for undercooling of the metal in the weld zone since heat input at weld pool is rapidly reduced in between pulse and background current of pulse tungsten inert gas welding [4 Pulse current results in a somewhat improved and more equiaxed grain structure in GTA welds. Surprisingly, typical persistent current welding produced predominantly columnar grain shapes. [5]. When compared to the conventional TIG welding process, the GTA welded AA (aluminium alloy) joint produced by pulsed current welding has superior ultimate tensile qualities [6]. The researchers investigated process parameter optimization in the pulsed TIG welding process of aluminium alloys by adjusting different gas mixes and discovered that the production of tiny dendritic microstructures resulted in the advancement of mechanical characteristics [7]. The metallographic examination reveals a fine grain structure at the weld pool, resulting in good mechanical characteristics. The current study is dedicated on obtaining the best process parameters in the PCGTAW process in order to achieve higher ultimate tensile strength.

ISBN - 978-93-95038-50-8

3. EXPERIMENTAL PROCEDURE

ASTM 106 Grade- B steel pipe with 5 mm thickness and 50 mm outer diameter is shown in Figure 2. is carefully chosen for the present work the most common angles for V grooves are 600 (2×300). The land has generally required a width of 1mm and the root opening between the parts to be welded is 1.5 mm

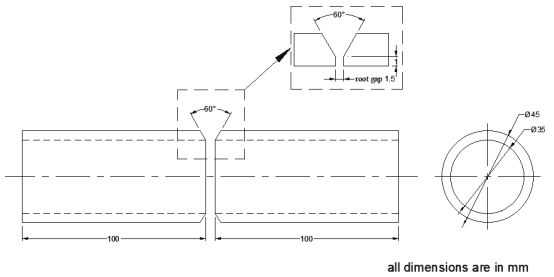

Figure 2: Schematic Diagram of ASTM 106 Grade B steel pipe

The chemical composition and mechanical properties of ASTM 106 Grade B steel are presented in Table 1 and 2.

Table 1: ASTM A 106 Grade B steel chemical composition

Element	Si	Ni	Mn	C	S	Mo	P	Cr	V	Cu
Weight (%)	0.27	0.014	0.60	0.21	0.01	0.007	0.015	0.057	0.001	0.017

Table 2: Mechanical Properties of ASTM A 106 Grade B steel

Hardness (Hv)	Tensile strength (MPa)	% Elongation	Yield strength (MPa)	Impact Strength (J)
160	410	32.2	303	128

Table 3: ER70S2 filler wire composition

Al	C	Cu	Mn	P	Si	S	Ti	Zr
0.10	0.06	0.15	1.10	0.012	0.50	0.012	0.10	0.09

Table 4: ER70S2 of filler wire mechanical properties

Yield Strength (MPa)	% Elongation	Ultimate tensile strength (MPa)
440	28	529

The PCGTAW experiments are conducted manually using the Indus Arc welding equipment and samples are shown in Figure 3. Taguchi design parameters and their levels are displayed in Table 3. The pipes are cleaned thoroughly before the conduction of experiments. Shielding gas of Argon with a flow rate of 14 lit /min. used to protect the weld pool with a constant speed of 2.09 mm/sec. to obtain maximum ultimate tensile strength.

ISBN - 978-93-95038-50-8

Figure 3: Samples of ASTM 106 Grade B Steel pipes, weldments

The multiple linear regression method was employed as the primary method in this investigation. MINITAB is used to create the regression equations. Equation 1 shows the general form of multiple linear regression models.

$$y = \beta_0+\beta_1X_1+\beta_2X_2+\beta_3X_3+.... \beta_nX_n \quad (1)$$

y = dependent variable

X_1, X_2, X_3 are independent variables

4. Results and Discussion

Table 5. lists the process variables and their ranges which were used in this study. Where X1, X2, X3, and X4 denote the pulse current, background current, pulse frequency, and pulse on, as well as their minimum and maximum values. The ASTM 106 Grade B steel pipes are joined using these range values.

Table 5: Factors and levels

Level	PC (A)	BC (A)	PF (Hz)	PO (%)
Notations	X_1	X_2	X_3	X_4
Range	180-220	100-120	4-8	40-60
Level 1	180	100	4	40
Level 2	200	110	6	50
Level 3	220	120	8	60

Table. 6 illustrates the results for ultimate tensile strength, impact strength, and microhardness derived from the experimental test conducted on 9 specimens utilizing the L9 orthogonal array while adjusting different process parameters. Process parameters are independent variables, while the produced values are dependent variables. The data in Tables 3 and 4 are modelled using the MINITAB software's linear regression.

$$y = \beta_0 + \beta_1X_1 + \beta_2X_2 + \beta_3X_3+ \beta_4X_4 \quad (2)$$

Table 6 shows the details of pulsed current GTAW experiments with different input process parameter levels to investigate the effect of input process parameters on output parameters. The Taguchi technique was used to adjust three of the four factors three levels, and all parameters were identified using an orthogonal array of L_9 (3^4) as the basis.

The arc efficiency for the pulsed current GTAW technique was set at 60%. The voltage was found to be 18V during the experiment. For the welding parameters PC, BC, PF, and Pulse on, a constant optimum welding speed of 2.09mm/sec was employed.

ISBN - 978-93-95038-50-8

Table 6: Values of ultimate tensile strength, impact strength and microhardness

S. No	Control Factors				Ultimate tensile strength	Impact strength	Micro hardness
	PC	BC	PF	PO			
Units	A	A	Hz	%	MPa	J	Hv
1	180	100	4	40	464.66	100	201
2	180	110	6	50	458.06	102	202
3	180	120	8	60	460.29	114	204
4	200	100	6	60	467.80	113	200
5	200	110	8	40	460.45	101	197
6	200	120	4	50	456.01	105	207
7	220	100	8	50	470.05	111	189
8	220	110	6	60	468.28	118	199
9	220	120	4	40	455.31	102	203

The independent variables pulse current, pulse frequency, background current, and pulse on are represented X_1, X_2, X_3, and X_4 respectively. The recorded results become the dependent variables. The following fitted model was obtained as shown in equation 3 by using MINITAB.

Regression Equation for ultimate tensile strength

Where X_1, X_2, X_3 and X_4 represent the pulse current (PC), background current (BC), pulse frequency (PF) and pulse on (PO) respectively, while 'y' represents the ultimate tensile strength.

The fitted model is $y = 463.15 + 1.77\ X_1 - 5.15\ X_2 + 0.31\ X_3 + 2.66\ X_4$ (3)

The following confirmatory experiments were conducted and given in Table. 7 to verify the regression equation produced and the optimal values of affecting parameters. Contribution percentages for each parameter: pulse current (200A), base current (100A), frequency (4Hz), and pulse on (50 %). Other confirmatory trials selected from 3^4 arrays confirm the regression equation predicted for ultimate tensile strength fairly closely (Table 7).

Table 7: Confirmatory experiments

S.No	Control factors				Responses			
	Pulse current (A)	Back ground current (A)	Pulse frequency (Hz)	Pulse on (%)	Ultimate tensile strength, MPa (Average), (X)	Predicted Ultimate tensile strength, MPa (Y)	Difference (X-Y)	Error (%)
1	180	100	4	40	465.885	462.74	-3.14	0.006
2	180	110	6	50	458.145	460.56	2.42	0.005
3	180	120	8	60	458.755	458.38	-0.37	0.000
4	200	100	6	60	466.095	470.14	4.05	0.0086
5	200	110	8	40	456.89	459.98	3.09	0.006
6	200	120	4	50	459.27	456.87	-2.4	0.005
7	220	100	8	50	463.96	469.56	5.6	0.011
8	220	110	6	60	462.755	466.45	3.7	0.007
9	220	120	4	40	456.795	456.29	-0.41	0.000

ISBN - 978-93-95038-50-8

Regression Equation for impact strength

The fitted model is $y= 88.33 + 2.50 X_1 - 0.50 X_2 + 0.50 X_3 + 7.00 X_4$ (4)

The following confirmatory experiments were conducted and given in Table 8 to verify the regression equation produced and the optimal values of affecting parameters. Contribution percentages for each parameter: pulse current (200A), base current (100A), frequency (4Hz), and pulse on (50 %). Other confirmatory trials selected from 3^4 arrays confirm the regression equation predicted for impact strength fairly closely (Table 8).

Table 8: Confirmatory experiments

S.No	Control factors				Responses			
	Pulse current, A	Back-ground current, A	Pulse frequency, Hz	Pulse on, %	Impact Strength (Average), MPa, (X)	Predicted impact strength, MPa, (Y)	Difference (X-Y)	Error (%)
1	180	100	4	40	100.32	97.83	-2.48	0.025
2	180	110	6	50	102.64	104.83	2.19	0.020
3	180	120	8	60	114.37	111.83	-2.54	0.022
4	200	100	6	60	113.89	114.83	0.94	0.008
5	200	110	8	40	101.91	100.83	-1.08	0.010
6	200	120	4	50	105.12	106.33	1.21	0.011
7	220	100	8	50	111.27	110.83	-0.44	0.0039
8	220	110	6	60	118.76	116.33	-2.4	0.020
9	220	120	4	40	102.02	102.33	0.31	0.003

Regression Equation for microhardness

The fitted model is $y= 202.56 - 2.667 X_1 + 4.000 X_2 - 2.833 X_3 + 0.333 X_4$ (5)

To verify the regression equation developed and validate optimized values of influencing parameters, the following confirmatory experiments were carried out and reported in Table 9. The percentage of contribution of each parameter pulse current (200A), base current (100A), frequency (4Hz), pulse on (50%). The regression equation predicted for microhardness is very close to other confirmatory experiments chosen among 3^4 arrays (Table 9).

Table 9: Confirmatory experiments

S.No	Control factors				Responses			
	Pulse current, A	Background current, A	Pulse frequency Hz	Pulse on, %	Microhardness (Average), (X)	Predicted microhardness(Y)	Difference (X-Y)	Error (%)
1	180	100	4	40	201.10	201.39	0.29	0.001
2	180	110	6	50	202.21	202.89	0.68	0.003
3	180	120	8	60	204.98	204.39	-0.59	0.002
4	200	100	6	60	200.56	196.55	-4.01	0.020
5	200	110	8	40	197.89	197.0	-0.89	0.004
6	200	120	4	50	207.34	207.05	-0.31	0.001
7	220	100	8	50	189.11	190.72	1.61	0.008
8	220	110	6	60	199.23	200.72	1.49	0.007
9	220	120	4	40	203.54	201.22	-2.32	0.011

ISBN - 978-93-95038-50-8

Table.10 displays the regression model coefficients generated from equations 3,4,5 by inserting process parameters from table 7, 8, 9.

Table 10: Regression model coefficients

Regression coefficients	Ultimate tensile strength (MPa)	Impact Strength (J)	Microhardness (Hv)
β_0	463.15	88.33	202.56
β_1	1.77	2.50	-2.667
β_2	-5.15	-0.50	4.00
β_3	0.31	0.50	-2.833
β_4	2.66	7.00	0.333

The regression equations for ultimate tensile strength, microhardness and impact strength are

Ultimate tensile strength = $463.15 + 1.77\ X_1 - 5.15\ X_2 + 0.31\ X_3 + 2.66\ X_4$

Impact strength = $88.33 + 2.50\ X_1 - 0.50\ X_2 + 0.50\ X_3 + 7.00\ X_4$

Microhardness = $202.56 - 2.667\ X_1 + 4.000\ X_2 - 2.833\ X_3 + 0.333\ X_4$

5. CONCLUSIONS

The improvement of ASTM 106 Grade B steel pipe joints created by pulsed TIG welding was investigated using the linear regression technique. The goal of the study is to establish a relationship between process variables and microhardness, impact strength, and the ultimate tensile strength of ASTM 106 Grade B steel pipe welds. As a result, experimental study was undertaken using the L9 orthogonal array, as well as linear regression analysis, to estimate and analyse ultimate tensile strength, impact strength, and microhardness in pulsed TIG welding. The experimental and anticipated results at 220 A, 100 A, 4 Hz, and 50% show that pulse current and background current affect ultimate tensile strength.

REFERENCES

1. Cleiton Carvalho Silvaa , Joaquim Teixeira de Assisb , " Residual Stress, Microstructure and Hardness of Thin-Walled Low-Carbon Steel Pipes Welded Manually, *Materials Research*. Vol 19, 2016, pp. 1215-1225. ISSN 1516 1439
2. B. Yelamasetti, G. Rajyalakshmi, and K. S. Kumar, "Mechanical and Microstructural Studies of Optimized Taguchi Grey Relational Analysis Of PCGTAW Process Parameters For Joining Monel 400 And AISI 316," *UPB Scientific Bulletin, Series B,* Vol. 83, Iss. 3, 2021 pp. 252-264, ISSN 1454-2331
3. K. Devendranath Ramkumar*,* "Effects of filler metals on the segregation, mechanical properties and hot corrosion behaviour of pulsed current gas tungsten arc welded super-austenitic stainless steel," *Journal of Manufacturing. Process.*, vol. 24, Oct. 2016 pp. 46–61. ISSN 1526-6125
4. Chennaiah MB, Kumar, Effect of Pulsed TIG Welding Parameters on the Microstructure and Micro-Hardness of AA6061 Joints, journal of materials science engineering, Vol 4, 2015, pp 1-4, ISSN 2169-0022,
5. G. M. Reddy, A. A. Gokhale, and K. P. Rao, "Optimisation of pulse frequency in pulsed current gas tungsten arc welding of aluminium–lithium alloy sheets," *Material Science Technology*, vol. 14, no. 1, Jan. 1998 pp. 61–66. ISSN 0267-0836.

6. N. Karunakaran and V. Balasubramanian, "Effect of pulsed current on temperature distribution, weld bead profiles and characteristics of gas tungsten arc welded aluminium alloy joints," *Transactions Nonferrous Metals Society China*, vol. 21, no. 2, Feb. 2011, pp. 278–286, ISSN 1003-6326.
7. P. Kumar, K. P. Kolhe, S. J. Morey, and C. K. Datta, "Process Parameters Optimization of an Aluminium Alloy with Pulsed Gas Tungsten Arc Welding (GTAW) Using Gas Mixtures," *Materials Sciences and Applications* , Vol.2 No.4, April 2011 ,pp 251-257, ISSN 2527-1034.
8. M.Sabzi, S.H.Mousavi, Anijdan, A.R.Eivani N.Park H.R.Jafarian "The effect of pulse current changes in PCGTAW on microstructural evolution, drastic improvement in mechanical properties, and fracture mode of dissimilar welded joint of AISI 316L-AISI 310S stainless steels", Materials Science and Engineering: A Volume 823, 2021, pp 141700, ISSN 0921-5093.
9. A. Prithiraj, I. O. Otunniyi, P. Osifo, and J. van der Merwe, "Corrosion behaviour of stainless and carbon steels exposed to sulphate – reducing bacteria from industrial heat exchangers," *Engineering Failure Analysis*, Vol No. 104, Oct. 2019, pp. 977–986, ISSN 1350-6307
10. M. Sarvghad, D. Del Aguila, and G. Will, "Optimized corrosion performance of a carbon steel in dilute sulfuric acid through heat treatment," *Applied Surface Science*, Vol. 491, Oct.2019, pp.460–468, ISSN 0169-4332
11. M. Daavari, S. A. S. Vanini, E. Fereiduni, and M. H. Rokni, "Mechanical and electrochemical behaviors of butt-weldedhigh-temperaturee steel pipes," *Engineering Failure Analysis*, Vol. 62, Apr 2016, pp. 287–299, ISSN 1350-6307
12. C. C. Silva, A. B. de Souza Neto, F. D. A. da Silva, F. E. S. de Freitas Júnior, and J. P. Farias, "Welding of ASTM A106 Gr. B steel pipes for high-temperature service – part 1 – residual stress analysis," *Welding International*, vol. 23, no. 4, Apr. 2009, pp. 270–281. ISSN 1754-2138
13. Manikandan, M, Arivazhagan, N, Arivarasu, M. Mageshkumar, K, Rajan, Deva N., Murugan, B. Arul, Prasanth, P, Sukumar, S, Vimalanathan, R, "Analysis of Metallurgical and Mechanical Properties of Continuous and Pulsed Current Gas Tungsten Arc Welded Alloy C-276 with Duplex Stainless Steel," *Transactions of the Indian Institute of Metals,* vol. 70, no. 3, Apr. 2017, pp. 661–669. ISSN 0972-2815.
14. R. Prabhu and, T. Alwarsamy, "Study and Investigations on Process Parameters for Bead Geometry during Cladding by Pulsed MIG Welding Process". *Bluff Body Edge Effect on Pressure-Hill and Zone of Influence,* Vol No 8, 2014, pp 722-729.
15. A. H. V. Pavan, K. S. N. Vikrant, G. Vimalan, and K. Singh, "Metallurgical analysis of SA-106 Gr. B pipe failure during hot bending," *Case Studies in Engineering Failure Analysis*, vol. 1, 2013, pp. 120–130.
16. S. S. M. Tavares, J. M. Pardal, R. R. Pinheiro, J. P. Gonçalves, and C. Scandian, "Failure of ASTM A-106 Gr. B tubes by creep and erosive wear," *Engineering Failure Analysis*, vol. 26, Dec. 2012, pp. 337–343.

Fire Safety Assessment Studies in High Rise Assembly Buildings using Fire Dynamic Simulator

Sanka SVD Sairam*, V Vinodh, T Subbananthan

Department of Space
Indian Space Research Organization,
Sriharikota, Andhra Pradesh, 524124
sanka.sairam@shar.gov.in

ABSTRACT

Indoors fires pose a significant threat in High rise assembly buildings especially with a lot of working personnel in various floors. In these type of buildings, fire protection, personnel and property safety play a key role. A study was carried out with Fire Dynamic Simulator (FDS) for a created model of High-rise assembly building with two different types of fire scenario to understand the spread of fire and smoke at various floors. Thus, by depicting a proper adoption of fire & smoke detection disposition considering these fire scenarios. The analysis was carried out by choosing the right type of positioning the detection method at various floors to minimize the response time.

Keywords: *Computer simulation, Multi-storey building fire, FDS, Smoke detection*

1. INTRODUCTION

Recently, computer simulation of fires has become a prominent tool for carrying out analysis and improvising of fire safety especially in production, process & assembly building dealing with explosion sensitive explosives. These usually require a high level of safety to prevent any type of fires near to process lines. The use of computer modelled Fire simulation itself presents a very understanding, economic and safe way of determination of potential fires for a given model. Fire Dynamic Simulator (FDS) is an Open Software developed by National Institute of Standards and Technology (NIST). FDS provides in aid to create the required model by defining any material properties. It solves the user created model with given set of inputs with assumption that the fire propagation is thermally driven (i.e. flow is of low-speed/low Mach) [1]. It also solves the other Thermo-chemical analysis equations like combustion of products, pyrolysis, heat transfers in conductive, convective & radiation between various phases like solid to gas, liquid to gas etc. [2]. The typical simple chemical reaction of fire in open environment used by FDS is as given below.

$$\text{Fuel} + 2\ \text{Air} \rightarrow \text{Products} \tag{1}$$

$$\text{Fuel} + 2\ (O_2 + 3.76\ N_2) \rightarrow x\ CO_2 + y\ H_2O + z\ N_2 \tag{2}$$

A graphical interface software that uses FDS was utilized to construct complex models for simulating different fire scenarios as per user requirements [3]. The software allows the user to visualise as well as construct the model in 3D. Computational Fluid Dynamics (CFD) in FDS solves the user model with given input boundary conditions by Navier-Strokes equation as per low speed approximations [2]. In our paper, two cases of indoor fires with different fuels were simulated in a High-rise assembly building. The fire model is rendered and observed for fire & smoke propagation over a period of time. The created model consists of various smoke detectors and thermocouples at each level to understand the smoke dynamics caused by each case of fire.

Corresponding author: Email: sanka.sairam@shar.gov.in

2. CREATION OF MODEL

Construction of Model was done through software having feature to import the 2D plan as a background image for creating model in 3D. The model generation is done in a rectangular Mesh of size 50 X 50 X 80 m with uniform cells of size 0.1 X 0.1 X 0.1 m for intended FDS simulation [4]. Thus, the entire domain space was divided into 500, 500 and 800 cells respectively in the direction of x, y and z axes.

The floor slabs and walls are of concrete material with 0.25 m thick. The building is in rectangular fashion with 30 (length) X 40 (width) m. The slabs are having partial openings to accommodate the vertical assembly operations at center. The typical construction creation of first floor slab and subsequent floors is shown in Figure 1. The design model of High-rise assembly building has 12 floors with floor to floor separation distance is 5 m. (Note: For understanding, the front entrance wall is in hide mode)

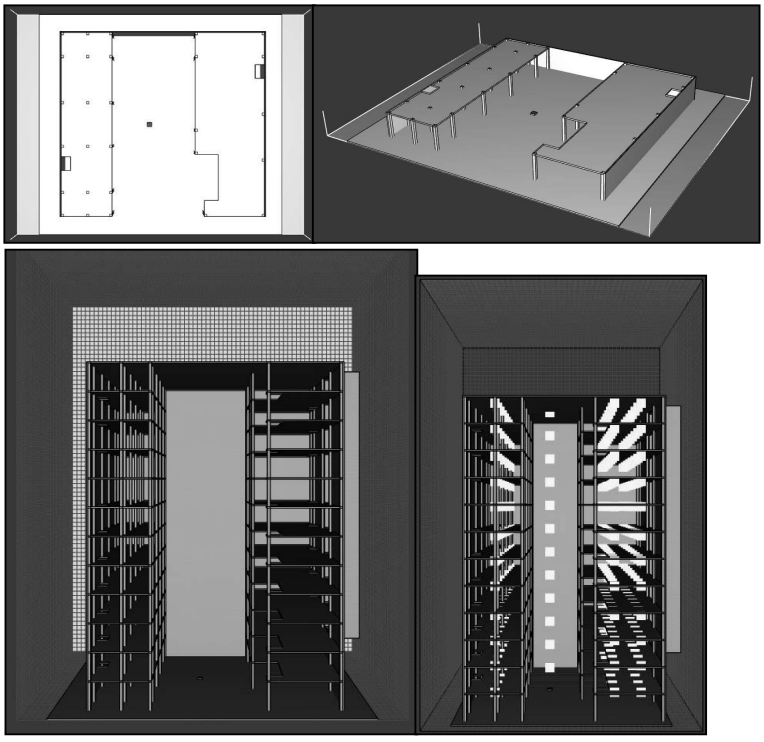

Figure 1: Stepwise construction of 3D model for High rise assembly building with Smoke Detectors & Thermocouples.

For ensuring the Open environment, computation boundary space of mesh is featured as Open vent at all directions except for ground. A stack of 1 X 1 X 0.25 m fuel is constructed in ground floor for generating fire. The top surface of the stack is maintained as burning surface (i.e. Burner) to enable the reaction initiation.

2.1. INPUTS TO MODEL

The modeling software requires the defining of the materials, surfaces, reaction and choosing of required results. In our model, we are generating a indoor fire with 2 different types of fuels i.e. cotton and wood at ground floor of the building so that fire developed in

ISBN - 978-93-95038-50-8

each case can be analyzed in an apt manner. The materials compositions along with reaction were given as input to the software [6]. The additional details like Heat of Combustion, pyrolysis, CO yield, Soot yield & Hydrogen Fraction were also provided for reaction [5] [7].

The characteristic Heat Release Rate (HRR) for the burning surface was obtained from experiments conducted. The typical profiles of HRR vs. Time graph were also co-related with profiles mentioned as per [5]. To get the temperature variation over the floors due to the fire in each case were depicted through positioning of 12 nos. of thermocouples above the burner surface. To understand the smoke propagation due to fires, 288 nos. smoke detectors of photoelectric type were positioned throughout the floors as shown in Figure 1. with obscuration threshold set at 7 %/m. The complete model is run in FDS simulation software for 200 seconds of fire simulation in Core i7-6700 @3.40 GHz, 8GB RAM.

3. RESULTS AND DISCUSSIONS

Based on the input parameters and boundary conditions given to the created model the CFD in FDS was run. The Figure 2. shows the illustration and visualization results of fire and smoke developments with time for wood & cotton fire scenarios.

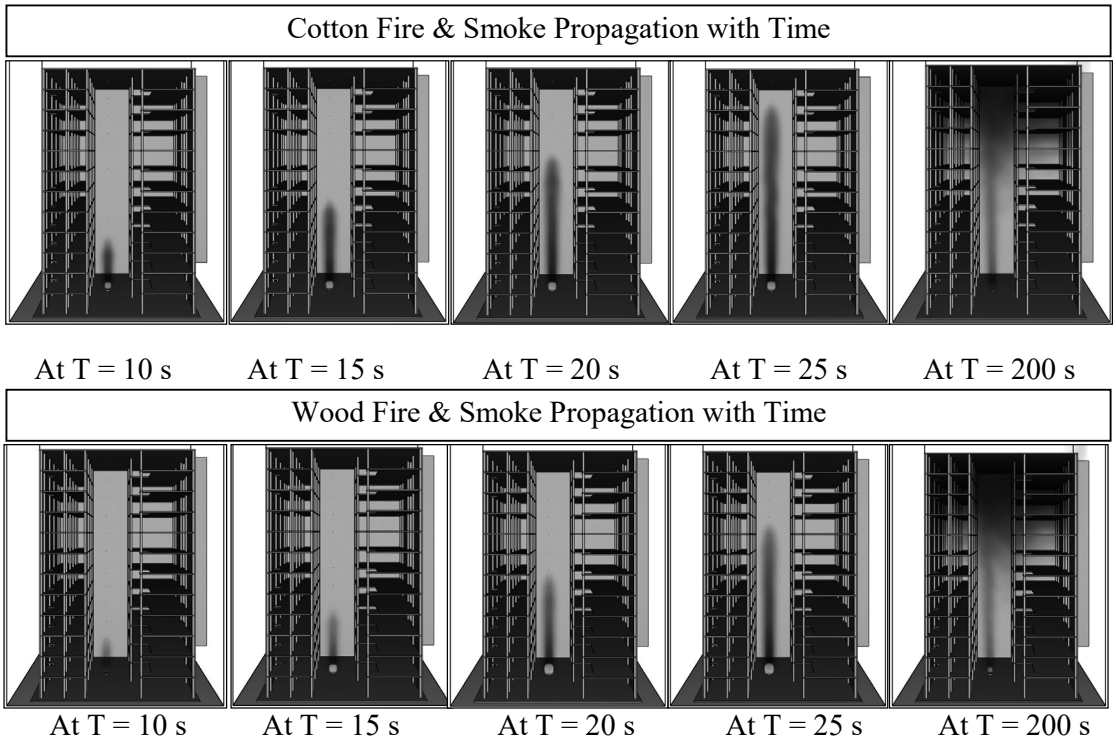

Figure 2: Result images of Fire & Smoke propagation with Time.

It was observed a maximum flame length of 2.514 m was observed at ~16 s. for cotton stack fire whereas 3.293 m of maximum flame length was observed at ~20 s. It was also observed that rise in smoke height is faster in case of cotton fires. A plot of obscuration of the photoelectric sensors' levels observed that have been triggered alarm (i.e. reaching threshold obscuration 7%/m) in both fires for simulated time were shown in below Figure 3. The first detector activation time observed for wood fire is 47.30 s where as for cotton fire is 46.09 s.

ISBN - 978-93-95038-50-8

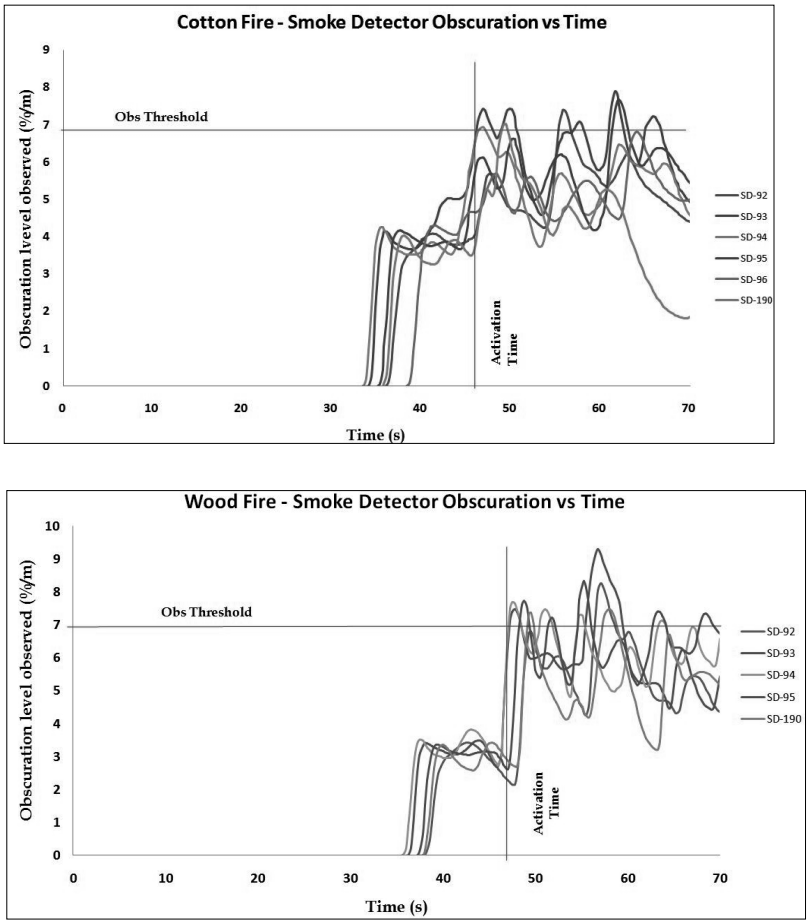

Figure 3: Plot of Obscuration of smoke detectors for wood & cotton fires with Time.

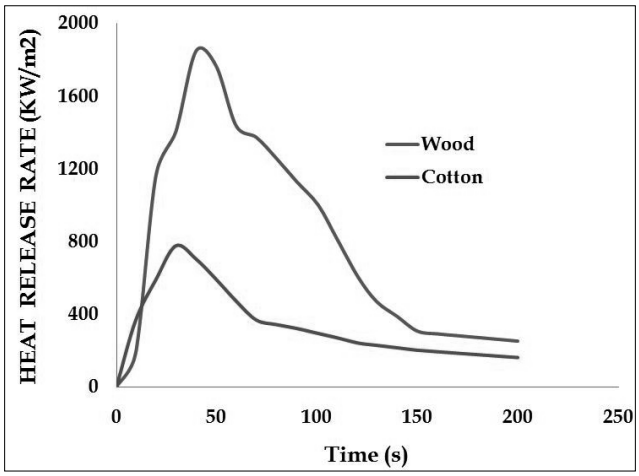

Figure 4: Plot of Heat release rate for wood & cotton fires with Time.

Plot of Heat release rate per unit area was shown in Figure 4 for both Cotton & Wood fire scenarios. Similarly, the temperature profiles observed in each floor was also depicted from the results is shown in Figure 5. A maximum of 184 ºC is observed for wood fire @ 44 s at 5-meter level where as a maximum of 107 ºC is observed @ 35 s for cotton. It is found that the temperature variation is decreasing for both fires on reaching top floors of assembly buildings.

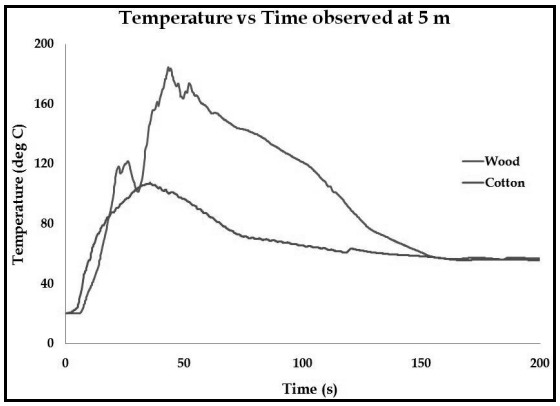

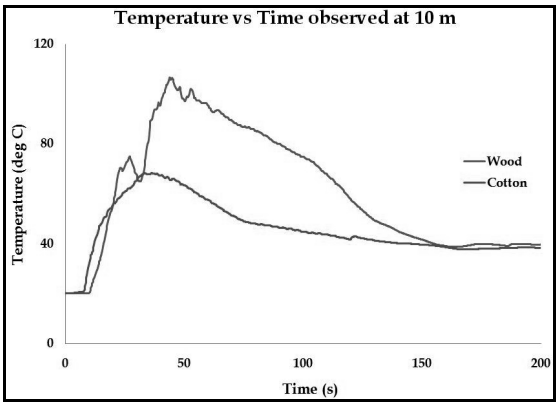

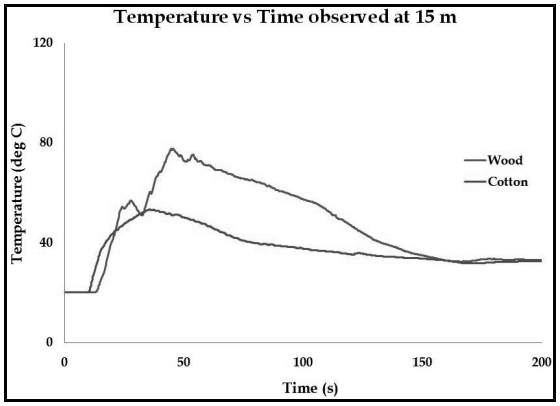

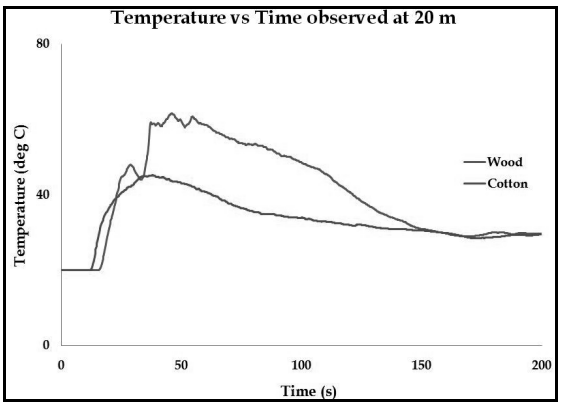

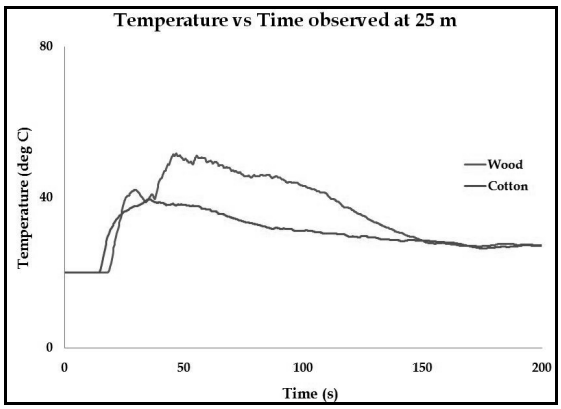

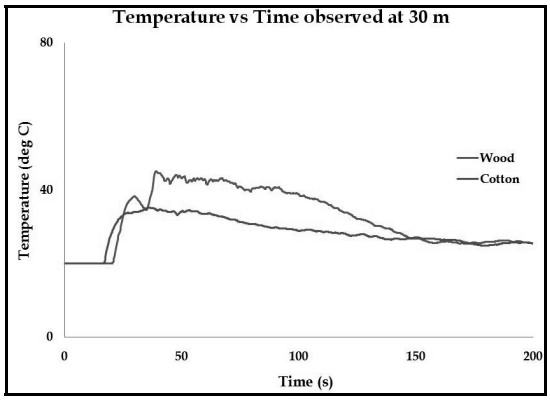

ISBN - 978-93-95038-50-8

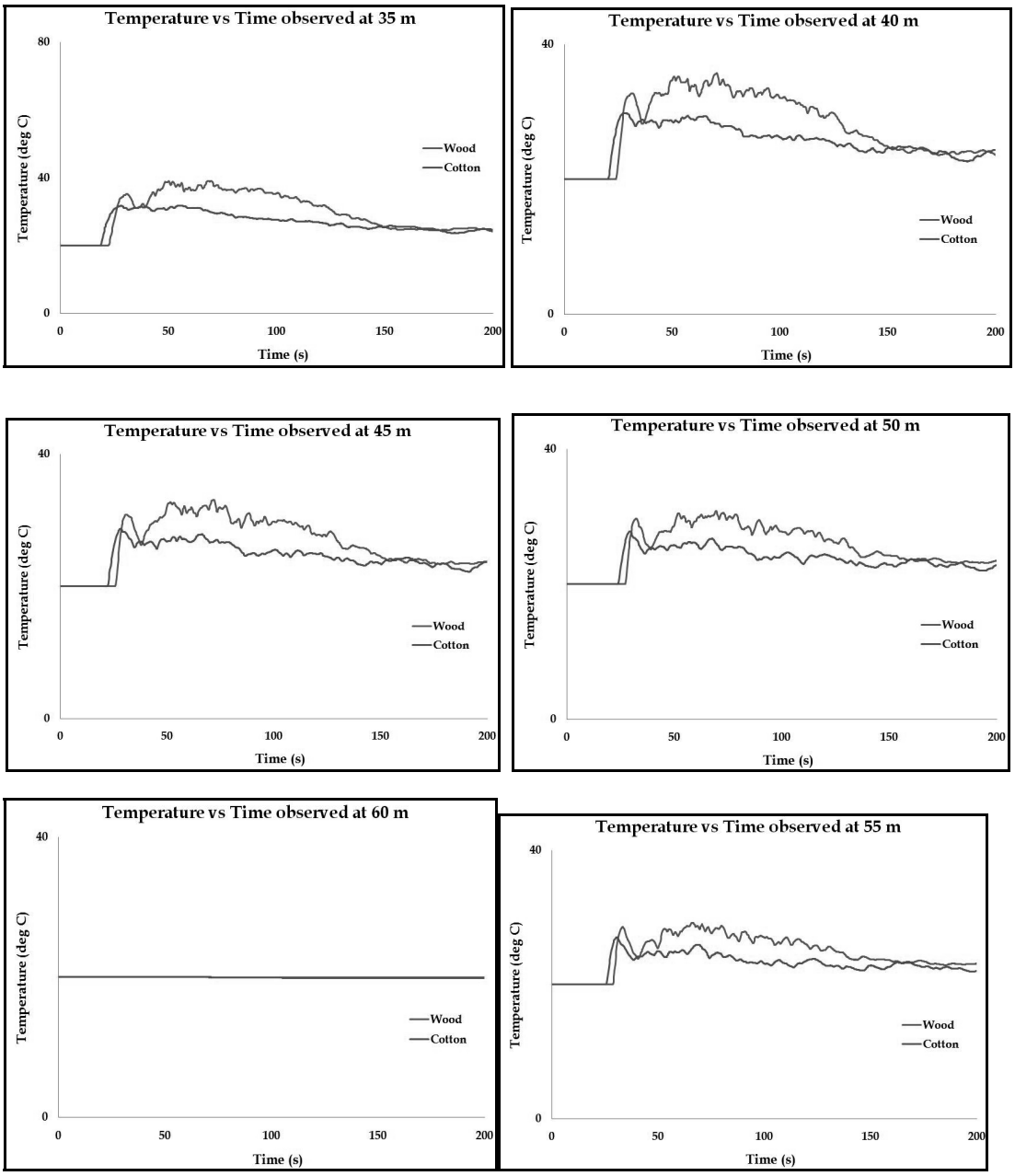

Figure 5: Plot of Temperature profiles for wood & cotton fires with Time.

4. CONCLUSION

A High-rise assembly building consisting of 12 floors was constructed in FDS to understand the two different fuel fires i.e. cotton and wood with identical stack dimensions. The entire building is equipped with 288 nos. of photoelectric smoke sensors and 12 nos. thermocouples at each floor to analyze the temperature and obscuration levels for entire simulation period of 200 s. It was observed that for both fire scenarios the smoke level reaches the ceiling height at around 47s. But the temperature values observed for wood fires is more than that of cotton fires. It is also inferred from results that the obscuration levels at top floors are filling significantly than at lower levels. Thus, from the data depicted we can

ISBN - 978-93-95038-50-8

see the Heat sensors with photoelectric type provided in lower floors provide a significant less response time where as the photoelectric type at top floor provides the efficient way to detect fires at top as well as bottom floors.

Additionally, for simulation of fires in further fine mesh for these types of complex structure geometry requires multi-core computer for processing the FDS simulations. Other flammable materials in addition to cotton & wood stack fires can also be added to the existing simulation for studying the impact of multi case fire scenarios. Also, aspects of safe evacuation from the fires at top levels of Multi-storey building can also be studied in future.

REFERENCES

1. Lukas Valasek, “The use of PyroSim graphical user interface for FDS simulation of a cinema fire”. International Journal of Mathematics and Computers in Simulation Issue 3, Volume 7, 2013.
2. Xinfeng Long, Xueqin Zhang & Bo Lou (2017): Numerical simulation of dormitory building fire and personnel escape based on Pyrosim and Pathfinder, Journal of the Chinese Institute of Engineers, DOI: 10.1080/02533839.2017.1300072”.
3. RADOJE B. JEVTIĆ, “Fire Simulation in House Conditions”. School of Electrical Engineering "Nikola Tesla", Niš Review paper UDC: 614.841.41:519.876.5DOI: 0.5937/tehnika1601160J
4. Rinne, Tuomo, Hietaniemi, Jukka & Hostikka, Simo, Rao, “Experimental Validation of the FDS Simulations of Smoke and Toxic Gas Concentrations”.
5. Morgan J. Hurley, "SFPE Handbook of Fire Protection Engineering", Fifth Edition. Chapter 7. Thermal Decomposition of Polymeric Materials.
6. Hong Zhang *et al.,* "Analysis of the indoor fire risk based on the Pyrosim simulation" Proceeding of IOP Conference Series: Earth and Environmental Science 2021 IOP Conf. Ser.: Earth Environ. Sci. 636 012002
7. Babrauskas, V., and Mulholland, G., "Smoke and Soot Data Determinations in the Cone Calorimeter," Mathematical Modeling of Fires, ASTM STP 983, American Society for Testing and Materials. Philadelphia, 1987, pp. 83-104.

ISBN - 978-93-95038-50-8

The Radar Cross Section of Marine Vessels

G. S*unil Sriharsha*, P.C. Bhuvana*, N. Harini*, Mallikarjun. Bangi, M. Jyoti++, G. Naresh Kumar++

*Students, GITAM, Telangana, India,
+Engineer, Hyderabad, Telangana, India
++Scientist, DRDL, Hyderabad, Telangana, India
Email: mallikarjun.bangimatam@gmail.com

ABSTRACT

This paper focuses on the estimation of ship RCS using High-Frequency Structure Simulator (HFSS). The results produced here have been compared to the estimates available in the open literature of a Canadian cargo ship named Teleost and also measured values. In this paper, the RCS of a Canadian marine ship named "Teleost" is presented. RCS depends on various parameters like shape, size, orientation, operating frequency and aspect angle. Simulations using Finite Element Method (FEM) in Ansys HFSS software for monostatic Radar Cross Section were made through 0.1MHz to 8MHz frequency. The results of the proposed method are compared with the existing measured values and simulated values available in open literature. The work is carried out using PEC and steel as the dielectric material to analyse the monostatic RCS values, and a broad comparison is made among previous values and the obtained values. The results of this proposed method are more accurate when compared to the previous works, and are very near to the measured values. The work is carried out using Perfectly Electrical Conductor (PEC) and steel as the materials. The simulations of these two materials are carried out individually, to analyze the Monostatic RCS values.

Keywords: *Radar cross-sections (RCS), High-Frequency, Surface Wave Radar (HFSWR) High-Frequency System Simulation (HFSS), Monostatic RCS, Perfectly Electrical Conductor (PEC)*

1. INTRODUCTION

Radar is the acronym for "RAdio Detection and Ranging". Radar uses radio waves (electro-magnetic waves). These waves have one of the largest wavelengths and smallest frequencies in the EM spectrum. Due to this, radio waves can travel long distances. This property of traveling long distance makes the most basic application of radar, that is ranging and detection. The distance measurement is one of the important applications of radar.

The basic concept of radar is, it transmits a Radio Frequency (RF) signal which is generated by the transmitter, which is radiated by the transmitting antenna and reflected from the reflecting object (target). A small portion of the reflected signal known as 'echo' returns to the radar receiver. Radar uses the 'echo' signal to determine the direction and distance of the reflecting object [1]. Radar can detect targets at near and far distances and it can also measure their range with precision, in all weather conditions, which is a major advantage when compared with other sensors. Usually radar provides exact location of target in range and angle. The change in target location can also be measured from the variation in range and angle with respective to time, by which the 'track' is possible.

Radar operates at different frequencies from a few Megahertz (MHz) to Gigahertz (GHz) within wide range of spectrum, where radar operation principles are the same at any frequency, but the practical implementation is widely different. Electromagnetic waves normally disperse incident energy in all directions when incident on a target. The spatial distribution of energy is called 'scattering', and the object itself is called as 'scatterer'. The energy scattered back to the source of the wave is called 'back-scattering', which mainly

*Corresponding author E-mail: mallikarjun.bangimatam@gmail.com

constitutes the radar echo of the objects. The intensity of the echo is described explicitly by the Radar Cross Section (RCS) of the object.

Therefore, it is critical in design and operation of radars to quantify or describe the echo, in terms of target characteristics as size, shape, and orientation. For this purpose, the target is described as an effective area or echo area terms, still found occasionally in contemporary technical literatures. [2] The Radar Cross Section (RCS) is defined in eq. 1

$$\sigma = \lim_{R \to \infty} 4\pi R^2 \left(\frac{|E_s|^2}{|E_0|^2} \right) \tag{1}$$

Where

- R is distance between radar and target
- E_0 is electric-field strength of incident wave on target
- Es is electric-field strength of scattered wave at radar.

RCS is also defined as a comparison of the scattered power density at the receiver to the incident power density at the target [3]. This definition also valid for the electric-field strengths and magnetic-field strengths of the incident and scattered. The basic tenets of RCS are as follows

1. RCS can be defined as the ability to reflect the radar electromagnetic waves.
2. RCS value tells how easily an object is detectable by radar.
3. RCS must be as low as possible for the benefit of not being detected.

Since, RCS is important factor to achieve stealth of an object, prediction and reduction of RCS become an important aspect while the vehicle is being built. Where prediction is defined as finding the RCS of an object, while reduction is a process of reducing the value of RCS. Prediction can be done in two ways, one being the conventional way, using the mathematical formulas and techniques available in the open literature and other way is the usage of simulation software's available. There are many commercially available software's that can predict the RCS value with high accuracy. Even there are many ways that focus on the reduction of RCS value. Some of them are the application of Radio Absorbing Materials (RAM), changing the dimensions of the vehicle, etc. RCS plays an important role in the understanding of the EM phenomenon of radar. The following methods are used for determining the RCS

- Geometrical Optics (GO)
- Physical Optics (PO)
- Geometrical Theory of Diffraction (GTD)
- Physical Theory of Diffraction (PTD).

The following techniques are used by commercial software's for the prediction of RCS are:

1. Methods of Moments (MoM): This type is used for linear and partial differential equations.
2. Finite Element Method (FEM): It is used for complex geometric shapes. In this method, the complex object is divided into smaller parts and the RCS of each smaller part is calculated and then added to get the RCS of the complex shape.
3. Finite Distance Time Domain (FDTD): It is the simplest and easiest to implement [4].

ISBN - 978-93-95038-50-8

The main objective of this paper is to find or predict the RCS of the objects by deploying a 3D model in ANSYS HFSS software and evaluating the performance by comparative study obtained from achieved results to results available in open literature. One of the oldest methods of finding the RCS value of any object in the lab is 'MACROSCOPE'.
There are many other software's that can be used to predict the RCS value of any object by simulating the conditions, which can be set by the user.

Here in this paper, ANSYS HFSS software is used for the prediction of the RCS value along with the shape and size of the object, which play a major role in predicting value of RCS. Factors like wind and water reflections (for naval applications) will affect the value of RCS (when measured physically).

Figure 1: Teleost Ship

2. LITERATURE SURVEY

The initial works on radar started in 1962, the authors discussed about the basics of the radar and its uses in [2]. One of the usages is to find RCS of an object. Taking a clue from research [2], the first major work on RCS and importance of RCS were discussed and published in the year 1978 by [5]. This discussion has led to the increase in attention towards RCS [6]. In [7], the author discusses a laboratory method to find (predict) the RCS using a software, which can be used to predict the RCS of any object. In the year 2006, work on 2 Canadian cargo ships was carried out to simulate the RCS values, using the HFSWR method and comparing the values with the originally measured value [8]. Taking a clue from the previous research of [8], authors discussed the effect of oceanic environment, and conducted a work in 2009, to calculate the practical effect of the oceanic environment on the value of RCS of any object in atmosphere. In 2012, one of the major researches was conducted on the prediction and the reduction of the RCS value for naval ships [9]. In [10], the authors have presented the different methods of predicting the RCS of ships and different parameters which will affect the value of RCS are presented.

In 2013, the authors have presented research on the (RAM) Radar Absorbing Material [11], they have di-electric properties. They are used to reduce the value of RCS of any ship or aircraft. RAM works on the principle of the object absorbing the electromagnetic wave energy to minimize the intensity of the reflected signal. The imaginary part in the dielectric constant leads to a reduction or decrease in the value of RCS.

In 2015, two major research works in the field of RCS are conducted. One research has worked on a combination of Frequency and Material Independent Reactions - Methods of moments 'FMIR-MoM' with the 'barycentric sub-division' to analyze the wide-band RCS of objects with 'PEC' material was discussed in [12]. Another research has worked on the different ways to calculate the RCS. Mainly techniques like Physical Optics (PO) and

Geometrical Optics (GO) are used to calculate the RCS. In [13] authors utilized software mechanism for the prediction of RCS. In 2017, for the first time, High-Frequency Ground Wave Radar (HFGWR) was used to predict the RCS of ships. With the use of HFGWR, the RCS value is significantly improved [14].

In 2018, RCS was used to calculate the dynamic human motions by virtual reality [15]. Authors used the Shooting and Bouncing Ray (SBR) technique. In this work, the human body was converted into a poly mesh and the SBR technique was used.

3. EXPERIMENT ANALYSIS

In this work, experimental analysis is carried out using ANSYS High Frequency System Simulation (HFSS). The Canadian marine vessel named 'Teleost' is illustrated fig. 1, and 3D models of side view and top view of the 'Teleost' ship are shown in fig. 3 and fig. 4. In addition, to this fig. II shows top view of a ship with respective to angles of incident fields referred to Port, Starboard, Bow and Stern. Here ship is modeled using Perfectly Electrical Conductor (PEC) material.

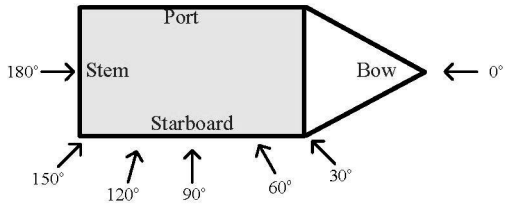

Figure 2: Teleost Ship Top View w.r.to incident angles

The Monostatic RCS values of the ship is obtained by taking the reference of the top view of the ship fig. 2.

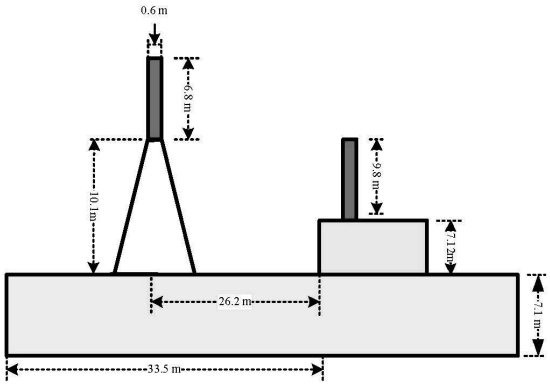

Figure 3: Ship Side View

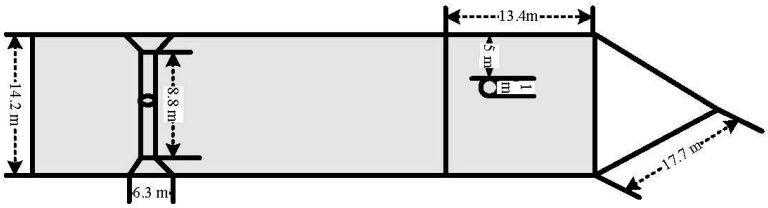

Figure 4: Ship Top View

Analysis are carried out using a frequency sweep ranging from 0.1 MHz to 8.0 MHz. Excitations are set up at the starboard angle of the ship. Boundaries are set up at the corners of the ship. The simulations are carried out using ANSYS HFSS 2019 software tool.

4. FEM ANALYSIS

Finite Element Method (FEM) subdivides a large system into smaller, simpler parts that are called finite elements. This is achieved by a particular space discretization in the space dimensions, which is implemented by the construction of a mesh of the object.

The finite element method formulation of a boundary value problem finally results in a system of algebraic equations. The method approximates the unknown function over the domain. The simple equations that model these finite elements are then assembled into a larger system of equations that models the entire problem. The FEM then approximates a solution by minimizing an associated error function via the calculus of variations. The Finite element breaking of the Teleost Ship is shown in fig. 5.

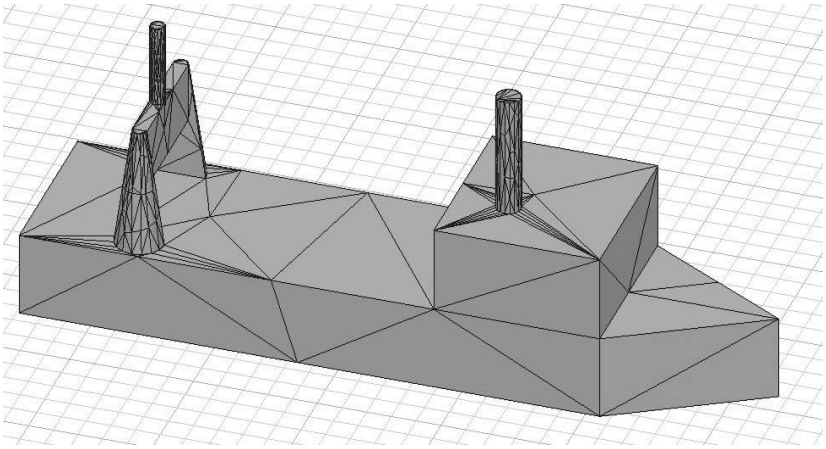

Figure 5: Finite Element breakdown

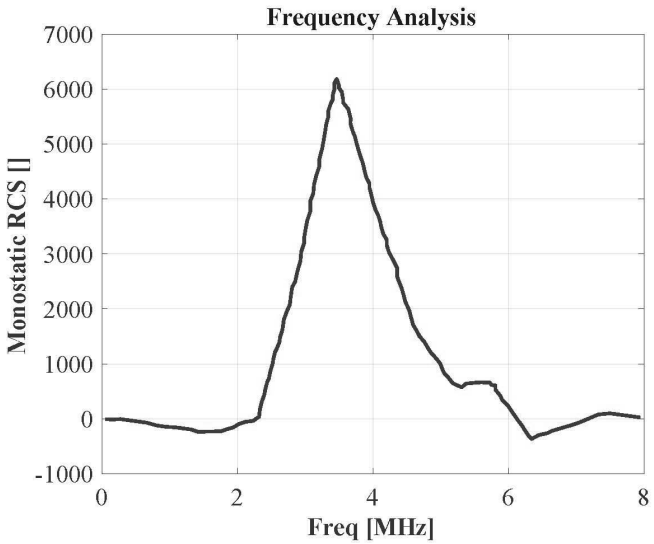

Figure 6: Frequency Analysis

4.1 RESULTS, DISCUSSIONS AND OBSERVATION

Analysis were carried out using FEM method on PEC material of 'Teleost' ship, and the observations are presented below in fig. 6. It is observed that a dip in the value of RCS at 6.5 MHz. One major reason behind that dip is the A-Frame mast in the Teleost ship (which can be observed in the fig 1). Where a mast is a spar, or arrangement of spars, which is erected more or less vertically on the center-line of a ship used for carrying sails, and derricks, which gives necessary aid to a navigation, for look-out position, signal yard, control position, radio aerial, or signal lamp.

From the simulations, fig. 6 shows a dip value at 6.5MHz and the Monostatic RCS value has a peak at 4 MHz. From this analysis, authors used only 4MHz frequency and tested at different parts of the ship. At the bow part of ship, the Monostatic RCS is 41.5dB, for starboard it is 42dB, and for stern it is 42dB, and whereas for port 39.5dB values are obtained for the PEC material. Table I shows the comparison of simulation values achieved and observed from previous literature [8], [16], for PEC material.

From the above values it can be noted that, for PEC material, the Monostatic returns obtained in this study have good gain, when compared with the values in [8], [16]. Here, authors not only considered PEC as a material, also considered Steel as another material and carried out for analysis. Simulation shows the observed values are 42.5dBat bow, 35dB for starboard, 32dB at the stern, and 41dB at the port.

Table 1: Comparison of the RCS Values of 2 different Papers to the Simulated Values

S.No.	Position of Consideration	Simulated values from [8]	Simulated values from [16]	Measured values from [16]	Simulated Values
1	Bow	41.9	38.4	40	41.5
2	StarBoard	42.2	34.4	42	42
3	Stern	40	36.4	40	42
4	Port	NA	32.5	43	39.5

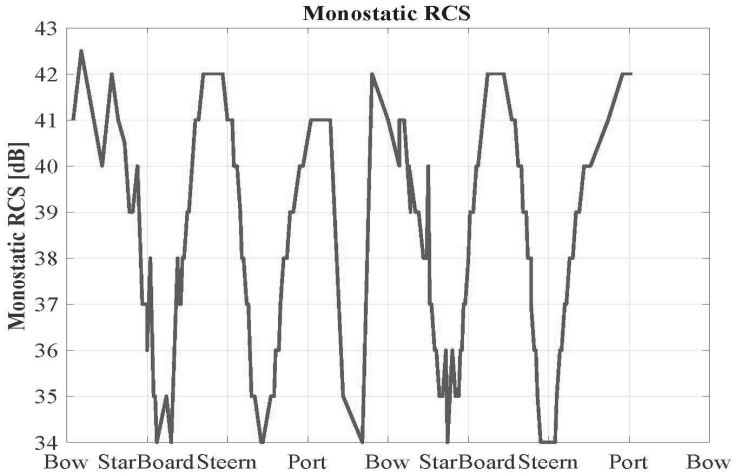

Figure 7: Monostatic RCS

Figure 7 shows Monostatic RCS values for various azimuth angles from (-180 to +180 or 0 to 360) of incident fields referred as the different parts of the ship mainly port, starboard, bow and stern.

Whereas fig. 8 shows the comparison of simulation values achieved and observed from previous literature [8], [16], shows the measured values and respective simulation values for PEC material. In fig. 8 'blue line' depicts the simulated RCS values, and 'Red Stars' shows physically measured values from [16]. The 'purple line' shows are the simulated values used by [8]. The 'yellow line' represents the RCS values obtained from simulation using ANSYS HFSS software for PEC material. The fig. 9 illustrates the comparison between PEC and steel as material with respective to various angles of incident fields.

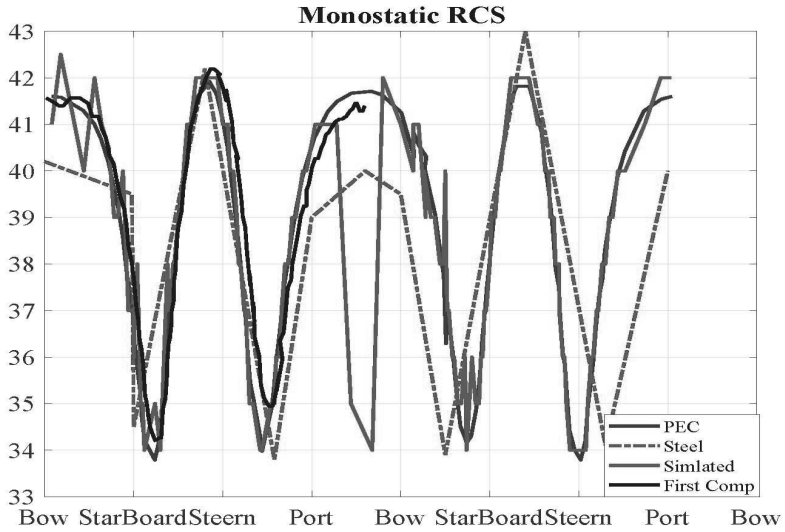

Figure 8: Comparison plot

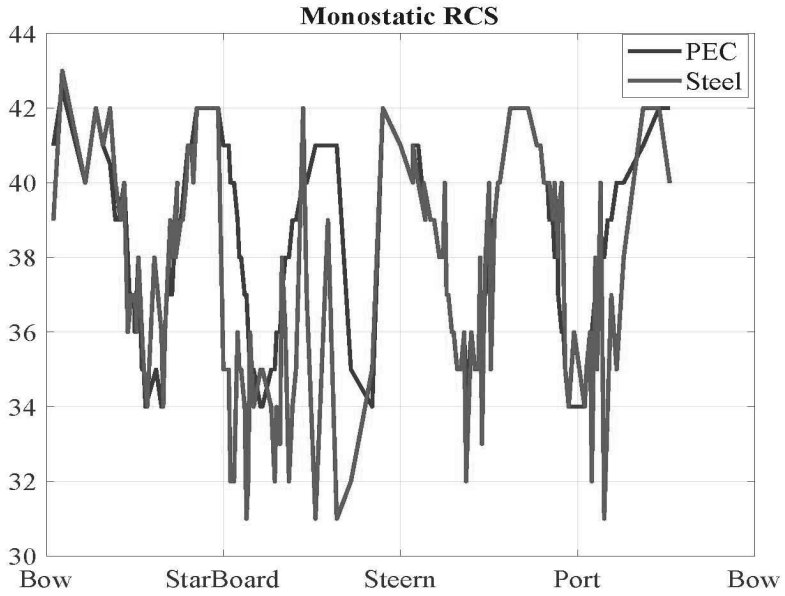

Figure 9: Steel vs PEC

5. CONCLUSION

In this paper the value of RCS of a Canadian ship "Teleost" which is modeled by PEC and steel materials is successfully predicted using HFSS and the Finite Element Method, the produced results prove to be better than the results in the existing literature. In future the effect of the environment on the value of RCS can also be studied.

ACKNOWLEDGEMENT

The authors thank the competent authorities of Defence Research and Development Laboratory (DRDL), Hyderabad for granting permission to publish this piece of work.

REFERENCES

1. G Richard Curry, Radar System Performance Modeling. Artech House, BOSTON LONDON, second edition ed., 2000.
2. M. I. Skolnik, "Introduction to radar," Radar handbook, vol. 2, p. 21, 1962.
3. MERRILL I. SKOLNIK, Radar Handbook. McGraw-Hill, Inc., second edition ed., 1992.
4. E. F. Knott, J. F. Schaeffer, and M. T. Tulley, Radar cross section. SciTech Publishing, 2004.
5. F. Paddison, C. Shipley, A. Maffett, and M. Dawson, "Radar cross section of ships," IEEE Transactions on Aerospace and Electronic Systems, no. 1, pp. 27–34, 1978.
6. D. W. Hess, "Introduction to rcs measurements," in 2008 Loughborough Antennas and Propagation Conference, pp. 37–44, 2008.
7. M. B. Heydari, M. Asgari, M. Zolfaghari, and N. Jafari, "Comparison of various full-wave softwares in calculating the rcs of simple objects," International Journal of Mechatronics, Electrical and Computer Technology (IJMEC), vol. 8, pp. 4002–4008, 2018.
8. H. Leong and H. Wilson, "An estimation and verification of vessel radar cross sections for high-frequency surface-wave radar," IEEE Antennas and Propagation Magazine, vol. 48, no. 2, pp. 11–16, 2006.
9. J. Khan, W. Duan, and S. Sherbaz, "Radar cross section prediction and reduction for naval ships," Journal of Marine science and application, vol. 11, no. 2, pp. 191–199, 2012.
10. V. D. Charris and J. M. G. Torres, "Analysis of radar cross section assessment methods and parameters affecting it for surface ships," Ciencia y tecnolog´ıa de buques, vol. 6, no. 11, pp. 91–106, 2012.
11. I. M. Jaber and H. I. Hammed, "Radar absorbing material (ram) and its effects on the radar detection range," Journal of Madenat Alelem University College, vol. 5, no. 2, pp. 6–15, 2013.
12. P. Du, Y. Shao, and J. J. Zhang, "Wideband rcs analysis of pec objects by combining fmir-mom with barycentric subdivision-based quadrature technique," in 2015 IEEE MTT-S International Microwave Workshop Series on Advanced Materials and Processes for RF and THz. Applications (IMWS-AMP), pp. 1–3, IEEE, 2015.
13. J.-T. Hwang et al., "Radar cross section analysis using physical optics and its applications to marine targets," Journal of Applied Mathematics and Physics, vol. 3, no. 02, p. 166, 2015.
14. K. Sun, B. Wen, and R. Wang, "Analysis of ship rcs detected by multifrequency hfgwr," International Journal of Antennas and Propagation, vol. 2017, 2017.
15. A. D. Singh, S. S. Ram, and S. Vishwakarma, "Simulation of the radar cross-section of dynamic human motions using virtual reality data and ray tracing," in 2018 IEEE Radar Conference (RadarConf18), pp. 1555–1560, IEEE, 2018.
16. S. K. Podilchak, H. Leong, R. Solomon, and Y. M. Antar, "Radar crosssection modeling of marine vessels in practical oceanic environments for high-frequency surface-wave radar," in 2009 IEEE Radar Conference, pp. 1–6, IEEE, 2009.

Radar Cross Section Modelling using Swerling Probability Density Function for Target Signal Strength Estimation

Raveen Kumar K[1], Sabina Esther K[2], MMV Dhanumjaya Rao[3], G Grahadurai[4]

Range Tracking Systems, RO, Satish Dhawan Space Centre,
Indian Space Research Organisation, Sriharikota, India. 524124
raveen.katakamu@shar.gov.in, sabina.k@shar.gov.in, mmvdrao@shar.gov.in, graha@shar.gov.in

ABSTRACT

SDSC SHAR, ISRO equipped with ground-based Precision Radars for tracking the launch vehicles for range safety operations and trajectory computations. The Design of Radar parameters, waveform generation and Receiver signal processing [4] always appears to be challenging owing to the wide effects it can cause on the performance of radars [3]. The radars under consideration are Tracking Radars, intended for track Launch Vehicle. It is designed for skin mode and Transponder mode operation which calls for accurate estimation of Signal strength to achieve sufficient link margin for a target complex Radar Cross Section (RCS) [6] at slant range.

In radar technology, scattering phenomenology is quantified by the target parameter RCS, σ can be modelled as random process. Probability density functions techniques are used to describe the target scattering and RCS estimation. Receiver that employs an envelope detector followed by a threshold decision technique [5]. The input to the receiver is composed of radar echo s(t) and additive zero mean white Gaussian noise n(t), with variance Ψ^2. The input noise is assumed to be spatially incoherent and uncorrelated with signal. The IF filter output is a complex random variable that is composed of either noise alone or noise plus target return signal. The noise quadrature components $n_I(t)$ and $n_Q(t)$ are uncorrelated zero mean low pass Gaussian noise with equal variance Ψ^2. The Joint Probability Density Functions of random variables is Rician PDF if target is available or Rayleigh PDF if noise alone present. Variations in radar-target geometry [8], target vibration, radar frequency, and polarization changes can lead to variations in target RCS, resulting in fluctuating targets having Swerling models [9] of target RCS fluctuation, The effect of these models on radar detection, signal strength estimation for a given radar parameters are considered.

Keywords: *Radar, RCS estimation, Probability Density Functions, Predicted Signal strength, SNR, Radar Range Equation, Swerling model, polarization etc.*

1. INTRODUCTION

The fundamental functions of radar systems are to search and track of detected targets. In all of these functions the radar performance is influenced by the strength of the signal coming into the radar receiver from the target of interest and by the strength of the signals that interfere with the target signal. In the special case of receiver thermal noise being the interfering signal, the ratio of target signal to noise power is called the signal-to-noise ratio (SNR). The ratio of the signal to the total interfering signal is the signal-to-interference ratio (SIR). Most of these interfering signals are noise-like and are therefore modelled as random processes [3]. To evaluate SIR the unknown, random, stochastic parameter is target RCS which need to be statistically estimated. The RCS is a function of target viewing angle relative to the transmitter and receiver antenna, the frequency of operation and polarization of the incident EM wave. RCS is a measure of not only how much of the incident EM wave is reflected from the target but also how much of the wave is intercepted by the target and how much is directed back toward the radar's receiver. Thus, these mechanisms interception, reflection, and directivity all interact to determine the RCS of a target. Radar Cross Section Modelling using Probability Density Functions [5] for Target Signal Strength Estimation discussed in detail in this paper. The paper describes a model which simulates and predicts the dynamic radar cross section (RCS) [6] for a moving Launch vehicle. The model simulates the Radar-Launch vehicle engagement dynamics which will affect the RCS. Consider a target (Rocket) consisting of a large number of individual scatterers as shown in Fig. 1 randomly distributed in space and each with approximately the same individual RCS.

ISBN - 978-93-95038-50-8 https://doi.org/10.37285/bsp.sasat2023.51

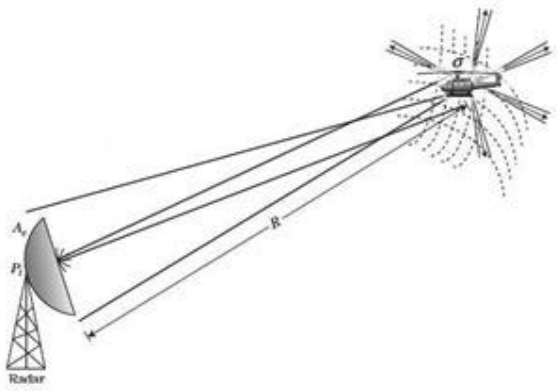

Figure 1: Radar and Rocket having multiple scatterers

The phase of the echoes from the various scatterers can then be assumed to be a random variable distributed uniformly on $(0,2\pi)$.

The radar under consideration is a Tracking Radar having specifications mentioned in the table.1, intended for track Launch Vehicle having trajectory in three-dimensional spherical coordinate system as shown in Fig.2. It is designed for skin mode and Transponder mode operation which calls for accurate estimation of Signal strength to achieve sufficient link margin for a target Complex RCS at 1000Km slant range.

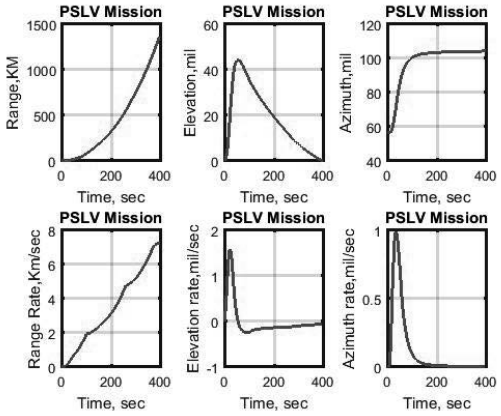

Figure 2: PSLV Mission Trajectory and its Rates

By taking into account the loses (L) involved during beam scanning, transmission, propagation and reception of radio waves. To these systems, clutter is considered to be an interfering return from a natural object such as precipitation, vegetation, soil and rocks, or the sea. The primary differences between clutter returns and receiver noise. Random noise, although varying with time. Clutter statistics can be similar to those of noise when the natural targets are composed of small, nearly equal-sized scatterers but can be quite different when the nature of the scatterers change or scatterers of differing types are present in the radar field of view. For this case, amplitude distributions having much longer “tails” than the Rayleigh distribution have been observed. Finally, although noise is independent of transmitted frequency, spatial position, and environmental parameters, clutter varies with all of these parameters, making clutter characterization very complex.

ISBN - 978-93-95038-50-8

Table 1: Radar Parameters to estimate signal strength

Radar parameter	Symbol	Value
Peak Power (KW)	P_t	1000
Frequency of Operation (MHz)	f	5660
Pulse width (nano sec)	τ	1000
Gain of Antenna (dB)	G_t, G_γ	45
Target Range (Km)	R	Based on Target Trajectory
Target Cross section (RCS)(sqm)	σ	To be estimated
Boltzmann constant(watt-sec/K)	K	1.38×10^{-23}
System Noise Temperature(K)	T	570
Receiver Bandwidth (MHz)	B	1.4
Receiver noise figure	F	3.5
Radar Losses(dB)	L_s	3

The radar beam illuminates a number of scatterers, each having a different reflectivity, σ_i, and distance, d_i, from the radar. The electric field amplitude (horizontal or vertical polarization component) measured at the radar due to the echo from the i-th scatterer will be proportional to the square root of the received power given by the radar range equation [2].

$$SNR = \frac{P_t G_t G_\gamma \lambda^2 \sigma}{(4\pi)^3 R^4 KTFBFL_s} \quad (1)$$

2. RADAR CROSS SECTION

Radar cross section [6] is a measure of power scattered in a given spatial direction when a target is illuminated by an incident wave. Another term for RCS is echo area. RCS is intended to characterize the target and not the effects of transmitter power, receiver sensitivity, and the distance or location between a target and the transmitter or receiver. Therefore, RCS is normalized to the power density of the incident wave at the target so that it does not depend on the distance from the illumination source to the target. This removes the effects of the transmitter power level and target distance. Mathematically, it is defined as 4π times the ratio of the power per unit solid angle scattered in a specified direction to the power per unit area in a plane wave incident on the scatterer from a specified direction. More precisely, it is the limit of that ratio as the distance from the scatterer to the point where the scattered power is measured approaches infinity.

$$\sigma = \underset{R\to\infty}{Lt}\ 4\pi R^2 \frac{|E^{scat}|^2}{|E^{inc}|^2} \quad (2)$$

Where E^{scat} is the scattered electric field, and E^{inc} is the field incident at the target. Three cases are distinguished: monostatic or backscatter; forward scattering; and bistatic scattering. A formal cross section may also be defined for the energy that is scattered, absorbed, or removed from the incident wave. A total cross section can also be defined that includes all of these effects. The scattered energy is of greatest practical interest because it represents the energy available for radar detection.

ISBN - 978-93-95038-50-8

The radar cross section of a target is a function of several attributes of the target like Target geometry and material composition, the radar observing the target called as aspect angle as shown in Fig.3 Transmitter and Receiver polarization, and frequency of operation.

Scattering Matrix for Linear Polarization

Radar cross section, as a scalar number, is a function of the polarization [1] of the incident and received wave. A more complete description of the interaction of the incident wave and the target is given by the polarization scattering matrix (PSM), which relates the scattered electric field vector E^{scat} to the incident field vector E^{inc}, component by component. In matrix notation, this is

$$\begin{bmatrix} E_v^{scat} \\ E_H^{scat} \end{bmatrix} = \begin{bmatrix} S_{VV} & S_{VH} \\ S_{HV} & S_{HH} \end{bmatrix} E^{inc} = \begin{bmatrix} S_{VV} & S_{VH} \\ S_{HV} & S_{HH} \end{bmatrix} \begin{bmatrix} E_v^{inc} \\ E_H^{inc} \end{bmatrix} \tag{3}$$

Scattering Matrix for Circular Polarization

In circular polarization, the electric field vector rotates in the plane perpendicular to the direction of propagation. The two orthogonal components of the electric field are called the right-handed circular [RC] and left-handed circular [LC].

Linear polarization can be transformed into circular polarization by shifting the phase of one of the two linear components by ±90 degrees. The choice between right- and left-handed circular is determined by the sign of the phase shift. Specifically, the RC and LC components of an electric field vector can be derived from the horizontal and vertical components

$$\begin{bmatrix} E_{RC}^t \\ E_{LC}^t \end{bmatrix} = \frac{1}{\sqrt{2}} \begin{bmatrix} 1 & j \\ 1 & -j \end{bmatrix} \begin{bmatrix} E_{HH}^t \\ E_{VV}^t \end{bmatrix} \tag{4}$$

The inverse transform to obtain linear polarization components from circular components is

$$\begin{bmatrix} E_{HH}^t \\ E_{VV}^t \end{bmatrix} = \frac{1}{\sqrt{2}} \begin{bmatrix} 1 & 1 \\ -j & j \end{bmatrix} \begin{bmatrix} E_{RC}^t \\ E_{LC}^t \end{bmatrix} \tag{5}$$

Received polarization can be defined in a similar manner. The LC and RC definitions change because the observer is now looking in the direction of propagation, which is from the target toward the receiver, while the radar system has defined LC and RC as viewed from the radar to the target. Therefore, with the superscript r denoting received field components

$$\begin{bmatrix} E_{RC}^\gamma \\ E_{LC}^\gamma \end{bmatrix} = \frac{1}{\sqrt{2}} \begin{bmatrix} 1 & -j \\ 1 & j \end{bmatrix} \begin{bmatrix} E_{HH}^t \\ E_{VV}^t \end{bmatrix} \tag{6}$$

which is seen to be the complex conjugate of the transmitted case. The circular polarization PSM contains no more information than the linear polarization PSM. If a linear PSM has been computed or measured, the corresponding circular PSM can be obtained by using equations.

$$\begin{bmatrix} S_{LL} & S_{LR} \\ S_{RL} & S_{RR} \end{bmatrix} = \frac{1}{\sqrt{2}} \begin{bmatrix} 1 & -j \\ 1 & j \end{bmatrix} \begin{bmatrix} S_{VV} & S_{VH} \\ S_{HV} & S_{HH} \end{bmatrix} \begin{bmatrix} 1 & 1 \\ -j & j \end{bmatrix} \tag{7}$$

Radar receiver [5] considered an envelope detector followed by threshold detection. The Input signal to the receiver is composed of radar echo signal s(t) and additive zero mean white Gaussian Noise n(t) with variance ψ^2. The input noise is assumed to be spatially

incoherent and uncorrelated with the signal. The output of the band pass IF filter is the signal v(t) and n(t).

$$v(t) = v_I(t) \cos \omega_0 t + v_Q(t) \sin \omega_0 t \tag{8}$$

In amplitude and phase form

$$v(t) = \gamma(t) \cos(\omega_o t) - \phi(t) \tag{9}$$

$\gamma(t)$ is the envelope of v(t), and phase $\phi(t)$, and $v_I(t)$, $v_0(t)$ are in phase and quadrature components as shown in Fig. 4

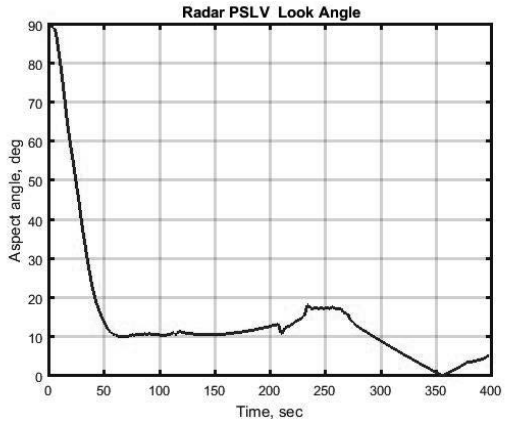

Figure 3: PSLV aspect Angle with respect to Radar

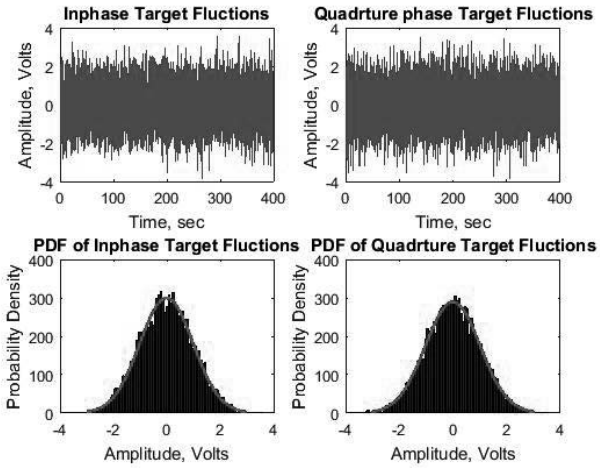

Figure 4: Receiver In & Quadrature Target Returns and Probability Density Functions

The Noise quadrature noise components $n_I(t)$, $n_0(t)$.

The Joint Probability Density Function of random variables.

$$f(n_I, n_Q) = \frac{1}{2\pi \psi^2} \exp\left(\frac{n_I^2 + n_Q^2}{2\psi^2} \right) \tag{10}$$

Signal amplitude and phase joint density PDF

$$f(\gamma, j) = \frac{1}{2\pi \psi^2} \exp\left(\frac{(r\cos j)^2 + (\gamma \sin j)^2}{2\psi^2} \right) \tag{11}$$

They are related by

$$f(\gamma,\phi) = |J|\, f(n_1, n_Q) \tag{12}$$

Where J is Jacobian [7] target Signal amplitude is given by

$$J = \begin{bmatrix} \frac{\partial n_1}{\partial \gamma} & \frac{\partial n_1}{\partial j} \\ \frac{\partial n_Q}{\partial \gamma} & \frac{\partial n_Q}{\partial j} \end{bmatrix} \begin{bmatrix} \cos\phi & \gamma \sin\phi \\ \sin\phi & \gamma \cos\phi \end{bmatrix} \tag{13}$$

The PDF of r(t) is Rician PDF if signal is present obtained by

$$f(\gamma) = \frac{\gamma}{\Psi^2} I_0\left(\frac{\gamma}{\Psi^2}\right) \exp\left(-\frac{\gamma^2}{2\Psi^2}\right) \tag{14}$$

The PDF of r(t) is Rayleigh PDF if noise is present

$$f(\gamma) = \frac{\gamma}{\Psi^2} \exp\left(-\frac{\gamma^2}{2\Psi^2}\right) \tag{15}$$

For large value of r PDF will tends to Gaussian PDF. The target locations are resembled in received signal envelope as Rayleigh and signal strength as exponential PDF as shown in Fig. 5. The use of a statistical description for radar cross section [1–3] in which the composite RCS σ of the scatterers within a single resolution cell is considered to be a random variable with a specified probability density function (PDF). The radar range equation, or RCS modelling as described in above PDF equations is used to estimate the mean RCS from received echo power measurements, and one of a variety of standard PDFs is used to describe the statistical variations of the RCS. Combined with the uncertainty of aspect angle, particularly before a target is detected, it is much more practical to use a statistical model as a simple way to capture the complexity of the target RCS. Rayleigh/exponential model is strictly accurate only in the limit of a very large number of scatterers, in practice it can be a good model for a target having as few as 10 or 20 significant scatterers. Fig.5 compares a histogram of the RCS.

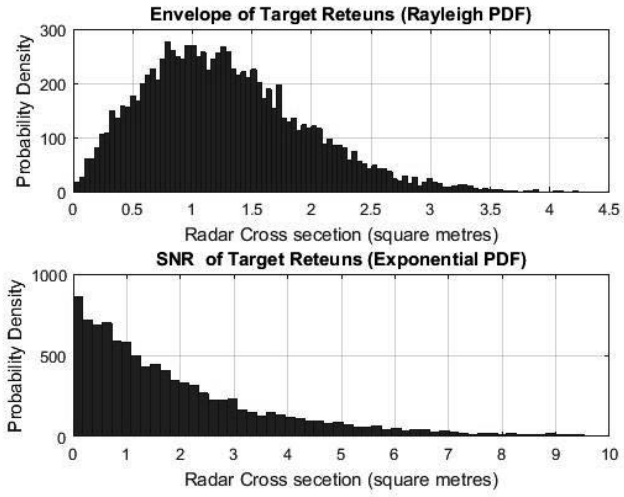

Figure 5: Envelope of Radar Detector and SNR PDFs

RCS is modelled with considering polarisation, frequency operation, aspect angle, Target dimensions, scan to scan fluctuation of Launch vehicle. Furthermore, received power at the radar (target echo only, not including noise or other interference) is proportional to target RCS as seen in the radar range equation. Thus, RCS fluctuations shown in Fig.6 result in received target power fluctuations.

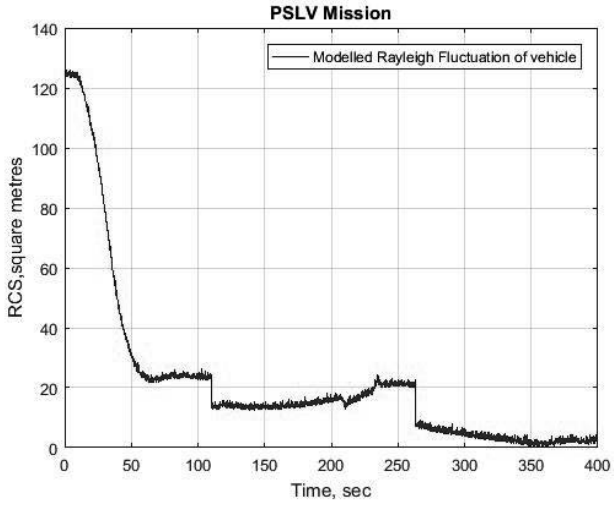

Figure 6: Modelled Radar Cross Section

After sizing of the Radar and Estimation of RCS (as modelled as random process) the signal strength as shown Fig. 7 is estimated for Radar for a given mission.

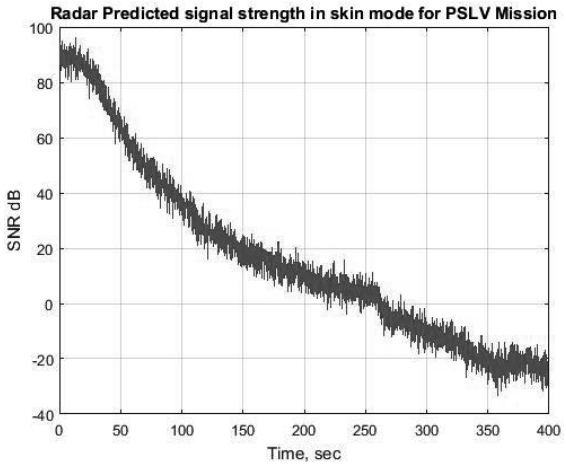

Figure 7: Estimated signal strength for Radar

3. CONCLUSIONS

The goal of this paper prior prediction of signal strength for Radar sizing. In the Radar Range Equation by modelling unknown Target RCS using swerling models with Rayleigh and Rician PDFs. The RCS evaluation of Launch vehicle by considering shape of launch vehicle in each stage, by considering input trajectory, Aspect angle of target. The Simulated Signal strength model is verified with real time trajectory the predicted signal strength by estimating RCS is matched with received signal strength in Real time.

ISBN - 978-93-95038-50-8

ACKNOWLEDGEMENT

The authors wish to thank Sri Rajarajan A, Director, SDSC SHAR for granting permission to publish this work. Authors acknowledge the Range Tracking Systems Group, Range Operations Entity of SDSC SHAR Sriharikota.

REFERENCES

1. Mott, H., Polarization in Antennas and Radar, Wiley, New York, 2012.
2. Blake, L.V., Radar Range-Performance Analysis, Artech House, Dedham, MA, 2009.
3. Barton, D.K., Radar System Analysis, Artech House, Dedham MA.
4. Skolnik, M.I., Introduction to Radar Systems, 3d ed., McGraw Hill, New York
5. Richards, M.A., Fundamentals of Radar Signal Processing, McGraw-Hill, New York
6. Knott, E.F., Shaeffer, J.F., and Tuley, M.T., Radar Cross Section, 2d ed., SciTech Publishing
7. Shnidman, D.A., "Calculation of Probability of Detection for Log-Normal Target Fluctuations," IEEE Transactions on Aerospace and Electronic Systems, vol. AES-27, no. 1, pp. 172– 174, January 1991
8. Shnidman, D.A., "Update on Radar Detection Probabilities and Their Calculation," IEEE Transactions on Aerospace and Electronic Systems, vol. AES-44, no. 1, pp. 380–383, January 2008.
9. Shnidman, D.A., "Calculation of Probability of Detection for Log-Normal Target Fluctuations," IEEE Transactions on Aerospace and Electronic Systems, vol. AES-27, no. 1, pp. 172– 174, 2011

Simulation of DSTATCOM for Distribution Generation based System with Various Algorithms

K. Bhavya[1], P.V.V. Rama Rao[2], L. Ravi Srinivas[3]

[1]Research Scholar, Assistant Professor, BVRIT HYDERABAD College of Engineering for Women, Hyderabad-500090
[2] Professor, Department of Electrical & Electronics Engineering, Maturi Venkata Subba Rao (M.V.S.R) Engineering College, Hyderabad
[3]Professor, Department of Electrical & Electronics Engineering, Gudlavalleru Engineering College, Gudlavalleru.
Email: [1]bhavya.k@bvrithyderabad.edu.in, [2]drramaraopvv@gmail.com, [3]lrsrinivas@gmail.com

ABSTRACT

The growth in protection devices in the field of power systems has been rising from the preceding years which enlarge life span of the power system. This paper aims at designing of various types of Custom Power Device (CPDs) for stabilizing the system under abnormal conditions like sudden switching of loads. One of the Custom Power Device Namely Distribution Static Compensator (DSTATCOM) has been proposed for dealing with various power quality issues. This work involves design of feedback control strategy with different algorithms like BAT algorithm and ANT colony optimization algorithm for controlling the parameters at the grid side and also at the load side. The three-phase grid connected system has been tested with various conditions with sudden occurrence of fault and also with sudden switching of various loads. The assessment of performance of algorithms has been verified for various parameters like PCC voltage, current, active power, reactive power and power factor. The proposed system is simulated using MATLAB and results are also analyzed.

Keywords: *Distribution Static Compensator (DSTATCOM), Custom Power Device (CPD), ANT Colony Algorithm, BAT Algorithm*

1. INTRODUCTION

The power demand is higher when compared to expansion of transmission system which is limited to certain capacity and so the electrical stresses will be larger which leads to different power quality issues like voltage sag, swell, interruptions, harmonics and oscillation in the system [1]. It also results in imbalance in the reactive power which has to be mitigated to avoid instability at the system side. So, it is required to control the reactive power along with the controlling of power flow through the transmission lines. This can be achieved with the usage of controller's through modern power electronic devices.

One of the modern technologies is flexible AC transmission system (FACTS) devices which are implemented for mitigating the various power quality issues. The FACTS are basically classified into three configurations- shunt devices, series devices and shunt-series devices. A type of shunt compensator has been designed in the proposed work to observe the performance of FACTS devices. The FACTS device requires the controlling of the gate signals of the inverter there by controlling the voltage, power flow through the line and so for controlling purpose, feedback controller is required.

The PID controller can be used for controlling the source and load parameters, but the disadvantage with the conventional PID controller is low dynamic performance and also involves oscillations at the output. The intelligent fuzzy [6] controller can be used which involves the design of membership functions and also framing of rules for the membership functions, but sometimes requires higher number of membership functions which leads to [7] complexity of the system. Neural network with back propagation algorithm can be designed

Corresponding author: E-mail: [1]bhavya.k@bvrithyderabad.edu.in

ISBN - 978-93-95038-50-8 https://doi.org/10.37285/bsp.sasat2023.52

with certain layers of input, output and hidden neurons, adjusting weights [8] to attain minimum error, but the disadvantage with the neural network is slow convergence rate. Genetic algorithm which works on the principle of natural evaluation can be applied for optimization problems but suffers with the problems of parameter tuning, [14-16] because of complicated cross over and mutation operators and also speed of convergence. So to overcome the above discussed disadvantages, ANT and BAT algorithm has been proposed which controls the source and also load side parameters.

The paper is organized as follows: Section I presents Introduction to the proposed system, Section II deals with the explanation of block diagram of proposed system with CPDs. Section III deals with the discussion of ANT algorithm Section IV deals with the software implementation and discussion of results. Section V deals with the conclusions drawn from the proposed work.

2. BLOCK DIAGRAM OF CUSTOM POWER DEVICES BASED DISTRIBUTION SYSTEM

The block diagram for the grid connected distribution system with CPDs has been revealed in below figure. It consists of three phase system with source [1-2] and load which are always connected and also consists of various loads like synchronous generator-based wind mill and induction generator-based wind mill which are connected and disconnected at various times. The Custom Power Devices namely DSTATCOM consisting of voltage source inverter connected in shunt with the system through shunt transformer. When an abnormal condition like occurrence of fault or sudden connection of load happens, there will be imbalance of voltage, current and also power. So, at that time, the algorithm-based controller operates generating error which will be fed for gate pulse generation for the CPD controller. Then Custom power Device will inject or absorb the power based up on the requirement there by controlling the parameters at Point of Common Coupling (PCC).

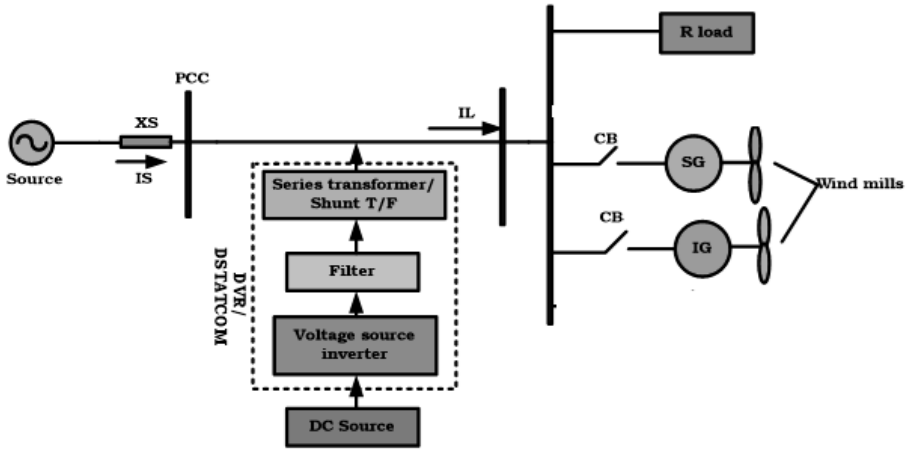

Figure 1: Block diagram of grid connected distribution system with CPDs

2.1. DISTRIBUTION STATIC COMPENSATOR (DSTATCOM)

The DSTATCOM is a custom power device which generates [2] three phase synchronous voltage with the supply voltages by means of DC source in combination with inverter by compensating reactive power also. In general, the voltage generated by the compensator will be always in phase with the line voltages, with no exchange of active power but there will be

exchange of reactive power in this case with the variation of amplitude of voltages. The compensator will always be connected in parallel with the line through the shunt transformer. Depending up on the amplitude of voltages, three conditions can be realized with the DSTATCOM.

Case 1: If the line voltage is less than the shunt voltage, the current of DSTATCOM leads the line voltage by 900, and then leading reactive power flows from the DSTATCOM.

Case 2: If the line voltage is more than the shunt voltage, the current of DSTATCOM lags the line voltage by 90^0, and then lagging reactive power flows from the DSTATCOM.

Case 3: If the line voltage is equal to the shunt voltage, then no reactive power flows from the DSTATCOM.

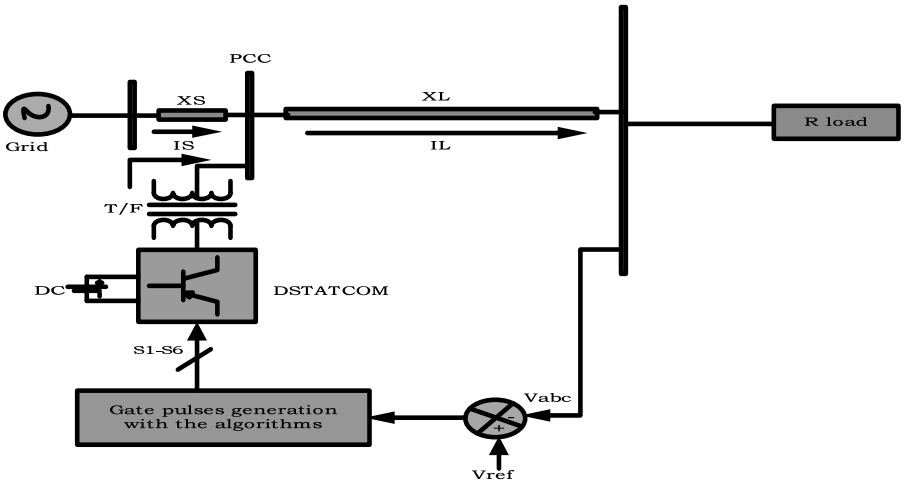

Figure 2: one-line diagram of power system with DSTATCOM

3. SOFTWARE REALIZATION OF DSTATCOM

The software implementation of the DG system with DSTATCOM has been implemented with various test cases like switching on of loads. Also, two algorithms namely ANT Colony optimization algorithm, BAT algorithm.

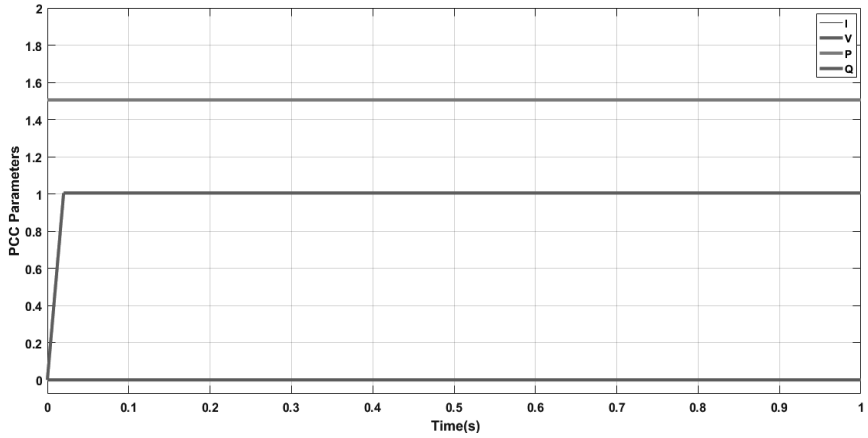

Figure 3: PCC Parameters of power system

The below table shows the rated parameters of the power system

Table 1: PCC Parameters of power system

Parameter	Rated values
Voltage	1pu
Current	1pu
Active power	1.5pu
Reactive power	0pu
Power factor	1pu

- **With fault condition in the power system**

The LLL fault has been created in the system at t=0.1s to t=0.65s and various algorithms have been tested for dynamic voltage restorer.

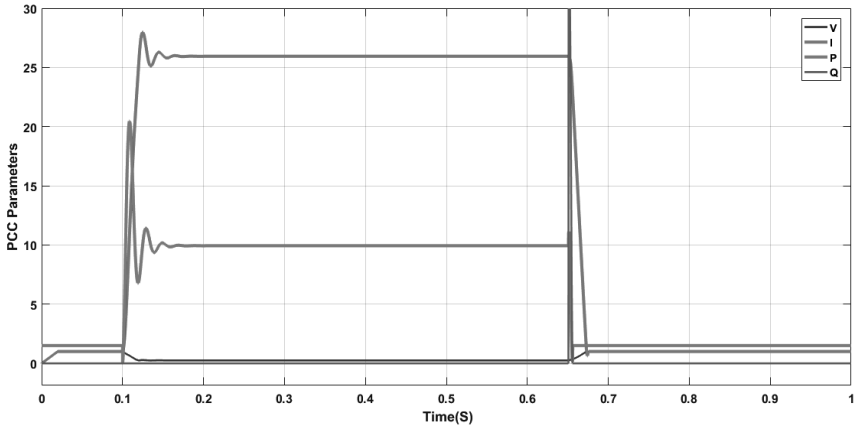

Figure 4 : PCC Parameters of power system under faulted condition

- ***DSTATCOM***

The power system has been simulated with grid at source side and load at the end side and the below waveform shows the PCC parameters at rated values.

The voltage has been almost remained constant, current has been maintained at 7.7times the rated value, active power has been maintained at 4times the rated value and reactive power is almost zero.

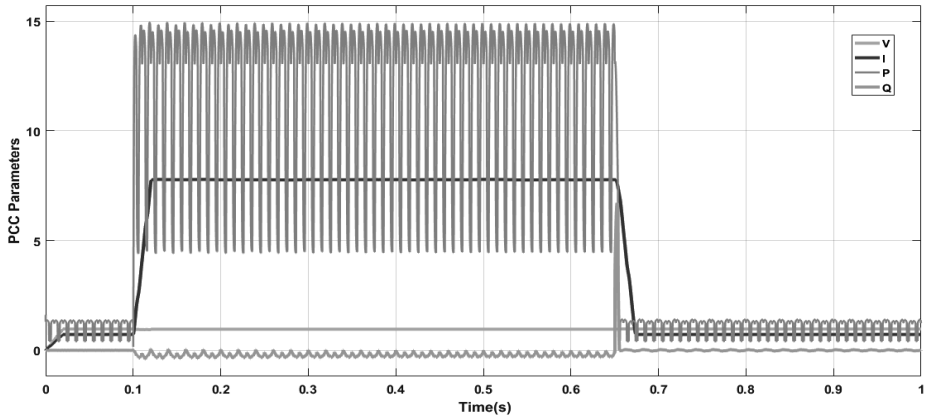

Figure 5 : PCC Parameters of power system under fault condition with DSTATCOM

Table 2: PCC Parameters with DSTATCOM using BAT, ANT algorithms

Parameter	Without CPDs	With CPD	
		BAT Algorithm	ANT Colony Algorithm
Voltage	0.998pu	0.96pu	0.6pu
Current	1.018pu	7.78pu	4.9pu
Active power	1.526pu	15pu	5.1pu
Reactive power	0.0001pu	0.0037pu	0.0037pu
Power factor	0.999pu	0.946pu	0.99pu

- ***With wind-based induction generator***

The wind turbine-based induction generator has been connected to the system at t=0.1s to t=0.65s and various algorithms have been tested for distribution static compensator.

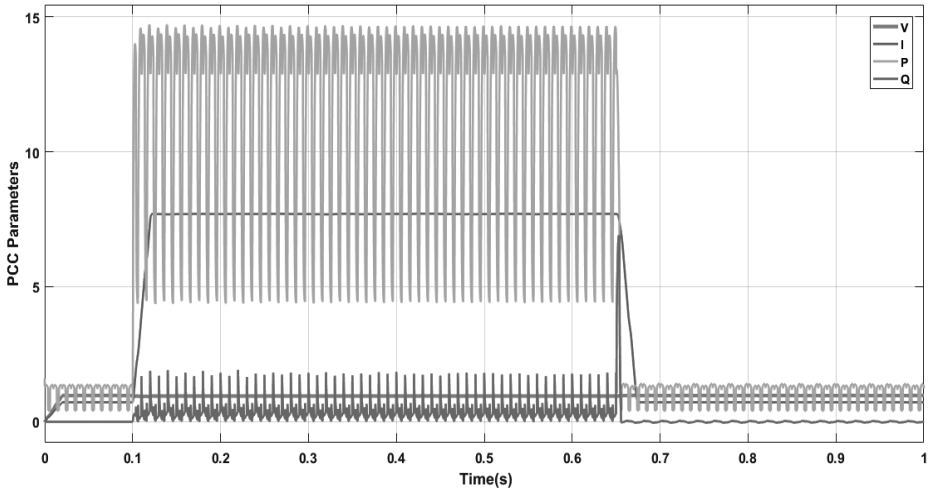

Figure 6: PCC Parameters of power system with induction generator with DSTATCOM

Table 3: PCC Parameters with induction generator, DSTATCOM, BAT, ANT algorithms

Parameter	Without CPDs	With CPDs	
		BAT Algorithm	ANT Colony Algorithm
Voltage	0.998pu	0.953pu	0.6pu
Current	1.018pu	7.7pu	3.5pu
Active power	1.526pu	14.6pu	5.9pu
Reactive power	0.0001pu	2pu	1.1pu
Power factor	0.999pu	0.95pu	0.95pu

- ***With wind based Synchronous generator***

The wind turbine based synchronous generator has been connected to the system at t=0.1s to t=0.65s and various algorithms have been tested for distribution static compensator.

ISBN - 978-93-95038-50-8

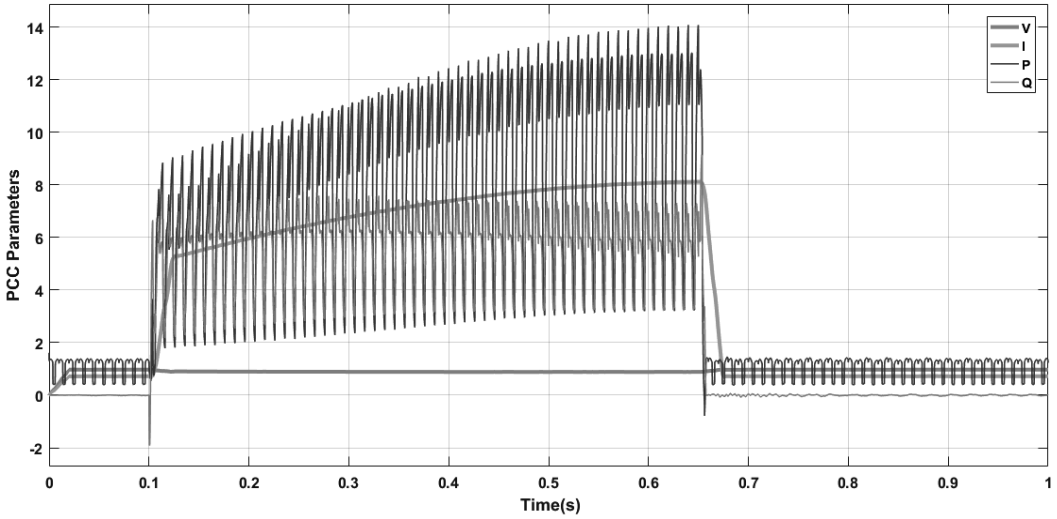

Figure 7: PCC Parameters of power system with synchronous generator with DSTATCOM

Table 4: PCC Parameters with synchronous generator, DSTATCOM BAT, ANT algorithms

Parameter	Without CPDs	With CPDs	
		BAT Algorithm	ANT Colony Algorithm
Voltage	0.998pu	0.89pu	0.59pu
Current	1.018pu	5.2pu	2.7pu
Active power	1.526pu	8.5pu	1.8pu
Reactive power	0.0001pu	7.1pu	3pu
Power factor	0.999pu	0.6pu	0.38pu

The DSTATCOM, DVR have been tested with three algorithms namely Weighted feedback, BAT, ANT algorithms for various conditions like fault occurrence, switching of synchronous generator, switching of induction generator, switching of RLC load where at every case DVR shows the better performance with weighted feedback algorithm than DSTATCOM with comparison of remaining two algorithms.

4.CONCLUSION

The Custom Power Devices Distribution Static Compensator has been proposed for dealing with various power quality issues in this paper. The design BAT algorithm and ANT colony optimization algorithm for controlling the parameters at the grid side and also at the load side have been proposed in this paper. The three-phase grid connected system has been tested with various conditions with sudden switching of various loads and the assessment of performance of algorithms has been verified in terms of various parameters like PCC voltage, current, active power, reactive power and power factor where the control strategy with ANT Colony Algorithm shows the better performance than the BAT algorithm. The entire system has been simulated using MATLAB/Simulink and also analysis of the results has been performed.

ISBN - 978-93-95038-50-8

REFERENCES

1. M. P. F. Asna and M. V. Manoj kumar, "DSTATCOM for Distribution System Having High PV Penetration," 2019 International Conference on Power Electronics Applications and Technology in Present Energy Scenario (PETPES), Mangalore, India, 2019, pp. 1-5, doi: 10.1109/PETPES47060.2019.9003912.
2. A. R. Gidd, A. D. Gore, S. B. Jondhale, O. V. Kadekar and M. P. Thakre, "Modeling, Analysis and Performance of a DSTATCOM for Voltage Sag Mitigation in Distribution Network," 2019 3rd International Conference on Trends in Electronics and Informatics (ICOEI), Tirunelveli, India, 2019, pp. 366-371, doi: 10.1109/ICOEI.2019.8862554.
3. M. Thirupathaiah, V. Ganesh and P. V. Prasad, "Enhancement of power quality in wind power distribution system using DVR and DSTATCOM based agent system," 2017 Innovations in Power and Advanced Computing Technologies (i-PACT), Vellore, 2017, pp. 1-9, doi: 10.1109/IPACT.2017.8244936.
4. A. Chorghade and V. A. Kulkarni Deodhar, "FACTS Devices for Reactive Power Compensation and Power Flow Control – Recent Trends," 2020 International Conference on Industry 4.0 Technology (I4Tech), Pune, India, 2020, pp. 217-221, doi: 10.1109/I4Tech48345.2020.9102640.
5. M. V. k. Reddy and T. Nireekshana, "Enhancement of Available Transfer Capability using FACTS Devices," 2019 International Conference on Intelligent Computing and Control Systems (ICCS), Madurai, India, 2019, pp. 869-874, doi: 10.1109/ICCS45141.2019.9065504.
6. G. R. Kumar, A. Rohith, G. Priyanka and G. Vamsipriya, "Multi-objective optimal economic emission power dispatch using Bat algorithm," 2017 Innovations in Power and Advanced Computing Technologies (i-PACT), Vellore, 2017, pp. 1-5, doi: 10.1109/IPACT.2017.8245076.
7. K. Loubna, B. Bachir and Z. Izeddine, "Optimal digital IIR filter design using ant colony optimization," 2018 4th International Conference on Optimization and Applications (ICOA), Mohammedia, 2018, pp. 1-5, doi: 10.1109/ICOA.2018.8370500.
8. L. Kritele, B. Benhala and I. Zorkani, "Ant Colony Optimization for Optimal Analog Filter Sizing," in Focus on Swarm Intelligence Research and Applications, Nova Science Publishers, pp. 193-220, 2017.
9. D. Chandra Sekhar, P.V. V Rama Rao, V. Ganesh, Weight Feedback Adaptive Multi Objective Cooperative Scheduling In Smart Grid Application, International Journal Of Recent Technology And Engineering (Ijrte) , Vol. 8 No.2, Pp.607-611,July 2019.
10. V. N. Kumar, M. Patowary, G. Panda and S. K. Prince, "Solar Plant Integration to Utility Grid with Improved Power Quality by using RNN-Hebbian-LMS Current Controller," 2018 IEEE Innovative Smart Grid Technologies - Asia (ISGT Asia), Singapore, 2018, pp. 546-551, doi: 10.1109/ISGT-Asia.2018.8467981.
11. A. Behuria, B. P. Mishra, P. Goel, A. Kar, S. Mohapatra and M. Chandra, "A novel variable step-size feedback Filtered-X LMS algorithm for acoustic noise removal," 2015 International Conference on Advances in Computing, Communications and Informatics (ICACCI), Kochi, 2015, pp. 166-171, doi: 10.1109/ICACCI.2015.7275603.
12. Asutosh Kar, Ambika Prasad Chanda, Sarthak Mohapatra and Mahesh Chandra, "An Improved Filtered-x Least Mean Square Algorithm for Acoustic Noise Suppression" in , Germany: Springer-Verlag, vol. 1, pp. 25-32, 2014.
13. A. Mohammadi, H. Asadi, S. Mohamed, K. Nelson and S. Nahavandi, "Multi objective and Interactive Genetic Algorithms for Weight Tuning of a Model Predictive Control-Based Motion Cueing Algorithm," in IEEE Transactions on Cybernetics, vol. 49, no. 9, pp. 3471-3481, Sept. 2019, doi: 10.1109/TCYB.2018.2845661.
14. X. Sun, C. Hu, G. Lei, Y. Guo and J. Zhu, "State Feedback Control for a PM Hub Motor Based on Gray Wolf Optimization Algorithm," in IEEE Transactions on Power Electronics, vol. 35, no. 1, pp. 1136-1146, Jan. 2020, doi: 10.1109/TPEL.2019.2923726.
15. M. S. Aslam, P. Shi and C. Lim, "Robust Active Noise Control Design by Optimal Weighted Least Squares Approach," in IEEE Transactions on Circuits and Systems I: Regular Papers, vol. 66, no. 10, pp. 3955-3967, Oct. 2019, doi: 10.1109/TCSI.2019.2910290.
16. S. Zhang and X. Zhao, "Distributed Power Allocation Based on LQG Regulator With Adaptive Weight and Switching Scheme for Cognitive Radio Networks," in IEEE Access, vol. 6, pp. 39180-39196, 2018, doi: 10.1109/ACCESS.2018.2856511.

Optimal Placement and Sizing of DSTATCOM in Radial Distribution System Using Gravitational Search Algorithm

U. Chandra Rao[1], Rama Rao PVV[2], and N Sumathi[3]

[1,3]Department of Electrical & Electronics Engineering, JNT University, Kakinada, A.P.- 533 003
[2]Department of Electrical & Electronics Engineering, MVSR Engineering College, Telangana. - 501510

ABSTRACT

In order to reduce power losses and improve the voltage profile of the Radial Distribution network, a Gravitational Search Algorithm (GSA) is described in this work. A backward forward load flow algorithm is taken as a base case and Loss Sensitivity Factors (LSF) are used for identifying the candidate buses for D-STATCOM placement whereas the optical allocation and sizing of D-STATCOM is done by using GSA. The proposed work has been evaluated using the industry-standard IEEE 33-Bus Radial Distribution Test network. The acquired results have been compared with the results obtained in Base Case, Genetic Approach (GA), Immune Algorithm (IA), Harmony Search Algorithm (HSA), Power Loss Index (PLI) technique, and Differential Evaluation Algorithm in order to verify the usefulness of the proposed algorithm (DEA). MATLAB software was used to run the simulation.

Keywords: Distribution STATIC Compensator (D-STATCOM), Gravitational Search Algorithm (GSA), Loss Sensitivity Factors, Optimal Allocation, Optimal Size, Power Loss Minimization, Radial Distribution System.

1. NOMENCLATURE

P_i, Q_i	Real and Reactive Powers at i^{th} bus
P_{Li}, Q_{Li}	Real and Reactive Load Powers at i^{th} bus
P_{Li+1}, Q_{Li+1}	Real and Reactive Load Powers at $(i+1)^{th}$ bus
P_{i+1}, Q_{i+1}	Real and Reactive Powers flow beyond $(i+1)^{th}$ bus
Z_j, Z_j'	Impedances of j^{th}branch/line before and after placing D-STATCOM
r_j, r_j'	Resistances of j^{th}branch/line before and after placing D-STATCOM
x_j, x_j'	Reactance of j^{th}branch/line before and after placing D-STATCOM
I_j	Current flow in j^{th}branch/line
V_i, V_{i+1}	Voltage magnitudes at the buses $i, i+1$ before placing D-STATCOM
V_i', V_{i+1}'	Voltage magnitudes at the buses $i, i+1$ after D-STATCOM Placement
θ_j	Phase angle of the current flow in j^{th}branch/line
δ_i, δ_{i+1}	Phase angles at the buses $i, i+1$ before placing D-STATCOM
δ_i', δ_{i+1}'	Phase angles at the buses $i, i+1$ after D-STATCOM Placement
$P_{T,Loss}$	Total Real Power Losses before placing D-STATCOM
$P_{T,Loss}^{with\ D-STAT}$ or $P_{D-STAT,TLoss}$	Total Active Power Losses after D-STATCOM installation.
$Q_{T,Loss}$	Total Reactive Power Losses before placing D-STATCOM
$Q_{loss(j)}$	Reactive power loss in j^{th}branch/line
$LSF_{(j)}$	Loss Sensitivity Factor (w.r.to. Reactive power) of j^{th}branch/line for D-STATCOM placement
I_{D-STAT}	D-STATCOM current

ISBN - 978-93-95038-50-8 https://doi.org/10.37285/bsp.sasat2023.53

$\frac{\pi}{2} + \delta'_{i+1}$	Phase angle of D-STATCOM current
V_{min}, V_{max}	Minimum and maximum voltage constraints for all buses
Q_{D-STAT}	Reactive power injected by D-STATCOM

2. INTRODUCTION

Now a day, a noteworthy ruin is faced by the distribution power system. When buses are moved far from the substation in distribution systems, the voltage at the buses decreases and there are significant losses. The lack of reactive power across the distribution network is the cause of the voltage reduction and excessive losses. The requirement of sufficient reactive power support to the appropriate locations is the most well-known method for improving power factor, voltage profile, and reducing line losses in distribution power systems. Increasing network losses and poor voltage regulation are caused by the expanding and complicated nature of electric distribution systems. According to studies, I^2R losses at the distribution level account for roughly 10 to 13% of the total power generated [1]. Deregulation worsens issues with the Radial Distribution System's power quality, including voltage swings, distortion, imbalance, sag, and insecurity (RDS). The aforementioned power quality issues prompt increment in power losses, response time is additionally decreased and furthermore influence power flow limits are reduced. Therefore, power system engineers should provide consumers with high-quality energy that has fewer power losses [2]. Shunt capacitors and series voltage regulators are the two common techniques for maintaining the distribution system's voltages within acceptable bounds. In any case, due to their step-by-step functioning, conventional series voltage regulators have a few disadvantages, including the inability to provide reactive power and relatively moderate reaction times [3-5]. When employed in a similar circuit with inductive components, shunt capacitors have the tendency to oscillate and are limited in their ability to create reactive power that is continually changing [6].

Several controllers have been used for effective series and shunt compensation. As a result of enhancements in the voltage and current handling capabilities of power electronic equipment that has taken into account the development of Flexible AC Transmission Systems (FACTS). It should be noted that FACTS devices respond quickly to changes in the state of the network. FACTS devices were first developed for transmission systems, but a similar concept known as D-FACTS devices or Custom Power Devices (CPDs) has started to be used in distribution systems [7-8]. Unbalanced loads, voltage sag, voltage swings, and voltage imbalance are some examples of power quality issues that can be resolved with a converter for shunt-linked voltage supplies called D-STATCOM. Over traditional reactive energy compensation devices, D-STATCOM offers a number of benefits, including low power losses, reduced harmonic output, high levels of regulatory functionality, low cost, and small size [9–14].

3. LITERATURE SURVEY

Few scholars, who have concentrated on the study of D-STATCOM placement and sizing in RDS, have created and deployed a number of algorithms for power loss mitigation and voltage augmentation in the distribution system. Authors *Mehdi Hosseini et.al.* proposed an analytical method for finding best location of DVR and D-STATCOM and concluded that D-STATCOM performance is superior than DVR in view of enhancing the voltage profile and power loss reduction but its size is comparatively high [7]. *Joseph Sanam et. al.* proposed an Exhaustive Search Method to minimize the power loss in IEEE 30-bus system by placing D-

STATCOM at 5th bus [15]. Researchers *Seyed Abbas Taher and Seyed Ahmadreza Afsari* was developed Immune Algorithm (IA) and concluded that the IA is more effective than Genetic Algorithm (GA) [16]. Authors *Yuvaraj.T et.al.* presented Bat Algorithm (BA) for D-STATCOMs allocation and sizing in RDS and said that BA converges quickly than IA [2]. Differential Evaluation Algorithm (DEA) was devised by Joseph Sanam et al. to reduce installation costs and energy loss costs while also improving voltage magnitudes [17]. Power Loss Index (PLI) Method was introduced by Atma Ram Gupta et al. to determine the ideal position for UPQC and DSTATCOM in RDS [8]. An analytical method for determining the ideal location and size of DSTATCOM was proposed by authors S M Suhail Hussain et al. They discovered that the method is efficient and simple to use [18]. Researchers Joseph Sanam et al. created a mathematical model of DSTATCOM and integrated it into backward forward load flow to account for reactive power [15]. The best location and size of D-STATCOM can be found by calculating the voltage stability index in RDS under various load scenarios, claim authors Abhinav Jain et al [19]. *T. Yuvaraj et. al.* proposed Harmony Search Algorithm under light load condition and Bat Algorithms for DSTATCOM allocation and sizing in RDS by considering light load, medium load and peak load conditions [20,21]. *K Subbarami Reddy et. al.* proposed Penguins Search Optimization Algorithm for optimal placement and sizing of DSTATCOM [22].

This paper organized as the Section I discuss the Nomenclature, introduction in section II and Literature Survey given in section III, section IV depicts problem formulation and Mathematical modelling of D-STATCOM is presented in Section V. While section VII discusses the simulation findings of the proposed work, section VI provides specifics about the gravitational search algorithm. Finally, section VIII has the conclusion.

4. PROBLEM FORMULATION

A. Power Flow Analysis [25]

The simple 2-bus Radial Distribution System (RDS) is shown in Figure 1.

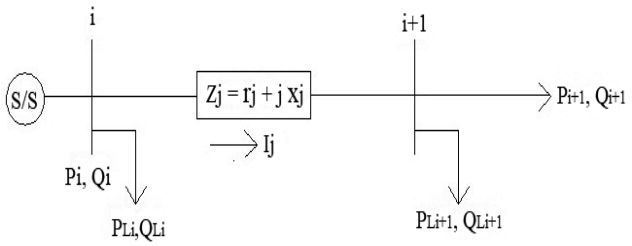

Figure 1: Single line diagram of a simple 2-Bus Radial Distribution System

The active (*Pi*) and reactive (*Qi*) powers that flows through branch 'j' are given as,

$$P_i = P_{i+1}^1 + r_j \frac{(P_{i+1}^{1\ 2} + Q_{i+1}^{1\ 2})}{V_{i+1}^2} \quad (1)$$

$$Q_i = Q_{i+1}^1 + x_j \frac{(P_{i+1}^{1\ 2} + Q_{i+1}^{1\ 2})}{V_{i+1}^2} \quad (2)$$

Where, $P_{i+1}^1 = P_{i+1} + P_{Li+1}$ and $Q_{i+1}^1 = Q_{i+1} + Q_{Li+1}$

The current measured within the branch "j" is represented as

$$I_j = \frac{V_i \angle \delta_i - V_{i+1} \angle \delta_{i+1}}{r_j + jX_j} \qquad \text{Also } I_j = \frac{P_i - j\,Q_i}{V_i \angle -\delta_i} \quad (3)$$

From Equation (3) the voltage magnitude at bus i and i+1 can be derived as

$$V_i = \left[V_{i+1}^2 + 2\left(\mathrm{P_i r_j} + \mathrm{Q_i x_j}\right) - (r_i^2 + Q_i^2)\ \frac{(P_i^2 + Q_i^2)}{V_i^2}\right]^{1/2} \quad (4)$$

$$V_{i+1} = \left[V_i^2 - 2\left(\mathrm{P_i r_j} + \mathrm{Q_i x_j}\right) + (r_i^2 + Q_i^2)\ \frac{(P_i^2 + Q_i^2)}{V_i^2}\right]^{1/2} \quad (5)$$

The phase angle at bus I and i+1 can be calculated similarly as

$$\delta_i = \delta_{i+1} - \tan^{-1}\left[\frac{(\mathrm{Q_i r_j} - \mathrm{P_i x_j})}{V_i^2 - (\mathrm{P_i r_j} + \mathrm{Q_i x_j})}\right] \quad (6)$$

$$\delta_{i+1} = \delta_i + \tan^{-1}\left[\frac{(\mathrm{Q_i r_j} - \mathrm{P_i x_j})}{V_i^2 - (\mathrm{P_i r_j} + \mathrm{Q_i x_j})}\right] \quad (7)$$

Calculated are line "j's" active and reactive power losses. using the formula

$$P_{loss(j)} = r_j\left[\frac{(P_i^2 + Q_i^2)}{V_i^2}\right] \quad (8)$$

$$\mathrm{Q_{loss(j)}} = \mathrm{x_j}\left[\frac{(\mathrm{P_i^2} + \mathrm{Q_i^2})}{\mathrm{V_i^2}}\right] \quad (9)$$

The total active and reactive power losses in the radial distribution system can be calculated using the following calculations (TAPL & TRPL)

TAPL

$$P_{T,Loss} = \sum_{j=1}^{Nb} r_j I_j^2 = \sum_{j=1}^{Nb} P_{loss(j)} = \sum_{j=1}^{Nb} P_{loss}(i, i+1) \quad (10)$$

TRPL

$$\mathrm{Q_{T,Loss}} = \sum_{j=1}^{Nb} x_j I_j^2 = \sum_{j=1}^{Nb} Q_{loss(j)} = \sum_{j=1}^{Nb} Q_{loss}(i, i+1) \quad (11)$$

Where, Nb represents the quantity of the branches.

B. Power Loss Calculation using D-STATCOM (D-STAT)

Following the installation of D-STATCOM in the distribution system, it is possible to calculate the active power losses through line 'j' in Fig. 1.

$$P_{D-STAT,loss(j)} = r_j\left[\frac{\left(P_{D-STAT_{(i)}^2} + Q_{D-STAT_{(i)}^2}\right)}{V_i^2}\right] \quad (12)$$

The radial distribution system's total active power losses (TAPL) can be computed as

$$P_{D-STAT,\ TLoss} = \sum_{j=1}^{Nb} P_{D-STAT,loss(j)} = \sum_{j=1}^{Nb} P_{D-STAT,loss}\ (i, i+1) \quad (13)$$

C. Loss Sensitivity Factors (LSFs)

By taking into account the first derivative of Q loss(j) in equation (9), which is related to the reactive power load Q (i, i+1), it is possible to determine the candidate bus for D-STATCOM deployment.

$$LSF_{(j)} = \frac{\partial Q_{loss(j)}}{\partial Q_{i,i+1}} \Rightarrow \frac{\partial Q_{loss(j)}}{\partial Q_j} = x_j \frac{2Q_i}{V_i^2} \quad (14)$$

The LSFs are obtained from the load flow in the base scenario (before compensation).

D. Objective Function

The suggested work's Objective Function (F) is provided by

$$Minimize\ (F) = min\ (P_{D-STAT,TLoss}) \quad (15)$$

The limitations on equality and inequality taken into account in this work include voltage constraints

$$V_{min} \leq |V_i| \leq V_{max} \qquad \text{i.e., } 0.95 \leq V_i \leq 1.05 \tag{16}$$

Reactive Power Constraint

$$Q_{D-STAT}^{min} \leq Q_{D-STAT} \leq Q_{D-STAT}^{max}$$

$$\text{i.e., } 1kVAr \leq Q_{D-STAT} \leq 2 \text{ MVAr} \tag{17}$$

5. MATHEMATICAL MODELING OF D-STATCOM

The D-STATCOM is a shunt connected voltage source converter that corrects power quality concerns like an unbalanced load, voltage sag, voltage volatility, and voltage unbalance. Figure 1 depicts the schematic diagram of a straightforward 2-bus RDS. Figure 2 displays the phasor diagram that corresponds to Figure 1. The voltage and current relationship from Fig. 1 can be shown in equation (20)

$$V_{i+1} \angle \delta_{i+1} = V_i \angle \delta_i - Z_j I_j \angle \theta_j \tag{18}$$

$V_i \angle \delta_i$ and $I_j \angle \theta_j$ can be derived from load flow equations.

In this study, D-STATCOM, which can only increase reactive power to the system, is utilised to control voltage under steady-state settings. The system's voltage $V_i \angle \delta_i$ must therefore be kept in quadrature with ID-STAT (i). D-STATCOM integration into the distribution system causes all bus voltages, particularly those of the buses close, to be in the D position.

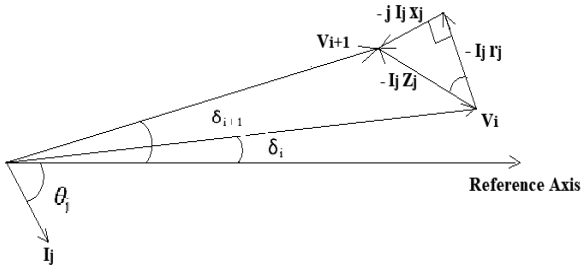

Figure 2: Phasor diagram of 2-bus Radial Distribution System shown in fig.1.

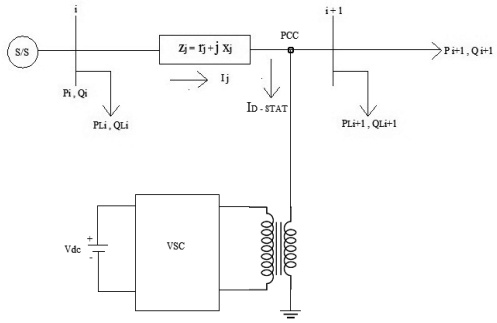

Figure 3: Schematic diagram of 2-bus RDS with D-STATCOM placement at $(i+1)^{th}$ bus.

STATCOM's and the network's branch currents vary in a steady state. Figure 3 shows the schematic for a 2-bus basic RDS where D-STATCOM is positioned on the (i+1)th bus to regulate voltage. STATCOM's and the network's branch currents vary in a steady state. Figure 3 shows the schematic for a 2-bus basic RDS where D-STATCOM is positioned on the (i+1) th bus to regulate voltage. The phasor diagram under this condition is shown in Figure 4. When D-STATCOM is connected, the voltage at the (i+1)th bus shifts from V (i+1) to V (i+1)'. In the phasor diagram shown in figure 4, the phase angle of the ith bus voltage V i, i.e., I is considered to be zero for ease of comprehension.

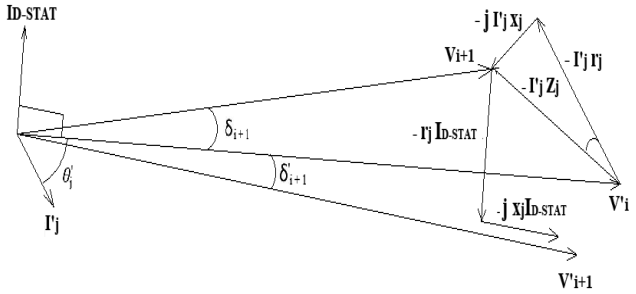

Figure 4: Phasor diagram of 2-bus RDS with D-STATCOM placement at (i+1)th Bus.

Therefore,

$$\angle I_{D\text{-}STAT} = \frac{\pi}{2} + \delta'_{i+1},\ \delta'_{i+1} < 0 \tag{19}$$

and voltage at (i+1)th bus after D-STATCOM placement is given by

$$V'_{i+1}\angle\delta'_{i+1} = V'_i\angle\delta'_i - (r_j + jx_j)I'_j\angle\theta'_j - (r_j + jx_j)I_{D-STAT}\angle\frac{\pi}{2} + \delta'_{i+1} \tag{20}$$

The voltage $V'_i\angle\delta'_i$ and current $I'_j\angle\theta'_j$ are obtained from the load flow calculations.

Therefore,

LHS of equation (22) can be written as

$$V'_{i+1}\angle\delta'_{i+1} = V'_{i+1}(cos\delta'_{i+1} + jsin\delta'_{i+1})$$

$$= V'_{i+1}cos\delta'_{i+1} + j\ V'_{i+1}sin\delta'_{i+1} \tag{21}$$

Similarly, RHS of equation (21) can be written as

$$V'_i\angle\delta'_i - (r_j + jx_j)I'_j\angle\theta'_j - (r_j + jx_j)I_{D-STAT}\angle\frac{\pi}{2} + \delta'_{i+1} \tag{22}$$

Having divided and equated the Real and Imaginary components on both sides of the equations. (23) & (24) then

Real Part ($V'_{i+1}cos\delta'_{i+1}$) is equal to

$$V'_i cos\delta'_i - r_j I'_j cos\theta'_j + r_j I_{D-STAT} sin\delta'_{i+1} + x_j I_{D-STAT} cos\delta'_{i+1} \quad (23)$$

The imaginary Part ($V'_{i+1}sin\delta'_{i+1}$) is equal to

$$V'_i sin\delta'_i - r_j I'_j \sin\theta'_j - x_j I'_j cos\theta'_j - r_j I_{D-STAT} cos\delta'_{i+1} + x_j I_{D-STAT} sin\ \delta'_{i+1} \quad (24)$$

Now, by taking some assumptions given below

$$y_1 = V'_i cos\delta'_i - r_j I'_j cos\theta'_j \quad (25)$$

$$y_2 = V'_i sin\ \delta'_i - r_j I'_j sin\theta'_j - x_j I'_j cos\theta'_j \quad (26)$$

$$y_3 = -r_j \quad (27)$$

$$y_4 = -x_j \quad (28)$$

$$m = V'_{i+1} \quad (29)$$

$$g_1 = I_{D-STAT} \quad (30)$$

$$g_2 = \delta'_{i+1} \quad (31)$$

Then the Real Part becomes as

$$mCos\ g_2 = y_1 - y_3 g_1 Sin\ g_2 - y_4 g_1 Cos\ g_2 \quad (32)$$

Therefore, $$g_1 = \frac{mCosg_2 - y_1}{-y_3 Sing_2 - y_4 Cosg_2} \quad (33)$$

And the Imaginary Part becomes as

$$mSin\ g_2 = y_2 + y_3 g_1 Cos\ g_2 - y_4 g_1 Sin\ g_2 \quad (34)$$

Therefore, $$g_1 = \frac{mSing_2 - y_2}{-y_3 Cosg_2 - y_4 Sing_2} \quad (35)$$

But the equations (35) & (36) both are equal.

Then

$$\frac{mCosg_2 - y_1}{-y_3 Sing_2 - y_4 Cosg_2} = \frac{mSing_2 - y_2}{-y_3 Cosg_2 - y_4 Sing_2} \quad (36)$$

After solving the above equation, we get

$$my_3 - Cosg_2(y_1 y_3 + y_2 y_4) + Sing_2(y_1 y_4 - y_2 y_3) = 0 \quad (37)$$

Again, taking some more assumptions given below

$$G_1 = y_1 y_4 - y_2 y_3 \quad (38)$$

$$G_2 = y_1 y_3 + y_2 y_4 \quad (39)$$

$$g = Sing_2 \tag{40}$$

Squaring on both sides of equation,

Then, $g^2 = Sin^2 g_2$ and $Cos^2 g_2 = \sqrt{(1-g^2)}$ (41)

Then equation (43) becomes as

$$my_3 - G_2\sqrt{1-g^2} + G_1\, g = 0 \tag{42}$$

$$my_3 + G_1\, g = G_2\sqrt{1-g^2} \tag{43}$$

Squaring on both sides and after simplifying,

Then, $(G_1^2 + G_2^2)g^2 + 2G_1 m y_3 g + (m^2 y_3^2 - G_2^2) = 0$ (44)

This is a quadratic equation with unknown parameter $'g'$ and it is obtained by solving using equation below.

$$g = \frac{-b \pm \sqrt{b^2-4ac}}{2a} \tag{45}$$

Where,

$$a = G_1^2 + G_2^2 = (y_1 y_4 - y_2 y_3) + (y_1 y_3 + y_2 y_4) \tag{46}$$

$$b = 2G_1 m y_3 = 2(y_1 y_4 - y_2 y_3)\,(V'_{i+1})(y_3) \tag{47}$$

$$c = m^2 y_3^2 - G_2^2 = [V'_{i+1}{}^2 * (-r_j)]^2 - (y_1 y_3 + y_2 y_4)^2 \tag{48}$$

There are currently two origins for "g." We look at the following boundary criteria to get the correct root value.

$$V'_{i+1} = V_{i+1} \text{ when } I_{D-STAT} = 0 \text{ and } \delta_{i+1} = \delta'_{i+1} \tag{49}$$

Then, the results shows that eqn. (45) is the correct root of $'g'$ which is given by

$$g = \frac{-b + \sqrt{b^2-4ac}}{2a} \tag{50}$$

The phase angle of the (i+1)th bus voltage is $g = Sing_2$

$$g_2 = Sin^{-1}(g) = Sin^{-1}\left[\frac{-b+\sqrt{b^2-4ac}}{2a}\right] \tag{51}$$

The amount of current that D-STATCOM injected is indicated as

$$|I_{D-STAT}| = g_1 = \frac{mCosg_2 - y_1}{-y_3 Sing_2 - y_4 Cosg_2} = \frac{V'_{i+1}Cos(\delta'_{i+1}) - y_1}{-y_3 Sin(\delta'_{i+1}) - y_4 Cos(\delta'_{i+1})} \tag{52}$$

In a similar manner, D-injected STATCOM's current's phase angle is given as

$$\angle I_{D\text{-}STAT} = \frac{\pi}{2} + \delta'_{i+1} = Sin^{-1}(g) \tag{53}$$

δFinally, The D-STATCOM injects reactive power that is provided by

$$jQ_{D-STAT} = (V'_{i+1}\angle\delta'_{i+1}) . \left(\mathrm{I}_{D-STAT}\angle\frac{\pi}{2} + \delta'_{i+1}\right)^{*} \quad (54)$$

Where, '*' represents the complex conjugate.

6. GRAVITATIONAL SEARCH ALGORITHM

The Gravitational Search Algorithm (GSA) was first developed by Esmat Rashedi and associates in 2009. Based on Newton's equations of motion and gravity, it is a brand-new meta-heuristic optimization method [26]. The steps listed below can be used to describe the GSA [27, 28].

The location of N masses (agents) is indicated as

$$U_j = \left(U_j^1, \ldots, U_j^c, \ldots, U_j^n\right) \text{ for i=1,2,3,……,N}$$

Where, U_j^d represents the position of j[th] mass in c[th] dimension.

The Gravitational Constant $G(t)$ at time (t) is given as

$$G(t) = G_0 e^{\left(\frac{-\delta t}{T}\right)}$$

G_0 and δ are initialised at the beginning and will be lowered to manage the search accuracy where T is the total number of iterations. Calculations are made of the internal masses (agents) and gravitational

$$mass_j(t) = \frac{Fit_j(t) - Worst(t)}{Best(t) - Worst(t)} \quad (55)$$

$$Mass_j(t) = \frac{mass_j(t)}{\sum_{k=1}^{N} mass_k(t)} \quad (56)$$

Where 〖Fit)] _j (t) is the fitness value of the jth mass at time (t), "Best" (t) and "Worst" (t) are the minimum and maximum fitness, respectively, and 〖Mass〗 _j(t)is the mass of the jth agent at time (t) h_{Best} is updated by

$$h_{Best} = H_{Best_Final} + \left[\frac{T-t}{T} X(100 - H_{Best_Final})\right]$$

H Best is the set of the first H masses (agents) with the best fitness value, while H (Best Final) is the set of the final H masses (agents) with the largest mass and the most recent fitness value.

F is the overall force.

$$F_{jk}^c = G \times \frac{M_j M_k}{R_{jk} + \tau} \times (U_k^c - U_j^c)$$

Where $R_{jk} = \left\|U_j, U_k\right\|_2 = \sqrt{\sum_{c=1}^{D} (U_k^c - U_j^c)^2}$

Where τ is small coefficient

On mass (agent) j in dimension c, the sum of the forces generated by the cth components of the forces from other agents will act.

$$F_j^c(t) = \sum_{k \in H_{Best}, k \neq j}^{N} rand_k F_{jk}^c(t)$$

A random number between 0 and 1 is called rand k.

Given by are the acceler*ation* $factor, velocity\ v, and\ location\ U$.

$$\alpha_j^c = \frac{F_j^c}{Mass_j}$$

$$v_j^c(t+1) = rand_j \times v_j^c(t) + a_j^c(t)$$

$$U_j^c(t+1) = U_j^c(t) + v_j^c(t+1)$$

$rand_j$ is random variable in interval (0,1)

7. SIMULATION RESULTS

The simulation was run in MATLAB (R2017a) version 9.2.0 on an Intel (R) core (TM), i5 processor-powered personal computer with 4GB of RAM. Throughout the simulation, some assumptions were made, including the initial gravitational constant "G0" being assumed to be 100, the population size, and the maximum number of iterations being assumed to be 50 and 100, respectively.

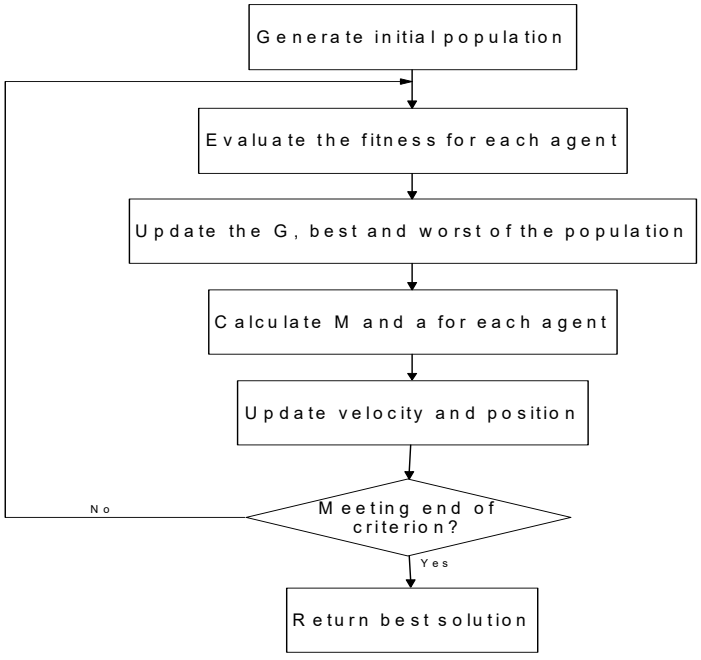

Figure 5: Basic Gravitational Search Algorithm Principles (GSA)

33-BUS RADIAL DISTRIBUTION TEST SYSTEM

Figure 6 shows the single line diagram of an IEEE 33-bus test system with 33 buses and 32 branches. The test system's buses and branches data were collected from [24]. 100 MVA and 12.66 kV are regarded as the basis voltage and base VA, respectively. The network's total active and reactive load powers are estimated to be 3.715 MW and 2.300 MVAr, respectively. The Total Active Power Losses (TAPL) and Total Reactive Power Losses (TRPL) calculated after running backward forward load flow in MATLAB as a base case are 210.98 kW and 143.13 kVAr, respectively. The bus with the lowest voltage magnitude is bus 18, which has a voltage of 0.9133 p.u. Voltage Sensitivity Factors (VSF) and Loss Sensitivity Factors (LSF) are employed to establish the best position.

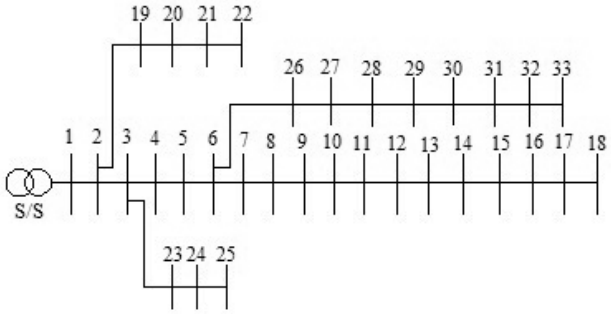

Figure 6: Standard IEEE 33-Bus Test System

for positioning D-STATCOM. The buses with the highest LSF and lowest VSF (VSF1.01) are selected as the candidate buses for allocation of D-STATCOM in RDS. The LSFs are determined using equation (19) from the base case load flow. If the buses have VSF values higher than 1.01, no compensation is necessary. The 29th bus is chosen as a candidate bus for D-STATCOM allocation in this paper.

Table 1: Voltage magnitudes at all buses without and with D-STATCOM placement

Bus No.	Voltage Magnitude (p.u.)		Bus No.	Voltage Magnitude (p.u.)	
	Without D-STATCOM	With D-STATCOM		Without D-STATCOM	With D-STATCOM
1	1	1	**18**	**0.9133**	**0.9259**
2	0.997	0.9975	19	0.9965	0.997
3	0.9829	0.9856	20	0.993	0.9934
4	0.9755	0.9797	21	0.9923	0.9927
5	0.9681	0.9741	22	0.9916	0.992
6	0.9497	0.9618	23	0.9794	0.982
7	0.9462	0.9583	24	0.9727	0.9754
8	0.9413	0.9535	25	0.9694	0.972
9	0.9351	0.9474	26	0.9477	0.9607
10	0.9294	0.9418	27	0.9452	0.9594
11	0.9286	0.9409	28	0.9337	0.956
12	0.9271	0.9395	29	0.9255	0.9538

Bus No.	Voltage Magnitude (p.u.)		Bus No.	Voltage Magnitude (p.u.)	
	Without D-STATCOM	With D-STATCOM		Without D-STATCOM	With D-STATCOM
13	0.921	0.9334	30	0.9219	0.9525
14	0.9187	0.9312	31	0.9178	0.9484
15	0.9173	0.9298	32	0.9169	0.9476
16	0.9159	0.9285	33	0.9166	0.9473
17	0.9139	0.9265	-	-	-

Cost of D-STATCOM [20]

The following equation can be used to determine the annual cost of D-STATCOM (57)

$$Cost_{D-STAT_{year}} = C_{D-STAT} * \left[\frac{(1+B^{\wedge})^{n_{D-STAT}} * B^{\wedge}}{(1+B^{\wedge})^{n_{D-STAT}} - 1}\right] \quad (57)$$

Where, $Cost_{D-STAT_{year}}$ is the annual cost of D-STATCOM

C_{D-STAT} is the D-STATCOM cost and it is 50 $/kVAr

B^ is the asset rate of return and it is taken as 0.1

n_{D-STAT} is the durability of D-STATCOM which is taken as 30.

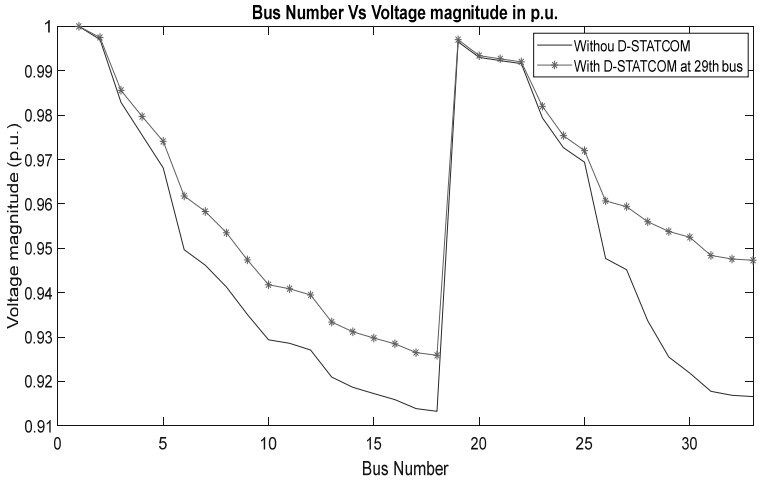

Figure 7: Voltage profile of the 33-bus RDS under the cases of without and with D-STATCOM placement at 29th bus

Total Cost Saving (TCS) [20]

The TCS is calculated by using the equation (70)

$$TCS = K_p(T \times P_{T,Loss}) - K_p(T \times P_{T,Loss}^{with\ D-STAT}) - (K_c \times Cost_{D-STAT_{year}}) \quad (58)$$

Table 2: Performance analysis of the proposed algorithm after installation of D-STATCOM in 33-bus RDS

		Base Case	IA [16]	BA [2]	HSA [20]	DEA [17]	Proposed (GSA)
Optimal Size(kVAr)		-	962.49	1250	1150	1252.7	1259.9
Location		-	12	30	30	30	29
TAPL (kW)		210.98	171.79	143.38	143.97	143.50	143.31
Reduction in APL	**kW**	-	39.19	67.6	67.01	67.48	67.67
	%	-	18.57	32.04	31.76	31.98	32.07
TRPL (kVAr)		143.13	115.26	96.17	96.47	-	96.35
Reduction in TRPL	**kW**	-	27.87	46.96	46.66	-	46.78
	%	-	19.47	32.80	32.59	-	32.68
Minimum Voltage (Bus Number)		0.9133	0.9258	0.9260	0.9236	0.9256	0.9259
Total Cost Saving ($)		-	11,130	24,545	24,264	27,211	31,194

Where K p, K (c), and T stand for the cost of energy losses, the time duration proportion, and the number of hours in a year, respectively, and their corresponding values are set to 0.06 $/kWh, 1 year, and 8760 hours, respectively.

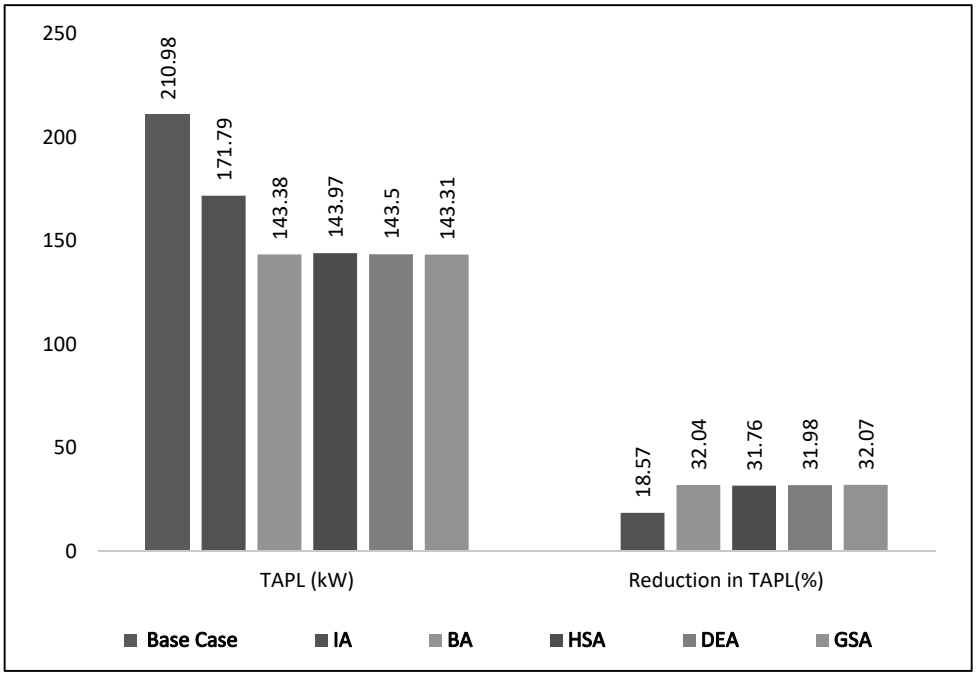

Figure 8: Comparison of GSA with other heuristic algorithms in view of Total Active Power Losses (TAPL) and % Reduction in TAPL

Voltage magnitudes at all buses without and with D-STATCOM placement bus are given in Table I. The voltage profile of the network without and with D-STATCOM allocation at 29th bus is plotted and shown in Figure 7. Comparison of GSA with other heuristic algorithms in view of Total Active Power Losses (TAPL) and % Reduction in TAPL shown in Figure 8 whereas Figure 9 shows the Performance comparison of TCS in GSA with other heuristic algorithms.

ISBN - 978-93-95038-50-8

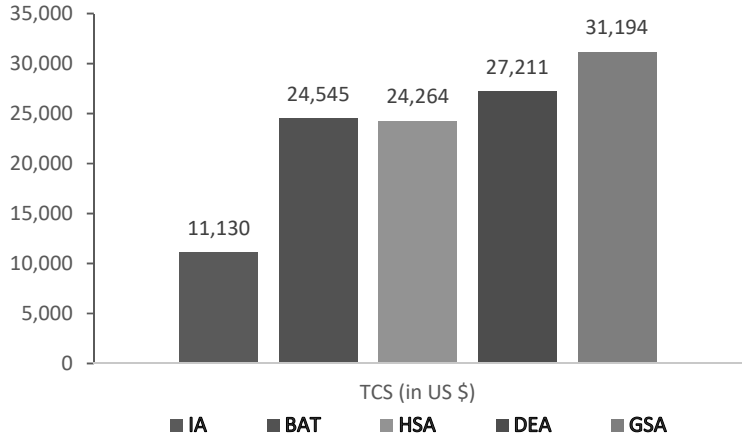

Figure 9: Performance comparison of TCS in GSA with other heuristic algorithms.

Table II contrasts existing and proposed algorithms for active and reactive power losses, ideal size and position, decrease in active and reactive power losses, and total annual cost savings (TCS). The D-STATCOM is located on the 12th bus, and Immune Algorithm [16] experiences more losses, per Table II. The losses in the Bat Algorithm are negligible even if the D-STATCOM is placed on the 30th bus in comparison to other existing algorithms [2]. The total active and reactive power losses in the suggested algorithm are 143.31 kW and 96.35 kVAr, respectively. Active and reactive power losses were reduced by 32.07% and 32.68% respectively, while the system's minimum voltage was raised to 0.9259 p.u. Particularly, the system's Total Yearly Cost Saving (TCS) of US$31,194 is the highest of any existing systems' total annual cost savings. This shows that the Gravitational Search Algorithm (GSA) under consideration outperformed all other algorithms. Particularly, the system's Total Yearly Cost Saving (TCS) of US$31,194 is the highest of any existing systems' total annual cost savings. This shows that the Gravitational Search Algorithm (GSA) under consideration outperformed all other algorithms.

8. CONCLUSION

In order to determine the ideal location and size for DSTATCOM in the RDS, the Gravitational Search Tool (GSA), a Newtonian Gravity-based optimization algorithm, has been demonstrated in this study. To reduce system power losses and increase bus voltage, the right location for DSTATCOM allocation is even more crucial. The best position of DSTATCOM is determined in this work using the LSF and VSF concept. LSF and VSF provide a better placement in terms of least power losses, most extreme TCS, and large bus extents in the RDS as compared to other dependability files. Results from the suggested technique are tested on a 33-bus RDS, and they are verified by additional heuristic algorithms. The DSTATCOM can be used to lower the overall power losses of the RDS, according to the study's findings. As a result, it is feasible to claim that the proposed algorithm considerably increases the operational suitability of the RDS and that it is a useful strategy to apply across all RDS in order to gain better execution.

ISBN - 978-93-95038-50-8

REFERENCES

1. Attia A. El-Fergany, Optimal capacitor allocations using evolutionary algorithms, IET Generation, Transmission & Distribution, 2013, doi: 10.1049/iet-gtd.2012.0661
2. Yuvaraj.T, Ravi.K, Devabalaji.K.R, DSTATCOM Allocation in the Radial Distribution Networks with Different Stability İndices using Bat Algorithm, Journal of Science, 30(4): 314-328 (2017).
3. Z. Gu and D. T. Rizy, Neural networks for combined control of capacitor banks and voltage regulators in distribution systems, IEEE Transactions on Power Delivery, Vol. 11, pp. 1921-1928, October 1996.
4. L. A. Kojovic, Coordination of distributed generation and step voltage regulator operations for improved distribution system voltage regulation, IEEE Power Engineering Society General Meeting, pp. 232 - 237, June 2006.
5. S. M. Ramsay, P. E. Cronin, R. J. Nelson, J. Bian and F. E. Menendez, Using distribution static compensators (D-STATCOMs) to extend the capability of voltage-limited distribution feeders, Rural Electric Power Conference, the 39th Annual Conference, pp. A4/1-A4/7, April 1996.
6. S. M. S. Hussain, M. Subbaramiah, An analytical approach for optimal location of D-STATCOM in radial distribution system, International Conference on Energy Efficient Technologies for Sustainability (ICEETS), pp. 1365-1369, April 2013.
7. Mehdi Hosseini, Heidar Ali Shayanfar, Mahmoud Fotuhi-Firuzabad, Modeling of Series and Shunt Distribution FACTS Devices in Distribution Systems Load Flow, J. Electrical Systems 4-4 (2008): 1-12.
8. Atma Ram Gupta, Ashwani Kumar, Performance Analysis of Radial Distribution Systems with UPQC and D-STATCOM, J. Inst. Eng. India Ser. B, Springer, DOI 10.1007/s40031-016-0254-4.
9. S. Xu, Q. Song, Y. Zhu, and W. Liu, Development of a D-STATCOM prototype based on cascade inverter with isolation transformer for unbalanced load compensation, IEEE International Conference on Industrial Technology, pp. 1051-1056., December, 2005.
10. H. Masdi, N. Mariun, S. Mahmud, A. Mohamed and S. Yusuf, Design of a prototype DSTATCOM for voltage sag mitigation, National Power and Energy Conference, pp. 61-66, November, 2004.
11. M.H. Haque, Compensation of distribution system voltage sag by DVR and D-STATCOM, 2001 IEEE Porto Power Tech Conference, Vol. 1, pp. 223-228, September, 2001.
12. P.S. Sensarma, K.R. Padiyar and V. Ramanarayanan, Analysis and performance evaluation of a distribution STATCOM for compensating voltage fluctuations, IEEE Transactions on Power Delivery, Vol. 16, pp. 259-264, April, 2001.
13. B. Blazic and I. Papic, A new mathematical model and control of D-StatCom for operation under unbalanced conditions, ELSEVIER, Electric Power Systems Research 72 (2004), pp. 279-287, July, 2004.
14. Jazebi S, Hosseinian SH, Vahidi B., DSTATCOM allocation in distribution networks considering reconfiguration using differential evolution algorithm. Energy Convers Manage 2011;52:2777–83.
15. Joseph Sanam, Sanjib Ganguly, and, A. K. Panda, Placement of DSTATCOM in Radial Distribution, Systems for the Compensation of Reactive Power, 2015 IEEE Innovative Smart Grid Technologies - Asia (ISGT ASIA), 2015, Pages 1-6.
16. Seyed Abbas Taher, Seyed Ahmadreza Afsari, Optimal location and sizing of DSTATCOM in distribution systems by immune algorithm, Electrical Power and Energy Systems 60 (2014) 34–44, ELSEVIER.
17. Joseph Sanam, Sanjib Ganguly, A.K.Panda, Chaduvula Hemanth, Optimization of energy loss cost of distribution networks with the optimal placement and sizing of DSTATCOM using Differential Evaluation Algorithm, Arab Journal of Sci. Eng (2017) 42:2851-2865.
18. S M Suhail Hussain, M Subbaramiah, An Analytical Approach for Optimal Location of DSTATCOM in Radial Distribution System, International Conference on Energy Efficient Technologies for Sustainability, 2013, Pages: 1365 – 1369.
19. Abhinav Jain, A R Gupta, Ashwani Kumar, An Efficient Method for D-STATCOM placement in Radial Distribution System, IEEE 6th India International Conference on Power Electronics (IICPE), 2014, Pages 1-6.
20. T. Yuvaraj, K. Ravi, and K. R. Devabalaji, Optimal Placement and sizing of DSTATCOM using Harmony Search Algorithm, ELSEVIER, International Conference on Alternative Energy in Developing Countries and Emerging Economies, 2015, 759-765.
21. T. Yuvaraj, K. Ravi, and K. R. Devabalaji, DSTATCOM allocation in distribution networks considering load variations using bat algorithm, Ain Shams Engineering Journal, 2015, http://dx.doi.org/10. 1016/j.asej.2015.08.006

22. K Subbarami Reddy, V Usha Reddy, Optimal Placement of DSTATCOM in Radial Distribution System using Fuzzy and Penguins Search Optimization Algorithm, International Journal of Innovative Research in Electrical, Electronics, Instrumentation and Control Engineering, ISSN: 2321 – 2004, Vol. 3, Issue 11, November 2015.
23. K.R. Devabalaji, K. Ravi, Optimal size and siting of multiple DG and DSTATCOM in radial distribution system using Bacterial Foraging Optimization Algorithm, Ain Shams Engineering Journal (2016) 7, 959–971, www.elsevier.com/locate/asej, www.sciencedirect.com
24. M M Aman, G B Jasman, A H A Bakar, H Mokhlis, A new approach for optimum simultaneous multi-DG distributed generation units placement and sizing based on maximization of system loadability using HPSO(Hybrid Particle Swarm Optimization) algorithm, Energy 66 (2014), 202-215 (Elsevier).
25. PVV Rama Rao, S Sivanagaraju, PV Prasad, Backward Forward Propagation Power Flow Method for Radial Distribution Systems, Journal of Electrical and Control Engineering, Vol.2, Issue 3,2012, PP 20-23.
26. Esmat Rashedi, Hossein Nezamabadi-pour, Saeid Saryazdi, GSA: A Gravitational Search Algorithm, Information Sciences 179 (2009) 2232-2248. (Elsevier).
27. Serhat Duman; Yusuf Sonmez; Ugur Guvenc; Nuran Yorukeren Application of gravitational search algorithm for optimal reactive power dispatch problem, 2011 International Symposium on Innovations in Intelligent Systems and Applications(2011), 519-523.
28. Aida Fazliana Abdul Kadir, Azah Mohamed, Hussain Shareef, An improved gravitational search algorithm for optimal placement and sizing of renewable distributed generation units in a distribution system for power quality enhancement, Journal of Renewable and Sustainable Energy 6, 033112, 2014.

Multi Objective Optimization of Process Parameters of Electro Discharge Machining On Nimonic 80A Using Grey Relational Analysis

K.L.Uday Kiran*, K.Saraswathamma, M.Rajesh

[1,2,3] Department of Mechanical Engineering, University College of Engineering,
Osmania University, Hyderabad, Telangana State
Email: udaykiran.kl@uceou.edu

ABSTRACT

Abrasive powder-mixed electrode coated electrical discharge machining (APMEC-EDM), a hybrid manufacturing process involving the use of a dielectric fluid mixed with abrasive powder and coated electrodes, combines the benefits of mechanical and thermal interactions. The aim of this article is to use a new approach of performance evaluation, gray relational analysis (GRA), to evaluate the effectiveness of optimizing multiple performance characteristics of APMEC-EDM of Nimonic80A Super alloy. The considered process parameter includes the five control factors namely pulse current (A), pulse ON time (Ton), pulse off time (Toff), Inter Electrode gap (mm) Aluminum powder concentration (g/L). The combination of L27 orthogonal array design of experiment with GRA enables to determine the optimal parameters for multiple responses. GRA is used to obtain a single performance index, gray relational grade through gray relational coefficient to optimize the APMEC-EDM process with lower tool wear rate, radial overcut, and higher material removal rate.

Keywords: *Electrical Discharge Machining, Gray Relational Analysis, Pulse on Time, Pulse off Time*

1. INTRODUCTION

Discharge Machining Process, which is also called electro-erosion machining process. When the gap voltage is sufficiently large (i.e. reaches the breakdown voltage of dielectric fluid), high power spark is produced, which increase the temperature about 10,000 degrees Celsius. By this way the metal is removed from the work piece [1].A major advantage of EDM is that the tool and the work piece do not come into contact [2]. In this process material is removed by controlled erosion through a series of electric sparks between the tool (electrode) and the work piece. The thermal energy of the sparks leads to intense heat conditions on the work piece causing melting and vaporizing of work piece material. Due to the high temperature of the sparks, not only work material is melted and vaporized, but the electrode material is also melted and vaporized, which is known as electrode wear (EW). The EW process is quite similar to the material removal mechanism as the electrode and the work piece are considered as a set of electrodes in EDM. Due to this wear, electrodes lose their dimensions resulting in inaccuracy of the cavities formed. During EDM, the main output parameters are the material removal rate (MRR) and Tool wear ratio (TWR). Electric discharge machining (EDM) is a non- traditional machining operating procedure in the manufacture of complex shaped dies, moulds and scathing parts used in automobile, aerospace, surgical and other industrial applications [3] Electrical-discharge machining (EDM) is extensively used for high strength materials. An analysis on the influence of current, Inter Electrode Gap, Pulse Duration and Different Powder Concentrations over MRR, TWR and ROC was performed. NIMONIC is a family of nickel based high-temperature low creep and high performance super alloys. NIMONIC alloys are primarily composed of nickel and chromium. Additives like aluminum, titanium and carbon are infused into alloy. NIMONIC alloys available commercially are NIMONIC 75, NIMONIC 80A, 81, 86, 252, NIMONIC PE11 and 16.

*Corresponding author: E-mail: udaykiran.kl@uceou.edu

The NIMONIC 80A has been used as a work piece material for the present experiment. It is a wrought, age-hardened alloy that is strengthened by additives like titanium, aluminum and carbon. It is manufactured by high-frequency melting and casting in air. It is similar to NIMONIC alloy 75. It has good corrosion and oxidation resistance. Its hardness value is 300HV.

Studies shows that the quality of the machined product depends on the selection of the process parameters and fixing the appropriate range of parameters. Shantisagar Biradar et al. [4] has optimized the process parameters of EDM for High Carbon High Chromium Die steel (HCHCr) using the titanium nitride coated copper electrode as the tool. The experiments were conducted using factorial design, analysis has been carried out using Grey Relational Analysis. Amitesh Goswani et al. [4] studied a multi response optimization method using utility concept for wire electrical discharge machining (WEDM) of Nimonic-80A alloy. The machining characteristics are material removal rate (MRR) and surface roughness (SR). They have done the experimentation using Taguchi's robust design methodology whereas process parameters are peak current, pulse on time and pulse off time. They reported that material removal rate and surface roughness increases with increase in pulse on time and decreases with increase in pulse-off time. The present aim of the Project is to optimize the process parameters of the EDM for machining of NIMONIC 80A using Grey Relational Grade and the percentage contribution of the parameters are found by using Analysis of Variance Method (ANOVA).

2. EXPERIMENTAL DETAILS

2.1. TOOL MATERIAL

In EDM tool material plays a very significant role in the Machining. In this present study an Copper electrode coated with Silver (3µ) thickness is used. The electrode dimensions are 10mm diameter and 50mm length respectively.

2.2. WORK MATERIAL

In this present study Nimonic 80A is used as the work material. The dimensions of the rectangular workpiece material are 15mm*5mm. The Fig 1 shows the electrode and workpice.

2.3. POWDER MATERIAL

The powder used in the present study is Aluminum metal powder of 325 mesh is used to mix in the dielectric. Aluminum powder concentration in the dielectric ranges from 3 to 9 g/l.

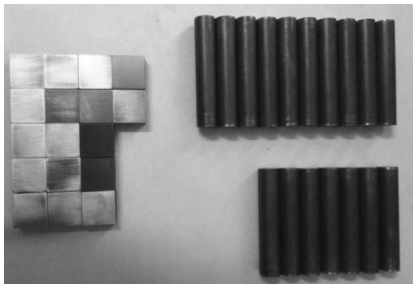

Figure 1: Workpiece and Electrode(Before Coating)

ISBN - 978-93-95038-50-8

3. RESEARCH METHODOLOGY

The selection of optimum machining parameters in EDM is an important step. Taguchi Optimization technique is single parameter optimization based on the signal to noise ratio [8]. Grey relational analysis is applied to optimize the parameters having multi-responses through grey relational grade. Furthermore, a statistical analysis of variance (ANOVA) is performed to see which process parameters are statistically significant. The steps involved are

3.1. SELECTION OF PROCESS PARAMETERS AND RESPONSE VARIABLES

The process parameters chosen and the levels of the variables are tabulated in the table 1. The response variables affected with respect to the process parameters are Material Removal Rate (MRR), Tool Wear rate (TWR) and Radial Over Cut (ROC).

Table 1: Levels of Process Parameters

Process Parameters	Units	Low level (-1)	Medium level (0)	High Level (-1)
Current	A	3	9	15
Pulse on time (ton)	µs	300	600	900
Pulse off time (toff)	µs	30	60	90
Inter electrode gap	mm	1	2	3
Aluminum powder concentration	g/l	3	6	9

3.2. DESIGN OF EXPERIMENTS

The Experiments were Performed randomly according to the L27 Orthogonal array generated using MINITAB. For each experiment different electrode (Silver Coated Copper Electrode) is used. The machining time considered for Nimonic 80A is 5 minutes. The arrangement of the experiments according to the L27 Orthogonal array is tabulated below with the Actual values.

Table 2: Design of Experiments with actual value

DOE	IEG (mm)	Current (A)	Powder Concentration (g/l)	On Time (µs)	Off Time (µs)
1	1	5	3	300	30
2	1	5	3	300	60
3	1	5	3	300	90
4	1	12	6	600	30
5	1	12	6	600	60
6	1	12	6	600	90
7	1	15	9	900	30
8	1	15	9	900	60
9	1	15	9	900	90
10	2	5	6	900	30
11	2	5	6	900	60
12	2	5	6	900	90

ISBN - 978-93-95038-50-8

13	2	12	9	300	30
14	2	12	9	300	60
15	2	12	9	300	90
16	2	15	3	600	30
17	2	15	3	600	60
18	2	15	3	600	90
19	3	5	9	600	30
20	3	5	9	600	60
21	3	5	9	600	90
22	3	12	3	900	30
23	3	12	3	900	60
24	3	12	3	900	90
25	3	15	6	300	30
26	3	15	6	300	60
27	3	15	6	300	90

4. EXPERIMENTAL SETUP

The whole experiments were carried out on an Electro Discharge Machining model ARD ARTM30D (Die-sinking type). White kerosene was used as dielectric fluid. The EDM machine tool is shown in Fig 3. Aluminum powder is added to the dielectric to examine the effect on responses. As concentration of powder is taken as one of the input variables it is difficult to maintain the total tank with 200 liters capacity. To minimize this, separate tray of one liter capacity was prepared and the different concentration levels were examined. The Workpieces are fitted with the help of Glue.

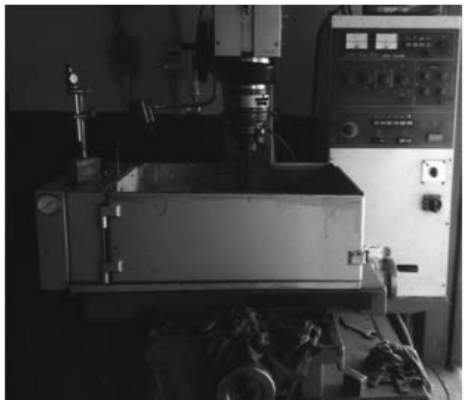

Figure 2: EDM setup

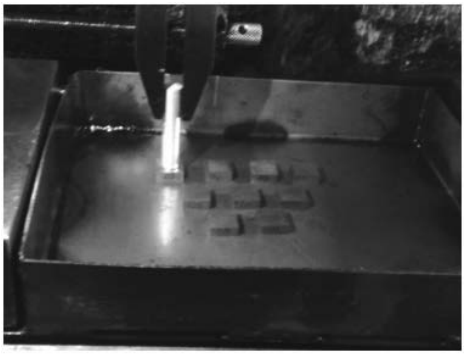

Figure 3: Arrangement of Workpieces in the Tray

5. CALCULATION OF RESPONSE VARIABLES

The experiments were conducted on all the 27 specimens with 5 minutes of machining time. The specimens and the electrodes are to be weighed before and after conducting the experiments. The Diameter of the electrode at the tip of the machining and the diameter of the hole produced are to be measured for every specimen using vernier calipers. The weights

and dia measured before and after the experiments are tabulated. The response variables (MRR, TWR, ROC) are calculated and are tabulated.

Material Removal Rate (MRR):

$$\text{MRR}=\frac{W_b-W_a}{t}\text{g/min}$$

Tool Wear Rate (TWR):

$$\text{TWR}=\frac{w_{tb}-w_{ta}}{t}\ \text{g/min}$$

Radial Over Cut (ROC):

$$\text{ROC}=\frac{D_h-D_t}{2}\ \text{mm}$$

t = time taken for Machining.

Table 3: Measured Weights, Diameter of tool and Workpiece along with the measured Response variables.

DOE	Wb (g)	WA (g)	MRR (g/min)	Wtb (g)	Wta (g)	TWR (g/min)	Dt (mm)	Dh (mm)	ROC (mm)
1	11.123	11.087	0.0072	34.689	34.673	0.0032	9.920	9.933	0.0067
2	11.163	11.123	0.008	34.868	34.820	0.0096	9.870	9.917	0.0233
3	11.132	11.096	0.0072	34.826	34.812	0.0028	9.860	9.877	0.0083
4	11.119	10.992	0.0254	34.761	34.743	0.0036	9.870	9.910	0.02
5	11.087	10.942	0.029	34.726	34.697	0.0058	9.930	10.007	0.0383
6	11.047	10.826	0.0442	34.774	34.736	0.0076	9.940	9.980	0.02
7	11.149	11.033	0.0232	34.796	34.727	0.0138	9.950	10.060	0.055
8	11.093	10.914	0.0358	34.829	34.801	0.0056	9.840	9.967	0.0633
9	11.104	10.881	0.0446	34.735	34.718	0.0034	9.930	9.867	-0.0317
10	11.094	11.071	0.0046	34.791	34.773	0.0036	9.950	9.980	0.015
11	11.152	11.131	0.0042	34.759	34.751	0.0016	9.920	10.083	0.0817
12	11.173	11.150	0.0046	34.718	34.704	0.0028	9.940	9.840	-0.05
13	11.156	10.703	0.0906	34.788	34.770	0.0036	9.970	10.120	0.075
14	11.171	10.590	0.1162	34.727	34.719	0.0016	9.920	10.120	0.1
15	11.093	10.570	0.1046	34.798	34.760	0.0076	9.930	10.013	0.0417
16	11.129	10.932	0.0394	34.489	34.461	0.0056	9.830	9.940	0.055
17	11.167	10.759	0.0816	34.776	34.737	0.0078	9.940	10.113	0.0867
18	11.089	10.585	0.1008	34.673	34.641	0.0064	9.960	10.123	0.0817
19	11.106	11.076	0.006	34.820	34.789	0.0062	9.850	9.767	-0.0417
20	11.122	11.096	0.0052	34.812	34.784	0.0056	9.910	9.880	-0.015
21	11.156	11.128	0.0056	34.743	34.713	0.006	9.910	9.553	-0.1783
22	11.100	10.936	0.0328	34.697	34.668	0.0058	9.950	10.000	0.025
23	11.153	10.974	0.0358	34.736	34.707	0.0058	9.900	10.057	0.0783
24	11.078	10.904	0.0348	34.727	34.698	0.0058	9.930	10.090	0.08
25	11.121	10.618	0.1006	34.801	34.771	0.006	9.900	10.157	0.1283
26	11.091	10.341	0.15	34.718	34.687	0.0062	9.940	10.133	0.0967
27	11.087	10.246	0.1682	34.773	34.742	0.0062	9.950	10.130	0.09

Where

W_b & W_a = Weight of the workpiece Before and After Machining.

W_{tb} & W_{ta} = Weight of Tool Before and After Machining.

D_t & D_h = Diameter of Tool and Hole respectively.

6. OPTIMIZATION OF RESPONSE VARIABLES

It is important for any process to follow optimal combination of process parameters to achieve desired output response by utilizing minimum possible resources. The Optimization of the Response Variables and the Effect of the Process paremeters on the Response Variables are calculated by using Analysis of Variance (ANOVA) method.

A CALCULATION OF S/N RATIO FOR MRR, TWR & ROC

A. Calculation of S/N Ratio For MRR: Taguchi's signal to noise ratio is the logarithmic function of desired output. S/N ratio is the ratio of the mean to standard deviation. Here mean refers to signal and standard deviation refers to noise. The ratio depends on the quality characteristic of the product/process to be optimized. A high value of S/N implies that signal is much higher than the random effects of noise factors. Process operation consistent with highest S/N always yields optimum quality with minimum variation.

As the material removal rate is the response which is to be maximum, so the larger is better will be considered in calculating the S/N ratios. The Higher the material removal rate indicates that the performance of the machining will be maximum. The calculated values of "Larger the Better S/N ratios" for MRR are in negative sign are tabulated.

$$\left(\frac{S}{N}\right)_{HB} = -10log_{10}(MSD_{HB})dB$$

$$MSD_{HB} = \frac{1}{n}\sum_{i=1}^{n}\frac{1}{Y_i^2}$$

B. Calculation of S/N Ratios for TWR: Low tool rate will permit the increase in the life of the tool, which means that the tool can be used for longer period of time without getting a change in the accuracy while machining. The sound to noise ratios for the tool wear rate are calculated using the formulae smaller the better. The sound to noise ratios for the Tool wear rate are calculated and tabulated.

$$\left(\frac{S}{N}\right)_{LB} = -10log_{10}(MSD_{LB})dB$$

$$MSD_{LB} = \frac{1}{n}\sum_{i=1}^{n}(Y_i^2)$$

C. Calculation of S/N ratios for ROC: Radial overcut is an error which is generated during the machining. It shouldn't be large as it may result in the improper contours. Hence smaller the better formulae was used to calculate the S/N Ratio's for the Radial Overcut and are tabulated.

$$\left(\frac{S}{N}\right)_{LB} = -10log_{10}(MSD_{LB})dB$$

$$MSD_{LB} = \frac{1}{n}\sum_{i=1}^{n}(Y_i^2)$$

Where

MSD = Mean Square Data

Yi = Response value of i^{th} experiment

n = Number of Replicants

Table 4: S/N Ratios of MRR, TWR & ROC

DOE	Powder Concen-tration (g/l)	IEG (mm)	Current (A)	Ton (µs)	Toff (µs)	MRR S/N Ratio	TWR S/N Ratio	ROC S/N Ratio
1	3	1	6	300	30	-42.853	49.8970	43.52183
2	3	1	6	300	60	-41.938	40.3545	32.64046
3	3	1	6	300	90	-42.853	51.0568	41.58362
4	3	2	12	600	30	-31.903	48.8739	33.9794
5	3	2	12	600	60	-30.752	44.7314	28.32847
6	3	2	12	600	90	-27.092	42.3837	33.9794
7	3	3	15	900	30	-32.69	37.2024	25.19275
8	3	3	15	900	60	-28.922	45.0362	23.96735
9	3	3	15	900	90	-27.013	49.3704	55.56303
10	6	2	6	900	30	-46.745	48.8739	36.47817
11	6	2	6	900	60	-47.535	55.9176	21.7591
12	6	2	6	900	90	-46.745	51.0568	43.52183
13	6	3	12	300	30	-20.857	48.8739	22.49877
14	6	3	12	300	60	-18.696	55.9176	20
15	6	3	12	300	90	-19.609	42.3837	27.60422
16	6	1	15	600	30	-28.09	45.0362	25.19275
17	6	1	15	600	60	-21.766	42.1581	21.24296
18	6	1	15	600	90	-19.931	43.8764	21.7591
19	9	3	6	600	30	-44.437	44.1521	41.58362
20	9	3	6	600	60	-45.68	45.0362	34.73517
21	9	3	6	600	90	-45.036	44.4369	55.56303
22	9	1	12	900	30	-29.683	44.7314	32.0412
23	9	1	12	900	60	-28.922	44.7314	22.12107
24	9	1	12	900	90	-29.168	44.7314	21.9382
25	9	2	15	300	30	-19.948	44.4369	17.83321
26	9	2	15	300	60	-16.478	44.1521	20.29447
27	9	2	15	300	90	-15.484	44.1521	20.91515

B) EFFECT OF PROCESS PARAMETERS ON RESPONSE VARIABLES:

The extent upto which the input variables effects the responses are to be identified. This is done by generating the response table using Minitab 18 Statistical Software.

Effect of Process Parameters on MRR: The Main effects plot is generated by taking the input variables with 3 levels in the Abcissa and Response variable (MRR) on the ordinate.

ISBN - 978-93-95038-50-8

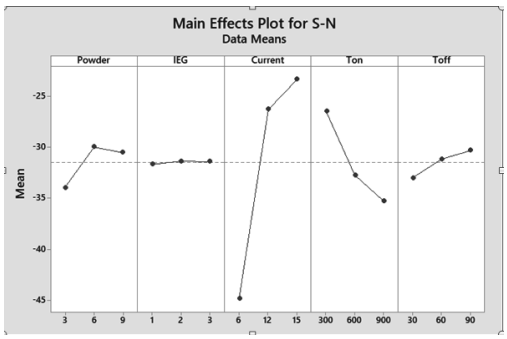

Figure 4: Main effects plot for MRR

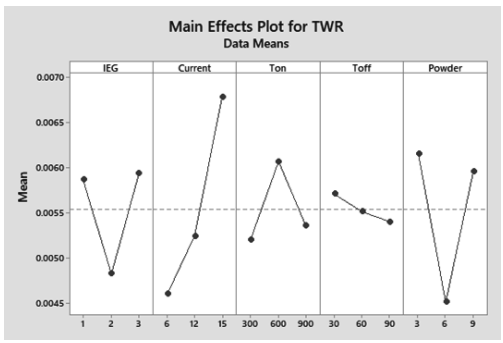

Figure 5: Main effects plot for TWR

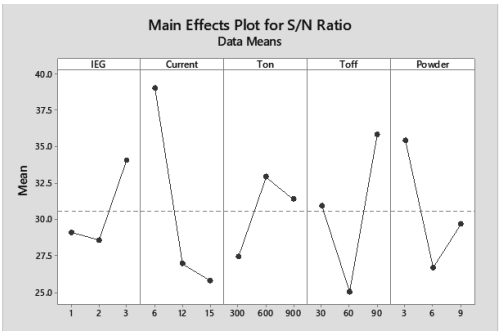

Figure 6: Main effects plot for roc

Response Table for MRR

The process parameters thus selected should be in such a way that MRR should be maximum. The levels at which the process parameters gives maximum MRR are generated by using Taguchi's technique. The so obtained values are tabulated in response Tables.

Table 5: Response table for MRR

Response Table for Signal to Noise Ratios					
Level	P C (g/l)	IEG (mm)	Current (A)	T_{on} (µs)	T_{off} (µs)
1	-34	-31.69	-44.87	-26.52	-33.02
2	-30	-31.41	-26.3	-32.74	-31.19
3	-30.54	-31.44	-23.37	-35.27	-30.33
Delta	4	0.28	21.5	8.75	2.7
Rank	3	5	1	2	4

The rank is generated for the different process parameters at different levels. The maximum values of the levels are considered as the MRR follows the Larger the better concept. The obtained Optimized values for MRR are Current (l3), Pulse on Time (l1), Powder Concentration (l2), Pulse off Time (l3) and IEG(l2).

The optimized parameters for MRR are

Current = 15 A

T_{on} = 300 µs
Powder concentration= 6 g/l
T_{off} = 90 µs
IEG = 2 mm

Response Table for TWR

Response Table for Signal to Noise Ratios					
Level	IEG (mm)	T_{on} (µs)	Current (A)	T_{off} (µs)	P C (g/l)
1	-33.08	-33.36	-33.56	-33.18	-33.1
2	-33.44	-32.96	-33.29	-33.29	-33.62
3	-33.17	-33.36	-32.84	-33.22	-32.97
Delta	0.37	0.4	0.73	0.1	0.65
Rank	4	3	1	5	2

The optimized parameters for TWR are

Current = 12 A
Powder concentration= 3 g/l
T_{on} = 300 µs
IEG = 1 mm
T_{off} = 30 µs

Response Table for ROC

Response Table for Signal to Noise Ratios					
Level	IEG (mm)	Current (A)	T_{on} (µs)	T_{off} (µs)	P C (g/l)
1	29.12	39.04	27.43	30.92	35.42
2	28.57	26.94	32.93	25.01	26.67
3	34.08	25.77	31.4	35.83	29.67
Delta	5.51	13.27	5.5	10.82	8.74
Rank	4	1	5	2	3

The rank is generated for the different process parameters at different levels. The minimum values of the levels are considered as the TWR follows the smaller the better concept. The obtained Optimized values for TWR are Current (l1), Powder concentration (l1), Pulse on Time(l3), Pulse off Time(l2)and IEG (l3).

The optimized parameters for ROC are

Current = 6 A
Powder Concentration = 3 g/l
T_{off} = 90 µs
T_{on} = 600 µs
IEG = 3 mm

ANOVA for Reponse Variables

ANOVA, a statistical tool, is used to identify any differences in the average performance of the set of items under test. The significant effect of process variables on the response parameters can be specified using ANOVA at a 95% confidence interval. ANOVA is calculated for all the response variables in order to know the effect of each process parameter

ISBN - 978-93-95038-50-8

on the response variable, and also to find out the contribution level of process parameters on the responses.

ANOVA for MRR, TWR & ROC

A Two way ANOVA was used for generation of the mean square value and sum of squares. F and P values are thus generated. The contribution table is also generated using ANOVA in Minitab.

Table 6: ANOVA for MRR

Source	DF	Seq SS	Contribution	Adj SS	Adj MS	F-Value	P-Value
Powder concentration (g/l)	2	0.797	0.15%	0.797	0.398	1.42	0.27
IEG (mm)	2	3.037	0.58%	3.037	1.518	5.42	0.016
Current (A)	2	480.535	91.06%	480.535	240.267	857.12	0
Pulse on Time (µs)	2	36.89	6.99%	36.89	18.445	65.8	0
Pulse off Time (µs)	2	1.941	0.37%	1.941	0.97	3.46	0.056
Error	16	4.485	0.85%	4.485	0.28		
Total	26	527.684	100.00%				

Table 7: ANOVA for TWR

Source	DF	Seq SS	Contribution	Adj SS	Adj MS	F-Value	P-Value
Powder concentration (g/l)	2	8.9767	24.16%	8.9767	4.4884	1.89	0.0183
IEG (mm)	2	0.2485	3.92%	0.24857	0.1242	0.52	0.602
Current (A)	2	10.9385	34.81%	10.9385	5.4692	1.98	0.0171
Pulse on Time (µs)	2	6.423	16.67%	6.423	3.2115	0.89	0.043
Pulse off Time (µs)	2	0.0286	0.45%	0.02867	0.0143	0.06	0.0942
Error	16	3.8011	19.98%	3.8011	0.2375		
Total	26	6.3376	100.00%				

Table 8: ANOVA for ROC

Source	DF	Seq SS	Contribution	Adj SS	Adj MS	F-Value	P-Value
IEG (mm)	2	0.000978	2.74%	0.000978	0.000489	1.08	0.364
Current (A)	2	0.013553	37.94%	0.013553	0.006777	14.94	0
Pulse on Time (µs)	2	0.003339	9.35%	0.003339	0.00167	3.68	0.048
Pulse off Time (µs)	2	0.003984	11.15%	0.003984	0.001992	4.39	0.03
Powder concentration (g/l)	2	0.006608	18.50%	0.006608	0.003304	7.29	0.006
Error	16	0.007257	20.32%	0.007257	0.000454		
Total	26	0.035719	100.00%				

If the P-value is lower than 0.05, they are considered to have a significant effect on the response variable. Thus the Percentage contribution of the process parameters on the response variables are found.

7. MULTI OBJECTIVE OPTIMIZATION

It is important for any process to follow optimal combination of process parameters to achieve desired output response by utilizing minimum possible resources. The optimal parameter setting for a single response may be detrimental for other responses at the same time. So a compromise has to be made and a multi-objective optimization has to be performed to arrive at an optimal parameter setting. Many optimization techniques have evolved over the years to optimize the parameters by solving multiple objective functions. One such technique is Grey Relational Analysis.

Grey Relational Analysis

In Grey Relational Analysis the multiple performance characteristics have been investigated with Grey Relational approach.In this approach the multiple performance characteristics can be converted into single grey relational grade. In the grey relational analysis, the grey relational grade is used to show the relationship among the sequences. If the two sequences are identical, then the value of grey relational grade is equal to 1. The grey relational grade also indicates the degree of influence that the comparability sequence could exert over the reference sequence. Therefore, if a particular comparability sequence is more important than the other comparability sequences to the reference, then the grey relational grade for that comparability sequence and reference sequence will be higher than other grey relational grades.

The steps involved in the Optimization of the process parameters using Grey Relational analysis are shown below:

- Step-1: Transformation of S/N ratio values from the original response values
- Step-2: Preprocessing of data to be performed for normalizing the raw data for analysis
- Step-3: Calculation of Grey Relational co-efficient to express the relationship between the ideal and actual normalized experimental results
- Step-4: Determination of Grey Relational grade by averaging the Grey Relational co-efficient corresponding toeach performance characteristics
- Step-5: Determination of the optimal factor and its level combination

STEP-1 Transformation of S/N ratio values from the original response values:

The S/N ratios for the response variables are already calculated and are tabulated in the table:

STEP-2: Normalizing the Raw Data

The S/N values are normalized and the values are tabulated

For Higher the better

$$Z_i = \frac{x_i - \min(x_i,\ i = 1, 2, \ldots, n)}{\max(x_i,\ i = 1, 2, \ldots, n) - \min(x_i,\ i = 1, 2, \ldots, n)}$$

For Smaller the better

$$Z_i = \frac{\max(x_i,\ i = 1, 2, \ldots, n) - x_i}{\max(x_i,\ i = 1, 2, \ldots, n) - \min(x_i,\ i = 1, 2, \ldots, n)}$$

The maximum and minimum values for MRR, TWR & ROC are taken respectively in the formulae 5.3 and 5.4 for normalization. The normalized values are tabulated in Table 5.2. The normalized S/N values ranges from 0 to 1.

DOE	Normalizing the S/N values

	MRR	TWR	ROC
1	0.1461	0.3217	0.3191
2	0.1746	0.8316	0.6075
3	0.1461	0.2597	0.3705
4	0.4877	0.3764	0.5721
5	0.5236	0.5977	0.7218
6	0.6378	0.7231	0.5721
7	0.4632	1	0.8049
8	0.5807	0.5814	0.8374
9	0.6403	0.3498	0
10	0.0247	0.3764	0.5058
11	0	0	0.8959
12	0.0247	0.2597	0.3191
13	0.8323	0.3764	0.8763
14	0.8998	0	0.9426
15	0.8713	0.7231	0.741
16	0.6067	0.5814	0.8049
17	0.804	0.7352	0.9096
18	0.8612	0.6434	0.8959
19	0.0967	0.6287	0.3705
20	0.0579	0.5814	0.552
21	0.078	0.6134	0
22	0.557	0.5977	0.6234
23	0.5807	0.5977	0.8864
24	0.573	0.5977	0.8912
25	0.8607	0.6134	1
26	0.969	0.6287	0.9348
27	1	0.6287	0.9183

Step-4: Calculation of Grey Relational Grade

$$y_i = - > \xi_i(k)$$

Where γi is the gray relational grade for the jth experiment and k is the number of performance characteristics.

The Grey Relational Grade is found out by taking the average of Response variables for the particular experiment. Average of three response variables were calculated and are shown in the Table

Table 9: Grey Relational coefficient for the Design of Experiments

ISBN - 978-93-95038-50-8

DOE	Powder concentration (g/l)	IEG (mm)	Current (A)	T_{on} (µs)	T_{off} (µs)	MRR	TWR	ROC	GRG
1	3	1	6	300	30	0.3693	0.4243	0.4234	0.4057
2	3	1	6	300	60	0.3773	0.7480	0.5603	0.5618
3	3	1	6	300	90	0.3693	0.4031	0.4427	0.4050
4	3	2	12	600	30	0.4939	0.4450	0.5388	0.4926
5	3	2	12	600	60	0.5121	0.5541	0.6425	0.5696
6	3	2	12	600	90	0.5799	0.6436	0.5388	0.5875
7	3	3	15	900	30	0.4822	1	0.7194	0.7339
8	3	3	15	900	60	0.5439	0.5443	0.7546	0.6143
9	3	3	15	900	90	0.5816	0.4347	0.3333	0.4499
10	6	2	6	900	30	0.3389	0.4450	0.5029	0.4289
11	6	2	6	900	60	0.3333	0.3333	0.8277	0.4981
12	6	2	6	900	90	0.3389	0.4031	0.4234	0.3885
13	6	3	12	300	30	0.7489	0.4450	0.8017	0.6652
14	6	3	12	300	60	0.8330	0.3333	0.8970	0.6878
15	6	3	12	300	90	0.7953	0.6436	0.6588	0.6992
16	6	1	15	600	30	0.5597	0.5443	0.7194	0.6078
17	6	1	15	600	60	0.7184	0.6538	0.8469	0.7397
18	6	1	15	600	90	0.7828	0.5837	0.8277	0.7314
19	9	3	6	600	30	0.3563	0.5738	0.4427	0.4576
20	9	3	6	600	60	0.3467	0.5443	0.5274	0.4728
21	9	3	6	600	90	0.3516	0.5640	0.3333	0.4163
22	9	1	12	900	30	0.5302	0.5541	0.5704	0.5516
23	9	1	12	900	60	0.5439	0.5541	0.8148	0.6376
24	9	1	12	900	90	0.5394	0.5541	0.8213	0.6383
25	9	2	15	300	30	0.7821	0.5640	1	0.7820
26	9	2	15	300	60	0.9416	0.5738	0.8846	0.8000
27	9	2	15	300	90	1	0.5738	0.8596	0.8111

5.1.5: Step-5: Determination of Optimum Parameters

The process parameters are now optimized using the grey relational grade. i.e. the grey relational grade is now assigned with the ranking system. The highest will be assigned as 1 and the rest follows. The Grey Relational grades are ranked as per their value and are tabulated in Table 9.

ISBN - 978-93-95038-50-8

Table 10: Ranking of Grey Relational Grade

DOE	Powder Concentration (g/l)	IEG (mm)	Current (A)	T_{on} (µs)	T_{off} (µs)	GRG	Rank
1	3	1	6	300	30	0.4056	25
2	3	1	6	300	60	0.5618	16
3	3	1	6	300	90	0.4050	26
4	3	2	12	600	30	0.4925	19
5	3	2	12	600	60	0.5695	15
6	3	2	12	600	90	0.5874	14
7	3	3	15	900	30	0.7338	5
8	3	3	15	900	60	0.6148	12
9	3	3	15	900	90	0.4498	22
10	6	2	6	900	30	0.4289	23
11	6	2	6	900	60	0.4981	18
12	6	2	6	900	90	0.3884	27
13	6	3	12	300	30	0.6651	9
14	6	3	12	300	60	0.6877	8
15	6	3	12	300	90	0.6992	7
16	6	1	15	600	30	0.6077	13
17	6	1	15	600	60	0.7396	4
18	6	1	15	600	90	0.7314	6
19	9	3	6	600	30	0.4575	21
20	9	3	6	600	60	0.4728	20
21	9	3	6	600	90	0.4163	24
22	9	1	12	900	30	0.5515	17
23	9	1	12	900	60	0.6376	11
24	9	1	12	900	90	0.6382	10
25	9	2	15	300	30	0.7820	3
26	9	2	15	300	60	0.7999	2
27	9	2	15	300	90	0.8111	1

Step-3: Calculation of Grey Relational Coefficient

$$\xi_i(k)=\frac{\Delta_{min}+\zeta\Delta_{max}}{\Delta_{0i}(k)+\zeta\Delta_{max}} \quad (5.5)$$

Where Δ is the Deviation sequence, Where Δ0i(k) is the deviation sequence of the reference sequence and compatibility sequence.ζ is distinguishing or identified coefficients. The value of ζ is the smaller and distinguished ability is the larger. ζ =0.5 is generally used.

The rank 1 represents the optimal solution for obtaining the Maximum MRR, Minimum TWR and ROC. The optimized properties thus obtained are Current at 15A, Inter Electrode Gap at 2mm, Powder concentration in dielectric at 9g/l, Pulse on time at 300µs &Pulse off time at 90µs.

ISBN - 978-93-95038-50-8

8. CONCLUSIONS

In this research , effect of machining response are Material Removal Rate, Tool Wear Rate and Radial Overcut of NIMONIC 80A with silver coated copper electrode have been investigated using EDM process by varying IEG, Powder concentration in di-electric, Current, Pulse On time and Pulse OFF time. Grey relational analysis is used in order to optimize the process parameters for the combined effects of MRR, TWR & ROC. Based on the experimental study, the following conclusions were made:

- Current is most significant parameter on Material Removal Rate (0.168 g), Tool Wear Rate (0.013 g) and Radial Over Cut (0.128 mm).
- For MRR the best process parameters are Current at 15 A, Ton at 300 µs, Powder concentration in dielectric at 6 g/l, Toff at 90 µs and IEG at 2 mm.
- The best process parameters to obtain the minimum tool wear rate are Current at 15 A, Powder concentration in dielectric at 9 g/l, Ton at 600 µs, IEG at 1 mm and Toff at 30 µs.
- The best process parameters to obtain the minimum radial overcut Current at 6 A, Powder concentration in dielectric at 3 g/l, Toff at 90 µs, Ton at 600 µs and IEG at 3 mm.
- The multi objective optimization is done using Grey Relational analysis and the obtained optimum values are Current at 15A, Inter Electrode Gap at 2mm, and Powder concentration in dielectric at 9g/l, Ton at 300µs and Toff at 90µs.

9. FUTURE SCOPE

Although the EDM machining has been thoroughly investigated for NIMONIC 80A work material, still there is a scope for future investigation. The following suggestions may prove useful for future work:

- The effect of machining parameters on recast layer thickness should be investigated.
- Study of effect of the process parameters flushing pressure and polarity etc. may also be investigated.
- Mathematical equations can be calculated in order to determine the change in MRR, TWR & ROC with respect to the change in the process parameters.

Finite element analysis can be done in order to calculate the Heat Affected zones of the required specimen with respect to the change in the parameters.

REFERENCES

1. M. Durairaj, D. Sudharsun, N. Swamynathan, Analysis of Process Parameters in Wire EDM with Stainless Steel using Single Objective Taguchi Method and Multi Objective Grey Relational Grade, International Conference On DESIGN AND MANUFACTURING, IConDM 2013,Procedia Engineering 64 (2013) 868 – 877.
2. Y. H. Guu& H. Hocheng, Effects of Work piece Rotation on Machinability during Electrical Discharge, Machining materials And Manufacturing Processes (2001) 16 (1), 91–101.
3. M Manohara, T Selvarajb, D Sivakumara, Experimental study to assess the effect of Electrode bottom profiles while machining Inconel 718 through EDM Process, Procedia Materials Science 6 (2014), 92-104.

ISBN - 978-93-95038-50-8

4. Amitesh Goswani and Jatinder kumar, “Investigation of Surface Integrity, Material Removal Rate and Wire Wear Ratio for WEDM of Nimonic 80a Alloy using GRA and Taguchi Method”, Engineering science and technology, an International Journal, 17 173-184, 2014.
5. Shantisagar Biradar, Panchal, Deepak and Gosavi, Vaibhav, “Optimization of EDM Process with Coated Electrode using GRA”, International Journal of Innovative Science, Engineering & Technology, 3:10, 323-328, 2016.
6. Ritesh Kumar Hui, “Experimental Investigation of Process Parameters and Optimization in EDM using Taguchi Method and Grey Relational Analysis”, International Journal of Engineering Research and General Science Volume 5, Issue 1, January-February, 2017.

ISBN - 978-93-95038-50-8

Mitigation of Voltage Sag and Swell in Smart Grid by using ANT-LION Intelligent Controller

D. Chandra Sekhar[1*], P.V. V Rama Rao[2] and R. Kiranmayi[3]

Department of Electrical and Electronics Engineering
[1]Research Scholar, JNTUCEA, JNTUA & Assistant Professor, Malla Reddy Engineering College, Secunderabad, Hyderabad.
[2]Professor, Maturi Venkata Subba Rao Engineering College, Hyderabad.
[3]Professor, JNTUCEA, JNTUA, Anathapuram
Email: dcsekhar@mrec.ac.in

ABSTRACT

In the operational condition of an electrical power system, the need for proper utilization with quality of utilization is primal. Where different types of quality measures are deployed such as the linear filters and adaptive filters to condition the current quality, a power flow controller is deployed to compensate for the dissipation losses or fault tolerance. Where efforts are made in enhancing power quality, efforts are also made in the utilization of it. With the rapid and ever-increasing demand for power supply and rapid increases in industrial and urbanization, the demand has exceeded the supply capacity of all generation systems. To compensate for the demanded power requirement, in addition to the existing power generation units, additional subunits are added to the power system to compensate for the demanded supply. Smart grids are designed as a cluster of various generation units and consumption units. The demanded power is processed in these smart grids and using a processing algorithm, these grids play a crucial part in adjusting the power supply allocation to compensate for it. Here, the grid systems are either designed for a concentric parameter or multi-objective monitoring in making a decision. The issue is with the complexity in the parameter validation, where multi-objective monitoring gives the benefit of accurate scheduling, the complexity in parameter monitoring is higher.

The main objective of the proposed is weight-defined parameter monitoring of power scheduling in multi-parameter monitoring, where the past approach of a preference-based scheduler is to be developed with different intelligent controller techniques like UNITED POWER FLOW CONTROLLER (UPFC) with ANT-LION optimization (ALO) algorithm is proposed and compared with ANFIS, Adaptive FLC, Reduced-order FL, FOPI, and FOFL. The PQ issue in the system is helped by the UPFC device. A shunt active power filter is used in series with an artificial neural network (ANN) with an ALO-based controller to improve UPFC performance by allaying current and voltage power quality (PQ) concerns. It proved that our proposed system is best in smart grid applications using MATLAB/Simulink.

Keywords: UPFC**,** ALO, ANFIS, Adaptive FLC, Reduced-order FL, FOPI and FOFL Smart Grid, MATLAB/ Simulink.

1. INTRODUCTION

There are no dispensing devices, nonlinear loads, or utilities employed as compensation in the electrical power system. This complicated structure guides the power system toward an unsteady energy source [1]. complicated energy systems known as "smart grids" (SGs) utilized two-way communication between distributed generation (DG), control systems, and loads to improve voltage stability, create the good utilization of RES, self-repair systems when a problem arises, and provide customers with the chance to control their electricity usage and save funds on maintenance cost [2]. Regardless of the complexity of most attacks, the Energy station represents a unique confrontational goal in the smart grid. [3].

Series and shunt compensators are combined in UPQC. Upgraded maximum frequencies, dynamic reactive and active energy control, voltage sag, voltage disbalance, voltage flicker, and voltage are all outcomes of its use [4]. Even from the end perspective, the user's PV technology has become the most enticing. Due to its dependability and simplicity, applications. However, scheme intricacies like load variations and parameter modifications

** Corresponding author: E-mail: dcsekhar@mrec.ac.in

may prevent PI/PID control from functioning normally even when it is perfectly aligned [6]. As an outcome of the power system's unsteady or disruption of synchronization, Due to a lack of dissipative torque, these vibrations become more intense. [7].

The major scheduling approach is defined as time-based operational, or demand based. In these systems, the power scheduling is operated based on the measurement of demanded power and the available generation [8-10]. Where advanced algorithms were deployed for proper decision-making, all the existing approaches were based on discrete parameter monitoring. Here, the characteristic of the demand variation is not been considered. Longer periodic observation of the demand may lead to a more accurate switching performance of the generation units.

The foremost contribution of the proposed methodology

- UPFC with ANT-LION optimization (ALO) algorithm is proposed and compared with ANFIS, Adaptive FLC, Reduced-order FL, FOPI, and FOFL to develop a weight-specified parameter tracking of power planning in multi-parametric monitoring, where the past method of priority scheduler is to be established.
- UPFC performance can be improved by easing concerns about current and voltage PQ by using an ANN with an ALO-based controller.
- To use and schedule the virtual generation plants in demand-supply, a hybrid system of virtual power units must be integrated and scheduled, from which a balance relation between generation and demand must be derived. Utilizing the MATLAB/Simulink environment, every parameter must be verified.

2. LITERATURE SURVEY

In this section, a few relevant works on intelligent controllers for smart grid performance are examined.

Rahbari, O, et.al., have offered a flexible control system that makes the smartest grids, electric cars with plugs, and renewable energy sources. This study suggests a workable solution to the issues associated with integrating renewable energies & into the electrical grid for electric vehicles, considering source generation unpredictability & uneven energy use, by using a new adaptive intelligent controller. It is suggested to use an innovative hybrid control strategy based on the optimum power flow issue and just a neuro-fuzzy adaptive inference system with particle swarm optimization resulting in a rise in the voltage's total harmonic distortion rather regularly.

Irfan, M. et.al., have proposed, Possibilities and difficulties in managing smart grids from a Pakistani perspective. This paper provides a thorough analysis of developments in smart grid control. The (ICT) methodologies are highlighted by the smart grid. Pakistan must make use of its natural resources, including wind, hydropower, and solar energy. To reduce future energy shortages, urgent action is required.

Bayindir, R. et.al., have suggested, Applications for smart grid technology. This study analysed data transmission methods, smart grid applications, and technological energy efficiency in smart grids. Scientists and engineers investigating the smart grid are expected to find this study to be a key source of direction.

Derakhshan, G. et.al., have discussed improving demand response programs in smart grids. The following four types of residential consumers were surveyed for this study, which was conducted on some residential houses in Tehran, Iran, during the summer: When payment costs for various periods are reduced, our optimization model employs the Shuffled

ISBN - 978-93-95038-50-8

Frog Leaping (SFL) algorithms & Teaching & Learning Based Optimization (TLBO)to plan smart grid utilization.

He, Y., et.al., have proposed, using an intelligent mechanism based on deep learning, the smart grid can identify fake information injection attacks in real-time. In this study, FDI assaults' behavioural characteristics are detected using deep learning methods. historical measurement data is employed, and the behavioural features are then used for real-time FDI attack identification.

Keshtkar, A. et.al, have proposed wireless sensors, smart grids, and fuzzy logic for smart home load reduction. In order to reduce the load on HVAC systems in houses, this study offers a fuzzy logic technique (FLA) that provides wireless sensors and smart grid incentives. A PCT that can handle TOU & RTP is being constructed in MATLAB/GUI to mimic a real thermostat. It functions as a "simulator engine" to assess FLA's effectiveness in various contexts. The main objective of energy systems and smart grids is the integration of household HVAC technologies in the context.

3. PROPOSED METHODOLOGY

The system's load demand increases as a result of the increased utility use brought on by urbanization and industrialization. Regarding protection and energy reliability and performance troubles, integrated approach sources are unable to satisfy the required energy needs in today's modern power grid. To resolve these issues, dispersed energy resources and RES have been utilized. The most cutting-edge technology currently in use, the RES system, can boost system steadiness and effectiveness. Among the most practical remedies for PQ problems like voltage sag, sale, and fluctuation is the FACT system. Therefore, UPFC is employed in the RES in this paper to address these power quality issues. A PV system that is linked to the smart grid makes up the suggested RES. The RES is linked to a smart grid, which results in issues with power quality due to nonlinear loads, critical loads, and unexpected loads. This results in a problem with reactive power mismatch and more voltage instability. The UPFC may be the best tool for dealing with power quality issues and enhancing voltage regulation in RES linked to the smart grid.

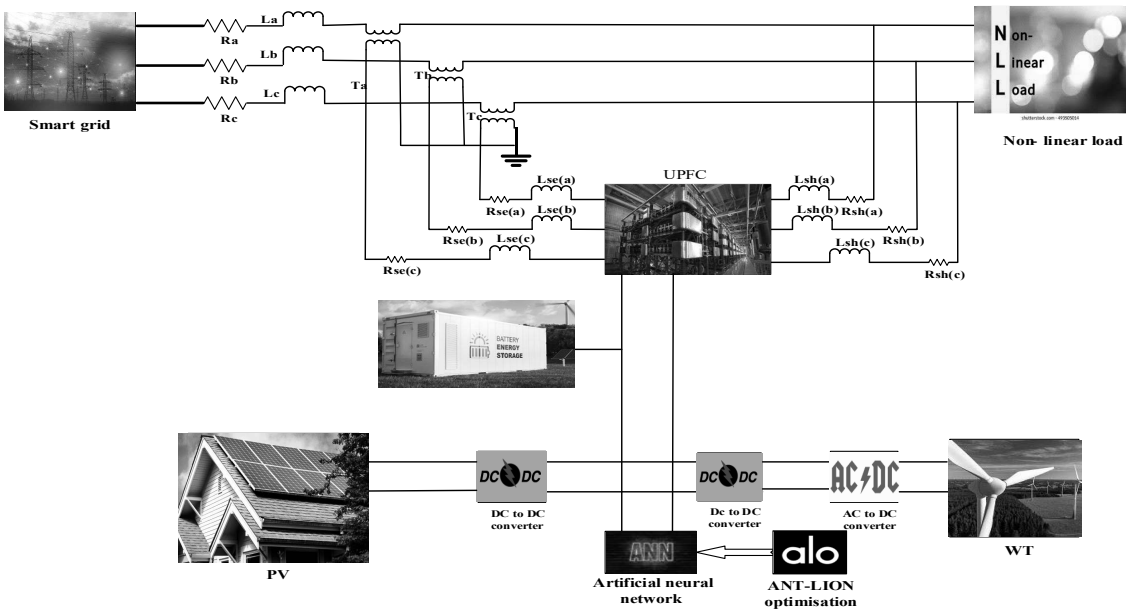

Figure 1: UPFC structure with smart grid connectivity and RES

The modeling approach is depicted in Fig. 1 and includes batteries and photovoltaics linked to a smart grid. To meet the needs of the customer, RES is used. The battery energy storage system is utilized to distribute essential electricity and store excess power generated by solar panels. Power quality issues in RES systems connected to the smart grid are the primary concern in maintaining stability and dependability conditions. To handle PQ difficulties including sag, swell, and fluctuation, a UPFC is constructed using a smart grid-connected RES system.

3.1. METHOD FOR STORING ENERGY IN BATTERIES

Systems that store energy in batteries are utilized to meet load demands when RES power supply is insufficient.

$$P^*_B = P^*_{RES}(t) + P^*_{MPPT}(t) - \frac{d\ [X(t)]}{dt} \quad (1)$$

$P^*_L(t)$ = Demand for system load,

P^*_B = Battery power.

An important battery feature known as the State of Charge (SOC) is linked to RES's inability to produce enough energy and excessive power production as shown in equation 1.

3.2. PV CELL ANALOGOUS CIRCUIT

The quantity of solar panels interconnected in a Photovoltaic system in series and parallel determines the voltage, current, open-circuit voltage & short-circuit current.

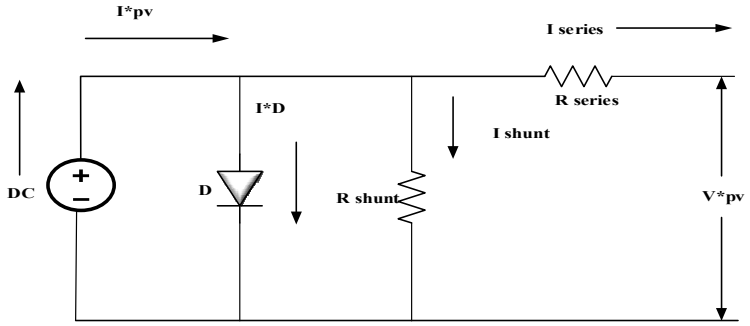

Figure 2: PV cell analogous circuit

3.2.1. DC-DC CONVERTER ANALOGOUS CIRCUIT

Figure 3 shows a circuit equivalent to a DC-DC boost converter. Switch 1 is initially closed, while switch 2 is initially in the open position. Inductor L's (I_L) current is now starting to rise from zero. The inductor current flows to the load at this point while the capacitor stores the charges, & switch-two is closed and switch one is opened. When the output voltage is stable, the ON-OFF states of switches 1 and 2 fairly represent the contingent excessive value of the output voltage current.

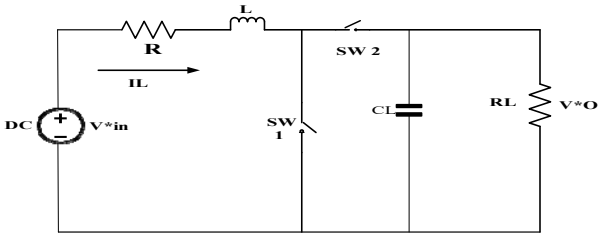

Figure 3: DC-DC converter analogous circuit

3.3 LOAD (SMART GRID, AC LOAD)

` The three-phase electric power system is the industry standard for generating, distributing, and transmitting alternating current (AC). It is a type of polyphase system, and in most cases, the most widely used way to transfer power in the world's electrical grids. It is also possible to use to power large motors and other heavy loads. Results and discussions

Case 1: Mitigation of Sag Signal

The voltage sag to be corrected in order to ensure linear and consistent system operation. By providing the necessary voltage with the help of UPFC, to meet the needs of the load, the voltage is rectified. The voltage from the source, injection voltage, and load voltage are all shown in a sag analysis in Figure 4.

ANFIS is contrasted with the modified sag signal produced by the proposed method. Signals that are already in use include Adaptive FLC, Reduced order FL, FOPI and FOFL. The suggested method corrects the sag signal in a time window of 0.15 to 0.3 seconds. Regarding sag correction, the suggested method performs better than convolutional alternatives.

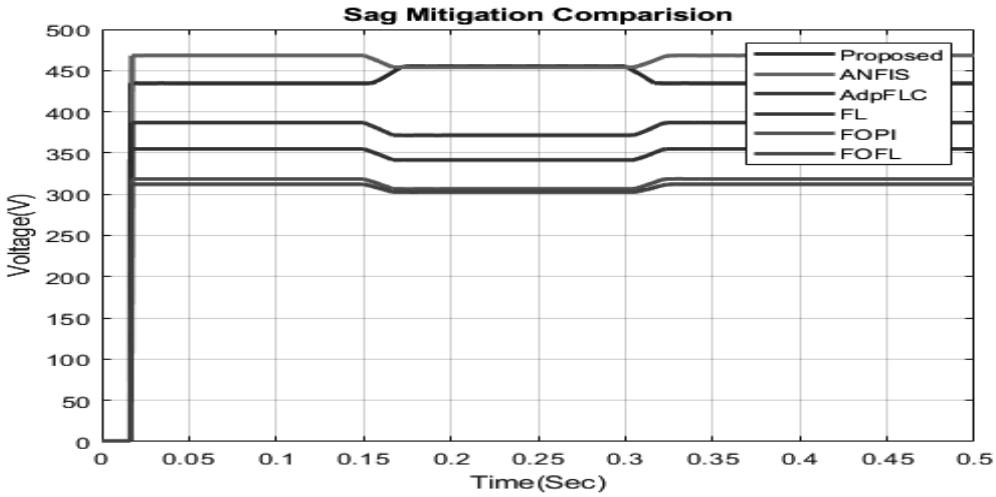

Figure 4: Comparison of sag mitigation

Case 2: Mitigation of Swell Signal

The performance of the suggested method is estimated using the swell condition. By combining the flaw with the source, the swell condition is introduced into the system. Examining the swell state, varying the sources, and rating the performances. Additionally, the injected voltage for the swell signal is compensated using the ANLINE built on the UPFC, and the compensated load voltage is ultimately reached at 440 V. The swell signal is decreased in the suggested method over a time interval of 0.15 to 0.3 sec.

In comparison to other techniques, the effectiveness of voltage swell alleviation As can be observed from this graph, the proposed method is better than ANFIS, Adaptive FLC, Reduced order FL, FOPI, and FOFL. In comparison to Reduced order FL, Adaptive FLC, and ANFIS, the swell signal is greatly diminished.

ISBN - 978-93-95038-50-8

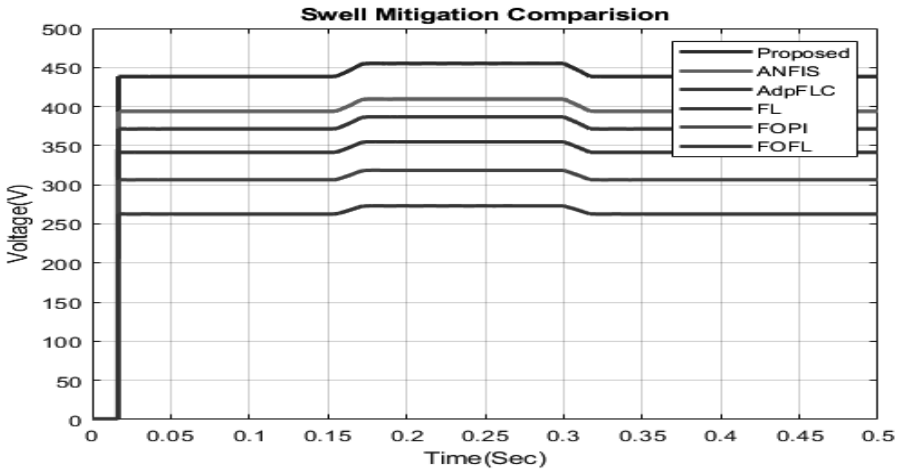

Figure 5: Comparison of Swell mitigation

6. CONCLUSIONS

This paper described the improvement of PQ carried out by the proper design of control techniques in a grid-connected RES with the load. The RES's irregularity causes PQ problems, which the ANT-LION optimization algorithm methodology attempts to address. The simulation results are used to analyze the various PQ troubles, such as voltage sag and harmonics, to show how superior the proposed work is. The proposed work's mitigation level is greater than that of the current algorithms. The percentage of THD, which is 2.07%, is also examined and contrasted with the THDs of traditional algorithms. In comparison to traditional algorithms, the suggested technique's UPFC with ANT-LION optimization algorithm is more effective.

REFERENCES

1. Ansal, V., 2020. ALO-optimized artificial neural network-controlled dynamic voltage restorer for compensation of voltage issues in the distribution system. *Soft Computing*, *24*(2), pp.1171-1184.
2. Radhika, A., Soundradevi, G. and Mohan Kumar, R., 2020. An effective compensation of power quality issues using MPPT-based cuckoo search optimization approach. *Soft Computing*, *24*(22), pp.16719-16725.
3. Gai, K., Wu, Y., Zhu, L., Xu, L. and Zhang, Y., 2019. Permissioned blockchain and edge computing empowered privacy-preserving smart grid networks. *IEEE Internet of Things Journal*, *6*(5), pp.7992-8004.
4. Nagaraju, G. and Shankar, S., 2020. Power quality improvement of wind energy conversion system with unified power quality controller: A hybrid control model. *Transactions of the Institute of Measurement and Control*, *42*(11), pp.1997-2010.
5. Kavuturu, K.V. and Narasimham, P.V.R.L., 2020. Multi-objective economic operation of modern power system considering weather variability using adaptive cuckoo search algorithm. *Journal of Electrical Systems and Information Technology*, *7*(1), pp.1-29.
6. Malik, S. and Suhag, S., 2020. A novel SSA tuned PI-TDF control scheme for mitigation of frequency excursions in a hybrid power system. *Smart Science*, *8*(4), pp.202-218.

7. Darvish Falehi, A., 2020. Optimal robust disturbance observer-based sliding mode controller using a multi-objective grasshopper optimization algorithm to enhance power system stability. *Journal of Ambient Intelligence and Humanized Computing*, *11*(11), pp.5045-5063.
8. Manuel, R. and Emayavaramban, G., 2022. PALONN: Parallel ant lion optimizer and artificial neural network for power flow control of the micro grid-connected system. *IETE Journal of Research*, *68*(2), pp.1225-1242.
9. Thumu, R., Harinadha Reddy, K. and Rami Reddy, C., 2021. Unified power flow controller in grid-connected hybrid renewable energy system for power flow control using an elitist control strategy. *Transactions of the Institute of Measurement and Control*, *43*(1), pp.228-247.
10. ElSayed, S.K. and Elattar, E.E., 2021. Slime Mold Algorithm for Optimal Reactive Power Dispatch Combining with Renewable Energy Sources. *Sustainability*, *13*(11), p.5831.

ISBN - 978-93-95038-50-8